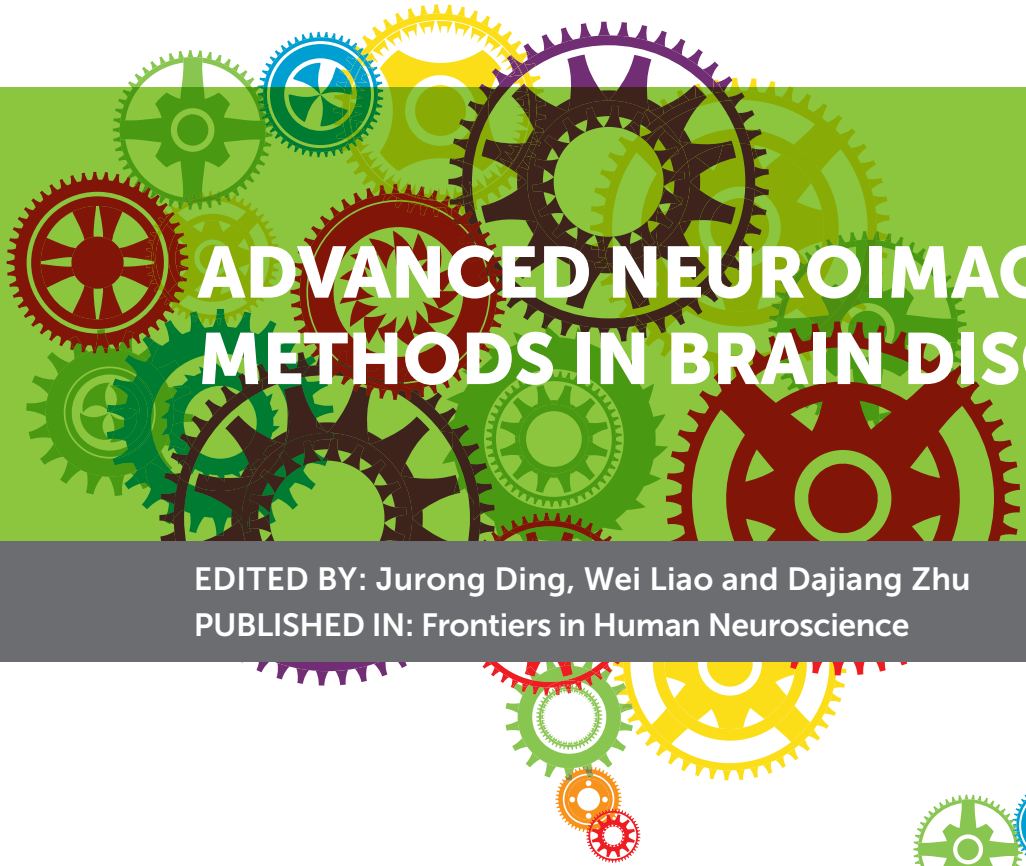

ADVANCED NEUROIMAGING METHODS IN BRAIN DISORDERS

EDITED BY: Jurong Ding, Wei Liao and Dajiang Zhu

PUBLISHED IN: Frontiers in Human Neuroscience

frontiers Research Topics

frontiers

ISSN 1664-8714
ISBN 978-2-88976-127-2
DOI 10.3389/978-2-88976-127-2

About Frontiers

Frontiers is more than just an open-access publisher of scholarly articles: it is a pioneering approach to the world of academia, radically improving the way scholarly research is managed. The grand vision of Frontiers is a world where all people have an equal opportunity to seek, share and generate knowledge. Frontiers provides immediate and permanent online open access to all its publications, but this alone is not enough to realize our grand goals.

Frontiers Journal Series

The Frontiers Journal Series is a multi-tier and interdisciplinary set of open-access, online journals, promising a paradigm shift from the current review, selection and dissemination processes in academic publishing. All Frontiers journals are driven by researchers for researchers; therefore, they constitute a service to the scholarly community. At the same time, the Frontiers Journal Series operates on a revolutionary invention, the tiered publishing system, initially addressing specific communities of scholars, and gradually climbing up to broader public understanding, thus serving the interests of the lay society, too.

Dedication to Quality

Each Frontiers article is a landmark of the highest quality, thanks to genuinely collaborative interactions between authors and review editors, who include some of the world's best academicians. Research must be certified by peers before entering a stream of knowledge that may eventually reach the public - and shape society; therefore, Frontiers only applies the most rigorous and unbiased reviews.
Frontiers revolutionizes research publishing by freely delivering the most outstanding research, evaluated with no bias from both the academic and social point of view. By applying the most advanced information technologies, Frontiers is catapulting scholarly publishing into a new generation.

What are Frontiers Research Topics?

Frontiers Research Topics are very popular trademarks of the Frontiers Journals Series: they are collections of at least ten articles, all centered on a particular subject. With their unique mix of varied contributions from Original Research to Review Articles, Frontiers Research Topics unify the most influential researchers, the latest key findings and historical advances in a hot research area! Find out more on how to host your own Frontiers Research Topic or contribute to one as an author by contacting the Frontiers Editorial Office: frontiersin.org/about/contact

ADVANCED NEUROIMAGING METHODS IN BRAIN DISORDERS

Topic Editors:
Jurong Ding, Sichuan University of Science and Engineering, China
Wei Liao, University of Electronic Science and Technology of China, China
Dajiang Zhu, University of Texas at Arlington, United States

Citation: Ding, J., Liao, W., Zhu, D., eds. (2022). Advanced Neuroimaging Methods in Brain Disorders. Lausanne: Frontiers Media SA. doi: 10.3389/978-2-88976-127-2

Table of Contents

frontiers | Frontiers in Human Neuroscience

EDITORIAL
published: 19 April 2022
doi: 10.3389/fnhum.2022.906323

Editorial: Advanced Neuroimaging Methods in Brain Disorders

Jurong Ding[1,2]*, *Wei Liao*[3,4] *and Dajiang Zhu*[5]

[1] School of Automation and Information Engineering, Sichuan University of Science and Engineering, Zigong, China, [2] Artificial Intelligence Key Laboratory of Sichuan Province, Sichuan University of Science and Engineering, Zigong, China, [3] The Clinical Hospital of Chengdu Brain Science Institute, School of Life Science and Technology, University of Electronic Science and Technology of China, Chengdu, China, [4] MOE Key Lab for Neuroinformation, High-Field Magnetic Resonance Brain Imaging Key Laboratory of Sichuan Province, University of Electronic Science and Technology of China, Chengdu, China, [5] Computer Science and Engineering, University of Texas at Arlington, Arlington, TX, United States

Keywords: neuroimaging, functional magnetic resonance imaging, brain network, machine learning, biomarkers

Editorial on the Research Topic

Advanced Neuroimaging Methods in Brain Disorders

The human brain is a large, interactive, and complex system, supporting our daily behavior and cognitive function. Researchers have been working on the mechanisms of the human brain, under healthy conditions and afflicted by different disorders for decades. Advanced neuroimaging techniques, such as magnetoencephalography (MEG), event-related potentials (ERPs), functional near-infrared spectroscopy (fNIRS), and magnetic resonance imaging (MRI), have been extensively utilized to explore the underlying principles of brain structural and functional architectures, as well as pathology alterations in various brain disorders. Especially, multi-modal neuroimaging techniques will in future provide a more comprehensive understanding of pathomechanism of brain disorders than single-modal techniques, which can be useful for early diagnosis and assessment of therapeutic effect and prognosis. In general, the development of robust neuroimaging analytical methods will fundamentally advance scientific understanding of the brain and facilitate numerous neuroscience and clinical research studies.

This Research Topic focuses on the recent developments of neuroimaging methods and their applications in various domains. In total, 19 contributions, including 16 original research articles, 2 study protocols, and one correction, were collected from internationally recognized researchers in the field.

MAGNETOENCEPHALOGRAPHY (MEG) AND EVENT-RELATED POTENTIALS (ERPS)

Using MEG recordings, Niu et al. explored the impact of antiepileptic drugs on cognition and neuromagnetic activities in children suffering from childhood epilepsy with centrotemporal spikes (CECTS). In this longitudinal study, children with CECTS after 1 year of treatment showed increased scores on cognitive assessment, as well as enhanced neural activity and functional connectivity of the default mode network (DMN). These results demonstrated that the normalization of aberrant DMN caused by antiepileptic drugs in children with CECTS likely explains the improvement of cognitive function.

OPEN ACCESS

Edited and reviewed by:
Mingzhou Ding,
University of Florida, United States

***Correspondence:**
Jurong Ding
jurongding@gmail.com

Specialty section:
This article was submitted to Brain Imaging and Stimulation, a section of the journal Frontiers in Human Neuroscience

Received: *28 March 2022*
Accepted: *31 March 2022*
Published: *19 April 2022*

Citation:
Ding J, Liao W and Zhu D (2022) Editorial: Advanced Neuroimaging Methods in Brain Disorders. Front. Hum. Neurosci. 16:906323. doi: 10.3389/fnhum.2022.906323

Event-related potential (ERPs) reflect brain activity and can be used to explore cognitive function. By using the ERPs technique, Wen et al. investigated the cognitive function and psychosocial factors between patients with major depressive disorder (MDD) with/without non-suicidal self-injury (NSSI) behavior and healthy controls. They found that patients with MDD with NSSI behavior exhibited impaired cognitive function, such as memory decline, attention and executive function deficits, and low-interference ability. The psychosocial factors contributing to NSSI behavior in adolescents with MDD were childhood abuse, lack of social support, and a sense of shame. Their findings highlight the risk factors for MDD with NSSI behavior, which can help the diagnosis and treatment of these patients.

FUNCTIONAL NEAR-INFRARED SPECTROSCOPY (FNIRS)

fNIRS, an optical neuroimaging technique, can provide quantitative hemodynamic responses to map the functional state of the brain. Zhang et al. proposed a quantitative power analysis model combining fNIRS technique and the Welch power spectrum estimation method to examine the brain functional activation of deceptive behavior. They found that spontaneous deceptive behaviors exhibited significantly higher power than controlled behavior. Meanwhile, the power existed a significant difference between the three cases (win-win, lose-win, and lose-lose conditions) for the spontaneous deceptive behavior not for the controlled behavior, suggesting that the reward system was only involved in the deception.

Using the fNIRS technique, Sun et al. evaluated narrowband resting-state functional connectivity (RSFC) at 14 frequency bands in 25 children with autism spectrum disorder (ASD) and 22 typically developing (TD) children. They reported that interhemispheric RSFC in several frequency bands was significantly decreased in ASD children. The difference in RSFC between the two groups was more pronounced in 0.01–0.02 Hz than in the other frequency bands, and the receiver operating characteristic analysis further demonstrated that 0.01–0.02 Hz RSFC showed an excellent discrimination ability between ASD and TD children, indicating that the narrowband RSFC might be a potential predictor of ASD.

MAGNETIC RESONANCE IMAGING (MRI)

Several MRI techniques, including magnetic resonance spectroscopy (MRS), susceptibility-weighted imaging (SWI), structural MRI, functional MRI (fMRI), and diffusion tensor imaging (DTI), can capture metabolic, functional, and structural changes in the brain and have caught the widespread attention of researchers. Using MRS, Sharma et al. investigated intra-subject reproducibility and repeatability of brain temperature. Their findings prove that MRS is a reliable and reproducible approach to measuring brain temperature, and may be utilized to non-invasively monitor brain temperature changes in health and disease. SWI is a useful tool for estimating iron deposition in the brain. One study used the SWI technique and machine learning methods to explore the relationship of brain iron deposition with the progression of Alzheimer's disease (AD) and found that AD progression-related regions were consistent with the regions reported from previous genetic association studies. Moreover, this study reported a new potential AD-related gene (MEF2C) (You et al.).

Using volumetric and vertex-wise shape analysis of structural MRI data, Gu et al. reported that patients with end-stage renal disease have subcortical structural atrophy, and the atrophy of the thalamus and accumbens was associated with cognitive dysfunction and sleep disorders, respectively. A structural covariance network (SCN) based on structural MRI data can characterize the synchronized topological patterns of brain regions during healthy or diseased states. To facilitate the use of SCN, Xu et al. developed a user-friendly graphical user interface software named "Brain Covariance Connectivity Toolkit" (BCCT) based on the MATLAB platform, which contained the SCN analysis, group comparison, and result-showing modules. This toolkit is convenient for researchers, especially clinical researchers, to perform brain covariance connectivity analysis.

Three resting-state fMRI (rs-fMRI) studies examined brain dysfunction in patients with different diseases. By measuring the static and dynamic amplitude of low-frequency fluctuations of rs-fMRI data in patients with chronic obstructive pulmonary disease, Lv et al. observed the altered static and dynamic brain activities in the basal ganglia and parahippocampal/hippocampal cortex in patients, as well as the relationship of these alterations with poor pulmonary function and semantic-memory impairments. Dry eye disease (DED) was investigated by combining rs-fMRI analysis methods and support vector machines in two studies. Yan et al. reported that patients with DED exhibited abnormal regional homogeneity (ReHo) values in the limbic-cortical circuits and the combination of ReHo values in the left middle cingulum and the left inferior occipital gyrus could be a neuroimaging biomarker to distinguish patients from healthy controls. In the study of Pan et al., reduced global-brain functional connectivity (FC) of the cerebello-thalamo-cortical network was found in patients with DED, and the FC values in the left thalamus can discriminate patients from controls with optimal accuracy, sensitivity, and specificity.

MULTI-MODAL NEUROIMAGING TECHNIQUES

Compared to single-modal measures, multi-modal neuroimaging analysis can provide complementary information to uncover the underlying brain mechanism. Qian et al. combined voxel-based morphometry (VBM) analysis and whole-volume psycho-physiological interactions analysis in multi-modal MRI data to assess gray matter volumes and FC alterations in individuals with betel quid dependency (BQD). Their results demonstrated that the caudate could be the structural basis of trait impulsivity and there existed abnormal frontostriatal connectivity in individuals with BQD. Combining structural and rs-fMRI techniques,

Li et al. reported common and specific functional alterations of the amygdala between MDD patients with and without anxiety, which were dependent on different amygdala subdivisions.

By combining DTI and rs-fMRI techniques, Wang et al. utilized the Dense Individualized and Common Connectivity-Based Cortical Landmarks (DICCCOL) method to evaluate fine-granularity structural and functional alterations in patients with attention deficit hyperactivity disorder (ADHD) from two independent samples. They observed four neighboring DICCCOLs near the left parietooccipital area with consistently discrepant fiber bundles and 78 consistent abnormal functional connectivities in ADHD patients across the two datasets. Their study provides a new approach for a multicenter and large sample ADHD study in the future. Using multi-modal neuroimaging data, Hu et al. examined gray matter volumes, seed-based FC, and DTI metrics (i.e., fractional anisotropy, axial, mean, and radial diffusivities) in patients with Wilson's disease. Their results revealed that aberrant white matter tracks in association fibers may account for prospective memory impairment, and gray matter volume changes in the association cortex have an indirect impact on global cognitive function by its abnormal FC in patients.

Pietrosanu et al. proposed a sparse group lasso method for multiple imaging modalities analysis to increase interpretability, generalizability, and stability and proved the advantage of their approach over independent sparse and joint sparse models in both simulation and neuroimaging results. Their study provides a stable and interpretable multi-modal imaging analysis framework for detecting brain structural changes in disease. In addition, two research teams shared their study protocol. Walker et al. described their study protocol for the Teen Inflammation Glutamate Emotion Research (TIGER) project, which will collect clinical, behavioral, and multi-modal imaging data to evaluate the associations among inflammation, glutamate levels, and neurodevelopmental trajectories in adolescents with depression. In a recent study protocol, Hu et al. reported the procedures for a prospective, multicenter, longitudinal cohort study, which aimed to establish an individual-based model for the prediction of communication impairment in children with bilateral cerebral palsy and periventricular white matter lesions at school entry by using machine learning algorithms and multi-modal MRI data acquired at an early age.

To summarize, the series of research articles and study protocols absorbed by this Research Topic shows the recent exciting achievements of advanced neuroimaging techniques and applications. We hope that these works will enrich our understanding of physiological and pathological mechanisms of the human brain from a neuroimaging perspective, and will further prompt the development of new imaging analytical methods and their application in more disease types.

AUTHOR CONTRIBUTIONS

All authors listed have made a substantial, direct, and intellectual contribution to the work and approved it for publication.

FUNDING

Grants from the Scientific Research Foundation of Sichuan University of Science and Engineering (2020RC31) supported JD.

Conflict of Interest: The authors declare that the research was conducted in the absence of any commercial or financial relationships that could be construed as a potential conflict of interest.

frontiers in Human Neuroscience

ORIGINAL RESEARCH
published: 25 September 2020
doi: 10.3389/fnhum.2020.572693

Reduced Global-Brain Functional Connectivity of the Cerebello-Thalamo-Cortical Network in Patients With Dry Eye Disease

Pan Pan[1], Shubao Wei[2], Yangpan Ou[1], Feng Liu[3], Huabing Li[4], Wenyan Jiang[2], Wenmei Li[5], Yiwu Lei[5], Wenbin Guo[1,6] and Shuguang Luo[2]**

[1] National Clinical Research Center for Mental Disorders, and Department of Psychiatry, The Second Xiangya Hospital of Central South University, Changsha, China, [2] Department of Neurology, The First Affiliated Hospital of Guangxi Medical University, Nanning, China, [3] Department of Radiology, Tianjin Medical University General Hospital, Tianjin, China, [4] Department of Radiology, The Second Xiangya Hospital of Central South University, Changsha, China, [5] Department of Radiology, The First Affiliated Hospital of Guangxi Medical University, Nanning, China, [6] The Third People's Hospital of Foshan, Foshan, China

OPEN ACCESS

Edited by:
Dajiang Zhu,
University of Texas at Arlington, United States

Reviewed by:
Lu Zhang,
University of Texas at Arlington, United States
Xi Jiang,
University of Electronic Science and Technology of China, China
Shijie Zhao,
Northwestern Polytechnical University, China

***Correspondence:**
Wenbin Guo
guowenbin76@csu.edu.cn
Shuguang Luo
robert58243@sohu.com

Specialty section:
This article was submitted to Brain Imaging and Stimulation, a section of the journal Frontiers in Human Neuroscience

Received: *15 June 2020*
Accepted: *24 August 2020*
Published: *25 September 2020*

Citation:
Pan P, Wei S, Ou Y, Liu F, Li H, Jiang W, Li W, Lei Y, Guo W and Luo S (2020) Reduced Global-Brain Functional Connectivity of the Cerebello-Thalamo-Cortical Network in Patients With Dry Eye Disease. Front. Hum. Neurosci. 14:572693. doi: 10.3389/fnhum.2020.572693

Background: The pathophysiology of patients with dry eye disease (DED) is associated with abnormal functional connectivity (FC). The present study aims to probe alterations of voxel-wise brain-wide FC in patient with DED at rest in an unbiased way.

Method: A total of 20 patients with DED and 23 controls matched by age, sex, and years of education underwent resting-state functional magnetic resonance imaging scans. Global-brain FC (GFC) was adopted to analyze the images. Support vector machine (SVM) was utilized to differentiate the patients from the controls.

Results: Compared with the controls, patients with DED exhibited decreased GFC in the right cerebellum lobule VIII/inferior semi-lunar lobule and left thalamus that belonged to the cerebello-thalamo-cortical network. The GFC values in the left thalamus were positively correlated to the illness duration ($r = 0.589$, $p = 0.006$) in the patients. Decreased GFC values in the left thalamus could be used to discriminate the patients from the controls with optimal accuracy, sensitivity and specificity (88.37, 85.00, and 91.30%).

Conclusions: Our findings indicate that decreased GFC in the brain regions associated with cerebello-thalamo-cortical network may provide a new insight for understanding the pathological changes of FC in DED. GFC values in the left thalamus may be utilized as a potential biomarker to identify the patients from the controls.

Keywords: dry eye disease, global-brain functional connectivity, network, functional magnetic resonance imaging, support vector machine

INTRODUCTION

The surface of the eyes is covered with a layer of tears. A stable tear film provides a comfortable environment to the eyes and serves as a good refractive media of the ocular surface (cornea, conjunctiva, accessory lacrimal gland and meibomian gland). Lack of tear membrane components will break the stability of the tear film resulting in ocular surface drying and the conjunctive

epithelium damaged by dehydration, known as dry eye syndrome (DED) (Pflugfelder et al., 1999, 2018; Brewitt and Sistani, 2001). DED, one of the most common ocular surface diseases, caused by a variety of factors, is characterized by the absence of mucous components in tears, abnormal distribution of tears on the ocular surface, and increased evaporation of tears (Tabbara and Sharara, 1998). The main clinical manifestations of DED include painful ocular symptoms often described as "burning and painful" (Lemp, 2007; Kalangara et al., 2017; Galor et al., 2018), visual impairment and unstable tear film with potential ocular surface damage, accompanied by increased tear osmotic pressure and ocular surface inflammation (Lemp, 2007). The aggravation of symptoms will lead to a range of serious eye disease including corneal abrasion, filamentous keratitis, and corneal ulcers eventually leading to nubecula and vision loss. However, the pathophysiology of DED remains unclear at present.

In recent years, "neurosensory abnormalities" have been added to the definition of DED (Craig et al., 2017). A growing literature suggested that dry eye symptoms in patients with DED should be better conceptualized as neuropathic eye pain, a manifestation of a central pain processing disorder (Galor et al., 2015; Kalangara et al., 2017; Levitt et al., 2017). Changes in surface microenvironment have taken place to control the secretion of ocular surface glands and blink activity through the ocular sensory pathway. Persistent changes will lead to ocular surface dyskinesia and neuropathic pain caused by functional dysfunction (Belmonte et al., 2017). Dysfunction is a medical condition that normal function of the body is impaired by autonomic dysfunction caused by cortical dysfunction (Liang et al., 2019). Previous studies showed that the occurrence of ocular surface pain is associated with tears deficiency, and repeated ocular sensory nerve injury is involved in the persistence of pain leading to transition from acute pain to chronic pain (Kalangara et al., 2017; Levitt et al., 2017). Sustained structural and functional changes in ocular sensory pathway could cause neuropathic pain and hypotonia of the ocular surface in patients with DED (Belmonte et al., 2017). Functional magnetic resonance imaging (fMRI) has been gradually applied in the clinical researches of DED. Research suggests that chronic peripheral nerve damage will lead to pathological neuroplasticity in the central nervous system (CNS) resulting in reduced nociceptor excitatory thresholds (Levitt et al., 2017). Previous researches showed that patients with DED had extensive alterations in brain function, and abnormal brain function played an important role in the maintenance and development of dry eye symptoms (Rahman et al., 2015; Levitt et al., 2017). fMRI has been used to explore abnormal functional activity in eye diseases such as glaucoma, amblyopia and corneal ulcers (Lin et al., 2012; Li et al., 2014; Rahman et al., 2015; Chen et al., 2017; Wang et al., 2017; Xu et al., 2019). However, it remains unclear whether patients with DED have abnormal GFC in certain brain regions.

To further clarify the pathophysiology of DED, a voxel-wise global-brain functional connectivity (GFC) approach was used to investigate the differences of functional organization between patients with DED and healthy controls. GFC is helpful to obtain voxel-wise whole-brain functional connectivity (FC) in an unbiased way (Li et al., 2016; Cui et al., 2018). Previous researches have demonstrated that GFC is a powerful and replicable data-driven analysis capable of identifying major intrinsic networks (Cole et al., 2009; Murrough et al., 2016). GFC provides an approach to measure the connectivity of all voxels in the brain relative to all other voxels by using a metric that does not require prior selection of seeds or networks (Meier et al., 2016; Zhurakovskaya et al., 2016; Cui et al., 2018; Pan et al., 2019a). Several researches of brain mechanisms have focused on the functional connectivity (FC) between preselected brain regions by using a region of interest (ROI) method (Pires et al., 2012; Meijer and Goraj, 2014; Giorgio and De Stefano, 2016; Lee et al., 2018). This approach is insufficient although the results from ROI are informative. Different ROI selection may yield different results due to potentially biased results based on preselected ROIs. In addition, it may not cover important brain regions associated with the core pathological changes in DED. By contrast, the novel aspect of the present study is that FC abnormalities in patients with DED were examined in a voxel-wise brain-wide way. GFC was considered as a suitable method to examine the differences in a large-scale functional organization in the brain for providing an unbiased way to measure brain function. Therefore, the purpose of the GFC method adopted in the study was to observe the mechanism of brain from the perspective of FC alterations across the whole brain. The potential FC alterations in patients with DED may be detected by this method. Finally, we used the receiver operating characteristic curve (ROC) and support vector machine (SVM) methods to investigate whether abnormal GFC in relevant brain areas could be considered as potential image biomarkers to discriminate patients from controls with good sensitivity and specificity.

MATERIALS AND METHODS

Subjects

A total of 20 right-handed patients with DED were recruited from the Frist Affiliated Hospital of Guangxi Medical University. DED was diagnosed according to DED diagnostic guidelines published by the Dry Eye Workshop in 2007 (Lemp, 2007). A total of 23 right-handed healthy controls without symptoms of neurological and ophthalmic disease were recruited from the local community at the same time. All participants aged from 18 to 65 years old. Most symptoms did not differ across different ages. However, burning sensation was common in patients aged 18∼45 years old, whereas photophobia was common in patients aged 46∼65 years old (Gao et al., 2011). Healthy controls were group-matched with the patients in terms of age, sex ratio, and years of education.

The exclusion criteria for patients with DED were as follows: (1) any history of connective tissue disease, such as rheumatoid arthritis and systemic lupus erythematosus; (2) any history hypertensive encephalopathy, metabolic encephalopathy, and lesions of the CNS caused by infection or other reasons. Healthy controls shared the following exclusion criteria: (1) any history of severe neurological diseases or ophthalmic diseases; (2) any history of serious surgery of internal medicine diseases; and (3) any family history of serious neuropsychiatric disorders or ophthalmic diseases in their first-degree relatives. The

participants who did not meet the standard for MRI or showed alterations under conventional MRI scans were also excluded.

The study was approved by the Local Ethics Committee of the First Affiliated Hospital of Guangxi Medical University. All procedures performed in the studies involving human participants were in accordance with the ethical standards of the institutional or national research committee and with the 1964 Helsinki declaration and its later amendments or comparable ethical standards. All participants were provided with a written informed consent before the experiment.

MRI Parameters

MRI images were captured by a Siemens 3.0T scanner. All participants were required to remain motionless and awake with their eyes closed. Participants were given soft earplugs and foam pads to reduce scanning noise and head motion. Resting-state functional images of slice-order type were obtained by an ascend type using the following parameters: repetition time/echo time = 2,000 ms/30 ms, inversion time = 900 ms, 30 slices, 64 × 64 matrix, 90° flip angle, 240 mm field of view, 4 mm slice thickness, 0.4 mm gap, and 250 volumes lasting for 500 s. After the scan, participants were asked some questions to confirm the wakefulness during the scan. For example, whether the participant fell asleep or the sound frequency of the machine changed during the scanning.

fMRI Data Analysis

Functional images were preprocessed automatically by using the DPABI software (Yan et al., 2016). Because there was time for participants to adapt to the scan environment, the first 10 volumes were removed to ensure a steady-state condition. We excluded the participants whose head movement was more than 2 mm of translation or 2° of rotation in any directions. The time series of fMRI were first corrected for within-scan acquisition time difference between slices and head motion. All realigned images were spatially normalized to the Montreal Neurological Institute (MNI) EPI space in SPM8 and resampled to 3 × 3 × 3 mm^3 (Liu et al., 2015). After normalization, the images were smoothed with 4 mm full width on the half maximum Gaussian kernel. Due to the limitation of imaging methods, the lesions of fMRI images were often hid in noise signals which might cause missed diagnosis and even misdiagnosis. The features of the lesion site would be more obvious after proper noise reduction pretreatment. The most common method of noise reduction is smooth. The smooth method is also used in previous studies on ophthalmic diseases (Chen et al., 2017; Wang et al., 2017; Xu et al., 2019). The time series were further linearly detrended and temporally band-pass filtered (0.01–0.08 Hz). Finally, several covariates were removed including Friston-24 head motion parameters obtained by rigid body correction, signal from white-matter centered region, and signal from cerebrospinal fluid. As described in a previous study, the global signal was not removed (Hahamy et al., 2014). The frame displacement (FD) value of each subject was calculated based on a previous study (Power et al., 2012). Scrubbing that removing time point with FD > 0.2 mm was used to control the effect of head motion.

GFC Analysis

The GFC method used in the study is similar to that used in our previous studies (Cui et al., 2018, 2020; Ding et al., 2019; Pan et al., 2019a,b; Li et al., 2020). GFC is a measure of functional connectivity of all voxels in the brain with respect to other voxels. For each participant, we calculated the average values of correlations between each voxel's time series and every other voxel in the gray matter of the whole brain in MATLAB, which was defined as GFC of this voxel. The threshold setting classified voxel with probability of >0.2 as gray matter, and the gray matter mask would be produced by the gray matter probability map in SPM8 (Liu et al., 2015). The GFC evaluation was defined as,

$$\mathrm{GFC} = \sum_{b=1}^{n} \frac{r(T_a, T_b)}{n-1}$$

The process of GFC involves calculating the Pearson correlation coefficients (r) between a given voxel's time series and all other voxels' time series, converting all correlations into Fisher z-scores matrix (Wang et al., 2015; Cui et al., 2018; Pan et al., 2019a,b; Li et al., 2020). The process generates a map for each participant, where each voxel value represents the average connectivity of the voxel with the rest of the brain. The GFC maps were generated by combining GFC of all voxels.

Two-sample *t*-tests were conducted on the GFC maps between patients with DED and healthy controls. The mean FD and age were used as covariates of no interest. The significance level was set as $p < 0.05$ by using the family wise error (FWE) correction method.

Correlation Analysis

Mean *z* values of the brain clusters with abnormal GFC were extracted. Pearson correlation analyses were performed to explore the relationship between abnormal GFC values and illness duration in the DED group after the normality of the data being checked. In the present study, we tested the independent hypotheses on the same data at the significance level of $p < 0.05$ through an approach of Bonferroni which was the strictest multiple test correction method.

TABLE 1 | Characteristics of the participants.

	Patients ($n = 20$)	Controls ($n = 23$)	*p*-value
Sex (male/female)	7/13	4/19	0.19[a]
Age (years)	52.55 ± 8.66	49.69 ± 6.51	0.23[b]
Education (years)	10.20 ± 3.56	8.61 ± 2.27	0.08[b]
FD (mm)	0.31 ± 0.20	0.39 ± 0.26	0.23[b]
Illness duration (months)	20.75 ± 15.37		

[a] *The p-value for sex distribution was obtained by a chi-square test.*
[b] *The p-values were obtained by independent-samples t-tests.*
FD, Framewise displacement.

Classification Analysis by Using SVM

As a good tool of classification especially suitable for the case of small samples (Vapnik, 1995), SVM was utilized to examine whether abnormal GFC values in brain areas could be applied to distinguish patients from controls (Chih-Chung and Chih-Jen, 2011) using the LIBSVM software package in the MATLAB. The type of kernel was the default Gaussian kernel in the LIBSVM. The classification performance of the unobserved data was evaluated by dividing the sample set into a training set and a test set. A random SVM cluster was constructed for classification and feature selection based on the brain fMRI data of the subjects. The LIBSVM adopted a "leave-one-out" method that was cross-validated to optimize parameters and obtain satisfactory sensitivity and specificity (Liu et al., 2015; Yan et al., 2016).

The receiver operating characteristic curve (ROC) analysis was used to validate the SVM results, once significant differences in GFC values were observed between the patients and the controls.

RESULTS

Characteristics of the Subjects

The sample of the present study included 20 patients with DED and 23 healthy controls. Continuous variables including age, years of education and FD were analyzed with two-sample *t*-tests. A Chi-squared test was utilized for sex distribution. Compared with the control group, age ($p = 0.23$), sex ration ($p = 0.19$), FD ($p = 0.23$), and years of education ($p = 0.08$) of the patient group were not statistically significant. The detailed information of demographic and clinical characteristics of the participants were showed in **Table 1**.

Group Differences in GFC

Compared with the controls, patients with DED exhibited decreased GFC in the right cerebellum lobule VIII/inferior semi-lunar lobule and left thalamus (**Figure 1** and **Table 2**). No brain region exhibited increased GFC in the patients relative to the controls.

Correlations Between GFC and Clinical Variable

As shown in **Figure 2**, a positive correlation was observed between GFC values in the left thalamus and illness duration in the patients ($r = 0.589$, $p = 0.006$).

Distinguishing Patients With DED From Controls

SVM analysis was utilized to determine whether abnormal GFC of these brain regions could distinguish patients with DED from healthy controls. Decreased GFC in the left thalamus exhibited the highest accuracy (88.37%), sensitivity (85.00%) and specificity

TABLE 2 | Regions with decreased GFC in the patients.

Cluster location	Peak (MNI)			Number of voxels	*T* value[a]
	x	y	z		
Right cerebellum lobule VIII/inferior semi-lunar lobule	24	−60	−48	32	−4.3311
Left thalamus	−18	−21	9	67	−4.1686

GFC, global-brain functional connectivity; MNI, Montreal Neurological Institute.
[a]*A negative T value represents decreased GFC in the patients relative to the controls.*

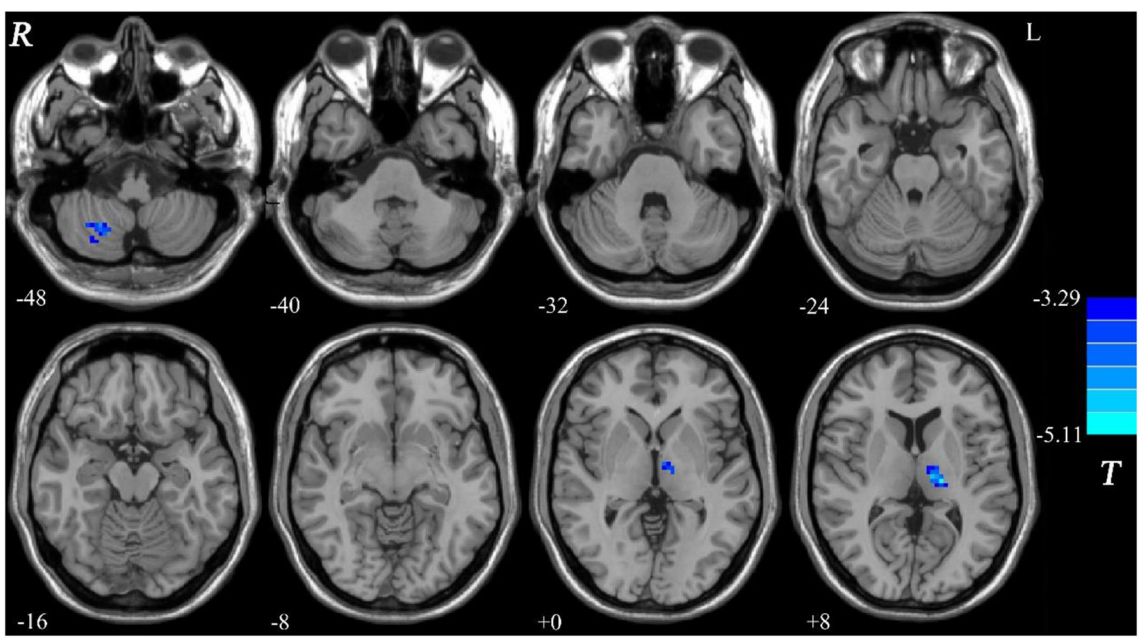

FIGURE 1 | Decreased GFC in patients with DED relative to healthy controls. GFC, global-brain functional connectivity; DED, dry eye disease.

(91.30%) that could be applied to identify the patients from the controls (**Figure 3**). As shown in **Figure 3** and **Table 3**, the accuracy of another brain region was unsatisfactory.

The SVM results were further validated by the ROC method. The results exhibited that the GFC values in the left thalamus could be applied to identify patients from controls with optimal specificity (95.00%) and sensitivity (78.26%) (**Figure 4** and **Table 4**).

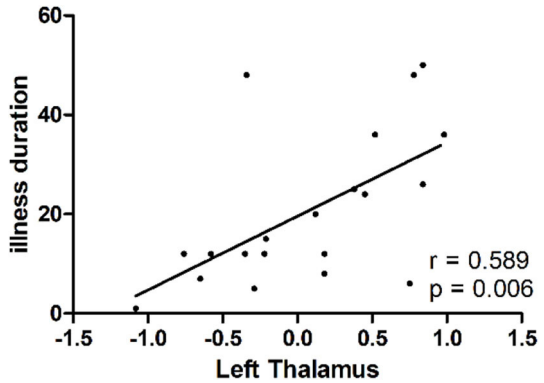

FIGURE 2 | A positive correlation ($r = 0.589$, $p = 0.006$) between GFC values in the left thalamus and illness duration in patients with dry eye disease. GFC, global-brain functional connectivity.

TABLE 3 | Differentiate the patients from the controls by GFC values in each brain region with the SVM method.

Brain regions	Accuracy	Sensitivity	Specificity
Right cerebellum lobule VIII/inferior semi-lunar lobule	76.74% (33/43)	75.00% (15/20)	78.26% (18/23)
Left thalamus	88.37% (38/43)	85.00% (17/20)	91.30% (21/23)

GFC, global-brain functional connectivity; SVM, support vector machines.

DISCUSSION

Compared with healthy controls, patients with DED exhibited significantly decreased GFC values in the cerebello-thalamo-cortical network including the thalamus and cerebellar lobule. Furthermore, GFC values in the left thalamus were positivity correlated with illness duration in the patients. GFC values in the left thalamus could correctly distinguish patients from healthy controls with optimal accuracy, sensitivity, and specificity.

Previous animal neurophysiological studies (Optican and Robinson, 1981; Barash et al., 1999) and human neurotrauma psychology studies (Waespe and Baumgartner, 1992; Panouillères et al., 2013) provided clear evidence that the cerebellum acted as an important role in the saccade adaptation. Alteration in the cerebellum lobule activity was associated with saccade adaptation (Guillaume et al., 2018). Spontaneous nystagmus might affect visual function in patients with unilateral cerebellar lobules and inferior semi-lunar lobule injury (Lee and Kim, 2020). The cerebellar lobule plays an important role in different coding of visual spatial cognition and visual working memory. The cerebellum lobule VIII was the most significantly activated area during above process (Sobczak-Edmans et al., 2016). A previous study observed functional separation between spatial coding and visual working memory processing in the cerebellum lobule (Brissenden et al., 2018). To sum up, cerebellum lobule may participate in the formation of visual working memory. The occurrence of visual impairment in patient with DED may be related to decreased GFC in the right cerebellum lobule VIII/inferior semi-lunar lobule.

The thalamus, located bilaterally around the third ventricle, is the largest elliptic gray matter mixed nucleus mass in the diencephalon. The main function of the thalamus as

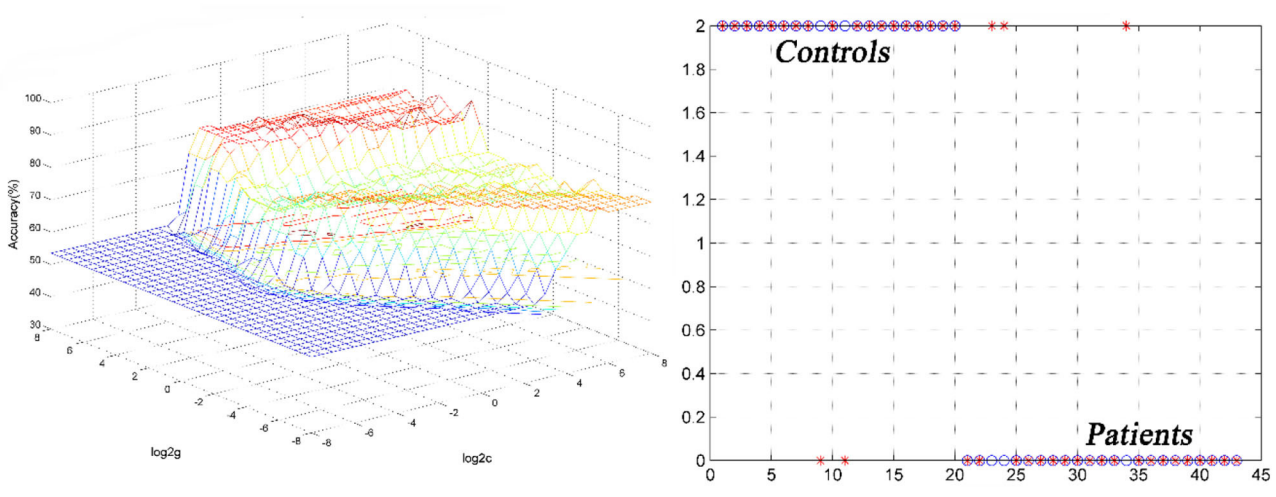

FIGURE 3 | 3D view of classified accuracy with best parameters using the GFC values in the left thalamus to differentiate the patients from the controls. The result was obtained in the LIBSVM using a "leave-one-out" approach with default Gaussian kernel. GFC, global-brain functional connectivity.

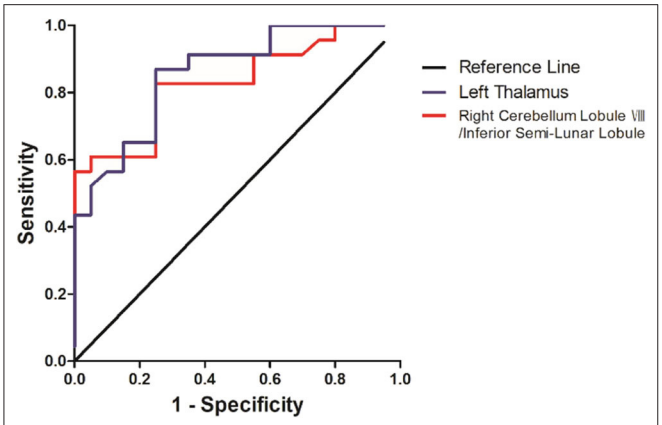

FIGURE 4 | Differentiating the patients from the controls with the receiver operating characteristic curve method by using the GFC values in the left thalamus and right cerebellum lobule VIII/inferior semi-lunar.

TABLE 4 | ROC analyses for differentiating the patients from the controls by using the GFC values.

Brain regions	Area under the curve	Cut-off point	Sensitivity	Specificity
Left thalamus	0.859	−0.3377	95.00% (19/20)	78.26% (18/23)
Right cerebellum lobule VIII/inferior semi-lunar lobule	0.830	0.0586	90.00% (18/20)	56.52% (13/23)

ROC, receiver operating characteristic curve; GFC, global-brain functional connectivity.

a relay station for the cerebral cortex to transmit damage information is to synthesize and distribute the sensory to different brain areas (Ab Aziz and Ahmad, 2006; Yen and Lu, 2013). Previous studies showed that the thalamus plays an important role in acute or chronic aching, anesthesia, and analgesia. The thalamus was often activated in fMRI experiments with pain (Heinke and Schwarzbauer, 2002; Martuzzi et al., 2010; Mhuircheartaigh et al., 2010). The descending inhibitory system composed of the thalamus and dorsal root ganglion transmitted aching information to the sensory cortex, and responded to aching during the transmission process and then gave feedback to external traumatic stimuli (Ab Aziz and Ahmad, 2006). Significantly decreased GFC in the left thalamus was observed in patients with DED in this study. Decreased GFC in the thalamus might lead to repeated nerve injury, which changed the stress activated state into the continuously activate state, and then made the pain threshold from enhancement to reduced feedback during the transformation of ocular pain from acute phase to persistent pain in patient with DED. Decreased GFC in the thalamus may be one cause of persistent eye aching in patients with DED. Notably, decreased GFC in the left thalamus was positivity correlated with illness duration in the patients. Abnormal GFC in the left thalamus may be affected the duration of the disease in patients with DED and provides theoretical basis for the pathophysiological of course of the disease in DED.

Specific interconnections exist widely between the thalamus and the cerebral cortex. The thalamic nuclei were connected with the corresponding cerebral cortex to form the thalamus-sensory projection system through these connections, and received and transmitted sensory information in this way (Klingner et al., 2013; Cheng et al., 2015; Penner et al., 2016). The cerebello-thalamo-cortical network was a complete functional network that could carry out visual information and pain information transmission, processing and response in both internal and external of the visual brain region. GFC alteration in the cerebello-thalamo-cortical network may be associated with visual impairment and persistent pain symptoms in patients with DED.

Abnormal GFC values might be utilized as potential biomarkers to identify patients from healthy controls. SVM analyses were conducted to determine whether the GFC values in the right cerebellum lobule VIII/inferior semi-lunar lobule and left thalamus could differentiate the patients from the controls with good sensitivities, specificities, and accuracies. Sensitivity or specificity higher than 0.75 indicated that decreased GFC in the left thalamus to go an accurate indicators (Gong et al., 2011). However, specificity < 0.6 for decreased GFC in right cerebellum lobule VIII/inferior semi-lunar lobule seems to be an indicator with poor accuracy. The accuracy, sensitivity and specificity of GFC values in the left thalamus were more than 0.8 (**Table 3**), which were optimal for the established diagnostic indicators (Swets, 1988). The ROC results were used to validate the SVM results, which showed that the area under the curve of the left thalamus was more than 0.7, an acceptable accuracy for established diagnostic indicators. Hence, we suggested that decreased GFC in the left thalamus could serve as a potential biomarker to discriminate the patients with DED from the controls.

Several limitations should be considered in the present study. First, the data size is small, the methods and results need to be validated on a larger data set. Second, clinical characteristics such as the data on age of onset were collected retrospectively which might have limited the accuracy of the information. Further assessment of other non-sensory manifestation could be used to provide a comprehensive explanation in patients with DED. Finally, the MNI template used in the study came from a Caucasian population which might bias the present findings from Chinese subjects.

CONCLUSION

Despite the limitation, the present study indicates that decreased GFC exists in brain regions of the cerebello-thalamo-cortical network in patients with DED. Decreased GFC values in the left thalamus may be utilized as a potential biomarker to differentiate the patients from the controls. Thus, this study provides new insights into the pathological changes of GFC in DED.

DATA AVAILABILITY STATEMENT

All datasets generated for this study are included in the article/supplementary material.

ETHICS STATEMENT

The studies involving human participants were reviewed and approved by Local Ethics Committee of the First Affiliated Hospital of Guangxi Medical University. The patients/participants provided their written informed consent to participate in this study.

AUTHOR CONTRIBUTIONS

WG and SL provided the conception of the work. SW, PP, YO, and WJ collected the data. FL, HL, WL, and YL were responsible for data analysis and interpretation. The manuscript was drafted by PP and critically revised by WG. All authors have given approval to final version of the manuscript. The manuscript was written through contributions of all authors.

FUNDING

This study was supported by grants from the National Key R&D Program of China (2016YFC1307100), the National Natural Science Foundation of China (Grant No. 81771447), and the Guangxi Appropriate Technology for Medical and Health Research and Development Project (Grant No. S201415-05).

ACKNOWLEDGMENTS

The authors thank all individuals with served as the research participants.

REFERENCES

Ab Aziz, C. B., and Ahmad, A. H. (2006). The role of the thalamus in modulating pain. *Malays. J. Med. Sci.* 13, 11–18.

Barash, S., Melikyan, A., Sivakov, A., Zhang, M., Glickstein, M., and Thier, P. (1999). Saccadic dysmetria and adaptation after lesions of the cerebellar cortex. *J. Neurosci.* 19, 10931–10939. doi: 10.1523/JNEUROSCI.19-24-10931.1999

Belmonte, C., Nichols, J., Cox, S., Brock, J., Begley, C., Bereiter, D., et al. (2017). TFOS DEWS II pain and sensation report. *Ocul. Surf.* 15, 404–437. doi: 10.1016/j.jtos.2017.05.002

Brewitt, H., and Sistani, F. (2001). Dry eye disease: the scale of the problem. *Surv. Ophthalmol.* 45(Suppl. 2), S199–202. doi: 10.1016/S0039-6257(00)00202-2

Brissenden, J. A., Tobyne, S. M., Osher, D. E., Levin, E. J., Halko, M. A., and Somers, D. C. (2018). Topographic cortico-cerebellar networks revealed by visual attention and working memory. *Curr. Biol.* 28, 3364–3372.e65. doi: 10.1016/j.cub.2018.08.059

Chen, W., Zhang, L., Xu, Y., Zhu, K., and Luo, M. (2017). Primary angle-closure glaucomas disturb regional spontaneous brain activity in the visual pathway: an fMRI study. *Neuropsychiatr. Dis. Treat* 13, 1409–1417. doi: 10.2147/NDT.S134258

Cheng, W., Palaniyappan, L., Li, M., Kendrick, K., Zhang, J., Luo, Q., et al. (2015). Voxel-Based, brain-wide association study of aberrant functional connectivity in schizophrenia implicates thalamocortical circuitry. *NPJ Schizophr.* 1:15016. doi: 10.1038/npjschz.2015.16

Chih-Chung, C., and Chih-Jen, L. (2011). Libsvm: a library for support vector machines. *ACM Trans. Intell. Syst. Technol.* 2:27. doi: 10.1145/1961189.1961199

Cole, M., Pathak, S., and Schneider, W. (2009). Identifying the brain's most globally connected regions. *NeuroImage* 49, 3132–3148. doi: 10.1016/j.neuroimage.2009.11.001

Craig, J. P., Nichols, K. K., Akpek, E. K., Caffery, B., Dua, H. S., Joo, C. K., et al. (2017). TFOS DEWS II definition and classification report. *Ocul. Surf.* 15, 276–283. doi: 10.1016/j.jtos.2017.05.008

Cui, G., Ou, Y., Chen, Y., Lv, D., Jia, C., Zhong, Z., et al. (2020). Altered global brain functional connectivity in drug-naive patients with obsessive-compulsive disorder. *Front. Psychiatr.* 11:98. doi: 10.3389/fpsyt.2020.00098

Cui, X., Liu, F., Chen, J., Xie, G., Wu, R., Zhang, Z., et al. (2018). Voxel-wise brain-wide functional connectivity abnormalities in first-episode, drug-naive patients with major depressive disorder. *Am. J. Med. Genet. B Neuropsychiatr. Genet.* 177, 447–453. doi: 10.1002/ajmg.b.32633

Ding, Y., Ou, Y., Su, Q., Pan, P., Shan, X., Chen, J., et al. (2019). Enhanced global-brain functional connectivity in the left superior frontal gyrus as a possible endophenotype for schizophrenia. *Front. Neurosci.* 13:145. doi: 10.3389/fnins.2019.00145

Galor, A., Felix, E., Feuer, W., Shalabi, N., Martin, E., Margolis, T., et al. (2015). Dry eye symptoms align more closely to non-ocular conditions than to tear film parameters. *Br. J. Ophthalmol.* 99, 1126–1129. doi: 10.1136/bjophthalmol-2014-306481

Galor, A., Moein, H. R., Lee, C., Rodriguez, A., Felix, E. R., Sarantopoulos, K. D., et al. (2018). Neuropathic pain and dry eye. *Ocul. Surf.* 16, 31–44. doi: 10.1016/j.jtos.2017.10.001

Gao, S., Zhao, X., Duan, C., and Wang, C. (2011). Clinical analysis of 1600 patients with dry eye syndrome at different ages. *Rec. Adv. Ophthalmol.* 31, 982–984. doi: 10.1159/rao.2010.0312

Giorgio, A., and De Stefano, N. (2016). Advanced structural and functional brain MRI in multiple sclerosis. *Semin. Neurol.* 36, 163–176. doi: 10.1055/s-0036-1579737

Gong, Q., Wu, Q., Scarpazza, C., Lui, S., Jia, Z., Marquand, A., et al. (2011). Prognostic prediction of therapeutic response in depression using high-field MR imaging. *Neuroimage* 55, 1497–1503. doi: 10.1016/j.neuroimage.2010.11.079

Guillaume, A., Fuller, J. R., Srimal, R., and Curtis, C. E. (2018). Cortico-cerebellar network involved in saccade adaptation. *J. Neurophysiol.* 120, 2583–2594. doi: 10.1152/jn.00392.2018

Hahamy, A., Calhoun, V., Pearlson, G., Harel, M., Stern, N., Attar, F., et al. (2014). Save the global: global signal connectivity as a tool for studying clinical populations with functional magnetic resonance imaging. *Brain Connect.* 4, 395–403. doi: 10.1089/brain.2014.0244

Heinke, W., and Schwarzbauer, C. (2002). *In vivo* imaging of anaesthetic action in humans: approaches with positron emission tomography (PET) and functional magnetic resonance imaging (fMRI). *Br. J. Anaesth.* 89, 112–122. doi: 10.1093/bja/aef155

Kalangara, J., Galor, A., Levitt, R., Covington, D., McManus, K., Sarantopoulos, C., et al. (2017). Characteristics of ocular pain complaints in patients with idiopathic dry eye symptoms. *Eye Contact Lens* 43, 192–198. doi: 10.1097/ICL.0000000000000249

Klingner, C., Langbein, K., Dietzek, M., Smesny, S., Witte, O., Sauer, H., et al. (2013). Thalamocortical connectivity during resting state in schizophrenia. *Eur. Arch. Psychiatr. Clin. Neurosci.* 264, 111–119. doi: 10.1007/s00406-013-0417-0

Lee, H., and Kim, H. A. (2020). Anatomical structure responsible for direction changing bilateral gaze-evoked nystagmus in patients with unilateral cerebellar infarction. *Medicine* 99:e19866. doi: 10.1097/MD.0000000000019866

Lee, U., Kim, M., Lee, K., Kaplan, C., Clauw, D., Kim, S., et al. (2018). Functional brain network mechanism of hypersensitivity in chronic pain. *Sci. Rep.* 8:243. doi: 10.1038/s41598-017-18657-4

Lemp, M. A. (2007). The definition and classification of dry eye disease: report of the definition and classification subcommittee of the international dry eye workshop 2007. *Ocul. Surf.* 5, 75–92. doi: 10.1016/S1542-0124(12)70081-2

Levitt, A., Galor, A., Chowdhury, A., Felix, E., Sarantopoulos, C., Zhuang, G., et al. (2017). Evidence that dry eye represents a chronic overlapping pain condition. *Mol. Pain* 13:1744806917729306. doi: 10.1177/1744806917729306

Li, H., Ou, Y., Liu, F., Chen, J., Zhao, J., Guo, W., et al. (2020). Reduced connectivity in anterior cingulate cortex as an early predictor for treatment response in drug-naive, first-episode schizophrenia: a global-brain functional

connectivity analysis. *Schizophr. Res.* 215, 337–343. doi: 10.1016/j.schres.2019.09.003

Li, T., Liu, Z., Li, J., Liu, Z., Tang, Z., Xie, X., et al. (2014). Altered amplitude of low-frequency fluctuation in primary open-angle glaucoma: a resting-state FMRI study. *Invest. Ophthalmol. Vis. Sci.* 56, 322–329. doi: 10.1167/iovs.14-14974

Li, T., Wang, Q., Zhang, J., Rolls, E., Yang, W., Palaniyappan, L., et al. (2016). Brain-wide analysis of functional connectivity in first-episode and chronic stages of schizophrenia. *Schizophr. Bul.l* 43, 436–448. doi: 10.1093/schbul/sbw099

Liang, L., Li, J., and Liu, Z. (2019). Focusing on the functional dry eye. *Zhonghua Yan Ke Za Zh*. 55, 885–890. doi: 10.3760/cma.j.issn.0412-4081.2019.12.003

Lin, X., Ding, K., Liu, Y., Yan, X., Song, S., and Jiang, T. (2012). Altered spontaneous activity in anisometropic amblyopia subjects: revealed by resting-state FMRI. *PLoS ONE* 7:e43373. doi: 10.1371/journal.pone.0043373

Liu, F., Guo, W., Fouche, J. P., Wang, Y., Wang, W., Ding, J., et al. (2015). Multivariate classification of social anxiety disorder using whole brain functional connectivity. *Brain Struct. Funct.* 220, 101–115. doi: 10.1007/s00429-013-0641-4

Martuzzi, R., Ramani, R., Qiu, M., Rajeevan, N., and Constable, R. T. (2010). Functional connectivity and alterations in baseline brain state in humans. *Neuroimage* 49, 823–834. doi: 10.1016/j.neuroimage.2009.07.028

Meier, T., Bellgowan, P., and Mayer, A. (2016). Longitudinal assessment of local and global functional connectivity following sports-related concussion. *Brain Imaging Behav.* 11, 129–140. doi: 10.1007/s11682-016-9520-y

Meijer, F., and Goraj, B. (2014). Brain MRI in Parkinson's disease. *Front. Biosci.* 6, 360–369. doi: 10.2741/e711

Mhuircheartaigh, R. N., Rosenorn-Lanng, D., Wise, R., Jbabdi, S., Rogers, R., and Tracey, I. (2010). Cortical and subcortical connectivity changes during decreasing levels of consciousness in humans: a functional magnetic resonance imaging study using propofol. *J. Neurosci.* 30, 9095–9102. doi: 10.1523/JNEUROSCI.5516-09.2010

Murrough, J., Abdallah, C., Anticevic, A., Collins, K., Geha, P., Averill, L., et al. (2016). Reduced global functional connectivity of the medial prefrontal cortex in major depressive disorder. *Hum. Brain Mapp.* 37, 3214–3223. doi: 10.1002/hbm.23235

Optican, L., and Robinson, D. A. (1981). Cerebellar-dependent adaptive control of primate saccadic system. *J. Neurophysiol.* 44, 1058–1076. doi: 10.1152/jn.1980.44.6.1058

Pan, P., Ou, Y., Su, Q., Liu, F., Chen, J., Zhao, J., et al. (2019a). Voxel-based global-brain functional connectivity alterations in first-episode drug-naive patients with somatization disorder. *J. Affect. Disord.* 254, 82–89. doi: 10.1016/j.jad.2019.04.099

Pan, P., Wei, S., Ou, Y., Jiang, W., Li, W., Lei, Y., et al. (2019b). Reduced global-brain functional connectivity and its relationship with symptomatic severity in cervical dystonia. *Front. Neurol.* 10:1358. doi: 10.3389/fneur.2019.01358

Panouillères, M., Alahyane, N., Urquizar, C., Salemme, R., Nighoghossian, N., Gaymard, B., et al. (2013). Effects of structural and functional cerebellar lesions on sensorimotor adaptation of saccades. *Exp. Brain Res.* 231, 1–11. doi: 10.1007/s00221-013-3662-6

Penner, J., Ford, K., Taylor, R., Schaefer, B., Théberge, J., Neufeld, R., et al. (2016). Medial prefrontal and anterior insular connectivity in early schizophrenia and major depressive disorder: a resting functional MRI evaluation of large-scale brain network models. *Front. Hum. Neurosci.* 10:132. doi: 10.3389/fnhum.2016.00132

Pflugfelder, S. C., Bian, F., Gumus, K., Farley, W., Stern, M. E., and De Paiva, C. S. (2018). Severity of Sjögren's syndrome keratoconjunctivitis sicca increases with increased percentage of conjunctival antigen-presenting cells. *Int. J. Mol. Sci.* 19:2760. doi: 10.3390/ijms19092760

Pflugfelder, S. C., Jones, D., Ji, Z., Afonso, A., and Monroy, D. (1999). Altered cytokine balance in the tear fluid and conjunctiva of patients with Sjögren's syndrome keratoconjunctivitis sicca. *Curr. Eye Res.* 19, 201–211. doi: 10.1076/ceyr.19.3.201.5309

Pires, C., Bahia, C., Rueda Lopes, F., Malfetano, F., Pereira, V., Kubo, T., et al. (2012). Brain MRI abnormalities in Brazilian patients with neuromyelitis optica. *J. Clin. Neurosci.* 19, 969–974. doi: 10.1016/j.jocn.2011.10.009

Power, J. D., Barnes, K. A., Snyder, A. Z., Schlaggar, B. L., and Petersen, S. E. (2012). Spurious but systematic correlations in functional connectivity MRI networks arise from subject motion. *Neuroimage* 59, 2142–2154. doi: 10.1016/j.neuroimage.2011.10.018

Rahman, M., Okamoto, K., Thompson, R., Katagiri, A., and Bereiter, D. A. (2015). Sensitization of trigeminal brainstem pathways in a model for tear deficient dry eye. *Pain* 156:942. doi: 10.1097/j.pain.0000000000000135

Sobczak-Edmans, M., Ng, T. H. B., Chan, Y. C., Chew, E., Chuang, K. H., and Chen, S. H. A. (2016). Temporal dynamics of visual working memory. *Neuroimage* 124, 1021–1030. doi: 10.1016/j.neuroimage.2015.09.038

Swets, J. A. (1988). Measuring the accuracy of diagnostic systems. *Science* 240, 1285–1293. doi: 10.1126/science.3287615

Tabbara, K. F., and Sharara, N. (1998). Dry eye syndrome. *Drugs Today* 34, 447–453. doi: 10.1358/dot.1998.34.5.485243

Vapnik, V. N. (1995). *The Nature Of Statistical Learning Theory* (New York, NY: Springer).

Waespe, W., and Baumgartner, R. (1992). Enduring dysmetria and impaired gain adaptivity of saccadic eye movements in Wallenberg's lateral medullary syndrome. *Brain J. Neurol. 115*, 1123–1146. doi: 10.1093/brain/115.4.1125

Wang, J., Li, T., Zhou, P., Wang, N., Xian, J., and He, H. (2017). Altered functional connectivity within and between the default model network and the visual network in primary open-angle glaucoma: a resting-state fMRI study. *Brain Imag. Behav.* 11, 1154–1163. doi: 10.1007/s11682-016-9597-3

Wang, L., Xia, M., Li, K., Zeng, Y., Su, Y., Dai, W., et al. (2015). The effects of antidepressant treatment on resting-state functional brain networks in patients with major depressive disorder. *Hum. Brain Mapp.* 36, 768–778. doi: 10.1002/hbm.22663

Xu, M., Liu, H., Tan, G., Su, T., Xiang, C., Wu, W., et al. (2019). Altered regional homogeneity in patients with corneal ulcer: a resting-state functional MRI study. *Front. Neurosci.* 13:743. doi: 10.3389/fnins.2019.00743

Yan, C. G., Wang, X. D., Zuo, X. N., and Zang, Y. F. (2016). DPABI: data processing & analysis for (resting-state) brain imaging. *Neuroinformatics* 14, 339–351. doi: 10.1007/s12021-016-9299-4

Yen, C. T., and Lu, P. L. (2013). Thalamus and pain. *Acta Anaesthesiol. Taiwan* 51, 73–80. doi: 10.1016/j.aat.2013.06.011

Zhurakovskaya, E., Paasonen, J., Shatillo, A., Lipponen, A., Salo, R., Aliev, R., et al. (2016). Global functional connectivity differences between sleep-like states in urethane anesthetized rats measured by fMRI. *PLoS ONE* 11:e0155343. doi: 10.1371/journal.pone.0155343

Conflict of Interest: The authors declare that the research was conducted in the absence of any commercial or financial relationships that could be construed as a potential conflict of interest.

frontiers in Human Neuroscience

STUDY PROTOCOL
published: 19 October 2020
doi: 10.3389/fnhum.2020.585512

Study Protocol for Teen Inflammation Glutamate Emotion Research (TIGER)

*Johanna C. Walker[1†], Giana I. Teresi[1†], Rachel L. Weisenburger[1], Jillian R. Segarra[1], Amar Ojha[2], Artenisa Kulla[1], Lucinda Sisk[3], Meng Gu[4], Daniel M. Spielman[4,5], Yael Rosenberg-Hasson[6,7], Holden T. Maecker[6,7], Manpreet K. Singh[8], Ian H. Gotlib[1] and Tiffany C. Ho[9,10]**

[1] Department of Psychology, Stanford University, Stanford, CA, United States, [2] Center for Neuroscience, University of Pittsburgh, Pittsburgh, PA, United States, [3] Department of Psychology, Yale University, New Haven, CT, United States, [4] Department of Radiology, Stanford University, Stanford, CA, United States, [5] Department of Electrical Engineering, Stanford University, Stanford, CA, United States, [6] Human Immune Monitoring Center, Stanford University, Stanford, CA, United States, [7] Department of Microbiology and Immunology, Stanford University, Stanford, CA, United States, [8] Department of Psychiatry and Behavioral Sciences, Stanford University, Stanford, CA, United States, [9] Weill Institute for Neurosciences, University of California, San Francisco, San Francisco, CA, United States, [10] Department of Psychiatry and Behavioral Sciences, University of California, San Francisco, San Francisco, CA, United States

OPEN ACCESS

Edited by:
Dajiang Zhu, University of Texas at Arlington, United States

Reviewed by:
Andrew Stephen Huhn, Johns Hopkins Medicine, United States
Shinichiro Nakajima, Keio University, Japan

***Correspondence:**
Tiffany C. Ho
Tiffany.Ho@ucsf.edu

[†] *These authors have contributed equally to this work*

Specialty section:
This article was submitted to Brain Imaging and Stimulation, a section of the journal Frontiers in Human Neuroscience

Received: *20 July 2020*
Accepted: *03 September 2020*
Published: *19 October 2020*

Citation:
Walker JC, Teresi GI, Weisenburger RL, Segarra JR, Ojha A, Kulla A, Sisk L, Gu M, Spielman DM, Rosenberg-Hasson Y, Maecker HT, Singh MK, Gotlib IH and Ho TC (2020) Study Protocol for Teen Inflammation Glutamate Emotion Research (TIGER). Front. Hum. Neurosci. 14:585512. doi: 10.3389/fnhum.2020.585512

This article provides an overview of the study protocol for the Teen Inflammation Glutamate Emotion Research (TIGER) project, a longitudinal study in which we plan to recruit 60 depressed adolescents (ages 13–18 years) and 30 psychiatrically healthy controls in order to examine the inflammatory and glutamatergic pathways that contribute to the recurrence of depression in adolescents. TIGER is the first study to examine the effects of peripheral inflammation on neurodevelopmental trajectories by assessing changes in cortical glutamate in depressed adolescents. Here, we describe the scientific rationale, design, and methods for the TIGER project. This article is intended to serve as an introduction to this project and to provide details for investigators who may be seeking to replicate or extend these methods for other related research endeavors.

Keywords: adolescence, depression, anterior cingulate cortex, magnetic resonance spectroscopy, glutamate

BACKGROUND

Depressive disorders, including Major Depressive Disorder (MDD), are the leading cause of disability worldwide, costing over $200 billion per year in the United States alone (Greenberg et al., 2015). This burden falls disproportionately on youth: by the age of 18, approximately 25% of individuals in the United States will experience a depressive episode (World Health Organization [WHO], 2017). The onset of depression during adolescence is known to adversely affect the course and prognosis of the disorder. Adolescent-onset depression is associated with longer, more severe, and more recurrent depressive episodes that are often refractory to treatment (Dunn and Goodyer, 2006; Fergusson et al., 2007; Naicker et al., 2013). Indeed, estimates of the probability of recurrence of depression are as high as 60% by 1 year (Birmaher and Arbelaez, 2002; Costello et al., 2002; Birmaher and Brent, 2007; Curry et al., 2011). Because adolescence is a period of significant neurodevelopment, the adverse impact of depression on ongoing brain maturation may explain, in part, why adolescent-onset depression is associated with more severe symptoms and a higher likelihood of recurrence than is adult-onset depression (Naicker et al., 2013).

Adolescence is a period characterized by major life transitions and heightened stress; stress is a frequent precipitant of MDD, a contributor to the course and maintenance of depressive symptoms, and a driver of neuroplasticity (Hammen, 2005; Ho, 2019). Moreover, depression itself is a stressful experience that may affect neurodevelopment through various psychobiological pathways. However, despite the consensus that stress affects neurodevelopmental processes (McEwen, 2012; Nelson and Gabard-Durnam, 2020), and that neurodevelopmental processes should be considered explicitly in models of adolescent MDD (Cicchetti and Rogosch, 2002; Lichenstein et al., 2016; Luby et al., 2016), we still know little about precisely how stress affects adolescent neurodevelopment in ways that increase risk of depression. Addressing this gap in knowledge requires research that takes a longitudinal approach to characterizing trajectories of brain development and depressive symptoms (Gotlib and Ordaz, 2016). In addition to the scarcity of longitudinal neuroimaging data on this topic, another major factor that limits our understanding of these processes is the lack of comprehensive integration of information across different modalities and neurobiological systems that are relevant to the study of adolescent stress, neurodevelopment, and depression.

Investigators have posited that inflammatory processes are critical in understanding how stress affects neurodevelopment in the context of depression (Miller et al., 2009; Ménard et al., 2016). It is well recognized that life stress activates the immune system by initiating a cascade of inflammatory responses, including increased production of pro-inflammatory cytokines in the peripheral nervous system (Miller et al., 2009). Critically, peripheral cytokines can cross the blood-brain barrier and alter its permeability (Banks et al., 2009), leading to increased inflammatory signaling in the central nervous system through the kynurenine pathway. Specifically, inflammatory cytokines activate the enzyme indoleamine-2,3 dioxygenase, which converts tryptophan (a precursor to serotonin) to kynurenine (Guillemin et al., 2001; Dantzer, 2017); a metabolite from this kynurenine pathway is quinolinic acid, which is a *N*-methyl-*D*-aspartate (NMDA) receptor agonist. The binding of quinolinic acid to NMDA receptors stimulates the production of glutamate; simultaneously, the inflammatory cascade initiated by the passage of peripheral cytokines into the central nervous system compromises the structural integrity of astrocytes and their ability to reuptake glutamate, as well as leads to damage of oligodendrocytes, the glial cells that produce myelin (Káradóttir and Attwell, 2007; Miller et al., 2009; Matute, 2011; Miller and Raison, 2016; Haroon et al., 2017). Thus, glutamatergic excitotoxicity through the kynurenine pathway and related pathways may be a key mechanism by which stress leads to the neurophenotypes commonly identified in depression, including gray matter loss (as measured by smaller limbic volumes, cortical thinning, and lower surface area), lower integrity of white matter microstructure in fronto-cingulate-limbic tracts (Aghajani et al., 2014; Bessette et al., 2014; LeWinn et al., 2014), and altered intrinsic fronto-cingulate-limbic connectivity (Connolly et al., 2013; Ho et al., 2014, 2015, 2017b; Kerestes et al., 2014). While neuroinflammation and mediators of the immune response in the central nervous system, such as microglia, cannot currently be measured non-invasively, technologies such as proton magnetic resonance spectroscopy (^{1}H-MRS) can be used to measure non-invasively the downstream effects of inflammation on neurotransmitter levels, including glutamate.

A number of studies using proton magnetic resonance spectroscopy (^{1}H-MRS), which permits non-invasive *in vivo* imaging of neurometabolites, have found reduced concentrations of glutamate or Glx (the sum of glutamate and glutamine, which is a proxy of glutamate metabolism as this signal is dominated by Glu) in multiple brain regions of depressed adults, including the anterior cingulate cortex (ACC) and medial frontal cortex (for a review, see Yüksel and Öngür, 2010; Sanacora et al., 2012; Moriguchi et al., 2019). Interestingly, these findings stand in contrast to the work reviewed above, which have consistently found *elevated* levels of Glu in response to stress and *higher* levels of Glu contributing to neurotoxicity (Miller et al., 2009; Miller and Raison, 2016; Haroon et al., 2017). Given that the vast majority (85.7%) of studies in the field have been in adults and not adolescents (Moriguchi et al., 2019), one possibility is that younger individuals with MDD exhibit higher levels of Glu in the ACC (and other cortical regions), but that over time, this results in depression-related cortical atrophy and, ultimately, reduced Glu compared to healthy controls. It is also important to note that with the exception of the study by Gabbay et al. (2017), which assessed 44 depressed adolescents, all of the prior MRS studies in depressed adolescents examining Glu (as described in Moriguchi et al., 2019) recruited relatively small sample sizes of depressed adolescents ($n < 20$), did not examine associations with inflammatory cytokines, and did not utilize longitudinal study designs to assess neurodevelopmental trajectories.

Indeed, no study to date has examined inflammation and its effects on glutamate levels and neurodevelopmental trajectories in adolescents with depression. Addressing this gap will help to elucidate whether (1) elevated inflammation and glutamate are already present in depressed adolescents or, alternatively, are consequences of chronic depression, as has been seen in adults with treatment-resistant depression; and (2) higher levels of inflammation and glutamate affect adolescent neurodevelopment in ways that increase risk for the development of subsequent episodes of depression. Moreover, researchers have posited that antioxidants, including glutathione and ascorbate, buffer against the neurotoxic effects of excessive glutamate in neurons, and may serve a neuroprotective role against glutamatergic excitotoxicity (Ballaz et al., 2013). That is, antioxidants may attenuate the effects of inflammation on glutamate, as well as the effects of inflammation-related glutamatergic neurotoxicity on neurodevelopment and depressive symptoms; these formulations, however, have not yet been tested.

The Teen Inflammation Glutamate Emotion Research (TIGER) study was developed to address these questions. We are using multimodal imaging to comprehensively assess neurophenotypes of depressive disorders and integrating information across traditionally disparate yet empirically relevant neurobiological systems (i.e., inflammatory and glutamatergic systems) to elucidate how neurodevelopment is affected in adolescents with depression. Specifically, we are testing the central hypothesis that glutamate mediates

the links between inflammation and the developmental trajectories of ACC connectivity over 18 months. We focused our investigation on the ACC because it is a large integrative region that spans multiple networks implicated in depression – including the salience network, the default mode network, and the central executive network – and subserves a host of functions commonly disrupted in depression, including emotion generative and regulatory processing, reward encoding, threat detection, learning, and error monitoring (Botvinick et al., 2004; Stevens et al., 2011; Kolling et al., 2016; Shenhav et al., 2016). Critically, the ACC undergoes significant maturation during adolescence (Power et al., 2011), and altered functional and structural connectivity of the ACC is one of the most robust neurophenotypes that has emerged in studies of adolescents with depression (Davey et al., 2012; Connolly et al., 2013; Ho et al., 2015, 2017b; Lichenstein et al., 2016). Specifically, in the TIGER project we seek to address the following questions (see **Figure 1**):

(1) Does glutamate concentration in the ACC mediate the associations between elevated pro-inflammatory cytokines and depressive neurophenotypes (measured by ACC connectivity)?
(2) Do antioxidants (as measured by glutathione and ascorbate) in the ACC moderate the associations among inflammation, ACC glutamate, and longitudinal trajectories of depressive neurophenotypes (measured by ACC connectivity)?
(3) What are baseline predictors of remission versus recurrence of depression over 18 months?

Finally, we are also recruiting a sample of psychiatrically healthy adolescents in order to examine the possibility that deviations from normative levels or trajectories in these neurobiological markers characterize adolescent depression.

METHODS AND STUDY DESIGN

Participants

Participants will be 60 depressed high school-aged adolescents (MDD) (ages 13–18 years) and 30 age- and sex-matched healthy controls (CTL) recruited from the San Francisco Bay Area community. See **Figure 2** for a list of inclusion/exclusion criteria for each diagnostic group. Participants will be recruited using flyers; advertisements on Craigslist, Nextdoor, and Facebook; and an internal referral program. The study has been approved by the Institutional Review Boards at Stanford University and the University of California, San Francisco. Participants and their parent(s)/legal guardian(s) will complete written assent and informed consent, respectively, and will be compensated for their participation.

Design and Procedures

The study will take place over an 18-month period, with three in-person laboratory sessions for all participants, approximately 9 months apart. Each timepoint (T1, T2, T3) will consist of two in-person visits (V1, V2) that will occur within 3 weeks of one another. T1 (V1) will include diagnostic and clinical interviews with adolescents and their parent(s)/legal guardian(s) to confirm the adolescent's eligibility, followed by self-report questionnaires. Once an adolescent is confirmed to be eligible, the participant will be invited to attend the second lab session (V2). V2 will include the MRI brain scan and a finger prick blood sample. These procedures will be repeated at T2 and T3. Between each of the three time points, participants will be asked to complete three surveys (2 online and 1 via phone call) from home every other month (e.g., M3, M5, M7, etc.). See **Figure 3** for more details.

Clinical and Behavioral Measures

Demographics

Participant age, sex assigned at birth, gender identity, sexual orientation, ethnicity, and race will be obtained through self-report questionnaires, while family socioeconomic status (income range and highest education of parent) will be obtained through parent-report.

Family History

To capture family history of psychiatric disorders, with a focus on mood disorders and suicide, in all first-degree blood-relatives of the participant, we will administer a modified version of the Family Interview for Genetic Studies (FIGS) (Gershon et al., 1988) to the adolescent's participating parent and/or legal guardian. If any endorsements of a down or elevated mood are made, the interviewer will continue into a screener probing for DSM-IV symptom criteria for depressive and bipolar disorders. A diagnosis will then be determined to be not present, suspected, or definite. In addition to asking about family history of depression and suicide, each parent will also be asked general screener questions to capture other significant psychiatric disorders: "*Did any [first degree relative] have any history of any psychiatric disorders or any problems with their nerves, emotions, or substance use? Did any see any professionals for their emotions or have any medications or treatments?*" All other suspected disorders captured in the general screener will be further probed, and information related to symptoms, diagnoses, professional treatment, and impairment will be used to determine whether the disorder was not present, suspected, or definite.

Pubertal Development

To measure pubertal development, we will be using self-report Tanner staging (Marshall and Tanner, 1968, 1970; Morris and Udry, 1980), wherein participants select how closely their pubic hair and breast/testes resemble an array of schematic drawings on a scale of 1 (prepubertal) to 5 (postpubertal). Self-report Tanner staging scores, particularly in older adolescents, have been found to be strongly correlated with physicians' physical examinations (Coleman and Coleman, 2002; Shirtcliff et al., 2009). As in previous studies of depressed adolescents, we will use the average of the pubic hair (i.e., adrenal) and breast/testes (i.e., gonadal) Tanner scores to index overall pubertal development (Ho et al., 2013, 2014, 2016). Female participants will also be asked to provide information on their menstrual cycle by providing approximate dates of their first period, as well their most recent periods at each timepoint. Participants will also

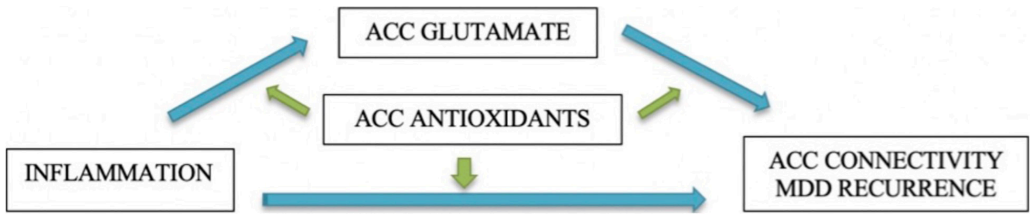

FIGURE 1 | Conceptual model and study aims. Green arrows indicate moderation of associations.

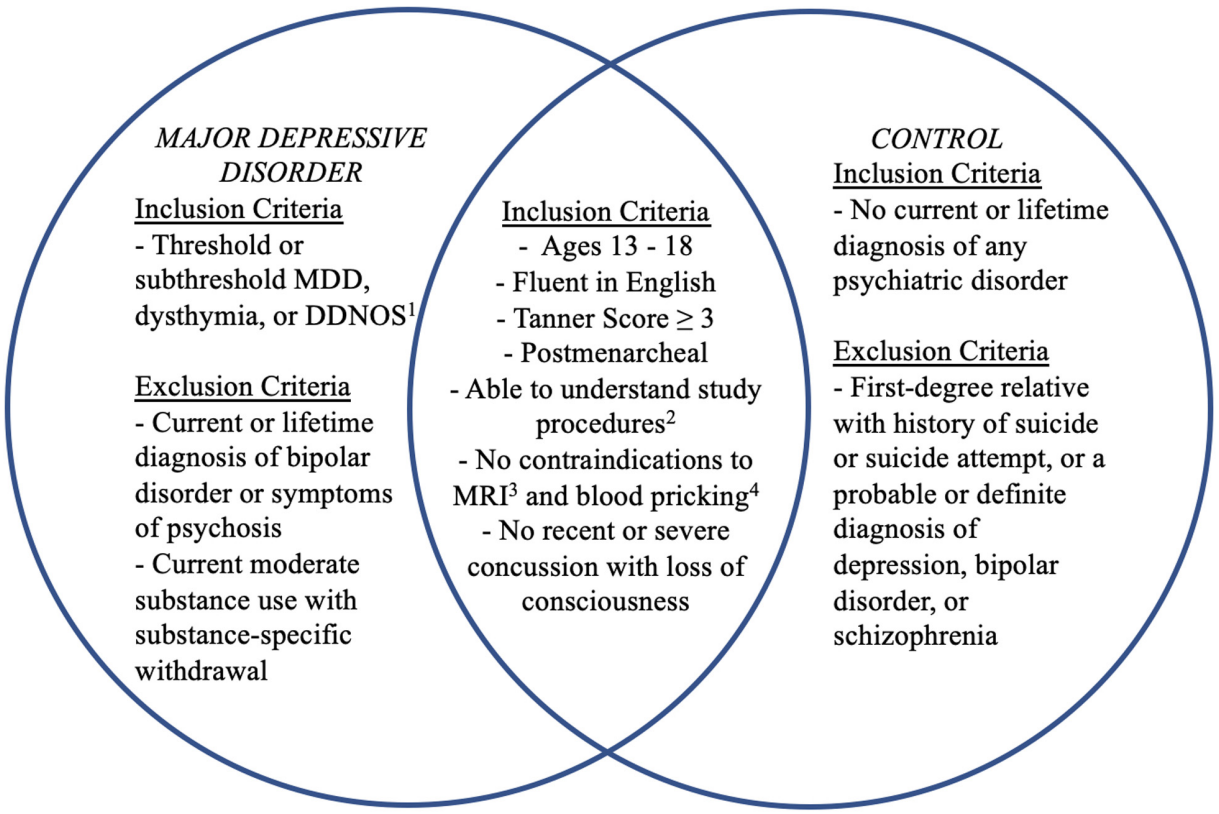

[1]If subthreshold for a depressive disorder via DSM-IV criteria, the participant must also have a minimum CDRS-R *t*-score of 55
[2]No current developmental or intellectual disorder that would interfere with or hinder a participant's ability to comprehend and properly follow study procedures
[3]Contraindications to MRI scanning include claustrophobia or presence of ferromagnetic metal in or on the body
[4]Contraindications to blood pricking include strong physiological and/or psychological aversion to blood, needles, and/or any step of the blood pricking procedure

FIGURE 2 | Inclusion and exclusion criteria for participants with Major Depressive Disorder (MDD) and healthy controls. CDRS-R, Children's Depression Rating Scale-Revised; DDNOS, depressive disorder not otherwise specified; MDD, Major Depressive Disorder; MRI, magnetic resonance imaging.

be asked to report on details of their current and past use of hormone contraceptives.

Depression and Psychiatric History (Clinical Interviews)

Participants and their parent(s)/legal guardian(s) will be administered the Kiddie Schedule for Affective Disorders and Schizophrenia Interview – Present and Lifetime Version (K-SADS-PL) (Kaufman et al., 2000), a semi-structured clinical interview designed to yield reliable and valid diagnoses of current and past history of psychiatric disorders according to DSM criteria. For the present study, we will be assessing present and lifetime history of the following Axis I disorders according to DSM-IV criteria: Depression, Mania (for the purpose of determining exclusion), Psychosis (for the purpose of determining exclusion), Alcohol Abuse and Dependence (for the purpose of determining exclusion), Panic Disorder, Social and Specific Phobia, Generalized Anxiety Disorder, Obsessive

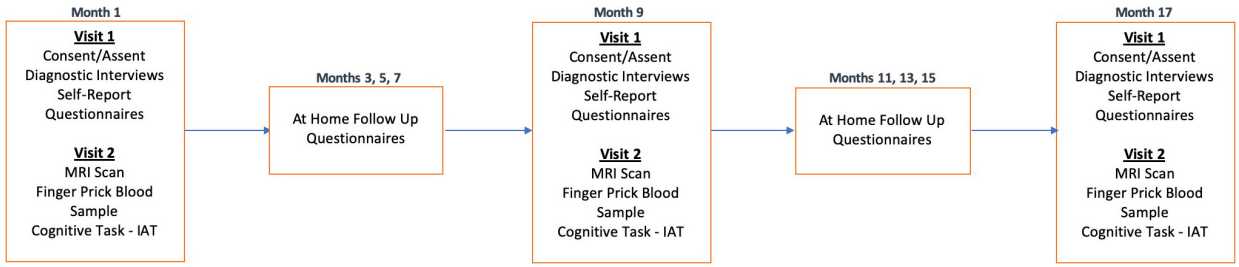

FIGURE 3 | Longitudinal study protocol. TIGER is a longitudinal study approximately 18-months long with 3 timepoints, approximately 9 months apart. Each timepoint will include two laboratory visits (Visit 1 and Visit 2). Every other month between laboratory sessions we will also obtain self-report measures of depression (RADS-2, PHQ-9) and anxiety (MASC-2), as well as information on any potential treatment changes. Please also see **Table 1** for a list of measures collected within each session visit at each timepoint.

TABLE 1 | Summary of primary measures in TIGER.

Method	Measure	Domain assessed	V1	V2	M
Clinical interview:	K-SADS-PL	Clinical diagnosis	X		
	CDRS-R	Depression symptom severity	X		
	C-SSR-S	Suicidal ideation and behaviors	X		
	SITBI	Non-suicidal self-injury	X		
	FIGS*	Family psychiatric history	X		
Self-report:	Tanner	Pubertal development	X		
	RADS-2	Depression symptom severity	X		X
	SIQ-JH	Explicit suicidal ideation	X		
	PHQ-9	Depression symptom severity	X		X
	MASC-2	Anxiety symptom severity	X		X
	MPVS	Bullying	X		
	STRAIN	Life stress	X		
	CTQ*	Childhood trauma	X		
	DERS*	Emotion regulation difficulties	X		
MRI:	T1-weighted SPGR	Grey and white matter		X	
	Resting-state fMRI	Functional connectivity		X	
	Diffusion-weighted MRI	Structural connectivity		X	
	^{1}H-MRS (ACC)	Glutamate, Glutathione, Ascorbate		X	
	ACC Glu	Glutamate		X	
	ACC GSH and ACC Asc	Antioxidants		X	
Cognitive task:	IAT – death version	Implicit suicidal ideation		X	
Blood:	IL-1β, IL-6, IL-10, TNF-α	Inflammation		X	

*Measures will be assessed at all three timepoints unless marked with a * which indicates the measure will only be administered at T1. Measures under column "M" are administered at the bi-monthly online follow-up assessments.*

Compulsive Disorder, Conduct Disorder, Oppositional Defiant Disorder, Disruptive Mood Dysregulation Disorder, and Post-Traumatic Stress Disorder. We will also be evaluating Attention Deficit Hyperactivity Disorder (ADHD) and Substance Use Disorders according to DSM-V criteria. The decision to rely on DSM-V criteria for ADHD was due to the later age cutoff for symptom presentation (age 12 versus age 7). The decision to rely on DSM-V criteria for substance use was due to the inclusion of substance-specific withdrawal symptoms. Moreover, there is compelling evidence across adolescents and substances that criteria for abuse and dependence in the DSM-IV reflect the same underlying condition rather than distinct nosologies (Hasin et al., 2013). Within each psychiatric module, ratings on a scale of 0 to 3 (no information to threshold) will be assigned to both the current and the most severe past episode. Age of onset, duration of episode, and number of episodes (if relevant) will be assessed for each disorder, as well as any academic, social, and familial impairment. To assess whether the participant has experienced remission or recurrence of a depressive disorder at T2 and T3, we will follow procedures from the Treatment for Adolescents with Depression Study (TADS) (Curry et al., 2011), and define recurrence as experiencing a clinically significant episode of depression following recovery (i.e., remission lasting a minimum of 8 weeks).

Additionally, to derive dimensional scores of depression severity, we will administer the Children's Depression Rating Scale-Revised (CDRS-R) (Poznanski and Mokros, 1996) to all participants and their parents. The CDRS-R is a clinician-rated

scale and one of the most widely used rating scales for assessing severity and change of depression symptoms for clinical research trials in pediatric depression (Isa et al., 2014). The CDRS-R is comprised of 17 questions, the first 14 of which are administered to both parent and adolescent participants, while the last three items are rated based on clinician observation and assess non-verbal characteristics such as depressed affect, listless speech, and hypoactivity. Interviewers will assign a total summary score integrating both parent and child interviews. Participants who are subthreshold for depressive disorders based on the K-SADS-PL but have a CDRS-R *t*-score $\geq$ 55 will be included (see **Figure 2**).

Depression (Self-Report)

Self-reported severity of symptoms will be assessed with the Reynolds Adolescent Depression Scale (RADS-2) (Reynolds, 2010), a 30-item questionnaire designed to assess severity of depressive symptoms in adolescents in both school and clinical settings (Reynolds, 2002). The RADS-2 was validated in an ethnically diverse North American sample of adolescents ages 11–20 years. In addition to a total severity score, the RADS-2 also generates scores on four specific dimensions of depression: *Dysphoric Mood*, *Anhedonia/Negative Affect*, *Negative Self-Evaluation*, and *Somatic Complaints*. We anticipate that data from the RADS-2 subscales will be useful for exploring hypotheses concerning subtypes of depression.

Finally, we will also administer the Patient Health Questionnaire-9 (PHQ-9), which is a nine-item questionnaire frequently used in both clinical and research settings to assess depression severity and symptom change (e.g., in response to treatment) in both adolescents and adults (Kroenke et al., 2001). We anticipate that data from the PHQ-9 will facilitate opportunities to combine our data with other studies across developmental populations.

Anxiety (Self-Report)

To assess symptoms of anxiety, we will administer the Multidimensional Anxiety Scale for Children (MASC-2) (March, 2012), a 39-item questionnaire which generates four subscales—*Social Anxiety*, *Separation Anxiety/Panic*, *Harm Avoidance*, and *Physical Symptoms*—based on six symptom domains: tense/restless, somatic/autonomic, perfectionism, anxious coping, humiliation/rejection, and performance fears. The MASC-2 has high convergent validity, both strong inter-rater and test–retest reliability, and has been widely used to assess anxiety within adolescents (March et al., 1997; Wei et al., 2014).

Suicidal Thoughts and Behaviors (Clinical Interviews)

Because depression is one of the strongest psychiatric risk factors for suicidal thoughts and behaviors (STBs) (Franklin et al., 2017; Ribeiro et al., 2018; Melhem et al., 2019), and because adolescence is a time when STBs rise (Nock et al., 2013), we will utilize multiple measures designed to assess STBs in adolescents, all of which are part of the Suicide Specialty Collection of the PhenX Toolkit[1].

[1]https://www.phenxtoolkit.org/sub-collections/view/3

Within the depression module of the K-SADS-PL, we will assess various levels of STBs – ranging from abstract thoughts, recurrent thoughts, suicidal ideation, suicidal acts (researching methods, obtaining materials, creating a plan), and suicide attempts. To supplement information from the K-SADS-PL and to further classify suicidal ideation and behavior, we will administer the pediatric version of the Columbia Suicide Severity Rating Scale (C-SSRS) (Posner et al., 2008). The C-SSRS is a semi-structured interview and has strong validity, internal consistency and high sensitivity (Posner et al., 2011; Gipson et al., 2015). Through administration of the C-SSRS, interviewers will assess the severity of suicidal ideation and gather information regarding the frequency, duration, and controllability of thoughts; possible deterrents to acting; and reasons for ideation. Interviewers will also utilize the C-SSRS to gather information about suicidal behaviors, including details regarding actual, interrupted, or aborted attempts as well as preparatory acts such as gathering materials or writing a suicide note.

Finally, given the co-occurrence of suicidal thoughts and attempts with non-suicidal self-injurious (NSSI) behaviors (Nock et al., 2006; Asarnow et al., 2011; Guan et al., 2012; Klonsky et al., 2013), we will also administer portions of the Self-Injurious Thoughts and Behavior Interview (SITBI) (Nock et al., 2007) to assess suicidal gestures and NSSI. The SITBI is a structured interview that assesses the history, frequency, and intensity of thoughts and behaviors related to non-suicidal self-injury. Ages of onset, as well as frequency of thoughts and behaviors in the last year (or since last visit, for T2 and T3 assessments), last month, and week prior to the assessment will also be obtained. Additionally, the SITBI includes questions assessing medical attention received for NSSI behaviors, as well as participants' perception that these NSSI thoughts and behaviors are likely to recur. The SITBI has high convergent validity, both strong inter-rater and test–retest reliability, and has been widely used with adolescents (van Alphen et al., 2017; Stewart et al., 2019; Vergara et al., 2019).

Suicidal Ideation (Self-Report)

To measure severity and frequency of suicidal ideation in the past month, we will administer the Suicidal Ideation Questionnaire–Junior High version (SIQ-JH) (Reynolds, 1987). The SIQ-JH is a 15-item measure designed for use with adolescents between the ages of 12–18 years, and has high internal consistency, test–retest reliability, and predictive validity (Reynolds, 1987).

Implicit Suicidal Ideation (Cognitive Task)

In addition to explicit or self-disclosed methods of suicidal ideation, we will administer a computerized task to probe suicidal ideation without relying on self-report, as there may be several reasons why an adolescent may not be truthful about their thoughts surrounding death or suicide (Nock et al., 2010). Specifically, we will be using the death-version of the implicit association test (IAT), which is a 5-min computerized task that will allow us to measure participants' response latencies to associations between self/not self-related stimuli and life/death-related stimuli to approximate the strength of each individual's association with self and death (Nock et al., 2010). The IAT

has been shown to have strong reliability (Cunningham et al., 2001; Nosek et al., 2005), construct validity (Lane et al., 2007), and sensitivity to clinical change in treatment (Teachman and Woody, 2003), and has also been used to predict severity of future suicidal ideation, non-suicidal self-injury, and attempt in adolescents (Cha et al., 2016; Glenn et al., 2019). Importantly, we have previously demonstrated in an independent community sample of adolescents (ages 9–13 years) that morphological alterations in the dorsal striatum – specifically the putamen and caudate – predict IAT bias scores 2 years later (Ho et al., 2018). Interestingly, putamen and caudate volumes did not predict SIQ-JH scores, suggesting that not only are dopaminergic striatal structures implicated in suicide risk, but also that neurobiological phenotypes may be better predictors of *objective* markers of suicide risk.

Life Stress

Given the key role of stress in our theoretical model, we will obtain comprehensive information on cumulative life stress in each participant using the Adolescent version of the Stress and Adversity Inventory (STRAIN) (Slavich et al., 2019). The Adolescent STRAIN is a self-administered computerized set of questions probing exposure to 75 distinct stressors, including 33 acute life events and 42 chronic difficulties. Through branching logic, additional questions are generated to assess the severity, frequency, timing, and duration of any endorsed stressor. The STRAIN also separates stressors occurring across different life domains (e.g., education, health) into five mutually exclusive types based on gold-standard stress assessments (Slavich and Shields, 2018): *Interpersonal Loss* (e.g., experiences characterized by the dissolution of relationships), *Physical Danger* (e.g., life-threatening circumstances, such as being robbed), *Entrapment* (e.g., circumstances that are difficult to escape, such as caring for a sibling with a disability), *Humiliation* (e.g., experiences characterized by social rejection, such as being mocked publicly), *Role Change/Disruption* (e.g., experiences marked by major life transitions, such as starting high school). Although the test–retest reliability of the Adolescent STRAIN has not yet been examined, its parent instrument, the Adult STRAIN, has been shown to exhibit excellent test–retest reliability (Slavich and Shields, 2018). More details on the psychometric properties of the Adolescent STRAIN can be found in Slavich et al., 2019.

Childhood Trauma Questionnaire

Meta-analytic and epidemiological evidence has shown that maltreatment experienced during childhood is significantly associated with depression in adolescents (McLaughlin et al., 2012; Humphreys et al., 2020; LeMoult et al., 2020), consistent with the formulation that adversity experienced during sensitive periods of development has an outsized effect on subsequent neurodevelopmental trajectories supporting mental health (Nelson and Gabard-Durnam, 2020). To measure adversity experienced during childhood, we will use the Childhood Trauma Questionnaire Short Form (CTQ-SF) (Bernstein et al., 2003), which is one of the most widely used measures of childhood maltreatment. The CTQ-SF is a reliable and empirically validated 28-item version of the original 70-item questionnaire (see Bernstein et al., 1994), and is rated on a 5-point scale. Along with a total score indexing severity of childhood trauma, the CTQ-SF has five clinical scales assessing childhood abuse and neglect: *Emotional Abuse*, *Physical Abuse*, *Sexual Abuse*, *Emotional Neglect*, and *Physical Neglect*. For readability, we administered an adapted version of the CTQ-SF in which we excluded the three-item validity scale, shortened item descriptions, and revised the directionality of reverse-scored items, which were neglect-related items only (e.g., "*There was someone in my family who helped me feel like I was important or special*" to "*I was never made to feel important*").

Peer Victimization

Since peer victimization and bullying have been linked with depressive symptoms in adolescents (Sweeting et al., 2006; Hong and Espelage, 2012; Stapinski et al., 2014), we also will administer the Multidimensional Peer Victimization Scale (MPVS) (Mynard and Joseph, 2000) to assess peer-related abuse. The MPVS is a self-report questionnaire comprised of 16 items that assess the frequency with which a child experienced certain types of peer victimization and manipulation in the last school year. Along with a total score indexing severity of peer victimization, the questionnaire generates four subscales: *Physical Victimization*, *Social Manipulation*, *Verbal Victimization*, and *Attacks on Property*. The MPVS has strong internal consistency, split-half reliability, and concurrent, convergent, and discriminant validity (Joseph and Stockton, 2018). Finally, to complement the MPVS, we also will query participants about recent experiences of bullying using an in-house measure. Participants will report whether or not they are currently being bullied, and if so, will describe who is bullying them (e.g., kids at school, in their grade or in class, in their neighborhood, family members), how many individuals are bullying them, and how they are being bullied.

Emotion Regulation

Given ample evidence that emotion regulation dysfunction is associated with the onset and recurrence of depression (Silk et al., 2003; Kuyken et al., 2006; Burwell and Shirk, 2007), we assessed emotion regulation strategies using the Difficulties in Emotion Regulation Scale (DERS) (Gratz and Roemer, 2003). The DERS is a 36-item measure which assesses emotion regulation tendencies and includes six subscales that assess different aspects of emotion regulation such as understanding, awareness and related behaviors. DERS has strong reliability and validity with adolescents (Weinberg and Klonsky, 2009; Neumann et al., 2010; Sarıtaş-Atalar et al., 2015) and adults (Orgeta, 2009; Kökönyei et al., 2014; Kaufman et al., 2016). Because the DERS was designed to assess trait level emotion regulation strategies (Hallion et al., 2018), we will only administer the DERS at T1.

Neuroimaging

All participants will complete the following MRI scans on a 3T Discovery MR750 (GE Medical Systems, Milwaukee, WI, United States) with a 32-channel head coil (Nova Medical, Wilmington, MA, United States) at the Stanford Center for Cognitive and Neurobiological Imaging. See **Table 2** for detailed acquisition parameters for each scan.

TABLE 2 | Summary of scan sequences and parameters.

	Voxel size (isometric mm, unless otherwise specified)	Number of slices (orientation)	FOV (cm)	TR/TE/TI (ms)	Number of volumes	Flip angle (°)	Duration (min:sec)
T1-weighted MRI	1.0	156 (axial)	25.6	8.2/3.2/600	N/A	12	3:40
Optimized PRESS (dACC)	Variable, not isometric	1 (oblique)	24.0	2000/35/NA	N/A	90	5:04
Optimized PRESS (rACC)	Variable	1 (axial)	24.0	2000/25/NA	N/A	90	5:04
Resting-state BOLD EPI	2.9	42 (oblique)	23.2	2000/30/NA	240	77	8:00
Resting-state fieldmap	2.9	42 (oblique)	22.4	700/4.5/NA	N/A	54	0:27
Diffusion-weighted MRI	2.0	64 (axial)	24.0	8500/94.2/NA	66 (60 $b = 2000$, 6 $b = 0$)	90	9:30
Diffusion-weighted MRI fieldmap	2.0	64 (axial)	24.0	700/4.5/NA	N/A	54	0:27
Quantitative T1	2.0	25 (axial)	24.0	3000/25/50	31	77	2:03 per scan (second scan with reverse phase-encoding)

T1-Weighted Anatomical MRI

A set of high-resolution T1-weighted anatomical images will be acquired using GE's "BRAVO" scan, which is a fast spoiled gradient-recalled (SPGR) sequence with parameters tuned to optimize tissue contrast. In addition to using images from this scan for prescribing voxels in the MRS scan (see below) and facilitating registration with the other images we will collect, we will also preprocess all T1-weighted MRI data using FreeSurfer 6.0 (Fischl et al., 2002)[2] to perform tissue segmentation and estimate subcortical gray matter volumes, cortical thickness, and surface area according to Desikan atlas (Desikan et al., 2006). Each segmentation will be manually checked for quality assurance according to the protocols established by the global consortium, Enhancing NeuroImaging Genetics through Meta-Analysis (ENIGMA)[3]. Outliers, defined as three absolute standard deviations away from the sample mean, will be flagged for additional visual inspection. Any structure that is poorly segmented will be excluded from further analysis only after careful visual inspection.

Magnetic Resonance Spectroscopy

To estimate concentrations of glutamate (Glu), glutathione (GSH), and ascorbate (Asc), we will use a proton magnetic resonance spectroscopy (^{1}H-MRS) scan based on a modification of the GE Healthcare PRESS product sequence, PROBE-p^{TM}. Two features were added to the product PROBE-p^{TM} sequence for improved localization: (1) 16 step phase cycling (EXORCYCLE on the two refocusing RF pulses) and (2) application of a sensitive point echo planar (EP) waveform during acquisition to further eliminate out-of-slice artifact in the logical z direction (Bodenhausen et al., 1977; Webb et al., 1994; Gu et al., 2018). To avoid suppression of Asc at 4.1 ppm, the bandwidth of the CHESS RF water suppression pulses will be reduced from 150 to 75 Hz. At T1, the location of the MRS voxel for the dorsal ACC (and rostral ACC), will be graphically prescribed manually following construction of the 3D T1-weighted anatomical scan (see above) using anatomical landmarks. At T2 and T3, we will use an automated voxel placement tool that uses non-linear warping between current native subject space and prior native subject space (i.e., at T1) to identify precise voxel locations in scanner space in real-time during data acquisition and to minimize bias in manual prescription[4].

All spectra of interest will be quantified using LCModel (Provencher, 2001; see **Table 3** for more details). Experimental GSH and Asc basis spectra will be acquired from custom built 50 mM GSH and Asc spherical phantoms with pH of 7.2 at 37°C in an otherwise synthetic basis set to improve accuracy

[2]http://surfer.nmr.mgh.harvard.edu/fswiki/recon-all

[3]http://enigma.ini.usc.edu/protocols/imaging-protocols/

[4]https://cni.stanford.edu/wiki/Spectro#Automated_magnetic_resonance_spectroscopy_voxel_placement_tools

TABLE 3 | Metabolites of interest imaged by magnetic resonance spectroscopy.

Metabolite	Abbreviation
Creatine	Cr
Glutamate	Glu
Glutathione	GSH
N-Acetylaspartate	NAA
Ascorbate	Asc
Glutamine	Gln
Glutamate + Glutamine	Glx
myo-Inositol	mI
Choline (Glycerophosphocholine + Phosphocholine)	Cho (GPC + PCH)
Creatine + Phosphocreatine	Cr + PCr

(due to the complexity of the GSH and Asc resonances and their dependence on temperature, simulated basis spectra are often inaccurate). All metabolite concentration levels will be expressed as ratios to total creatine (i.e., sum of creatine and phosphocreatine) levels (which are relatively high and stable across different tissue types of the brain, and thus, often used as an internal reference standard for characterizing other spectra). In addition to quantifying concentrations of Glu (and GSH and Asc), because of the dynamic cycling between glutamine (Gln) and Glu (extracellular Glu is converted into Gln in astrocytes before being released and taken up by neurons where it is synthesized into Glu or GABA; Ramadan et al., 2013), we will also consider the total sum of Glu and Gln (Glx), and the ratio of Glu to Gln as complementary indices of glutamate metabolism. Finally, because *N*-acetylaspartate (NAA) is present almost exclusively in neurons and is widely considered a marker of neuronal health, whereas myo-inositol (mI) and choline (Cho) are found mostly in glial cells (Brand et al., 1993; Griffin et al., 2002), we will also explore these neurometabolites in analyses specific to gray and white matter, respectively. We will use the Cramér–Rao lower bounds (CRLB), a measure of the reliability of the fit, with a quality criterion set at <35% for each individual metabolite. Tissue segmentation (e.g., percentage of gray matter) in prescribed voxels will also be used as a potential covariate.

Resting-State fMRI

To examine intrinsic functional connectivity, we will acquire resting-state T2*-weighted BOLD fMRI data using an echo planar image (EPI) sequence. Resting-state fMRI data will be pre-processed using standard methods in AFNI and FSL that we have implemented based on previous work from our group (Connolly et al., 2013, 2017; Ho et al., 2015, 2017b; Sacchet et al., 2016; Ordaz et al., 2018; Schwartz et al., 2019). Specifically, EPI timeseries data will be despiked, slice-time and motion corrected, then subsequently aligned to the T1-weighted images using a local Pearson correlation method (Saad et al., 2009), and spatially smoothed. We will then submit the pre-processed data into a voxelwise multiple linear regression to regress out effects from non-brain and physiological processes (mean signal from WM and CSF, 6 motion parameters at each time point, 6 motion parameters at the prior time point, and the square of each of these 12 motion parameters); the resulting residuals will then be bandpass filtered ($0.009 < f < 0.08$ Hz), demeaned, and used for subsequent analyses. For the purposes of testing study aims, we will conduct group-level independent components analysis (ICA) followed by dual regression. Group ICA is a data-driven multivariate signal-processing method that spatially clusters fMRI data based on the strength of their temporal correlations (Kiviniemi et al., 2003; Beckmann et al., 2009); when followed by dual regression, this approach has higher test–retest reliability than seed-based functional connectivity (Zuo et al., 2010; Smith et al., 2014). Based on previous work from our group and others implicating dorsal and rostral ACC connectivity in adolescent depression (Ho et al., 2015, 2017b; Lichenstein et al., 2016), we will focus on connectivity of a component of the salience network, which is anchored in the dorsal ACC and enjoys robust connectivity with the anterior insula and subcortical structures (Seeley et al., 2007; Menon and Uddin, 2010; Power et al., 2010), and a component of the default mode network, which includes rostral ACC, medial prefrontal cortex, and the posterior cingulate cortex (Andrews-Hanna et al., 2010). See **Figure 4** for more details.

Diffusion-Weighted MRI

Diffusion-weighted (DW) MRI data will be acquired using a modified version of the GE Healthcare DW-EPI sequence with dual spin echo scans, where the polarity of the second 180° pulse is inverted relative to the first 180°, thereby causing off-resonance signal from fat to get defocused and reducing fat-shift artifacts (Reese et al., 2003; Sarlls et al., 2011). Given evidence in the literature implicating the cingulum bundles, which are major white matter tracts connecting ACC with prefrontal cortex (cingulum cingulate), along with the ACC and hippocampus (cingulum hippocampus), and the uncinate fasciculus (a major white matter tract connecting the amygdala with prefrontal cortex) with depression in adolescents (LeWinn et al., 2014; Lichenstein et al., 2016), we will focus our analyses on white matter microstructure of these fronto-cingulate-limbic tracts, with a specific focus on tracts that cross the ACC. Specifically, we will acquire diffusion-weighted MRI (dMRI) sequence using an echo planar imaging sequence with isotropic voxels sampling 96 directions. All dMRI data will be pre-processed (e.g., registration, eddy-current and motion correction, resampling) based on VISTA tools[5] that have been implemented by our team previously in adolescents (Ho et al., 2017a). Diffusion tensors will be fit using least squares to generate voxelwise fractional anisotropy (FA) maps. Whole brain deterministic fiber tracking will be performed with Automated Fiber Quantification (AFQ)[6]. The seeds for tractography will be selected from a uniform 1 mm 3D grid spanning the whole brain mask for voxels with FA > 0.3. Path tracing will proceed until FA < 0.15 or until the minimum angle between the current and previous path segments >30°. AFQ-derived segmentations of major white matter tracts including the cingulum have been validated in children and adolescents (Yeatman et al., 2012; Ho et al., 2017a, 2020). Importantly, we have used these pre-processing and tractography methods to successfully segment the cingulum tracts in adolescents (Ho et al., 2020), and compute FA as well as other diffusivity metrics (mean diffusivity, axial diffusivity, and radial diffusivity). See **Figure 4** for more details.

Quantitative MRI

R1 (1/T1), which can be computed from a quantitative MRI (qMRI) scan, has been shown to be a promising complement to DWI for quantifying myelin *in vivo* using MRI (Koenig et al., 1990; Stüber et al., 2014). Moreover, recent evidence suggests that lower R1 is associated with MDD in adults (Sacchet and Gotlib, 2017). We will use a slice-shuffled inversion-recovery simultaneous multi-slice EPI sequence with in-plane acceleration followed by a second scan with reversed phase encoding in order to correct for signal distortion. After running FSL's *top-up*

[5]http://vistalab.stanford.edu/software

[6]https://github.com/jyeatman/AFQ

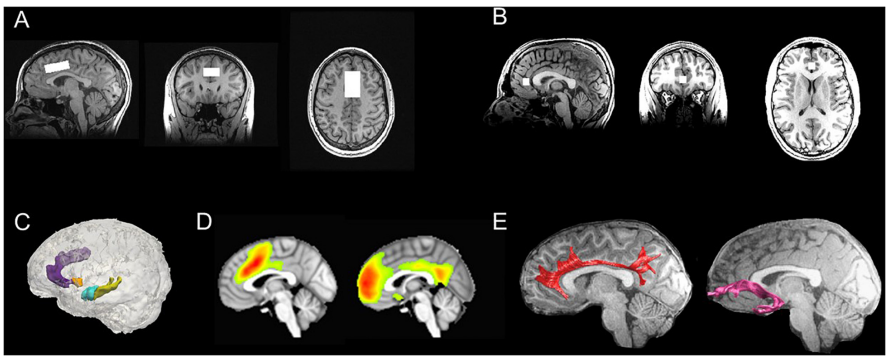

FIGURE 4 | Multimodal neuroimaging scans in TIGER. **(A)** Representative dorsal ACC voxel from the MRS scan; **(B)** Representative rostral ACC voxel from the MRS scan; **(C)** Representative FreeSurfer-based segmentations of the dorsal ACC (light purple), rostral ACC (dark purple), striatum (orange), hippocampus (yellow), and amygdala (blue); **(D)** Group-level computations of the salience network anchored in the dorsal ACC (left) and default mode network anchored in the medial prefrontal cortex/rostral ACC and cingulate gyrus (right) derived from resting-state fMRI data using ICA (all maps thresholded at $t_{68} > 3.93$; $\alpha = 0.0001$); **(E)** Representative tractography of the cingulum bundles (red) and uncinate fasciculus (pink), which are two major white matter tracts that connect fronto-cingulate-limbic structures. ACC, anterior cingulate cortex; ICA, independent components analysis; MRS, magnetic resonance spectroscopy; TIGER, Teen Inflammation Glutamate Emotion Research.

to estimate and correct for distortions, we will use non-linear least squares modeling to estimate T1 signal per voxel[7] and then compute the inverse of the result to obtain a voxelwise map of R1 values.

Inflammatory Cytokines

To measure inflammatory cytokines, we will use a dried blood spot (DBS) protocol. Five blood spots, comprising approximately 150–250 μL per spot, will be collected using mini contact-activated lancets (BD 366594 Microtainer, BD Biosciences, San Jose, CA, United States) to prick the finger after the participant runs their non-dominant hand under hot water for 2 min. Blood spots will be collected on 3 mm filter paper cards (Whatman #903, GE Healthcare, Piscataway, NJ, United States) and will then be dried overnight at room temperature before being transferred to Ziplock bags with a desiccant for storage in a −20°C freezer. All extraction and analysis will take place at the Human Immune Monitoring Center (HIMC) at Stanford University. Prior to analysis, all samples will be extracted, prepared, and diluted 3 fold in the Luminex assay buffer prior to running the 62-plex Luminex assays (eBioscience; San Diego, CA, United States), and then run through a dedicated flow cytometry-based platform, the Luminex FlexMap 3D. The 62-plex Luminex assays use antibody-conjugated bead sets to detect analytes in a multiplexed sandwich immunoassay format. Each bead in the set is identified by a unique spectral barcode of two dyes which is excited by a red laser. The quantity of bound protein will be read via a biotin-conjugated dector antibody bound to streptavidin-phycoerythrin. The streptavidin-phycoerythrin conjugate is excited by the second laser (green). In addition to the 62-plex beads, each well will also contain Assay Chex beads (Radix BioSolutions), which are process control beads that will allow us to normalize the data based on potential confounds (e.g., non-specific binding; Maecker et al., 2020). All data will be analyzed using MasterPlex software (Hitachi Software Engineering America Ltd., MiraiBio Group). Although both median fluorescence intensity (MFI) and calculated concentration values (in pg/mL) will be reported for each analyte, based on prior work demonstrating advantages of using MFI over concentration values for low abundant analytes (Breen et al., 2016), we will conduct all statistical analyses using MFI values. Although we are able to obtain more than 60 analytes using the Luminex assays, to minimize multiple comparisons and pursue hypothesis-driven analyses based on prior literature relating inflammatory cytokines with depression (Howren et al., 2009; Liu et al., 2012; Raison et al., 2013; Valkanova et al., 2013), we will focus on interleukin (IL)-1β, IL-6, IL-10, and tumor necrosis factor (TNF)-α, as these cytokines have also been shown to be assayed reliably from DBS (Miller and McDade, 2012; Skogstrand et al., 2012). Critically, the cytokines we will assay using the described DBS protocol have been validated against plasma obtained through a venipuncture from the same individuals collected at the same time using standard protocols from the field ($R^2 = 0.82$; Rosenberg-Hasson et al., 2014).

Statistical Approach and Power Analyses

In this proposed longitudinal study, 60 depressed adolescents will be repeatedly assessed over a considerably long period, allowing for reasonable inference regarding the longitudinal relationships among inflammation, Glu, and ACC connectivity. The core analysis strategy in this project is longitudinal mixed effects modeling (Raudenbush and Bryk, 2002; Singer et al., 2003), where we fully utilize the repeatedly measured primary outcomes of neurophenotypes (i.e., ACC connectivity). For all mixed effects models, maximum likelihood (ML) estimation will be used, which will allow individuals who have outcome data at one or more assessment points to be included in our final analysis.

First, we will employ standard correlation and linear regression analyses to test linear associations among baseline

[7]https://github.com/cni/t1fit/blob/master/t1_fitter.py

measurements of inflammation, ACC Glu, ACC GSH, ACC Asc, and depression severity, which will provide important insights regarding the relationships across these key variables. Based on the medium effect sizes ($r = 0.45$–0.75) reported in the literature on associations between pro-inflammatory cytokine levels and depression (Liu et al., 2012), between GSH and depression in a pilot study of 11 adults with and 10 adults without depression (Lapidus et al., 2014), and in our pilot data in an independent sample of 22 adolescents with familial risk of mood disorders with elevated depression symptoms who do not meet criteria for MDD ($r = 0.31$), the estimated power to detect a significant association between all our key variables will range from **0.65 to 0.90** with $N = 60$.

To test the hypothesis of our primary aim that glutamate concentrations in the ACC mediate the associations between higher levels of pro-inflammatory cytokines and depressive neurophenotypes (e.g., cingulum FA), we will conduct separate (one for each outcome) mediation models to test whether the effects of T1 cytokines on longitudinal trajectories in these depressive phenotypes are mediated through early changes (changes between T1 and T2) in ACC Glu. We will follow the eligibility and analytical criteria of MacArthur approach for mediator analysis (Kraemer et al., 2002; Kraemer and Gibbons, 2009), which will be examined by two tests: (1) whether T1 cytokines are significantly correlated with early changes (change between T1 and T2) in ACC Glu (eligibility criteria for mediators); and (2) whether early changes in ACC Glu are significantly correlated with longitudinal trajectories (i.e., estimated slopes) of depressive neurophenotypes (analytical criteria for mediators). Previous studies have documented moderately strong associations between Glu and inflammatory cytokines (Sanacora et al., 2012) as well as between Glu and MDD (Moriguchi et al., 2019); however, none have related Glu in ACC with cytokines specifically and no studies have examined whether changes in Glu are associated with longitudinal trajectories in neurophenotypes (i.e., with resting-state or white matter connectivity). Thus, using a conservative effect size of $r = 0.4$ for both tests, assuming 15% missing data by T3, and conservatively assuming ICC = 0.7 for ACC connectivity based on previous longitudinal MRI studies (Bonekamp et al., 2007; Thomason et al., 2011), we estimate that the power to analytically identify ACC Glu as a mediator is **0.79**. Because of the absence of data in the literature on whether GSH and/or Asc are potential moderators of associations among inflammation, Glu and depressive neurophenotypes, we will focus on hypothesis generation and clinical significance (effect sizes) for the second aim of our study.

Finally, we will use linear models to compare recurrence and remission status by T3 from T1 levels of cytokines, GSH and Asc in ACC, and Glu in ACC. We will also use the intercepts and slopes of ACC connectivity that are estimated from our mixed effects models to compare the groups on longitudinal trajectories of neurophenotypes. Because there are no studies to date comparing trajectories of ACC connectivity in either adolescents or adults with recurrent MDD with recovered counterparts, we estimated power according to effect sizes reported in changes in depressive symptoms between these two groups in adults ($r = 0.68$–0.78; Vittengl et al., 2007). Under these assumptions, and assuming 15% attrition by T3 ($N = 51$), the estimated power to detect group differences is **0.87**.

DISCUSSION

In summary, in the TIGER study we are comprehensively assessing neurobiological phenotypes of MDD and identifying predictors of recurrence of depression in adolescents. The main aims of this longitudinal study are three-fold: (1) to determine whether glutamate in the ACC mediates the associations between elevated pro-inflammatory cytokines and depressive neurophenotypes; (2) to examine whether antioxidants, such as glutathione and ascorbate, moderate the associations among ACC glutamate concentrations, peripheral levels of inflammation, and longitudinal trajectories of ACC connectivity; (3) to identify neurobiological and clinical predictors of the recurrence of depression over 18 months.

This study is novel in its multimodal approach of examining stress-related mechanisms that contribute to the development and persistence of depression in adolescents. By identifying predictors and mechanisms of the recurrence of depression in adolescents, we are taking an important initial step in generating subtypes or biotypes (i.e., scientifically informed neural subtypes) of depression that will elucidate our understanding of the phenomenology of depression and inform treatment strategies. For example, it is likely that not all depressed adolescents exhibit heightened inflammation or ACC glutamate (relative to healthy controls); those who do may represent a distinct subtype or biotype of depression that does not respond well to first-line treatments. Although TIGER is not a treatment study, we will be able to explore such possibilities, which may inform future research seeking to examine or monitor the efficacy of novel treatments for adolescent depression.

Moreover, given the heterogeneity in subject selection, sample size, scan sequence parameters, field of strength of scanner, and voxel location in previous studies using MRS to examine neurometabolites implicated in depression (Yüksel and Öngür, 2010; Luykx et al., 2012; Moriguchi et al., 2019), a major strength of the multimodal neuroimaging approach of TIGER is that it allows us to integrate information from multiple neuroimaging modalities (e.g., fMRI, diffusion MRI) to enable us to reconcile these potential discrepancies in the literature and gain a more precise understanding of glutamatergic abnormalities underlying MDD (Salvadore and Zarate, 2010; Mathews et al., 2012). Finally, because of the comprehensive clinical and neurobiological data we will be collecting, we will also be in a position to explore additional hypotheses and projects spanning topics outside the main aims of the study, including identifying correlates and predictors of STBs, NSSI behaviors, and examining the contribution of the type and timing of stress to the onset, course, and neurophenotypes of depression.

Although our study has a number of strengths, it also has important limitations. First, we expect some attrition by the end of this longitudinal study, which may reduce statistical

power to test all study aims. While we explicitly assumed 15% attrition by the end of the study in our power analyses and are utilizing mixed effects modeling which can account for some missing data (Little and Rubin, 2002), unanticipated events (i.e., COVID-19 pandemic) may further reduce our statistical power. Thus, larger investigations will be necessary to replicate our findings before they can be translated to clinical practice. Second, the age range for inclusion in our study is fairly broad. We selected this age range based on epidemiological rates of the onset of depression (Breslau et al., 2017) while seeking to maximize feasibility in recruitment. Moreover, because we will be assessing adolescents across a relatively wider age range, we will be positioned to model age-related associations in ACC connectivity across the study sample that will allow us estimate patterns of typical and atypical (i.e., depression) trajectories. Nevertheless, it will be important for future investigations to consider recruiting a sample with minimal variability in age in order to better understand the effects of stress-related inflammation and glutamate on neurodevelopment. Third, data collection will occur primarily in laboratory-based settings, which may reduce the generalizability of our study results with respect to the severity and range of symptom profiles, given that a minimum level of functioning is necessary for attending in-lab assessments. Future investigations that rely on naturalistic and easily acquired data are needed to generate scalable markers of behavior and cognition that are neurobiologically validated in order to facilitate the widespread identification of depression (including subtypes or biotypes) in adolescents. Fourth, there are also potential circadian effects on inflammatory markers and neurometabolite concentrations that also need to be considered, particularly in light of compelling evidence of disturbances of sleep and circadian biology in depression (Clarke and Harvey, 2012; Orchard et al., 2020; Walker et al., 2020). While we will be collecting time of day for each measure we collect, which can be used as covariates in sensitivity analyses, future work will be needed to more comprehensively assess circadian rhythms, as well as sleep chronotype and other related factors, on these variables and their processes. Finally, although we are including adolescents who have subthreshold depression according to DSM criteria, dimensional frameworks that conceptualize and characterize the heterogeneity of symptom presentation found in mood and anxiety disorders more broadly (e.g., RDoC and HiTOP; Cuthbert and Insel, 2013; Kotov et al., 2017) are particularly promising approaches to generating novel brain-based models that can lead to the effective treatment – and possibly prevention – of these debilitating conditions.

In conclusion, the TIGER project will collect comprehensive neurobiological, clinical, and cognitive data to assess the associations between inflammatory and glutamatergic pathways to predict the recurrence of depression in adolescents. The ultimate aim of the TIGER project is to set the foundation for brain-based models of depression in adolescents by elucidating neurobiological mechanisms that facilitate risk identification and treatment decisions, and by informing research focused on the development of novel treatment targets for this particularly vulnerable population.

ETHICS STATEMENT

The studies involving human participants were reviewed and approved by Stanford University Institutional Review Board and University of California, San Francisco Institutional Review Board. Participants under the age of 18 provided written informed assent and their parent(s)/legal guardian(s) provided written informed consent on their behalf. Participants 18 and older provided written informed consent.

AUTHOR CONTRIBUTIONS

TH, IG, MS, MG, DS, YR-H, and HM designed the study. TH obtained funding for the study. JW, GT, RW, JS, and TH wrote the first draft of the manuscript. All authors contributed to the writing of the manuscript.

FUNDING

This work was supported by the National Institutes of Health (K01MH117442 to TH, R37MH101495 to IG), the Klingenstein Third Generation Foundation (Child and Adolescent Depression Fellow Award to TH), the Stanford Maternal and Child Health Research Institute (Early Career Award and K Support Award to TH), the Stanford Center for Cognitive and Neurobiological Imaging (Seed Grant to TH), and the Ray and Dagmar Dolby Family Fund (to TH). The funding agencies played no role in the preparation, review, or approval of this manuscript.

ACKNOWLEDGMENTS

We would like to thank Drs. Laima Baltusis, Andrew Krystal, Thomas McDade, George Slavich, Owen Wolkowitz, Hua Wu, Duan Xu, and Tony Yang for guidance and consultation on various aspects of this project.

REFERENCES

Aghajani, M., Veer, I., Van Lang, N., Meens, P., Van den Bulk, B., Rombouts, S., et al. (2014). Altered white-matter architecture in treatment-naive adolescents with clinical depression. *Psychol. Med.* 44, 2287–2298. doi: 10.1017/S0033291713003000

Andrews-Hanna, J. R., Reidler, J. S., Sepulcre, J., Poulin, R., and Buckner, R. L. (2010). Functional-anatomic fractionation of the brain's default network. *Neuron* 65, 550–562. doi: 10.1016/j.neuron.2010.02.005

Asarnow, J. R., Porta, G., Spirito, A., Emslie, G., Clarke, G., Wagner, K. D., et al. (2011). Suicide attempts and nonsuicidal self-injury in the treatment of resistant depression in adolescents: findings from the TORDIA trial.

J. Am. Acad. Child Adolesc. Psychiatry 50, 772–781. doi: 10.1016/j.jaac.2011.04.003

Ballaz, S., Morales, I., Rodríguez, M., and Obeso, J. A. (2013). Ascorbate prevents cell death from prolonged exposure to glutamate in an in vitro model of human dopaminergic neurons. *J. Neurosci. Res.* 91, 1609–1617. doi: 10.1002/jnr.23276

Banks, W. A., Lynch, J. L., and Price, T. O. (2009). "Cytokines and the blood–brain barrier," in *The Neuroimmunological Basis of Behavior and Mental Disorders*, eds A. Siegel and S. S. Zalcman (Boston, MA: Springer).

Beckmann, C. F., Mackay, C. E., Filippini, N., and Smith, S. M. (2009). Group comparison of resting-state FMRI data using multi-subject ICA and dual regression. *NeuroImage* 47:S148. doi: 10.1016/S1053-8119(09)71511-3

Bernstein, D. P., Fink, L., Handelsman, L., Foote, J., Lovejoy, M., Wenzel, K., et al. (1994). Initial reliability and validity of a new retrospective measure of child abuse and neglect. *Am. J. Psychiatry* 151, 1132–1136. doi: 10.1176/ajp.151.8.1132

Bernstein, D. P., Stein, J. A., Newcomb, M. D., Walker, E., Pogge, D., Ahluvalia, T., et al. (2003). Development and validation of a brief screening version of the Childhood Trauma Questionnaire. *Child Abuse Negl.* 27, 169–190. doi: 10.1016/S0145-2134(02)00541-0

Bessette, K. L., Nave, A. M., Caprihan, A., and Stevens, M. C. (2014). White matter abnormalities in adolescents with major depressive disorder. *Brain Imaging Behav.* 8, 531–541. doi: 10.1007/s11682-013-9274-8

Birmaher, B., and Arbelaez, C. (2002). Course and outcome of child and adolescent major depressive disorder. *Child Adolesc. Psychiatr. Clin. N. Am.* 11, 619–637. doi: 10.1016/S1056-4993(02)00011-1

Birmaher, B., and Brent, D. (2007). Practice parameter for the assessment and treatment of children and adolescents with depressive disorders. *J. Am. Acad. Child Adolesc. Psychiatry* 46, 1503–1526. doi: 10.1097/chi.0b013e318145ae1c

Bodenhausen, G., Freeman, R., and Turner, D. L. (1977). Suppression of artifacts in two-dimensional J spectroscopy. *J. Magn. Reson. Imaging* 27, 511–514. doi: 10.1016/0022-2364(77)90016-6

Bonekamp, D., Nagae, L. M., Degaonkar, M., Matson, M., Abdalla, W. M. A., Barker, P. B., et al. (2007). Diffusion tensor imaging in children and adolescents: reproducibility, hemispheric, and age-related differences. *NeuroImage* 34, 733–742. doi: 10.1016/j.neuroimage.2006.09.020

Botvinick, M. M., Cohen, J. D., and Carter, C. S. (2004). Conflict monitoring and anterior cingulate cortex: an update. *Trends Cogn. Sci.* 8, 539–546. doi: 10.1016/j.tics.2004.10.003

Brand, A., Richter-Landsberg, C., and Leibfritz, D. (1993). Multinuclear NMR studies on the energy metabolism of glial and neuronal cells. *Dev. Neurosci.* 15, 289–298. doi: 10.1159/000111347

Breen, R., Hannan, D. F., Rottman, D. B., and Whelan, C. T. (2016). *Understanding Contemporary Ireland: State, Class and Development in the Republic of Ireland*. Cham: Springer.

Breslau, J., Gilman, S. E., Stein, B. D., Ruder, T., Gmelin, T., and Miller, E. (2017). Sex differences in recent first-onset depression in an epidemiological sample of adolescents. *Transl. Psychiatry* 7:e1139. doi: 10.1038/tp.2017.105

Burwell, R. A., and Shirk, S. R. (2007). Subtypes of rumination in adolescence: associations between brooding, reflection, depressive symptoms, and coping. *J. Clin. Child Adolesc. Psychol.* 36, 56–65. doi: 10.1080/15374410709336568

Cha, C. B., Augenstein, T. M., Frost, K. H., Gallagher, K., D'Angelo, E. J., and Nock, M. K. (2016). Using implicit and explicit measures to predict nonsuicidal self-injury among adolescent inpatients. *J. Am. Acad. Child Adolesc. Psychiatry* 55, 62–68. doi: 10.1016/j.jaac.2015.10.008

Cicchetti, D., and Rogosch, F. A. (2002). A developmental psychopathology perspective on adolescence. *J. Consult. Clin. Psychol.* 70, 6–20. doi: 10.1037/0022-006X.70.1.6

Clarke, G., and Harvey, A. G. (2012). The complex role of sleep in adolescent depression. *Child Adolesc. Psychiatr. Clin. N. Am.* 21, 385–400. doi: 10.1016/j.chc.2012.01.006

Coleman, L., and Coleman, J. (2002). The measurement of puberty: a review. *J. Adolesc.* 25, 535–550. doi: 10.1006/jado.2002.0494

Connolly, C. G., Ho, T. C., Blom, E. H., LeWinn, K. Z., Sacchet, M. D., Tymofiyeva, O., et al. (2017). Resting-state functional connectivity of the amygdala and longitudinal changes in depression severity in adolescent depression. *J. Affect. Disord.* 207, 86–94. doi: 10.1016/j.jad.2016.09.026

Connolly, C. G., Wu, J., Ho, T. C., Hoeft, F., Wolkowitz, O., Eisendrath, S., et al. (2013). Resting-state functional connectivity of subgenual anterior cingulate cortex in depressed adolescents. *Biol. Psychiatry* 74, 898–907. doi: 10.1016/j.biopsych.2013.05.036

Costello, E. J., Pine, D. S., Hammen, C., March, J. S., Plotsky, P. M., Weissman, M. M., et al. (2002). Development and natural history of mood disorders. *Biol. Psychiatry* 52, 529–542. doi: 10.1016/S0006-3223(02)01372-0

Cunningham, W. A., Preacher, K. J., and Banaji, M. R. (2001). Implicit attitude measures: consistency, stability, and convergent validity. *Psychol. Sci.* 12, 163–170. doi: 10.1111/1467-9280.00328

Curry, J., Silva, S., Rohde, P., Ginsburg, G., Kratochvil, C., Simons, A., et al. (2011). Recovery and recurrence following treatment for adolescent major depression. *Arch. Gen. Psychiatry* 68, 263–269. doi: 10.1001/archgenpsychiatry.2010.150

Cuthbert, B. N., and Insel, T. R. (2013). Toward the future of psychiatric diagnosis: the seven pillars of RDoC. *BMC Med.* 11:126. doi: 10.1186/1741-7015-11-126

Dantzer, R. (2017). Role of the kynurenine metabolism pathway in inflammation-induced depression – Preclinical approaches. *Curr. Top. Behav. Neurosci.* 31, 117–138. doi: 10.1007/7854_2016_6

Davey, C. G., Yücel, M., Allen, N. B., and Harrison, B. J. (2012). Task-related deactivation and functional connectivity of the subgenual cingulate cortex in major depressive disorder. *Front. Psychiatry* 3:14. doi: 10.3389/fpsyt.2012.00014

Desikan, R. S., Ségonne, F., Fischl, B., Quinn, B. T., Dickerson, B. C., Blacker, D., et al. (2006). An automated labeling system for subdividing the human cerebral cortex on MRI scans into gyral based regions of interest. *NeuroImage* 31, 968–980. doi: 10.1016/j.neuroimage.2006.01.021

Dunn, V., and Goodyer, I. M. (2006). Longitudinal investigation into childhood- and adolescence-onset depression: psychiatric outcome in early adulthood. *Br. J. Psychiatry* 188, 216–222. doi: 10.1192/bjp.188.3.216

Fergusson, D. M., Boden, J. M., and Horwood, L. J. (2007). Recurrence of major depression in adolescence and early adulthood, and later mental health, educational and economic outcomes. *Br. J. Psychiatry* 191, 335–342. doi: 10.1192/bjp.bp.107.036079

Fischl, B., Salat, D. H., Busa, E., Albert, M., Dieterich, M., Haselgrove, C., et al. (2002). Whole brain segmentation: automated labeling of neuroanatomical structures in the human brain. *Neuron* 33, 341–355. doi: 10.1016/s0896-6273(02)00569-x

Franklin, J. C., Ribeiro, J. D., Fox, K. R., Bentley, K. H., Kleiman, E. M., Huang, X., et al. (2017). Risk factors for suicidal thoughts and behaviors: a meta-analysis of 50 years of research. *Psychol. Bull.* 143, 187–232. doi: 10.1037/bul0000084

Gabbay, V., Bradley, K. A., Mao, X., Ostrover, R., Kang, G., and Shungu, D. C. (2017). Anterior cingulate cortex γ-aminobutyric acid deficits in youth with depression. *Transl. Psychiatry* 7:e1216. doi: 10.1038/tp.2017.187

Gershon, E. S., DeLisi, L. E., Hamovit, J., Nurnberger, J. I., Maxwell, M. E., Schreiber, J., et al. (1988). A controlled family study of chronic psychoses: schizophrenia and schizoaffective disorder. *Arch. Gen. Psychiatry* 45, 328–336. doi: 10.1001/archpsyc.1988.01800280038006

Gipson, P. Y., Agarwala, P., Opperman, K. J., Horwitz, A., and King, C. A. (2015). Columbia-suicide severity rating scale: predictive validity with adolescent psychiatric emergency patients. *Pediatr. Emerg. Care* 31, 88–94. doi: 10.1097/PEC.0000000000000225

Glenn, C. R., Millner, A. J., Esposito, E. C., Porter, A. C., and Nock, M. K. (2019). Implicit identification with death predicts suicidal thoughts and behaviors in adolescents. *J. Clin. Child Adolesc. Psychol.* 48, 263–272. doi: 10.1080/15374416.2018.1528548

Gotlib, I. H., and Ordaz, S. J. (2016). The importance of assessing neural trajectories in pediatric depression. *JAMA Psychiatry* 73, 9–10. doi: 10.1001/jamapsychiatry.2015.2453

Gratz, K. L., and Roemer, L. (2003). Multidimensional assessment of emotion regulation and dysregulation: development, factor structure, and initial validation of the difficulties in emotion regulation scale. *J. Psychopathol. Behav. Assess.* 14, 41–54. doi: 10.1023/b:joba.0000007455.08539.94

Greenberg, P. E., Fournier, A.-A., Sisitsky, T., Pike, C. T., and Kessler, R. C. (2015). The economic burden of adults with major depressive disorder in the United States (2005 and 2010). *J. Clin. Psychiatry* 76, 155–162. doi: 10.4088/JCP.14m09298

Griffin, J. L., Bollard, M., Nicholson, J. K., and Bhakoo, K. (2002). Spectral profiles of cultured neuronal and glial cells derived from HRMAS (1)H NMR spectroscopy. *NMR Biomed.* 15, 375–384. doi: 10.1002/nbm.792

Gu, M., Hurd, R., Noeske, R., Baltusis, L., Hancock, R., Sacchet, M. D., et al. (2018). GABA editing with macromolecule suppression using an improved

MEGA-SPECIAL sequence. *Magn. Reson. Med.* 79, 41–47. doi: 10.1002/mrm.26691

Guan, K., Fox, K. R., and Prinstein, M. J. (2012). Nonsuicidal self-injury as a time-invariant predictor of adolescent suicide ideation and attempts in a diverse community sample. *J. Consult. Clin. Psychol.* 80, 842–849. doi: 10.1037/a0029429

Guillemin, G. J., Kerr, S. J., Smythe, G. A., Smith, D. G., Kapoor, V., Armati, P. J., et al. (2001). Kynurenine pathway metabolism in human astrocytes: a paradox for neuronal protection. *J. Neurochem.* 78, 842–853. doi: 10.1046/j.1471-4159.2001.00498.x

Hallion, L. S., Steinman, S. A., Tolin, D. F., and Diefenbach, G. J. (2018). Psychometric properties of the difficulties in emotion regulation scale (DERS) and its short forms in adults with emotional disorders. *Front. Psychol.* 9:539. doi: 10.3389/fpsyg.2018.00539

Hammen, C. (2005). Stress and depression. *Annu. Rev. Clin. Psychol.* 1, 293–319. doi: 10.1146/annurev.clinpsy.1.102803.143938

Haroon, E., Miller, A. H., and Sanacora, G. (2017). Inflammation, glutamate, and glia: a trio of trouble in mood disorders. *Neuropsychopharmacology* 42, 193–215. doi: 10.1038/npp.2016.199

Hasin, D. S., O'Brien, C. P., Auriacombe, M., Borges, G., Bucholz, K., Budney, A., et al. (2013). DSM-5 criteria for substance use disorders: recommendations and rationale. *Am. J. Psychiatry* 170, 834–851. doi: 10.1176/appi.ajp.2013.12060782

Ho, T. C. (2019). Stress and neurodevelopment in adolescent depression. *Biol. Psychiatry* 86:e33. doi: 10.1016/j.biopsych.2019.09.012

Ho, T. C., Cichocki, A. C., Gifuni, A. J., Catalina Camacho, M., Ordaz, S. J., Singh, M. K., et al. (2018). Reduced dorsal striatal gray matter volume predicts implicit suicidal ideation in adolescents. *Soc. Cogn. Affect. Neurosci.* 13, 1215–1224. doi: 10.1093/scan/nsy089

Ho, T. C., Colich, N. L., Sisk, L. M., Oskirko, K., Jo, B., and Gotlib, I. H. (2020). Sex differences in the effects of gonadal hormones on white matter microstructure development in adolescence. *Dev. Cogn. Neurosci.* 42:100773. doi: 10.1016/j.dcn.2020.100773

Ho, T. C., Connolly, C. G., Henje Blom, E., LeWinn, K. Z., Strigo, I. A., Paulus, M. P., et al. (2015). Emotion-dependent functional connectivity of the default mode network in adolescent depression. *Biol. Psychiatry* 78, 635–646. doi: 10.1016/j.biopsych.2014.09.002

Ho, T. C., King, L. S., Leong, J. K., Colich, N. L., Humphreys, K. L., Ordaz, S. J., et al. (2017a). Effects of sensitivity to life stress on uncinate fasciculus segments in early adolescence. *Soc. Cogn. Affect. Neurosci.* 12, 1460–1469. doi: 10.1093/scan/nsx065

Ho, T. C., Sacchet, M. D., Connolly, C. G., Margulies, D. S., Tymofiyeva, O., Paulus, M. P., et al. (2017b). Inflexible functional connectivity of the dorsal anterior cingulate cortex in adolescent major depressive disorder. *Neuropsychopharmacology* 42, 2434–2445. doi: 10.1038/npp.2017.103

Ho, T. C., Wu, J., Shin, D. D., Liu, T. T., Tapert, S. F., Yang, G., et al. (2013). Altered cerebral perfusion in executive, affective, and motor networks during adolescent depression. *J. Am. Acad. Child Adolesc. Psychiatry* 52, 1076.e2–1091.e2. doi: 10.1016/j.jaac.2013.07.008

Ho, T. C., Yang, G., Wu, J., Cassey, P., Brown, S. D., Hoang, N., et al. (2014). Functional connectivity of negative emotional processing in adolescent depression. *J. Affect. Disord.* 155, 65–74. doi: 10.1016/j.jad.2013.10.025

Ho, T. C., Zhang, S., Sacchet, M. D., Weng, H., Connolly, C. G., Henje Blom, E., et al. (2016). Fusiform gyrus dysfunction is associated with perceptual processing efficiency to emotional faces in adolescent depression: a model-based approach. *Front. Psychol.* 7:40. doi: 10.3389/fpsyg.2016.00040

Hong, J. S., and Espelage, D. L. (2012). A review of research on bullying and peer victimization in school: an ecological system analysis. *Aggress. Violent Behav.* 17, 311–322. doi: 10.1016/j.avb.2012.03.003

Howren, M. B., Lamkin, D. M., and Suls, J. (2009). Associations of depression with C-reactive protein, IL-1, and IL-6: a meta-analysis. *Psychos. Med.* 71, 171–186. doi: 10.1097/PSY.0b013e3181907c1b

Humphreys, K. L., LeMoult, J., Wear, J. G., Piersiak, H. A., Lee, A., and Gotlib, I. H. (2020). Child maltreatment and depression: a meta-analysis of studies using the childhood trauma questionnaire. *Child Abuse Negl.* 102:104361. doi: 10.1016/j.chiabu.2020.104361

Isa, A., Bernstein, I., Trivedi, M., Mayes, T., Kennard, B., and Emslie, G. (2014). Childhood depression subscales using repeated sessions on children's depression rating scale – revised (CDRS-R) scores. *J. Child Adolesc. Psychopharmacol.* 24, 318–324. doi: 10.1089/cap.2013.0127

Joseph, S., and Stockton, H. (2018). The multidimensional peer victimization scale: a systematic review. *Aggress. Viol. Behav.* 42, 96–114. doi: 10.1016/j.avb.2018.07.009

Káradóttir, R., and Attwell, D. (2007). Neurotransmitter receptors in the life and death of oligodendrocytes. *Neuroscience* 145, 1426–1438. doi: 10.1016/j.neuroscience.2006.08.070

Kaufman, E. A., Xia, M., Fosco, G., Yaptangco, M., Skidmore, C. R., and Crowell, S. E. (2016). The difficulties in emotion regulation scale short form (DERS-SF): validation and replication in adolescent and adult samples. *J. Psychopathol. Behav. Assess.* 38, 443–455. doi: 10.1007/s10862-015-9529-3

Kaufman, J., Birmaher, B., Brent, D. A., Ryan, N. D., and Rao, U. (2000). K-SADS-PL. *J. Am. Acad. Child Adolesc. Psychiatry* 39, 1208–1208. doi: 10.1097/00004583-200010000-00002

Kerestes, R., Davey, C. G., Stephanou, K., Whittle, S., and Harrison, B. J. (2014). Functional brain imaging studies of youth depression: a systematic review. *NeuroImage Clin.* 4, 209–231. doi: 10.1016/j.nicl.2013.11.009

Kiviniemi, V., Kantola, J. H., Jauhiainen, J., Hyvärinen, A., and Tervonen, O. (2003). Independent component analysis of nondeterministic fMRI signal sources. *NeuroImage* 19(2 Pt 1), 253–260. doi: 10.1016/s1053-8119(03)00097-1

Klonsky, E. D., May, A. M., and Glenn, C. R. (2013). The relationship between nonsuicidal self-injury and attempted suicide: converging evidence from four samples. *J. Abnorm. Psychol.* 122, 231–237. doi: 10.1037/a0030278

Koenig, S. H., Brown, R. D. III, Spiller, M., and Lundbom, N. (1990). Relaxometry of brain: why white matter appears bright in MRI. *Magn. Reson. Med.* 14, 482–495. doi: 10.1002/mrm.1910140306

Kökönyei, G., Urbán, R., Reinhardt, M., Józan, A., and Demetrovics, Z. (2014). The difficulties in emotion regulation scale: factor structure in chronic pain patients. *J. Clin. Psychol.* 70, 589–600. doi: 10.1002/jclp.22036

Kolling, N., Wittmann, M. K., Behrens, T. E. J., Boorman, E. D., Mars, R. B., and Rushworth, M. F. S. (2016). Value, search, persistence and model updating in anterior cingulate cortex. *Nat. Neurosci.* 19, 1280–1285. doi: 10.1038/nn.4382

Kotov, R., Krueger, R. F., Watson, D., Achenbach, T. M., Althoff, R. R., Bagby, R. M., et al. (2017). The hierarchical taxonomy of psychopathology (HiTOP): a dimensional alternative to traditional nosologies. *J. Abnorm. Psychol.* 126, 454–477. doi: 10.1037/abn0000258

Kraemer, H. C., and Gibbons, R. D. (2009). Why does the randomized clinical trial methodology so often mislead clinical decision making? Focus on moderators and mediators of treatment. *Psychiatr. Ann.* 39, 736–745. doi: 10.3928/00485713-20090625-06

Kraemer, H. C., Wilson, G. T., Fairburn, C. G., and Agras, W. S. (2002). Mediators and moderators of treatment effects in randomized clinical trials. *Arch. Gen. Psychiatry* 59, 877–883. doi: 10.1001/archpsyc.59.10.877

Kroenke, K., Spitzer, R. L., and Williams, J. B. W. (2001). The PHQ-9. *J. Gen. Intern. Med.* 16, 606–613. doi: 10.1046/j.1525-1497.2001.016009606.x

Kuyken, W., Watkins, E., Holden, E., and Cook, W. (2006). Rumination in adolescents at risk for depression. *J. Affect. Disord.* 96, 39–47. doi: 10.1016/j.jad.2006.05.017

Lane, K. A., Banaji, M. R., Nosek, B. A., and Greenwald, A. G. (2007). "Understanding and using the implicit association test: IV," in *Implicit Measures of Attitudes*, eds B. Wittenbrink and N. Schwarz (New York, NY: The Guilford Press).

Lapidus, K. A. B., Gabbay, V., Mao, X., Johnson, A., Murrough, J. W., Mathew, S. J., et al. (2014). In vivo (1)H MRS study of potential associations between glutathione, oxidative stress and anhedonia in major depressive disorder. *Neurosci. Lett.* 569, 74–79. doi: 10.1016/j.neulet.2014.03.056

LeMoult, J., Humphreys, K. L., Tracy, A., Hoffmeister, J. A., Ip, E., and Gotlib, I. H. (2020). Meta-analysis: exposure to early life stress and risk for depression in childhood and adolescence. *J. Am. Acad. Child Adolesc. Psychiatry* 59, 842–855. doi: 10.1016/j.jaac.2019.10.011

LeWinn, K. Z., Connolly, C. G., Wu, J., Drahos, M., Hoeft, F., Ho, T. C., et al. (2014). White matter correlates of adolescent depression: structural evidence

for frontolimbic disconnectivity. *J. Am. Acad. Child Adolesc. Psychiatry* 53, 899.e7–909.e7. doi: 10.1016/j.jaac.2014.04.021

Lichenstein, S. D., Verstynen, T., and Forbes, E. E. (2016). Adolescent brain development and depression: a case for the importance of connectivity of the anterior cingulate cortex. *Neurosci. Biobehav. Rev.* 70, 271–287. doi: 10.1016/j.neubiorev.2016.07.024

Little, R. J., and Rubin, D. B. (2002). *Statistical Analysis with Missing Data*. New York, NY: John Wiley & Sons.

Liu, Y., Ho, R. C.-M., and Mak, A. (2012). Interleukin (IL)-6, tumour necrosis factor alpha (TNF-α) and soluble interleukin-2 receptors (sIL-2R) are elevated in patients with major depressive disorder: a meta-analysis and meta-regression. *J. Affect. Disord.* 139, 230–239. doi: 10.1016/j.jad.2011.08.003

Luby, J. L., Belden, A. C., Jackson, J. J., Lessov-Schlaggar, C. N., Harms, M. P., Tillman, R., et al. (2016). Early childhood depression and alterations in the trajectory of gray matter maturation in middle childhood and early adolescence. *JAMA Psychiatry* 73, 31–38. doi: 10.1001/jamapsychiatry.2015.2356

Luykx, J. J., Laban, K. G., van den Heuvel, M. P., Boks, M. P., Mandl, R. C., Kahn, R. S., et al. (2012). Region and state specific glutamate downregulation in major depressive disorder: a meta-analysis of (1)H-MRS findings. *Neurosci. Biobehav. Rev.* 36, 198–205. doi: 10.1016/j.neubiorev.2011.05.014

Maecker, H. T., Rosenberg-Hasson, Y., Kolstad, K. D., Steen, V. D., and Chung, L. S. (2020). A novel utility to correct for plate/batch/lot and nonspecific binding artifacts in luminex data. *J. Immunol.* 204, 3425–3433. doi: 10.4049/jimmunol.2000017

March, J. S. (2012). *Multidimensional Anxiety Scale for Children*, 2nd Edn. North Tonawanda, NY: Multi-Health Systems.

March, J. S., Parker, J. D. A., Sullivan, K., Stallings, P., and Conners, C. K. (1997). The multidimensional anxiety scale for children (MASC): factor structure, reliability, and validity. *J. Am. Acad. Child Adolesc. Psychiatry* 36, 554–565. doi: 10.1097/00004583-199704000-00019

Marshall, W. A., and Tanner, J. M. (1968). Growth and physiological development during adolescence. *Annu. Rev. Med.* 19, 283–300. doi: 10.1146/annurev.me.19.020168.001435

Marshall, W. A., and Tanner, J. M. (1970). Variations in the pattern of pubertal changes in boys. *Arch. Dis. Child.* 45, 13–23. doi: 10.1136/adc.45.239.13

Mathews, D. C., Henter, I. D., and Zarate, C. A. (2012). Targeting the glutamatergic system to treat major depressive disorder: rationale and progress to date. *Drugs* 72, 1313–1333. doi: 10.2165/11633130-000000000-00000

Matute, C. (2011). Glutamate and ATP signaling in white matter pathology. *J. Anat.* 219, 53–64. doi: 10.1111/j.1469-7580.2010.01339.x

McEwen, B. S. (2012). Brain on stress: how the social environment gets under the skin. *Proc. Natl. Acad. Sci. U.S.A.* 109(Suppl. 2), 17180–17185. doi: 10.1073/pnas.1121254109

McLaughlin, K. A., Greif Green, J., Gruber, M. J., Sampson, N. A., Zaslavsky, A. M., and Kessler, R. C. (2012). Childhood adversities and first onset of psychiatric disorders in a national sample of US adolescents. *Arch. Gen. Psychiatry* 69, 1151–1160. doi: 10.1001/archgenpsychiatry.2011.2277

Melhem, N. M., Porta, G., Oquendo, M. A., Zelazny, J., Keilp, J. G., Iyengar, S., et al. (2019). Severity and Variability of Depression Symptoms Predicting Suicide Attempt in High-Risk Individuals. *JAMA Psychiatry* 76, 603–613. doi: 10.1001/jamapsychiatry.2018.4513

Ménard, C., Hodes, G. E., and Russo, S. J. (2016). Pathogenesis of depression: insights from human and rodent studies. *Neuroscience*, 321, 138–162. doi: 10.1016/j.neuroscience.2015.05.053

Menon, V., and Uddin, L. Q. (2010). Saliency, switching, attention and control: a network model of insula function. *Brain Struct. Func.* 214, 655–667. doi: 10.1007/s00429-010-0262-0

Miller, A. H., Maletic, V., and Raison, C. L. (2009). Inflammation and its discontents: the role of cytokines in the pathophysiology of major depression. *Biol. Psychiatry* 65, 732–741. doi: 10.1016/j.biopsych.2008.11.029

Miller, A. H., and Raison, C. L. (2016). The role of inflammation in depression: from evolutionary imperative to modern treatment target. *Nat. Rev. Immunol.* 16, 22–34. doi: 10.1038/nri.2015.5

Miller, E. M., and McDade, T. W. (2012). A highly sensitive immunoassay for interleukin-6 in dried blood spots. *Am. J. Hum. Biol.* 24, 863–865. doi: 10.1002/ajhb.22324

Moriguchi, S., Takamiya, A., Noda, Y., Horita, N., Wada, M., Tsugawa, S., et al. (2019). Glutamatergic neurometabolite levels in major depressive disorder: a systematic review and meta-analysis of proton magnetic resonance spectroscopy studies. *Mol. Psychiatry* 24, 952–964. doi: 10.1038/s41380-018-0252-9

Morris, N. M., and Udry, J. R. (1980). Validation of a self-administered instrument to assess stage of adolescent development. *J. Youth Adolesc.* 9, 271–280. doi: 10.1007/BF02088471

Mynard, H., and Joseph, S. (2000). Development of the multidimensional peer-victimization scale. *Aggress. Behav.* 26, 169–178. doi: 10.1002/(sici)1098-2337(2000)26:2<169::aid-ab3>3.0.co;2-a

Naicker, K., Galambos, N. L., Zeng, Y., Senthilselvan, A., and Colman, I. (2013). Social, demographic, and health outcomes in the 10 years following adolescent depression. *J. Adolesc Health* 52, 533–538. doi: 10.1016/j.jadohealth.2012.12.016

Nelson, C. A., and Gabard-Durnam, L. J. (2020). Early adversity and critical periods: neurodevelopmental consequences of violating the expectable environment. *Trends Neurosci.* 43, 133–143. doi: 10.1016/j.tins.2020.01.002

Neumann, A., van Lier, P. C., Gratz, K. L., and Koot, H. M. (2010). Multidimensional assessment of emotion regulation difficulties in adolescents using the difficulties in emotion regulation scale. *Assessment* 17, 138–149. doi: 10.1177/1073191109349579

Nock, M. K., Green, J. G., Hwang, I., McLaughlin, K. A., Sampson, N. A., Zaslavsky, A. M., et al. (2013). Prevalence, correlates and treatment of lifetime suicidal behavior among adolescents: results from the national comorbidity survey replication – adolescent supplement (NCS-A). *JAMA Psychiatry* 70:55. doi: 10.1001/2013.jamapsychiatry.55

Nock, M. K., Holmberg, E. B., Photos, V. I., and Michel, B. D. (2007). Self-Injurious Thoughts and Behaviors Interview: development, reliability, and validity in an adolescent sample. *Psychol. Assess.* 19, 309–317. doi: 10.1037/1040-3590.19.3.309

Nock, M. K., Joiner, T. E., Gordon, K. H., Lloyd-Richardson, E., and Prinstein, M. J. (2006). Non-suicidal self-injury among adolescents: diagnostic correlates and relation to suicide attempts. *Psychiatry Res.* 144, 65–72. doi: 10.1016/j.psychres.2006.05.010

Nock, M. K., Park, J. M., Finn, C. T., Deliberto, T. L., Dour, H. J., and Banaji, M. R. (2010). Measuring the suicidal mind: implicit cognition predicts suicidal behavior. *Psychol. Sci.* 21, 511–517. doi: 10.1177/0956797610364762

Nosek, B. A., Greenwald, A. G., and Banaji, M. R. (2005). Understanding and using the implicit association test: II. method variables and construct validity. *Pers. Soc. Psychol. Bull.* 31, 166–180. doi: 10.1177/0146167204271418

Orchard, F., Gregory, A. M., Gradisar, M., and Reynolds, S. (2020). Self-reported sleep patterns and quality amongst adolescents: cross-sectional and prospective associations with anxiety and depression. *J. Child Psychol. Psychiatry* [Epub ahead of print]. doi: 10.1111/jcpp.13288

Ordaz, S. J., Goyer, M. S., Ho, T. C., Singh, M. K., and Gotlib, I. H. (2018). Network basis of suicidal ideation in depressed adolescents. *J. Affect. Disord.* 226, 92–99. doi: 10.1016/j.jad.2017.09.021

Orgeta, V. (2009). Specificity of age differences in emotion regulation. *Aging Ment. Health* 13, 818–826. doi: 10.1080/13607860902989661

Posner, K., Brent, D., Lucas, C., Gould, M., Stanley, B., Brown, G., et al. (2008). *Columbia-Suicide Severity Rating Scale (C-SSRS)*. New York, NY: Columbia University Medical Center.

Posner, K., Brown, G. K., Stanley, B., Brent, D. A., Yershova, K. V., Oquendo, M. A., et al. (2011). The columbia–suicide severity rating scale: initial validity and internal consistency findings from three multisite studies with adolescents and adults. *Am. J. Psychiatry* 168, 1266–1277. doi: 10.1176/appi.ajp.2011.10111704

Power, J. D., Cohen, A. L., Nelson, S. M., Wig, G. S., Barnes, K. A., Church, J. A., et al. (2011). Functional network organization of the human brain. *Neuron* 72, 665–678. doi: 10.1016/j.neuron.2011.09.006

Power, J. D., Fair, D. A., Schlaggar, B. L., and Petersen, S. E. (2010). The development of human functional brain networks. *Neuron* 67, 735–748. doi: 10.1016/j.neuron.2010.08.017

Poznanski, E. O., and Mokros, H. B. (1996). *Children's Depression Rating Scale, Revised (CDRS-R)*. Los Angeles: Western Psychological Services.

Provencher, S. W. (2001). Automatic quantitation of localized in vivo 1H spectra with LCModel. *NMR Biomed.* 14, 260–264. doi: 10.1002/nbm.698

Raison, C. L., Rutherford, R. E., Woolwine, B. J., Shuo, C., Schettler, P., Drake, D. F., et al. (2013). A randomized controlled trial of the tumor necrosis factor antagonist infliximab for treatment-resistant depression: the role of baseline inflammatory biomarkers. *JAMA Psychiatry* 70, 31–41. doi: 10.1001/2013.jamapsychiatry.4

Ramadan, S., Lin, A., and Stanwell, P. (2013). Glutamate and glutamine: a review of in vivo MRS in the human brain. *NMR Biomed.* 26, 1630–1646. doi: 10.1002/nbm.3045

Raudenbush, S. W., and Bryk, A. S. (2002). *Hierarchical Linear Models: Applications and Data Analysis Methods*. Thousand Oaks, CA: SAGE.

Reese, T. G., Heid, O., Weisskoff, R. M., and Wedeen, V. J. (2003). Reduction of eddy-current-induced distortion in diffusion MRI using a twice-refocused spin echo. *Magn. Reson. Med.* 49, 177–182. doi: 10.1002/mrm.10308

Reynolds, W. M. (1987). *Suicidal Ideation Questionnaire-Junior*. Odessa, FL: Psychological Assessment Resources, 16–18.

Reynolds, W. M. (2002). *Manual for the Reynolds Adolescent Depression Scale—Second Edition (RADS-2)*. Lutz, FL: Psychological Assessment Resources.

Reynolds, W. M. (2010). *Reynolds Adolescent Depression Scale. In The Corsini Encyclopedia of Psychology*. Atlanta: American Cancer Society, 1–1.

Ribeiro, J. D., Huang, X., Fox, K. R., and Franklin, J. C. (2018). Depression and hopelessness as risk factors for suicide ideation, attempts and death: meta-analysis of longitudinal studies. *Br. J. Psychiatry* 212, 279–286. doi: 10.1192/bjp.2018.27

Rosenberg-Hasson, Y., Hansmann, L., Liedtke, M., Herschmann, I., and Maecker, H. T. (2014). Effects of serum and plasma matrices on multiplex immunoassays. *Immunol. Res.* 58, 224–233. doi: 10.1007/s12026-014-8491-6

Saad, Z. S., Glen, D. R., Chen, G., Beauchamp, M. S., Desai, R., and Cox, R. W. (2009). A new method for improving functional-to-structural MRI alignment using local Pearson correlation. *NeuroImage* 44, 839–848. doi: 10.1016/j.neuroimage.2008.09.037

Sacchet, M. D., and Gotlib, I. H. (2017). Myelination of the brain in major depressive disorder: an in vivo quantitative magnetic resonance imaging study. *Sci. Rep.* 7:2200. doi: 10.1038/s41598-017-02062-y

Sacchet, M. D., Ho, T. C., Connolly, C. G., Tymofiyeva, O., Lewinn, K. Z., Han, L. K., et al. (2016). Large-scale hypoconnectivity between resting-state functional networks in unmedicated adolescent major depressive disorder. *Neuropsychopharmacology* 41, 2951–2960. doi: 10.1038/npp.2016.76

Salvadore, G., and Zarate, C. A. Jr. (2010). Magnetic resonance spectroscopy studies of the glutamatergic system in mood disorders: a pathway to diagnosis, novel therapeutics, and personalized medicine? *Biol. Psychiatry* 68, 780–782. doi: 10.1016/j.biopsych.2010.09.011

Sanacora, G., Treccani, G., and Popoli, M. (2012). Towards a glutamate hypothesis of depression: an emerging frontier of neuropsychopharmacology for mood disorders. *Neuropharmacology* 62, 63–77. doi: 10.1016/j.neuropharm.2011.07.036

Sarıtaş-Atalar, D., Gençöz, T., and Özen, A. (2015). Confirmatory factor analyses of the difficulties in emotion regulation scale (DERS) in a Turkish adolescent sample. *Eur. J. Psychol. Assess.* 31, 12–19. doi: 10.1027/1015-5759/a000199

Sarlls, J. E., Pierpaoli, C., Talagala, S. L., and Luh, W. M. (2011). Robust fat suppression at 3T in high-resolution diffusion-weighted single-shot echo-planar imaging of human brain. *Magn. Reson. Med.* 66, 1658–1665. doi: 10.1002/mrm.22940

Schwartz, J., Ordaz, S. J., Ho, T. C., and Gotlib, I. H. (2019). Longitudinal decreases in suicidal ideation are associated with increases in salience network coherence in depressed adolescents. *J. Affect. Disord.* 245, 545–552. doi: 10.1016/j.jad.2018.11.009

Seeley, W. H., Menon, V., Schatzberg, A. F., Keller, J., Glover, G. H., Kenna, H., et al. (2007). Dissociable intrinsic connectivity networks for salience processing and executive control. *J. Neurosci.* 27, 2349–2356. doi: 10.1523/JNEUROSCI.5587-06.2007

Shenhav, A., Cohen, J. D., and Botvinick, M. M. (2016). Dorsal anterior cingulate cortex and the value of control. *Nat. Neurosci.* 19, 1286–1291. doi: 10.1038/nn.4384

Shirtcliff, E. A., Dahl, R. E., and Pollak, S. D. (2009). Pubertal development: correspondence between hormonal and physical development. *Child Dev.* 80, 327–337. doi: 10.1111/j.1467-8624.2009.01263.x

Silk, J. S., Steinberg, L., and Morris, A. S. (2003). Adolescents' emotion regulation in daily life: links to depressive symptoms and problem behavior. *Child Dev.* 74, 1869–1880. doi: 10.1046/j.1467-8624.2003.00643.x

Singer, J. D., Willett, J. B., Willett, C. W. E. P. J. B., and Willett, J. B. (2003). *Applied Longitudinal Data Analysis: Modeling Change and Event Occurrence*. Oxford: Oxford University Press.

Skogstrand, K., Thysen, A. H., Jørgensen, C. S., Rasmussen, E. M., Andersen, ÅB., Lillebaek, T., et al. (2012). Antigen-induced cytokine and chemokine release test for tuberculosis infection using adsorption of stimulated whole blood on filter paper and multiplex analysis. *Scand. J. Clin. Lab. Investig.* 72, 204–211. doi: 10.3109/00365513.2011.649014

Slavich, G. M., and Shields, G. S. (2018). Assessing lifetime stress exposure using the stress and adversity inventory for adults (Adult STRAIN): an overview and initial validation. *Psychos. Med.* 80, 17–27. doi: 10.1097/PSY.0000000000000534

Slavich, G. M., Stewart, J. G., Esposito, E. C., Shields, G. S., and Auerbach, R. P. (2019). The stress and adversity inventory for adolescents (Adolescent STRAIN): associations with mental and physical health, risky behaviors, and psychiatric diagnoses in youth seeking treatment. *J. Child Psychol. Psychiatry* 60, 998–1009. doi: 10.1111/jcpp.13038

Smith, D. V., Utevsky, A. V., Bland, A. R., Clement, N., Clithero, J. A., Harsch, A. E., et al. (2014). Characterizing individual differences in functional connectivity using dual-regression and seed-based approaches. *NeuroImage* 95, 1–12. doi: 10.1016/j.neuroimage.2014.03.042

Stapinski, L. A., Bowes, L., Wolke, D., Pearson, R. M., Mahedy, L., Button, K. S., et al. (2014). Peer victimization during adolescence and risk for anxiety disorders in adulthood: a prospective cohort study. *Depress. Anxiety* 31, 574–582. doi: 10.1002/da.22270

Stevens, F. L., Hurley, R. A., and Taber, K. H. (2011). Anterior cingulate cortex: unique role in cognition and emotion. *J. Neuropsychiatry Clin. Neurosci.* 23, 121–125. doi: 10.1176/jnp.23.2.jnp121

Stewart, J. G., Shields, G. S., Esposito, E. C., Cosby, E. A., Allen, N. B., Slavich, G. M., et al. (2019). Life stress and suicide in adolescents. *J. Abnorm. Child Psychol.* 47, 1707–1722. doi: 10.1007/s10802-019-00534-5

Stüber, C., Morawski, M., Schäfer, A., Labadie, C., Wähnert, M., Leuze, C., et al. (2014). Myelin and iron concentration in the human brain: a quantitative study of MRI contrast. *NeuroImage* 93(Pt 1), 95–106. doi: 10.1016/j.neuroimage.2014.02.026

Sweeting, H., Young, R., West, P., and Der, G. (2006). Peer victimization and depression in early-mid adolescence: a longitudinal study. *Br. J. Educ. Psychol.* 76(Pt 3), 577–594. doi: 10.1348/000709905X49890

Teachman, B. A., and Woody, S. R. (2003). Automatic processing in spider phobia: implicit fear associations over the course of treatment. *J. Abnorm. Psychol.* 112, 100–109. doi: 10.1037/0021-843X.112.1.100

Thomason, M. E., Dennis, E. L., Joshi, A. A., Joshi, S. H., Dinov, I. D., Chang, C., et al. (2011). Resting-state fMRI can reliably map neural networks in children. *NeuroImage* 55, 165–175. doi: 10.1016/j.neuroimage.2010.11.080

Valkanova, V., Ebmeier, K. P., and Allan, C. L. (2013). CRP, IL-6 and depression: a systematic review and meta-analysis of longitudinal studies. *J. Affect. Disord.* 150, 736–744. doi: 10.1016/j.jad.2013.06.004

van Alphen, N. R., Stewart, J. G., Esposito, E. C., Pridgen, B., Gold, J., and Auerbach, R. P. (2017). Predictors of rehospitalization for depressed adolescents admitted to acute psychiatric treatment. *J. Clin. Psychiatry* 78, 592–598. doi: 10.4088/JCP.15m10326

Vergara, G. A., Stewart, J. G., Cosby, E. A., Lincoln, S. H., and Auerbach, R. P. (2019). Non-Suicidal self-injury and suicide in depressed adolescents: impact of peer victimization and bullying. *J. Affect. Disord.* 245, 744–749. doi: 10.1016/j.jad.2018.11.084

Vittengl, J. R., Clark, L. A., Dunn, T. W., and Jarrett, R. B. (2007). Reducing relapse and recurrence in unipolar depression: a comparative meta-analysis of cognitive-behavioral therapy's effects. *J. Consult. Clin. Psychol.* 75, 475–488. doi: 10.1037/0022-006X.75.3.475

Walker, W. H., Walton, J. C., DeVries, A. C., and Nelson, R. J. (2020). Circadian rhythm disruption and mental health. *Transl. Psychiatry* 10, 1–13. doi: 10.1038/s41398-020-0694-0

Webb, P. G., Sailasuta, N., Kohler, S. J., Raidy, T., Moats, R. A., and Hurd, R. E. (1994). Automated single-voxel proton MRS: technical development

and multisite verification. *Magn. Reson. Med.* 31, 365–373. doi: 10.1002/mrm.1910310404

Wei, C., Hoff, A., Villabø, M. A., Peterman, J., Kendall, P. C., Piacentini, J., et al. (2014). Assessing anxiety in youth with the multidimensional anxiety scale for children. *J. Clin. Child Adolesc. Psychol.* 43, 566–578. doi: 10.1080/15374416.2013.814541

Weinberg, A., and Klonsky, E. D. (2009). Measurement of emotion dysregulation in adolescents. *Psychol. Assess.* 21, 616–621. doi: 10.1037/a0016669

World Health Organization [WHO] (2017). *Depression and Other Common Mental Disorders: Global Health Estimates (No. WHO/MSD/MER/*2017.2). Geneva: World Health Organization.

Yeatman, J. D., Dougherty, R. F., Myall, N. J., Wandell, B. A., and Feldman, H. M. (2012). Tract profiles of white matter properties: automating fiber-tract quantification. *PLoS One* 7:e49790. doi: 10.1371/journal.pone.0049790

Yüksel, C., and Öngür, D. (2010). Magnetic resonance spectroscopy studies of glutamate-related abnormalities in mood disorders. *Biol. Psychiatry* 68, 785–794. doi: 10.1016/j.biopsych.2010.06.016

Zuo, X. N., Kelly, C., Adelstein, J. S., Klein, D. F., Castellanos, F. X., and Milham, M. P. (2010). Reliable intrinsic connectivity networks: test-retest evaluation using ICA and dual regression approach. *NeuroImage* 49, 2163–2177. doi: 10.1016/j.neuroimage.2009.10.080

Conflict of Interest: The authors declare that the research was conducted in the absence of any commercial or financial relationships that could be construed as a potential conflict of interest.

frontiers in Human Neuroscience

ORIGINAL RESEARCH
published: 29 October 2020
doi: 10.3389/fnhum.2020.578913

Higher Trait Impulsivity and Altered Frontostriatal Connectivity in Betel-Quid Dependent Individuals

Zhaoxin Qian[1†], Shaohui Liu[2†], Xueling Zhu[3], Lingyu Kong[3], Neng Liu[4], Dongcui Wang[3], Canhua Jiang[5], Zhongyuan Zhan[5] and Fulai Yuan[2]*

[1]Department of Emergency, Xiangya Hospital, Central South University, Changsha, China, [2]Health Management Center, Xiangya Hospital, Central South University, Changsha, China, [3]Department of Radiology, Xiangya Hospital, Central South University, Changsha, China, [4]Department of Nursing, Xiangya Hospital, Central South University, Changsha, China, [5]Department of Oral and Maxillofacial Surgery, Xiangya Hospital, Central South University, Changsha, China

OPEN ACCESS

Edited by:
Wei Liao,
University of Electronic Science and Technology of China, China

Reviewed by:
Tao Liu,
Hainan General Hospital, China
Yuan Zhong,
Nanjing Normal University, China

***Correspondence:**
Fulai Yuan
fulaiyuan2010@163.com

[†]These authors have contributed equally to this work

Specialty section:
This article was submitted to Brain Imaging and Stimulation, a section of the journal Frontiers in Human Neuroscience

Received: *01 July 2020*
Accepted: *22 September 2020*
Published: *29 October 2020*

Citation:
Qian Z, Liu S, Zhu X, Kong L, Liu N, Wang D, Jiang C, Zhan Z and Yuan F (2020) Higher Trait Impulsivity and Altered Frontostriatal Connectivity in Betel-Quid Dependent Individuals. Front. Hum. Neurosci. 14:578913. doi: 10.3389/fnhum.2020.578913

Objective: Betel quid dependency (BQD) is characterized by functional and structural brain alterations. Trait impulsivity may influence substance dependence by impacting its neurobiological underpinnings in the frontostriatal circuit. However, little is known about the trait impulsivity and its neural correlates in individuals with BQD.

Methods: Forty-eight participants with BQD and 22 normal controls (NCs) were recruited and scanned on a 3T MRI scanner. Barratt impulsiveness scale (BIS) was used to measure trait impulsivity: motor, attention, and no plan impulsivity. We used voxel-based morphometry (VBM) to assess the relationship between trait impulsivity and gray matter volumes. The relevant clusters identified were served as regions of interest (ROI) seeds. The whole-volume psycho-physiological interactions (PPI) analysis was used to investigate the changes of functional connectivity related to ROI seeds in the cue-reactivity task condition (BQ and control images).

Results: Behaviorally, the BQD group showed significantly higher trait impulsivity including motor and no plan impulsivity than the NCs group. VBM analyses showed that motor impulsivity was negatively associated with gray matter volume of right caudate in the whole sample. No difference in gray matter volume between the two groups was observed. PPI analyses showed that there was a significantly decreased functional connectivity between the right caudate and right dorsolateral prefrontal cortex (DLPFC) when watching BQ related images than control images in individuals with BQD. Furthermore, functional connectivity between the right caudate and right DLPFC was negatively correlated with BQ dependency scores.

Conclusions: Our study demonstrated the structural basis of trait impulsivity in the caudate and provided evidence for abnormal interactions within frontostriatal circuitsin individuals with BQD, which may provide insight into the selection of potential novel therapeutic targets for the treatment of BQ dependency.

Keywords: betel quid dependence, trait impulsivity, frontostriatal circuit, PPI, functional connectivity

INTRODUCTION

Betel quid (BQ, the product of areca nut, which is the fruit of the areca palm) is among the most widely used psychoactive substances worldwide along with tobacco, alcohol, and caffeine (Boucher and Mannan, 2002; Yen et al., 2018). With a chemical structure analogous to that of nicotine (Lord et al., 2002), BQ has been recognized as a group 1 carcinogen by International Agency for Cancer Research (World Health Organization, 2004), and categorized as "addiction" with heavy use (Mirza et al., 2011; Papke et al., 2015). There are more than 600 million people using BQ within the Indo-Asia-Pacific biogeographic region, and its use is spreading into Asian migrant communities in western countries in recent years (Gupta and Warnakulasuriya, 2002; Lee et al., 2018). In mainland China, BQ is most commonly used in Hunan and Hainan provinces with different eating styles (Zhang and Reichart, 2007). The negative consequences of excessive BQ use have been reported to be correlated with the risk of oral potentially malignant disorder, oral cancer, and other health consequences (Lee et al., 2003; Jacob et al., 2004; Tilakaratne et al., 2006; Mehrtash et al., 2017). Although these clinical phenomena are well-known, the pathophysiological mechanism of BQ dependency (BQD) remains unclear.

Like other psychoactive substances, a high quantity of BQ use is addictive. The research suggested a substantial proportion of BQ users showed signs of dependence, which were associated with the number of chews per day, years of chewing, education, and the inclusion of tobacco in the quid (Benegal et al., 2008; Mirza et al., 2011). A betel quid dependency scale (BQDS) was developed to assess the degree of dependency in BQ users (Herzog et al., 2014), which had been proved with good reliability and validity in our previous studies (Yuan et al., 2017a,b; Zhu et al., 2017, 2018). In a recent study of 8,922 participants across six Asian communities (Taiwan, China, Malaysia, Indonesia, Nepal, and Sri Lanka), betel-quid use disorder was found to meet the Diagnostic and Statistical Manual of Mental Disorders (fifth edition; DSM-V) criteria for a substance use disorder and had a high prevalence among BQ users (Lee et al., 2018).

Functional neuroimaging studies have implicated BQ addiction involves brain structural and functional alterations (Kessler, 2012). Based on recent lines of evidence, individuals with BQ dependency have been documented to be associated with changes in the prefrontal cortex (PFC), insula, anterior cingulate cortex, hippocampal/hypothalamus, cerebellum, frontotemporal and frontoparietal, which are implicated in reward, impulsivity and cognitive systems in the brain (Chen et al., 2015; Liu et al., 2015, 2016a,b; Huang et al., 2017; Yuan et al., 2017a; Zhu et al., 2017; Weng et al., 2018). For example, our previous study suggested heavy BQ users with decreased gray matter volumes in the prefrontal cortex (Zhu et al., 2018), altered white matter integrity in anterior thalamic radiation, and disrupted default mode network connectivity (Zhu et al., 2017). Furthermore, the duration of BQ use and the severity of BQ dependency were reported to be associated with the majority of brain alterations in BQ users. However, the neural mechanism underlying BQD remains largely unclear, and further investigation is needed.

Impulsivity, as a kind of personality trait, is characterized by the propensity to act quickly and without regard for negative consequences (Dalley et al., 2011). Despite the variability in samples and the diversity in measures of impulsivity, the relationship between impulsivity and substance addiction has been widely investigated (Matt et al., 2001; Baker and Yardley, 2002; Shillington and Clapp, 2002). Impulsivity was regarded as one risk factor for the development and maintenance of substance misuse problems, especially in alcohol (Lejuez et al., 2010; Ming et al., 2017), nicotine (Joos et al., 2013), and methamphetamine dependency (Simons and Carey, 2002).

With the development of neuroimaging techniques, the neural bases underlying trait impulsivity have gained much attention in recent literature. Evidence from functional neuroimaging data implies that trait impulsivity may influence substance dependency by impacting its neurobiological underpinnings in the frontostriatal circuit (Knutson et al., 2001; Moreno-López et al., 2012), such as the striatum (caudate and putamen), prefrontal regions, orbitofrontal cortex and anterior cingulate cortex (Horn et al., 2003; Forstmann et al., 2008; Andrews-Hanna et al., 2011; Diekhof et al., 2012). Structural neuroimaging studies have reported the structural manifestation of impulsivity in the prefrontal regions and striatum not only in healthy individuals (Cho et al., 2013; Tschernegg et al., 2015) but also in patients with psychiatric conditions, such as alcoholics (Beck et al., 2009), pathological gambling (Koehler et al., 2015), major depressive disorders (Dombrovski et al., 2012) and psychopathy (Glenn et al., 2010). However, the relationship between impulsivity and the frontostriatal circuit remains unknown in BQ addiction.

To the best of our knowledge, no research has investigated the trait impulsivity deficits and its neural correlates in individuals with BQD. In the current study, our first aim was to measure the characteristics of trait impulsivity by using the Barratt impulsiveness scale (BIS) in the BQD group (Patton et al., 1995). The second goal was to examine the structural manifestation of trait impulsivity by investigating the association of trait impulsivity and gray matter volumes. Then, the relevant areas identified were served as regions of interest (ROI) seeds. A whole-volume psycho-physiological interactions (PPI) analysis was conducted to investigate the changes of functional connectivity related to ROI seeds in the cue-reactivity task condition (BQ and control images). We hypothesized that compared with healthy controls, individuals with BQD showed abnormal impulsivity, which would correlate with the frontostriatal circuit. The results of this study could help to understand the underlying psychological and neural bases of BQ use, and further have potential implications for treating and preventing BQ dependency.

MATERIALS AND METHODS

Participants

Participants (N = 70, all males) were recruited from Changsha, Hunan province. We recruited two groups of participants: BQD group (N = 48) and normal controls (NCs) group (N = 22). Individuals with BQD were recruited from the outpatient department in Xiangya Hospital of Central South University. Structured Clinical Interview was used to determine if the BQD group met the DSM-V criteria for substance use disorders (average scored on 7.63 ± 1.70). The NCs group were recruited through a combination of targeted site sampling, advertisement, and snowball sampling referrals.

All participants were screened with the Structured Clinical Interview for DSM-IV Axis I disorders and were excluded for any of the following: past or current Axis I disorder, including but not limited to major depressive disorder and/or any anxiety disorders; current or past other substance use; pregnancy or current breastfeeding; unstable medical or neurological illness; the history of severe head trauma; and the presence of metal implants precluding a magnetic resonance imaging (MRI) scan. Additionally, none of the participants was diagnosed as alcohol or smoking dependency as measured by the AUDIT (Alcohol Use Disorders Identification Test) and the FTND (Fagerstrom Test for Nicotine Dependence) respectively. Diagnosis and exclusion criteria were corroborated by two licensed psychiatrists.

A detailed history of BQ use was identified for everyone with BQD: age of first BQ use, duration (years) of BQ use, and estimated BQ use per day (g). This study only included males because there was significantly less problem with BQ use in females (Lee et al., 2018). The study was approved by the Institutional Review Board at Xiangya Hospital of Central South University. All participants provided written informed consent after the study procedures were explained to them thoroughly.

Procedures

All participants were asked to come to Xiangya Hospital and finish the behavior measures and MRI scans. They got compensation for their time devoting to this study (on average about 1-h interview and 30 min MRI scan). All of them were required to be abstinent (4 h) from tobacco, alcohol, and caffeine drinking before the interview. The MRI scans included a high-resolution structural scan and a session of fMRI scan with the cue-reactivity task. The cue reactivity task was a frequently used task to investigate the brain functional mechanism of individuals with addiction (Kühn and Gallinat, 2011).

Behavior Measures

Barratt Impulsiveness Scale (BIS)

The BIS is a self-report questionnaire designed to assess the personality/behavioral construct of impulsiveness, which has been widely used in impulsivity research for the last 50 years (Patton et al., 1995). As a 30-item rated on a five-point scale, it includes three subscales: motor, attention, and no plan subscales. The motor scale comprises items that reflect acting without thinking. The attention scale includes items measuring poor concentration/attentiveness with those reflecting cognitive instability. The no plan scale measures an orientation focused on the immediate present that fails to consider future effects. The BIS exhibited high degrees of reliability and validity in both English and Chinese version (Yao et al., 2007; Huang et al., 2013). The Chinese version of the BIS used in this current study exhibited high internal consistency, with a Cronbach's alpha value of 0.81, 0.78, and 0.83 for three subscales.

Betel Quid Dependence Scale (BQDS)

The BQDS is a widely used scale for diagnosing the dependency of BQ (Lee et al., 2012). As a 16-item self-report instrument, the BQDS comprises of three factors: "physical and psychological urgent need," "increasing dose," and "maladaptive use." The BQDS was found to have good internal consistency (alpha = 0.92) and construct validity, which exhibited high degrees of reliability and validity in both the English-speaking and Chinese-speaking chewers (Herzog et al., 2014; Zhu et al., 2017).

MRI Scans

All MRI images were acquired by using a Siemens 3.0T Prisma scanner at Xiangya Hospital. Standard settings were used to perform the scan. For example, foam pads were used to minimize head motion. Participants were instructed to keep their head very still during the structural scan and respond to the instructions when doing functional scans. Stimulus presentation, the timing of all stimuli, and response events were achieved by using Matlab (Mathworks) and Psychtoolbox[1] on an IBM-compatible PC. Participants' responses were collected online using an MRI-compatible button box.

The structural scan was performed using T1 MPRAGE sequence, covering the whole brain with the following scanning parameters: TR/TE = 2,110 ms/3.18 ms, matrix = 256 × 256, number of slices = 256, and voxel size = 0.7 × 0.7 × 0.7 mm^3, sagittal slice position. The functional scan was performed using EPI sequence with the following parameters: TR/TE = 2,000 ms/30 ms, matrix = 64 × 64, number of slices = 75, voxel size = 2.34 × 2.34 × 2.00 mm^3.

Cue Reactivity Task

Participants performed one session of the cue reactivity task inside the scanner. During this task, two types of cues were presented: the BQ and control images. There were 20 images for each category, and each image was presented three times. To keep all participants awake during the passive view task, 10 animal images were presented twice (see **Figure 1**). These images were presented with a random order with each image for 3 s with a 1-s intertrial interval. Participants were instructed to press a button whenever they saw an animal. The correct ratio and reaction in the cueing task were served as the behavior data of the task.

Data Analysis Procedure

Behavioral measures were first compared between two groups to find the differences of demographic as well as the impulsivity measure. Then significant trait impulsivity characteristics were correlated with structural MRI data in the whole sample to find their anatomical bounds. The structural MRI data were analyzed

[1] www.psychtoolbox.org

FIGURE 1 | The illustration of stimulus presentation. Different types of images [Betel quid (BQ), control, and animal] were randomly presented for 3 s with 1 s interstimulus interval. Participants were instructed to press a button when seeing an animal image.

by the voxel-based morphometry (VBM) method, which has been widely used in neuroimaging studies (Ashburner and Friston, 2000; Good et al., 2001; He et al., 2013). Significant clusters in the VBM analysis were served as ROI seeds to do the PPI analysis. The PPI maps were then compared between the two groups. All tests were corrected for multiple comparisons with Bonferroni correction.

VBM Analysis

VBM analysis was implemented in FSL_VBM (Smith et al., 2004), which has been widely used to analyze the structural MRI data. The processing steps were standardized: brains were extracted by using BET (Smith, 2002) and segmented into gray matter, white matter, and CSF by using FAST4 (Zhang et al., 2001). Two steps of registration (linear and non-linear) were performed to register the gray-matter partial volume images to the standard space (MNI152). A study-specific template was created by averaging all normalized images. Lastly, the resulting images of gray matter volume were smoothed with an isotropic Gaussian kernel (3 mm). Statistics were performed with FSL non-parametric permutation methods (Randomise v2.1; Nichols and Holmes, 2002). Statistical analysis using the general linear model was used to identify the correlation between gray matter volumes and trait impulsivity. The null distribution at each voxel was constructed using 10,000 random permutations. Multiple comparisons were corrected across the whole brain using the threshold-free cluster enhancement (TFCE). Additionally, we also performed the analysis to compare the difference of gray matter volume between the BQD and NCs group.

fMRI Data Analysis

fMRI data preprocessing and statistical analyses were carried out by FSL[2]. Images were realigned to compensate for small residual head movements (Jenkinson and Smith, 2001). Translational movement parameters never exceeded one voxel in any direction for any participant. Data were spatially smoothed using a five-mm full-width-half-maximum (FWHM) Gaussian kernel and were filtered using a nonlinear high pass filter with a 100-s cutoff. A two-step registration procedure was used whereby EPI images were first registered to the MPRAGE structural image, and then into standard MNI space, using affine transformations (Jenkinson and Smith, 2001). Registration from MPRAGE structural image to standard space was further refined using FNIRT nonlinear registration (Andersson et al., 2007a,b).

Statistical analyses were performed in the native image space, with the statistical maps normalized to the standard space before higher-level analyses. The data was modeled at the first-level using a general linear model within FSL's FILM module. As illustrated before Andersson et al. (2007a,b), brain activations were modeled for BQ, control, and animal images separately. The event onsets were convolved with canonical hemodynamic response function (HRF, double-gamma) to generate regressors. Temporal derivatives were included as covariates of no interest to improve statistical sensitivity. The six-movement parameters were also included as covariates in the model.

PPI Analysis

PPI analysis was performed by FSL[3]. Two interaction terms of BQ and control images with the ROIs were entered into the model. Group analyses were performed to examine group differences between interactions and to specifically find the difference in brain connectivity in BQD and NCs groups. Group images were evaluated with a height threshold of $Z > 3.1$ and a cluster probability of $p < 0.05$, corrected for whole-brain multiple comparisons based on Gaussian random field theory. The education was included as a covariate for all fMRI analyses.

RESULTS

Demographic Results

Table 1 showed the demographic and impulsivity characteristics for all participants. According to **Table 1**, the BQD and NCs group were matched on age (BQD: 34.85 ± 8.10 years; NCs: 32.05 ± 6.25 years; $t_{(68)} = 1.44$, $p = 0.15$), and BMI (BQD: 25.07 ± 3.74 kg/m^2; NCs: 23.32 ± 3.84 kg/m^2; $t_{(68)} = 1.81$,

[2]www.fmrib.ox.ac.uk/fsl

[3]https://fsl.fmrib.ox.ac.uk/fsl/fslwiki/PPI

TABLE 1 | Demographic and impulsivity characteristics of participants (M ± SD).

	BQD	NCs	Statistics
N	48	22	-
Age (years)	34.85 ± 8.10	32.05 ± 6.25	$t_{(68)} = 1.44$, $p = 0.150$
Education (years)	11.62 ± 2.83	17.82 ± 2.82	$t_{(68)} = -6.19$, $p < 0.001$*
BMI (kg/m^2)	25.07 ± 3.74	23.32 ± 3.84	$t_{(68)} = 1.81$, $p = 0.080$
BQDS	59.63 ± 14.55	-	-
Duration of BQ use (years)	15.23 ± 7.10	-	-
Age of first BQ use	17.13 ± 6.67	-	-
Estimated BQ use per day (g)	40.19 ± 33.11	-	-
BIS_Motor	25.52 ± 5.86	20.59 ± 4.29	$t_{(68)} = 3.53$, $p = 0.001$*
BIS_Attention	36.83 ± 4.13	37.73 ± 4.31	$t_{(68)} = -0.83$, $p = 0.410$
BIS_No Plan	39.27 ± 4.72	36.73 ± 3.55	$t_{(68)} = 3.06$, $p = 0.003$*
Cue_CR	0.99 ± 0.03	0.97 ± 0.05	$t_{(68)} = 1.77$, $p = 0.160$
Cue_RT (ms)	609.5 ± 138.1	618.8 ± 144.3	$t_{(68)} = -0.25$, $p = 0.800$

*Significant at $p < 0.05$.

$p = 0.08$). However, they did show significant difference on years of education (BQD: 11.62 ± 2.83 years; NCs: 17.82 ± 2.82 years; $t_{(68)} = -6.19$, $p < 0.001$). Years of education was entered as a covariate for the following analysis. **Table 1** illustrated the difference of trait impulsivity between the two groups. Results suggested that the BQD group showed higher motor and no plan impulsivity than the NCs group. Both groups performed very well in the cue-reactivity task (over 97% of the correct ratio of detecting animals). There was no significant difference in terms of either the correct ratio or reaction time between groups.

VBM Results

VBM correlation analysis aimed to investigate the structural bonding of the trait impulsivity characteristics. The result of correlation analysis suggested that scores of motor impulsivity were negatively correlated with the volume of right caudate in the whole group (both BQD and NCs group; **Figure 2A**, right caudate, blue area, MNI coordinates: 8, 14, −2; 81 voxels, $Z = 4.74$). Moreover, the right caudate volume was negatively correlated with BQDS scores in the BQD group ($r_{(48)} = -0.441$, $p = 0.002$). Also, no significant difference was found between cognitive impulsivity, no plan impulsivity, and gray matter volumes between BQD and NCs group.

PPI Results

The right caudate which showed a significant correlation with motor impulsivity was used as the ROI to do the PPI analysis. PPI results suggested that in contrast to viewing control images, viewing BQ related images would decrease functional connectivity between the right caudate and right dorsolateral prefrontal cortex (DLPFC) in the BQD group (**Figure 2B**, DLPFC, red area, MNI coordinates: 54, 28, −2; 57 voxels, $Z = 4.38$). Furthermore, correlation analysis showed that functional connectivity between right caudate and right DLPFC was negatively correlated with BQDS scores in the BQD group (**Figure 2C**, $r_{(48)} = -0.417$, $p = 0.003$).

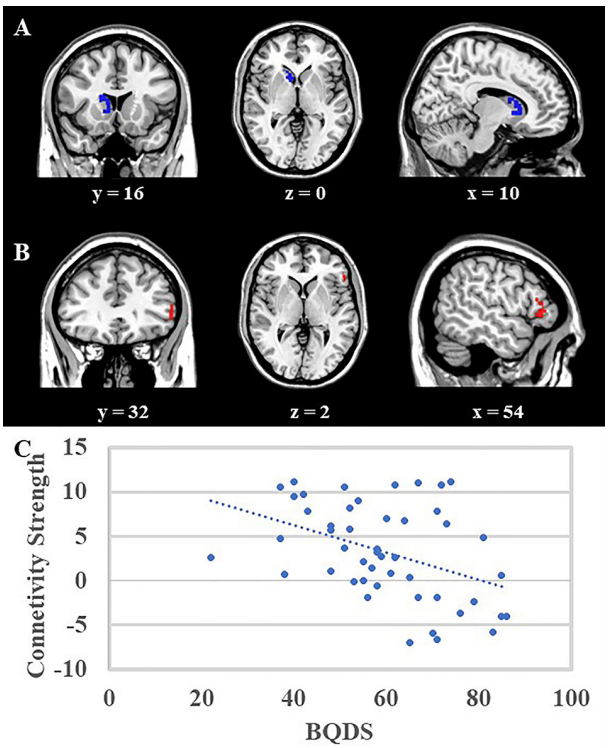

FIGURE 2 | **(A)** Voxel-Based Morphometry (VBM) analysis showed that the right caudate (blue area, MNI coordinates: 8, 14, −2; 81 voxels, $Z = 4.74$) was negatively correlated with scores of motor impulsivity, and no other results were found. **(B)** Psycho-Physiological Interactions (PPI) analysis suggested that in contrast to view control images, viewing BQ related images would decrease functional connectivity between right caudate and right DLPFC (red area, MNI coordinates: 54, 28, −2, 57 voxels, $Z = 4.38$). Both results were mapped onto a standard brain and displayed with coronal, axial, and sagittal views respectively. The numbers below represented the slice numbers. **(C)** The scatter plot of correlation analysis between functional connectivity (right caudate and right DLPFC) and BQDS scores in the BQD group.

DISCUSSION

To our knowledge, the current study provided the first empirical evidence to demonstrate the behavioral and neural differences of trait impulsivity between the BQD and NCs group. Consistent with our hypothesis, the BQD group showed significantly higher motor impulsivity and no plan impulsivity than the NCs group. Motor impulsivity was negatively associated with gray matter volume in right caudate in the whole group. Compared with the

NCs group, the BQD group showed less functional connectivity between right caudate and right DLPFC when viewing BQ related images than control images, which was more profound in participants with higher BQDS score.

This current study highlighted the trait impulsivity deficit in the BQD group. Substance misusers have been widely reported to score higher on measures of trait impulsivity despite a variety of measures of impulsivity (Dawe et al., 2004; Crews and Boettiger, 2009). So far, evidence has been accumulated for the relationship between impulsive behaviors and substance use and abuse (Baker and Yardley, 2002; de Wit, 2009). One study found that high trait impulsivity predicted the switch to compulsive cocaine-taking (Belin et al., 2008). Another study detected a positive relationship between the frequency of marijuana use and the number of marijuana-related problems that were greatest in those with high trait impulsivity scores (Simons and Carey, 2002). Similar evidence also came from internet addiction (Cao et al., 2007), sexual addiction (Bancroft and Vukadinovic, 2004), as well as other substance addiction (Kreek et al., 2005). Our study extends these prior findings by providing new evidence for increased motor and no plan impulsivity in individuals with BQ dependency.

The present study provided evidence for a negative correlation between gray matter volume in right caudate and motor impulsivity, which supported previous reports on the structural manifestation of trait impulsivity in the striatum (including caudate and putamen). In healthy individuals, a negative relationship was revealed between impulsivity scores assessed by BIS and gray matter volumes of the putamen bilaterally (Cho et al., 2013). In psychiatric disorders, Babbs et al. (2013) reported a negative correlation between trait impulsivity and caudate activity in response to a milkshake in the overweight group. Other studies suggested that structural and functional asymmetry of the caudate was associated with impulsivity deficits in participants with attention-deficit/hyperactivity disorder (Schrimsher et al., 2002; Dang et al., 2016). Although reports on gray matter changes reflecting high impulsivity in the striatum were inconsistent (Glenn et al., 2010), our results provide new evidence for a negative relationship between trait impulsivity and right caudate by the results that higher motor impulsivity was associated with less right caudate volume and further support the notion that the right caudate is involved in the pathophysiology of trait impulsivity in substance addiction.

Finally, this current study revealed decreased functional connectivity between right caudate and DLPFC in individuals with BQD (viewing BQ related images vs. control images). Anatomically, the dorsal striatum (caudate and putamen) receives projections primarily from the association cortex (mainly DLPFC), sensory, and motor areas (Alexander et al., 1986). Neuroimaging studies in addiction reveal the critical roles of the frontostriatal circuit, which are mainly associated with reward (striatum) and cognitive control (prefrontal cortex; Noël et al., 2013; He et al., 2017, 2019; Wei et al., 2017; Chen et al., 2018). It is worth noting that the striatum and prefrontal cortex are intermodulations by frontostriatal circuits (Volkow et al., 2011, 2012; Saad et al., 2019). The interactions between the striatum and prefrontal cortex are especially important to investigate the underlying neural mechanism of addiction, such as smoking (Kober et al., 2010) and internet gaming disorder (Yuan K. et al., 2017; Kim and Kang, 2018). Previous studies revealed structural and functional alterations in the prefrontal cortex and caudate in individuals with BQD relative to healthy controls (Liu et al., 2016b; Sariah et al., 2019). However, the interaction between the prefrontal cortex and caudate in BQ users with dependency has never been investigated. Our findings contribute to filling this gap by showing that reduced functional connectivity between right caudate and right DLPFC in individuals with BQD. Furthermore, it should be noted that functional connectivity between right caudate and DLPFC was revealed to be negatively associated severity of BQ dependency, which implies the effect of BQ use on the frontostriatal circuits.

It was important to note some of the limitations of this study. Firstly, the study used an imbalanced sample. Future research involving a balanced sample and larger sample sizes may help address some of these additional questions. Secondly, this study only recruited male participants, so it should be cautious in generalizing the findings of this study to the females. Then, the cross-sectional nature of this study can't make causal association conclusions about BQ use and impulsivity. Longitudinal studies should be employed in the future to assess the longer-term effect of BQ use on impulsivity in individuals with BQD. Lastly, we also screened some participants with symptoms of depression and/or anxiety. BQ use may be associated with higher depression or anxiety. We will carry out future studies to investigate this topic.

In conclusion, we revealed increased motor and no plan impulsivity in individuals with BQD relative to healthy controls. Motor impulsivity was negatively associated with gray matter volume of right caudate in the whole group. Compared with the NCs group, the BQD group showed less functional connectivity between right caudate and right DLPFC when viewing BQ related images than control images, which was more profound in participants with higher BQDS scores. Our study sheds light on the pathology of trait impulsivity in individuals with BQD, which may provide insight into the selection of key targeted brain regions for interventions aiming to decrease motor impulsivity levels in betel-quid chewers.

DATA AVAILABILITY STATEMENT

The raw data supporting the conclusions of this article will be made available by the authors, without undue reservation.

ETHICS STATEMENT

The studies involving human participants were reviewed and approved by the Institutional Review Board at Xiangya Hospital of Central South University. The patients/participants provided their written informed consent to participate in this study.

AUTHOR CONTRIBUTIONS

FY, ZQ, and SL conceived and designed the experiments. SL, NL, and CJ conducted the experiments and collected data. DW

and ZZ analyzed the results. ZQ, SL, XZ, and LK wrote the main manuscript text. All authors reviewed the manuscript. All authors contributed to the article and approved the submitted version.

FUNDING

This work was supported by research grants from the National Natural Science Foundation of China (grant number 61972460 to XZ and 61802443 to FY), Foundation for the Author of National Excellent Doctoral Dissertation of People's Republic China (FANEDD; grant number 201411 to XZ), Natural Science Foundation of Hunan Province (grant number 2019JJ20037 to XZ, 2020JJ4883 to LK, and 2020JJ4923 to FY), Philosophy and Social Science Foundation of Hunan Province (grant number 17YBA426 to FY and 16YBA036 to XZ), Youth Research of Xiangya Hospital, Central South University (grant number 2017Q19 to FY), and the introduction of overseas talents and intelligence projects of Hunan Province (grant number 2019YZ3023 to NL).

REFERENCES

Alexander, G. E., DeLong, M. R., and Strick, P. L. (1986). Parallel organization of functionally segregated circuits linking basal ganglia and cortex. *Annu. Rev. Neurosci.* 9, 357–381. doi: 10.1146/annurev.ne.09.030186.002041

Andersson, J. L. R., Jenkinson, M., and Smith, S. (2007a). Non-linear optimisation. *FMRIB Technical Report TR07JA1.* Available online at: www.fmrib.ox.ac.uk/analysis/techrep. Accessed October 3, 2020.

Andersson, J. L. R., Jenkinson, M., and Smith, S. (2007b). Non-linear registration, aka Spatial normalisation. *FMRIB Technical Report TR07JA2.* Available online at: www.fmrib.ox.ac.uk/analysis/techrep. Accessed October 3, 2020.

Andrews-Hanna, J. R., Mackiewicz, S. K. L., Claus, E. D., Burgess, G. C., Luka, R., Banich, M. T., et al. (2011). Cognitive control in adolescence: neural underpinnings and relation to self-report behaviors. *PLoS One* 6:e21598. doi: 10.1371/journal.pone.0021598

Ashburner, J., and Friston, K. J. (2000). Voxel-based morphometry—the methods. *NeuroImage* 11, 805–821. doi: 10.1006/nimg.2000.0582

Babbs, R. K., Sun, X., Felsted, J., Chouinard-Decorte, F., Veldhuizen, M. G., and Small, D. M. (2013). Decreased caudate response to milkshake is associated with higher body mass index and greater impulsivity. *Physiol. Behav.* 121, 103–111. doi: 10.1016/j.physbeh.2013.03.025

Baker, J. R., and Yardley, J. K. (2002). Moderating effect of gender on the relationship between sensation seeking-impulsivity and substance use in adolescents. *J. Child Adolesc. Subst. Abuse* 12, 27–43. doi: 10.1300/J029v12n01_02

Bancroft, J., and Vukadinovic, Z. (2004). Sexual addiction, sexual compulsivity, sexual impulsivity, or what? Toward a theoretical model. *J. Sex Res.* 41, 225–234. doi: 10.1080/00224490409552230

Beck, A., Schlagenhauf, F., Wustenberg, T., Hein, J., Kienast, T., Kahnt, T., et al. (2009). Ventral striatal activation during reward anticipation correlates with impulsivity in alcoholics. *Biol. Psychiatry* 66, 734–742. doi: 10.1016/j.biopsych.2009.04.035

Belin, D., Mar, A. C., Dalley, J. W., Robbins, T. W., and Everitt, B. J. (2008). High impulsivity predicts the switch to compulsive cocaine-taking. *Science* 320, 1352–1355. doi: 10.1126/science.1158136

Benegal, V., Rajkumar, R. P., and Muralidharan, K. (2008). Does areca nut use lead to dependence? *Drug Alcohol Depend.* 97, 114–121. doi: 10.1016/j.drugalcdep.2008.03.016

Boucher, B. J., and Mannan, N. (2002). Metabolic effects of the consumption of Areca catechu. *Addict. Biol.* 7, 103–110. doi: 10.1080/13556210120091464

Cao, F., Su, L., Liu, T., and Gao, X. (2007). The relationship between impulsivity and Internet addiction in a sample of Chinese adolescents. *Eur. Psychiatry* 22, 466–471. doi: 10.1016/j.eurpsy.2007.05.004

Chen, R., Li, D. P., Turel, O., Sørensen, T. A., Bechara, A., Li, Y., et al. (2018). Decision making deficits in relation to food cues influence obesity: a triadic neural model of problematic eating. *Front. Psychiatry* 9:264. doi: 10.3389/fpsyt.2018.00264

Chen, F., Zhong, Y., Zhang, Z., Xu, Q., Liu, T., Pan, M., et al. (2015). Gray matter abnormalities associated with betel quid dependence: a voxel-based morphometry study. *Am. J. Transl. Res.* 7, 364–374.

Cho, S. S., Pellecchia, G., Aminian, K., Ray, N., Segura, B., Obeso, I., et al. (2013). Morphometric correlation of impulsivity in medial prefrontal cortex. *Brain Topogr.* 26, 479–487. doi: 10.1007/s10548-012-0270-x

Crews, F. T., and Boettiger, C. A. (2009). Impulsivity, frontal lobes and risk for addiction. *Pharmacol. Biochem. Behav.* 93, 237–247. doi: 10.1016/j.pbb.2009.04.018

Dalley, J. W., Everitt, B. J., and Robbins, T. W. (2011). Impulsivity, compulsivity, and top-down cognitive control. *Neuron* 69, 680–694. doi: 10.1016/j.neuron.2011.01.020

Dang, L. C., Samanez-Larkin, G. R., Young, J. S., Cowan, R. L., Kessler, R. M., and Zald, D. H. (2016). Caudate asymmetry is related to attentional impulsivity and an objective measure of ADHD-like attentional problems in healthy adults. *Brain Struct. Funct.* 221, 277–286. doi: 10.1007/s00429-014-0906-6

Dawe, S., Gullo, M. J., and Loxton, N. J. (2004). Reward drive and rash impulsiveness as dimensions of impulsivity: implications for substance misuse. *Addict. Behav.* 29, 1389–1405. doi: 10.1016/j.addbeh.2004.06.004

de Wit, H. (2009). Impulsivity as a determinant and consequence of drug use: a review of underlying processes. *Addict. Biol.* 14, 22–31. doi: 10.1111/j.1369-1600.2008.00129.x

Diekhof, E. K., Nerenberg, L., Falkai, P., Dechent, P., Baudewig, J., and Gruber, O. (2012). Impulsive personality and the ability to resist immediate reward: an fMRI study examining interindividual differences in the neural mechanisms underlying self-control. *Hum. Brain Mapp.* 33, 2768–2784. doi: 10.1002/hbm.21398

Dombrovski, A. Y., Siegle, G. J., Szanto, K., Clark, L., Reynolds, C. F., and Aizenstein, H. (2012). The temptation of suicide: striatal gray matter, discounting of delayed rewards and suicide attempts in late-life depression. *Psychol. Med.* 42, 1203–1215. doi: 10.1017/S0033291711002133

Forstmann, B. U., Jahfari, S., Scholte, H. S., Wolfensteller, U., van den Wildenberg, W. P., and Ridderinkhof, K. R. (2008). Function and structure of the right inferior frontal cortex predict individual differences in response inhibition: a model-based approach. *J. Neurosci.* 28, 9790–9796. doi: 10.1523/JNEUROSCI.1465-08.2008

Glenn, A. L., Raine, A., Yaralian, P. S., and Yang, Y. (2010). Increased volume of the striatum in psychopathic individuals. *Biol. Psychiatry* 67, 52–58. doi: 10.1016/j.biopsych.2009.06.018

Good, C., Johnsrude, I., Ashburner, J., Henson, R., Friston, K., and Frackowiak, R. (2001). A voxel-based morphometric study of ageing in 465 normal adult human brains. *NeuroImage* 14, 21–36. doi: 10.1006/nimg.2001.0786

Gupta, P. C., and Warnakulasuriya, S. (2002). Global epidemiology of areca nut usage. *Addict. Biol.* 7, 77–83. doi: 10.1080/13556210020091437

He, Q., Huang, X., Zhang, S., Turel, O., Ma, L., and Bechara, A. (2019). Dynamic causal modeling of insular, striatal and prefrontal cortex activities during a food-specific go/nogo task. *Biol. Psychiatry Cogn. Neurosci. Neuroimaging* 4, 1080–1089. doi: 10.1016/j.bpsc.2018.12.005

He, Q., Turel, O., Brevers, D., and Bechara, A. (2017). Excess social media use in normal populations is associated with amygdala-striatal but not with prefrontal morphology. *Psychiatry Res. Neuroimaging* 269, 31–35. doi: 10.1016/j.pscychresns.2017.09.003

He, Q., Xue, G., Chen, C., Chen, C., Lu, Z.-L., and Dong, Q. (2013). Decoding the neuroanatomical basis of reading ability: a multivoxel morphometric study. *J. Neurosci.* 33, 12835–12843. doi: 10.1523/JNEUROSCI.0449-13.2013

Herzog, T. A., Murphy, K. L., Little, M. A., Suguitan, G. S., Pokhrel, P., and Kawamoto, C. T. (2014). The betel quid dependence scale: replication and

extension in a Guamanian sample. *Drug Alcohol Depend.* 138, 154–160. doi: 10.1016/j.drugalcdep.2014.02.022

Horn, N. R., Dolan, M., Elliott, R., Deakin, J. F. W., and Woodruff, P. W. R. (2003). Response inhibition and impulsivity: an fMRI study. *Neuropsychologia* 41, 1959–1966. doi: 10.1016/s0028-3932(03)00077-0

Huang, C. Y., Li, C. S., Fang, S. C., Wu, C. S., and Liao, D. L. (2013). The reliability of the Chinese version of the Barratt Impulsiveness Scale version 11, in abstinent, opioid-dependent participants in Taiwan. *J. Chin. Med. Assoc.* 76, 289–295. doi: 10.1016/j.jcma.2013.01.005

Huang, X., Pu, W., Liu, H., Li, X., Greenshaw, A. J., Dursun, S. M., et al. (2017). Altered brain functional connectivity in betel quid-dependent chewers. *Front. Psychiatry* 8:239. doi: 10.3389/fpsyt.2017.00239

World Health Organization (2004). *International Agency for Research on Cancer (IARC) Monograph on the Evaluation of Carcinogenic Risks to Humans. Betel-Quid and Areca-nut Chewing and Some Areca-nut-Derived Nitrosamines*. Lyon, France: IARC.

Jacob, B. J., Straif, K., Thomas, G., Ramadas, K., Mathew, B., Zhang, Z. F., et al. (2004). Betel quid without tobacco as a risk factor for oral precancers. *Oral Oncol.* 40, 697–704. doi: 10.1016/j.oraloncology.2004.01.005

Jenkinson, M., and Smith, S. (2001). A global optimisation method for robust affine registration of brain images. *Med. Image Anal.* 5, 143–156. doi: 10.1016/s1361-8415(01)00036-6

Joos, L., Goudriaan, A. E., Schmaal, L., De Witte, N. A. J., Van den Brink, W., Sabbe, B. G. C., et al. (2013). The relationship between impulsivity and craving in alcohol dependent patients. *Psychopharmacology* 226, 273–283. doi: 10.1007/s00213-012-2905-8

Kessler, R. C. (2012). The costs of depression. *Psychiatr. Clin. North. Am.* 35, 1–14. doi: 10.1016/j.psc.2011.11.005

Kim, J., and Kang, E. (2018). Internet game overuse is associated with an alteration of fronto-striatal functional connectivity during reward feedback processing. *Front. Psychiatry* 9:371. doi: 10.3389/fpsyt.2018.00371

Knutson, B., Fong, G. W., Adams, C. M., Varner, J. L., and Hommer, D. (2001). Dissociation of reward anticipation and outcome with event-related fMRI. *Neuroreport* 12, 3683–3687. doi: 10.1097/00001756-200112040-00016

Kober, H., Mende-Siedlecki, P., Kross, E. F., Weber, J., Mischel, W., Hart, C. L., et al. (2010). Prefrontal-striatal pathway underlies cognitive regulation of craving. *Proc. Natl. Acad. Sci. U S A* 107, 14811–14816. doi: 10.1073/pnas.1007779107

Koehler, S., Hasselmann, E., Wustenberg, T., Heinz, A., and Romanczuk-Seiferth, N. (2015). Higher volume of ventral striatum and right prefrontal cortex in pathological gambling. *Brain Struct. Funct.* 220, 469–477. doi: 10.1007/s00429-013-0668-6

Kreek, M. J., Nielsen, D. A., Butelman, E. R., and LaForge, K. S. (2005). Genetic influences on impulsivity, risk taking, stress responsivity and vulnerability to drug abuse and addiction. *Nat. Neurosci.* 8, 1450–1457. doi: 10.1038/nn1583

Kühn, S., and Gallinat, J. (2011). Common biology of craving across legal and illegal drugs—a quantitative meta-analysis of cue-reactivity brain response. *Eur. J. Neurosci.* 33, 1318–1326. doi: 10.1111/j.1460-9568.2010.07590.x

Lee, C.-Y., Chang, C.-S., Shieh, T.-Y., and Chang, Y.-Y. (2012). Development and validation of a self-rating scale for betel quid chewers based on a male-prisoner population in Taiwan: the Betel Quid Dependence Scale. *Drug Alcohol Depend.* 121, 18–22. doi: 10.1016/j.drugalcdep.2011.07.027

Lee, C. H., Ko, Y. C., Huang, H. L., Chao, Y. Y., Tsai, C. C., Shieh, T. Y., et al. (2003). The precancer risk of betel quid chewing, tobacco use and alcohol consumption in oral leukoplakia and oral submucous fibrosis in southern Taiwan. *Br. J. Cancer* 88, 366–372. doi: 10.1038/sj.bjc.6600727

Lee, C. H., Ko, A. M., Yang, F. M., Hung, C. C., Warnakulasuriya, S., Ibrahim, S. O., et al. (2018). Association of DSM-5 betel-quid use disorder with oral potentially malignant disorder in 6 betel-quid endemic asian populations. *JAMA Psychiatry* 75, 261–269. doi: 10.1001/jamapsychiatry.2017.4307

Lejuez, C. W., Magidson, J. F., Mitchell, S. H., Sinha, R., Stevens, M. C., and de Wit, H. (2010). Behavioral and biological indicators of impulsivity in the development of alcohol use, problems and disorders. *Alcohol. Clin. Exp. Res.* 34, 1334–1345. doi: 10.1111/j.1530-0277.2010.01217.x

Liu, T., Li, J., Huang, S., Zhao, Z., Yang, G., Pan, M., et al. (2015). Neurochemical abnormalities in anterior cingulate cortex on betel quid dependence: a 2D (1)H MRS investigation. *Am. J. Transl. Res.* 7, 2795–2804.

Liu, T., Li, J., Zhang, Z., Xu, Q., Lu, G., Huang, S., et al. (2016a). Altered long- and short-range functional connectivity in patients with betel quid dependence: a resting-state functional MRI study. *Cell Physiol. Biochem.* 40, 1626–1636. doi: 10.1159/000453212

Liu, T., Li, J., Zhao, Z., Zhong, Y., Zhang, Z., Xu, Q., et al. (2016b). Betel quid dependence is associated with functional connectivity changes of the anterior cingulate cortex: a resting-state fMRI study. *J. Transl. Med.* 14:33. doi: 10.1186/s12967-016-0784-1

Lord, G. A., Lim, C. K., Warnakulasuriya, S., and Peters, T. J. (2002). Chemical and analytical aspects of areca nut. *Addict. Biol.* 7, 99–102. doi: 10.1080/13556210120091455

Matt, M., William, G. I., Lisa, N. L., Steve, M., and Irene, E. (2001). Origins and consequences of age at first drink. I. Associations with substance-use disorders, disinhibitory behavior and psychopathology and P3 amplitude. *Alcohol. Clin. Exp. Res.* 25, 1156–1165. doi: 10.1111/j.1530-0277.2001.tb02330.x

Mehrtash, H., Duncan, K., Parascandola, M., David, A., Gritz, E. R., Gupta, P. C., et al. (2017). Defining a global research and policy agenda for betel quid and areca nut. *Lancet Oncol.* 18, e767–e775. doi: 10.1016/S1470-2045(17)30460-6

Ming, Q., Zhong, X., Zhang, X., Pu, W., Dong, D., Jiang, Y., et al. (2017). State-independent and dependent neural responses to psychosocial stress in current and remitted depression. *Am. J. Psychiatry* 174, 971–979. doi: 10.1176/appi.ajp.2017.16080974

Mirza, S. S., Shafique, K., Vart, P., and Arain, M. I. (2011). Areca nut chewing and dependency syndrome: is the dependence comparable to smoking? a cross sectional study. *Subst. Abuse Treat. Prev. Policy* 6:23. doi: 10.1186/1747-597X-6-23

Moreno-López, L., Catena, A., Fernández-Serrano, M. J., Delgado-Rico, E., Stamatakis, E. A., Pírez-García, M., et al. (2012). Trait impulsivity and prefrontal gray matter reductions in cocaine dependent individuals. *Drug Alcohol Depend.* 125, 208–214. doi: 10.1016/j.drugalcdep.2012.02.012

Nichols, T., and Holmes, A. (2002). Nonparametric permutation tests for functional neuroimaging: a primer with examples. *Hum. Brain Mapp.* 15, 1–25. doi: 10.1002/hbm.1058

Noël, X., Brevers, D., and Bechara, A. (2013). A neurocognitive approach to understanding the neurobiology of addiction. *Curr. Opin. Neurobiol.* 23, 632–638. doi: 10.1016/j.conb.2013.01.018

Papke, R. L., Horenstein, N. A., and Stokes, C. (2015). Nicotinic activity of arecoline, the psychoactive element of "betel nuts", suggests a basis for habitual use and anti-inflammatory activity. *PLoS One* 10:e0140907. doi: 10.1371/journal.pone.0140907

Patton, J. H., Stanford, M. S., and Barratt, E. S. (1995). Factor structure of the Barratt impulsiveness scale. *J. Clin. Psychol.* 51, 768–774. doi: 10.1002/1097-4679(199511)51:6<768::aid-jclp2270510607>3.0.co;2-1

Saad, L., Sartori, M., Pol Bodetto, S., Romieu, P., Kalsbeek, A., Zwiller, J., et al. (2019). Regulation of brain DNA methylation factors and of the orexinergic system by cocaine and food self-administration. *Mol. Neurobiol.* 56, 5315–5331. doi: 10.1007/s12035-018-1453-6

Sariah, A., Liu, Z., Pu, W., Liu, H., Xue, Z., and Huang, X. (2019). Structural and functional alterations in betel-quid chewers: a systematic review of neuroimaging findings. *Front. Psychiatry* 10:16. doi: 10.3389/fpsyt.2019.00016

Schrimsher, G. W., Billingsley, R. L., Jackson, E. F., and Moore, B. D. (2002). Caudate nucleus volume asymmetry predicts attention-deficit hyperactivity disorder (ADHD) symptomatology in children. *J. Child Neurol.* 17, 877–884. doi: 10.1177/088307380201700122001

Shillington, A. M., and Clapp, J. D. (2002). Beer and bongs: differential problems experienced by older adolescents using alcohol only compared to combined alcohol and marijuana use. *Am. J. Drug Alcohol Abuse* 28, 379–397. doi: 10.1081/ada-120002980

Simons, J. S., and Carey, K. B. (2002). Risk and vulnerability for marijuana use problems: the role of affect dysregulation. *Psychol. Addict. Behav.* 16, 72–75. doi: 10.1037/0893-164X.16.1.72

Smith, S. (2002). Fast robust automated brain extraction. *Hum. Brain Mapp.* 17, 143–155. doi: 10.1002/hbm.10062

Smith, S., Jenkinson, M., Woolrich, M., Beckmann, C., Behrens, T., Johansen-Berg, H., et al. (2004). Advances in functional and structural MR image analysis and implementation as FSL. *NeuroImage* 23, S208–S219. doi: 10.1016/j.neuroimage.2004.07.051

Tilakaratne, W. M., Klinikowski, M. F., Saku, T., Peters, T. J., and Warnakulasuriya, S. (2006). Oral submucous fibrosis: review on aetiology and pathogenesis. *Oral Oncol.* 42, 561–568. doi: 10.1016/j.oraloncology.2005.08.005

Tschernegg, M., Pletzer, B., Schwartenbeck, P., Ludersdorfer, P., Hoffmann, U., and Kronbichler, M. (2015). Impulsivity relates to striatal gray matter volumes in humans: evidence from a delay discounting paradigm. *Front. Hum. Neurosci.* 9:384. doi: 10.3389/fnhum.2015.00384

Volkow, N. D., Wang, G.-J., Fowler, J. S., and Tomasi, D. (2012). Addiction circuitry in the human brain. *Ann. Rev. Pharmacol. Toxicol.* 52, 321–336. doi: 10.1146/annurev-pharmtox-010611-134625

Volkow, N. D., Wang, G. J., Fowler, J. S., Tomasi, D., and Telang, F. (2011). Addiction: beyond dopamine reward circuitry. *Proc. Natl. Acad. Sci. U S A* 108, 15037–15042. doi: 10.1073/pnas.1010654108

Wei, L., Zhang, S., Turel, O., Bechara, A., and He, Q. (2017). A tripartite neurocognitive model of internet gaming disorder. *Front. Psychiatry* 8:285. doi: 10.3389/fpsyt.2017.00285

Weng, J. C., Chou, Y. S., Huang, G. J., Tyan, Y. S., and Ho, M. C. (2018). Mapping brain functional alterations in betel-quid chewers using resting-state fMRI and network analysis. *Psychopharmacology* 235, 1257–1271. doi: 10.1007/s00213-018-4841-8

Yao, S., Yang, H., Zhu, X., Auerbach, R. P., Abela, J. R., Pulleyblank, R. W., et al. (2007). An examination of the psychometric properties of the Chinese version of the Barratt Impulsiveness Scale, 11th version in a sample of Chinese adolescents. *Percept. Mot. Skills* 104, 1169–1182. doi: 10.2466/pms.104.4.1169-1182

Yen, H. Y., Chen, P. H., Ko, Y. C., Chiang, S. K., Chang, Y. Y., and Shiah, Y. J. (2018). Betel quid chewing, personality and mood: betel quid chewing associated with low extraversion and negative mood. *Subst. Use Misuse* 53, 1782–1787. doi: 10.1080/10826084.2018.1432652

Yuan, F., Kong, L., Zhu, X., Jiang, C., Fang, C., and Liao, W. (2017a). Altered gray-matter volumes associated with betel quid dependence. *Front. Psychiatry* 8:139. doi: 10.3389/fpsyt.2017.00139

Yuan, F., Zhu, X., Kong, L., Shen, H., Liao, W., and Jiang, C. (2017b). White matter integrity deficit associated with betel quid dependence. *Front. Psychiatry* 8:201. doi: 10.3389/fpsyt.2017.00201

Yuan, K., Yu, D., Cai, C., Feng, D., Li, Y., Bi, Y., et al. (2017). Frontostriatal circuits, resting state functional connectivity and cognitive control in internet gaming disorder. *Addict. Biol.* 22, 813–822. doi: 10.1111/adb.12348

Zhang, Y., Brady, M., and Smith, S. (2001). Segmentation of brain MR images through a hidden Markov random field model and the expectation-maximization algorithm. *IEEE Trans. Med. Imaging* 20, 45–57. doi: 10.1109/42.906424

Zhang, X., and Reichart, P. A. (2007). A review of betel quid chewing, oral cancer and precancer in Mainland China. *Oral Oncol.* 43, 424–430. doi: 10.1016/j.oraloncology.2006.08.010

Zhu, X. L., Liu, S. H., Liao, W. H., Kong, L. Y., Jiang, C. H., and Yuan, F. L. (2018). Executive function deficit in betel-quid-dependent chewers: mediating role of prefrontal cortical thickness. *J. Psychopharmacol.* 32, 1362–1368. doi: 10.1177/0269881118806299

Zhu, X., Zhu, Q., Jiang, C., Shen, H., Wang, F., Liao, W., et al. (2017). Disrupted resting-state default mode network in betel quid-dependent individuals. *Front. Psychol.* 8:84. doi: 10.3389/fpsyg.2017.00084

Conflict of Interest: The authors declare that the research was conducted in the absence of any commercial or financial relationships that could be construed as a potential conflict of interest.

frontiers in Human Neuroscience

ORIGINAL RESEARCH
published: 09 November 2020
doi: 10.3389/fnhum.2020.574758

Abnormal Spontaneous Brain Activities of Limbic-Cortical Circuits in Patients With Dry Eye Disease

Haohao Yan[1], *Xiaoxiao Shan*[1], *Shubao Wei*[2], *Feng Liu*[3], *Wenmei Li*[2], *Yiwu Lei*[2], *Wenbin Guo*[1,4]* and *Shuguang Luo*[2]*

[1] Department of Psychiatry, National Clinical Research Center for Mental Disorders, The Second Xiangya Hospital of Central South University, Changsha, China, [2] Department of Neurology, The First Affiliated Hospital of Guangxi Medical University, Nanning, China, [3] Department of Radiology, Tianjin Medical University General Hospital, Tianjin, China, [4] Department of Psychiatry, The Third People's Hospital of Foshan, Foshan, China

Whether brain function is altered in patients with dry eye disease (DED) remains unclear. Twenty patients with DED and 23 healthy controls (HCs) were scanned using resting-state functional magnetic resonance imaging. Regional homogeneity (ReHo) and support vector machine (SVM) were used to analyze the imaging data. Relative to the HCs, the patients with DED showed significantly increased ReHo values in the left inferior occipital gyrus (IOG), left superior temporal gyrus, and right superior medial prefrontal cortex, and significantly decreased ReHo values in the right superior frontal gyrus/middle frontal gyrus and bilateral middle cingulum (MC). SVM results indicated that the combination of ReHo values in the left MC and the left IOG in distinguishing patients with DED from HCs had a sensitivity of 95.00%, a specificity of 91.30%, and an accuracy of 93.02%. The present study found that the patients with DED had abnormal ReHo values in the limbic-cortical circuits. A combination of ReHo values in the left MC and the left IOG could be applied as a potential imaging biomarker to distinguish patients with DED from HCs. The dysfunction of limbic-cortical circuits may play an important role in the pathophysiology of DED.

Keywords: dry eye disease, resting-state functional magnetic resonance imaging, regional homogeneity, support vector machine, limbic-cortical circuits

OPEN ACCESS

Edited by:
Wei Liao,
University of Electronic Science and Technology of China, China

Reviewed by:
Qiu Jiang,
Southwest Normal University, China
Yong Xu,
First Hospital of Shanxi Medical University, China

***Correspondence:**
Wenbin Guo
guowenbin76@csu.edu.cn
Shuguang Luo
robert58243@sohu.com

Specialty section:
This article was submitted to Brain Imaging and Stimulation, a section of the journal Frontiers in Human Neuroscience

Received: *21 June 2020*
Accepted: *06 October 2020*
Published: *09 November 2020*

Citation:
Yan H, Shan X, Wei S, Liu F, Li W, Lei Y, Guo W and Luo S (2020) Abnormal Spontaneous Brain Activities of Limbic-Cortical Circuits in Patients With Dry Eye Disease. Front. Hum. Neurosci. 14:574758. doi: 10.3389/fnhum.2020.574758

INTRODUCTION

Dry eye disease (DED) is a common health problem because of its morbidity, prevalence (5–35%), and cost implications (Smith, 2007; Messmer, 2015). DED is more frequently reported by women than by men, and its likelihood increases with age (Moss et al., 2000; Schaumberg et al., 2003). Dry eye (DE) is defined as "a multifactorial disease of the ocular surface characterized by a loss of homeostasis of the tear film accompanied by ocular symptoms, in which tear film instability and hyperosmolarity, ocular surface inflammation and damage, and neurosensory abnormalities play etiological roles" by the Tear Film and Ocular Surface Society Dry Eye Workshop II (Craig et al., 2017). "Neurosensory abnormalities" are indeed included in the DE definition, but the neuropathophysiology mechanism of DED remains unclear.

The tear film plays an important role in providing a refractive interface for the optical light path, and protection and lubrication for the ocular surface (Willcox et al., 2017). The major ingredients of the tear film are aqueous tear, lipid components, and mucins. Aqueous tear is mainly produced

by lacrimal glands. Lipid components are generally synthesized by meibomian glands. Mucins are mainly synthesized by conjunctival goblet cells (Ellingham et al., 1999) and stratified squamous epithelial cells (Argüeso et al., 2003). DED may be caused by the dysfunction of these glands and cells (Mathers, 2000; Mantelli and Argüeso, 2008) or the neuronal circuits regulating tear secretion (van Bijsterveld et al., 2003; Dartt, 2009). In DED, aberrations and scattering induced by alterations of the tear film directly cause disturbances in vision quality (Benito et al., 2011; Tan et al., 2015). In addition to visual disturbance, most patients with DED also complain of ocular discomfort accompanied by increased blinks. Ocular discomfort comprises ocular fatigue and unpleasant sensations such as pain, itching, and dryness. The unpleasant sensations are induced by the pathological processes affecting the trigeminal sensory nerves innervating the ocular and periocular tissues. In some studies, the terms "dryness," "itching," "foreign body sensation," and "burning" are applied to describe the ocular pain associated with DED (Mertzanis et al., 2005; Kalangara et al., 2016). Ocular pain is an uncomfortable and unpleasant sensory and emotional experience induced by the interconnected peripheral nervous system (PNS) and central nervous system (CNS). The enhanced excitability of central pain pathways result from the local activation of microglia and weakened inhibitory descending modulation (Tulleuda et al., 2011). The inhibitory descending control systems come from higher brain centers and modulate ascending excitatory nociceptive pathways by influencing the trigeminal and spinal sensory input (Tracey and Mantyh, 2007; Khasabov et al., 2015). However, the role of descending control systems in DED has not been comprehensively studied. Ocular pain in patients with DED is mainly induced by peripheral insults to the innervated ocular and periocular tissues. However, in certain circumstances, ocular pain in patients with DED is induced by direct injuries to, or dysfunctions of, the cortical and subcortical structures, which process the peripheral nociceptive input, the peripheral nociceptive sensory neurons located in the trigeminal and dorsal root ganglion, and the higher-order neurons located in the spinal cord, brain stem, and thalamus (von Hehn et al., 2012; Belmonte et al., 2015). This pain is called "neuropathic pain." An emerging concern is that a subset of DED should be represented as a chronic neuropathic pain (Kalangara et al., 2016). In DED, the persistent deficiency of tears results in peripheral nerve damage and ocular inflammation. Peripheral nerve damage and ocular inflammation have complex interactions (Ordovas-Montanes et al., 2015). Long-term peripheral nerve damage and ocular inflammation induce alterations in the structures and functions of PNS and CNS involved in ocular sensory pathways (Belmonte et al., 2015, 2017; Rahman et al., 2015; Levitt et al., 2017), thereby leading to neuropathic pain and central sensitization. Central sensitization is caused by decreased activation thresholds and abnormal amplifying signals within the CNS through neuroplastic processes (Latremoliere and Woolf, 2009; Galor et al., 2015). In DED, the increased blinks result from the enhanced activities of the ocular surface sensory nerve evoked by the stimulation of an unstable tear film (Nakamori et al., 1997) and/or from the redistribution of the tear film over the cornea to obtain enhanced image quality (Tan et al., 2015). The level of dopamine released by the basal ganglia can modulate the blink rate in DED, as observed in a rat model study (Kaminer et al., 2011).

In sum, one can reasonably hypothesize that abnormal brain function plays an important role in DED symptoms' maintenance and development. Abnormal brain structure and function in Sjögren syndrome, a subset of DED (Craig et al., 2017), have been reported in many neuroimaging studies. A study applied computed tomography and magnetic resonance imaging (MRI) and identified 24 patients with white matter abnormalities from a total of 49 patients with Sjögren syndrome with DE (Akasbi et al., 2012). White matter hyperintensities were also found in patients with Sjögren syndrome in the studies that applied MRI and voxel-based morphometry (Tzarouchi et al., 2011, 2014). In a study that applied voxel-wise and global brain volume analyses, the patients with Sjögren syndrome showed lower white matter volumes, not gray matter volumes, than the healthy controls (HCs) (Lauvsnes et al., 2014). Another study found decreased gray matter volume in the cortex and cerebellum in patients with Sjögren syndrome (Tzarouchi et al., 2011). A study applied resting-state functional magnetic resonance imaging (rs-fMRI) and functional connectivity analysis and found altered hippocampal functional connectivity in patients with primary Sjögren syndrome (Zhang et al., 2020). Another study applied rs-fMRI and regional homogeneity (ReHo) analysis and found abnormal ReHo values in the frontoparietal junction area and visual cortex in patients with Sjögren syndrome (Xing et al., 2018). Nevertheless, whether brain function is altered in DED remains unclear. Therefore, a study on brain function will facilitate the understanding of the underlying neuropathophysiology of DED.

Herein, we applied rs-fMRI to map functional brain and decipher spontaneous cerebral neuro-activities. Since Bharat Biswal et al.'s study using rs-fMRI (Biswal et al., 1995), rs-fMRI has been widely used to map functional brain and decipher spontaneous cerebral neuro-activities by measuring the blood oxygen level-dependent (BOLD) signal. Relative to task-based fMRI, rs-fMRI can observe cerebral neurophysiological processes without requiring task performance. Therefore, applying rs-fMRI avoids the potential limitation of applying task-based fMRI in fMRI studies.

After accessing the neuroimaging data of patients with DED and HCs via rs-fMRI, ReHo was utilized to depict the local features of BOLD signals and thus reflect the local synchronization of spontaneous brain activities. Kendall's coefficient concordance (KCC) of the voxel similarity of the time series of a given voxel with the nearest neighboring voxels was applied to measure the ReHo values (Zang et al., 2004). ReHo has been successfully utilized to explore the abnormalities of regional functional synchronization in some ophthalmologic illnesses, such as glaucoma, amblyopia, and corneal ulcer (Lin et al., 2012; Chen et al., 2017; Xu et al., 2019). However, whether patients with DED have abnormal ReHo in certain brain regions, particularly in the brain sensory and visual processing regions, remains unclear.

Support vector machine (SVM) learning is a robust classification tool. This supervised learning algorithm is

usually used to recognize patterns and analyze data. Relative to Bayesian networks, decision trees, and artificial neural networks, SVM has significant strengths, such as high accuracy, direct geometric interpretation, and excellent mathematical tractability (Zhang and Wu, 2012). Moreover, SVM does not need large training samples to avoid overfitting (Li et al., 2010); this feature is particularly effective in classification when the sample size is small (Chen and Chen, 2017). Therefore, SVM was applied in this work to determine whether abnormal ReHo values in certain brain areas could be used to distinguish patients with DED from HCs.

We hypothesized that patients with DED would show abnormal ReHo in certain brain regions, particularly in the brain sensory and visual processing regions, and that such abnormal ReHo in relevant regions might serve as possible imaging biomarkers to distinguish patients with DED from HCs via SVM.

MATERIALS AND METHODS

Participants

A total of 20 right-handed patients with DED (age ≥18 years) were eligible to participate in the whole study. The diagnosis of DED was confirmed by an ophthalmologist by using DED diagnostic guidelines published in 2007 by the Dry Eye Workshop (Lemp, 2007). The exclusion criteria were as follows: (1) patients with other ophthalmic diseases, such as glaucoma, cataract, diabetic retinopathy, and amblyopia; (2) patients with a history of metabolic encephalopathy, hypertensive encephalopathy, CNS infection, and CNS lesions induced by other causes; and (3) patients who were pregnant.

We recruited 23 right-handed HCs (age ≥18 years) from the community. The sex ratio, age, and years of education of the HCs and patients were group-matched. They were also interviewed using the DED diagnostic guidelines published in 2007 by the Dry Eye Workshop. They were excluded if they had a history of neuropsychiatric illness or brain injury or if they were pregnant.

The ethics committee of the First Affiliated Hospital of Guangxi Medical University approved the study. The study was executed according to the Helsinki Declaration. All participants provided an informed written consent.

Scan Acquisition

In this study, rs-fMRI was performed using a Siemens 3.0 T scanner and a standard head coil. The participants lay on the scanner bed with their eyes closed. They were instructed to remain calm and awake. They used foam pads and soft earplugs to reduce head motion and scanning noise. A gradient-echo-planar imaging (EPI) sequence was used to acquire the imaging data with the following parameters: repetition time = 2,000 ms, echo time = 30 ms, 30 slices, 90° flip angle, 64 × 64 matrix, 240 mm field of view, 4 mm slice thickness, 0.4 mm gap, and 250 volumes (500 s).

Data Preprocessing

Statistical parametric mapping software (SPM12; http://www.fil.ion.ucl.ac.uk/spm/) and the Data Processing Assistant for Resting-State fMRI were applied to preprocess the images. The first 10 images of each participant were discarded due to unstable initial MRI signals. We corrected the fMRI images for head motion and acquisition delay between slices. The participants must have translations of <2 mm and rotations of <2° in the x, y, or z axis. Thereafter, all imaging data were spatially normalized to the standard Montreal Neurological Institute (MNI) EPI template in SPM12 and sampled again to 3 mm cubic voxels. The resulting fMRI images were subjected to bandpass filtering (0.01–0.08 Hz) and time-course linear detrending to reduce the influence of high-frequency physiological noise and low-frequency drift.

ReHo Analysis

ReHo is an rs-fMRI measurement that is utilized to explore regional functional synchronization. The Resting-State fMRI Data Analysis Toolkit (REST, http://resting-fmri.sourceforge.net) was utilized to conduct the ReHo analysis. Individual ReHo maps were produced by calculating the KCC of the time series of a given voxel with those of its nearest voxels (26 voxels). The formula for calculating the KCC value was introduced in a previous study (Zang et al., 2004). The ReHo maps were normalized to reduce the influence of individual variations on the KCC values by dividing the KCC values among each voxel by the whole brain average KCC. Thereafter, the ReHo maps were smoothed with a Gaussian kernel of 4 mm full width at half maximum.

Statistical Analysis

SPSS 18.0 (Chicago, IL) was used to compare the demographic characteristics of the two groups. To assess the differences in sex distribution, we performed a chi-square test on the two groups. For the differences in ages and years of education, we performed two-sample *t*-tests. The differences in the ReHo values of the HCs and patients with DED were compared by two-sample *t*-tests with years of education and age as the covariates of no interest. The Gaussian random field method was utilized to correct for multiple comparisons with the REST software (voxel significance: $P < 0.001$, cluster significance: $P < 0.05$).

Correlation Analysis

To assess the possible relationship between abnormal ReHo values and illness duration in patients with DED, we conducted Pearson's correlation analyses between the abnormal ReHo values and illness duration (significance level: $P < 0.05$). In the correlation analysis, the average values of the clusters with abnormal ReHo were used.

Classification Analysis

Classification analysis was performed to examine whether ReHo values and a combination of ReHo values in relevant regions could serve as possible imaging biomarkers to distinguish patients with DED from HCs. SVM analysis was applied to the classification analysis by using the LIBSVM software package (http://www.csie.ntu.edu.tw/~cjlin/libsvm/) in MATLAB. SVM was performed to measure the capacity of the abnormal ReHo values to distinguish patients with DED from HCs. In SVM,

differences between groups are learned by a training dataset, and classification performance in unobserved data is evaluated by a test dataset. To train data, we provided label pairs $(x_i, c_i), i = 1, \ldots, l$. In the label pairs, $x_i \in R^n$, with x_i representing ReHo values and c_i represents class label. Class label "$c = +1$" was assigned to the patients with DED, and "$c = 0$" was assigned to the HCs. We applied Gaussian radial basis function kernel and Grid search method to implement parameter optimization. We also conducted a "leave-one-out" cross-validation approach in the LIBSVM software to obtain the highest specificity and sensitivity. The form of radial basis function kernel used in the present study is "$K(x_i, x_j) = e^{-y\|x_i - x_j\|^2}$" (Liu et al., 2018).

RESULTS

Characteristics of Participants

A total of 20 patients with DED and 23 HCs were recruited in the study. The two groups did not show significant differences in sex ratio ($P = 0.19$), age ($P = 0.23$) or years of education ($P = 0.10$). The detailed characteristics of the participants are shown in **Table 1**.

TABLE 1 | Characteristics of participants.

Variables	Patients ($n = 20$)	Controls ($n = 23$)	p-value
Age (years)	52.55 ± 8.66	49.70 ± 6.51	0.23[b]
Sex (male/female)	7/13	4/19	0.19[a]
Years of education (years)	10.20 ± 3.56	8.61 ± 2.27	0.10[b]
Illness duration (months)	20.75 ± 15.37		

[a] *The p-value for sex distribution was obtained by a chi-square test.*
[b] *The p-values were obtained by two samples t-tests.*

Differences in ReHo Values of Patients With DED and HCs

Relative to the HCs, the patients with DED showed significantly enhanced ReHo in the left inferior occipital gyrus (IOG), left superior temporal gyrus (STG), and right superior medial prefrontal cortex (MPFC), and significantly reduced ReHo in the right superior frontal gyrus (SFG)/middle frontal gyrus (MFG) and bilateral middle cingulum (MC). Detailed information is presented in **Table 2** and **Figure 1**.

TABLE 2 | Regions with abnormal ReHo values in patients.

Cluster location	Peak (MNI)			Number of voxels	T-value
	x	y	z		
Left inferior occipital gyrus	−45	−81	−12	36	3.8793
Left superior temporal gyrus	−63	−15	6	30	4.2411
Right superior MPFC	18	39	51	79	3.9433
Right superior frontal gyrus/middle frontal gyrus	24	3	48	30	−4.4578
Right middle cingulum	12	−21	36	84	−4.8042
Left middle cingulum	−9	−6	36	33	−4.1881

ReHo, regional homogeneity; MNI, Montreal Neurological Institute; MPFC, medial prefrontal cortex.

Correlation Analysis Result

No correlation was observed between ReHo values and illness duration in patients with DED at the $P < 0.05$ level.

SVM Result

Figure 2 presents the accuracies for distinguishing patients with DED from HCs based on the ReHo values of six detected brain regions and a combination of these clusters. In the combination of ReHo values in the left MC and left IOG, 40 subjects were correctly classified with the highest accuracy. This combination was the optimal combination with a sensitivity of 95.00%, a specificity of 91.30%, and an accuracy of 93.02% (**Figure 3**).

DISCUSSION

Relative to the HCs, the patients with DED showed abnormal ReHo in the limbic-cortical circuits. Increased or decreased ReHo values in the patients with DED, relative to the HCs, indicated spontaneous brain activities in certain regions having more or less synchronization. No correlation was found between the ReHo values in these brain regions and illness duration in the patients. Moreover, the SVM analysis showed that a combination of ReHo values in the left MC and left IOG could facilitate the differentiation of the patients with DED from the HCs with satisfactory sensitivities, specificities, and accuracies.

Increased ReHo Values in Left IOG, Left STG, and Right Superior MPFC

The occipital gyrus is the visual cortex, a crucial brain region for visual processing. The IOG plays a critical role in visual processing, particularly in visual processing of faces, and is known as the occipital face area. In neuroimaging studies, participants showed more activity in the IOG when observing faces than when observing other stimuli (Sergent et al., 1992; Liu et al., 2010). A damaged IOG results in the impaired identity recognition of faces (Allison et al., 1994; Rossion et al., 2003). The electrical stimulation of the IOG induces impairments in the perception of facial features and configurations (Pitcher et al., 2007; Jonas et al., 2012). Moreover, the IOG has connections to the limbic system, and a number of studies have shown neural networks consisting of the amygdala and the IOG being responsible for the visual processing of faces (Rossion et al., 2011; Sato et al., 2017). In the present study, we found significantly increased ReHo in the left IOG of the patients with DED relative to the HCs, and this result indicated reinforced activities in this brain area. Reinforced activities in the left IOG enhance visual processing. DED impairs vision, especially functional vision, in patients (Miljanović et al., 2007). Hence, increased ReHo values in the left IOG may compensate for visual impairment in patients with DED.

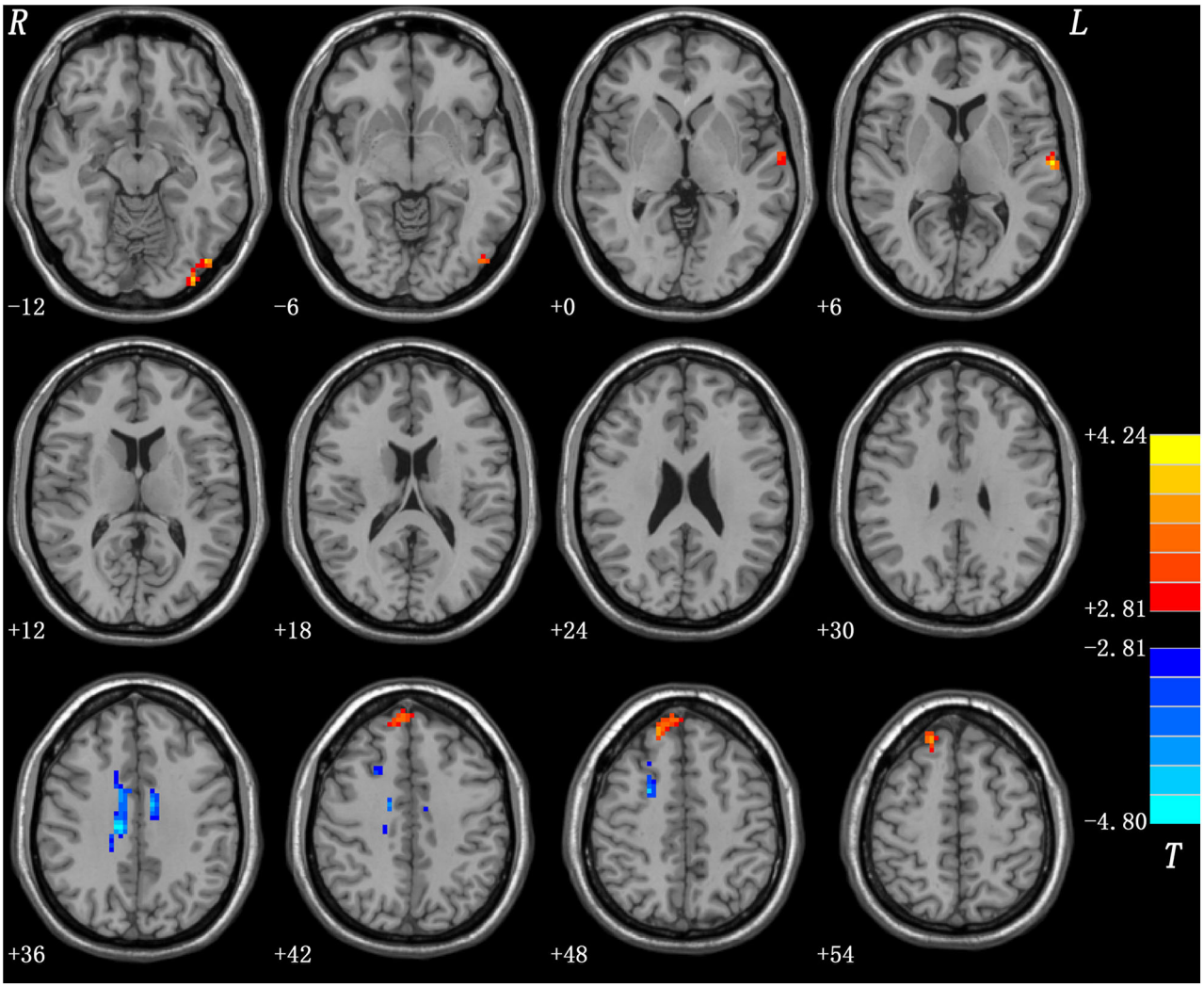

FIGURE 1 | Regions with abnormal ReHo in patients with DED. Red and blue denote increased and decreased ReHo in patients with DED, respectively. DED, dry eye disease; ReHo, regional homogeneity.

Repetitive transcranial magnetic stimulation creating "virtual lesions" in the STG results in disturbed visual search (Ellison et al., 2004). Another study applied intraoperative electrical stimulation and found that the inactivation of the STG induces a disturbed visual search (Gharabaghi et al., 2006). Event-related potential (Reale et al., 2007) and fMRI (Robins et al., 2009) studies have suggested that the STG plays an important role in the integration of auditory—visual cues. The STG has connections to the limbic system. The connection between the amygdala and the STG may be correlated with auditory input and the transfer of complex sensory information (Kosmal et al., 1997). Small STG and amygdala were found in patients with schizophrenia relative to HCs, and these features may be correlated with auditory hallucinations (Barta et al., 1990; Yoshida et al., 2009). In the present study, we found increased ReHo values in the left STG of the patients with DED. Therefore, increased ReHo values in the left STG may also account for visual impairment in patients with DED.

MPFC plays a crucial role in fear extinction (Milad and Quirk, 2002; Milad et al., 2004; Santini et al., 2004). A rat under persistent stress shows structural and functional changes in the MPFC (Radley et al., 2006, 2008). The MPFC is a part of the brain's reward system, and stimulating it can induce an antidepressant effect (Tzschentke, 2000; Hamani et al., 2010). The MPFC has connections to the limbic system. In these connections, the amygdala–MPFC circuit is involved in emotional processing (Delli Pizzi et al., 2017; Thijssen et al., 2017). In the present study, we found significantly increased ReHo in the right superior MPFC in the patients with DED. Patients with DED often complain of negative moods, such as depression or anxiety (Li et al., 2011; van der Vaart et al., 2015). Therefore, significantly increased ReHo in the right superior

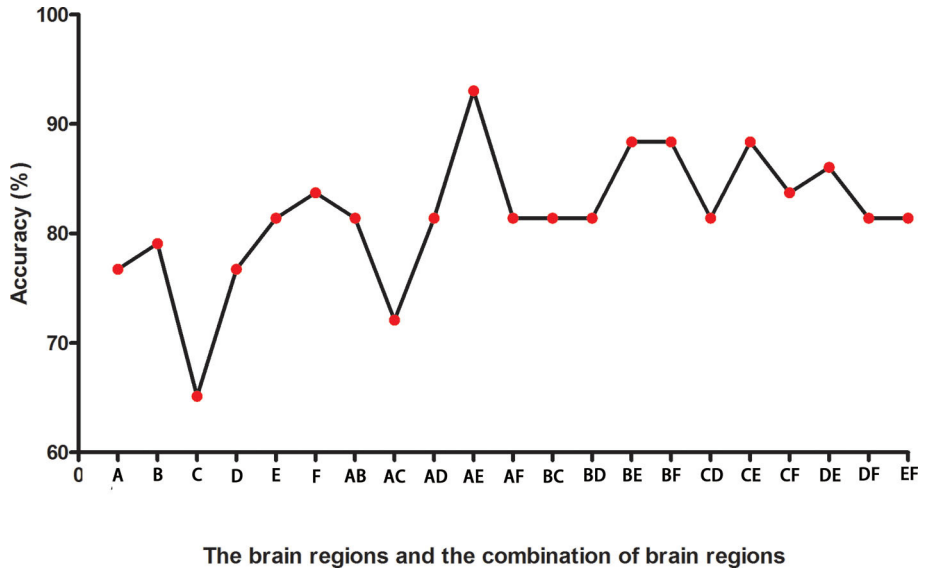

FIGURE 2 | The accuracies in differentiating patients from controls of six brain regions with abnormal ReHo values and combinations of them. A represents the left middle cingulum; B represents the right middle cingulum; C represents the right superior MPFC; D represents the right superior frontal gyrus/middle frontal gyrus; E represents the left inferior occipital gyrus; F represents the left superior temporal gyrus. ReHo, regional homogeneity; MPFC, medial prefrontal cortex.

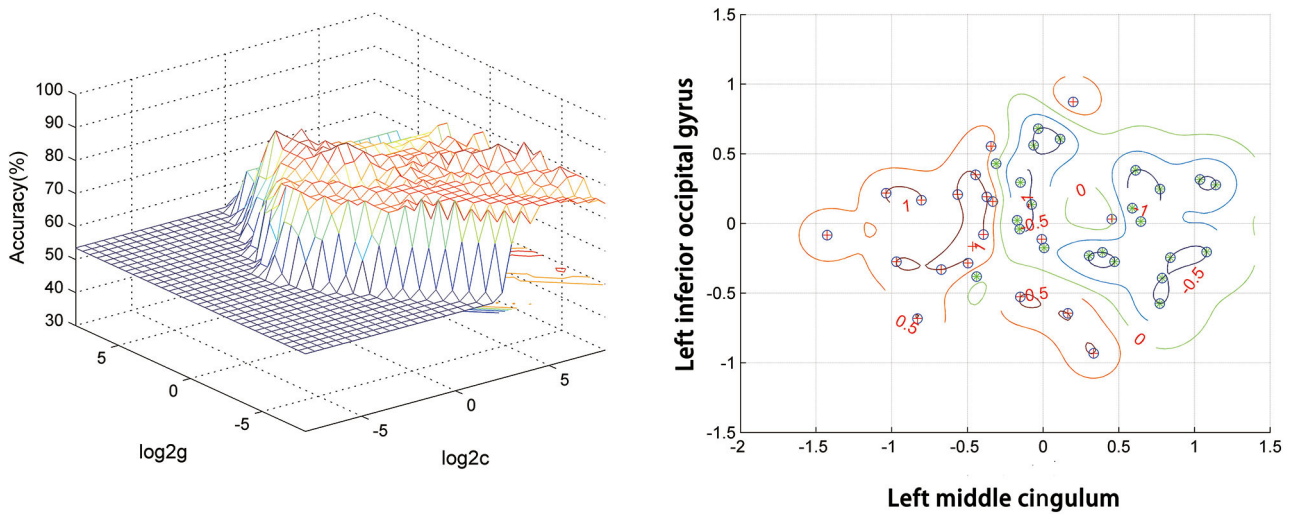

FIGURE 3 | SVM analysis of the combination of ReHo values in the left middle cingulum and the left inferior occipital gyrus. Sensitivity = 95.00%, specificity = 91.30%, and accuracy = 93.02%. SVM, support vector machines; ReHo, regional homogeneity.

MPFC may be correlated with a negative mood in patients with DED, although anxiety and depression severity were not assessed in the present study.

Decreased ReHo Values in the Right SFG/MFG and Bilateral MC

The right SFG generally plays a crucial role in cognitive control and emotion regulation (Rose et al., 2011; Tully et al., 2014; McDonald et al., 2020). The SFG is also involved in the experience of pain. Fulbright et al. found that the SFG, especially the right SFG, shows pain-related activation when an individual experiences pain stimuli (Fulbright et al., 2001). The frontal cortex and cingulum are parts of the "pain matrix," which transforms nociceptive signals into a perception of pain and perceived pain intensity (Rainville, 2002; Tracey and Mantyh, 2007; Legrain et al., 2011; Favilla et al., 2014). The MFG and SFG play a vital role in modulating the nociceptive pathways of the cortical and subcortical regions (Yang et al., 2013). Decreased gray matter volume in the MFG (Absinta et al., 2012; Yang et al., 2013) and SFG (Lutz et al., 2008) was observed in painful diseases,

such as cluster headaches and fibromyalgia. In the present study, we found significantly decreased ReHo values in the right SFG and MFG in the patients with DED relative to the HCs. In a majority of the patients with DED, ocular pain was a major discomfort. Hence, the dysfunction of the right SFG and MFG may be related to pain in patients with DED.

Mazzola et al. found that the stimulation of the insular cortex can evoke a pain sensation around the eye (Mazzola et al., 2006). A number of studies have found that ocular neurons have projections to the posterior thalamus and the parabrachial area and not to the main somatosensory thalamic areas (Meng et al., 1997; Aicher et al., 2013). Connections exist across the insular cortex, amygdala, and cingulate cortex, thereby suggesting the crucial role of the cerebral limbic system in the autonomic aspects of pain and affection of patients with DED (Bernard et al., 1996). The cingulate cortex is a critical region of the "pain matrix" (Favilla et al., 2014). The MC is a part of the limbic system, which is involved in emotional processing when an individual experiences pain (Zubieta et al., 2003). In the present study, we found significantly decreased ReHo values in the bilateral MC of the patients with DED relative to the HCs. In sum, the decreased ReHo values of the bilateral MC may be related to pain in patients with DED.

In the present study, we found significantly increased ReHo values in the left IOG and left STG, both of which may compensate for visual impairment in patients with DED. Increased ReHo values were also noted in the right superior MPFC, and they may be correlated with a negative mood in patients with DED. The IOG, STG, and MPFC have strong connections to the amygdala. We also found significantly decreased ReHo values in the right SFG/MFG and bilateral MC, and they may be related to the pain of patients with DED; all these four brain regions together make up the "pain matrix." The amygdala and cingulate gyrus are part of the limbic system. The cerebral limbic system has a key role in the autonomic aspects of pain of DED patients (Bernard et al., 1996). Hence, the abnormal ReHo values found in these brain regions of the patients with DED suggested that limbic-cortical circuits may play a crucial role in the pathophysiology of DED. The dysfunction of the limbic-cortical circuits and DED symptoms may be reciprocal, and the heterogeneity of clinically observed DED symptoms can be explained by the dysfunction of the limbic-cortical circuits in combination with active intrinsic compensatory processes.

A previous study suggested that a specificity or sensitivity of more than 0.7 could be considered as an acceptable level for establishing a diagnostic index (Swets, 1988), whereas a specificity or sensitivity of <0.7 might lead to poor accuracy as a diagnostic indicator (Gong et al., 2011; Zhu et al., 2018; Li et al., 2019). In the present study, the SVM result showed that the combination of ReHo values in the left MC and left IOG in distinguishing patients with DED from HCs had a sensitivity of 95.00%, a specificity of 91.30%, and an accuracy of 93.02%. Therefore, this combination of ReHo values is appropriately applied as a potential image biomarker to distinguish patients with DED from HCs. In the correlation analysis, no correlation was observed between the ReHo values and illness duration of the patients with DED. This result suggested that the illness duration had no effect on the ReHo values.

Several limitations of the present study should be raised. The sample size is small, and it may lead to low-reliability results. Moreover, we cannot divide patients into different subgroups due to the small sample size. Large sample size studies are needed. The MNI template used in the present study was produced from a Caucasian population, and the results may be biased to Chinese subjects.

CONCLUSION

In the present study, patients with DED had abnormal ReHo values in the limbic-cortical circuits. A combination of ReHo values in the left MC and the left IOG could be applied as potential imaging biomarkers to distinguish patients with DED from HCs. The dysfunction of the limbic-cortical circuits may play an important role in the pathophysiology of DED.

DATA AVAILABILITY STATEMENT

The raw data supporting the conclusions of this article will be made available by the authors, without undue reservation.

ETHICS STATEMENT

The studies involving human participants were reviewed and approved by the ethics committee of the First Affiliated Hospital of Guangxi Medical University. The patients/participants provided their written informed consent to participate in this study.

AUTHOR CONTRIBUTIONS

WG and SL designed the study. SW, FL, WL, YL, XS, and HY collected the original imaging data. WG and FL analyzed the imaging data. WG, XS, and HY wrote the manuscript. All the authors contributed and approved the final manuscript.

FUNDING

This study was supported by grants from the National Key R&D Program of China (2016YFC1307100), National Natural Science Foundation of China (81771447), the Natural Science Foundation of Hunan (Grant No. 2020JJ4784), and Guangxi Appropriate Technology for Medical and Health Research and Development Project (S201415-05).

ACKNOWLEDGMENTS

All subjects were acknowledged for participating in this study.

REFERENCES

Absinta, M., Rocca, M. A., Colombo, B., Falini, A., Comi, G., and Filippi, M. (2012). Selective decreased grey matter volume of the pain-matrix network in cluster headache. *Cephalalgia* 32, 109–115. doi: 10.1177/0333102411431334

Aicher, S. A., Hermes, S. M., and Hegarty, D. M. (2013). Corneal afferents differentially target thalamic- and parabrachial-projecting neurons in spinal trigeminal nucleus caudalis. *Neuroscience* 232, 182–193. doi: 10.1016/j.neuroscience.2012.11.033

Akasbi, M., Berenguer, J., Saiz, A., Brito-Zerón, P., Pérez-De-Lis, M., Bové, A., et al. (2012). White matter abnormalities in primary Sjögren syndrome. *QJM* 105, 433–443. doi: 10.1093/qjmed/hcr218

Allison, T., Ginter, H., McCarthy, G., Nobre, A. C., Puce, A., Luby, M., et al. (1994). Face recognition in human extrastriate cortex. *J. Neurophysiol.* 71, 821–825. doi: 10.1152/jn.1994.71.2.821

Argüeso, P., Spurr-Michaud, S., Russo, C. L., Tisdale, A., and Gipson, I. K. (2003). MUC16 mucin is expressed by the human ocular surface epithelia and carries the H185 carbohydrate epitope. *Invest. Ophthalmol. Vis. Sci.* 44, 2487–2495. doi: 10.1167/iovs.02-0862

Barta, P. E., Pearlson, G. D., Powers, R. E., Richards, S. S., and Tune, L. E. (1990). Auditory hallucinations and smaller superior temporal gyral volume in schizophrenia. *Am. J. Psychiatry* 147, 1457–1462. doi: 10.1176/ajp.147.11.1457

Belmonte, C., Acosta, M. C., Merayo-Lloves, J., and Gallar, J. (2015). What causes eye pain? *Curr. Ophthalmol. Rep.* 3, 111–121. doi: 10.1007/s40135-015-0073-9

Belmonte, C., Nichols, J. J., Cox, S. M., Brock, J. A., Begley, C. G., Bereiter, D. A., et al. (2017). TFOS DEWS II pain and sensation report. *Ocul. Surf.* 15, 404–437. doi: 10.1016/j.jtos.2017.05.002

Benito, A., Pérez, G. M., Mirabet, S., Vilaseca, M., Pujol, J., Marín, J. M., et al. (2011). Objective optical assessment of tear-film quality dynamics in normal and mildly symptomatic dry eyes. *J. Cataract Refract. Surg.* 37, 1481–1487. doi: 10.1016/j.jcrs.2011.03.036

Bernard, J. F., Bester, H., and Besson, J. M. (1996). Involvement of the spino-parabrachio -amygdaloid and -hypothalamic pathways in the autonomic and affective emotional aspects of pain. *Prog. Brain Res.* 107, 243–255. doi: 10.1016/S0079-6123(08)61868-3

Biswal, B., Yetkin, F. Z., Haughton, V. M., and Hyde, J. S. (1995). Functional connectivity in the motor cortex of resting human brain using echo-planar MRI. *Magn. Reson. Med.* 34, 537–541. doi: 10.1002/mrm.1910340409

Chen, H., and Chen, L. (2017). Support vector machine classification of drunk driving behaviour. *Int. J. Environ. Res. Public Health* 14:108. doi: 10.3390/ijerph14010108

Chen, W., Zhang, L., Xu, Y. G., Zhu, K., and Luo, M. (2017). Primary angle-closure glaucomas disturb regional spontaneous brain activity in the visual pathway: an fMRI study. *Neuropsychiatr. Dis. Treat.* 13, 1409–1417. doi: 10.2147/NDT.S134258

Craig, J. P., Nichols, K. K., Akpek, E. K., Caffery, B., Dua, H. S., Joo, C. K., et al. (2017). TFOS DEWS II definition and classification report. *Ocul. Surf.* 15, 276–283. doi: 10.1016/j.jtos.2017.05.008

Dartt, D. A. (2009). Neural regulation of lacrimal gland secretory processes: relevance in dry eye diseases. *Prog. Retin. Eye Res.* 28, 155–177. doi: 10.1016/j.preteyeres.2009.04.003

Delli Pizzi, S., Chiacchiaretta, P., Mantini, D., Bubbico, G., Ferretti, A., Edden, R. A., et al. (2017). Functional and neurochemical interactions within the amygdala-medial prefrontal cortex circuit and their relevance to emotional processing. *Brain Struct. Funct.* 222, 1267–1279. doi: 10.1007/s00429-016-1276-z

Ellingham, R. B., Berry, M., Stevenson, D., and Corfield, A. P. (1999). Secreted human conjunctival mucus contains MUC5AC glycoforms. *Glycobiology* 9, 1181–1189. doi: 10.1093/glycob/9.11.1181

Ellison, A., Schindler, I., Pattison, L. L., and Milner, A. D. (2004). An exploration of the role of the superior temporal gyrus in visual search and spatial perception using TMS. *Brain* 127(Pt 10), 2307–2315. doi: 10.1093/brain/awh244

Favilla, S., Huber, A., Pagnoni, G., Lui, F., Facchin, P., Cocchi, M., et al. (2014). Ranking brain areas encoding the perceived level of pain from fMRI data. *Neuroimage* 90, 153–162. doi: 10.1016/j.neuroimage.2014.01.001

Fulbright, R. K., Troche, C. J., Skudlarski, P., Gore, J. C., and Wexler, B. E. (2001). Functional MR imaging of regional brain activation associated with the affective experience of pain. *AJR Am. J. Roentgenol.* 177, 1205–1210. doi: 10.2214/ajr.177.5.1771205

Galor, A., Levitt, R. C., Felix, E. R., Martin, E. R., and Sarantopoulos, C. D. (2015). Neuropathic ocular pain: an important yet underevaluated feature of dry eye. *Eye* 29, 301–312. doi: 10.1038/eye.2014.263

Gharabaghi, A., Fruhmann Berger, M., Tatagiba, M., and Karnath, H. O. (2006). The role of the right superior temporal gyrus in visual search-insights from intraoperative electrical stimulation. *Neuropsychologia* 44, 2578–2581. doi: 10.1016/j.neuropsychologia.2006.04.006

Gong, Q., Wu, Q., Scarpazza, C., Lui, S., Jia, Z., Marquand, A., et al. (2011). Prognostic prediction of therapeutic response in depression using high-field MR imaging. *Neuroimage* 55, 1497–1503. doi: 10.1016/j.neuroimage.2010.11.079

Hamani, C., Diwan, M., Macedo, C. E., Brandão, M. L., Shumake, J., Gonzalez-Lima, F., et al. (2010). Antidepressant-like effects of medial prefrontal cortex deep brain stimulation in rats. *Biol. Psychiatry* 67, 117–124. doi: 10.1016/j.biopsych.2009.08.025

Jonas, J., Descoins, M., Koessler, L., Colnat-Coulbois, S., Sauvée, M., Guye, M., et al. (2012). Focal electrical intracerebral stimulation of a face-sensitive area causes transient prosopagnosia. *Neuroscience* 222, 281–288. doi: 10.1016/j.neuroscience.2012.07.021

Kalangara, J. P., Galor, A., Levitt, R. C., Felix, E. R., Alegret, R., and Sarantopoulos, C. D. (2016). Burning eye syndrome: do neuropathic pain mechanisms underlie chronic dry eye? *Pain Med.* 17, 746–755. doi: 10.1093/pm/pnv070

Kaminer, J., Powers, A. S., Horn, K. G., Hui, C., and Evinger, C. (2011). Characterizing the spontaneous blink generator: an animal model. *J. Neurosci.* 31, 11256–11267. doi: 10.1523/JNEUROSCI.6218-10.2011

Khasabov, S. G., Malecha, P., Noack, J., Tabakov, J., Okamoto, K., Bereiter, D. A., et al. (2015). Activation of rostral ventromedial medulla neurons by noxious stimulation of cutaneous and deep craniofacial tissues. *J. Neurophysiol.* 113, 14–22. doi: 10.1152/jn.00125.2014

Kosmal, A., Malinowska, M., and Kowalska, D. M. (1997). Thalamic and amygdaloid connections of the auditory association cortex of the superior temporal gyrus in rhesus monkey (Macaca mulatta). *Acta Neurobiol. Exp.* 57, 165–188.

Latremoliere, A., and Woolf, C. J. (2009). Central sensitization: a generator of pain hypersensitivity by central neural plasticity. *J. Pain* 10, 895–926. doi: 10.1016/j.jpain.2009.06.012

Lauvsnes, M. B., Beyer, M. K., Appenzeller, S., Greve, O. J., Harboe, E., Gøransson, L. G., et al. (2014). Loss of cerebral white matter in primary Sjögren's syndrome: a controlled volumetric magnetic resonance imaging study. *Eur. J. Neurol.* 21, 1324–1329. doi: 10.1111/ene.12486

Legrain, V., Iannetti, G. D., Plaghki, L., and Mouraux, A. (2011). The pain matrix reloaded: a salience detection system for the body. *Prog. Neurobiol.* 93, 111–124. doi: 10.1016/j.pneurobio.2010.10.005

Lemp, M. A. (2007). The definition and classification of dry eye disease: report of the definition and classification subcommittee of the international dry eye workShop 2007. *Ocul. Surf.* 5, 75–92. doi: 10.1016/S1542-0124(12)70081-2

Levitt, A. E., Galor, A., Chowdhury, A. R., Felix, E. R., Sarantopoulos, C. D., Zhuang, G. Y., et al. (2017). Evidence that dry eye represents a chronic overlapping pain condition. *Mol. Pain* 13:1744806917729306. doi: 10.1177/1744806917729306

Li, D., Yang, W., and Wang, S. (2010). Classification of foreign fibers in cotton lint using machine vision and multi-class support vector machine. *Comput. Electron. Agric.* 74, 274–279. doi: 10.1016/j.compag.2010.09.002

Li, H., Guo, W., Liu, F., Chen, J., Su, Q., Zhang, Z., et al. (2019). Enhanced baseline activity in the left ventromedial putamen predicts individual treatment response in drug-naive, first-episode schizophrenia: results from two independent study samples. *EBioMedicine* 46, 248–255. doi: 10.1016/j.ebiom.2019.07.022

Li, M., Gong, L., Sun, X., and Chapin, W. J. (2011). Anxiety and depression in patients with dry eye syndrome. *Curr. Eye Res.* 36, 1–7. doi: 10.3109/02713683.2010.519850

Lin, X., Ding, K., Liu, Y., Yan, X., Song, S., and Jiang, T. (2012). Altered spontaneous activity in anisometropic amblyopia subjects: revealed by resting-state FMRI. *PLoS ONE* 7:e43373. doi: 10.1371/journal.pone.0043373

Liu, J., Harris, A., and Kanwisher, N. (2010). Perception of face parts and face configurations: an FMRI study. *J. Cogn. Neurosci.* 22, 203–211. doi: 10.1162/jocn.2009.21203

Liu, Y., Zhang, Y., Lv, L., Wu, R., Zhao, J., and Guo, W. (2018). Abnormal neural activity as a potential biomarker for drug-naive first-episode adolescent-onset schizophrenia with coherence regional homogeneity and support vector machine analyses. *Schizophr. Res.* 192, 408–415. doi: 10.1016/j.schres.2017.04.028

Lutz, J., Jäger, L., de Quervain, D., Krauseneck, T., Padberg, F., Wichnalek, M., et al. (2008). White and gray matter abnormalities in the brain of patients with fibromyalgia: a diffusion-tensor and volumetric imaging study. *Arthritis Rheum.* 58, 3960–3969. doi: 10.1002/art.24070

Mantelli, F., and Argüeso, P. (2008). Functions of ocular surface mucins in health and disease. *Curr. Opin. Allergy Clin. Immunol.* 8, 477–483. doi: 10.1097/ACI.0b013e32830e6b04

Mathers, W. D. (2000). Why the eye becomes dry: a cornea and lacrimal gland feedback model. *CLAO J.* 26, 159–165.

Mazzola, L., Isnard, J., and Mauguière, F. (2006). Somatosensory and pain responses to stimulation of the second somatosensory area (SII) in humans. A comparison with SI and insular responses. *Cereb. Cortex* 16, 960–968. doi: 10.1093/cercor/bhj038

McDonald, B., Becker, K., Meshi, D., Heekeren, H. R., and von Scheve, C. (2020). Individual differences in envy experienced through perspective-taking involves functional connectivity of the superior frontal gyrus. *Cogn. Affect. Behav. Neurosci.* 20, 783–797. doi: 10.3758/s13415-020-00802-8

Meng, I. D., Hu, J. W., Benetti, A. P., and Bereiter, D. A. (1997). Encoding of corneal input in two distinct regions of the spinal trigeminal nucleus in the rat: cutaneous receptive field properties, responses to thermal and chemical stimulation, modulation by diffuse noxious inhibitory controls, and projections to the parabrachial area. *J. Neurophysiol.* 77, 43–56. doi: 10.1152/jn.1997.77.1.43

Mertzanis, P., Abetz, L., Rajagopalan, K., Espindle, D., Chalmers, R., Snyder, C., et al. (2005). The relative burden of dry eye in patients' lives: comparisons to a U.S. normative sample. *Invest Ophthalmol. Vis. Sci.* 46, 46–50. doi: 10.1167/iovs.03-0915

Messmer, E. M. (2015). The pathophysiology, diagnosis, and treatment of dry eye disease. *Dtsch. Arztebl. Int.* 112, 71–81, quiz 82. doi: 10.3238/arztebl.2015.0071

Milad, M. R., and Quirk, G. J. (2002). Neurons in medial prefrontal cortex signal memory for fear extinction. *Nature* 420, 70–74. doi: 10.1038/nature01138

Milad, M. R., Vidal-Gonzalez, I., and Quirk, G. J. (2004). Electrical stimulation of medial prefrontal cortex reduces conditioned fear in a temporally specific manner. *Behav. Neurosci.* 118, 389–394. doi: 10.1037/0735-7044.118.2.389

Miljanović, B., Dana, R., Sullivan, D. A., and Schaumberg, D. A. (2007). Impact of dry eye syndrome on vision-related quality of life. *Am. J. Ophthalmol.* 143, 409–415. doi: 10.1016/j.ajo.2006.11.060

Moss, S. E., Klein, R., and Klein, B. E. (2000). Prevalence of and risk factors for dry eye syndrome. *Arch. Ophthalmol.* 118, 1264–1268. doi: 10.1001/archopht.118.9.1264

Nakamori, K., Odawara, M., Nakajima, T., Mizutani, T., and Tsubota, K. (1997). Blinking is controlled primarily by ocular surface conditions. *Am. J. Ophthalmol.* 124, 24–30. doi: 10.1016/S0002-9394(14)71639-3

Ordovas-Montanes, J., Rakoff-Nahoum, S., Huang, S., Riol-Blanco, L., Barreiro, O., and von Andrian, U. H. (2015). The regulation of immunological processes by peripheral neurons in homeostasis and disease. *Trends Immunol.* 36, 578–604. doi: 10.1016/j.it.2015.08.007

Pitcher, D., Walsh, V., Yovel, G., and Duchaine, B. (2007). TMS evidence for the involvement of the right occipital face area in early face processing. *Curr. Biol.* 17, 1568–1573. doi: 10.1016/j.cub.2007.07.063

Radley, J. J., Rocher, A. B., Miller, M., Janssen, W. G., Liston, C., Hof, P. R., et al. (2006). Repeated stress induces dendritic spine loss in the rat medial prefrontal cortex. *Cereb. Cortex* 16, 313–320. doi: 10.1093/cercor/bhi104

Radley, J. J., Rocher, A. B., Rodriguez, A., Ehlenberger, D. B., Dammann, M., McEwen, B. S., et al. (2008). Repeated stress alters dendritic spine morphology in the rat medial prefrontal cortex. *J. Comp. Neurol.* 507, 1141–1150. doi: 10.1002/cne.21588

Rahman, M., Okamoto, K., Thompson, R., Katagiri, A., and Bereiter, D. A. (2015). Sensitization of trigeminal brainstem pathways in a model for tear deficient dry eye. *Pain* 156, 942–950. doi: 10.1097/j.pain.0000000000000135

Rainville, P. (2002). Brain mechanisms of pain affect and pain modulation. *Curr. Opin. Neurobiol.* 12, 195–204. doi: 10.1016/S0959-4388(02)00313-6

Reale, R. A., Calvert, G. A., Thesen, T., Jenison, R. L., Kawasaki, H., Oya, H., et al. (2007). Auditory-visual processing represented in the human superior temporal gyrus. *Neuroscience* 145, 162–184. doi: 10.1016/j.neuroscience.2006.11.036

Robins, D. L., Hunyadi, E., and Schultz, R. T. (2009). Superior temporal activation in response to dynamic audio-visual emotional cues. *Brain Cogn.* 69, 269–278. doi: 10.1016/j.bandc.2008.08.007

Rose, J. E., McClernon, F. J., Froeliger, B., Behm, F. M., Preud'homme, X., and Krystal, A. D. (2011). Repetitive transcranial magnetic stimulation of the superior frontal gyrus modulates craving for cigarettes. *Biol. Psychiatry* 70, 794–799. doi: 10.1016/j.biopsych.2011.05.031

Rossion, B., Caldara, R., Seghier, M., Schuller, A. M., Lazeyras, F., and Mayer, E. (2003). A network of occipito-temporal face-sensitive areas besides the right middle fusiform gyrus is necessary for normal face processing. *Brain* 126(Pt 11), 2381–2395. doi: 10.1093/brain/awg241

Rossion, B., Dricot, L., Goebel, R., and Busigny, T. (2011). Holistic face categorization in higher order visual areas of the normal and prosopagnosic brain: toward a non-hierarchical view of face perception. *Front. Hum. Neurosci.* 4:225. doi: 10.3389/fnhum.2010.00225

Santini, E., Ge, H., Ren, K., Peña de Ortiz, S., and Quirk, G. J. (2004). Consolidation of fear extinction requires protein synthesis in the medial prefrontal cortex. *J. Neurosci.* 24, 5704–5710. doi: 10.1523/JNEUROSCI.0786-04.2004

Sato, W., Kochiyama, T., Uono, S., Matsuda, K., Usui, K., Usui, N., et al. (2017). Bidirectional electric communication between the inferior occipital gyrus and the amygdala during face processing. *Hum. Brain Mapp.* 38, 4511–4524. doi: 10.1002/hbm.23678

Schaumberg, D. A., Sullivan, D. A., Buring, J. E., and Dana, M. R. (2003). Prevalence of dry eye syndrome among US women. *Am. J. Ophthalmol.* 136, 318–326. doi: 10.1016/S0002-9394(03)00218-6

Sergent, J., Ohta, S., and MacDonald, B. (1992). Functional neuroanatomy of face and object processing. A positron emission tomography study. *Brain* 115(Pt 1), 15–36. doi: 10.1093/brain/115.1.15

Smith, J. A. (2007). The epidemiology of dry eye disease: report of the epidemiology subcommittee of the international dry eye workshop 2007. *Ocul. Surf.* 5, 93–107. doi: 10.1016/S1542-0124(12)70082-4

Swets, J. A. (1988). Measuring the accuracy of diagnostic systems. *Science* 240, 1285–1293. doi: 10.1126/science.3287615

Tan, C. H., Labbé, A., Liang, Q., Qiao, L., Baudouin, C., Wan, X., et al. (2015). Dynamic change of optical quality in patients with dry eye disease. *Invest. Ophthalmol. Vis. Sci.* 56, 2848–2854. doi: 10.1167/iovs.14-15757

Thijssen, S., Muetzel, R. L., Bakermans-Kranenburg, M. J., Jaddoe, V. W., Tiemeier, H., Verhulst, F. C., et al. (2017). Insensitive parenting may accelerate the development of the amygdala-medial prefrontal cortex circuit. *Dev. Psychopathol.* 29, 505–518. doi: 10.1017/S0954579417000141

Tracey, I., and Mantyh, P. W. (2007). The cerebral signature for pain perception and its modulation. *Neuron* 55, 377–391. doi: 10.1016/j.neuron.2007.07.012

Tulleuda, A., Cokic, B., Callejo, G., Saiani, B., Serra, J., and Gasull, X. (2011). TRESK channel contribution to nociceptive sensory neurons excitability: modulation by nerve injury. *Mol. Pain* 7:30. doi: 10.1186/1744-8069-7-30

Tully, L. M., Lincoln, S. H., Liyanage-Don, N., and Hooker, C. I. (2014). Impaired cognitive control mediates the relationship between cortical thickness of the superior frontal gyrus and role functioning in schizophrenia. *Schizophr. Res.* 152, 358–364. doi: 10.1016/j.schres.2013.12.005

Tzarouchi, L. C., Tsifetaki, N., Konitsiotis, S., Zikou, A., Astrakas, L., Drosos, A., et al. (2011). CNS involvement in primary Sjogren syndrome: assessment of gray and white matter changes with MRI and voxel-based morphometry. *AJR Am. J. Roentgenol.* 197, 1207–1212. doi: 10.2214/AJR.10.5984

Tzarouchi, L. C., Zikou, A. K., Tsifetaki, N., Astrakas, L. G., Konitsiotis, S., Voulgari, P., et al. (2014). White matter water diffusion changes in primary Sjögren syndrome. *AJNR Am. J. Neuroradiol.* 35, 680–685. doi: 10.3174/ajnr.A3756

Tzschentke, T. M. (2000). The medial prefrontal cortex as a part of the brain reward system. *Amino Acids* 19, 211–219. doi: 10.1007/s007260070051

van Bijsterveld, O. P., Kruize, A. A., and Bleys, R. L. (2003). Central nervous system mechanisms in Sjögren's syndrome. *Br. J. Ophthalmol.* 87, 128–130. doi: 10.1136/bjo.87.2.128

van der Vaart, R., Weaver, M. A., Lefebvre, C., and Davis, R. M. (2015). The association between dry eye disease and depression and anxiety in a large population-based study. *Am. J. Ophthalmol.* 159, 470–474. doi: 10.1016/j.ajo.2014.11.028

von Hehn, C. A., Baron, R., and Woolf, C. J. (2012). Deconstructing the neuropathic pain phenotype to reveal neural mechanisms. *Neuron* 73, 638–652. doi: 10.1016/j.neuron.2012.02.008

Willcox, M. D. P., Argüeso, P., Georgiev, G. A., Holopainen, J. M., Laurie, G. W., Millar, T. J., et al. (2017). TFOS DEWS II tear film report. *Ocul. Surf.* 15, 366–403. doi: 10.1016/j.jtos.2017.03.006

Xing, W., Shi, W., Leng, Y., Sun, X., Guan, T., Liao, W., et al. (2018). Resting-state fMRI in primary Sjögren syndrome. *Acta Radiol.* 59, 1091–1096. doi: 10.1177/0284185117749993

Xu, M. W., Liu, H. M., Tan, G., Su, T., Xiang, C. Q., Wu, W., et al. (2019). Altered regional homogeneity in patients with corneal ulcer: a resting-state functional MRI study. *Front. Neurosci.* 13:743. doi: 10.3389/fnins.2019.00743

Yang, F. C., Chou, K. H., Fuh, J. L., Huang, C. C., Lirng, J. F., Lin, Y. Y., et al. (2013). Altered gray matter volume in the frontal pain modulation network in patients with cluster headache. *Pain* 154, 801–807. doi: 10.1016/j.pain.2013.02.005

Yoshida, T., McCarley, R. W., Nakamura, M., Lee, K., Koo, M. S., Bouix, S., et al. (2009). A prospective longitudinal volumetric MRI study of superior temporal gyrus gray matter and amygdala-hippocampal complex in chronic schizophrenia. *Schizophr. Res.* 113, 84–94. doi: 10.1016/j.schres.2009.05.004

Zang, Y., Jiang, T., Lu, Y., He, Y., and Tian, L. (2004). Regional homogeneity approach to fMRI data analysis. *Neuroimage* 22, 394–400. doi: 10.1016/j.neuroimage.2003.12.030

Zhang, X. D., Zhao, L. R., Zhou, J. M., Su, Y. Y., Ke, J., Cheng, Y., et al. (2020). Altered hippocampal functional connectivity in primary Sjögren syndrome: a resting-state fMRI study. *Lupus* 29, 446–454. doi: 10.1177/0961203320908936

Zhang, Y., and Wu, L. (2012). Classification of fruits using computer vision and a multiclass support vector machine. *Sensors* 12, 12489–12505. doi: 10.3390/s120912489

Zhu, F., Liu, F., Guo, W., Chen, J., Su, Q., Zhang, Z., et al. (2018). Disrupted asymmetry of inter- and intra-hemispheric functional connectivity in patients with drug-naive, first-episode schizophrenia and their unaffected siblings. *EBioMedicine* 36, 429–435. doi: 10.1016/j.ebiom.2018.09.012

Zubieta, J. K., Ketter, T. A., Bueller, J. A., Xu, Y., Kilbourn, M. R., Young, E. A., et al. (2003). Regulation of human affective responses by anterior cingulate and limbic mu-opioid neurotransmission. *Arch. Gen. Psychiatry* 60, 1145–1153. doi: 10.1001/archpsyc.60.11.1145

Conflict of Interest: The authors declare that the research was conducted in the absence of any commercial or financial relationships that could be construed as a potential conflict of interest.

frontiers in Human Neuroscience

ORIGINAL RESEARCH
published: 13 November 2020
doi: 10.3389/fnhum.2020.594830

Assessing Fine-Granularity Structural and Functional Connectivity in Children With Attention Deficit Hyperactivity Disorder

*Peng Wang[1,2,3], Xi Jiang[4,5], Hanbo Chen[5], Shu Zhang[6], Xiang Li[7], Qingjiu Cao[1,2], Li Sun[1,2], Lu Liu[1,2], Binrang Yang[3] and Yufeng Wang[1,2]**

[1] Peking University Sixth Hospital, Institute of Mental Health, Beijing, China, [2] National Clinical Research Center for Mental Disorders and the Key Laboratory of Mental Health, Ministry of Health (Peking University), Beijing, China, [3] Shenzhen Children's Hospital, Shenzhen, China, [4] School of Life Sciences and Technology, MOE Key Lab for Neuroinformation, University of Electronic Science and Technology of China, Chengdu, China, [5] Cortical Architecture Imaging and Discovery Lab, Department of Computer Science and Bioimaging Research Center, University of Georgia, Athens, GA, United States, [6] School of Computer Science, Northwestern Polytechnical University, Xi'an, China, [7] Massachusetts General Hospital, Harvard Medical School, Boston, MA, United States

OPEN ACCESS

Edited by:
Jurong Ding,
Sichuan University of Science and Engineering, China

Reviewed by:
Liang Zhan,
University of Pittsburgh, United States
Lu Zhang,
The University of Texas at Arlington, United States

***Correspondence:**
Yufeng Wang
wangyf@bjmu.edu.cn

Specialty section:
This article was submitted to Brain Imaging and Stimulation, a section of the journal Frontiers in Human Neuroscience

Received: *14 August 2020*
Accepted: *16 October 2020*
Published: *13 November 2020*

Citation:
Wang P, Jiang X, Chen H, Zhang S, Li X, Cao Q, Sun L, Liu L, Yang B and Wang Y (2020) Assessing Fine-Granularity Structural and Functional Connectivity in Children With Attention Deficit Hyperactivity Disorder. Front. Hum. Neurosci. 14:594830. doi: 10.3389/fnhum.2020.594830

Attention deficit hyperactivity disorder (ADHD) was considered to be a disorder with high heterogeneity, as various abnormalities were found across widespread brain regions in recent neuroimaging studies. However, remarkable individual variability of cortical structure and function may have partially contributed to these discrepant findings. In this work, we applied the Dense Individualized and Common Connectivity-Based Cortical Landmarks (DICCCOL) method to identify fine-granularity corresponding functional cortical regions across different subjects based on the shape of a white matter fiber bundle and measured functional connectivities between these cortical regions. Fiber bundle pattern and functional connectivity were compared between ADHD patients and normal controls in two independent samples. Interestingly, four neighboring DICCCOLs located close to the left parietooccipital area consistently exhibited discrepant fiber bundles in both datasets. The left precentral gyrus (DICCCOL 175, BA 6) and the right anterior cingulate gyrus (DICCCOL 321, BA 32) had the highest connection number among 78 pairs of abnormal functional connectivities with good cross-sample consistency. Furthermore, abnormal functional connectivities were significantly correlated with ADHD symptoms. Our studies revealed novel fine-granularity structural and functional alterations in ADHD.

Keywords: attention deficit hyperactivity disorder, fMRI, resting state, functional connectivity, diffusion tensor imaging, structural connectivity

INTRODUCTION

Attention deficit hyperactivity disorder (ADHD) is one of the most common neurobehavioral psychiatric disorders of childhood, and its prevalence rates based on teacher reports were an estimated 5.47% (Polanczyk et al., 2014). The typical symptoms are characterized as excessive inattention, hyperactivity/impulsiveness, or their combinations (Cortese, 2012). Over the past

several decades, functional and structural neuroimaging data provided a promising opportunity to understand this disorder better by revealing various differences in brain regions between ADHD patients and controls (Albajara Saenz et al., 2019). The classical prefrontal–striatal model (Castellanos et al., 2006) of ADHD could be extended to include other neural circuits and their relationships from the perspective of large-scale brain networks (Bush, 2010; Castellanos and Proal, 2012). The studies of resting-state functional connectivity also highlight the importance of brain interval connection.

The scattered brain areas that exhibit neuroactivities at resting state are called default mode network (DMN), which includes medial prefrontal cortex, precuneus/posterior cingulate cortex, lateral parietal cortex, and inferior temporal lobule. Previous studies have shown that the synchronization of neural activity (functional connectivity; Friston et al., 1993) within the default network and between the default network and the task-positive network is closely related to cognitive function. For example, a stronger negative correlation between default network and frontal–parietal network is associated with better behavioral performance (Kelly et al., 2008). An experiment comparing 24-h sleep deprivation state with natural arousal state showed that sleep deprivation increased the variation of subjects' reaction time in behavioral performance, and this phenomenon was related to the functional connectivity within DMN and the weakening of negative correlation between component DMN and external brain network (De Havas et al., 2012). Recently, studies using electroencephalogram have also proved the relationship between the variation of behavioral performance and the synchronization of brain activity (Gerrits et al., 2019; Machida et al., 2019; Kucyi et al., 2020). This association also exists in the ADHD population. In ADHD children, stronger frontal–striatal functional connectivity at the resting state is associated with better executive function, especially the inhibitory control (Li et al., 2014). Abnormal thalamo-caudate functional connectivity is associated with poor spatial working memory in ADHD children (Mills et al., 2012). In ADHD adults, functional connectivity within DMN and between DMN and attention network was associated with cognitive performance (Mowinckel et al., 2017).

A recent review also confirmed that the abnormal synchrony among brain regions in resting state is one of the characteristics of ADHD, mainly the decreasing synchronization between the anterior and posterior regions of DMN and the absence of anticorrelation between DMN and task-positive network (Posner et al., 2014; Castellanos and Aoki, 2016). In youths with ADHD, the anticorrelation between the dorsal anterior cingulate cortex (ACC) and DMN structures, including the posterior cingulate cortex, is decreased (Sun et al., 2012). Other studies with similar findings in the adult/child population (Sato et al., 2012; Hoekzema et al., 2014; Kumar et al., 2020). Furthermore, methylphenidate hydrochloride, as the most commonly used effective medication for the treatment of ADHD, can normalize the deactivation of the ventromedial prefrontal cortex (vmPFC) and posterior cingulate gyrus and improve cognitive performance (Peterson et al., 2009; Liddle et al., 2011). Multiple studies also confirmed that medication could normalize the DMN function connectivity of ADHD patients (Pereira-Sanchez and de Castro Manglano, 2017) and improve their cognitive task performance (Mowinckel et al., 2017). In conclusion, studying the relationship between brain regions from the whole-brain level, rather than a single region or network, is necessary for ADHD research.

However, in the ADHD research field, high heterogeneity has become an important issue (Luo et al., 2019). In addition to the complex etiology, individual differences in brain structure and function are also important factors. In the studies on the relationship between brain regions, how to define "brain regions" in different brains is a critical problem. The consensus is that the research results of functional connectivity based on seed points [regions of interest (ROIs)] are easily affected by the selection of seed points, which is a relatively subjective process (Power et al., 2012). Due to the possible heterogeneity inside the selected brain regions and the complexity of the human brain, the results may vary with the size of the selected "brain region." Using an activation experiment to define ROI could reduce the feasibility and repeatability of the research. To define ROI by meta-analysis according to the ROIs in previous studies, we need to ignore the possible differences in brain structure among individuals, and previous experiments could also have the problem in selecting ROI. In the previous studies of functional connectivity, a very small change in the ROI will greatly change the results. This phenomenon is largely due to the limitations of functional magnetic resonance imaging (fMRI) technology (Zhu et al., 2011; Li et al., 2013).

Furthermore, regarding the future clinical application of resting-state fMRI (RS-fMRI), pointed out that one of the future directions would be big sample data, and acquiring large samples needs multisite data sharing. Big data from a single site may produce statistically significant but trivial results, whereas no result is believable until it has been replicated in multiple independent datasets (Castellanos et al., 2013). Big data would be a possible solution to the heterogeneity of ADHD fMRI research, but it also faces the problem of individual differences in human brain structure and function. In four independent ADHD datasets, Wang et al. (2017) applied several commonly used resting-state analysis, including regional homogeneity, amplitude of low-frequency fluctuation, and degree centrality, and found that there were no overlapping abnormal brain regions among datasets, although three of the four datasets were collected in the same site. In addition to the high heterogeneity of ADHD, due to the complexity and individual differences of the human brain, the co-registration process of fMRI data may also be one of the relevant factors. At present, the common method in fMRI researches (74% of 9,400 fMRI studies; Derrfuss and Mar, 2009) is to register the brains of different individuals on a unified Talairach or Montreal Neurological Institute template to define corresponding brain regions. Due to the lack of accurate information on the boundaries of brain regions and the large differences in the structure/function of brain regions among individuals, the results largely depend on the algorithm of the registration step (Zhang and Cootes, 2011).

Therefore, in the ADHD fMRI study, under the demand of multicenter data sharing, considering the individual brain

differences, a method to define brain regions with fine-granularity and better structural/functional consistency across brains is warranted.

The Dense Individualized and Common Connectivity-based Cortical Landmarks (DICCCOL; Zhu et al., 2013) system defined 358 individualized landmarks with structural and functional consistency across different brains. The physiological basis of this method is the "connectional fingerprint concept" (Passingham et al., 2002), which premised that each brain's cytoarchitectonic area has a unique set of extrinsic inputs and outputs that largely determines the functions that each brain area performs. This close relationship between structure and function had been supported by some evidence (Honey et al., 2009; Li et al., 2010; Zhu et al., 2012). Therefore, 358 DICCCOLs are 358 landmarks on the cortex with consistent similar fiber bundle patterns across individual subjects. Because of this good functional consistency across different brains, DICCCOL could be one of the most promising methods that may help us to observe ADHD without the interference of individual variability of cortical structure and function. For the same reason, DICCCOL also provides better comparability for results from different datasets. Another benefit of applying DICCCOL in researching psychiatric disorders is the potential usage for white-matter (WM) abnormity detection. ADHD was considered a psychiatric disorder with WM abnormity based on previous diffusion tensor imaging (DTI) research (van Ewijk et al., 2012; Aoki et al., 2018). Also, we have found some discrepant DICCCOLs in ADHD patients with different fiber bundle patterns (Wang et al., 2013).

Thus, in the current study, we adopted the DICCCOL system in two independent ADHD datasets. We hypothesized that children with ADHD (1) exhibit abnormal fiber bundle, (2) exhibit abnormal resting functional connectivities, and (3) exhibit consistent abnormalities across independent datasets.

MATERIALS AND METHODS

Subjects

This study includes two independent datasets. These two datasets were collected for different purposes and using different scan parameters. Previous analysis of these datasets has been published elsewhere separately (An et al., 2013; Cao et al., 2013). Only diffusion-weighted MRI and RS-fMRI scans were used in the current study. The following inclusion criteria were used for the ADHD group: (a) age between 8 and 14 years at the time point of the scan; (b) diagnosis of ADHD by a clinician using the Schedule for Affective Disorders and Schizophrenia for School-Age Children–Present and Lifetime Version (Kaufman et al., 2000); and (c) right-handedness. The following exclusion criteria were used: (a) other Axis-I psychiatric diagnoses; (b) IQ < 80 using the Chinese Wechsler Intelligence Scale for Children (Gong and Cai, 1993); (c) psychotropic medication history; and (d) any significant medical or neurological conditions or a history of head injury. In the two datasets, the inclusion and exclusion criteria of the control group were basically the same as those of the ADHD group, but the subjects in the control group did not meet the diagnostic criteria of ADHD. There are 25 ADHD-combined-type children and 45 age- and sex-matched controls in dataset 1. For dataset 2, 11 ADHD-combined-type children and 26 controls who matched in age and sex are included. The demographic characteristics of all participants are shown in **Table 1**.

The ADHD Rating Scale-IV forms were collected from the parents of ADHD children to assess the severity of ADHD

TABLE 1 | Demographic characteristics of two datasets.

		ADHD	Control	*p*
Dataset 1 diffusion-weighted MRI	Number (m/f)	25 (24/1)	45 (35/10)	$p = 0.09$
	Age (years)	11.05 (1.68)	11.00 (1.40)	$p = 0.89$
	IQ	108.1 (16.7)	121.3 (13.6)	$p < 0.001$
	Inattention scores	27.0 (12.2)	16.1 (4.0)	$p < 0.001$
	Impulsivity scores	27.2 (11.1)	15.1 (4.0)	$p < 0.001$
Dataset 1 fMRI (6 participants were excluded for head motion)	Number (m/f)	23 (22/1)	41 (31/10)	$p = 0.09$
	Age (years)	11.08 (1.67)	11.06 (1.40)	$p = 0.96$
	IQ	108.65 (16.97)	122.27 (13.61)	$p < 0.001$
	Inattention scores	26.77 (4.00)	16.15 (3.87)	$p < 0.001$
	Impulsivity scores	25.36 (7.44)	15.27 (3.94)	$p < 0.001$
Dataset 2	Number (m/f)	11 (11/0)	26 (26/0)	
	Age (years)	11.71 (2.13)	11.98 (1.77)	$p = 0.69$
	IQ	114.36 (13.86)	119.04 (12.80)	$p = 0.33$
	Inattention scores	28.00 (4.38)	15.23 (2.54)	$p < 0.001$
	Impulsivity scores	25.55 (5.91)	13.04 (3.86)	$p < 0.001$

Values are mean (standard deviation). Six subjects in Dataset 1 were excluded for head motion during fMRI preprocessing.

symptoms. Written informed consent was obtained from each parent, and each child agreed to participate. The Institutional Review Board at the Health Center of Peking University approved this study.

Imaging Parameters

Both two datasets with multimodal diffusion-weighted/RS-fMRI data are acquired in a SIEMENS TRIO 3T scanner at the State Key Laboratory of Cognitive Neuroscience and Learning, Beijing Normal University. The diffusion-weighted MRI images of dataset 1 are acquired using the following parameters: 49 axial slices, repetition time (TR) = 7,200 ms, echo time (TE) = 104 ms, flip angle = 90°, 64 diffusion directions, b = 1,000 s/mm2, thickness = 2.5 mm, slice spacing = 0 mm, and acquisition matrix = 128 × 128. As for dataset 2, the diffusion-weighted MRI images are acquired by following parameters: 47 axial slices, TR = 6,900 ms, TE = 104 ms, flip angle = 90°, 64 diffusion directions, b = 1,000 s/mm2, thickness = 2.5 mm, slice spacing = 2.5 mm, and acquisition matrix = 128 × 128. The RS-fMRI images of these two datasets shared similar parameters. They were acquired using an echo-planar imaging sequence with 33 axial slices, TR = 2,000 ms, TE = 30 ms, flip angle = 90°, slice thickness = 3 mm, slice spacing = 3.6 mm, in-plane resolution = 64 × 64, and 240 volumes.

Image Preprocessing

Preprocessing of the diffusion-weighted MRI data include brain skull removal, head motion correction, and eddy current correction. Subsequently, fibers tracts, gray matter and WM tissue segmentations (Liu et al., 2007), and the cortical surface were generated based on the diffusion-weighted MRI data (Liu et al., 2008). Specifically, fiber tracking was performed via the MEDINRIA[1]. The fractional anisotropy threshold was 0.2, and the minimum fiber length was 20 mm. Brain tissue segmentation was conducted on the diffusion-weighted MRI data directly (Liu et al., 2007). Our DICCCOL landmark is identified based on WM fiber tracts and located on WM cortical surface derived from DTI data. So, we performed segmentation on DTI data directly instead of structural MRI to avoid any structural MRI-DTI registration error. Based on the WM tissue map, the cortical surface was reconstructed using the marching cubes algorithm (Liu et al., 2008). The RS-fMRI data preprocessing steps include motion correction, spatial smoothing, slice time correction, global drift removal, and bandpass filtering (0.01–0.1 Hz) via FSL FEAT software[2]. The DTI space was used as the standard space. RS-fMRI data were registered to the DTI space via the FSL FLIRT software (Jenkinson and Smith, 2001).

Dense Individualized and Common Connectivity-Based Cortical Landmark Identification

We defined 358 DICCCOL ROIs (Zhu et al., 2013) based on diffusion-weighted MRI data on each participant's brain. As mentioned earlier, this method has been proven to be reasonably consistent and reproducible in over 240 brains (Zhu et al., 2013). In brief, the DICCCOL prediction process is based on the consistency of WM fiber connection patterns across brains, and it is composed of three major steps: initial landmark selection, optimization of landmark locations, and determination of group-wise consistent DICCCOLs. Details of the process can be found in the previous publication (Zhu et al., 2013).

In the discussed steps, the shape of each fiber bundle will be quantified as a "trace-map." In this way, the morphological differences between fiber bundles can be quantified as "trace-map distance." The specific algorithm can be found in the previous publication (Li et al., 2010). According to our previous work (Wang et al., 2013), among ADHD patients, specific DICCCOL ROIs show a significantly higher trace-map distance to the given models compared with the normal controls. In the current study, using the same one-side t-test method ($p < 0.05$), abnormal DICCCOL ROIs in each dataset were identified. Then, we investigated whether there are overlapped results between the two datasets.

Functional Connectivity Analysis

Because the DICCCOL method is based on the "Connectional Fingerprint Concept" (Passingham et al., 2002), which simply stated that only brain landmarks with similar WM fiber bundle morphology are considered to have functional correspondence among different individual brains and thus can be used as an ROI of functional analysis, in the current research, only DICCCOL ROIs without significant group differences in the trace-map distance were involved in resting-state functional connectivity analysis.

After the co-registration between fMRI and diffusion-weighted MRI data, we extracted the RS-fMRI BOLD signals of each DICCCOL ROI for each participant. Functional connectivities were calculated for each pair of DICCCOL ROIs. After Fisher's r-to-z transform, we conducted between-group comparison ($p < 0.05$). Again, by overlapping the result of two datasets, we got a relatively consistent abnormal functional connectivity map.

Correlation Analysis Between Functional Connectivity and Symptom Severity

To study the relationship between ADHD symptoms (ADHD-RS score) and abnormal functional connectivity with good cross-sample universality, we applied generalized linear regression, with covariances including age/sex/IQ.

RESULTS

Demographic Data

The information for the demographics/clinical data of the participants is summarized in **Table 1**. For the analysis of continuous variables, a t-test was used to compare means. Categorical variables were compared with the chi-square test. The differences in sex and age were not significant.

[1]http://www-sop.inria.fr/asclepios/software/MedINRIA/

[2]http://fsl.fmrib.ox.ac.uk/fsl/feat5/

Discrepant Dense Individualized and Common Connectivity-Based Cortical Landmarks in Attention Deficit Hyperactivity Disorder

As expected, in the ADHD group, certain DICCCOL ROIs displayed notably higher trace-map distance compared with the control group, which indicated that the fiber bundle patterns at these locations have higher variability. Four DICCCOL ROIs (DICCCOL numbers: 34, 37, 38, and 44) among them were shared by both datasets. The positions and trace map distance of these four DICCCOL ROIs, as well as the shape of the fiber bundles, are shown in **Figure 1**. The information of all 358 DICCCOL fiber bundle patterns and comparison between groups can be found in the **Supplementary Materials.**

Results of Functional Connectivity Analysis

The 78 consistent abnormal functional connectivities in the ADHD group across datasets are shown in **Figure 2**. Among the abnormal functional connectivities, 10 were related to DICCCOL 175, and nine were related to DICCCOL 321.

Results of Correlation Analysis Between Functional Connectivity and Symptom Severity

Three of the 78 overlapping functional connectivities (Z score) significantly predicted the ADHD parent rating scale score. The result is shown in **Figure 3**. Based on the previous study that labeled DICCCOLs with functional meaning (Yuan et al., 2013), the physiological significance of these three functional connectivities is shown in **Table 2**.

DISCUSSION

In the current study, after the DICCCOL prediction procedure, we found that ADHD patients showed notably discrepant fiber bundle patterns on a number of DICCCOLs, and four of them were shared by both datasets. As shown in **Figure 1**, DICCCOLs

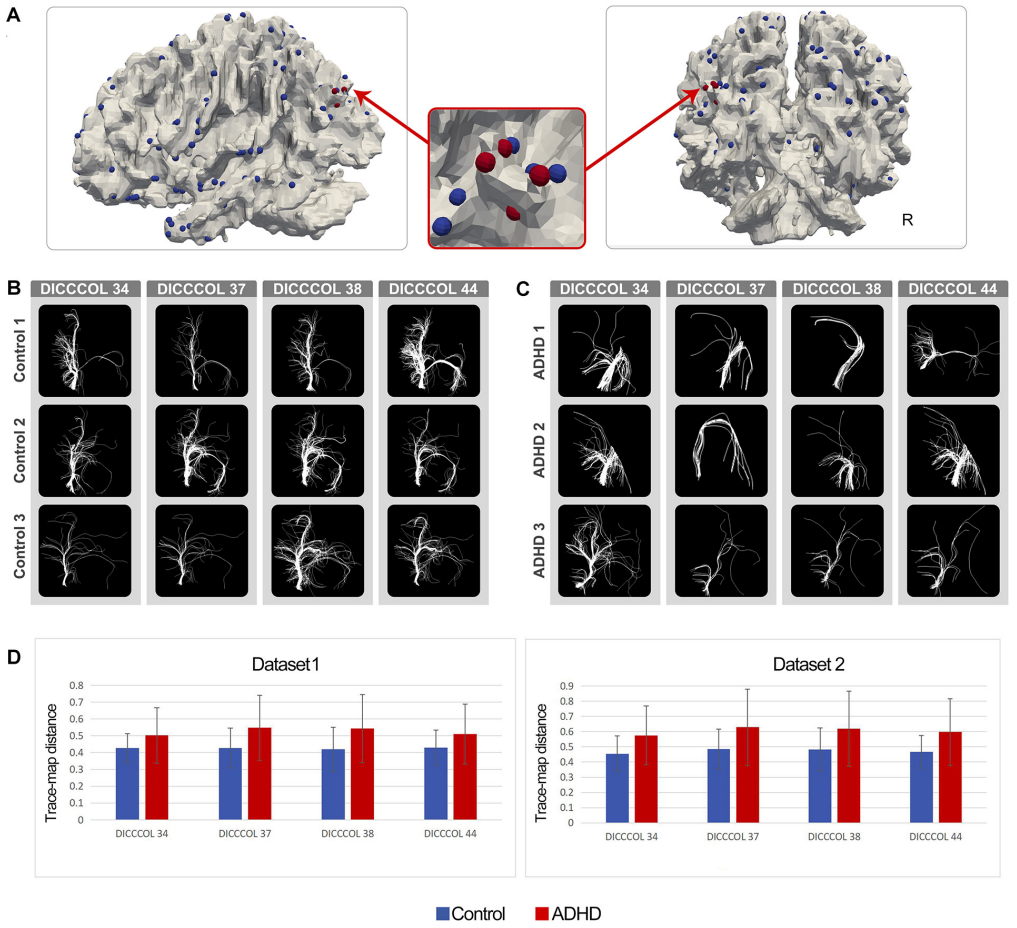

FIGURE 1 | (A) Distribution of DICCCOLs: 34, 37, 38, and 44 (four red bubbles); **(B)** Fiber bundle of DICCCOLs 34, 37, 38, and 44 in three random NC brains; each row represents a participant; **(C)** Fiber bundle of DICCCOLs 34, 37, 38, and 44 in three random ADHD patients' brains; each row represents a participant; **(D)** Trace-map distance of DICCCOLs 34, 37, 38, and 44 in dataset 1 and dataset 2.

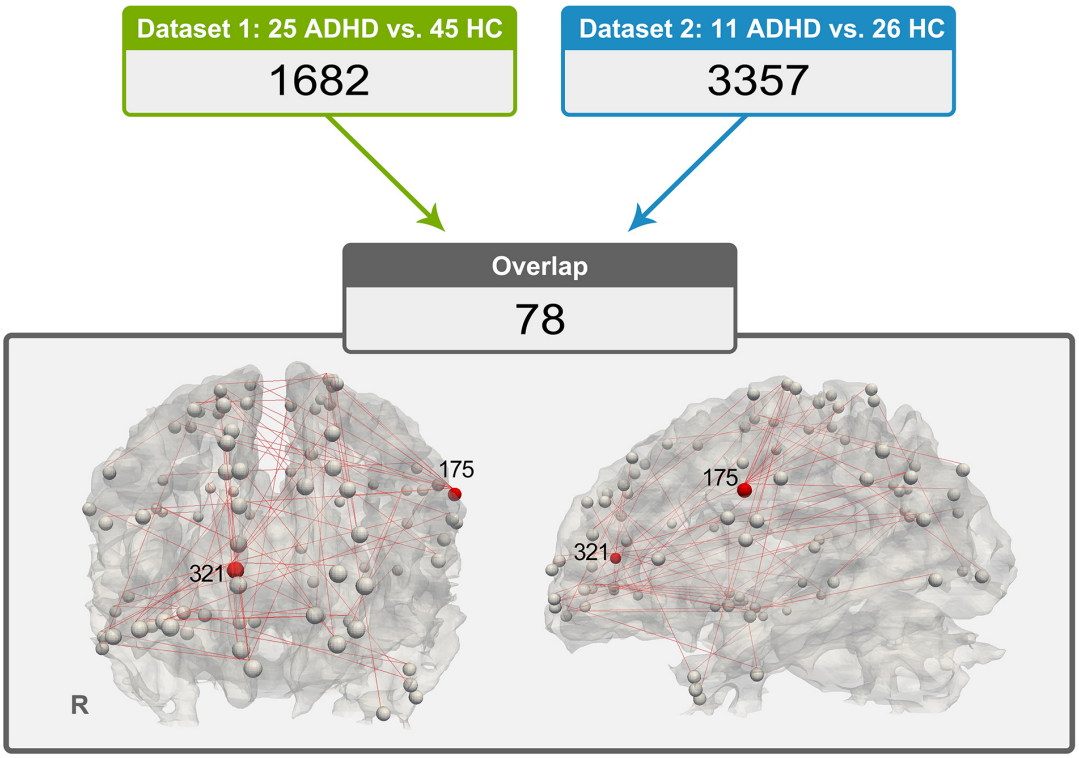

FIGURE 2 | Distribution of 78 pairs of discrepant functional connectivity, which could indicate the importance of DICCCOL nos. 321 and 175 in this abnormal network (a relatively large number of red lines are connected).

34, 37, 38, and 44 were located near the left parietooccipital junction and had a very close spatial position. In addition, 78 abnormal functional connectivities exhibited good cross-sample consistency. Three of them were significantly related to the severity of ADHD symptoms.

The DICCCOL method established 358 individual landmarks on each participant's brain. DICCCOLs with the same number were considered to have good functional correspondence among different participants. A meta-analysis labeled each DICCCOL with functional meaning by registering them to 1,110 previous task-fMRI research (Yuan et al., 2013). The result interpretation of the current study is based on this publication.

We found that DICCCOL nos. 34, 37, 38, and 44, located near the junction of the left parietal and occipital lobe, exhibited abnormal fiber bundle structure in the ADHD group. These four DICCCOLs were very close in spatial location, and there were no other DICCCOLs between them. Therefore, we speculated that these four DICCCOLs might be small subregions of a larger functional brain region. These abnormalities of the four adjacent landmarks may indicate the structural and, thus, functional (Passingham et al., 2002) abnormalities in this larger brain region. Furthermore, among the 358 landmarks all over the brain, only four adjacent ones of them were found, which also highlighted the significance of this large brain area in the pathological mechanism of ADHD. According to previous meta-analysis (Yuan et al., 2013), the functions of these four DICCCOLs are undefined. DICCCOL nos. 34, 37, 38, and 44 were located in the left posterior parietal lobe/upper occipital lobe, and its spatial distribution was similar to the DMN components. The most consistent components of the DMN are medial regions (medial prefrontal, posterior cingulate/precuneus) and lateral regions (posterior parietal lobe) of the brain. These structures are usually reduced in activity in cognitive tasks requiring attention (Raichle et al., 2001; Raichle, 2014). Therefore, it can also explain that these four DICCCOLs were not activated in as much as 1,110 previous studies and thus were labeled as undefined (Yuan et al., 2013). So, the results of the current study supported the hypothesis that ADHD patients have abnormalities in posterior DMN.

By applying functional connectivity analysis between DICCCOL ROIs with no difference in WM fiber bundle morphology, we obtained 1,682 functional connectivities with between-group differences in dataset 1 and 3,357 in dataset 2. Seventy-eight of them exhibited good consistency across datasets. Interestingly, we found that a quarter (19 of 78) of these abnormal functional connectivities were associated with DICCCOL ROI nos. 175 and 321. Therefore, these two DICCCOLs with abnormal functional connectivities, which are consistently shown in two separate datasets, may play an important role in the pathogenesis of ADHD.

According to the previous meta-analysis (Yuan et al., 2013), DICCCOL 175 was located in the left precentral gyrus and was related to "Cognition. Speech. Language. Working Memory. Attention." Functional and structural abnormalities of the precentral gyrus are common in ADHD studies. In a recent

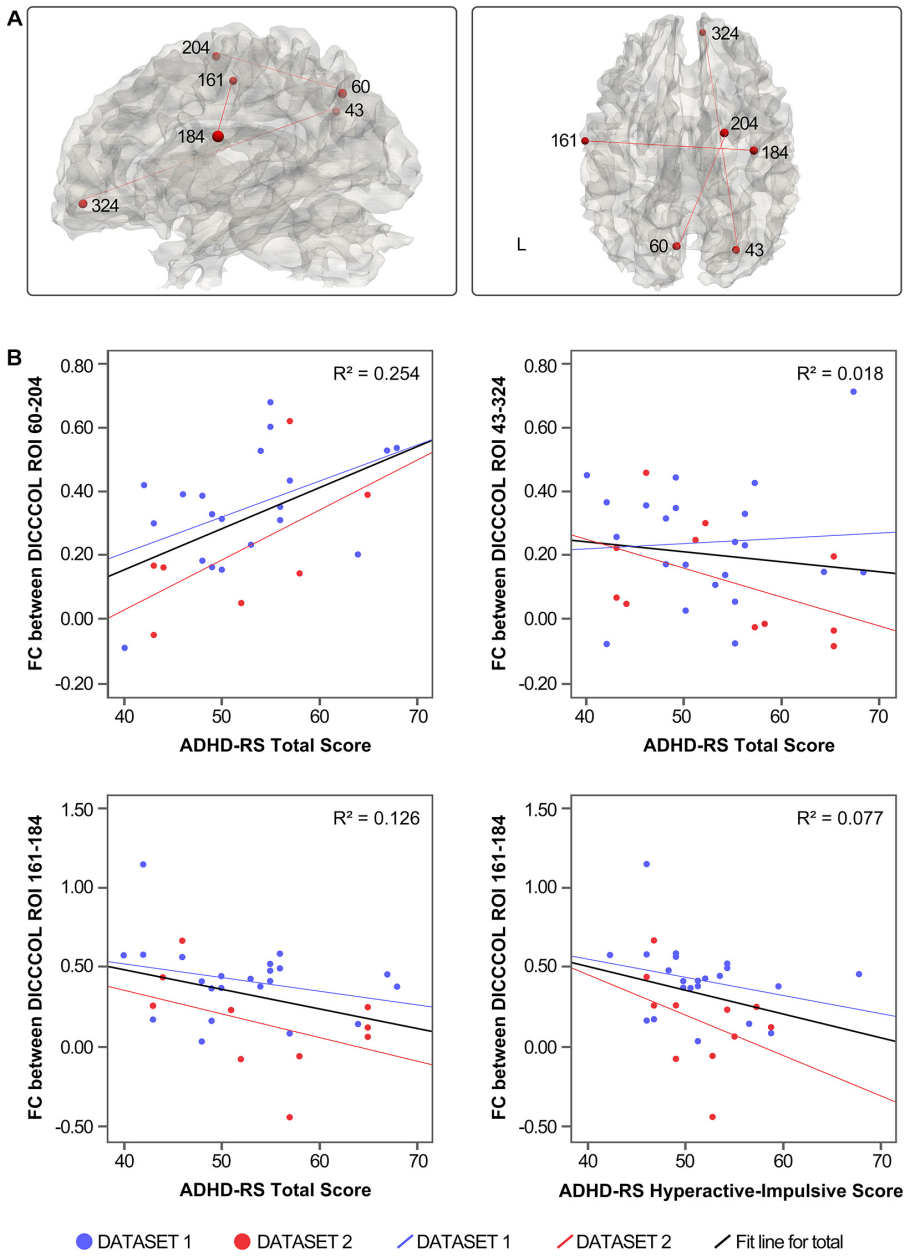

FIGURE 3 | (A) Distribution of functional connectivities. **(B)** Correlation between functional connectivities and symptom severity.

TABLE 2 | Physiological significance of functional connectivity related to the severity of ADHD symptoms.

DICCCOL number	Location	Brodmann area	Function
60	Left precuneus	7	None
~204	Right superior frontal gyrus	6	Cognition, Language, Memory.
43	Right precuneus	19	Cognition, Attention, Language
~324	Right anterior cingulate	10	None
161	Right precentral gyrus	4	Action, Attention, Memory, Emotion
~184	Left precentral gyrus	43	Action, Language, Emotion, Language

resting-state functional connectivity study of ADHD, Guo also used whole-brain functional connectivity to classify features for machine learning and found that two of the four features with the best discriminability were related to the precentral gyrus, namely the precentral gyrus–prefrontal lobe and the precentral gyrus–superior temporal gyrus (Guo et al., 2020). In a young adult with ADHD, Krista found that the cerebral cortex thickness of the precentral and postcentral gyrus was the only brain regions associated with the persistence of ADHD, and the cluster in the precentral gyrus was close to that of DICCCOL 175 (Lisdahl et al., 2016). Bernis found that the cortical of the bilateral precentral gyrus and supplementary motor area in ADHD children was thicker than that in normal controls, and the thickness was positively correlated with the severity of ADHD symptoms (Sutcubasi Kaya et al., 2018). Therefore, in the current study, the abnormal functional connectivity of the 175 DICCCOL ROI supported the findings in previous researches. Considering that ADHD children are asked to "keep still" during a scan, for individuals with more prominent hyperactivity symptoms, it is necessary to suppress motor-related impulses. This finding may reflect the inhibition of motor impulse in ADHD children under a resting state.

DICCCOL 321 located in the right anterior cingulate gyrus is related to cognition and emotion (Yuan et al., 2013). During the various task, such as go/no go, response inhibition, attention, and hypoactivity of ACC were found by fMRI, PET, and event-related potential in ADHD patients (Rubia et al., 1999; Durston et al., 2003, 2007). A meta-analysis that included 16 task state functional brain image studies also found that ACC was one of the brain regions with consistent hypoactivity in ADHD patients across studies (Dickstein et al., 2006). In addition, after the DMN interference hypothesis was put forward (Kelly et al., 2008), ACC has been widely concerned because of its weak negative correlation with DMN components in ADHD children and adults (Sato et al., 2012; Sun et al., 2012). Furthermore, the efficacy of stimulant treatment in patients with ADHD-combined type is related to the volume of right ACC (Semrud-Clikeman et al., 2014). In ADHD adults, using single-voxel proton magnetic resonance spectroscopy, glutamate levels in the ACC were higher than the control group and positively correlated with ADHD symptomatology (Bauer et al., 2016). Therefore, the abnormal ACC functional connectivities found in this study are consistent with previous studies, reflecting the abnormal brain activity outside the default network of ADHD patients under resting state.

The functional connectivities related to ADHD symptoms were mostly between the default network components and other brain networks, such as the right precuneus and the right ACC (DICCCOL 43–324) and left precuneus and right superior frontal gyrus (DICCCOL 60–204), which reflected the abnormal function of DMN and other networks in resting state. In addition, functional connectivity between the bilateral precentral gyrus (DICCCOL 161–184) was associated with hyperactivity impulse scores. Together with the discussed findings of abnormal functional connectivity in the precentral gyrus (DICCCOL 175), this finding highlights the significance of abnormal activity of the precentral gyrus in patients with ADHD under resting state. In contrast, there is no functional connectivities related to the inattention score of ADHD-RS, which may be related to the low demand on attention level in the resting state. This issue could be verified in the future by combining task and resting-state scans.

The current study has the following limitations: (1) we abandoned some abnormal DICCCOLs during fMRI analysis, so 322 DICCCOLs are not a perfect representation of the "whole-brain;" however, the brain activity with more ADHD characteristics may be reflected in these DICCCOLs. As mentioned in *Method*, because these abnormal DICCCOLs do not have good WM fiber bundle morphological similarity, we cannot arbitrarily determine their functional correspondence. This is the temporary limitation of the DICCCOL method and a critical issue to be overcome in the application of future disease research. (2) The "connectional fingerprint concept" (Passingham et al., 2002) is a theory based on healthy individuals, so its application in the disease population needs to be cautious. (3) Small sample size may influence the results; also, the imbalance of sample size will lead to lower statistical efficiency. The findings of the current study need to be validated on a larger multicenter sample.

In this study, we used the DICCCOL method and replicated some findings consistent with previous studies on two independent ADHD samples, and some unique findings were also found: there were morphological abnormalities in the WM tracts in the left posterior cortex of the DMN in children with ADHD; in the resting state, the abnormal functional connectivities with good cross-sample consistency mainly involved attention, motion, emotion, and working memory (DICCCOL 175/321). This study provides a new possibility for multicenter and large sample ADHD study in the future. Although the physiological significance of the part of the DICCCOL landmarks is still unclear, Castellanos points out that effective biomarkers do not necessarily have a clear neurophysiological significance or explanation (Castellanos et al., 2013). From this point of view, DICCCOL, which is easy to operate and has good interindividual functional consistency, is a possible direction for the clinical application of resting-state fMRI.

DATA AVAILABILITY STATEMENT

The raw data supporting the conclusions of this article will be made available by the authors, without undue reservation.

ETHICS STATEMENT

The studies involving human participants were reviewed and approved by the Institutional Review Board at the Health Center of Peking University. Written informed consent to participate in this study was provided by the participants' legal guardian/next of kin.

AUTHOR CONTRIBUTIONS

YW, PW, and SZ: conception and design. PW, XJ, HC, SZ, XL, BY, and YW: analysis and interpretation. PW, QC, LS, and LL: data collection. PW and SZ writing the manuscript. XJ and QC: critical revision of the manuscript. PW, SZ, and XJ: statistical analysis. YW: overall responsibility. All authors contributed to the article and approved the submitted version.

FUNDING

This study was funded by the National High Technology Research and Development Program of China (863 Program) (No. 2008AA022605), the National Basic Research Development Program of China (973 program) (No. 2014CB846104), the National Natural Science Foundation of China (No. 81000594), and the Sanming Project of Medicine in Shenzhen "The ADHD research group from Peking University Sixth hospital" (No. SZSM201612036).

ACKNOWLEDGMENTS

Thanks are due to Meilin Wang for kind assistance in figure editing and valuable discussion on results. The authors thank all the children and adolescents who participated in the research.

SUPPLEMENTARY MATERIAL

The Supplementary Material for this article can be found online at: https://www.frontiersin.org/articles/10.3389/fnhum.2020.594830/full#supplementary-material

REFERENCES

Albajara Saenz, A., Villemonteix, T., and Massat, I. (2019). Structural and functional neuroimaging in attention-deficit/hyperactivity disorder. *Dev. Med. Child. Neurol.* 61, 399–405. doi: 10.1111/dmcn.14050

An, L., Cao, X. H., Cao, Q. J., Sun, L., Yang, L., Zou, Q. H., et al. (2013). Methylphenidate normalizes resting-state brain dysfunction in boys with attention deficit hyperactivity disorder. *Neuropsychopharmacology* 38, 1287–1295. doi: 10.1038/npp.2013.27

Aoki, Y., Cortese, S., and Castellanos, F. X. (2018). Research review: diffusion tensor imaging studies of attention-deficit/hyperactivity disorder: meta-analyses and reflections on head motion. *J. Child Psychol. Psychiatry* 59, 193–202. doi: 10.1111/jcpp.12778

Bauer, J., Werner, A., Kohl, W., Kugel, H., Shushakova, A., Pedersen, A., et al. (2016). Hyperactivity and impulsivity in adult attention-deficit/hyperactivity disorder is related to glutamatergic dysfunction in the anterior cingulate cortex. *World J. Biol. Psychiatry* 19, 538–546. doi: 10.1080/15622975.2016.1262060

Bush, G. (2010). Attention-deficit/hyperactivity disorder and attention networks. *Neuropsychopharmacology* 35, 278–300. doi: 10.1038/npp.2009.120

Cao, Q., Shu, N., An, L., Wang, P., Sun, L., Xia, M. R., et al. (2013). Probabilistic diffusion tractography and graph theory analysis reveal abnormal white matter structural connectivity networks in drug-naive boys with attention deficit/hyperactivity disorder. *J. Neurosci.* 33, 10676–10687. doi: 10.1523/JNEUROSCI.4793-12.2013

Castellanos, F. X., and Aoki, Y. (2016). Intrinsic functional connectivity in attention-deficit/hyperactivity disorder: a science in development. *Biol. Psychiatry Cogn. Neurosci. Neuroimag.* 1, 253–261. doi: 10.1016/j.bpsc.2016.03.004

Castellanos, F. X., Di Martino, A., Craddock, R. C., Mehta, A. D., and Milham, M. P. (2013). Clinical applications of the functional connectome. *Neuroimage* 80, 527–540. doi: 10.1016/j.neuroimage.2013.04.083

Castellanos, F. X., and Proal, E. (2012). Large-scale brain systems in ADHD: beyond the prefrontal-striatal model. *Trends Cogn. Sci.* 16, 17–26. doi: 10.1016/j.tics.2011.11.007

Castellanos, F. X., Sonuga-Barke, E. J., Milham, M. P., and Tannock, R. (2006). Characterizing cognition in ADHD: beyond executive dysfunction. *Trends Cogn. Sci.* 10, 117–123. doi: 10.1016/j.tics.2006.01.011

Cortese, S. (2012). The neurobiology and genetics of Attention-Deficit/Hyperactivity Disorder (ADHD): what every clinician should know. *Eur. J. Paediatr. Neurol.* 16, 422–433. doi: 10.1016/j.ejpn.2012.01.009

De Havas, J. A., Parimal, S., Soon, C. S., and Chee, M. W. (2012). Sleep deprivation reduces default mode network connectivity and anti-correlation during rest and task performance. *Neuroimage* 59, 1745–1751. doi: 10.1016/j.neuroimage.2011.08.026

Derrfuss, J., and Mar, R. A. (2009). Lost in localization: the need for a universal coordinate database. *Neuroimage* 48, 1–7. doi: 10.1016/j.neuroimage.2009.01.053

Dickstein, S. G., Bannon, K., Castellanos, F. X., and Milham, M. P. (2006). The neural correlates of attention deficit hyperactivity disorder: an ALE meta-analysis. *J. Child Psychol. Psychiatry* 47, 1051–1062. doi: 10.1111/j.1469-7610.2006.01671.x

Durston, S., Davidson, M. C., Mulder, M. J., Spicer, J. A., Galvan, A., Tottenham, N., et al. (2007). Neural and behavioral correlates of expectancy violations in attention-deficit hyperactivity disorder. *J. Child Psychol. Psychiatry* 48, 881–889. doi: 10.1111/j.1469-7610.2007.01754.x

Durston, S., Tottenham, N. T., Thomas, K. M., Davidson, M. C., Eigsti, I. M., Yang, Y., et al. (2003). Differential patterns of striatal activation in young children with and without ADHD. *Biol. Psychiatry* 53, 871–878. doi: 10.1016/s0006-3223(02)01904-2

Friston, K. J., Frith, C. D., Liddle, P. F., and Frackowiak, R. S. (1993). Functional connectivity: the principal-component analysis of large (PET) data sets. *J. Cereb. Blood Flow Metab.* 13, 5–14. doi: 10.1038/jcbfm.1993.4

Gerrits, B., Vollebregt, M. A., Olbrich, S., van Dijk, H., Palmer, D., Gordon, E., et al. (2019). Probing the "Default Network Interference Hypothesis". With EEG: an rdoc approach focused on attention. *Clin. EEG Neurosci.* 50, 404–412. doi: 10.1177/1550059419864461

Gong, Y., and Cai, T. (1993). *Wechsler Intelligence Scale for Chinese Children (C-WISC)*. Changsha: Hunan Map Press.

Guo, X., Yao, D., Cao, Q., Liu, L., Zhao, Q., Li, H., et al. (2020). Shared and distinct resting functional connectivity in children and adults with attention-deficit/hyperactivity disorder. *Transl. Psychiatry* 10:65. doi: 10.1038/s41398-020-0740-y

Hoekzema, E., Carmona, S., Ramos-Quiroga, J. A., Richarte Fernandez, V., Bosch, R., Soliva, J. C., et al. (2014). An independent components and functional connectivity analysis of resting state fMRI data points to neural network dysregulation in adult ADHD. *Hum. Brain Mapp.* 35, 1261–1272. doi: 10.1002/hbm.22250

Honey, C. J., Sporns, O., Cammoun, L., Gigandet, X., Thiran, J. P., Meuli, R., et al. (2009). Predicting human resting-state functional connectivity from structural connectivity. *Proc. Natl. Acad. Sci. U S A.* 106, 2035–2040. doi: 10.1073/pnas.0811168106

Jenkinson, M., and Smith, S. (2001). A global optimisation method for robust affine registration of brain images. *Med. Image Anal.* 5, 143–156. doi: 10.1016/s1361-8415(01)00036-6

Kaufman, J., Birmaher, B., Ryan, N., and Rao, U. (2000). K-Sads-Pl. *J. Am. Acad. Child Adolesc. Psychiatry* 39:1208. doi: 10.1097/00004583-200010000-00002

Kelly, A. M. C., Uddin, L. Q., Biswal, B. B., Castellanos, F. X., and Milham, M. P. (2008). Competition between functional brain networks mediates behavioral variability. *Neuroimage* 39, 527–537. doi: 10.1016/j.neuroimage.2007.08.008

Kucyi, A., Daitch, A., Raccah, O., Zhao, B., Zhang, C., Esterman, M., et al. (2020). Electrophysiological dynamics of antagonistic brain networks reflect attentional fluctuations. *Nat. Commun.* 11:325. doi: 10.1038/s41467-019-14166-2

Kumar, U., Arya, A., and Agarwal, V. (2020). Neural network connectivity in ADHD children: an independent component and functional connectivity analysis of resting state fMRI data. *Brain Imag. Behav*. doi: 10.1007/s11682-019-00242-0 Online ahead of print.

Li, F., He, N., Li, Y., Chen, L., Huang, X., Lui, S., et al. (2014). Intrinsic brain abnormalities in attention deficit hyperactivity disorder: a resting-state functional MR imaging study. *Radiology* 272, 514–523. doi: 10.1148/radiol.14131622

Li, K., Guo, L., Faraco, C., Zhu, D., Deng, F., Zhang, T., et al. (2010). "Individualized ROI optimization via maximization of group-wise consistency of structural and functional profiles," in *Paper Presented at the Advances in Neural Information Processing Systems*, (Noida: NIPS).

Li, K., Zhu, D., Guo, L., Li, Z., Lynch, M. E., Coles, C., et al. (2013). Connectomics signatures of prenatal cocaine exposure affected adolescent brains. *Hum. Brain Mapp.* 34, 2494–2510. doi: 10.1002/hbm.22082

Liddle, E. B., Hollis, C., Batty, M. J., Groom, M. J., Totman, J. J., Liotti, M., et al. (2011). Task-related default mode network modulation and inhibitory control in ADHD: effects of motivation and methylphenidate. *J. Child Psychol. Psychiatry* 52, 761–771. doi: 10.1111/j.1469-7610.2010.02333.x

Lisdahl, K., Tamm, L., Epstein, J., Jernigan, T., Molina, B., Hinshaw, S., et al. (2016). The impact of ADHD persistence, recent cannabis use, and age of regular cannabis use onset on subcortical volume and cortical thickness in young adults. *Drug Alcohol Depend.* 161, 135–146. doi: 10.1016/j.drugalcdep.2016.01.032

Liu, T., Li, H., Wong, K., Tarokh, A., Guo, L., and Wong, S. T. (2007). Brain tissue segmentation based on DTI data. *Neuroimage* 38, 114–123. doi: 10.1016/j.neuroimage.2007.07.002

Liu, T., Nie, J., Tarokh, A., Guo, L., and Wong, S. T. (2008). Reconstruction of central cortical surface from brain MRI images: method and application. *Neuroimage* 40, 991–1002. doi: 10.1016/j.neuroimage.2007.12.027

Luo, Y., Weibman, D., Halperin, J. M., and Li, X. (2019). A review of heterogeneity in Attention Deficit/Hyperactivity Disorder (ADHD). *Front. Hum. Neurosci.* 13:42. doi: 10.3389/fnhum.2019.00042

Machida, K., Murias, M., and Johnson, K. A. (2019). Electrophysiological correlates of response time variability during a sustained attention task. *Front. Hum. Neurosci.* 13:363. doi: 10.3389/fnhum.2019.00363

Mills, K. L., Bathula, D., Dias, T. G., Iyer, S. P., Fenesy, M. C., Musser, E. D., et al. (2012). Altered cortico-striatal-thalamic connectivity in relation to spatial working memory capacity in children with ADHD. *Front. Psychiatry* 3:2. doi: 10.3389/fpsyt.2012.00002

Mowinckel, A. M., Alnæs, D., Pedersen, M. L., Ziegler, S., Fredriksen, M., Kaufmann, T., et al. (2017). Increased default-mode variability is related to reduced task-performance and is evident in adults with ADHD. *NeuroImage: Clin.* 16, 369–382. doi: 10.1016/j.nicl.2017.03.008

Passingham, R. E., Stephan, K. E., and Kotter, R. (2002). The anatomical basis of functional localization in the cortex. *Nat. Rev. Neurosci.* 3, 606–616. doi: 10.1038/nrn893

Pereira-Sanchez, V., and de Castro Manglano, P. (2017). The effects of medication on default mode network (DMN) connectivity in attention deficit/hyperactivity disorder (ADHD): bibliographic review. *Eur. Psychiatry* 41:S629. doi: 10.1016/j.eurpsy.2017.01.1022

Peterson, B. S., Potenza, M. N., Wang, Z., Zhu, H., Martin, A., Marsh, R., et al. (2009). An FMRI study of the effects of psychostimulants on default-mode processing during stroop task performance in youths with ADHD. *Am. J. Psychiatry* 166, 1286–1294. doi: 10.1176/appi.ajp.2009.08050724

Polanczyk, G. V., Willcutt, E. G., Salum, G. A., Kieling, C., and Rohde, L. A. (2014). ADHD prevalence estimates across three decades: an updated systematic review and meta-regression analysis. *Int. J. Epidemiol.* 43, 434–442. doi: 10.1093/ije/dyt261

Posner, J., Park, C., and Wang, Z. (2014). Connecting the dots: a review of resting connectivity MRI studies in attention-deficit/hyperactivity disorder. *Neuropsychol. Rev.* 24, 3–15. doi: 10.1007/s11065-014-9251-z

Power, J. D., Barnes, K. A., Snyder, A. Z., Schlaggar, B. L., and Petersen, S. E. (2012). Spurious but systematic correlations in functional connectivity MRI networks arise from subject motion. *Neuroimage* 59, 2142–2154. doi: 10.1016/j.neuroimage.2011.10.018

Raichle, M. E. (2014). Default mode network. *Annu. Rev. Neurosci.* 38, 433–447.

Raichle, M. E., MacLeod, A. M., Snyder, A. Z., Powers, W. J., Gusnard, D. A., and Shulman, G. L. (2001). A default mode of brain function. *Proc. Natl. Acad. Sci. U S A.* 98, 676–682. doi: 10.1073/pnas.98.2.676

Rubia, K., Overmeyer, S., Taylor, E., Brammer, M., Williams, S. C., Simmons, A., et al. (1999). Hypofrontality in attention deficit hyperactivity disorder during higher-order motor control: a study with functional MRI. *Am. J. Psychiatry* 156, 891–896. doi: 10.1176/ajp.156.6.891

Sato, J. R., Hoexter, M. Q., Castellanos, X. F., and Rohde, L. A. (2012). Abnormal brain connectivity patterns in adults with ADHD: a coherence study. *PLoS One* 7:e45671. doi: 10.1371/journal.pone.0045671

Semrud-Clikeman, M., Pliszka, S. R., Bledsoe, J., and Lancaster, J. (2014). Volumetric MRI differences in treatment naive and chronically treated adolescents with ADHD-combined type. *J. Atten. Disord.* 18, 511–520. doi: 10.1177/1087054712443158

Sun, L., Cao, Q., Long, X., Sui, M., Cao, X., Zhu, C., et al. (2012). Abnormal functional connectivity between the anterior cingulate and the default mode network in drug-naive boys with attention deficit hyperactivity disorder. *Psychiatry Res.* 201, 120–127. doi: 10.1016/j.pscychresns.2011.07.001

Sutcubasi Kaya, B., Metin, B., Tas, Z. C., Buyukaslan, A., Soysal, A., Hatiloglu, D., et al. (2018). Gray matter increase in motor cortex in pediatric ADHD: a voxel-based morphometry study. *J. Atten. Disord.* 22, 611–618. doi: 10.1177/1087054716659139

van Ewijk, H., Heslenfeld, D. J., Zwiers, M. P., Buitelaar, J. K., and Oosterlaan, J. (2012). Diffusion tensor imaging in attention deficit/hyperactivity disorder: a systematic review and meta-analysis. *Neurosci. Biobehav. Rev.* 36, 1093–1106. doi: 10.1016/j.neubiorev.2012.01.003

Wang, J. B., Zheng, L. J., Cao, Q. J., Wang, Y. F., Sun, L., Zang, Y. F., et al. (2017). Inconsistency in abnormal brain activity across cohorts of ADHD-200 in children with attention deficit hyperactivity disorder. *Front. Neurosci.* 11:320. doi: 10.3389/fnins.2017.00320

Wang, P., Zhu, D., Li, X., Chen, H., Jiang, X., Sun, L., et al. (2013). "Identifying functional connectomics abnormality in attention deficit hyperactivity disorder," in *Paper Presented at the Biomedical Imaging (ISBI), 2013 IEEE 10th International Symposium on*, (Piscataway, NJ: IEEE).

Yuan, Y., Jiang, X., Zhu, D., Chen, H., Li, K., Lv, P., et al. (2013). Meta-analysis of functional roles of DICCCOLs. *Neuroinformatics* 11, 47–63. doi: 10.1007/s12021-012-9165-y

Zhang, P., and Cootes, T. F. (2011). Automatic part selection for groupwise registration. *Inf. Process Med. Imag.* 22, 636–647. doi: 10.1007/978-3-642-22092-0_52

Zhu, D., Li, K., Faraco, C. C., Deng, F., Zhang, D., Guo, L., et al. (2012). Optimization of functional brain ROIs via maximization of consistency of structural connectivity profiles. *Neuroimage* 59, 1382–1393. doi: 10.1016/j.neuroimage.2011.08.037

Zhu, D., Li, K., Guo, L., Jiang, X., Zhang, T., Zhang, D., et al. (2013). DICCCOL: dense individualized and common connectivity-based cortical landmarks. *Cereb. Cortex* 23, 786–800. doi: 10.1093/cercor/bhs072

Zhu, D., Zhang, D., Faraco, C., Li, K., Deng, F., Chen, H., et al. (2011). Discovering dense and consistent landmarks in the brain. *Inf. Process Med. Imag.* 22, 97–110. doi: 10.1007/978-3-642-22092-0_9

Conflict of Interest: The authors declare that the research was conducted in the absence of any commercial or financial relationships that could be construed as a potential conflict of interest.

frontiers in Human Neuroscience

ORIGINAL RESEARCH
published: 23 December 2020
doi: 10.3389/fnhum.2020.598435

Repeatability and Reproducibility of *in-vivo* Brain Temperature Measurements

Ayushe A. Sharma[1,2,3]*, *Rodolphe Nenert*[3,4], *Christina Mueller*[1], *Andrew A. Maudsley*[5], *Jarred W. Younger*[1] and *Jerzy P. Szaflarski*[2,3,4,6]

[1] Department of Psychology, University of Alabama at Birmingham (UAB), Birmingham, AL, United States, [2] Department of Neurobiology, University of Alabama at Birmingham (UAB), Birmingham, AL, United States, [3] University of Alabama at Birmingham Epilepsy Center (UABEC), Birmingham, AL, United States, [4] Department of Neurology, University of Alabama at Birmingham (UAB), Birmingham, AL, United States, [5] Department of Radiology, Miller School of Medicine, University of Miami, Miami, FL, United States, [6] Department of Neurosurgery, University of Alabama at Birmingham (UAB), Birmingham, AL, United States

Background: Magnetic resonance spectroscopic imaging (MRSI) is a neuroimaging technique that may be useful for non-invasive mapping of brain temperature (i.e., thermometry) over a large brain volume. To date, intra-subject reproducibility of MRSI-based brain temperature (MRSI-t) has not been investigated. The objective of this repeated measures MRSI-t study was to establish intra-subject reproducibility and repeatability of brain temperature, as well as typical brain temperature range.

Methods: Healthy participants aged 23–46 years ($N = 18$; 7 females) were scanned at two time points ∼12-weeks apart. Volumetric MRSI data were processed by reconstructing metabolite and water images using parametric spectral analysis. Brain temperature was derived using the frequency difference between water and creatine (T_{CRE}) for 47 regions of interest (ROIs) delineated by the modified Automated Anatomical Labeling (AAL) atlas. Reproducibility was measured using the coefficient of variation for repeated measures (COVrep), and repeatability was determined using the standard error of measurement (SEM). For each region, the upper and lower bounds of Minimal Detectable Change (MDC) were established to characterize the typical range of T_{CRE} values.

Results: The mean global brain temperature over all subjects was 37.2°C with spatial variations across ROIs. There was a significant main effect for time [$F_{(1,\ 1,591)} = 37.0$, $p < 0.0001$] and for brain region [$F_{(46,\ 1,591)} = 2.66$, $p < 0.0001$]. The time*brain region interaction was not significant [$F_{(46,\ 1,591)} = 0.80$, $p = 0.83$]. Participants' T_{CRE} was stable for each ROI across both time points, with ROIs' COVrep ranging from 0.81 to 3.08% (mean COVrep = 1.92%); majority of ROIs had a COVrep <2.0%.

Conclusions: Brain temperature measurements were highly consistent between both time points, indicating high reproducibility and repeatability of MRSI-t. MRSI-t may be a promising diagnostic, prognostic, and therapeutic tool for non-invasively monitoring brain temperature changes in health and disease. However, further studies of healthy

OPEN ACCESS

Edited by:
Dajiang Zhu,
University of Texas at Arlington, United States

Reviewed by:
Edith V. Sullivan,
Stanford University, United States
Esin Ozturk Isik,
Bogaziçi University, Turkey
Hironaka Igarashi,
Niigata University, Japan

***Correspondence:**
Ayushe A. Sharma
sharma87@uab.edu

Specialty section:
This article was submitted to Brain Imaging and Stimulation, a section of the journal Frontiers in Human Neuroscience

Received: *24 August 2020*
Accepted: *30 November 2020*
Published: *23 December 2020*

Citation:
Sharma AA, Nenert R, Mueller C, Maudsley AA, Younger JW and Szaflarski JP (2020) Repeatability and Reproducibility of in-vivo Brain Temperature Measurements. Front. Hum. Neurosci. 14:598435. doi: 10.3389/fnhum.2020.598435

participants with larger sample size(s) and numerous repeated acquisitions are imperative for establishing a reference range of typical brain T_{CRE}, as well as the threshold above which T_{CRE} is likely pathological.

Keywords: MRS, brain temperature, MR thermometry, neuroinflammation, neuroimaging

INTRODUCTION

Neuroinflammation is increasingly implicated in the initiation and maintenance of a number of neurodegenerative diseases, including multiple sclerosis, Alzheimer's Disease, and epilepsy (Lucas et al., 2006; Amor et al., 2010; Maroso et al., 2010). In these disease states, neuroinflammatory cells (e.g., microglia) do not return to quiescence and instead become chronically activated, ultimately propelling a structural, functional, and biochemical neurodegenerative state (Devinsky et al., 2013; Albrecht et al., 2016; Chen et al., 2016). Elucidating what drives and sustains neuroinflammation is a critical goal in the field, especially in the disease states where chronic, low-level neuroinflammatory phenomena result in negative consequences. For example, as demonstrated by findings from studies of animal models of epilepsy and resected human epileptic tissue, sustained neuroinflammation causes chronic hyperexcitability, lower seizure threshold, and neuronal death (Aronica et al., 2010; Maroso et al., 2010; Ravizza et al., 2011; Vezzani and Friedman, 2011; Vezzani et al., 2019). A neuroimaging-based biomarker of neuroinflammation may allow tracking disease progression, treatment response, and associated comorbidities and cognitive impairments; such a tool may even identify a way to prevent these phenomena in the first place (Sharma and Szaflarski, 2020).

Structural magnetic resonance imaging (sMRI) is often considered the gold-standard for pinpointing neurological pathophysiology, but is frequently inadequate in localizing focal tissue abnormalities. For example, in treatment-resistant epilepsy patients, surgical resection of the epileptogenic zone is the only approach that can grant seizure freedom (Noe et al., 2013; Jehi, 2018). Surgical planning is straightforward in patients with sMRI-detectable lesions, but challenging in the 20–30% patients who are MR-negative (Salmenpera et al., 2007; Jobst and Cascino, 2015; Muhlhofer et al., 2017). Moreover, patients with sMRI-detectable lesions experience 2.5–2.9 times better surgical outcomes than those with normal sMRIs (Salmenpera et al., 2007; Giorgio and De Stefano, 2010; Téllez-Zenteno et al., 2010; Finke, 2018; Alberts et al., 2020; Sharma and Szaflarski, 2020). Despite sMRI's capacity to pinpoint major structural abnormalities (e.g., large ischemic lesions), the data demonstrate its diminished sensitivity and specificity for detecting the smaller, more focalized neuroinflammatory phenomena (Barr et al., 1997; Kälviäinen and Salmenperä, 2002; Blümcke et al., 2012; Sharma and Szaflarski, 2020). Therefore, there is a need to identify a sensitive and specific *in vivo* biomarker of neuroinflammatory pathophysiology. Other currently available approaches are invasive and/or costly (e.g., lumbar puncture, positron emission tomography [PET]). Further, PET relies on the use of radioisotopes that *may* localize key neuroinflammatory cells, but variable quantitative accuracy, limited bioavailability, and unclear specificity of ligand-target binding are critical gaps that limit its clinical utility (Vivash and OBrien, 2016; Best et al., 2019; Dickstein et al., 2019; Ghadery et al., 2019; Hamelin et al., 2019; Sharma and Szaflarski, 2020). Thus, the question remains: how can we non-invasively localize neuroinflammation in a living human brain?

Since the focal inflammatory response generates focal changes in temperature, brain temperature mapping may be a promising proxy for diagnosing and monitoring the progression of neurological diseases characterized by metabolic and homeostatic disruptions (Ene Mrozek et al., 2012; Wang et al., 2014). Brain temperature correlates well with systemic temperature during healthy states, generally measuring 0.5–1°C higher than core body temperature (Rossi et al., 2001; Wang et al., 2014). During pathological processes such as neuroinflammation, increased metabolic demands overwhelm the brain's already limited cooling mechanisms and drive brain temperature 1–2°C higher than core body temperature (Rossi et al., 2001). As neuroinflammatory phenomena such as leukocyte extravasation and accumulation, blood brain barrier permeability, and even cerebral edema increase, so does the brain temperature (Dietrich et al., 1996, 1998; Chatzipanteli et al., 2000; Sharma and Hoopes, 2003).

Of the ways we can measure brain temperature, magnetic resonance spectroscopic imaging (MRSI) is the most non-invasive and economical. Brain temperature can be derived from MRSI data by calculating the frequency difference between the temperature-sensitive water peak and one or more metabolite peaks that are temperature-insensitive (Maudsley et al., 2017). MRSI-based brain temperature (MRSI-t) measurement correlates well with the recordings of implanted probes, as indicated by phantom and experimental studies (Cady et al., 1995; Corbett et al., 1995). Brain temperature has already been approximated using MRSI in a number of contexts: healthy adults, ischemic stroke, neonatal encephalopathy, myalgic encephalitis/chronic fatigue syndrome, and rheumatoid arthritis (Maudsley et al., 2010; Mueller et al., 2019, 2020; Zhang et al., 2020). The majority of previous studies have performed MRSI-t measurements only at a single brain location or limited spatial region, but it has recently been demonstrated that the measurement can be obtained using a volumetric echo-planar

Abbreviations: MRSI, Magnetic resonance spectroscopic imaging; MRSI-t, MRSI-based brain temperature; ROI(s), Region(s) of interest; COVrep, Coefficient of variation for repeated measures; SEM, Standard error of measurement; MDC, Minimal Detectable Change; T_{CRE}, MRSI-based brain temperature calculated according to the equation $T_{CRE} = -102.61(\Delta_{H20-CRE}) + 206.1°C$; tCre, creatine + phosphocreatine (total creatine); tCho, total choline; NAA, N-acetylaspartate; Glx, combined signal from glutamine and glutamate; MI, myo-inositol.

spectroscopic imaging (EPSI) acquisition to create temperature maps over a large fraction of the brain volume (Maudsley et al., 2006, 2017). Limited data are available on the reproducibility and reliability of MRSI-t using volumetric EPSI. Previous work has established intra-subject reproducibility of serial EPSI acquisitions in a limited sample ($N = 2$) at 5 1-week intervals, as well as that of successive EPSI acquisitions (2 per session) in a larger sample ($N = 32$) (Maudsley et al., 2010; Veenith et al., 2014). However, the reproducibility and repeatability of MRSI-t using volumetric EPSI has only been established in a small sample ($N = 10$), with 3 acquisitions separated by 1-week intervals (Zhang et al., 2020). Thus, the available data do not mirror a real-life clinical situation in which participants are typically exposed to a treatment/intervention for 12–16 weeks before a second measurement is collected.

To date, no study has investigated whether intra-subject reproducibility is maintained in a larger sample of healthy control participants with longer duration between scans. Additionally, all previous studies have only reported the coefficient of variation (COV) and intraclass correlation coefficients as measures of reproducibility and repeatability; these data are useful, but the exact boundary at which a given region's brain temperature is normal vs. above-normal (i.e., areas of focal neuroinflammation or other pathophysiological phenomena) remains uncertain (Maudsley et al., 2010; Zhang et al., 2020). Before MRSI-t can be used as a clinical tool for *in vivo* assessment of neuroinflammation, we must determine whether MRSI-based brain temperature estimates are reliable and reproducible over typical study periods. In addition to establishing bounds of normal global and region-level brain temperature, it is critical that we determine the bounds at which brain temperature is above-normal in each region. The objective of this study was to establish intra-subject reproducibility and repeatability of brain temperature derivations in healthy participants scanned twice, ∼12 weeks apart. In addition to establishing typical mean brain temperature across regions, we aimed to define the bounds of typical vs. atypical (i.e., possibly abnormal) brain temperature by calculating region-level measures of Minimum Detectable Change (MDC). We hypothesized that mean brain temperature would range from 37.0 to 37.5°C. We also hypothesized that MDC would indicate brain temperatures to be atypical if ≥ 0.5°C above mean brain temperature.

METHODS

Participants

Healthy adult participants were recruited from the local area via word of mouth and IRB-approved study flyers. Interested participants contacted study personnel via phone or email. Participants were scheduled for their first study visit pending a phone screen for inclusion criteria and MR compatibility. The primary inclusionary criteria were: (1) age of 18–65 years, (2) no history of neurological disease or injury (e.g., traumatic brain injury), (3) ability to undergo MRI at 3-Tesla (e.g., no metal implants or claustrophobia), and (4) negative urine pregnancy test if female of childbearing potential. Of importance is that participants' self-reported history of neurological disease or injury was collected during phone screening; no neurological examinations were performed, and medical records were not reviewed unless patient history was questionable. Written informed consent was obtained from all participants before collecting any clinical measures or imaging data.

Study Visits

Participants completed two study visits scheduled at the University of Alabama at Birmingham (UAB) Civitan International Neuroimaging Laboratory housed in the UAB Highlands Hospital. For most participants ($N = 14$), visits were scheduled 10–12 weeks apart; for the last 4 participants recruited, the second study visit was delayed by 5–7 weeks due to COVID-19 research restrictions. The mean overall time between visits was 11.33 ± 2.59 weeks. During each study visit, participants completed 2 self-report questionnaires: the Hospital Anxiety and Depression Scale (HADS) and the Profile of Mood States (POMS) (Zigmond and Snaith, 1983; McNair et al., 1989). Prior to imaging, tympanic temperature measurements were collected using a Braun Pro 4000 ThermoScan aural thermometer; this measure was included due to evidence that tympanic temperature can reliably reflect brain temperature and to make sure there were no individual temperature elevations that could affect brain temperature measurements (Mariak et al., 2003).

Data Acquisition

Participants were scanned on a 3T Siemens Magnetom Prisma scanner using a 20-channel head coil. T1-weighted structural images were acquired using a magnetization-prepared rapid gradient echo sequence with the following parameters: repetition time (TR) = 2,400 ms; echo time (TE) = 2.22 ms; flip angle = 8°; 208 slices (0.8 mm thick); matrix = 256 × 256.

Whole-brain metabolite MRSI data were collected using a 3-dimensional EPSI sequence with spin-echo excitation with the following parameters: TR_1 = 1,500 ms (TR for metabolite data), TR_2 = 511 ms (TR for water reference data), TE = 17.6 ms, lipid inversion-nulling with TI = 198 ms; FOV = 280 × 280 × 180 mm, sampled with 50 × 50 × 18 k-space points. A separate MRSI dataset was acquired using an interleaved acquisition without water suppression and served as the water reference signal; with the exception of TR, these data were acquired with identical spatial and spectral parameters as the metabolite MRSI data. Spectral sampling used 1,000 sample points with 2,500 Hz spectral width; with resampling and combination of the odd and even echoes, this was reduced to 500 points and 1,250 Hz (Metzger and Hu, 1997). Prior to MRSI data acquisition, we performed off-resonance frequency correction, and shimming to reduce magnetic field inhomogeneities. Shimming consisted of a 3D automatic shim by the scanner, followed by an interactive shim to achieve a peak FWHM ≤30 Hz (Zeinali-Rafsanjani et al., 2018).

We also acquired 2D arterial spin labeling (ASL) perfusion scans to rule out perfusion-related contributions to brain temperature and metabolite concentration measurements (Zhu et al., 2009; Ene Mrozek et al., 2012; Rango et al., 2015). ASL data were acquired using a Proximal Inversion with Control of Off-Resonance Effects (PICORE) labeling scheme for

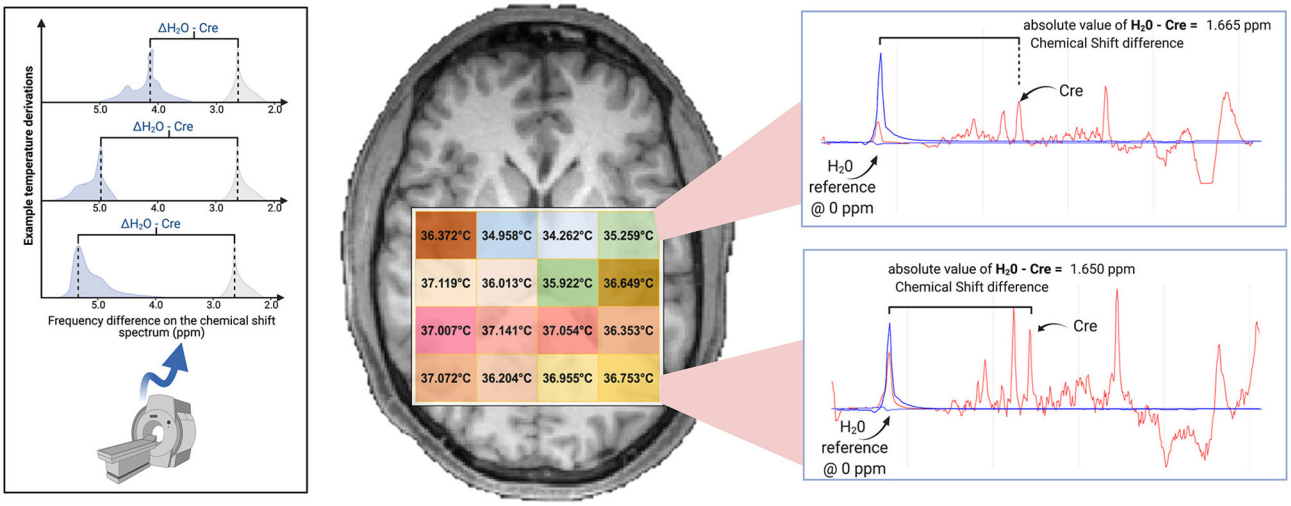

FIGURE 1 | Brain temperature can be non-invasively derived from volumetric magnetic resonance spectroscopic imaging (MRSI) data by calculating the frequency difference between the temperature-sensitive water peak and one or more metabolite peaks that are temperature-insensitive (*left**). When using creatine as the reference, voxel-level brain temperature can be calculated according to the following equation: $T_{CRE} = -102.61(\Delta_{H20-CRE}) + 206.1°C$, $\Delta_{H20-CRE}$ = chemical shift difference between the creatine and water resonances. Example T_{CRE} calculations are provided for a participant's single tissue slice (*right*). Representative spectra illustrate $\Delta_{H20-CRE}$ derivations, with plots depicting a water-suppressed metabolite spectrum (*red line*), with an overlay that indicates the location of the reference water signal (*blue line)*. Spectral plots were created within the Metabolite Imaging and Data Analysis System (MIDAS) software package, and the figure was created using BioRender. *Adapted from Dehkharghani et al. (2015).

background suppression. Sixty pairs of label/control ASL images were collected in the axial direction at a single inversion time of 1,800 ms, TR = 2500 sms, TE = 16.18 ms, 12 slices, 4 × 4 × 10 mm voxels.

Data Processing

Image reconstruction and spectral processing was completed within the Metabolite Imaging and Data Analysis System (MIDAS) software package (Maudsley et al., 2006). Raw metabolite and water MRSI data were reconstructed with interpolation to 50 × 50 × 36 voxels and spatial smoothing. This yielded 5.6 × 5.6 × 5 mm voxels, with a voxel volume of ∼0.1568 cm^3. Processing included B_0 inhomogeneity correction and formation of individual metabolite maps using a parametric spectral modeling method to quantify relative peak areas and resonance frequencies for resonances of N-acetylaspartate (NAA), creatine (tCre), choline (tCho), and water, as described by Maudsley et al. (2006). For repeat studies, each MRSI dataset was spatially registered to the T1-weighted image of the first study. Voxel-level brain temperature was then calculated using the chemical shift difference between the creatine and water resonances ($\Delta_{H20-CRE}$; **Figure 1**), according to the equation $T_{CRE} = -102.61(\Delta_{H20-CRE}) + 206.1°C$ (Maudsley et al., 2017). The creatine resonance was selected for the frequency reference as it is broadly distributed within the cells and, as such, is less sensitive to cellular-level changes of magnetic susceptibility with neuronal orientation (Maudsley et al., 2017). We provide an example of raw MRSI metabolite and temperature data in **Figure 2**. The resultant MRSI-t maps were then spatially registered to Montreal Neurological Institute (MNI) template at 2 mm isotropic voxel resolution, which was also aligned with a modified version of the Automated Anatomical Labeling (AAL) atlas that delineated 47 regions of interest (ROIs) (Tzourio-Mazoyer et al., 2002; Maudsley et al., 2017).

Following initial processing, the atlas was mapped into subject space using an inverse spatial transformation algorithm within the MIDAS Project Review and Analysis (PRANA) module (Maudsley et al., 2006). The Map Integrated Spectrum (MINT) module within MIDAS was then used to compute mean estimates of metabolite concentrations, metabolite ratios, and brain temperature within each of the atlas-defined brain regions. Spectral integration was limited to voxels that had a fitted metabolite linewidth between 2 and 12 Hz, and voxels were excluded if they had an outlying values of 2.5 times the standard deviation of all valid voxels in the image (Maudsley et al., 2006).

ASL data were processed using ASLtbx batch scripts with Statistical Parametric Mapping (SPM12; http://www.fil.ion.ucl.ac.uk) running in MatLab R2019b (The MathWorks, Inc., Natick, MA, USA) (Wang et al., 2008). Images were motion-corrected and smoothed with a 6 mm full-width-at-half-maximum (FWHM) Gaussian kernel to diminish motion artifacts and decrease noise for subsequent image subtraction. Cerebral blood flow (CBF) was quantified in ml/100 g/min using simple subtraction between each tag/control pair (120 smoothed volumes, 60 pairs). Each participant's mean CBF maps were then 1) registered to high-resolution structural space with affine registration, followed by 2) non-linear registration to MNI space.

Data Analysis

Descriptive statistics and correlation analyses were conducted in IBM SPSS Version 26.0 (www.ibm.com/products/spss-statistics). Reproducibility of MRSI-t based T_{CRE} was evaluated using

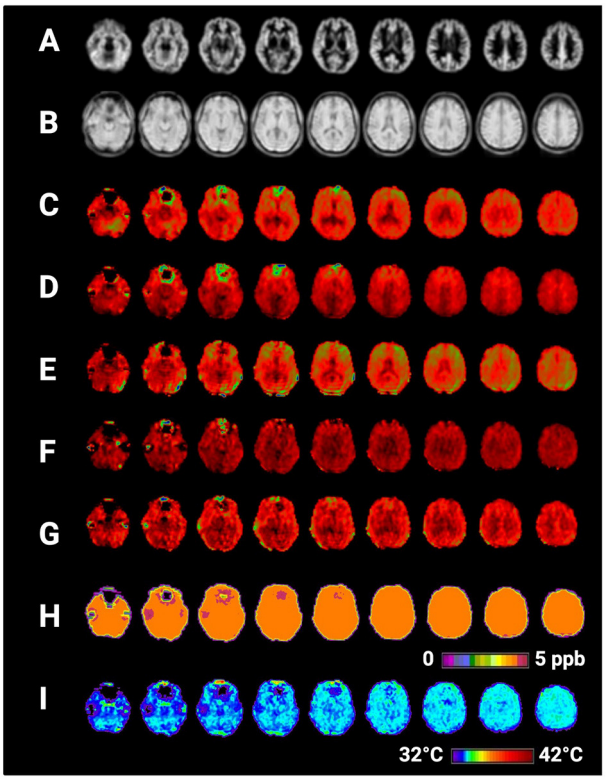

FIGURE 2 | Selected axial slices showing raw metabolite and brain temperature maps derived from a single participant's volumetric magnetic resonance spectroscopic imaging data (MRSI) data. Shown are **(A)** normalized gray matter volumes, **(B)** water reference signal, **(C)** total creatine (creatine + phosphocreatine), **(D)** total choline, **(E)** NAA (N-acetylaspartate), **(F)** myo-inositol, **(G)** Glx (combined signal from glutamine and glutamate), **(H)** frequency difference between water and creatine ($\Delta_{H2O-CRE}$), **(I)** brain temperature calculated according to the equation $T_{CRE} = -102.61(\Delta_{H2O-CRE}) + 206.1°C$. Raw MRSI data were visualized within the Metabolite Imaging and Data Analysis System (MIDAS) software package, and the figure was created using BioRender.

the coefficient of variation for repeated measures (COVrep) (Shechtman, 2013). Reliability was evaluated with the Standard Error of Measurement (SEM = square root of the MS_{ERROR} term from 2-way mixed ANOVA used to compute Cronbach's Alpha) (Weir, 2005). Minimal Detectable Change (MDC) was then calculated from SEM to provide a clinically meaningful basis for evaluating T_{CRE} changes over repeated measures. Standard MDC was calculated at the 68th confidence interval (CI) (Weir, 2005). To investigate temporal and spatial variation in T_{CRE}, we performed a linear mixed effects analysis using GraphPad Prism version 8.0 for Mac (GraphPad Software, La Jolla, CA, USA, www.graphpad.com).

In a secondary analysis, the relationship between T_{CRE} and brain metabolites and/or metabolite ratios implicated in neuroinflammatory disease was assessed. Metabolites were quantified within MIDAS as previously described, with metabolite concentrations corrected in reference to water and CSF percentage (Maudsley et al., 2009; Lecocq et al., 2015; Zhang et al., 2020). Since quantification did not account for metabolite and reference relaxation, our analyses were based on metabolite values in institutional units (I.U.) (Kreis et al., 1993; Maudsley et al., 2009). Metabolites of interest included myo-inositol, choline, NAA, and the combined signal of glutamine and glutamate (Glx) (Oz et al., 2014). Myo-inositol (MI) is a glial marker, with increased levels indicating glial activation or proliferation seen in neuroinflammation (Haris et al., 2011). Choline (total choline, tCho) is expressed in cell membranes, with increased levels indicating high cell turnover during inflammatory processes (Oz et al., 2014). NAA indicates neuronal health, with lower values representing axonal loss (Moffett et al., 2007; Oz et al., 2014). Due to evidence of creatine (total creatine, tCre) as a reference metabolite, metabolites were also evaluated on the basis of their ratios with tCre (Maudsley et al., 2017). Spearman's rho (r_s) correlation coefficients were calculated between T_{CRE}, each metabolite ratio of interest, and tympanic temperature using a two-tailed threshold of $p < 0.05$. Variables with $r_s > |0.5|$ were evaluated as predictors of T_{CRE} in a multiple regression model. Independent samples *t*-tests assessed hemispheric (right vs. left) differences in region-level T_{CRE}. Independent samples *t*-tests contrasting sex differences in global and region-level T_{CRE} were planned but not performed due to unequal sex distribution in the final dataset. Data quality was evaluated on the basis of (1) number of accepted voxels (%) following processing and (2) spectral linewidth.

Paired samples *t*-tests of participants' mean CBF maps contrasted cerebral perfusion between the two time points. This served as a measure of whether brain temperature differences—if present—could be attributed to perfusion differences.

RESULTS

Participant Demographics and Metabolite Measures

Twenty-one participants were recruited; 18 completed all study procedures and were included in the analyses ($N = 7$ females). The mean age was 30.39 ± 7.47 years (range 23–46 years). Descriptive statistics for study measures of temperature, blood flow, and inflammatory metabolite ratios were tabulated for both time points; global within-subject differences from time1 to time2 were computed with repeated measures *t*-tests (**Table 1**). The repeated measures *t*-tests revealed significant increase in HADS sub-scale Depression scores [$t(17) = -4.12$, $p = 0.001$], though this change was not clinically significant and scores remained in the normal range (0–7) for both time points (Zigmond and Snaith, 1983). Additionally, there was a global reduction in mean NAA/tCre, $t(17) = 2.19$, $p = 0.04$. Mean T_{CRE} was 37.00°C at time1 and 37.40°C at time2, with a global mean T_{CRE} of 37.2°C across both time points. Box-and-whisker plots of T_{CRE} calculated at both time points are provided in **Figure 3**.

Brain Temperature Reproducibility, Reliability, and Minimal Detectable Change

The COVrep, our measure of reproducibility, ranged from 0.81 to 3.08% (mean 1.92%) across 47 ROIs, with 30 ROIs having a

TABLE 1 | Descriptive statistics for clinical and imaging-derived measures of temperature, blood flow, average metabolite values (in institutional units), and metabolite ratios.

	time1 ($N = 18$)	time2 ($N = 18$)	time1 vs. time2
Heart rate (bpm)	73.50 ± 11.40	74.17 ± 17.12	$t(17) = -0.20$, $p = 0.84$
HADS, depression	1.72 ± 1.96	2.72 ± 2.27	$t(17) = -4.12$, $p = 0.001$
HADS, anxiety	5.33 ± 2.63	4.83 ± 2.36	$t(17) = 0.89$, $p = 0.39$
POMS, TMD	−0.39 ± 20.75	0.06 ± 18.89	$t(17) = -0.18$, $p = 0.85$
Tympanic temperature (°C)	36.73 ± 0.30	36.65 ± 0.19	$t(17) = 0.98$, $p = 0.34$
Global T_{CRE} (°C)	37.00 ± 0.62	37.40 ± 0.94	$t(17) = -1.28$, $p = 0.22$
Global CBF (ml/100 g/min)	70.77 ± 6.15	71.03 ± 4.24	$t(17) = 0.21$, $p = 0.84$
tCre	26270.0 ± 1807	26844.98 ± 1345.20	$t(17) = -1.91$, $p = 0.07$
tCho	5279.00 ± 664.10	5288.66 ± 723.35	$t(17) = -0.10$, $p = 0.93$
NAA/tCre	1.35 ± 0.24	1.26 ± 0.09	$t(17) = 2.19$, $p = 0.04$
Glx/tCre	0.66 ± 0.06	0.64 ± 0.05	$t(17) = 1.76$, $p = 0.10$
MI/tCre	0.55 ± 0.08	0.59 ± 0.22	$t(17) = -0.63$, $p = 0.53$

**All measures are in I.U., institutional units unless otherwise specified.*

HADS, Hospital Anxiety and Depression Scale; POMS, Profile of Mood States; TMD, total mood disturbance; CBF, cerebral blood flow; tCho, total choline; tCre, creatine + phosphocreatine (total creatine); NAA/tCre, N-acetylaspartate ratio to tCre; Glx/tCr, ratio of combined signal from glutamine and glutamate to tCre; MI/tCre, myo-inositol ratio to tCre; I.U., institutional units.

COVrep < 2.0%. SEM ranged from 0.365 to 2.713 (mean 1.295 ± 0.647) (**Table 2**). The highest COVrep (3.08%) was in the R Fusiform Gyrus. Mean brain temperature was the lowest in the R and L putamen, R and L pallidum, R and L hippocampus, L and R anterior cingulum, R and L thalamus, and R insula (**Table 2**). Mean brain temperature was highest in the R occipital lobe, L and R precuneus, R and L frontal lobes, and R and L cuneus.

Based on the MDC, the T_{CRE} at which we consider brain temperature as atypical varies across brain regions (**Table 2**, **Figure 4**). When considering MDC computations at the 68th CI, the upper bounds of brain temperature indicating above-typical T_{CRE} ranged from 37.57 to 41.49°C (mean 39.03 ± 1.14°C); the lower bounds indicating below-typical T_{CRE} ranged from 33.74 to 36.91°C (mean 35.37 ± 0.80°C). According to MDC calculations, the T_{CRE} at which values are considered above-typical were highest in the following regions: R and L frontal lobes (41.49, 40.99°C), R occipital lobe (41.38°C), L precentral gyrus (41.13°C), and L and R parietal lobes (40.92, 41.03°C) (**Table 2**, **Figure 4**). In addition to assessing these ROI-based measures, brain temperature maps visualized brain temperature changes within participants from time1 to time2 (**Figure 5**).

Spatial and Temporal Variations in Brain Temperature

A linear mixed effects model investigated the variation of T_{CRE} across 47 brain regions over 2 time points. Fixed effects included time, brain region, and the interaction of time*brain region, with participants considered random effects. In the case of a statistically significant interaction, we planned follow-up tests to assess pairwise differences using simple effects analysis. *P*-values were corrected for multiple comparisons by controlling the False Discovery Rate (FDR=0.05) with the two-stage step-up method of Benjamini and Yekutieli (2001). The interaction of time*brain region was not significant [$F_{(46,\ 1,591)} = 0.80$, $p = 0.83$]. There was a significant main effect for time [$F_{(1,\ 1,591)} = 37.0$, $p < 0.0001$], and for brain region [$F_{(46,\ 1,591)} = 2.66$, $p < 0.0001$].

Within-Subjects Variation in Cerebral Blood Flow

Voxel-level repeated measures *t*-tests did not find significant within-subjects differences in mean CBF when comparing time1 vs. time 2; the same results were found when mean T_{CRE} was included as a covariate. Further, participants' global CBF values did not change significantly from time1 to time2, as indicated by paired samples *t*-tests [$t(17) = 0.21$, $p = 0.84$]. At time1, mean global CBF was 70.77 ± 6.15 mL/100 g/min. At time2, mean global CBF was 71.03 ± 4.24 mL/100 g/min (**Table 1**). Mean CBF ranged from 56.66 to 79.99 mL/100 g/min (**Figure 5**). Each participant's mean CBF maps for time1 and time2 are visualized alongside T_{CRE} maps (**Figure 5**). Mean CBF for all participants across both time points was 70.90 mL/100 g/min.

Relationship Between Brain Temperature and Other Physiological Variables

For major metabolites (tCre, tCho, NAA, and MI), COVrep (%) values are provided in **Table 3**. In contrast to T_{CRE}, metabolite concentrations varied substantially across time. For tCho, mean COVrep was 12.49% (range 3.13–84.52%); with the removal of outlying values for the R Precentral Gyrus, the COVrep range for tCho became limited to 3.13–34.44%. For tCre, mean COVrep was 10.38% (range 4.35–22.08%). For NAA, mean COVrep was 6.93% (range 2.68–28.44%). Lastly, mean COVrep for MI was 16.05% (range 6.41–41.97%).

Spearman correlations were run to test the relationship between T_{CRE} and the ratios MI/tCre, NAA/tCre, and Glx/tCre (**Table 4**). There was a strong, positive correlation between T_{CRE} and NAA/tCre ($r_s = 0.678$, $p < 0.0001$), and a strong negative correlation between T_{CRE} and tCho/tCre ($r_s = -0.575$, $p < 0.0001$). There was a moderate, positive statistically significant

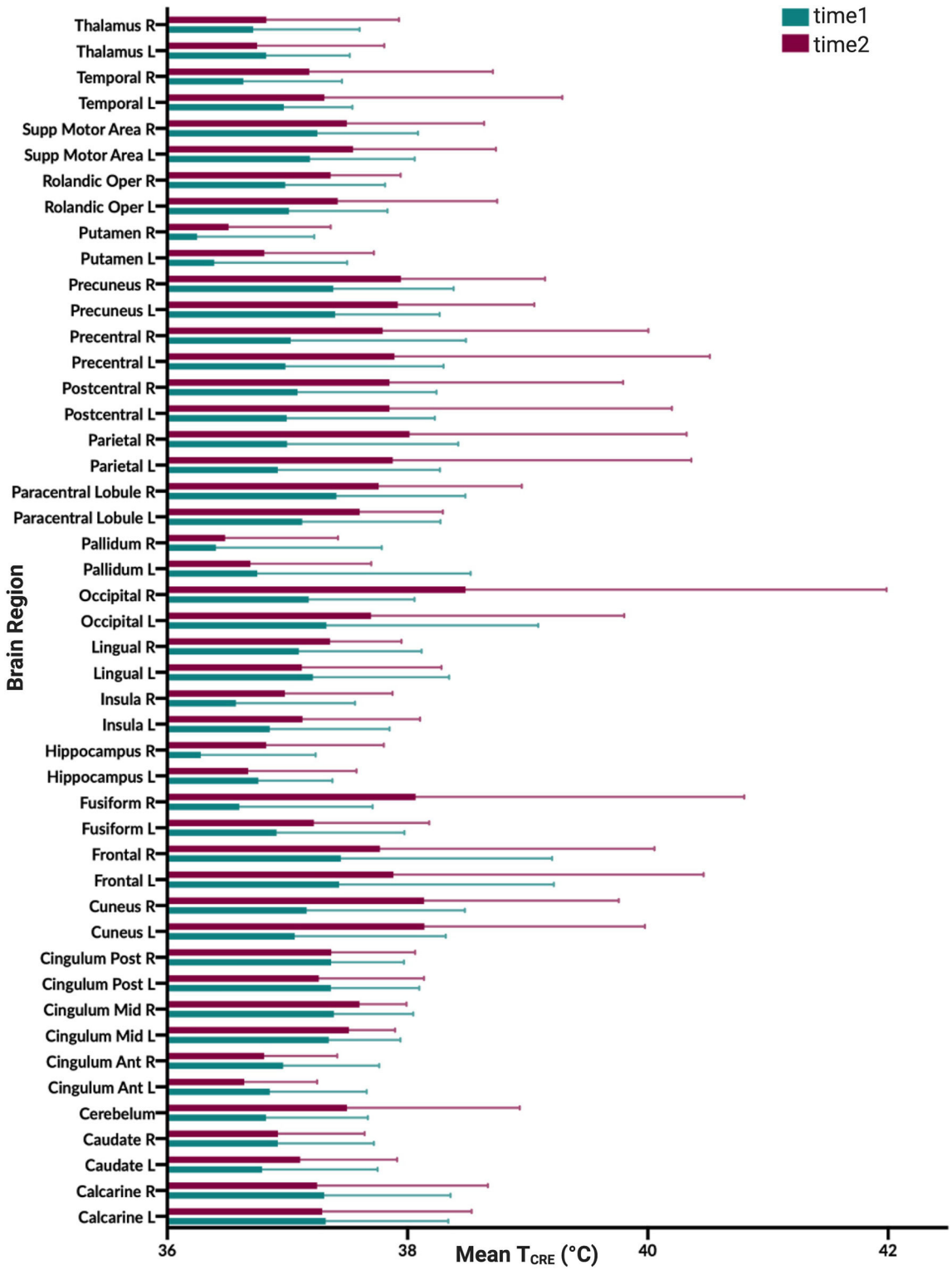

FIGURE 3 | Graphical illustration of mean brain temperature for time1 (mean 37.0°C) and time2 (37.4°C) across 47 regions of interest (ROIs) delineated by the modified Automated Anatomical Labeling (AAL) atlas. Brain temperature was non-invasively derived from volumetric magnetic resonance spectroscopic imaging (MRSI) data, using the following equation: $T_{CRE} = -102.61(\Delta_{H20-CRE}) + 206.1°C$, where $\Delta_{H20-CRE}$ = chemical shift difference between the creatine and water resonances. For each brain region, colored bars (time1, teal; time2, burgundy), reflect the mean T_{CRE}; whiskers indicate range of T_{CRE} values beyond the mean. The mean global brain temperature over all subjects was 37.2°C with spatial variations across regions (37.57–41.49°C). There was a significant main effect for time [$F_{(1,\ 1,591)} = 37.0$, $p < 0.0001$] and for brain region [$F_{(46,\ 1,591)} = 2.66$, $p < 0.0001$]. The time*brain region interaction was not significant [$F_{(46,1,591)} = 0.80$, $p = 0.83$].

TABLE 2 | Mean MRSI-based brain temperature (T_{CRE}) in 47 ROIs for both time points time1 (T_1) and time2 (T_2), their standard deviations (SD), and corresponding reproducibility and reliability statistics.

ROI	Scan	*n*	Mean	SD	COVrep (%)	SEM	MDC
L Calcarine	T_1	18	37.320	1.019	1.85	1.131	1.600
	T_2	18	37.289	1.244			
R Calcarine	T_1	18	37.306	1.052	2.24	1.288	1.822
	T_2	18	37.247	1.421			
L Caudate	T_1	18	36.788	0.963	1.66	0.733	1.036
	T_2	18	37.106	0.807			
R Caudate	T_1	18	36.921	0.800	1.73	0.827	1.170
	T_2	18	36.922	0.721			
Cerebellum	T_1	18	36.822	0.848	2.10	1.141	1.614
	T_2	18	37.497	1.436			
L Anterior Cingulum	T_1	17	36.853	0.807	1.29	0.581	0.822
	T_2	17	36.641	0.606			
R Anterior Cingulum	T_1	17	36.965	0.799	1.11	0.511	0.722
	T_2	17	36.806	0.610			
L Mid Cingulum	T_1	18	37.345	0.597	0.81	0.365	0.516
	T_2	18	37.512	0.383			
R Mid Cingulum	T_1	18	37.387	0.661	0.88	0.421	0.595
	T_2	18	37.600	0.391			
L Posterior Cingulum	T_1	18	37.363	0.735	1.41	0.824	1.165
	T_2	18	37.262	0.875			
R Posterior Cingulum	T_1	18	37.364	0.605	1.36	0.696	0.985
	T_2	18	37.366	0.698			
L Cuneus	T_1	18	37.062	1.257	2.50	1.522	2.153
	T_2	18	38.140	1.835			
R Cuneus	T_1	18	37.161	1.316	2.65	1.586	2.243
	T_2	18	38.138	1.620			
L Frontal Lobe	T_1	18	37.431	1.787	2.88	2.713	3.837
	T_2	18	37.884	2.582			
R Frontal Lobe	T_1	17	37.445	1.759	2.56	2.395	3.387
	T_2	17	37.771	2.285			
L Fusiform Gyrus	T_1	18	36.909	1.065	1.60	0.831	1.176
	T_2	18	37.221	0.959			
R Fusiform Gyrus	T_1	18	36.601	1.108	3.08	2.179	3.082
	T_2	18	38.067	2.735			
L Hippocampus	T_1	18	36.758	0.616	1.55	0.879	1.243
	T_2	18	36.674	0.902			
R Hippocampus	T_1	18	36.278	0.956	2.13	1.016	1.437
	T_2	18	36.824	0.980			
L Insula	T_1	18	36.854	0.996	1.92	1.022	1.446
	T_2	18	37.126	0.978			
R Insula	T_1	18	36.572	0.991	1.93	0.934	1.321
	T_2	18	36.979	0.897			
L Lingual Gyrus	T_1	18	37.213	1.134	1.89	1.111	1.572
	T_2	18	37.120	1.161			
R Lingual Gyrus	T_1	18	37.096	1.021	1.61	0.853	1.206
	T_2	18	37.355	0.594			
L Occipital Lobe	T_1	18	37.326	1.761	1.33	0.731	1.033
	T_2	18	37.696	2.106			
R Occipital Lobe	T_1	18	37.179	0.879	2.98	2.507	3.546
	T_2	18	38.484	3.504			
L Pallidum	T_1	18	36.749	1.776	2.58	1.195	1.691
	T_2	18	36.693	1.005			
R Pallidum	T_1	17	36.406	1.381	2.70	1.292	1.828
	T_2	17	36.483	0.939			
L Paracentral Lobule	T_1	18	37.124	1.151	1.49	0.663	0.937
	T_2	18	37.603	0.692			
R Paracentral Lobule	T_1	18	37.409	1.073	1.66	1.430	2.023
	T_2	18	37.761	1.190			
L Parietal Lobe	T_1	18	36.921	1.349	2.57	2.564	3.627
	T_2	18	37.877	2.485			
R Parietal Lobe	T_1	18	36.998	1.424	2.47	2.414	3.414
	T_2	18	38.016	2.307			
L Postcentral Gyrus	T_1	18	36.994	1.232	2.35	2.420	3.422
	T_2	18	37.851	2.350			
R Postcentral Gyrus	T_1	18	37.084	1.157	1.88	2.003	2.833
	T_2	18	37.850	1.944			
L Precentral Gyrus	T_1	18	36.984	1.315	2.57	2.609	3.690
	T_2	18	37.891	2.625			
R Precentral Gyrus	T_1	18	37.028	1.459	2.40	2.216	3.133
	T_2	18	37.793	2.211			
L Precuneus	T_1	18	37.399	0.867	1.69	1.222	1.728
	T_2	18	37.920	1.134			
R Precuneus	T_1	18	37.382	1.002	1.73	1.341	1.897
	T_2	18	37.944	1.201			
L Putamen	T_1	18	36.392	1.105	2.18	1.029	1.455
	T_2	18	36.808	0.911			
R Putamen	T_1	18	36.248	0.975	1.89	0.872	1.233
	T_2	18	36.511	0.849			
L Rolandic Operculum	T_1	18	37.013	0.821	1.76	1.289	1.823
	T_2	18	37.419	1.328			
R Rolandic Operculum	T_1	18	36.983	0.830	1.51	0.757	1.071
	T_2	18	37.360	0.582			
L Supplemental Motor Area	T_1	18	37.187	0.872	1.66	1.301	1.840
	T_2	18	37.547	1.190			
R Supplemental Motor Area	T_1	17	37.251	0.837	1.67	1.295	1.831
	T_2	17	37.496	1.142			
L Temporal Lobe	T_1	18	36.971	0.569	1.24	1.111	1.571
	T_2	18	37.308	1.981			
R Temporal Lobe	T_1	18	36.634	0.822	1.72	1.197	1.694
	T_2	18	37.182	1.529			
L Thalamus	T_1	18	36.823	0.696	1.57	0.853	1.207
	T_2	18	36.748	1.059			
R Thalamus	T_1	18	36.715	0.886	1.94	1.004	1.420
	T_2	18	36.824	1.104			

For each ROI, reproducibility was measured with the coefficient of variation for repeated measures (COVrep). The standard error of measurement (SEM) provided a measure of reliability. Minimal Detectable Change (MDC) was calculated from SEM to provide a clinically meaningful basis for evaluating T_{CRE} changes over repeated measures.
MRSI, magnetic resonance spectroscopic imaging; ROI, region of interest; n, number of observations; R, right; L, left.

correlation between T_{CRE} and Glx/tCre, $r_s = 0.458$, $p = 0.001$. Lastly, there was a weak, negative correlation of statistical significance between T_{CRE} and MI/tCre, $r_s = -0.322$, $p = 0.027$. Based on results of correlation analysis, a multiple regression was performed to predict T_{CRE} from tCho/tCre, NAA/tCre, Glx/tCre, and MI/tCre. However, none of the metabolite ratios were significant predictors of T_{CRE}. The mean distribution of tCho/tCre, NAA/tCre, Glx/tCre, and MI/tCre across regions at time1 is included in **Figure 6**.

There were no significant differences in brain temperature when comparing left and right ROIs at $p < 0.05$, corrected for FDR. Due to unequal sex distribution of our participants in the final dataset, we did not perform independent samples *t*-tests to evaluate sex differences in global and regional T_{CRE}.

Assessing Quality and Spectral Resolution

Our data were of moderate to high quality as indicated by the spectral resolution and total percentage of voxels included in our final analysis. An average of 75.18% of voxels within the brain met quality criteria across both timepoints (76.47 ± 10.68% of voxels at T_1, 73.89 ± 12.39% of voxels at T_2), with a range of 48.13% to 89.53%. As indicated by the mean linewidth of 7.31 Hz (range, 6.39 to 8.69) our data also had high spectral resolution.

We performed *post-hoc* correlation analysis of SEM, COVrep, mean T_{CRE}, and ROI size to determine if there was an association between reproducibility, repeatability, T_{CRE}, and region size. ROI size was calculated by multiplying the mean # of voxels in each region (pre-processing) by the mean % accepted voxels after processing. To adjust for varying scale, SEM, COVrep, mean T_{CRE}, and ROI size were z-transformed. Reproducibility and repeatability (COVrep*SEM) had a strong positive correlation ($r = 0.805$, $p < 0.001$) (**Table 5**). Mean T_{CRE} had a moderate positive correlation with both SEM ($r = 0.487$, $p < 0.001$) and ROI size ($r = 0.626$, $p < 0.001$) (**Table 5**). Finally, in addition to its association with mean T_{CRE}, ROI size had a moderate positive correlation with SEM ($r = 0.524$, $p < 0.001$) (**Table 5**).

DISCUSSION

Main Findings

In this study, a global brain temperature of 37.2°C was found, with spatial variations across ROIs consistent with previous studies (Cady et al., 1995, 2011; Zhang et al., 2020). Also consistent with previous studies was a significant main effect for time [$F_{(1, 1,591)} = 37.0$, $p < 0.0001$], and for brain region [$F_{(46, 1,591)} = 2.66$, $p < 0.0001$]. The central aim of this study was to evaluate whether intra-subject reproducibility is maintained in a large sample of healthy participants with longer duration between scans than previously investigated. Though this study acquired MRSI-t data with a much greater time interval between acquisitions (∼12 weeks apart), the COVrep ranged from 0.81 to 3.08% (mean COVrep = 1.92%), with 30 ROIs having a COVrep < 2.0%. Thus, T_{CRE} was stable across all 47 ROIs and paralleled results of previous studies of serial acquisitions or those separated by 1-week intervals (Maudsley et al., 2010; Thrippleton et al., 2014; Zhang et al., 2020). Another important question was whether timepoint has an impact on the mean brain temperature within a given ROI. Mixed effects analysis confirmed that the effect of time does not depend on ROIs, as indicated by the lack of a significant interaction [time*brain region, $F_{(46, 1,591)} = 0.80$, $p = 0.83$)]. Thus, in the absence of neuropathology, the effect of time likely exerts a global change in brain temperature that equally impacts all brain regions. Interestingly, the highest T_{CRE} was found in (1) posterior regions affected by anterior-posterior gradient effects (L and R occipital lobe, L and R cuneus, L and R precuneus), and 2) large peripheral cortical regions (L and R frontal lobes, R parietal, L and R occipital). Large posterior regions demonstrated higher T_{CRE} with more within-subject variability and greater SEM. Based on MDC, atypical T_{CRE} ranged from 37.57 to 41.49°C. MDC was calculated at the 68th confidence interval (CI), but future work with larger sample sizes and more repeated acquisitions may enable MDC calculation at the 90th or 95th CIs. Based on the aforementioned findings, our study confirms previous findings of spatial brain temperature variations from structure to structure; even if time has a significant effect, this effect is distributed over regions, and does not change in magnitude as a function of ROI.

Though T_{CRE} correlated moderately with some of the neuroinflammatory metabolites, the regression model indicated that none were significant predictors. Thus, the relationship between T_{CRE} and neuroinflammatory metabolites could not be fully assessed in this population, as would be expected for healthy participants without neuroinflammatory pathophysiology. Creatine was among the most stable brain metabolites (COVrep = 10.38%), though NAA still demonstrated far less variability between timepoints. Consistent with previous investigations, myo-inositol was the least stable across time points (COVrep = 16.05%) (Brooks et al., 1999; Wellard et al., 2005; Okada et al., 2007; Zhang et al., 2020). Myo-inositol quantification is technically challenging due to low signal-to-noise ratio, which primarily stems from the distributed signal of 6 hydrogen atoms and spectral overlap with spectra of other metabolites (e.g., Glx) (Haris et al., 2011). Previous studies have demonstrated substantial variability of MI globally and across regions. Choline demonstrated a wider range of COVrep across ROIs (range 3.13–84.52%), as compared to MI. This unexpected finding may result from scanner-specific anomalies, increased cellular or brain activity, or even undocumented physiological phenomena (e.g., injury or illness). Given the small body of repeatability data for volumetric MRSI, more studies are necessary before the reliability, variability, and expected range of metabolite and brain temperature values can be solidified for healthy populations or region to region.

Maudsley et al. previously established tCre as the reference metabolite for brain temperature derivations; this is because of its even distribution across cellular compartments (at least in the absence of disease), which renders tCre the least susceptible to gray matter (GM) and white matter (WM) tissue-dependency frequency shifts (Maudsley et al., 2017). Given the difficulty of separating GM and WM within each ROI, we used tCre as our reference metabolite. However, it is not always the case that tCre is well-distributed or best reference metabolite—especially when considering neurodegenerative conditions characterized by significant changes in bioenergetics/metabolism. The posterior

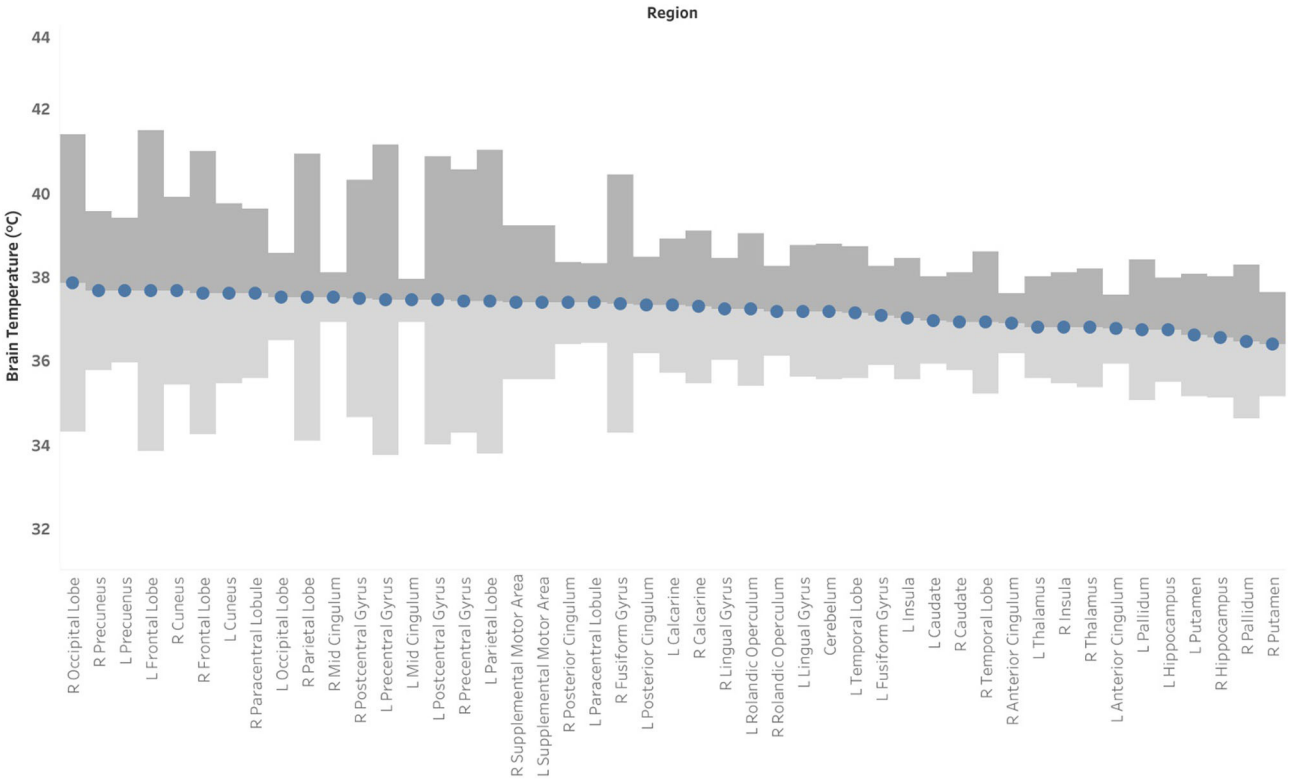

FIGURE 4 | Mean brain temperature for 47 brain regions delineated by the Automated Anatomical Labeling (AAL) atlas, with estimates of the upper and lower bounds of Minimal Detectable Change (MDC) at which temperatures may be above- or below-typical, respectively. Brain temperature was non-invasively derived from volumetric magnetic resonance spectroscopic imaging (MRSI) data. Voxel-level brain temperature was calculated according to the following equation: $T_{CRE} = -102.61(\Delta_{H20-CRE}) + 206.1°C$, where $\Delta_{H20-CRE}$ = chemical shift difference between the creatine and water resonances. The upper bounds of MDC are indicated in dark gray bands, and the lower bounds of MDC are indicated in light gray bands.

regions that indicated higher brain temperature and greater variability could be the result of anterior-posterior gradient due to acquisition, but may also be the result of visual stimulation effects from watching movies during acquisition (Kauppinen et al., 2008; Rango et al., 2015). Future studies would benefit from acquiring data both with and without in-scanner visual stimulation.

Limitations and Other Considerations

Our study was limited by the heterogeneity of the participant population, limited age range (no participants >46 years), and acquisition-related methods that are inherently variable between- and within-participants. Additionally, we did not monitor or control for a number of variables that could alter brain temperature, including circadian rhythms, diurnal changes, hormonal variations (e.g., due to menstruation), or even environmental conditions (e.g., temperature in the scanner room). Our methodological limitations stem from two issues that critically impact all MRSI-t data: (1) magnetic field inhomogeneities and (2) interfering signal from water-containing structures (e.g., the aqueous humor of the eyes). Shimming during EPSI acquisition can substantially reduce magnetic field inhomogeneities and improve signal-to-noise ratio by adjusting spectral linewidth, but the process is time-consuming and difficult without substantial training. Due to investigators' extensive training in manual shimming, automated shimming was followed by interactive shimming to optimize signal resolution and data quality. All participants' data were acquired a peak FWHM $\leq$30 Hz as recommended (Zeinali-Rafsanjani et al., 2018). Though shimming greatly improves spectral linewidth, it cannot correct the spatial inhomogeneities present across structures and even within large brain regions—additionally, it is unclear whether these spatial inhomogeneities are truly artifact or a reflection of actual physiological processes. Signals from water-containing structures are typically masked with the placement of a saturation band placement during data acquisition. While this is effective to an extent, the saturation band is a 3D rectangular slab of fixed bounds and shape—it can only be angled to cover the eyes and sphenoidal sinuses, and there is currently no capacity for altering the curvature of the band. Depending on each participant's structural anatomy, the saturation band may cut off regions of cortex in the frontal areas. Additionally, the placement and angling of this slab cannot be replicated from subject-to-subject or even within a subject across time points. As with our own data, these issues can result in missing or even heavily

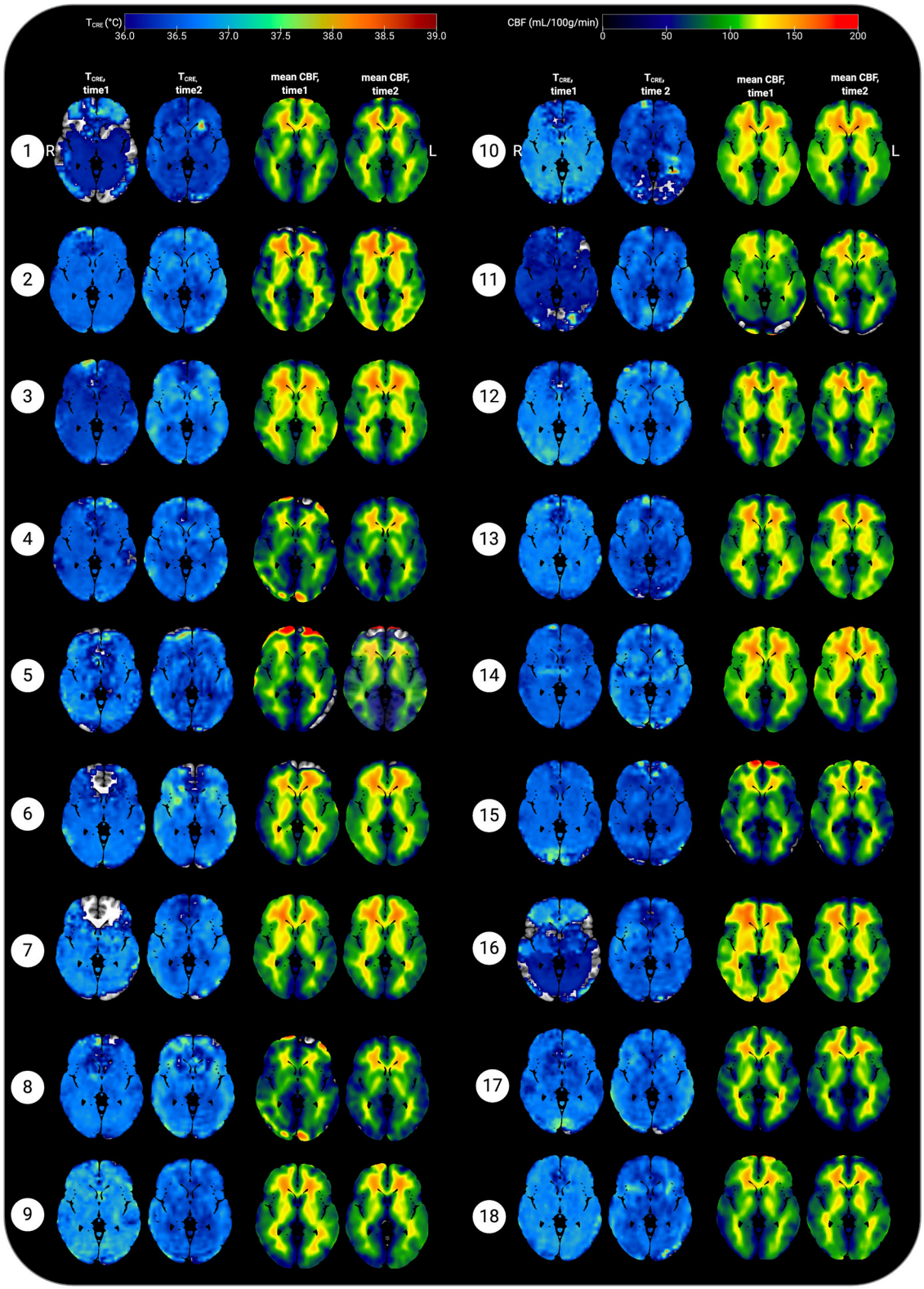

FIGURE 5 | Representative axial slices showing brain temperature (T_{CRE}) and cerebral blood flow (CBF) for 18 healthy participants at time 1 and time 2. Brain temperature was non-invasively measured using volumetric magnetic resonance spectroscopic imaging (MRSI) data, with calculation according to the following equation: $T_{CRE} = -102.61(\Delta_{H20-CRE}) + 206.1°C$, $\Delta_{H20-CRE}$ = chemical shift difference between the creatine and water resonances. Mean CBF maps (ml/100 g/min) were generated following processing of arterial spin labeling (ASL) data, with voxel-level CBF quantified using simple subtraction between each tag/control pair (120

(Continued)

FIGURE 5 | smoothed volumes, 60 pairs) for 18 participants. Mean T_{CRE} and CBF maps were resliced and co-registered to Montreal Neurological Institute template space with the Statistical Parametric Mapping (SPM12) toolbox running in MatLab R2019b. All data are visualized for axial view of the same slice ($z = 8$; L, left; R; right). The T_{CRE} color scale ranges from 36.0 to 39°C, with dark to light blue coloring indicating T_{CRE} values within the typical range. The majority of voxels demonstrate T_{CRE} <37.5°C, with a mean of 37.0°C for time1 and 37.4°C for time2 (global mean of 37.2°C). As demonstrated by the time1 and time2 maps and the global COVrep of 1.92%, there was a minimal variation in participants' data from time1 to time2. For some participants' data, brain regions were excluded from analysis due to technical reasons; these areas are represented by regions where the template brain is exposed. Each participant's mean CBF maps for time1 and time 2 are visualized alongside T_{CRE} maps; as with T_{CRE} mean CBF varies little from time1 to time2. Spatial T_{CRE} variations did not vary as a function of cerebral perfusion as indicated by mean CBF. The open-source software MRIcroGL (McCausland Center for Brain Imaging, University of South Carolina; https://www.mccauslandcenter.sc.edu/mricrogl/) was used to overlay mean T_{CRE} and CBF maps on the MNI single-participant template for 3D renderings of participant data. The figure was created using BioRender.

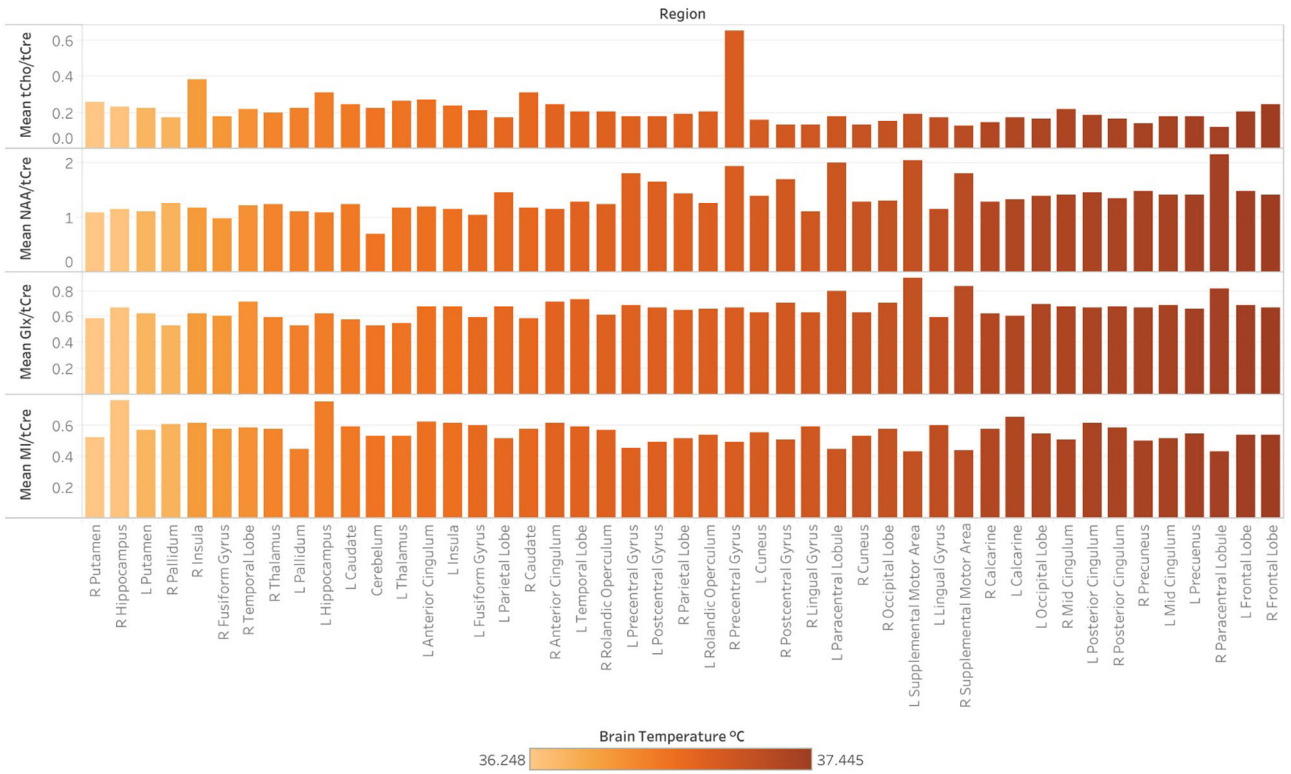

FIGURE 6 | Regional differences in the concentration of major metabolites ratios, as indicated by magnetic resonance spectroscopic imaging (MRSI) data collected at 3-Tesla at a single timepoint (time1). Following the processing of MRSI data within the Metabolite Imaging and Data Analysis System (MIDAS) software package, metabolite ratios were quantified using the Map Integrated Spectrum (MINT) module within MIDAS. Spectral integration was limited to voxels that had a fitted metabolite linewidth between 2 and 12 Hz, and voxels were excluded if they had an outlying values of 2.5 times the standard deviation of all valid voxels in the image. Metabolite ratios were derived for 47 brain regions delineated by the Automated Anatomical Labeling (AAL) atlas. Ratios for the following metabolites in reference to creatine (tCre) are demonstrated: choline (tCho), N-acetylaspartate (NAA), Glx (combined signal from glutamine and glutamate), and myo-inositol (MI). Mean tCho/tCre, NAA/tCre, Glx/tCre, and MI/tCRE across regions at time1, with regions ordered (left to right) by ascending mean T_{CRE} at time1 and corresponding coloring metabolite ratio data.

contaminated metabolite and temperature data for impacted ROIs, as voxels may not contain sufficient information or signals of sufficient quality.

A countless number of phenomena could theoretically impact brain temperature and weaken the ability to maintain sufficient reproducibility and reliability. Functional activity, time of day, and even transient hormonal fluctuations such as menstruation may impact MRSI-t-based estimates (Ene Mrozek et al., 2012). Thrippleton et al. limited data acquisition to afternoon hours to minimize diurnal temperature variation, and went so far as to recruit only male subjects to avoid the hormonal fluctuations that may impact brain temperature in females (Thrippleton et al., 2014). They additionally instructed their participants to refrain from eating, drinking, exercising, or going outdoors within 1 h of scanning; even the temperature of the scanner room was regulated to obtain the most precise measurements (Thrippleton et al., 2014). These methods may be the reason for low error in repeated measurements (0.14°C), with less deviation between successive measurements. Of course, not all studies have the capacity to limit such phenomena, and one could argue that varied reference data in both sexes and across a varied number of experimental situations is imperative for fully understanding

TABLE 3 | Coefficient of variation (COVrep, %) for major metabolites.

	COVrep (%)			
Brain region	**tCho**	**tCre**	**MI**	**NAA**
L Calcarine	7.27	8.94	5.47	13.43
R Calcarine	11.63	14.42	10.59	13.00
L Caudate	12.03	7.93	8.53	22.89
R Caudate	19.00	10.67	6.62	24.31
Cerebellum	10.61	17.31	28.44	20.28
L Anterior Cingulum	6.20	8.78	4.71	14.59
R Anterior Cingulum	6.85	6.41	3.43	12.83
L Mid Cingulum	9.62	9.44	3.18	13.89
R Mid Cingulum	5.26	11.24	2.68	17.67
L Posterior Cingulum	4.73	6.45	5.01	7.19
R Posterior Cingulum	10.62	6.10	4.58	6.41
L Cuneus	7.29	10.71	7.58	9.37
R Cuneus	8.04	12.06	11.11	11.07
L Frontal Lobe	4.33	7.18	4.76	8.68
R Frontal Lobe	12.79	4.39	3.28	9.58
L Fusiform Gyrus	15.91	10.46	10.02	18.75
R Fusiform Gyrus	10.84	13.19	19.78	20.94
L Hippocampus	12.45	11.14	7.72	11.01
R Hippocampus	15.24	10.46	10.74	12.08
L Insula	3.13	6.79	3.48	19.45
R Insula	34.44	6.60	4.63	17.07
L Lingual Gyrus	10.53	12.34	10.68	17.38
R Lingual Gyrus	16.60	13.27	13.28	16.60
L Occipital Lobe	5.76	9.93	6.63	11.15
R Occipital Lobe	9.08	12.74	8.48	9.53
L Pallidum	12.41	10.15	8.04	41.97
R Pallidum	12.70	17.14	8.88	37.91
L Paracentral Lobule	17.79	17.57	6.26	22.12
R Paracentral Lobule	16.46	20.08	5.93	29.10
L Parietal Lobe	4.47	6.30	3.49	6.54
R Parietal Lobe	10.22	5.44	4.29	6.77
L Postcentral Gyrus	10.16	10.10	4.18	9.89
R Postcentral Gyrus	10.58	11.64	4.13	12.59
L Precentral Gyrus	11.91	12.20	4.56	16.17
R Precentral Gyrus	84.52	11.54	4.72	14.53
L Precuneus	6.94	5.99	4.21	7.87
R Precuneus	7.82	6.65	3.09	10.72
L Putamen	6.23	6.94	4.91	30.85
R Putamen	13.48	9.99	7.32	22.54
L Rolandic Operculum	4.07	6.96	4.25	7.96
R Rolandic Operculum	4.72	8.29	4.30	9.05
L Supplemental Motor Area	14.95	19.46	7.08	32.60
R Supplemental Motor Area	22.56	22.08	4.86	25.93
L Temporal Lobe	3.70	4.35	3.78	8.12
R Temporal Lobe	8.23	5.15	6.17	6.48
L Thalamus	11.69	8.28	7.63	14.71
R Thalamus	21.24	12.43	8.35	20.60

L, left; R, right; tCho, total choline; tCre, creatine + phosphocreatine (total creatine); MI, myo-inositol; NAA, N-acetylaspartate.

TABLE 4 | Spearman correlations between metabolite ratios and brain temperature.

	T_{CRE}	tCho/tCre	NAA/tCre	Glx/tCre	MI/tCre
T_{CRE}	–	−0.575	0.678		
tCho/tCre	−0.575	–	−0.464		
NAA/tCre	0.678	−0.464	–	0.623	−0.603
Glx/tCre			0.623	–	
MI/tCre			−0.603		–

All correlations significant at the 0.01 level (2-tailed).
T_{CRE}, brain temperature calculated according to the equation $T_{CRE} = -102.61(\Delta_{H20-CRE}) + 206.1°C$; tCho, total choline; tCre, creatine + phosphocreatine (total creatine); NAA, N-acetylaspartate; Glx, combined signal from glutamine and glutamate); MI, myo-inositol.

TABLE 5 | Pearson correlations between measures of reproducibility and repeatability (SEM and COVrep), mean T_{CRE}, and ROI size.

	SEM, z-score	**COVrep, z-score**	**Mean T_{CRE}, z-score**	**ROI Size, z-score**
SEM, z-score	–	0.805	0.487	0.524
COVrep, z-score	0.805	–		
Mean T_{CRE}, z-score	0.487		–	0.626
ROI size, z-score	0.524		0.626	–

All correlations significant at the 0.01 level (2-tailed).
MRSI, magnetic resonance spectroscopic imaging; ROI, region of interest; n, number of observations; T_{CRE}, brain temperature derived using the frequency difference between H and creatine; ROI, region of interest; COVrep, coefficient of variation for repeated measures; SEM, standard error of measurement.

MRSI-t-based temperature estimates. Additionally, the calibrated equation we used for deriving T_{CRE} was developed on a more dated scanner model than that used for our study. There is disagreement over whether a calibrated formula derived phantom data is a worthwhile endeavor (Verius et al., 2019; Annink et al., 2020). The difference is minimal for short TE MRSI-t, but significant for long TE MRSI-t, resulting in a mean difference between derivations of up to 0.15°C (Annink et al., 2020). Given this small but possibly significant difference, future studies would benefit from developing a calibrated temperature formula that accounts for conditions at their particular scanner. It is worth noting that a calibration would only impact the intercept of the temperature calculation, with no impact on the slope. Thus, calibration would have little impact on outcomes if all participants' data are acquired with the same sequence and identical temperature equation.

Conclusions

MRSI-t is a reliable and reproducible approach to measuring brain temperature, though future studies of larger sample size with more repeated acquisitions over long duration are necessary. We must also determine whether MRSI-t measurements of brain temperature are sensitive to the phenomenon we are attempting to visualize. Since this study included healthy

participants only, the relationship between brain temperature and neuroinflammatory metabolites could not be fully assessed. Thus, the reference data this study provides must be applied to assessing patients with focal neuroinflammation. Before MRSI-t-based temperature can be utilized clinically, it is imperative to determine (1) if this tool can isolate focal brain temperature increases in regions of neuroinflammation and (2) if it can differentiate those with neuroinflammatory pathophysiology from those who are healthy.

DATA AVAILABILITY STATEMENT

The datasets presented in this article are not readily available because of participant privacy. De-identified data will be made available upon reasonable request with IRB and data sharing approvals in place. Requests to access the datasets should be directed to Ayushe Sharma, sharma87@uab.edu.

ETHICS STATEMENT

All procedures involving human participants or their protected health information were conducted in accordance with study procedures approved by the University of Alabama at Birmingham Institutional Review Board. Written informed consent was obtained from all individual participants involved in the study.

AUTHOR CONTRIBUTIONS

AAS, RN, and JPS: methodology and writing – review and editing. AAS and RN: data acquisition and processing. AAS and AAM: methodology, data curation, and data visualization. CM, AAM, and JWY: review and editing. AAS: formal analysis and writing—original draft. JPS: project supervision, funding acquisition, conceptualization, review, and writing—review and editing. All authors: listed have made substantial, direct, and intellectual contributions to the work.

FUNDING

This work was supported by State of Alabama General Fund (Carly's Law) and the UAB Epilepsy Center supported this study. AAS is currently supported by an institutional training grant (T32-NS061788-13) from the National Institute of Neurological Disorders and Stroke (NINDS).

ACKNOWLEDGMENTS

The authors thank Dr. Adam Goodman for helpful discussions regarding data analyses and visualization. This study was presented in part at the Annual Meeting of the Organization for Human Brain Mapping, Montreal, CA, 2020 (virtual presentation).

REFERENCES

Alberts, M. J., Faulstich, M. E., and Gray, L. (2020). *Stroke With Negative Brain Magnetic Resonance Imaging*. Available online at: http://ahajournals.org (accessed July 19, 2020).

Albrecht, D. S., Granziera, C., Hooker, J. M., and Loggia, M. L. (2016). *In vivo* imaging of human neuroinflammation. *ACS Chem. Neurosci.* 7, 470–483. doi: 10.1021/acschemneuro.6b00056

Amor, S., Puentes, F., Baker, D., and Van Der Valk, P. (2010). Inflammation in neurodegenerative diseases. *Immunology* 129, 154–169. doi: 10.1111/j.1365-2567.2009.03225.x

Annink, K. V., Groenendaal, F., Cohen, D., van der Aa, N. E., Alderliesten, T., Dudink, J., et al. (2020). Brain temperature of infants with neonatal encephalopathy following perinatal asphyxia calculated using magnetic resonance spectroscopy. *Pediatr. Res.* 88, 279–284. doi: 10.1038/s41390-019-0739-3

Aronica, E., Fluiter, K., Iyer, A., Zurolo, E., Vreijling, J., van Vliet, E. A., et al. (2010). Expression pattern of miR-146a, an inflammation-associated microRNA, in experimental and human temporal lobe epilepsy. *Eur. J. Neurosci.* 31, 1100–1107. doi: 10.1111/j.1460-9568.2010.07122.x

Barr, W. B., Ashtari, M., and Schaul, N. (1997). Bilateral reductions in hippocampal volume in adults with epilepsy and a history of febrile seizures. *J. Neurol. Neurosurg. Psychiatry* 63, 461–467. doi: 10.1136/jnnp.63.4.461

Benjamini, Y., and Yekutieli, D. (2001). The control of the false discovery rate in multiple testing under dependency. *Ann. Stat.* 29, 1165–1188. doi: 10.1214/aos/1013699998

Best, L., Ghadery, C., Pavese, N., Tai, Y. F., and Strafella, A. P. (2019). New and Old TSPO PET radioligands for imaging brain microglial activation in neurodegenerative disease. *Curr. Neurol. Neurosci. Rep.* 19:24. doi: 10.1007/s11910-019-0934-y

Blümcke, I., Coras, R., Miyata, H., and Özkara, C. (2012). Defining clinico-neuropathological subtypes of mesial temporal lobe epilepsy with hippocampal sclerosis. *Brain Pathol.* 22, 402–411. doi: 10.1111/j.1750-3639.2012.00583.x

Brooks, W. M., Friedman, S. D., and Stidley, C. A. (1999). Reproducibility of 1H-MRS *in vivo*. *Magn. Reson. Med.* 41, 193–197. doi: 10.1002/(SICI)1522-2594(199901)41:1<193::AID-MRM27>3.0.CO;2-P

Cady, E. B., D'Souza, P. C., Penrice, J., and Lorek, A. (1995). The estimation of local brain temperature by *in vivo* 1H magnetic resonance spectroscopy. *Magn. Reson. Med.* 33, 862–867. doi: 10.1002/mrm.1910330620

Cady, E. B., Penrice, J., and Robertson, N. J. (2011). Improved reproducibility of MRS regional brain thermometry by "amplitude-weighted combination." *NMR Biomed.* 24, 865–872. doi: 10.1002/nbm.1634

Chatzipanteli, K., Alonso, O. F., Kraydieh, S., and Dietrich, W. D. (2000). Importance of posttraumatic hypothermia and hyperthermia on the inflammatory response after fluid percussion brain injury: biochemical and immunocytochemical studies. *J. Cereb. Blood Flow Metab.* 20, 531–542. doi: 10.1097/00004647-200003000-00012

Chen, W. W., Zhang, X., and Huang, W. J. (2016). Role of neuroinflammation in neurodegenerative diseases (Review). *Mol. Med. Rep.* 13, 3391–3396. doi: 10.3892/mmr.2016.4948

Corbett, R. J. T., Laptook, A. R., Tollefsbol, G., and Kim, B. (1995). Validation of a noninvasive method to measure brain temperature *in vivo* using 1H NMR spectroscopy. *J. Neurochem.* 64, 1224–1230. doi: 10.1046/j.1471-4159.1995.64031224.x

Dehkharghani, S., Mao, H., Howell, L., Zhang, X., Pate, K. S., Magrath, P. R., et al. (2015). Proton resonance frequency chemical shift thermometry: experimental design and validation toward high-resolution noninvasive temperature monitoring and *in vivo* experience in a non-human primate model of acute ischemic stroke. *Am. J. Neuroradiol.* 36, 1128–1135. doi: 10.3174/ajnr.A4241

Devinsky, O., Vezzani, A., Najjar, S., De Lanerolle, N. C., and Rogawski, M. A. (2013). Glia and epilepsy: excitability and inflammation. *Trends Neurosci.* 36, 174–184. doi: 10.1016/j.tins.2012.11.008

Dickstein, L. P., Liow, J., Austermuehle, A., Zoghbi, S., Inati, S. K., Zaghloul, K., et al. (2019). Neuroinflammation in neocortical epilepsy measured by PET imaging of translocator protein. *Epilepsia* 60:15967. doi: 10.1111/epi.15967

Dietrich, W. D., Alonso, O., Busto, R., Prado, R., Zhao, W., Dewanjee, M. K., et al. (1998). Posttraumatic cerebral ischemia after fluid percussion brain injury:

an autoradiographic and histopathological study in rats. *Neurosurgery* 43, 585–593. doi: 10.1097/00006123-199809000-00105

Dietrich, W. D., Alonso, O., Halley, M., and Busto, R. (1996). Delayed posttraumatic brain hyperthermia worsens outcome after fluid percussion brain injury: a light and electron microscopic study in rats. *Neurosurgery* 38, 533–541. doi: 10.1227/00006123-199603000-00023

Ene Mrozek, S., Vardon, F., and Geeraerts, T. (2012). Brain temperature: physiology and pathophysiology after brain injury. *Anesthesiol. Res. Pract.* 2012:989487. doi: 10.1155/2012/989487

Finke, C. (2018). Diagnosing MRI-negative autoimmune diseases. *Neurol. Neuroimmunol. Neuroinflammation* 5:e457. doi: 10.1212/NXI.0000000000000457

Ghadery, C., Best, L. A., Pavese, N., Tai, Y. F., and Strafella, A. P. (2019). PET evaluation of microglial activation in non-neurodegenerative brain diseases. *Curr. Neurol. Neurosci. Rep.* 19:38. doi: 10.1007/s11910-019-0951-x

Giorgio, A., and De Stefano, N. (2010). Cognition in multiple sclerosis: relevance of lesions, brain atrophy and proton MR spectroscopy. *Neurol. Sci.* 31, S245–S248. doi: 10.1007/s10072-010-0370-x

Hamelin, L., Lagarde, J., Dorothé, G., Leroy, C., Labit, M., Comley, R. A., et al. (2019). Early and protective microglial activation in alzheimer's disease: a prospective study using 18 F-DPA-714 PET imaging. *Brain* 139, 1252–1264. doi: 10.1093/brain/aww017

Haris, M., Cai, K., Singh, A., Hariharan, H., and Reddy, R. (2011). *In vivo* mapping of brain myo-inositol. *Neuroimage* 54, 2079–2085. doi: 10.1016/j.neuroimage.2010.10.017

Jehi, L. (2018). The epileptogenic zone: concept and definition. *Epilepsy Curr.* 18, 12–16. doi: 10.5698/1535-7597.18.1.12

Jobst, B. C., and Cascino, G. D. (2015). Resective epilepsy surgery for drug-resistant focal epilepsy: a review. *JAMA - J. Am. Med. Assoc.* 313, 285–293. doi: 10.1001/jama.2014.17426

Kälviäinen, R., and Salmenperä, T. (2002). "Do recurrent seizures cause neuronal damage? A series of studies with MRI volumetry in adults with partial epilepsy," *in Progress in Brain Research* (Elsevier), 279–295. doi: 10.1016/S0079-6123(02)35026-X

Kauppinen, R. A., Vidyasagar, R., Childs, C., Balanos, G. M., and Hiltunen, Y. (2008). Assessment of human brain temperature by1H MRS during visual stimulation and hypercapnia. *NMR Biomed.* 21, 388–395. doi: 10.1002/nbm.1204

Kreis, R., Ernst, T., and Ross, B. D. (1993). Absolute quantitation of water and metabolites in the human brain. II. metabolite concentrations. *J. Magn. Reson. Ser. B* 102, 9–19. doi: 10.1006/jmrb.1993.1056

Lecocq, A., Le Fur, Y., Maudsley, A. A., Le Troter, A., Sheriff, S., Sabati, M., et al. (2015). Whole-brain quantitative mapping of metabolites using short echo three-dimensional proton MRSI. *J. Magn. Reson. Imaging* 42, 280–289. doi: 10.1002/jmri.24809

Lucas, S.-M., Rothwell, N. J., and Gibson, R. M. (2006). The role of inflammation in CNS injury and disease. *Br. J. Pharmacol.* 147(Suppl. 1), S232–S240. doi: 10.1038/sj.bjp.0706400

Mariak, Z., White, M. D., Lyson, T., and Lewko, J. (2003). Tympanic temperature reflects intracranial temperature changes in humans. *Pflugers Arch. Eur. J. Physiol.* 446, 279–284. doi: 10.1007/s00424-003-1021-3

Maroso, M., Balosso, S., Ravizza, T., Liu, J., Aronica, E., Iyer, A. M., et al. (2010). Toll-like receptor 4 and high-mobility group box-1 are involved in ictogenesis and can be targeted to reduce seizures. *Nat. Med.* 16, 413–419. doi: 10.1038/nm.2127

Maudsley, A. A., Darkazanli, A., Alger, J. R., Hall, L. O., Schuff, N., Studholme, C., et al. (2006). Comprehensive processing, display and analysis for *in vivo* MR spectroscopic imaging. *NMR Biomed.* 19, 492–503. doi: 10.1002/nbm.1025

Maudsley, A. A., Domenig, C., Govind, V., Darkazanli, A., Studholme, C., Arheart, K., et al. (2009). Mapping of brain metabolite distributions by volumetric proton MR spectroscopic imaging (MRSI). *Magn. Reson. Med.* 61, 548–559. doi: 10.1002/mrm.21875

Maudsley, A. A., Domenig, C., and Sheriff, S. (2010). Reproducibility of serial whole-brain MR Spectroscopic Imaging. *NMR Biomed.* 23, 251–256. doi: 10.1002/nbm.1445

Maudsley, A. A., Goryawala, M. Z., and Sheriff, S. (2017). Effects of tissue susceptibility on brain temperature mapping. *Neuroimage* 146, 1093–1101. doi: 10.1016/j.neuroimage.2016.09.062

McNair, D., Lorr, M., and Doppleman, L. (1989). *Profile of Mood States (POMS) Manual.* San Diego, CA: Educational and Industrial Testing Service.

Metzger, G., and Hu, X. (1997). Application of interlaced fourier transform to echo-planar spectroscopic imaging. *J. Magn. Reson.* 125, 166–170. doi: 10.1006/jmre.1997.1114

Moffett, J., Ross, B., Arun, P., Madhavarao, C., and Namboodiri, A. (2007). N-Acetylaspartate in the CNS: from neurodiagnostics to neurobiology. *Prog. Neurobiol.* 81, 89–131. doi: 10.1016/j.pneurobio.2006.12.003

Mueller, C., Lin, J. C., Sheriff, S., Maudsley, A. A., and Younger, J. W. (2019). Evidence of widespread metabolite abnormalities in myalgic encephalomyelitis/chronic fatigue syndrome: assessment with whole-brain magnetic resonance spectroscopy. *Brain Imaging Behav.* 14, 562–572. doi: 10.1007/s11682-018-0029-4

Mueller, C., Lin, J. C., Thannickal, H. H., Daredia, A., Denney, T. S., Beyers, R., et al. (2020). No evidence of abnormal metabolic or inflammatory activity in the brains of patients with rheumatoid arthritis: results from a preliminary study using whole-brain magnetic resonance spectroscopic imaging (MRSI). *Clin. Rheumatol.* 39, 1765–1774. doi: 10.1007/s10067-019-04923-5

Muhlhofer, W., Tan, Y.-L., Mueller, S. G., and Knowlton, R. (2017). MRI-negative temporal lobe epilepsy-what do we know? *Epilepsia* 58, 727–742. doi: 10.1111/epi.13699

Noe, K., Sulc, V., Wong-Kisiel, L., Wirrell, E., Van Gompel, J. J., Wetjen, N., et al. (2013). Long-term outcomes after nonlesional extratemporal lobe epilepsy surgery. *JAMA Neurol.* 70, 1003–1008. doi: 10.1001/jamaneurol.2013.209

Okada, T., Sakamoto, S., Nakamoto, Y., Kohara, N., and Senda, M. (2007). Reproducibility of magnetic resonance spectroscopy in correlation with signal-to-noise ratio. *Psychiatry Res. Neuroimaging* 156, 169–174. doi: 10.1016/j.pscychresns.2007.03.007

Oz, G., Alger, J. R., Barker, P. B., Bartha, R., Bizzi, A., Boesch, C., et al. (2014). Clinical proton MR spectroscopy in central nervous system disorders. *Radiology* 270, 658–679. doi: 10.1148/radiol.13130531

Rango, M., Bonifati, C., and Bresolin, N. (2015). Post-activation brain warming: a 1-H MRS thermometry study. *PLoS ONE* 10:e0127314. doi: 10.1371/journal.pone.0127314

Ravizza, T., Balosso, S., and Vezzani, A. (2011). Inflammation and prevention of epileptogenesis. *Neurosci. Lett.* 497, 223–230. doi: 10.1016/j.neulet.2011.02.040

Rossi, S., Roncati Zanier, E., Mauri, I., Columbo, A., and Stocchetti, N. (2001). Brain temperature, body core temperature, and intracranial pressure in acute cerebral damage. *J. Neurol. Neurosurg. Psychiatry* 71, 448–454. doi: 10.1136/jnnp.71.4.448

Salmenpera, M., Symms, M. R., Rugg-Gunn, F. J., Boulby, P. A., Free, S. L., Barker, J., et al. (2007). Evaluation of quantitative magnetic resonance imaging contrasts in MRI-negative refractory focal epilepsy * §Tuuli. *Epilepsia* 48, 229–237. doi: 10.1111/j.1528-1167.2007.00918.x

Sharma, A. A., and Szaflarski, J. P. (2020). *In vivo* imaging of neuroinflammatory targets in treatment-resistant epilepsy. *Curr. Neurol. Neurosci. Rep.* 20:5. doi: 10.1007/s11910-020-1025-9

Sharma, H. S., and Hoopes, P. J. (2003). Hyperthermia induced pathophysiology of the central nervous system. *Int. J. Hyperthermia.* 19, 325–354. doi: 10.1080/0265673021000054621

Shechtman, O. (2013). *The Coefficient of Variation as an Index of Measurement Reliability*. (Berlin, Heidelberg: Springer), 39–49. doi: 10.1007/978-3-642-37131-8_4

Téllez-Zenteno, J. F., Ronquillo, L. H., Moien-Afshari, F., and Wiebe, S. (2010). Surgical outcomes in lesional and non-lesional epilepsy: a systematic review and meta-analysis. *Epilepsy Res.* 89, 310–318. doi: 10.1016/j.eplepsyres.2010.02.007

Thrippleton, M. J., Parikh, J., Harris, B. A., Hammer, S. J., Semple, S. I. K., Andrews, P. J. D., et al. (2014). Reliability of MRSI brain temperature mapping at 1.5 and 3 T. *NMR Biomed.* 27, 183–190. doi: 10.1002/nbm.3050

Tzourio-Mazoyer, N., Landeau, B., Papathanassiou, D., Crivello, F., Etard, O., Delcroix, N., et al. (2002). Automated anatomical labeling of activations in SPM using a macroscopic anatomical parcellation of the MNI MRI single-subject brain. *Neuroimage* 15, 273–289. doi: 10.1006/nimg.2001.0978

Veenith, T. V., Mada, M., Carter, E., Grossac, J., Newcombe, V., Outtrim, J., et al. (2014). Comparison of inter subject variability and reproducibility of whole brain proton spectroscopy. *PLoS ONE* 9:e115304. doi: 10.1371/journal.pone.0115304

Verius, M., Frank, F., Gizewski, E., and Broessner, G. (2019). Magnetic resonance spectroscopy thermometry at 3 tesla: importance of calibration measurements. *Ther. Hypothermia Temp. Manag.* 9, 146–155. doi: 10.1089/ther.2018.0027

Vezzani, A., Balosso, S., and Ravizza, T. (2019). Neuroinflammatory pathways as treatment targets and biomarkers in epilepsy. *Nat. Rev. Neurol.* 15, 459–472. doi: 10.1038/s41582-019-0217-x

Vezzani, A., and Friedman, A. (2011). Brain inflammation as a biomarker in epilepsy. *Biomark. Med.* 5, 607–614. doi: 10.2217/bmm.11.61

Vivash, L., and OBrien, T. J. (2016). Imaging microglial activation with TSPO PET: lighting up neurologic diseases? *J. Nucl. Med.* 57, 165–168. doi: 10.2967/jnumed.114.141713

Wang, H., Wang, B., Normoyle, K. P., Jackson, K., Spitler, K., Sharrock, M., et al. (2014). Brain temperature and its fundamental properties: a review for clinical neuroscientists. *Front. Neurosci.* 8:307. doi: 10.3389/fnins.2014.00307

Wang, Z., Aguirre, G. K., Rao, H., Wang, J., Fernández-Seara, M. A., Childress, A. R., et al. (2008). Empirical optimization of ASL data analysis using an ASL data processing toolbox: ASLtbx. *Magn. Reson. Imaging* 26, 261–269. doi: 10.1016/j.mri.2007.07.003

Weir, J. P. (2005). Quantifying test-retest reliability using the intraclass correlation coefficient and the SEM. *J. Strength Cond. Res.* 19, 231–240. doi: 10.1519/00124278-200502000-00038

Wellard, R. M., Briellmann, R. S., Jennings, C., and Jackson, G. D. (2005). Physiologic variability of single-voxel proton MR spectroscopic measurements at 3T. *Am. J. Neuroradiol.* 26, 585–590.

Zeinali-Rafsanjani, B., Faghihi, R., Mosleh-Shirazi, M. A., Moghadam, S.-M., Lotfi, M., Jalli, R., et al. (2018). MRS shimming: an important point which should not be ignored. *J. Biomed. Phys. Eng.* 8, 261–270.

Zhang, Y., Taub, E., Mueller, C., Younger, J., Uswatte, G., DeRamus, T. P., et al. (2020). Reproducibility of whole-brain temperature mapping and metabolite quantification using proton magnetic resonance spectroscopy. *NMR Biomed.* 33:e4313. doi: 10.1002/nbm.4313

Zhu, M., Ackerman, J. J. H., and Yablonskiy, D. A. (2009). Body and brain temperature coupling: The critical role of cerebral blood flow. *J. Comp. Physiol. B Biochem. Syst. Environ. Physiol.* 179, 701–710. doi: 10.1007/s00360-009-0352-6

Zigmond, A. S., and Snaith, R. P. (1983). The hospital anxiety and depression scale. *Acta Psychiatr. Scand.* 67, 361–370. doi: 10.1111/j.1600-0447.1983.tb09716.x

Conflict of Interest: The authors declare that the research was conducted in the absence of any commercial or financial relationships that could be construed as a potential conflict of interest.

frontiers in Human Neuroscience

CORRECTION
published: 26 November 2021
doi: 10.3389/fnhum.2021.780797

Corrigendum: Repeatability and Reproducibility of *in-vivo* Brain Temperature Measurements

Ayushe A. Sharma[1,2,3]*, *Rodolphe Nenert*[3,4], *Christina Mueller*[1], *Andrew A. Maudsley*[5], *Jarred W. Younger*[1] *and Jerzy P. Szaflarski*[2,3,4,6]

[1] Department of Psychology, University of Alabama at Birmingham (UAB), Birmingham, AL, United States, [2] Department of Neurobiology, University of Alabama at Birmingham (UAB), Birmingham, AL, United States, [3] University of Alabama at Birmingham Epilepsy Center (UABEC), Birmingham, AL, United States, [4] Department of Neurology, University of Alabama at Birmingham (UAB), Birmingham, AL, United States, [5] Department of Radiology, Miller School of Medicine, University of Miami, Miami, FL, United States, [6] Department of Neurosurgery, University of Alabama at Birmingham (UAB), Birmingham, AL, United States

Keywords: MRS, brain temperature, MR thermometry, neuroinflammation, neuroimaging

A Corrigendum on

Repeatability and Reproducibility of *in-vivo* Brain Temperature Measurements
by Sharma, A. A., Nenert, R., Mueller, C., Maudsley, A. A., Younger, J. W., and Szaflarski, J. P. (2020). Front. Hum. Neurosci. 14:598435. doi: 10.3389/fnhum.2020.598435

In the original article, there was a mistake in ***Figure 1*** as published.

The original figure was adapted from Dehkharghani et al. (2015), but this adaptation was not appropriately described and referenced in the manuscript. We apologize for this oversight. The figure has been revised: the adapted portion has been replaced with a new graphic and the caption now appropriately indicates that a portion was adapted from a previously published article. The corrected ***Figure 1*** appears below.

The authors apologize for this error and state that this does not change the scientific conclusions of the article in any way. The original article has been updated.

REFERENCES

Dehkharghani, S., Mao, H., Howell, L., Zhang, X., Pate, K. S., Magrath, P. R., et al. (2015). Proton resonance frequency chemical shift thermometry: experimental design and validation toward high-resolution noninvasive temperature monitoring and *in vivo* experience in a non-human primate model of acute ischemic stroke. *Am. J. Neuroradiol.* 36, 1128–1135. doi: 10.3174/ajnr.A4241

Edited and reviewed by:
Dajiang Zhu,
University of Texas at Arlington, United States

***Correspondence:**
Ayushe A. Sharma
sharma87@uab.edu

Specialty section:
This article was submitted to Brain Imaging and Stimulation, a section of the journal Frontiers in Human Neuroscience

Received: *21 September 2021*
Accepted: *04 November 2021*
Published: *26 November 2021*

Citation:
Sharma AA, Nenert R, Mueller C, Maudsley AA, Younger JW and Szaflarski JP (2021) Corrigendum: Repeatability and Reproducibility of in-vivo Brain Temperature Measurements. Front. Hum. Neurosci. 15:780797. doi: 10.3389/fnhum.2021.780797

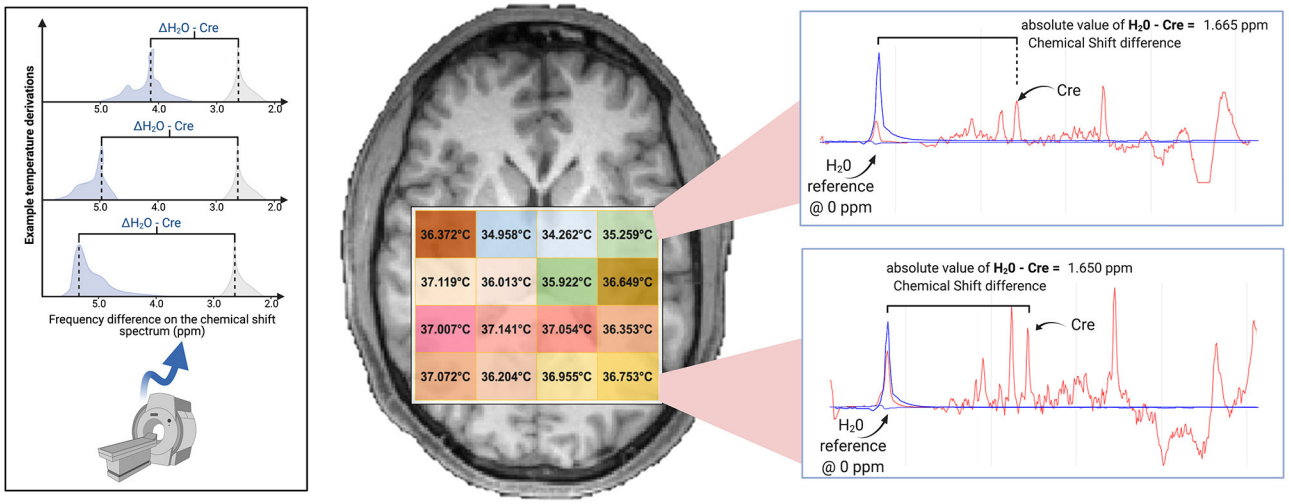

FIGURE 1 | Brain temperature can be non-invasively derived from volumetric magnetic resonance spectroscopic imaging (MRSI) data by calculating the frequency difference between the temperature-sensitive water peak and one or more metabolite peaks that are temperature-insensitive (*left*[*]). When using creatine as the reference, voxel-level brain temperature can be calculated according to the following equation: $T_{CRE} = -102.61(\Delta_{H20-CRE}) + 206.1°C$, $\Delta_{H20-CRE}$ = chemical shift difference between the creatine and water resonances. Example T_{CRE} calculations are provided for a participant's single tissue slice (*right*). Representative spectra illustrate $\Delta_{H20-CRE}$ derivations, with plots depicting a water-suppressed metabolite spectrum (*red line*), with an overlay that indicates the location of the reference water signal (*blue line)*. Spectral plots were created within the Metabolite Imaging and Data Analysis System (MIDAS) software package, and the figure was created using BioRender. [*]Adapted from Dehkharghani et al. (2015).

frontiers in Human Neuroscience

ORIGINAL RESEARCH
published: 15 January 2021
doi: 10.3389/fnhum.2020.580238

Abnormal Static and Dynamic Local-Neural Activity in COPD and Its Relationship With Pulmonary Function and Cognitive Impairments

Zhi Lv[1,2†], Qingqing Chen[3†], Yinling Jiang[2], Panpan Hu[4], Lei Zhang[3], Tongjian Bai[4], Kai Wang[4], Yongsheng Wang[2] and Xiaoyun Fan[1*]*

[1] Department of Geriatric Respiratory and Critical Care Medicine, The First Affiliated Hospital of Anhui Medical University, Hefei, China, [2] Department of Pulmonary, The Second People's Hospital of Hefei (The Affiliated Hefei Hospital of Anhui Medical University), Hefei, China, [3] The Fifth Ward, Department of Tuberculosis, Anhui Chest Hospital, Hefei, China, [4] Department of Neurology, The First Affiliated Hospital of Anhui Medical University, Hefei, China

OPEN ACCESS

Edited by:
Wei Liao,
University of Electronic Science and Technology of China, China

Reviewed by:
Feng Liu,
Tianjin Medical University General Hospital, China
Qiang Xu,
Nanjing University, China

***Correspondence:**
Yongsheng Wang
13305657779@189.cn
Xiaoyun Fan
13956988552@163.com

[†]These authors have contributed equally to this work

Specialty section:
This article was submitted to Brain Imaging and Stimulation, a section of the journal Frontiers in Human Neuroscience

Received: 05 July 2020
Accepted: 11 December 2020
Published: 15 January 2021

Citation:
Lv Z, Chen Q, Jiang Y, Hu P, Zhang L, Bai T, Wang K, Wang Y and Fan X (2021) Abnormal Static and Dynamic Local-Neural Activity in COPD and Its Relationship With Pulmonary Function and Cognitive Impairments. Front. Hum. Neurosci. 14:580238. doi: 10.3389/fnhum.2020.580238

Patients with chronic obstructive pulmonary disease (COPD) are characterized by attenuated pulmonary function and are frequently reported with cognitive impairments, especially memory impairments. The mechanism underlying the memory impairments still remains unclear. We applied resting-state functional magnetic resonance imaging (RS-fMRI) to compare the brain local activities with static and dynamic amplitude of low-frequency fluctuations (sALFF, dALFF) among patients with COPD ($n = 32$) and healthy controls (HC, $n = 30$). Compared with HC, COPD patients exhibited decreased sALFF in the right basal ganglia and increased dALFF in the bilateral parahippocampal/hippocampal gyrus. The reduced the left basal ganglia was associated with lower oxygen partial pressure. Besides, the increased dALFF in the left hippocampal/parahippocampal cortex was associated with poor semantic-memory performance and the increased dALFF in the left hippocampal/parahippocampal cortex was associated the forced vital capacity. The present study revealed the abnormal static and dynamic local-neural activities in the basal ganglia and parahippocampal/hippocampal cortex in COPD patient and its relationship with poor lung function and semantic-memory impairments.

Keywords: chronic obstructive pulmonary disease, semantic memory, resting-state functional MRI, dynamic, amplitude of low-frequency fluctuation

INTRODUCTION

Chronic obstructive pulmonary disease (COPD) is a chronic disease of the lungs and a leading cause of significant mortality and disability (Watz et al., 2008). According to the WHO, COPD is the fourth leading cause of death and will be the third leading cause of death by 2030. Cognitive dysfunction is one of the most important comorbidities of COPD, which must be cautiously considered. It has been reported that 12–88% of patients with COPD present with cognitive impairments (Hynninen et al., 2005), either globally or in single cognitive domains (Dodd et al., 2010), especially memory deficits (Cleutjens et al., 2014). However, the pathogenesis of cognitive impairments remains unclear.

Multiple studies have revealed the relationship between cerebral structural lesions and poor respiratory function (Liao et al., 1999; Sachdev et al., 2006). Considering the direct relation between hypoxia and neuronal functional activity, COPD patients may be more susceptible to neuronal functional alterations. Hence, it is more reasonable from a functional view to explore the neural substance underlying cognitive impairments in COPD. Indeed, it is widely known that cognitive processing requires activity in the relevant cerebral regions (task-related neuronal activity). However, compared with task-related neuronal activity, spontaneous neuronal activity actually consumes more brain energy (Raichle and Mintun, 2006) and has been linked with multiple cognitive processes, such as spatial orientation and memory (Greicius et al., 2003). Spontaneous neuronal activity refers to the activity intrinsically generated by the brain that is not attributable to particular information inputs or outputs (Fox and Raichle, 2007).

Recently, spontaneous activity has been indexed by various approaches, such as resting-state functional connectivity (RSFC) and regional homogeneity (ReHo). These indexes reflect functional coupling between distinct brain regions, spatially remote and local, respectively (Friston, 2002; Zang et al., 2004), but not direct neuronal activity. As regional measures of spontaneous activity, the regional amplitude of low-frequency fluctuations (ALFF) has been extensively used to represent spontaneous neuronal activity (Zang et al., 2007). The ALFF were shown to be closely associated with other classical measures of brain activation, such as PET (Tomasi et al., 2013), and have been widely used to measure the neural substrates of several cognitive processes, including language learning and working memory (Zou et al., 2013; Deng et al., 2016). Besides, abnormal ALFF have been linked to cognitive dysfunction in various neurological disorders, such as Alzheimer's disease (Wang et al., 2011). Recently, there have also been studies that investigated the alterations in neuronal activity in patients with COPD using ALFF (Wenjing et al., 2018; Lu et al., 2019). For example, Lu et al. (2019) found decreased ALFF in bilateral basal ganglia areas and the aberrant ALFF value was correlated with PaO_2 and the pulmonary ventilation function.

However, most of these studies on local spontaneous neuronal activity have focused on measuring static ALFF (sALFF), which is based on the implicit assumption that brain activity remains temporally stationary during the entire scanning period. Recently, mounting evidence has suggested there are time-varying characteristics of brain local activity (Hutchison et al., 2013; Allen et al., 2014; Liu et al., 2017), which was always indexed by the dynamic amplitude of low-frequency fluctuation (dALFF). Importantly, the dALFF has been frequently associated with cognitive performance in healthy people (Fornito et al., 2012) and patients with cognitive impairments (Fiorenzato et al., 2019). However, whether patients with COPD exhibit abnormal dALFF remains unclear. In the present study, we aimed to explore the static and dynamic local neuronal activities and their relationships to cognitive deficit in patients with COPD. We assumed that COPD patients present aberrant static and dynamic ALFF and these abnormal local activities may be related to cognitive impairments in COPD patients.

MATERIALS AND METHODS

Participants

Thirty-two patients with COPD were recruited from the Hefei Second People's Hospital, Hefei, China. The patients were diagnosed according to the Global Initiative for Chronic Obstructive Lung Disease (GOLD) guidelines from 2013 and met other necessary inclusion criteria: (1) no current mental disorders or neurological illness or related history; (2) no history of substance abuse; (3) no comorbidities such as diabetes, liver failure, cardiovascular disease, neurological disorders, or malignant tumor; (4) years of schooling >5; (5) eligible head motion (<3 mm, 3°); (6) no claustrophobia or other contraindications of an MRI scan. Finally, thirty-two patients were included in the final analysis. Thirty healthy subjects were also enrolled and matched according to gender, age, and education via local advertisements. All participants were carefully screened in a diagnostic interview to rule out current or past significant medical illness or mental disorders. The present study was approved by the Anhui Medical University Ethics Committee, and written informed consent was obtained from all participants.

Laboratory Tests

Within 3 days of MRI scanning, a standardized pulmonary function test was performed to evaluate the function of pulmonary ventilation in all participants. In addition, an arterial blood gas analysis was performed for all patients.

Cognitive Test

The present study primarily focused on the semantic memory, assessed by a category verbal fluency test (CVFT). During the CVFT, participants were required to say as many words as possible describing a vegetable within 1 min. One point was scored when participants gave a correct term for the correct description of the vegetable. The total score was used as a record of memory performance for further analysis.

MRI Data Acquisition

Structural and functional MRI images of participants were acquired at the University of Science and Technology of China, Anhui Province, with a 3-T scanner (Discovery GE750w, General Electric). Before image acquisition, all participants were asked to keep their eyes closed and body still, and not to think of anything in particular. T1-weighted anatomical images were acquired in the sagittal orientation [TR/TE = 8.16/3.18 ms; flip angle = 12°; field of view (FOV) = 256 × 256 mm^2; voxel size = 1 × 1 × 1 mm^3; slice thickness= 1 mm; 188 slices]. Functional MRI (BOLD) images were composed of 217 echo-planar imaging volumes (TR/TE = 2,400/30 ms; flip angle = 90°; FOV = 192 × 192 mm^2; voxel size = 3 × 3 × 3 mm^3; slice thickness = 3 mm; matrix size = 64 × 64; 46 continuous slices).

Functional Data Preprocessing

Functional MRI data were preprocessed using the Data Processing Assistant for Resting-State Functional MR Imaging toolkit (Chao-Gan and Yu-Feng, 2010). For each participant, we applied the following processing steps: discarding the

first 10 volumes to allow for magnetization equilibrium; slice timing correction; realignment to account for head motion; co-registered structural images with the mean functional image and then segmented into gray matter, white matter, and cerebrospinal fluid; the gray matter maps were non-linearly co-registered to the tissue probability maps in the Montreal Neurological Institute (MNI) space; normalization functional volume to the MNI space using the parameters estimated during non-linear co-registration at a resolution of $3 \times 3 \times 3$ mm^3; nuisance regressors with 24 Friston motion parameters, white matter high signal, cerebrospinal fluid signal and global signals as regressors; filtering with a temporal band pass of 0.01–0.1 Hz, and spatial smoothing (Gaussian kernel $= 4 \times 4 \times 4$ mm^3). Finally, motion scrubbing was conducted using the cubic spline method to minimize the influence of the time points with high motion [frame-wise displacement (FD) >0.5], as well as that of one time point prior to, and two time points following, each of these high motion time points.

Static Amplitude of Low-Frequency Fluctuations (sALFF)

After preprocessing, the filtered time series was converted to the frequency domain using a fast Fourier transform. The square root of the power at each frequency was calculated to obtain amplitude values. The ALFF was calculated as the sum of the amplitude values in the 0.01–0.1 Hz low-frequency power range. To reduce the global effects of variability across participants, the ALFF was normalized to the mean within-brain ALFF value for each participant.

Dynamic Amplitude of Low-Frequency Fluctuations (dALFF)

The sliding window approach was used to calculate the dALFF using DynamicBC software (Liao et al., 2014). Based on previous recommendations, we chose 30 repetition times (TRs) (72 s) as the window length (Leonardi and Van De Ville, 2015; Li et al., 2018), and the window was shifted by 40% of the window length (12 TRs, 28.8 s). There were 207 TRs for our data and, hence, 15 windows constituted the full time series. For the time series in each window, the ALFF map was calculated using the procedures described above for the sALFF calculation. To study the temporal variability of ALFF, the standard deviation (SD) of ALFF at each voxel was calculated across sliding-window dynamics, then the coefficient of variation (CV: SD/mean) map was calculated, i.e., dALFF. Additionally, selected parameters, especially the length of window and span (overlap), are key factors in the computation of dynamics. To validate our findings, we conducted auxiliary analyses with another span (one TR, 2.4 s) and two window lengths [40 TRs (96 s) and 50 TRs (120 s)].

Statistical Analysis

The Pearson's χ^2 test and two-sample *t*-tests were applied to compare the demographic and clinical characteristics of the two groups (gender, age, educational years, clinical symptoms, and semantic memory performance) with SPSS 23. Voxel-wise two-sample *t*-tests within the gray matter mask were performed to quantitatively compare the differences in the sALFF and dALFF values between the two groups with gender, age, educational years, and head motion indexed by frame-wise displacement (FD) as covariates with the software of DPABI (http://rfmri.org/dpabi). Statistical maps for sALFF and dALFF were corrected using the Gaussian Random Field method at the threshold of $p < 0.001$ at the voxel level and $p < 0.05$ at the cluster level (cluster size >40 voxel). Spearman's correlation analyses were conducted to examine the associations between the significantly different sALFF and dALFF values between groups and behavioral performance. Significance for correlations was determined by $p < 0.05$ (two-tailed), with no correction.

RESULTS

Demographic and Clinical Characteristics

Thirty-two patients with COPD and 30 healthy controls were included in the final analysis. No significant differences were found between the two groups in terms of age or gender. Compared with the HC, participants with COPD had lower scores in the CVFT. **Table 1** presents the demographic characteristics of the two groups.

Group Comparison of sALFF

We explored the differences in sALFF between the two groups based on voxel level. Compared with HC, there were lower sALFF in the left basal ganglia (cluster size = 66; peak coordinate = −24, 0, 0) (shown in **Figure 1**). No other regions demonstrating significantly different sALFF between the two groups were found.

TABLE 1 | Demographic and clinical characteristic.

	COPD	HC	[b]T value/χ^2	*p*-value
Gender (Male/female)[a]	30/2	27/3	0.29	0.59
Age	71.94 ± 5.52	71.10 ± 3.95	0.68	0.50
Educational years	6.03 ± 2.60	6.17 ± 2.13	−0.22	0.82
PH	7.40 ± 0.040			
PaO_2	83.68 ± 22.87			
$PaCO_2$	43.75 ± 10.70			
FEV_1	0.95 ± 0.44			
FVC	1.84 ± 0.71			
FEV_1/FVC	0.51 ± 0.088			
CVFT	12.69 ± 2.38			
sALFF in BG	0.67 ± 0.10	0.80 ± 0.11	−4.97	<0.001
dALFF in LHIP	0.29 ± 0.08	0.19 ± 0.04	6.03	<0.001
dALFF in RHIP	0.25 ± 0.05	0.18 ± 0.04	6.76	<0.001

[a]*Data are presented as mean ± standard deviation except Gender.*
[b]*Comparisons were performed using the chi-square test for the variable of Gender and independent samples t-tests for other variables.*
COPD, chronic obstructive pulmonary disease; HC, healthy control; PH, pondus hydrogenii; PaO_2, partial pressure of oxygen; $PaCO_2$, partial pressure of carbon dioxide; FVC, forced vital capacity; FEV_1, forced expiratory volume in the first second; CVFT, category verbal fluency test; sALFF, static amplitude of low-frequency fluctuations; dALFF, dynamic amplitude of low-frequency fluctuations; BG, basal ganglia; RHIP, right hippocampal/parahippocampal cortex; LHIP, hippocampal/parahippocampal cortex.

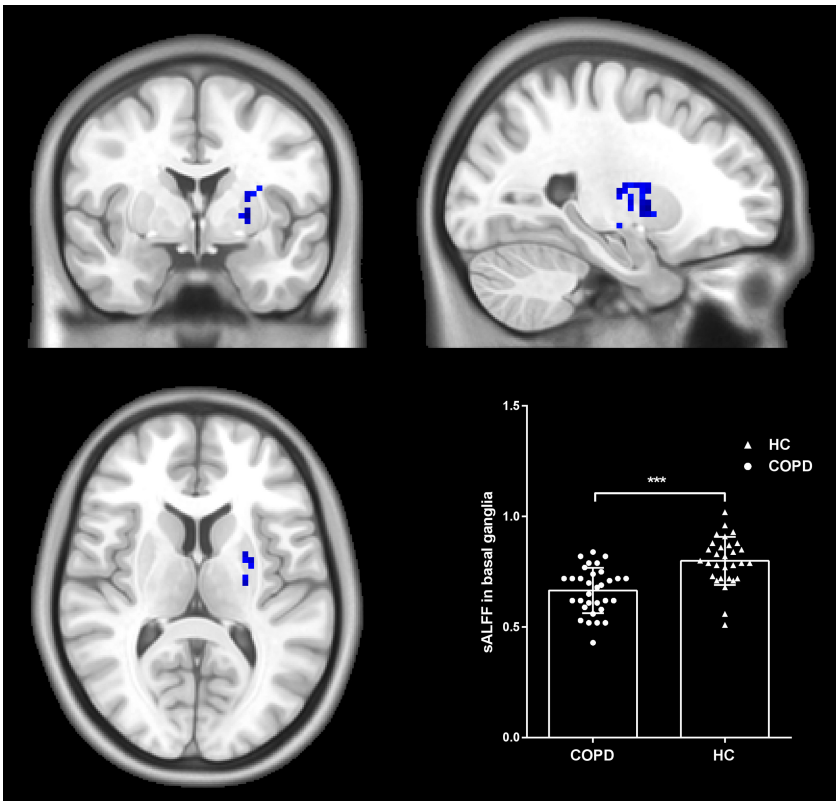

FIGURE 1 | Group differences in sALFF. Patients with COPD showed decreased sALFF in the left basal ganglia compared to HC. Statistical maps were corrected via the Gaussian Random Field (GRF) method at a threshold of voxel $P < 0.001$, cluster $P < 0.05$ (with 7.6*8.0*6.7 mm^3 as estimate smoothness kernel). Scatter plots present sALFF of each participant in the two groups. ***$p < 0.001$.

Group Comparison of dALFF

The differences in dALFF between the two groups were also examined based on voxel level. Compared with HC, patients with COPD exhibited decreased dALFF in the bilateral hippocampal/parahippocampal cortex (cluster = 48, peak coordinate = 27, −39, 0; cluster size = 50, peak coordinate = −27, −51, −3) (shown in **Figure 2**). The validation analysis with different sliding-window lengths also revealed decreased dALFF in the bilateral hippocampal/parahippocampal cortex in the COPD group (**Supplementary Figure 1**).

Relationship Between sALFF and dALFF Clinical Characteristics and Behavioral Performance

The reduced sALFF in the left basal ganglia were lower oxygen partial pressure ($r = 0.544$, $p = 0.001$). Besides, the increased dALFF in the left hippocampal/parahippocampal cortex were associated with poor semantic-memory performance ($r = 0.544$, $p = 0.001$) and the increased dALFF in the left hippocampal/parahippocampal cortex were associated with the forced vital capacity ($r = 0.544$, $p = 0.001$). The sALFF in the left basal ganglia were negatively related with dALFF in the bilateral hippocampal/parahippocampal cortex ($r = -0.360$, $p = 0.004$ for the left and $r = -0.341$, $p = 0.007$). There was no significant relationship of other clinical characteristics with sALFF, or dALFF (see **Table 2**).

DISCUSSION

In the present study, we aimed to reveal brain functional alterations in COPD patients and their relationships to cognitive dysfunction. We found that COPD patients exhibited decreased local spontaneous activity in the left basal ganglia. We also observed a novel temporal dynamic alteration in the local spontaneous activity in the bilateral parahippocampal/hippocampal gyrus. Importantly, there were significant relationships between static and dynamic local spontaneous activities and clinical characteristics (both pulmonary function and semantic-memory performance).

Increasing evidence has suggested that patients with COPD display abnormal local spontaneous neuronal activity. Lu et al. have demonstrated lower local spontaneous activity in the bilateral basal ganglia among COPD patients indexed with static ALFF (sALFF), which is consistent with our results (Lu et al., 2019). Lower sALFF in the basal ganglia was associated with poor pulmonary function. Their deep location in the brain may contribute to the susceptibility of basal ganglia to persistent hypoxia (Schindler et al., 2016), due to neurovascular-coupling

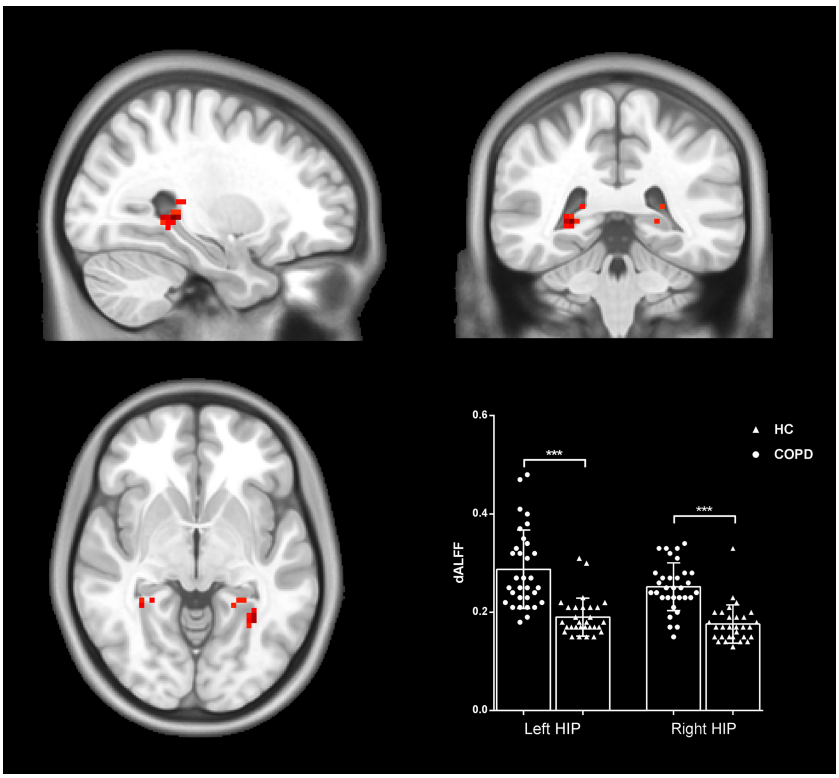

FIGURE 2 | Group differences in dALFF. Patients with COPD showed increased dALFF in the bilateral hippocampal/parahippocampal cortex. Statistical maps were corrected via the Gaussian Random Field (GRF) method at a threshold of voxel $P < 0.001$, cluster $P < 0.05$ (with 9.5*10.2*8.7 mm^3 as estimate smoothness kernel). Scatter plots present sALFF of each participant in the two groups. ***$p < 0.001$.

TABLE 2 | Correlations between clinical characteristics and brain function.

	PH	PaO_2	$PaCO_2$	FEV_1	FVC	FEV_1/FVC	CVFT	sALFF in Put	dALFF in LHIP	dALFF in RHIP
PH	-	0.107	**−0.514****	**0.362***	0.196	**0.441***	0.141	0.214	−0.014	−0.156
PaO_2	-	-	−0.192	0.193	0.130	0.080	0.195	**0.562****	0.089	0.219
$PaCO_2$	-	-	-	**−0.403***	−0.234	**−0.437***	−0.157	−0.082	−0.148	0.216
FEV_1	-	-	-	-	**0.914*****	**0.478****	0.314	−0.080	−0.202	−0.300
FVC	-	-	-	-	-	0.140	0.265	−0.185	−0.231	**−0.357***
FEV_1/FVC	-	-	-	-	-	-	0.299	0.073	−0.146	−0.029
CVFT	-	-	-	-	-	-	-	0.030	**−0.579*****	−0.121
sALFF in BG	-	-	-	-	-	-	-	-	**−0.360****	**−0.341****
dALFF in LHIP	-	-	-	-	-	-	-	-	-	0.348
dALFF in RHIP	-	-	-	-	-	-	-	-	-	-

*$p < 0.05$; **$p < 0.01$; ***$p < 0.001$.

alterations. Basal ganglia are a group of subcortical nuclei that provide functions in the motor and multiple cognitive domains, including executive functions (Monchi et al., 2006). The reduced local activity has been linked with executive dysfunction in COPD patients and other neuropsychiatric disorders (Maciel et al., 2016; Lu et al., 2019). Notably, basal ganglia is also involved in semantic processing (Viñas-Guasch and Wu, 2017). Studies involving lesion imaging have suggested that lesions in the basal ganglia may impair verbal-fluency performance (Chouiter et al., 2016). Considering the fact that the verbal fluency test reflects both executive and semantic processing, we speculate that the lower local spontaneous activity in the basal ganglia may be related to executive dysfunction and semantic impairments.

Besides the basal ganglia, the hippocampal cortex is another brain structure that is sensitive to hypoxia (Dunn et al., 1999). This phenomenon may be attributed to the relative lack of capillary anastomoses between intrahippocampal vessels (Perosa et al., 2020). In line with this concept, our results revealed

abnormal local activity in the hippocampal/parahippocampal cortex and the significant relationship between local activity and poor pulmonary function. The hippocampal/parahippocampal cortex is critical for episodic memory (Düzel et al., 2001) and consolidation of long-term memory (Frey and Frey, 2008) and contributes to many other cognitive domains, such as semantic memory (Sheldon and Moscovitch, 2012). Hippocampal dysfunction has been linked to semantic-memory impairments (Bai et al., 2019). Consistent with this, the present study has found an association between hippocampal activity and CVFT performance, which most likely relies on the medial temporal cortex, which mediates the storage and retrieval of semantic knowledge (Henry and Crawford, 2004).

Notably, this work took an innovative approach that investigated the temporal variability of local brain activity in COPD. Mounting studies suggest that brain dynamics reflect the functional capacity of the neural system (Kucyi et al., 2016) and more readily predict cognitive and affective conditions (Wang et al., 2019; Cui et al., 2020). Using a novel dALFF method, we revealed the abnormal enhanced dynamics of hippocampal local activity, which imply abnormal stability in the hippocampal local activity. Intriguingly, there were negatively significant relationships between sALFF in basal ganglia and dALFF in bilateral hippocampal/parahippocampal cortex. Physiological meanings of these relationships are still unclear. We speculate that the alteration of sALFF and dALFF may play an intermediary role between anoxia and memory impairments.

There are several limitations inherent in the present study. First, the sample size was too small, which may have led to sampling bias. Further studies with larger sample sizes are needed to replicate our results. Second, the data on arterial blood gas analysis and pulmonary function were lacking for healthy controls, although all healthy controls were screened rigorously by a physician to exclude possible hypoxemia and poor pulmonary function. Third, patients in the present study were not drug-free, and thus we cannot eliminate the confounding effects of drugs on our findings.

CONCLUSION

These limitations notwithstanding, our results indicate that semantic-memory impairments in COPD patients are linked with abnormal static and dynamic local-neural activity in the basal ganglia and parahippocampal/hippocampal cortex, which may be modulated by poor pulmonary function.

DATA AVAILABILITY STATEMENT

The raw data supporting the conclusions of this article will be made available by the authors, without undue reservation.

ETHICS STATEMENT

The studies involving human participants were reviewed and approved by the Hefei Second People's Hospital Ethics Committee. The patients/participants provided their written informed consent to participate in this study.

AUTHOR CONTRIBUTIONS

ZL, QC, YW, and XF designed the study. YJ, PH, and LZ acquired behavior and imaging data. TB and KW help for analyzing the clinical and imaging data. ZL, QC, and XF wrote this article, which all authors have reviewed. All authors contributed to the article and approved the submitted version.

FUNDING

This work was supported by the National Key R&D Program of China (No. 2018YFC1314200), National Natural Science Foundation of China (No. U1803126), and Guanghua Program [No. (2018) 125-16] and Second People's Hospital of Hefei Foundation (2020qnjj12).

ACKNOWLEDGMENTS

We would like to thank operators of the Center for Biomedical Engineering, University of Science and Technology of China, for MRI data scanning. We also acknowledge all participants who volunteered to participate in the present study.

SUPPLEMENTARY MATERIAL

The Supplementary Material for this article can be found online at: https://www.frontiersin.org/articles/10.3389/fnhum.2020.580238/full#supplementary-material

REFERENCES

Allen, E. A., Damaraju, E., Plis, S. M., Erhardt, E. B., Eichele, T., and Calhoun, V. D. (2014). Tracking whole-brain connectivity dynamics in the resting state. *Cereb. Cortex* 24, 663–676. doi: 10.1093/cercor/bhs352

Bai, T., Wei, Q., Xie, W., Wang, A., Wang, J., Ji, G. J., et al. (2019). Hippocampal-subregion functional alterations associated with antidepressant effects and cognitive impairments of electroconvulsive therapy. *Psychol. Med.* 49, 1357–1364. doi: 10.1017/S0033291718002684

Chao-Gan, Y., and Yu-Feng, Z. (2010). DPARSF: a MATLAB toolbox for "Pipeline" data analysis of resting-state fMRI. *Front. Syst. Neurosci*. 4:13. doi: 10.3389/fnsys.2010.00013

Chouiter, L., Holmberg, J., Manuel, A. L., Colombo, F., Clarke, S., Annoni, J. M., et al. (2016). Partly segregated cortico-subcortical pathways support phonologic and semantic verbal fluency: a lesion study. *Neuroscience* 329, 275–283. doi: 10.1016/j.neuroscience.2016.05.029

Cleutjens, F. A. H. M., Spruit, M. A., Ponds, R. W. H. M., Dijkstra, J. B., Franssen, F. M. E., Wouters, E. F. M., et al. (2014). Cognitive functioning in obstructive lung disease: results from the United Kingdom biobank. *J. Am. Med. Dir. Assoc.* 15, 214–219. doi: 10.1016/j.jamda.2013.12.007

Cui, Q., Sheng, W., Chen, Y., Pang, Y., Lu, F., Tang, Q., et al. (2020). Dynamic changes of amplitude of low-frequency fluctuations in patients with generalized anxiety disorder. *Human Brain Mapp.* 41, 1667–1676. doi: 10.1002/hbm.24902

Deng, Z., Chandrasekaran, B., Wang, S., and Wong, P. C. M. (2016). Resting-state low-frequency fluctuations reflect individual differences in spoken language learning. *Cortex* 76, 63–78. doi: 10.1016/j.cortex.2015.11.020

Dodd, J. W., Getov, S. V., and Jones, P. W. (2010). Cognitive function in COPD. *Eur. Respir. J.* 35, 913–922. doi: 10.1183/09031936.00125109

Dunn, J. F., Wadghiri, Y. Z., and Meyerand, M. E. (1999). Regional heterogeneity in the brain's response to hypoxia measured using BOLD MR imaging. *Magn. Reson. Med.* 41, 850–854. doi: 10.1002/(SICI)1522-2594(199904)41:4andlt;850::AID-MRM27andgt;3.0.CO;2-L

Düzel, E., Vargha-Khadem, F., Heinze, H. J., and Mishkin, M. (2001). Brain activity evidence for recognition without recollection after early hippocampal damage. *Proc. Natl. Acad. Sci. U.S.A.* 98, 8101–8106. doi: 10.1073/pnas.131205798

Fiorenzato, E., Strafella, A. P., Kim, J., Schifano, R., Weis, L., Antonini, A., et al. (2019). Dynamic functional connectivity changes associated with dementia in Parkinson's disease. *Brain* 142, 2860–2872. doi: 10.1093/brain/awz192

Fornito, A., Harrison, B. J., Zalesky, A., and Simons, J. S. (2012). Competitive and cooperative dynamics of large-scale brain functional networks supporting recollection. *Proc. Natl. Acad. Sci. U.S.A.* 109, 12788–12793. doi: 10.1073/pnas.1204185109

Fox, M. D., and Raichle, M. E. (2007). Spontaneous fluctuations in brain activity observed with functional magnetic resonance imaging. *Nat. Rev. Neurosci.* 8, 700–711. doi: 10.1038/nrn2201

Frey, S., and Frey, J. U. (2008). "Synaptic tagging" and "cross-tagging" and related associative reinforcement processes of functional plasticity as the cellular basis for memory formation. *Prog. Brain Res.* 169, 117–143. doi: 10.1016/S0079-6123(07)00007-6

Friston, K. (2002). Beyond phrenology: what can neuroimaging tell us about distributed circuitry? *Ann. Rev. Neurosci.* 25, 221–250. doi: 10.1146/annurev.neuro.25.112701.142846

Greicius, M. D., Krasnow, B., Reiss, A. L., and Menon, V. (2003). Functional connectivity in the resting brain: a network analysis of the default mode hypothesis. *Proc. Natl. Acad. Sci. U.S.A.* 100, 253–258. doi: 10.1073/pnas.0135058100

Henry, J. D., and Crawford, J. R. (2004). A meta-analytic review of verbal fluency performance following focal cortical lesions. *Neuropsychology* 18, 284–295. doi: 10.1037/0894-4105.18.2.284

Hutchison, R. M., Womelsdorf, T., Allen, E. A., Bandettini, P. A., Calhoun, V. D., Corbetta, M., et al. (2013). Dynamic functional connectivity: promise, issues, and interpretations. *Neuroimage* 80, 360–378. doi: 10.1016/j.neuroimage.2013.05.079

Hynninen, K. M., Breitve, M. H., Wiborg, A. B., Pallesen, S., and Nordhus, I. H. (2005). Psychological characteristics of patients with chronic obstructive pulmonary disease: a review. *J. Psychosom. Res.* 59, 429–443. doi: 10.1016/j.jpsychores.2005.04.007

Kucyi, A., Hove, M. J., Esterman, M., Hutchison, R. M., and Valera, E. M. (2016). Dynamic brain network correlates of spontaneous fluctuations in attention. *Cereb Cortex* 27, 1831–1840. doi: 10.1093/cercor/bhw029

Leonardi, N., and Van De Ville, D. (2015). On spurious and real fluctuations of dynamic functional connectivity during rest. *Neuroimage* 104, 430–436. doi: 10.1016/j.neuroimage.2014.09.007

Li, J., Duan, X., Cui, Q., Chen, H., and Liao, W. (2018). More than just statics: temporal dynamics of intrinsic brain activity predicts the suicidal ideation in depressed patients. *Psychol. Med.* 49, 852–860. doi: 10.1017/S0033291718001502

Liao, D., Higgins, M., Bryan, N. R., Eigenbrodt, M. L., Chambless, L. E., Lamar, V., et al. (1999). Lower pulmonary function and cerebral subclinical abnormalities detected by MRI: the atherosclerosis risk in communities study. *Chest* 116, 150–156. doi: 10.1378/chest.116.1.150

Liao, W., Wu, G. R., Xu, Q., Ji, G. J., Zhang, Z., Zang, Y. F., et al. (2014). DynamicBC: a MATLAB toolbox for dynamic brain connectome analysis. *Brain Connectivity* 4, 780–790. doi: 10.1089/brain.2014.0253

Liu, F., Wang, Y., Li, M., Wang, W., Li, R., Zhang, Z., et al. (2017). Dynamic functional network connectivity in idiopathic generalized epilepsy with generalized tonic-clonic seizure. *Human Brain Mapp.* 38, 957–973. doi: 10.1002/hbm.23430

Lu, C. Q., Xu, W., Zeng, C. H., Ge, L. Y., Wang, Y. C., Meng, X. P., et al. (2019). Altered amplitude of low-frequency fluctuation in basal ganglia correlates to pulmonary ventilation function in COPD patients: a resting-state fMRI study. *Brain Behav.* 9:e01336. doi: 10.1002/brb3.1336

Maciel, R. O., Ferreira, G. A., Akemy, B., and Cardoso, F. (2016). Executive dysfunction, obsessive-compulsive symptoms, and attention deficit and hyperactivity disorder in systemic lupus erythematosus: evidence for basal ganglia dysfunction? *J. Neurol. Sci.* 360, 94–e01397. doi: 10.1016/j.jns.2015.11.052

Monchi, O., Petrides, M., Strafella, A. P., Worsley, K. J., and Doyon, J. (2006). Functional role of the basal ganglia in the planning and execution of actions. *Ann. Neurol.* 59, 257–264. doi: 10.1002/ana.20742

Perosa, V., Priester, A., Ziegler, G., Cardenas-Blanco, A., Dobisch, L., Spallazzi, M., et al. (2020). Hippocampal vascular reserve associated with cognitive performance and hippocampal volume. *Brain* 143, 622–634. doi: 10.1093/brain/awz383

Raichle, M. E., and Mintun, M. A. (2006). Brain work and brain imaging. *Ann. Rev. Neurosci.* 29, 449–476. doi: 10.1146/annurev.neuro.29.051605.112819

Sachdev, P. S., Anstey, K. J., Parslow, R. A., Wen, W., Maller, J., Kumar, R., et al. (2006). Pulmonary function, cognitive impairment and brain atrophy in a middle-aged community sample. *Dement. Geriatr. Cogn. Disord.* 21, 300–308. doi: 10.1159/000091438

Schindler, T., Stevenson, G., Jayatilake, S., Gilbert, Y., Oei, J. L., and Welsh, A. (2016). Reference ranges for neonatal basal ganglia perfusion as measured by fractional moving blood volume. *Neonatology* 109, 91–96. doi: 10.1159/000441466

Sheldon, S., and Moscovitch, M. (2012). The nature and time-course of medial temporal lobe contributions to semantic retrieval: an fMRI study on verbal fluency. *Hippocampus* 22, 1451–1466. doi: 10.1002/hipo.20985

Tomasi, D., Wang, G. J., and Volkow, N. D. (2013). Energetic cost of brain functional connectivity. *Proc. Natl. Acad. Sci. U.S.A.* 110, 13642–13647. doi: 10.1073/pnas.1303346110

Viñas-Guasch, N., and Wu, Y. J. (2017). The role of the putamen in language: a meta-analytic connectivity modeling study. *Brain Struct. Funct.* 222, 3991–4004. doi: 10.1007/s00429-017-1450-y

Wang, P., Li, R., Liu, B., Wang, C., Huang, Z., Dai, R., et al. (2019). Altered static and temporal dynamic amplitude of low-frequency fluctuations in the background network during working memory states in mild cognitive impairment. *Front. Aging Neurosci.* 11:152. doi: 10.3389/fnagi.2019.00152

Wang, Z., Yan, C., Zhao, C., Qi, Z., Zhou, W., Lu, J., et al. (2011). Spatial patterns of intrinsic brain activity in mild cognitive impairment and Alzheimer's disease: a resting-state functional MRI study. *Human Brain Mapp.* 32, 1720–1740. doi: 10.1002/hbm.21140

Watz, H., Waschki, B., Boehme, C., Claussen, M., Meyer, T., and Magnussen, H. (2008). Extrapulmonary effects of chronic obstructive pulmonary disease on physical activity. *Am. J. Respir. Crit. Care Med.* 177, 743–751. doi: 10.1164/rccm.200707-1011OC

Wenjing, W., Haijun, L., Dechang, P., Juan, L., Huizhen, X., Honghui, Y., et al. (2018). Abnormal intrinsic brain activities in stable patients with COPD: a resting-state functional MRI study. *Neuropsychiatr. Dis. Treat. Vol.* 14, 2763–2772. doi: 10.2147/NDT.S180325

Zang, Y., Jiang, T., Lu, Y., He, Y., and Tian, L. (2004). Regional homogeneity approach to fMRI data analysis. *NeuroImage* 22, 394–400. doi: 10.1016/j.neuroimage.2003.12.030

Zang, Y. F., He, Y., Zhu, C. Z., Cao, Q. J., Sui, M. Q., Liang, M., et al. (2007). Altered baseline brain activity in children with ADHD revealed by resting-state functional MRI. *Brain Dev.* 29, 83–91. doi: 10.1016/j.braindev.2006.07.002

Zou, Q., Ross, T. J., Gu, H., Geng, X., Zuo, X. N., Hong, L. E., et al. (2013). Intrinsic resting-state activity predicts working memory brain activation and behavioral performance. *Human Brain Mapp.* 34, 3204–3215. doi: 10.1002/hbm.22136

Conflict of Interest: The authors declare that the research was conducted in the absence of any commercial or financial relationships that could be construed as a potential conflict of interest.

frontiers in Human Neuroscience

ORIGINAL RESEARCH
published: 18 January 2021
doi: 10.3389/fnhum.2020.606238

A Look Into the Power of fNIRS Signals by Using the Welch Power Spectral Estimate for Deception Detection

Jiang Zhang[1], Jingyue Zhang[1], Houhua Ren[2], Qihong Liu[3], Zhengcong Du[4], Lan Wu[5], Liyang Sai[6,7], Zhen Yuan[8], Site Mo[1] and Xiaohong Lin[6]**

[1] College of Electrical Engineering, Sichuan University, Chengdu, China, [2] China Mobile (Chengdu) Industrial Research Institute, Chengdu, China, [3] College of Biomedical Engineering, Sichuan University, Chengdu, China, [4] School of Information Science and Technology, Xichang University, Xichang, China, [5] Sichuan Cancer Hospital and Institute, Chengdu, China, [6] Institutes of Psychological Sciences, Hangzhou Normal University, Hangzhou, China, [7] Department of Psychology, Zhejiang Normal University, Jinhua, China, [8] Bioimaging Core, Faculty of Health Sciences, University of Macau, Taipa, China

OPEN ACCESS

Edited by:
Dajiang Zhu,
University of Texas at Arlington,
United States

Reviewed by:
Lei Xi,
Southern University of Science and Technology, China
Jiaying Xiao,
Central South University, China

***Correspondence:**
Site Mo
mosite@scu.edu.cn
Xiaohong Lin
zhulin24show@hotmail.com

Specialty section:
This article was submitted to Brain Imaging and Stimulation, a section of the journal Frontiers in Human Neuroscience

Received: 14 September 2020
Accepted: 30 November 2020
Published: 18 January 2021

Citation:
Zhang J, Zhang J, Ren H, Liu Q, Du Z, Wu L, Sai L, Yuan Z, Mo S and Lin X (2021) A Look Into the Power of fNIRS Signals by Using the Welch Power Spectral Estimate for Deception Detection. Front. Hum. Neurosci. 14:606238. doi: 10.3389/fnhum.2020.606238

Neuroimaging technologies have improved our understanding of deception and also exhibit their potential in revealing the origins of its neural mechanism. In this study, a quantitative power analysis method that uses the Welch power spectrum estimation of functional near-infrared spectroscopy (fNIRS) signals was proposed to examine the brain activation difference between the spontaneous deceptive behavior and controlled behavior. The power value produced by the model was applied to quantify the activity energy of brain regions, which can serve as a neuromarker for deception detection. Interestingly, the power analysis results generated from the Welch spectrum estimation method demonstrated that the spontaneous deceptive behavior elicited significantly higher power than that from the controlled behavior in the prefrontal cortex. Meanwhile, the power findings also showed significant difference between the spontaneous deceptive behavior and controlled behavior, indicating that the reward system was only involved in the deception. The proposed power analysis method for processing fNIRS data provides us an additional insight to understand the cognitive mechanism of deception.

Keywords: functional near-infrared spectroscopy, power, Welch power spectrum estimation, deception, quantitative analysis

INTRODUCTION

Deception is a universally existing sociopsychological phenomenon, involving such psychological activities as perception, memory, thinking, and imagination (Depaulo et al., 2003; Crossman and Lewis, 2006; Talwar and Kang, 2008; Kang, 2013). To date, great efforts have been made to reveal the neurobiological basis of deception. For example, electroencephalography (EEG)/event-related potential (ERP) (Fukuda, 2001; Carrión et al., 2010), functional magnetic resonance imaging (fMRI) (Harada et al., 2009; Abe, 2011; Gamer et al., 2012), functional near-infrared spectroscopy (fNIRS) (Bhutta et al., 2015; Zhang et al., 2016), and various data analysis methods (Christ et al., 2009; Zhang et al., 2016) were used to elicit the neural mechanisms underlying deception. Nevertheless,

the neural mechanisms for deception still remains unclear, and the related data analysis methods need to be developed.

Because of poor EEG/ERP inherent spatial resolution, researchers are not better enabled to know about the brain regions involved in deception until the advent of fMRI (Fukuda, 2001; Harada et al., 2009; Carrión et al., 2010; Abe, 2011). Compared to fMRI, fNIRS can be operated in a portable, comfortable, and quiet way with fewer body constraints (Beurskens et al., 2014). fNIRS that relies on the hemodynamic responses to infer brain activation has also been extensively utilized to inspect the cognition and brain disorders (Hoshi, 2009; Izzetoglu et al., 2007; Caliandro et al., 2013; Yuan, 2013; Ding et al., 2014; Ren et al., 2019). In particular, fNIRS as an optical neuroimaging tool can provide the quantitative hemodynamic information including oxyhemoglobin (HbO) and deoxyhemoglobin concentration changes, which plays an important role in the study of cognitive processing in the frontal/prefrontal cortex (PFC) (Izzetoglu et al., 2007; Hoshi, 2009; Caliandro et al., 2013; Yuan, 2013; Ding et al., 2014; Ren et al., 2019). More importantly, fNIRS has exhibited its unbeatable advantages in deception detection that involves the inspection of executive functions in PFC including withholding the truth and response monitoring (Hoshi, 2003; Kovelman et al., 2008; Ayaz et al., 2012). Despite all these, deception still remains a profound paradigm for studying human behaviors, in view of the great complexity of deception in different environments and thus the limited understanding of neural mechanisms underlying various situations.

In view of the fact that the neural activities are accompanied by energy and power variation, the power changes of hemodynamic response, capable of reflecting brain activity intensity (Buxton et al., 2004; Zhang et al., 2010b), this study proposes a power analysis method based on the Welch power spectrum estimation of fNIRS signals including hemodynamic information, in a bid to quantify the brain hemodynamic responses associated with deception underlying various behavior states. The Welch power spectrum algorithm, as an effective spectral estimation method without seriously destroying the resolution, can significantly reduce the variance of spectral estimation by segmenting data through overlapping and adding windows in time domain (Welch, 1967; Proakis et al., 2003). We have made extensive efforts in acquiring data, documents, or information regarding the application of power analysis of fNIRS in exploring brain functional activity, which turns out to be a very rarely adopted practice, with little references available. But we do find the power measure produced by the power analysis model capable of quantifying the brain activity energy in different brain regions during a short-time period, and it has been applied in fMRI and EEG (Zhang et al., 2010a; Radulescu et al., 2012; Gonzalez et al., 2016). And this leads us to assume that the power of fNIRS may also be able to serve as a neuromarker to unveil the brain power difference between the spontaneous deceptive and controlled behavior. In short, the novel measure in fNIRS proposed in this study is rather reasonably expected to be a valuable new approach to better understanding the cognitive mechanism associated with deception.

MATERIALS AND METHODS

Participants

Twenty-five participants (14 females and 11 males; all aged 19–22 years) were recruited for the fNIRS experiments. All participants were right handed, who had no reported histories of brain diseases. Participants were instructed to sign informed consent documents prior to data acquisition. The protocol of this study was approved by the ethics committees of the Zhejiang Normal University, and the experimental tests were performed in accordance with the guidelines.

Tasks and Procedures

The paradigm adopted for the present study consisted of two blocks: one for spontaneous deceptive behavior and the other for controlled behavior. The spontaneous deceptive behavior block contained 40 event-related trials, whereas the controlled behavior block had 30 trials. The stimuli ended as soon as participants respond, and each trial included a 2 s prestimuli period, followed by an 11 s post-stimulus and recovery period with a white fixation cross displayed in the center of the monitor screen to make sure the hemodynamic response returned to the baseline (**Figure 1**).

During the stimuli period of each trial, participants were instructed to play a computer poker game with an opponent in a separated room. The winner was the poker game player who scored more points in each round (trial). For the spontaneous deceptive behavior stimuli, only the opponent picked up the first card of the poker game, and then only the participant who was able to see both his (her) and the opponent's cards needed sent the final results of the competition (answers) to the opponent by pressing a button. The winner (the participant or the opponent) should be rewarded some amount of money. Interestingly, if the participant won the game for each round, he (she) generally sent the correct answer (win–win) to the opponent, whereas when the participant lost the game, he (she) might send a false answer to the opponent (lose–win) to receive a reward by deception or send the correct answer to lose the game (lose–lose). Among the 40-trial spontaneous deceptive behavior stimuli, 10 were for the win case, 30 for the lose case. Participants did not need to lie in the win case, whereas participants could lie for more money in the lose case. Therefore, 30 trials were designed for lose case to maintain the trials for lie (lose–win) or truth telling (lose–lose) were enough (about 10) for calculation.

By contrast, for the controlled behavior stimuli, participants needed to follow instructions on the computer screen to tell the truth or lie. In addition, the winner was not awarded any money for the controlled behavior task. The controlled behavior task consisted of three conditions: participants won the poker game and then sent the right answer (win–win) to the computer, and participants lost the game and sent the false (lose–win) or the true answer (lose–lose) to the computer. Ten trial tests were respectively, performed for each of the three conditions (i.e., win–win, lose–win, and lose–lose). And the test cases of spontaneous and controlled behaviors were provided in **Table 1**. Participants received rewards after they finished the whole experiment.

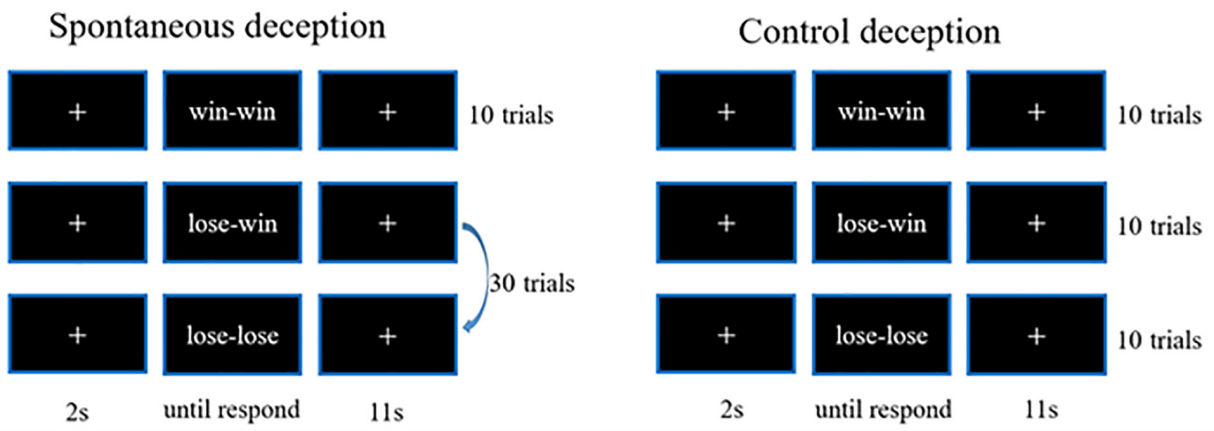

FIGURE 1 | The schematic of paradigm for deception tests.

TABLE 1 | Test cases of the spontaneous and controlled behaviors.

Categories	Spontaneous behavior (S)			Controlled behavior (C)		
Cases	a	b	c	a	b	c
Real answer	Win	Lose	Lose	Win	Lose	Lose
Participant' answer	Win	Win	Lose	Win	Win	Lose
Results	Truth	Deception	Truth	Truth	Deception	Truth

Data Acquisition and Preprocessing

fNIRS recordings were performed with a CW fNIRS system (ETG-4000, Hitachi Medical Co., Japan; 24 channels with eight laser sources and eight optical detectors). The optodes were placed on a 9 × 9 cm patch that was able to cover the frontal lobe (**Figures 2A,B**). The distance between each source and each detector was 30 mm; the sampling rate of the ETG-4000 system was 10 Hz, and the wavelengths of laser sources used were 695 and 830 nm. A three-dimensional (3D) magnetic space digitizer (EZT-DM401, Hitachi Medical Corporation, Japan) was utilized to measure the 3D spatial location of each optode on each participant's scalp. And then the NIRS-SPM software (Ye et al., 2009) was used to access each channel's mean MNI standard coordinates (Singh et al., 2005), which are provided in **Table A1**.

The fNIRS data were first processed by using a 0.01 Hz temporal high-pass filter and subsequently 0.3 Hz low-pass filter to remove baseline drifts and pulsation due to the heartbeat (Ding et al., 2014; Sai et al., 2014). In this study, only HbO signals were processed for further power analysis because of its high signal-to-noise ratio (Homae et al., 2007; Lu et al., 2010; Ding et al., 2014). Two participants were excluded from further analysis because of the poor quality of their optical data (possibly due to poor contact between the optodes and the scalp). Next, the datasets were segmented in relation to different markers that included three types of triggers for the spontaneous behaviors and three

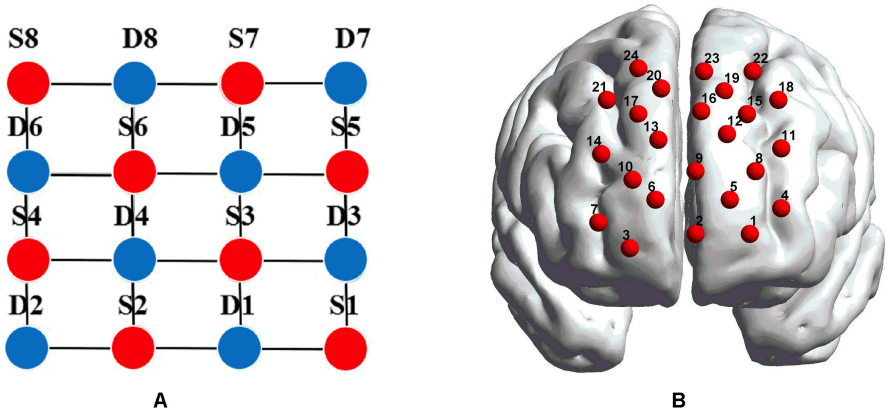

FIGURE 2 | (A) The distribution of laser sources and optical detector pair. The red dots represent the laser sources, whereas the light detectors are denoted by the blue dots, and the gray lines define the generated 24 channels. **(B)** The placements of the 24 channels in the dorsal bilateral frontal region. **(B)** was obtained by importing the 3D coordinates measured by a 3D digitizer into BrainNet Viewer to generate the configuration of 24 channels.

additional categories of triggers for the control behaviors (i.e., the win–win, lose–win, and lose–lose behaviors).

Data Analysis

For the trial-averaged HbO data from all channels, the PWELCH function in MATLAB is first used to calculate the Welch power spectral density (PSD) (Welch, 1967; Proakis et al., 2003) for each time series relevant to each channel and each participant. Interestingly, previous studies (Efron and Tibshirani, 1993) showed that the Welch algorithm can break down the original signal into L overlapped segments. Consequently, the Welch power spectrum estimation algorithm of HbO signal $x(n)$ is defined as follows:

1) The signal $x(n)$ with length N is divided into L data segments with length M, and the data segment is allowed to overlap, and N is the number of data points for each trial. The Welch power spectrum of $x_i(n)$, data segment i, is denoted as $P_i(w)$ (Proakis et al., 2003),

$$P_i\ (w) = \frac{1}{MU}\left|\sum_{n=0}^{M-1} x_i(n)d_2(n)e^{-jwn}\right|^2 \quad (1)$$

in which $U = \frac{1}{M}\sum_{n=0}^{M-1} d_2^2(n)$ is the normalized factor that ensures that the obtained power spectrum is asymptotically unbiased estimation; $d_2(n)$ is the window function, and w is the angular frequency.

2) After calculating the Welch power spectrum of each data segment, we then generate the mean power spectrum of all L segments and obtain the Welch power spectrum estimation of the whole HbO signal $x(n)$ (Proakis et al., 2003),

$$p\ (w) = \frac{1}{L}\sum_{i=1}^{L} P_i(w) = \frac{1}{MUL}\sum_{i=1}^{L}\left|\sum_{n=0}^{M-1} x_i(n)d_2(n)e^{-jwn}\right|^2 \quad (2)$$

3) Once the Welch power spectrum estimation of the mth channel for kth participant $p_{m,k}(w)$ is determined, the power is generated, which is the sum of PSD from all angular frequencies,

$$P_{m,k} = \sum_{w} p_{m,k}\ (w) \quad (3)$$

in which $P_{m,k}$ is the power of the mth channel from the kth participant.

In addition, the standardized indicators for power are used to eliminate the effects of individual differences, in which $P_{m,k}$ is standardized,

$$\text{Standard}.P_{m,k} = P_{m,k}/\text{mean}(P_k) \quad (4)$$

where Standard.$P_{m,k}$ is the standardized form of $P_{m,k}$, P_k denotes the data vector with the total power from 24 channels for the kth subject, and mean(P_k) is the mean value of the data vector P_k .

As a result, a single power was produced for each channel from each participant based on Eqs 1–3, and then the power was standardized with Eq. 4. Further statistical analysis was performed by using the standardized indicator measures to identify the channels that exhibited significant difference between various conditions (Efron and Tibshirani, 1993; Nichols and Holmes, 2001; Manly, 2006; Zhang et al., 2010a, 2011).

RESULTS AND DISCUSSION

The Welch power spectrum estimation of HbO signals was first generated for each channel from each subject. Although the power spectrum at characteristic points may be specified as the index of brain functional activation, brain activity may affect the power of signals at multiple frequencies. So we calculated the changes of average power for fNIRS signals in time domain. In order to obtain the average power in time domain by power spectrum, it is necessary to calculate the power of signals within all frequency bands. And the power as a novel neuromarker was produced for each channel from each subject, which was utilized as a quantitative measure for the following statistical analysis.

To inspect the neural correlates of deception, the paired t statistical test based on power measure was performed to examine the brain power differences between the spontaneous and controlled behaviors for the win–win, lose–win, and lose–lose cases. Interestingly, it was discovered from **Figure 3** that for the win–win case, the spontaneous behavior exhibited significantly larger power than that from the controlled behavior in the frontopolar area (BA10, channel 04, and channel 09) and dorsolateral PFC (DLPFC) (BA09, channel 17). Meanwhile, the results in **Figure 4** showed that for the lose–win case, the spontaneous deceptive behavior exhibited significantly higher power than the controlled behavior in the frontopolar area (BA10, channel 04), whereas the power for the controlled behavior was significantly enhanced as compared to that from the spontaneous behavior in the DLPFC (BA09, channel 12). In addition, we

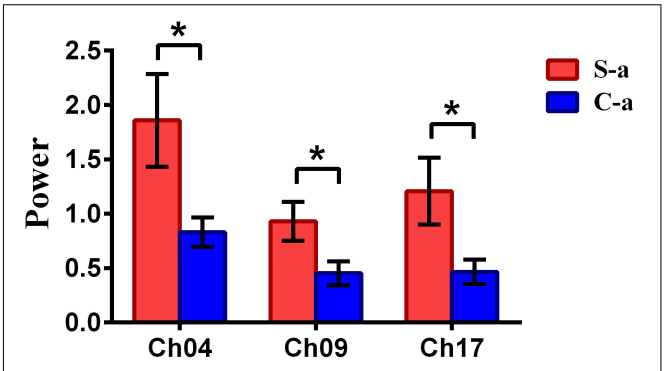

FIGURE 3 | The channels with statistically significant difference in the power (mean ± SE) between the spontaneous deceptive and controlled behavior for the win–win case. The red and blue colors denote the spontaneous deceptive and controlled behavior, respectively. The horizontal axes denote the channels with statistically significant differences, and the vertical axes denotes the power (mean ± SE) of the channels. *$p < 0.05$ (the p-values are from t-test to show the difference between the spontaneous deceptive and controlled behavior for the win–win condition.) Here S-a represents the win–win case under the conditions of spontaneous behavior (case of spontaneous behavior in **Table 1**). C-a represents the win–win case under the conditions of control behavior.

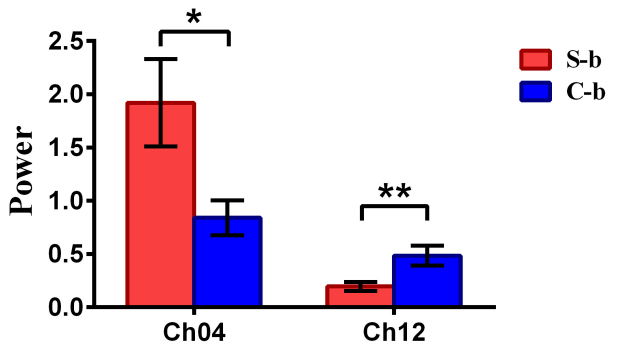

FIGURE 4 | The channels with statistically significant difference in the power (mean ± SE) between the spontaneous deceptive and controlled behavior for the lose–win case. The red and blue colors denote the spontaneous deceptive and controlled behavior, respectively. The horizontal axes denote the channels with statistically significant differences, and the vertical axes denote the power (mean ± SE) of the channels. *$p < 0.05$ and **$p < 0.01$. (The p-values are from t-test to show the difference between the spontaneous deceptive and controlled behavior for the lose–win condition.) Here S-b represents the lose–win case under the conditions of spontaneous behavior. C-b represents the lose–win case under the conditions of control behavior.

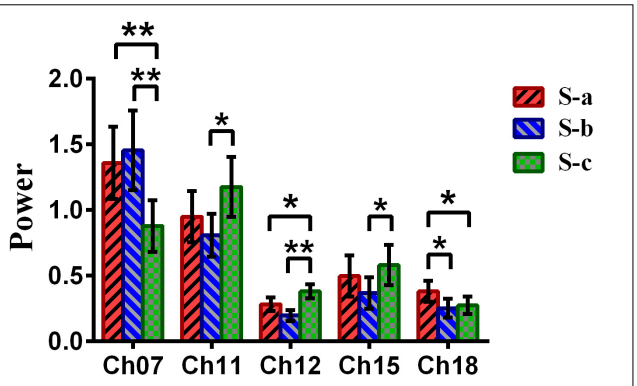

FIGURE 6 | The channels with statistically significant differences in the power (mean ± SE) between the win–win, lose–win, and lose–lose cases underlying spontaneous deceptive behavior. The red, blue, and green colors represent the win–win, lose–win, and lose–lose condition, respectively. The horizontal axes denote the channels with statistically significant differences, and the vertical axes denote the power (mean ± SE) of the channels. *$p < 0.05$ and **$p < 0.01$. (The p-values are from the repeated-measures analysis of variance measure for the win–win, lose–win, and lose–lose cases underlying the spontaneous deceptive behavior.)

discovered that for the lose–lose case, the brain power for the controlled behavior was significantly higher in the frontopolar area (BA10, channel 07) than that from the spontaneous behavior (**Figure 5**). However, this is not the case for the brain power in DLPFC (BA09, channel 17), in which the spontaneous behavior exhibited higher value as compared to the controlled behavior.

Repeated-measures analysis of variance (ANOVA) measure was performed to explore the difference between the win–win, lose–win, and lose–lose conditions for the spontaneous deceptive behavior. The results in **Figure 6** demonstrated that the power between the three cases exhibited significant difference in several brain regions, although this is not the case for the controlled behavior. For example, *post hoc* analysis for the spontaneous behavior showed that for the win–win case, the brain activation in DLPFC (BA09, channel 18) was significantly increased as compared to that from the lose–win case. In addition, compared with the lose–lose case, the lose–win case showed enhanced brain activation in the frontopolar area (BA10, channel 07). Meanwhile, the lose–lose case also exhibited significantly higher power than the lose–win case in the DLPFC (BA46, channel 11; BA09, channels 12 and 15). In particular, compared with the lose–lose case, the win–win case showed significantly higher brain power in the frontopolar area (BA10, channel 07) and DLPFC (BA09, channel 18). Further, the lose–lose case as well manifested significantly higher power than the win–win case in the DLPFC (BA09, channel 12).

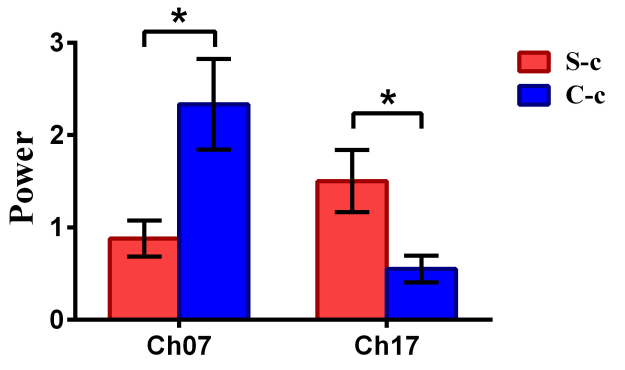

FIGURE 5 | The channels with statistically significant difference in the power (mean ± SE) between the spontaneous deceptive and controlled behavior for the lose–lose case. The red and blue colors denote the spontaneous deceptive and controlled behavior, respectively. The horizontal axes denote the channels with statistically significant differences, and the vertical axes denote the power (mean ± SE) of the channels. *$p < 0.05$. (The p-values are from t-test to show the difference between the spontaneous deceptive and controlled behavior for the lose–win condition.) Here S-c represents the lose–lose case under the conditions of spontaneous behavior. And C-c represents the lose–lose case under the conditions of control behavior.

In this study, fNIRS was used to inspect the neural mechanism of deception by using the measure of power, built on the basis of the Welch power spectrum estimation. The analysis of signals was not conducted directly based on the changes of signal amplitude at a certain instantaneous time point, but on quantitative comparison and analysis of the changes of power within all frequency bands between different cases. The analysis results of the power within all bands may not be consistent with the results of the amplitude variation of the fNIRS signal at a certain instantaneous time point, due to the fact that the amplitude at a single instantaneous time point is more susceptible to noise. Statistical analysis including the paired t test and the ANOVA measure was performed to examine the brain power difference between the spontaneous and controlled behaviors. The power spectrum approach has turned out to be able to detect neural activities for the whole brain using detection tools such as fMRI and EEG (Marchini and Ripley, 2000; Moritz et al., 2003; Duff et al., 2008; Gonzalez et al., 2016). But ours is the

first ever study, to the best of our knowledge, that combines the power analysis model and fNIRS data to quantitatively examine the brain functional activation with deception. We discovered that the spontaneous deceptive behaviors exhibited significantly higher power than the controlled behavior. The analysis results also demonstrated that the power can be an effective neuromarker to reveal the complex neural mechanism associated with deception. Interestingly, the identified brain regions such as the right DLPFC (BA09), the left DLPFC (BA46), and the frontopolar area (BA10) are involved in the planning of complex and coordinated movements (Baker et al., 1996; Hoshi and Tanji, 2000), which plays an essential role in higher-level cognitive processing, particularly the goal-processing operations (Fincham et al., 2002) and executing an action. In addition, previous reports also illustrated that the function of DLPFC including BA09 and BA46 is related to the executive function such as response control (Menon et al., 2001; Ridderinkhof et al., 2004). Importantly, during the stimuli period of spontaneous deceptive behavior, participants needed to make a decision on whether to tell truth or lie to the opponent, which might demand more cognitive efforts. By contrast, for the controlled behavior, participants were required to follow the instructions on the computer screen, which did not involve obvious cognitive efforts. Consequently, compared with that from the controlled behavior, enhanced brain power was discovered in the left frontopolar region and right DLPFC for the spontaneous behavior. Our results were also in line with previous findings that the functional brain networks of spontaneous deceptive behavior exhibited significant difference as compared to that from the controlled behavior (Zhang et al., 2016).

Meanwhile, the analysis results (**Figure 6**) of repeated-measures ANOVA are shown, which was performed to examine the brain power difference between the three conditions underlying the spontaneous deceptive behavior. Importantly, we discovered that there existed significant difference between the three cases during the performance of spontaneous behavior task. The brain regions that exhibited statistically significant power difference were the right frontopolar area (BA10) and the DLPFC (the left DLPFC, BA09, and BA46). Interestingly, previous fMRI studies also demonstrated that the PFC including the frontopolar area and DLPFC is the major cortical region within the "reward" neural network (Pochon et al., 2002; Haber and Knutson, 2010). Hence, the fMRI findings showed good agreement with our results regarding the activated brain regions. In addition, the results in **Figure 6** demonstrated that there were statistical differences in the frontopolar area and the DLPFC between the case of truth-telling and lying. In the truth-telling cases (win–win, lose–lose), the participants' answer were consistent with the real answer. However, for the lose–win case, participants needed to report the opposite of real answer to lie for receiving the reward. The frontopolar area and the DLPFC are parts of the anterior PFC and have been identified to play an important role in the processing of response control, which is discovered as the central of lying (Kozel et al., 2005; Priori et al., 2008; Mameli et al., 2010). It might be because of the differences that the participants choose to lie to get a reward or to present the fact as honest, which caused the significant differences in the frontopolar area and the DLPFC underlying the cases of using a truth-telling or a lying to deceive during the spontaneous behavior.

CONCLUSION

To the best of our knowledge, it was the first time that the power analysis model, which combined the neuroimaging tool fNIRS and the Welch power spectrum estimation method, was utilized for the quantitative analysis of brain power in deception with different behavior states. We discovered that the demanding executive tasks under the spontaneous behavior produced significantly higher power than those under the controlled behavior in the PFC including the left frontopolar area and the right DLPFC. These findings showed that the power analysis method can provide us supplementary reference information to explore the neural mechanism of deception.

DATA AVAILABILITY STATEMENT

The original contributions presented in the study are included in the article/supplementary material, further inquiries can be directed to the corresponding author/s.

ETHICS STATEMENT

The studies involving human participants were reviewed and approved by the Ethics Committees of the Zhejiang Normal University and the experimental tests were performed in accordance with the guidelines. The patients/participants provided their written informed consent to participate in this study.

AUTHOR CONTRIBUTIONS

JiaZ proposed the analysis method for processing fNIRS data. XL and LS designed the experiments. JiaZ and HR analyzed the data. XL prepared the **Figures 1**, **2B**. HR prepared the **Figures 3–6** and **Table 1**. XL and HR prepared the **Table A1** and **Figure 2A**. JiaZ, HR, ZY, JinZ, XL, SM, and ZD wrote the manuscript. The others provided supports to this study during the experiments. All authors contributed to the article and approved the submitted version.

FUNDING

This research was supported by the National Natural Science Foundation of China (Grant No. 61876114) and Sichuan Science and Technology Program (Grant No. 2018TJPT0008, Science and Technology Department of Sichuan Province, China). This work was also supported in part by Liangshan State Science and Technology Program (Grant No. 18YYJS0073).

REFERENCES

Abe, N. (2011). How the brain shapes deception: an integrated review of the literature. *Neuroscientist* 17, 560–574. doi: 10.1177/1073858410393359

Ayaz, H., Shewokis, P. A., Bunce, S., Izzetoglu, K., Willems, B., and Onaral, B. (2012). Optical brain monitoring for operator training and mental workload assessment. *Neuroimage* 59, 36–47. doi: 10.1016/j.neuroimage.2011.06.023

Baker, S. C., Rogers, R. D., Owen, A. M., Frith, C. D., Dolan, R. J., and Frackowiak, R. S. (1996). Neural systems engaged by planning: a pet study of the tower of london task. *Neuropsychologia* 34, 515–526. doi: 10.1016/0028-3932(95)00133-6

Beurskens, R., Helmich, I., Rein, R., and Bock, O. (2014). Age-related changes in prefrontal activity during walking in dual-task situations: a fNIRS study. *Int. J. Psychophysiol.* 92, 122–128. doi: 10.1016/j.ijpsycho.2014.03.005

Bhutta, M. R., Hong, M. J., Kim, Y. H., and Hong, K. S. (2015). Single-trial lie detection using a combined fNIRS-polygraph system. *Front. Psychol.* 6:709. doi: 10.3389/fpsyg.2015.00709

Buxton, R. B., Uludag, K., Dubowitz, D. J., and Liu, T. T. (2004). Modeling the hemodynamic response to brain activation. *Neuroimage* 23, S220–S233.

Caliandro, P., Silvestri, G., Padua, L., Bianchi, M. L., Simbolotti, C., Russo, G., et al. (2013). fNIRS evaluation during a phonemic verbal task reveals prefrontal Hypometabolism in patients affected by myotonic dystrophy type 1. *Clin. Neurophysiol.* 124, 2269–2276. doi: 10.1016/j.clinph.2013.05.010

Carrión, R. E., Keenan, J. P., and Sebanz, N. (2010). A truth that's told with bad intent: an ERP study of deception. *Cognition* 114, 105–110. doi: 10.1016/j.cognition.2009.05.014

Christ, S. E., Essen, D. C. V., Watson, J. M., Brubaker, L. E., and Mcdermott, K. B. (2009). The contributions of prefrontal cortex and executive control to deception: evidence from activation likelihood estimate meta-analyses. *Cereb. Cortex* 19, 1557–1566. doi: 10.1093/cercor/bhn189

Crossman, A. M., and Lewis, M. (2006). Adults' ability to detect children's lying. *Behav. Sci. Law* 24, 703–715. doi: 10.1002/bsl.731

Depaulo, B. M., Lindsay, J. J., Malone, B. E., Muhlenbruck, L., Charlton, K., and Cooper, H. (2003). Cues to deception. *Psychol. Bull.* 129, 74–118.

Ding, X. P., Sai, L., Fu, G., Liu, J., and Lee, K. (2014). Neural correlates of second-order verbal deception: a functional near-infrared spectroscopy (fNIRS) study. *Neuroimage* 87, 505–514. doi: 10.1016/j.neuroimage.2013.10.023

Duff, E. P., Johnston, L. A., Xiong, J., Fox, P. T., Mareels, I., and Egan, G. F. (2008). The power of spectral density analysis for mapping endogenous BOLD signal fluctuations. *Hum. Brain Mapp.* 29, 778–790. doi: 10.1002/hbm.20601

Efron, B., and Tibshirani, R. J. (1993). *An Introduction to the Bootstrap*. Boca Raton, FL: CRC Press.

Fincham, J. M., Carter, C. S., Van, V. V., Stenger, V. A., and Anderson, J. R. (2002). Neural mechanisms of planning: a computational analysis using event-related fMRI. *Proc. Natl. Acad. Sci. U.S.A.* 99:3346. doi: 10.1073/pnas.052703399

Fukuda, K. (2001). Eye blinks: new indices for the detection of deception. *Int. J. Psychophysiol.* 40, 239–245. doi: 10.1016/s0167-8760(00)00192-6

Gamer, M., Klimecki, O., Bauermann, T., Stoeter, P., and Vossel, G. (2012). fMRI-activation patterns in the detection of concealed information rely on memory-related effects. *Soc. Cogn. Affect. Neurosci.* 7, 506–515. doi: 10.1093/scan/nsp005

Gonzalez, S. L., Reeb-Sutherland, B. C., and Nelson, E. L. (2016). Quantifying motor experience in the infant brain: EEG power, coherence, and mu desynchronization. *Front. Psychol.* 7:216. doi: 10.3389/fpsyg.2016.00216

Haber, S. N., and Knutson, B. (2010). The reward circuit: linking primate anatomy and human imaging. *Neuropsychopharmacology* 35, 4–26. doi: 10.1038/npp.2009.129

Harada, T., Itakura, S., Xu, F., Lee, K., Nakashita, S., Saito, D. N., et al. (2009). Neural correlates of the judgment of lying: a functional magnetic resonance imaging study. *Neurosci. Res.* 63, 24–34. doi: 10.1016/j.neures.2008.09.010

Homae, F., Watanabe, H., Nakano, T., and Taga, G. (2007). Prosodic processing in the developing brain. *Neurosci. Res.* 59, 29–39. doi: 10.1016/j.neures.2007.05.005

Hoshi, E., and Tanji, J. (2000). Integration of target and body-part information in the premotor cortex when planning action. *Nature* 408, 466–470. doi: 10.1038/35044075

Hoshi, Y. (2003). Functional near-infrared optical imaging: utility and limitations in human brain mapping. *Psychophysiology* 40, 511–520. doi: 10.1111/1469-8986.00053

Hoshi, Y. (2009). "Near-infrared spectroscopy for studying higher cognition," in *Neural Correlates of Thinking. On Thinking*, Vol. 1, eds E. Kraft, B. Gulyás, and E. Pöppel (Berlin: Springer), 83–93. doi: 10.1007/978-3-540-68044-4_6

Izzetoglu, M., Bunce, S., Izzetoglu, K., Onaral, B., and Pourrezaei, K. (2007). Function brain imaging using near-infrared technology-assessing cognitive activity in real-life situations. *IEEE Eng. Med. Biol. Mag.* 26, 38–46.

Kang, L. (2013). Little liars: development of verbal deception in children. *Child Dev. Perspect.* 7, 91–96. doi: 10.1111/cdep.12023

Kovelman, I., Shalinsky, M. H., Berens, M. S., and Petitto, L. A. (2008). Shining new light on the brain's 'bilingual signature:' a functional near infrared spectroscopy investigation of semantic processing. *Neuroimage* 39, 1457–1471. doi: 10.1016/j.neuroimage.2007.10.017

Kozel, F. A., Johnson, K. A., Mu, Q., Grenesko, E. L., Laken, S. J., and George, M. S. (2005). Detecting deception using functional magnetic resonance imaging. *Biol. Psychiatry* 58, 605–613. doi: 10.1016/j.biopsych.2005.07.040

Lu, C. M., Zhang, Y. J., Biswal, B. B., Zang, Y. F., Peng, D. L., and Zhu, C. Z. (2010). Use of fNIRS to assess resting state functional connectivity. *J. Neurosci. Meth.* 186, 242–249. doi: 10.1016/j.jneumeth.2009.11.010

Mameli, F., Mrakic-Sposta, S., Vergari, M., Fumagalli, M., Macis, M., and Ferrucci, R. (2010). Dorsolateral prefrontal cortex specifically processes general - but not personal - knowledge deception: multiple brain networks for lying. *Behav. Brain Res.* 211, 164–168. doi: 10.1016/j.bbr.2010.03.024

Manly, B. F. J. (2006). *Randomization, Bootstrap and Monte Carlo Methods in Biology*. Boca Raton, FL: CRC Press.

Marchini, J. L., and Ripley, B. D. (2000). A new statistical approach to detecting significant activation in Functional MRI. *Neuroimage* 12, 366–380. doi: 10.1006/nimg.2000.0628

Menon, V., Adleman, N. E., White, C. D., Glover, G. H., and Reiss, A. L. (2001). Error-related brain activation during a go/nogo response inhibition task. *Hum. Brain Mapp.* 12, 131–143. doi: 10.1002/1097-0193(200103)12:3<131::aid-hbm1010>3.0.co;2-c

Moritz, C. H., Rogers, B. P., and Meyerand, M. E. (2003). Power spectrum ranked independent component analysis of a periodic fMRI complex motor paradigm. *Hum. Brain Mapp.* 18, 111–122. doi: 10.1002/hbm.10081

Nichols, T. E., and Holmes, A. P. (2001). Nonparametric permutation tests for functional neuroimaging: a primer with examples. *Hum. Brain Mapp.* 15, 1–25. doi: 10.1002/hbm.1058

Pochon, J. B., Levy, R., Fossati, P., Lehericy, S., Poline, J. B., and Pillon, B. (2002). The neural system that bridges reward and cognition in humans: an fMRI study. *Proc. Natl. Acad. Sci. U.S.A.* 99, 5669–5674. doi: 10.1073/pnas.082111099

Priori, A., Mameli, F., Cogiamanian, F., Marceglia, S., Tiriticco, M., and Mrakic-Sposta, S. (2008). Lie-specific involvement of dorsolateral prefrontal cortex in deception. *Cereb. Cortex* 18, 451–455. doi: 10.1093/cercor/bhm088

Proakis, J. G., Nikias, C. L., Rader, C. M., Ling, F., Moonen, M., and Proudler, I. K. (2003). *Algorithms for Statistical Signal Processing*. Beijing: Tsinghua University Press.

Radulescu, A. R., Rubin, D., Strey, H. H., and Mujica-Parodi, L. R. (2012). Power spectrum scale invariance identifies prefrontal dysregulation in paranoid schizophrenia. *Hum. Brain Map.* 33, 1582–1593. doi: 10.1002/hbm.21309

Ren, H., Wang, M. Y., He, Y., Du, Z., Zhang, J., Zhang, J., et al. (2019). A novel phase analysis method for examining fNIRS neuroimaging data associated with Chinese/English sight translation. *Behav. Brain Res.* 361, 151–158. doi: 10.1016/j.bbr.2018.12.032

Ridderinkhof, K. R., Wildenberg, W. P. M. V. D., Segalowitz, S. J., and Carter, C. S. (2004). Neurocognitive mechanisms of cognitive control: the role of prefrontal cortex in action selection, response inhibition, performance monitoring, and reward-based learning. *Brain Cogn.* 56, 129–140. doi: 10.1016/j.bandc.2004.09.016

Sai, L., Zhou, X., Ding, X. P., Fu, G., and Sang, B. (2014). Detecting concealed information using functional near-infrared spectroscopy. *Brain Topogr.* 27, 652–662. doi: 10.1007/s10548-014-0352-z

Singh, A. K., Okamoto, M., Dan, H., Jurcak, V., and Dan, I. (2005). Spatial registration of multichannel multi-subject fNIRS data to MNI space without MRI. *Neuroimage* 27, 842–851. doi: 10.1016/j.neuroimage.2005.05.019

Talwar, V., and Kang, L. (2008). Social and cognitive correlates of children's lying behavior. *Child Dev.* 79, 866–881. doi: 10.1111/j.1467-8624.2008.01164.x

Welch, P. D. (1967). The use of fast Fourier transform for the estimation of power spectra: a method based on time averaging over short, modified periodogram. *IEEE Trans. Audio Electroacoust.* 15, 70–73. doi: 10.1109/tau.1967.1161901

Ye, J. C., Tak, S., Jang, K. E., Jung, J. W., and Jang, J. D. (2009). NIRS-SPM: statistical parametric mapping for near-infrared spectroscopy. *Neuroimage* 44, 428–447. doi: 10.1016/j.neuroimage.2008.08.036

Yuan, Z. (2013). Combining independent component analysis and Granger causality to investigate brain network dynamics with fNIRS measurements. *Biomed. Opt. Express* 4, 2629–2643. doi: 10.1364/boe.4.002629

Zhang, J., Chen, H., Fang, F., and Liao, W. (2010a). Convolution power spectrum analysis for fMRI data based on prior image signal. *IEEE Trans. Biomed. Engin.* 57, 343–352. doi: 10.1109/tbme.2009.2031098

Zhang, J., Chen, H., Fang, F., and Liao, W. (2010b). Quantitative analysis of asymmetrical cortical activity based on power spectrum changes. *Brain Topogr.* 23, 257–268. doi: 10.1007/s10548-010-0136-z

Zhang, J., Lin, X., Fu, G., Sai, L., Chen, H., and Yang, J. (2016). Mapping the small-world properties of brain networks in deception with functional near-infrared spectroscopy. *Sci. Rep.* 6:25297.

Zhang, J., Tuo, X. G., Yuan, Z., Liao, W., and Chen, H. F. (2011). Analysis of fMRI data using an integrated principal component analysis and supervised affinity propagation clustering approach. *IEEE Trans. Biomed. Eng.* 58, 3184–3196. doi: 10.1109/tbme.2011.2165542

Conflict of Interest: The authors declare that the research was conducted in the absence of any commercial or financial relationships that could be construed as a potential conflict of interest.

APPENDIX

TABLE A1 | The mean 3D MNI coordinates and associated brain regions for the 24 channels.

Channels	MNI coordinates (x, y, z)			Brodmann area	Probability of overlap
Ch01	−21	71	0	11—Orbitofrontal area	0.57
Ch02	−2	70	0	10—Frontopolar area	0.89
Ch03	21	72	−5	11—Orbitofrontal area	0.74
Ch04	−32	65	9	10—Frontopolar area	0.88
Ch05	−14	73	12	10—Frontopolar area	1
Ch06	12	73	12	10—Frontopolar area	1
Ch07	32	68	4	10—Frontopolar area	0.66
Ch08	−23	67	22	10—Frontopolar area	0.88
Ch09	−2	67	22	10—Frontopolar area	1
Ch10	20	70	19	10—Frontopolar area	1
Ch11	−32	55	30	46—Dorsolateral prefrontal cortex	0.97
Ch12	−13	62	35	9—Dorsolateral prefrontal cortex	0.50
Ch13	11	65	33	10—Frontopolar area	0.67
Ch14	31	58	28	46—Dorsolateral prefrontal cortex	0.77
Ch15	−20	52	42	9—Dorsolateral prefrontal cortex	0.93
Ch16	−4	56	43	9—Dorsolateral prefrontal cortex	0.95
Ch17	18	55	42	9—Dorsolateral prefrontal cortex	0.99
Ch18	−31	39	47	9—Dorsolateral prefrontal cortex	0.95
Ch19	−12	47	50	9—Dorsolateral prefrontal cortex	0.90
Ch20	10	49	51	9—Dorsolateral prefrontal cortex	0.84
Ch21	29	42	47	9—Dorsolateral prefrontal cortex	0.98
Ch22	−22	34	57	8—Includes Frontal eye fields	0.75
Ch23	−5	39	57	8—Includes Frontal eye fields	0.85
Ch24	18	37	58	8—Includes Frontal eye fields	0.76

frontiers in Human Neuroscience

ORIGINAL RESEARCH
published: 15 February 2021
doi: 10.3389/fnhum.2021.634113

Common and Specific Alterations of Amygdala Subregions in Major Depressive Disorder With and Without Anxiety: A Combined Structural and Resting-State Functional MRI Study

Yao Yao Li[1†], Xiao kang Ni[2†], Ya feng You[2†], Yan hua Qing[2], Pei rong Wang[3], Jia shu Yao[2], Ke ming Ren[2], Lei Zhang[2], Zhi wei Liu[4], Tie jun Song[4], Jinhui Wang[5], Yu-Feng Zang[6], Yue di Shen[7] and Wei Chen[2,8,9]**

[1] Department of Psychiatry, Hangzhou Seventh People's Hospital, Hangzhou, China, [2] Department of Psychiatry, Sir Run Run Shaw Hospital, Zhejiang University School of Medicine, Hangzhou, China, [3] Zhejiang Academy of Traditional Chinese Medicine, Hangzhou, China, [4] Clinical Laboratory, Sir Run Run Shaw Hospital, Zhejiang University School of Medicine, Hangzhou, China, [5] Guangdong Key Laboratory of Mental Health and Cognitive Science, Center for Studies of Psychological Application, Institute for Brain Research and Rehabilitation, South China Normal University, Guangzhou, China, [6] Zhejiang Key Laboratory for Research in Assessment of Cognitive Impairments, Hangzhou, China, [7] Department of Diagnostics, School of Medicine, Hangzhou Normal University, Hangzhou, China, [8] Department of Psychology and Behavioral Sciences, Zhejiang University, Hangzhou, China, [9] Key Laboratory of Medical Neurobiology of Zhejiang Province, Hangzhou, China

Anxious major depressive disorder is a common subtype of major depressive disorder; however, its unique neural mechanism is not well-understood currently. Using multimodal MRI data, this study examined common and specific alterations of amygdala subregions between patients with and without anxiety. No alterations were observed in the gray matter volume or intra-region functional integration in either patient group. Compared with the controls, both patient groups showed decreased functional connectivity between the left superficial amygdala and the left putamen, and between the right superficial amygdala and the bilateral anterior cingulate cortex and medial orbitofrontal cortex, while only patients with anxiety exhibited decreased activity in the bilateral laterobasal and superficial amygdala. Moreover, the decreased activity correlated negatively with the Hamilton depression scale scores in the patients with anxiety. These findings provided insights into the pathophysiologic processes of anxious major depressive disorder and may help to develop new and effective treatment programs.

Keywords: major depressive disorder, multimodal MRI, amygdala subregion, anxiety, functional connectivity

OPEN ACCESS

Edited by:
Wei Liao,
University of Electronic Science and Technology of China, China

Reviewed by:
Yifeng Wang,
Sichuan Normal University, China
Lixia Tian,
Beijing Jiaotong University, China

****Correspondence:***
Yue di Shen
shenyd5@126.com
Wei Chen
srrcw@zju.edu.cn

[†]These authors have contributed equally to this work

Specialty section:
This article was submitted to Brain Imaging and Stimulation, a section of the journal Frontiers in Human Neuroscience

Received: *27 November 2020*
Accepted: *22 January 2021*
Published: *15 February 2021*

Citation:
Li YY, Ni Xk, You Yf, Qing Yh, Wang Pr, Yao Js, Ren Km, Zhang L, Liu Zw, Song Tj, Wang J, Zang Y-F, Shen Yd and Chen W (2021) Common and Specific Alterations of Amygdala Subregions in Major Depressive Disorder With and Without Anxiety: A Combined Structural and Resting-State Functional MRI Study. Front. Hum. Neurosci. 15:634113. doi: 10.3389/fnhum.2021.634113

INTRODUCTION

Major depressive disorder (MDD) is a common mental disorder that affects more than 300 million people globally (Gaspersz et al., 2017a). MDD is becoming the leading cause of disability worldwide and contributes significantly to the global disease burden. MDD is a clinically heterogeneous disease with multiple subtypes, among which anxious MDD (AMDD) is one of the most common, with a prevalence of 40–60% (Gaspersz et al., 2017a). Compared with non-anxious MDD

(nAMDD), patients with AMDD often suffer from more severe depressive illness (Wiethoff et al., 2010; Goldberg et al., 2014), greater functional impairment (Rao and Zisook, 2009; Goldberg and Fawcett, 2012), reduced response to antidepressant treatment (Fava et al., 2008; Ionescu et al., 2014), and a higher risk of suicide (Seo et al., 2011; Gaspersz et al., 2017b). Thus, it is clinically significant to explore the unique neural mechanism underlying this specific MDD subtype, which could help to develop new and effective treatment programs for AMDD.

The amygdala, which is located in the medial part of the anterior temporal lobe, is one of the most important structures in the limbic system (Ongur and Price, 2000). It plays a vital role in emotion processing and regulation (Phillips and Swartz, 2014). Mounting evidence from multimodal MRI studies has indicated that the amygdala is widely implicated in the pathophysiology of depression, as characterized by structural and functional alterations in patients (Savitz and Drevets, 2009; Licznerski and Duman, 2013; Fonseka et al., 2018). With respect to AMDD, a previous study used diffusion and structural MRI and showed no significant differences in volume or white matter integrity of the amygdala between patients with AMDD and nAMDD (Delaparte et al., 2017). Analogously, analyses of functional MRI (fMRI) revealed that patients with AMDD and those with nAMDD exhibited common patterns of abnormal activation and connectivity of the amygdala compared with controls (Etkin and Schatzberg, 2011; van Tol et al., 2012). However, it is worth noting that all the above studies treated the amygdala as a unified structure. Recent evidence indicates anatomical and functional heterogeneity of the human amygdala, which can be divided into three major subdivisions: The laterobasal amygdala (LBA), the superficial amygdala (SFA), and the centromedial amygdala (CMA) (Amunts et al., 2005; Ball et al., 2007). These subregions exhibit different connectivity patterns in healthy individuals (Li et al., 2012) and show unique alterations in MDD (Wang et al., 2017) and anxiety disorder (Qin et al., 2014). However, whether and how the amygdala subregions are differentially involved in AMDD are largely unknown.

In the present study, we investigated common and specific structural and functional brain alterations of amygdala subregions between patients with AMDD and those with nAMDD by combining structural MRI and resting-state fMRI (R-fMRI). Specifically, for each subregion of the amygdala, we compared 26 patients with AMDD and 23 patients with nAMDD vs. 30 healthy controls (HCs) in terms of regional gray matter volume (GMV) using structural MRI, and amplitude of low frequency fluctuation (ALFF), cross-correlation coefficients of spontaneous low-frequency (COSLOF), and seed-based functional connectivity (sFC) using R-fMRI. We hypothesized that compared with the HCs, patients with AMDD and nAMDD had common and specific alterations in the amygdala that were dependent on the subregions.

MATERIALS AND METHODS

Participants

All patients included in this study were screened from an ongoing follow-up project that aims to explore the relationships between baseline brain architecture and clinical outcomes of patients with MDD after antidepressant treatment using multimodal MRI data. According to the aim of the current study, 49 patients with MDD (26 AMDD and 23 nAMDD) were selected. MDD was diagnosed according to the Diagnostic and Statistical Manual of Mental Disorders, 4th Edition, Text Revision (DSM-IV-TR) criteria, using the Structured Clinical Interview for DSM-V (SCID)-I. Exclusion criteria for MDD included (1) patients who could not undergo an MRI examination because of claustrophobia, metallic implants, or other contraindication for MRI; (2) patients with severe suicidal tendency; (3) pregnant or lactating women; (4) any severe physical diseases as assessed by personal history; (5) a history of organic brain disorders, neurological disorders, other psychiatric disorders, cardiovascular diseases, head trauma, or loss of consciousness; and (6) a history of substance abuse, including tobacco, alcohol, or other psychoactive substances. The patients were recruited from outpatients and inpatients of the Sir Run Run Shaw Hospital, School of Medicine, Zhejiang University, Hangzhou, China. All patients were free of psychotropic medications for at least 4 weeks before the MRI scan and had a Hamilton depression rating (HAMD) score $\geq$ 14. We chose a HAMD $\geq$ 14 instead of 18 as in our previous studies (Shen et al., 2015; Sheng et al., 2018) to maximize the sample size of the current study. Out of the 49 patients, 26 were categorized as having AMDD in terms a HAMD anxiety/somatization factor score $\geq$ 7 (Fava et al., 2008). In addition, a cohort of 30 HCs was enrolled using community recruitment via an advertisement. All HCs had no lifetime history of psychiatric or neurological illness and no lifetime history of substance abuse. All participants were right-handed Han Chinese individuals, aged 18–60 years old, and had a mood Disorder Questionnaire (MDQ) score $<$ 7. Demographic and clinical characteristics of all the participants are summarized in **Table 1**. This study was approved by the Ethics Committee of the Sir Run Run Shaw Hospital, School of Medicine, Zhejiang University, and the Affiliated Hospital of Hangzhou Normal University. All participants gave written informed consent.

MRI Data Acquisition

All MRI data were acquired on a 3.0 T MR scanner (GE Discovery MR750, GE Medical Systems, Milwaukee, WI, USA) equipped with an eight-channel head coil array in the Center for Cognition and Brain Disorders, Hangzhou Normal University, China. During the scan, all participants were instructed to lie quietly in the scanner with their eyes closed, to keep their head still, but awake, and to try not to think of anything systematically. High-resolution T1-weighted images were acquired with a three-dimensional spoiled gradient-recalled sequence with the following parameters: 176 axial slices; repetition time (TR) = 8.1 ms; echo time (TE) = 3.1 ms; ip angle (FA) = 8°; field of view (FOV) = 250 × 250 mm^2; matrix = 256 × 256; slice thickness = 1.0 mm; and no gap. The R-fMRI images were acquired axially using a single-shot, gradient-recalled echo planar imaging sequence parallel to the line of the anterior–posterior commissure: 37 slices; TR = 2,000 ms; TE = 30 ms; FA = 90°; FOV = 220 × 220 mm^2; matrix = 128 × 128; slice thickness

TABLE 1 | Demographics and clinical measures of all participants.

	HCs ($n = 30$)	AMDD ($n = 26$)	NAMDD ($n = 23$)	*P*-value
Age (years)	39.233 ± 12.484	41.308 ± 10.884	36 ± 10.135	0.264
Gender (M/F)	12/18	11/15	15/8	0.147
HAMD		22.808 ± 4.578	18.044 ± 2.931	<0.001
Anxiety/somatization factor scores		8.769 ± 1.704	5.348 ± 0.714	<0.001
Others		14.039 ± 3.893	12.696 ± 2.883	0.181
Duration of illness (years)		0.2 – 13	0.1 – 16	0.277
Age of onset (years)		37.654 ± 12.614	31.696 ± 9.665	0.073

HCs, healthy controls; AMDD, anxious major depressive disorder; NAMDD, non-anxious major depressive disorder; M, male; F, female; HAMD, Hamilton Rating Scale for Depression.

= 3.2 mm; and no gap. The scan lasted for 368 s in total and included 184 volumes for each participant.

Definition of Amygdala Subregions

The amygdala subregions were determined using stereotaxic, probabilistic maps of cytoarchitectonic boundaries (Amunts et al., 2005) and implemented in FSL's Juelich histological atlas (https://fsl.fmrib.ox.ac.uk/fsl/fslwiki/). All amygdala subregions were created in the standard Montreal Neurological Institute (MNI) space by selecting only voxels with a probability of at least 50% of belonging to each subdivision.

Structural MRI Data Analysis

Structural images were processed by using the cat toolbox (http://www.neuro.uni-jena.de/cat/) for the SPM12 (http://www.fil.ion.ucl.ac.uk/spm/software/spm12/). Briefly, individual structural images were first segmented into GM, white matter, and cerebrospinal fluid on the basis of an adaptive Maximum A Posterior technique. The resultant GM maps were then normalized to the MNI space by using a high-dimensional "DARTEL" approach and modulated to compensate for spatial normalization effects. Finally, for each amygdala subregion, the mean GMV was obtained for each participant by averaging the GMV values across the voxels within the subregion.

R-fMRI Data Analysis

All R-fMRI data preprocessing was implemented using GRETNA (Wang et al., 2015b) based on the SPM12 software (http://www.fil.ion.ucl.ac.uk/spm/software/spm12/). After discarding the first five volumes to allow for magnetic saturation, we conducted slice timing (Sinc interpolation), head motion correction (six-parameter rigid-body transformation), spatial normalization (via tissue segmentation of individual structural images using the unified segment) and resampling ($3 \times 3 \times 3$ mm^3), and smoothing (Gaussian kernel with a 6-mm full width at half maximum). No patients were excluded according to the head motion criteria of > 2.5 mm in displacement or > 2.5° in rotation in any direction (the maximum head motion was 2.275 mm in translation and 1.617° in rotation over all participants). To ensure functional specificity of the amygdala subregions, all regions of interest (ROIs) were masked out before spatial smoothing. The smoothed images subsequently underwent removal of linear trends and band-pass filtering (0.01–0.08 Hz). Finally, the white matter signals, cerebrospinal fluid signals, and 24-parameter head motion profiles (Friston et al., 1996) were regressed out from each voxel's time series. The white matter signals and cerebrospinal fluid signals were obtained by averaging signals in masks derived from the corresponding tissue probability maps in the SPM12 toolbox (thres = 0.8) (Wang et al., 2015a). The high threshold was chosen to ensure that the resultant mask was "entirely" from white matter or CSF. Notably, all the nuisance signals were also band-pass filtered (0.01–0.08 Hz) (Hallquist et al., 2013).

After preprocessing, three measures were used to comprehensively characterize the functional architecture of each amygdala subregions, including ALFF, COSLOF, and sFC. (1) ALFF. For each voxel within a given amygdala subregion, the time series was first converted to the frequency domain using a fast Fourier transformation. The square root of the power spectrum was then computed and summed across a predefined frequency interval (0.01–0.08 Hz). The ALFF for the given amygdala subregion was finally calculated as the mean summed square root across voxels within the subregion. ALFF measures the strength or intensity of low-frequency oscillations embedded in spontaneous neural activity (Zang et al., 2007). (2) COSLOF. For any pair of voxels within a given amygdala subregion, the Pearson correlation coefficient was first computed between their time series. This resulted in a correlation matrix with a dimensionality of $n \times n$ (n = the number of voxels in the given subregion). The COSLOF for the given amygdala subregion was then computed as the mean of all the elements in the upper triangular portion of the correlation matrix. COSLOF reflects the overall functional integration within a given region (Li et al., 2002). (3) sFC. For each voxel within a given amygdala subregion, the time series was first extracted and then correlated with the time series of each voxel over the entire brain. This resulted in six whole-brain FC maps for each participant. The functional connectivity maps further underwent a Fisher's r-to-z transformation to improve the normality. Notably, the sFC analysis was restricted in a gray matter mask that was obtained by thresholding the gray matter tissue probability map in the SPM12 toolbox (thres = 0.4). The relatively loose threshold was chosen to ensure sufficient search space for gray matter.

Statistical Analysis

For the demographic data, one-way analysis of variance (ANOVA) and chi-square tests were used to compare age

and gender data among the three groups, respectively. For the clinical data, two-sample *t*-tests were used to compare HAMD anxiety/somatization factor scores, HAMD without anxiety/somatization factor scores, age of onset, and duration of illness between the two patient groups. For multimodal MRI-based GMV, ALFF, and COSLOF of each amygdala subregion, one-way ANOVA was used to infer differences among the three groups, followed by a Bonferroni method to correct for multiple comparisons across subregions. For the whole-brain sFC maps, a voxel-wise F-test was performed to infer differences among the three groups. A cluster-level family-wise error rate procedure was used to determine significant clusters by combining a voxel-level $P < 0.001$ and an extend-level $P < 0.05$. *Post-hoc* pair-wise comparisons were further performed with two-sample *t*-tests when significant main effects were observed. For the sFC, the *post-hoc* comparisons were conducted on the intra-cluster mean FC strength. Finally, non-parametric Spearman correlations were used to test the relationships between multimodal MRI-based amygdala alterations and clinical variables (HAMD anxiety/somatization factor scores, HAMD without anxiety/somatization factor scores, duration of illness, and age of onset) in each patient group. Again, the Bonferroni method was used to correct for multiple comparisons.

RESULTS

Demographic and Clinical Characteristics

As shown in **Table 1**, there were no significant differences in age or gender among the three groups ($P > 0.05$). Both patient groups did not differ significantly in their HAMD without anxiety/somatization factor scores, age of onset, or duration of illness ($P > 0.05$). As expected, the HAMD scores were significantly higher in the AMDD group than the nAMDD group ($P < 0.001$) because of their higher anxiety/somatization factor scores ($P < 0.001$).

Structural GMV of Amygdala Subregions

No significant differences were observed in the GMV for any amygdala subregion among the three groups ($P > 0.05$, Bonferroni corrected).

Functional ALFF of Amygdala Subregions

Significant main effects ($P < 0.05$, Bonferroni corrected) were found for the ALFF of the bilateral LBA (left: $P = 0.002$; right: $P = 0.007$) and SFA (left: $P = 0.003$; right: $P = 0.002$), but not the bilateral CMA ($P > 0.05$), among the three groups (**Figure 1**). *Post-hoc* comparisons revealed a common pattern of HCs > nAMDD > AMDD that were shared by the four subregions, while only the differences between the patients with AMDD and HCs were significant ($P < 0.05$, Bonferroni corrected).

Functional COSLOF of Amygdala Subregions

No significant differences were observed in the COSLOF for any amygdala subregion among the three groups ($P > 0.05$, Bonferroni corrected).

Functional sFC of Amygdala Subregions

Significant main effects ($P < 0.05$, FWE corrected) were observed for the left SFA-based sFC in a cluster that primarily embraced the left putamen (**Figure 2A**) and for the right SFA-based sFC in a cluster that was predominantly involved in the bilateral anterior cingulate cortex (ACC) and medial orbital parts of the bilateral superior frontal gyri (ORBsupmed) (**Figure 2B**). Further *post-hoc* comparisons revealed that both patient groups showed significantly decreased FC compared with those of the HCs, but with no significant differences between them (**Figure 2C**). For the bilateral CMA and LBA, no regions were found to show significant main effects among the three groups ($P > 0.05$, FWE corrected).

Relationships Between Functional Characteristics of Amygdala Subregions and Clinical Variables

Significant negative correlations were observed for the ALFF of the left LBA and SFA with HAMD without anxiety/somatization factor scores in the patients with AMDD ($r = -0.645$ and -0.622, respectively, $P < 0.05$, Bonferroni corrected) rather than in those with nAMDD ($P > 0.05$) (**Figure 3**). No significant correlations were found between ALFF and other clinical variables or between sFC and any clinical variables.

DISCUSSION

This study investigated the structural and functional alterations of amygdala subregions in patients with AMDD and nAMDD vs. HCs. Our results showed common and specific amygdala alterations between patients with AMDD and nAMDD that were dependent on different amygdala subdivisions. These findings provide new insights into the unique neural mechanism underlying AMDD.

Numerous studies have examined the amygdala volume in MDD; however, inconsistent even opposing results were obtained (Munn et al., 2007; Tang et al., 2007). Many factors may collectively account for the discrepancy, in which the clinical heterogeneity of the patients and the functional heterogeneity of the amygdala might be two key ones. Focusing on individual amygdala subregions in MDD patients with and without anxiety, we showed that there were no significant GMV differences in the patients compared with those in the HCs for any amygdala subregion. This is consistent with previous studies showing an unchanged amygdala volume in MDD (Bremner et al., 2000; Frodl et al., 2004; Munn et al., 2007; Lorenzetti et al., 2010). Moreover, no significant GMV differences were observed between the two patient groups for any amygdala subregion. This is in line with a previous study showing no significant volume differences of the whole amygdala between patients with anxious unipolar major depressive disorder and those with non-anxious unipolar major depressive disorder (Delaparte et al., 2017). These findings collectively suggest that gray matter volume of the amygdala is not a suitable sign to differentiate anxious depressed from non-anxious depressed individuals. Notably, there are a number of other variables that may confound results for the

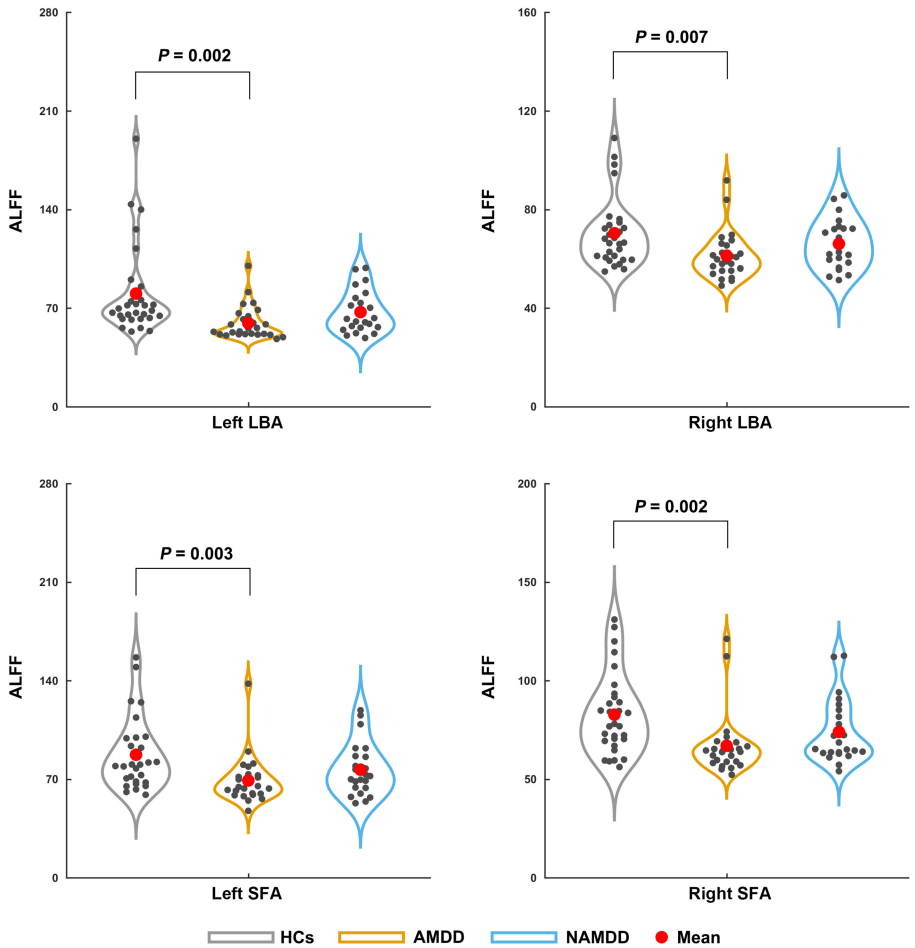

FIGURE 1 | Differences in the ALFF of amygdala subregions among the groups. Significant ALFF decreases in the bilateral LBA and SFA were observed in patients with AMDD but not in those with nAMDD compared with the HCs. ALFF, amplitude of low frequency fluctuation; LBA, laterobasal amygdala; SFA, superficial amygdala; AMDD, anxious major depressive disorder; nAMDD, non-anxious major depressive disorder; HCs, healthy controls.

amygdala volume, including depression duration or number of episodes (Frodl et al., 2003; MacMaster et al., 2008; Kronenberg et al., 2009), antidepressant medication (Hamilton et al., 2008), suicidal tendency (Monkul et al., 2007; Spoletini et al., 2011), genetic variations (Zetzsche et al., 2008; Savitz and Drevets, 2009), and the state of MDD (van Eijndhoven et al., 2009; Malykhin et al., 2012; Zavorotnyy et al., 2018). Further studies are needed to examine the reproducibility of our findings by taking these factors into consideration to gain a more comprehensive picture of amygdala volume abnormalities in MDD. In addition, postmortem neuroanatomical studies may further clarify the issue by examining, for example, neuron or glia numbers or densities at the cellular level (Rubinow et al., 2016).

In addition to structural GMV, we characterized the functional organization of the amygdala subregions from the perspectives of local fluctuation amplitude, intra-region functional integration, and inter-regional functional communication. First, we found that patients with AMDD showed significantly decreased ALFF in the bilateral SFA and the LBA compared with those in the HCs. The SFA and LBA are closely related to emotional processing and regulation: The SFA is mainly involved in olfactory function (Heimer and Van Hoesen, 2006; Moreno and Gonzalez, 2007) and affective processes (Roy et al., 2009), and the LBA plays a central role in modulating the fear response and evaluating sensory information (Jovanovic and Ressler, 2010). In contrast, the CMA is mainly associated with the generation of behavioral responses through projections to the brainstem and cortical and striatal regions (Roy et al., 2009). Accordingly, our results suggest that AMDD selectively affects local spontaneous brain activity of emotion-related amygdala subregions. However, no significant ALFF differences were found between patients with nAMDD and HCs for any amygdala subregion. Therefore, the observed ALFF alterations in SFA and LBA appear to be specific to AMDD. This implies that the SFA and the LBA may be involved in the pathophysiological processes of AMDD and may serve as potential biomarkers to differentiate AMDD from nAMDD. However, no significant differences were found in the ALFF of the bilateral SFA and the LBA between the two patient groups.

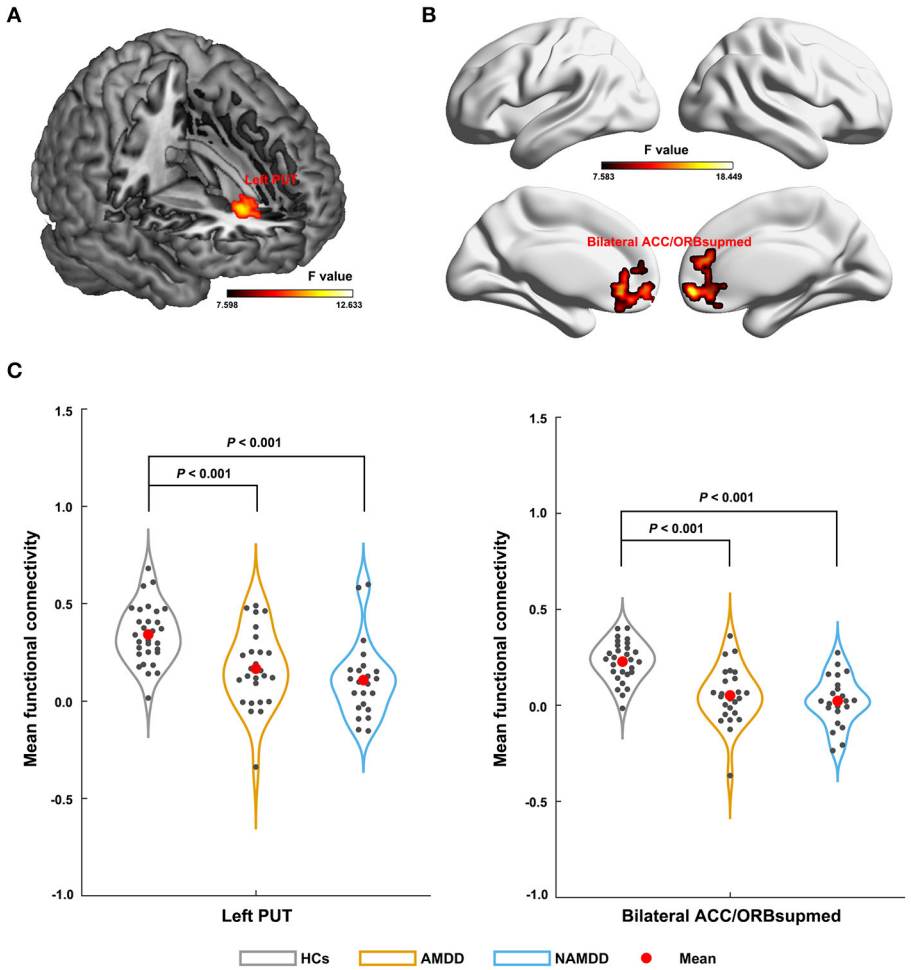

FIGURE 2 | Differences in sFC of amygdala subregions among groups. The left SFA-based sFC **(A)**; the right SFA-based sFC **(B)**; Significant sFC decreases were observed in both the patient groups compared with that in the HCs between the left SFA and the left putamen, and between the right SFA and the bilateral anterior cingulate cortex and medial orbital parts of the bilateral superior frontal gyri **(C)**. PUT, putamen; ACC, anterior cingulate cortex; ORBsupmed, medial orbital part of the superior frontal gyrus; AMDD, anxious major depressive disorder; nAMDD, non-anxious major depressive disorder; HCs, healthy controls.

These findings imply that there may exist a trend effect in the observed ALFF alterations from nAMDD to AMDD. Notably, using a whole-brain voxel-wise analysis, two previous studies found increased ALFF in the bilateral amygdala in patients with MDD compared with that in HCs (Du et al., 2016; Chen et al., 2017). The discrepancy might be caused by different scales at which the analyses were performed (i.e., voxel-level vs. region-level) or because of the differentiation of AMDD and nAMDD in the current study. Moreover, we found that decreased ALFF in the left LBA and SFA were negatively correlated with the HAMD without anxiety/somatization factor scores in the AMDD patients. The HAMD without anxiety/somatization factor scores include several factors, such as cognitive disturbance, retardation, sleep disturbance, and weight loss. These factors represent different symptom clusters that are closely related to the characteristics and medication of the disease. Thus, the ALFF decreases may underlie the specific symptoms in patients with AMDD. Further studies are needed to deepen our understanding on this point by examining the associations between alterations of amygdala subregions and each factor in a larger sample size.

Second, no significant difference was found in the COSLOF among the three groups for each amygdala subregion. This suggests intact functional integration within each amygdala subregion in patients with MDD, regardless of the status of anxiety.

Finally, compared with the HCs, both patients with AMDD and those with nAMDD exhibited decreased functional connectivity of the bilateral SFA, with no significant differences between the two patient groups. This suggests that functional connectivity reductions of the SFA might serve as intrinsic features for MDD. Mounting evidence from both animal and human studies indicates that the SFA typically shows connectivity with the limbic system to form a neural circuit that is closely associated with affective processes (Moreno and Gonzalez, 2007; Goossens et al., 2009; Roy et al., 2009; Gabard-Durnam et al., 2014). Since affective disturbances are commonly

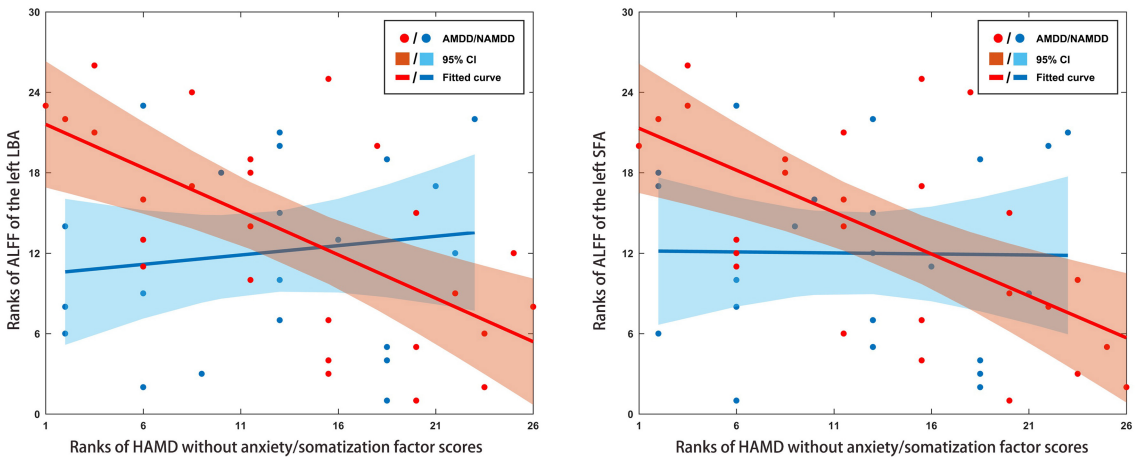

FIGURE 3 | Scatter plots of relationships between altered ALFF of amygdala subregions and clinical variables in patients. Significant negative correlations were observed for the ALFF of the left LBA and SFA with HAMD without anxiety/somatization factor scores in the AMDD group, but not in the nAMDD group. ALFF, amplitude of low frequency fluctuation; LBA, laterobasal amygdala; SFA, superficial amygdala; AMDD, anxious major depressive disorder; nAMDD, non-anxious major depressive disorder; HAMD, Hamilton Rating Scale for Depression.

observed in MDD, regardless of subtype, it is plausible to observe disrupted functional connectivity of the SFA in both AMDD and nAMDD. However, a previous task-fMRI study showed common deficits in both activation and connectivity of the amygdala among patients with MDD, patients with anxiety, and comorbid subjects, suggesting a shared origin between anxiety and depression (Etkin and Schatzberg, 2011). Specifically, the right SFA showed decreased functional connectivity with the bilateral ACC and ORBsupmed in both MDD groups. Both the ACC and ORBsupmed are parts of the prefrontal cortex and are related to emotional processing and regulation (Mayberg et al., 2002; Milad and Rauch, 2007). Numerous previous studies demonstrated the existence of functional connectivity between the amygdala and different parts of the prefrontal regions (e.g., the ACC, and the ventral prefrontal and orbitofrontal cortex) in healthy individuals (Zald and Pardo, 1997; Hariri et al., 2003; Ochsner et al., 2004) and disruptions of these connectivities in MDD (Almeida et al., 2009; Versace et al., 2010; Etkin and Schatzberg, 2011). The disruptions imply impaired prefrontal modulation of the amygdala in MDD, which may contribute to emotional disturbances in patients suffering from the disease. Here, our findings further suggested that the disruptions are selectively targeted to the SFA in MDD. As for the left SFA, decreased functional connectivity with the left putamen was found in both MDD groups, as compared with that in the HCs. The putamen belongs to the dorsal striatum and is thought to play a crucial role in the development of mood disorders. For instance, one animal study found that the putamen was significantly different between anhedonic-like and resilient animals, indicating important implications of the putamen in anhedonia (Delgado y Palacios et al., 2014), which is one of the core symptoms of depression. Thus, the disrupted interaction between the left SFA and the putamen may be involved in the pathological mechanism of depression, in particular the origin of anhedonia. It should be noted that to what extent the findings from animal studies apply to humans remain to be determined due to the limitation of cross-species homologies. This issue can be partially addressed in the future by establishing cross-species correspondence in brain structures via network approaches (Goulas et al., 2015).

Several limitations of this study should be mentioned. First, the sample size was relatively small, which may limit the generalizability of our findings. Second, about half of the patients were treated with psychotropic medication before the MRI scan, which may have significantly modulated their functional brain organization (Wang et al., 2015c; Abdallah et al., 2017; Sheng et al., 2018). Although all patients were free of psychotropic medications for at least 4 weeks before the MRI scan, we cannot fully exclude the possible long-term effects of medication. Studies on non-medicated patients are expected in the future to examine to what extent the current findings are contaminated by this factor. Third, similar to previous studies, we employed dimensional diagnosis to define AMDD, based on the severity of anxiety symptoms in MDD, as measured by the HAMD anxiety/somatization factor. However, the anxiety/somatization factor only contains seven items representing anxiety symptoms and thus may suffer from the risk of misclassification to some extent. Nevertheless, it should be noted that a previous study in Level 1 of the Sequenced Treatment Alternatives to Relieve Depression indicated that the association between anxious unipolar major depressive disorder and poorer treatment outcome was independent of how we defined anxious unipolar major depressive disorder (Fava et al., 2008). Future studies are required to replicate the current findings by integrating multiple dimension diagnosis to minimize the classification error. Fourth, although spatial smoothing was performed after masking out all amygdala subregions to ensure functional specificity, the signals in the amygdala subregions might still be polluted by those from regions adjacent to them. Future studies are required to address this issue by using more sophisticated methods, such as orthogonalization. Finally, several previous studies have shown that MDD-related alterations in both local

fluctuation amplitude and interregional functional connectivity are frequency-dependent (Yue et al., 2015; He et al., 2016; Wang et al., 2016). It would be interesting to investigate whether the observed amygdala alterations are modulated by choices of different frequency intervals.

CONCLUSION

In summary, we demonstrated common and specific functional alterations of the amygdala between patients with AMDD and those with nAMDD. Moreover, the alterations were dependent on the functional features chosen and different amygdala subregions. These findings deepen our understanding neural mechanisms underlying anxiety co-morbid with MDD and have implications for future development of new and effective treatment programs.

DATA AVAILABILITY STATEMENT

The original contributions presented in the study are included in the article/supplementary material, further inquiries can be directed to the corresponding authors.

ETHICS STATEMENT

The studies involving human participants were reviewed and approved by The ethics committee of Sir Run Run Shaw Hospital, Zhejiang University School of Medicine. The patients/participants provided their written informed consent to participate in this study.

AUTHOR CONTRIBUTIONS

YL, XN, and YY conducted the statistical analysis and drafted the initial manuscript. YQ, PW, JY, KR, LZ, ZL, and TS contributed to the conduct of the study. JW conducted the data analysis. Y-FZ and JW were responsible for the interpretation of MRI data. WC and JW reviewed and revised the manuscript. WC and YS designed and supervised the study. All authors contributed to the article and approved the submitted version.

FUNDING

This work was supported by the National Key Research & Development Program of China (2017YFC1310502 and 2016YFC1307200), the NSFC Projects of International Cooperation and Exchanges (8161101010), the National Natural Science Foundation of China (81671764 and 81671350), the Key Project of the Department of Science and Technology of Zhejiang Province (2018C03023), the Department of Science and Technology of Zhejiang Province (2016F50046), the Science and Technology Program of Hangzhou Municipality (20190101A10), and the Project of Chinese Traditional Medicine of Zhejiang Province (2020ZX012).

REFERENCES

Abdallah, C. G., Averill, L. A., Collins, K. A., Geha, P., Schwartz, J., Averill, C., et al. (2017). Ketamine treatment and global brain connectivity in major depression. *Neuropsychopharmacology* 42, 1210–1219. doi: 10.1038/npp.2016.186

Almeida, J. R., Versace, A., Mechelli, A., Hassel, S., Quevedo, K., Kupfer, D. J., et al. (2009). Abnormal amygdala-prefrontal effective connectivity to happy faces differentiates bipolar from major depression. *Biol. Psychiatry* 66, 451–459. doi: 10.1016/j.biopsych.2009.03.024

Amunts, K., Kedo, O., Kindler, M., Pieperhoff, P., Mohlberg, H., Shah, N. J., et al. (2005). Cytoarchitectonic mapping of the human amygdala, hippocampal region, and entorhinal cortex: intersubject variability and probability maps. *Anat. Embryol. (Berl.)* 210, 343–352. doi: 10.1007/s00429-005-0025-5

Ball, T., Rahm, B., Eickhoff, S. B., Schulze-Bonhage, A., Speck, O., and Mutschler, I. (2007). Response properties of human amygdala subregions: evidence based on functional MRI combined with probabilistic anatomical maps. *PLoS ONE* 2:e307. doi: 10.1371/journal.pone.0000307

Bremner, J. D., Narayan, M., Anderson, E. R., Staib, L. H., Miller, H. L., and Charney, D. S. (2000). Hippocampal volume reduction in major depression. *Am. J. Psychiatry* 157, 115–118. doi: 10.1176/ajp.157.1.115

Chen, V. C., Shen, C. Y., Liang, S. H., Li, Z. H., Hsieh, M. H., Tyan, Y. S., et al. (2017). Assessment of brain functional connectome alternations and correlation with depression and anxiety in major depressive disorders. *PeerJ.* 5:e3147. doi: 10.7717/peerj.3147

Delaparte, L., Yeh, F. C., Adams, P., Malchow, A., Trivedi, M. H., Oquendo, M. A., et al. (2017). A comparison of structural connectivity in anxious depression versus non-anxious depression. *J. Psychiatr. Res.* 89, 38–47. doi: 10.1016/j.jpsychires.2017.01.012

Delgado y Palacios, R., Verhoye, M., Henningsen, K., Wiborg, O., and Van der Linden, A. (2014). Diffusion kurtosis imaging and high-resolution MRI demonstrate structural aberrations of caudate putamen and amygdala after chronic mild stress. *PLoS ONE* 9:e95077. doi: 10.1371/journal.pone.0095077

Du, L., Wang, J., Meng, B., Yong, N., Yang, X., Huang, Q., et al. (2016). Early life stress affects limited regional brain activity in depression. *Sci. Rep.* 6:25338. doi: 10.1038/srep25338

Etkin, A., and Schatzberg, A. F. (2011). Common abnormalities and disorder-specific compensation during implicit regulation of emotional processing in generalized anxiety and major depressive disorders. *Am. J. Psychiatry* 168, 968–978. doi: 10.1176/appi.ajp.2011.10091290

Fava, M., Rush, A. J., Alpert, J. E., Balasubramani, G. K., Wisniewski, S. R., Carmin, C. N., et al. (2008). Difference in treatment outcome in outpatients with anxious versus nonanxious depression: a STAR*D report. *Am. J. Psychiatry* 165, 342–351. doi: 10.1176/appi.ajp.2007.06111868

Fonseka, T. M., MacQueen, G. M., and Kennedy, S. H. (2018). Neuroimaging biomarkers as predictors of treatment outcome in Major Depressive Disorder. *J. Affect. Disord.* 233, 21–35. doi: 10.1016/j.jad.2017.10.049

Friston, K. J., Williams, S., Howard, R., Frackowiak, R. S., and Turner, R. (1996). Movement-related effects in fMRI time-series. *Magn. Reson. Med.* 35, 346–355. doi: 10.1002/mrm.1910350312

Frodl, T., Meisenzahl, E. M., Zetzsche, T., Born, C., Jager, M., Groll, C., et al. (2003). Larger amygdala volumes in first depressive episode as compared to recurrent major depression and healthy control subjects. *Biol. Psychiatry* 53, 338–344. doi: 10.1016/S0006-3223(02)01474-9

Frodl, T., Meisenzahl, E. M., Zetzsche, T., Höhne, T., Banac, S., Schorr, C., et al. (2004). Hippocampal and amygdala changes in patients with major depressive disorder and healthy controls during a 1-year follow-up. *J. Clin. Psychiatry* 65, 492–499. doi: 10.4088/JCP.v65n0407

Gabard-Durnam, L. J., Flannery, J., Goff, B., Gee, D. G., Humphreys, K. L., Telzer, E., et al. (2014). The development of human amygdala functional connectivity at rest from 4 to 23 years: a cross-sectional study. *Neuroimage* 95, 193–207. doi: 10.1016/j.neuroimage.2014.03.038

Gaspersz, R., Lamers, F., Kent, J. M., Beekman, A. T., Smit, J. H., van Hemert, A. M., et al. (2017a). Longitudinal predictive validity of the DSM-5 anxious

distress specifier for clinical outcomes in a large cohort of patients with major depressive disorder. *J. Clin. Psychiatry* 78, 207–213. doi: 10.4088/JCP.15m10221

Gaspersz, R., Lamers, F., Kent, J. M., Beekman, A. T. F., Smit, J. H., van Hemert, A. M., et al. (2017b). Anxious distress predicts subsequent treatment outcome and side effects in depressed patients starting antidepressant treatment. *J. Psychiatr. Res.* 84, 41–48. doi: 10.1016/j.jpsychires.2016.09.018

Goldberg, D., and Fawcett, J. (2012). The importance of anxiety in both major depression and bipolar disorder. *Depress Anxiety* 29, 471–478. doi: 10.1002/da.21939

Goldberg, D. P., Wittchen, H. U., Zimmermann, P., Pfister, H., and Beesdobaum, K. (2014). Anxious and non-anxious forms of major depression: familial, personality, and symptom characteristics. *Psychol. Med.* 44:1223. doi: 10.1017/S0033291713001827

Goossens, L., Kukolja, J., Onur, O. A., Fink, G. R., Maier, W., Griez, E., et al. (2009). Selective processing of social stimuli in the superficial amygdala. *Hum. Brain Mapp.* 30, 3332–3338. doi: 10.1002/hbm.20755

Goulas, A., Schaefer, A., and Margulies, D. S. (2015). The strength of weak connections in the macaque cortico-cortical network. *Brain Struct. Funct.* 220, 2939–2951. doi: 10.1007/s00429-014-0836-3

Hallquist, M. N., Hwang, K., Luna, B. The nuisance of nuisance regression: spectral misspecification in a common approach to resting-state fMRI preprocessing reintroduces noise and obscures functional connectivity. *Neuroimage.* (2013) 82, 208–25. doi: 10.1016/j.neuroimage.2013.05.116

Hamilton, J. P., Siemer, M., and Gotlib, I. H. (2008). Amygdala volume in major depressive disorder: a meta-analysis of magnetic resonance imaging studies. *Mol. Psychiatry* 13, 993–1000. doi: 10.1038/mp.2008.57

Hariri, A. R., Mattay, V. S., Tessitore, A., Fera, F., and Weinberger, D. R. (2003). Neocortical modulation of the amygdala response to fearful stimuli. *Biol. Psychiatry* 53, 494–501. doi: 10.1016/S0006-3223(02)01786-9

He, Z., Cui, Q., Zheng, J., Duan, X., Pang, Y., Gao, Q., et al. (2016). Frequency-specific alterations in functional connectivity in treatment-resistant and -sensitive major depressive disorder. *J. Psychiatr. Res.* 82, 30–39. doi: 10.1016/j.jpsychires.2016.07.011

Heimer, L., and Van Hoesen, G. W. (2006). The limbic lobe and its output channels: implications for emotional functions and adaptive behavior. *Neurosci. Biobehav. Rev.* 30, 126–147. doi: 10.1016/j.neubiorev.2005.06.006

Ionescu, D. F., Niciu, M. J., Richards, E. M., and Zarate, C. A. Jr. (2014). Pharmacologic treatment of dimensional anxious depression: a review. *Prim. Care Companion CNS Disord.* 16:PCC.13r01621. doi: 10.4088/PCC.13r01621

Jovanovic, T., and Ressler, K. J. (2010). How the neurocircuitry and genetics of fear inhibition may inform our understanding of PTSD. *Am. J. Psychiatry* 167, 648–662. doi: 10.1176/appi.ajp.2009.09071074

Kronenberg, G., Tebartz van Elst, L., Regen, F., Deuschle, M., Heuser, I., and Colla, M. (2009). Reduced amygdala volume in newly admitted psychiatric in-patients with unipolar major depression. *J. Psychiatr. Res.* 43, 1112–1117. doi: 10.1016/j.jpsychires.2009.03.007

Li, S. J., Li, Z., Wu, G., Zhang, M. J., Franczak, M., and Antuono, P. G. (2002). Alzheimer disease: evaluation of a functional MR imaging index as a marker. *Radiology* 225, 253–259. doi: 10.1148/radiol.22510 11301

Li, Y., Qin, W., Jiang, T., Zhang, Y., and Yu, C. (2012). Sex-dependent correlations between the personality dimension of harm avoidance and the resting-state functional connectivity of amygdala subregions. *PLoS ONE* 7:e35925. doi: 10.1371/journal.pone.0035925

Licznerski, P., and Duman, R. S. (2013). Remodeling of axo-spinous synapses in the pathophysiology and treatment of depression. *Neuroscience* 251, 33–50. doi: 10.1016/j.neuroscience.2012.09.057

Lorenzetti, V., Allen, N. B., Whittle, S., and Yücel, M. (2010). Amygdala volumes in a sample of current depressed and remitted depressed patients and healthy controls. *J. Affect. Disord.* 120, 112–119. doi: 10.1016/j.jad.2009.04.021

MacMaster, F. P., Mirza, Y., Szeszko, P. R., Kmiecik, L. E., Easter, P. C., Taormina, S. P., et al. (2008). Amygdala and hippocampal volumes in familial early onset major depressive disorder. *Biol. Psychiatry* 63, 385–390. doi: 10.1016/j.biopsych.2007.05.005

Malykhin, N. V., Carter, R., Hegadoren, K. M., Seres, P., and Coupland, N. J. (2012). Fronto-limbic volumetric changes in major depressive disorder. *J. Affect. Disord.* 136, 1104–1113. doi: 10.1016/j.jad.2011.10.038

Mayberg, H. S., Silva, J. A., Brannan, S. K., Tekell, J. L., Mahurin, R. K., McGinnis, S., et al. (2002). The functional neuroanatomy of the placebo effect. *Am. J. Psychiatry* 159, 728–737. doi: 10.1176/appi.ajp.159.5.728

Milad, M. R., and Rauch, S. L. (2007). The role of the orbitofrontal cortex in anxiety disorders. *Ann. N. Y. Acad. Sci.* 1121, 546–561. doi: 10.1196/annals.1401.006

Monkul, E. S., Hatch, J. P., Nicoletti, M. A., Spence, S., Brambilla, P., Lacerda, A. L., et al. (2007). Fronto-limbic brain structures in suicidal and non-suicidal female patients with major depressive disorder. *Mol. Psychiatry* 12, 360–366. doi: 10.1038/sj.mp.4001919

Moreno, N., and Gonzalez, A. (2007). Evolution of the amygdaloid complex in vertebrates, with special reference to the anamnio-amniotic transition. *J. Anat.* 211, 151–163. doi: 10.1111/j.1469-7580.2007.00780.x

Munn, M. A., Alexopoulos, J., Nishino, T., Babb, C. M., Flake, L. A., Singer, T., et al. (2007). Amygdala volume analysis in female twins with major depression. *Biol. Psychiatry* 62, 415–422. doi: 10.1016/j.biopsych.2006.11.031

Ochsner, K. N., Ray, R. D., Cooper, J. C., Robertson, E. R., Chopra, S., Gabrieli, J. D., et al. (2004). For better or for worse: neural systems supporting the cognitive down- and up-regulation of negative emotion. *Neuroimage* 23, 483–499. doi: 10.1016/j.neuroimage.2004.06.030

Ongur, D., and Price, J. L. (2000). The organization of networks within the orbital and medial prefrontal cortex of rats, monkeys and humans. *Cereb. Cortex* 10, 206–219. doi: 10.1093/cercor/10.3.206

Phillips, M. L., and Swartz, H. A. (2014). A critical appraisal of neuroimaging studies of bipolar disorder: toward a new conceptualization of underlying neural circuitry and a road map for future research. *Am. J. Psychiatry.* 171, 829–843. doi: 10.1176/appi.ajp.2014.13081008

Qin, S., Young, C. B., Duan, X., Chen, T., Supekar, K., and Menon, V. (2014). Amygdala subregional structure and intrinsic functional connectivity predicts individual differences in anxiety during early childhood. *Biol. Psychiatry* 75, 892–900. doi: 10.1016/j.biopsych.2013.10.006

Rao, S., and Zisook, S. (2009). Anxious depression: clinical features and treatment. *Curr. Psychiatry Rep.* 11, 429–436. doi: 10.1007/s11920-009-0065-2

Roy, A. K., Shehzad, Z., Margulies, D. S., Kelly, A. M., Uddin, L. Q., Gotimer, K., et al. (2009). Functional connectivity of the human amygdala using resting state fMRI. *Neuroimage* 45, 614–626. doi: 10.1016/j.neuroimage.2008.11.030

Rubinow, M. J., Mahajan, G., May, W., Overholser, J. C., Jurjus, G. J., Dieter, L., et al. (2016). Basolateral amygdala volume and cell numbers in major depressive disorder: a postmortem stereological study. *Brain Struct. Funct.* 221, 171–184. doi: 10.1007/s00429-014-0900-z

Savitz, J. B., and Drevets, W. C. (2009). Imaging phenotypes of major depressive disorder: genetic correlates. *Neuroscience* 164, 300–330. doi: 10.1016/j.neuroscience.2009.03.082

Seo, H. J., Jung, Y. E., Kim, T. S., Kim, J. B., Lee, M. S., Kim, J. M., et al. (2011). Distinctive clinical characteristics and suicidal tendencies of patients with anxious depression. *J. Nerv. Ment. Dis.* 199, 42–48. doi: 10.1097/NMD.0b013e3182043b60

Shen, Y., Yao, J., Jiang, X., Zhang, L., Xu, L., Feng, R., et al. (2015). Sub-hubs of baseline functional brain networks are related to early improvement following two-week pharmacological therapy for major depressive disorder. *Hum. Brain Mapp.* 36, 2915–2927. doi: 10.1002/hbm.22817

Sheng, J., Shen, Y., Qin, Y., Zhang, L., Jiang, B., Li, Y., et al. (2018). Spatiotemporal, metabolic, and therapeutic characterization of altered functional connectivity in major depressive disorder. *Hum. Brain Mapp.* 39, 1957–1971. doi: 10.1002/hbm.23976

Spoletini, I., Piras, F., Fagioli, S., Rubino, I. A., Martinotti, G., Siracusano, A., et al. (2011). Suicidal attempts and increased right amygdala volume in schizophrenia. *Schizophr. Res.* 125, 30–40. doi: 10.1016/j.schres.2010.08.023

Tang, Y., Wang, F., Xie, G., Liu, J., Li, L., Su, L., et al. (2007). Reduced ventral anterior cingulate and amygdala volumes in medication-naive females with major depressive disorder: a voxel-based morphometric magnetic resonance imaging study. *Psychiatry Res.* 156, 83–86. doi: 10.1016/j.pscychresns.2007.03.005

van Eijndhoven, P., van Wingen, G., van Oijen, K., Rijpkema, M., Goraj, B., Jan Verkes, R., et al. (2009). Amygdala volume marks the acute state in the early course of depression. *Biol. Psychiatry* 65, 812–818. doi: 10.1016/j.biopsych.2008.10.027

van Tol, M. J., Demenescu, L. R., van der Wee, N. J., Kortekaas, R., Marjan, M. A. N., Boer, J. A., et al. (2012). Functional magnetic resonance imaging correlates

of emotional word encoding and recognition in depression and anxiety disorders. *Biol. Psychiatry* 71, 593–602. doi: 10.1016/j.biopsych.2011.11.016

Versace, A., Thompson, W. K., Zhou, D., Almeida, J. R., Hassel, S., Klein, C. R., et al. (2010). Abnormal left and right amygdala-orbitofrontal cortical functional connectivity to emotional faces: state versus trait vulnerability markers of depression in bipolar disorder. *Biol. Psychiatry* 67, 422–431. doi: 10.1016/j.biopsych.2009.11.025

Wang, J., Wang, X., He, Y., Yu, X., Wang, H., and He, Y. (2015a). Apolipoprotein E ε4 modulates functional brain connectome in Alzheimer's disease. *Hum. Brain Mapp.* 36, 1828–1846. doi: 10.1002/hbm.22740

Wang, J., Wang, X., Xia, M., Liao, X., Evans, A., and He, Y. (2015b). GRETNA: a graph theoretical network analysis toolbox for imaging connectomics. *Front. Hum. Neurosci.* 9:386. doi: 10.3389/fnhum.2015.00386

Wang, J., Wei, Q., Bai, T., Zhou, X., Sun, H., Becker, B., et al. (2017). Electroconvulsive therapy selectively enhanced feedforward connectivity from fusiform face area to amygdala in major depressive disorder. *Soc. Cogn. Affect. Neurosci.* 12, 1983–1992. doi: 10.1093/scan/nsx100

Wang, L., Kong, Q., Li, K., Su, Y., Zeng, Y., Zhang, Q., et al. (2016). Frequency-dependent changes in amplitude of low-frequency oscillations in depression: a resting-state fMRI study. *Neurosci. Lett.* 614, 105–111. doi: 10.1016/j.neulet.2016.01.012

Wang, L., Xia, M., Li, K., Zeng, Y., Su, Y., Dai, W., et al. (2015c). The effects of antidepressant treatment on resting-state functional brain networks in patients with major depressive disorder. *Hum. Brain Mapp.* 36, 768–778. doi: 10.1002/hbm.22663

Wiethoff, K., Bauer, M., Baghai, T. C., Möller, H. J., Fisher, R., Hollinde, D., et al. (2010). Prevalence and treatment outcome in anxious versus nonanxious depression: results from the German Algorithm Project. *J. Clin. Psychiatry* 71, 1047–1054. doi: 10.4088/JCP.09m05650blu

Yue, Y., Jia, X., Hou, Z., Zang, Y., and Yuan, Y. (2015). Frequency-dependent amplitude alterations of resting-state spontaneous fluctuations in late-onset depression. *Biomed. Res. Int.* 2015:505479. doi: 10.1155/2015/505479

Zald, D. H., and Pardo, J. V. (1997). Emotion, olfaction, and the human amygdala: amygdala activation during aversive olfactory stimulation. *Proc. Natl. Acad. Sci. U.S.A.* 94, 4119–4124. doi: 10.1073/pnas.94.8.4119

Zang, Y. F., He, Y., Zhu, C. Z., Cao, Q. J., Sui, M. Q., Liang, M., et al. (2007). Altered baseline brain activity in children with ADHD revealed by resting-state functional MRI. *Brain Dev.* 29, 83–91. doi: 10.1016/j.braindev.2006.07.002

Zavorotnyy, M., Zollner, R., Schulte-Gustenberg, L. R., Wulff, L., Schoning, S., Dannlowski, U., et al. (2018). Low left amygdala volume is associated with a longer duration of unipolar depression. *J. Neural. Transm. (Vienna)* 125, 229–238. doi: 10.1007/s00702-017-1811-y

Zetzsche, T., Preuss, U. W., Bondy, B., Frodl, T., Zill, P., Schmitt, G., et al. (2008). 5-HT1A receptor gene C−1019 G polymorphism and amygdala volume in borderline personality disorder. *Genes Brain Behav.* 7, 306–313. doi: 10.1111/j.1601-183X.2007.00353.x

Conflict of Interest: The authors declare that the research was conducted in the absence of any commercial or financial relationships that could be construed as a potential conflict of interest.

frontiers in Human Neuroscience

ORIGINAL RESEARCH
published: 23 February 2021
doi: 10.3389/fnhum.2021.641616

Stable Anatomy Detection in Multimodal Imaging Through Sparse Group Regularization: A Comparative Study of Iron Accumulation in the Aging Brain

Matthew Pietrosanu[1], Li Zhang[1], Peter Seres[2], Ahmed Elkady[3], Alan H. Wilman[2], Linglong Kong[1] and Dana Cobzas[4,5]**

[1] Department of Mathematical and Statistical Sciences, University of Alberta, Edmonton, AB, Canada, [2] Department of Biomedical Engineering, University of Alberta, Edmonton, AB, Canada, [3] Department of Biomedical Engineering, McGill University, Montreal, QC, Canada, [4] Department of Computing Science, University of Alberta, Edmonton, AB, Canada, [5] Department of Computer Science, MacEwan University, Edmonton, AB, Canada

OPEN ACCESS

Edited by:
Dajiang Zhu,
University of Texas at Arlington,
United States

Reviewed by:
Lu Zhang,
University of Texas at Arlington,
United States
Xiao Li,
Northwestern Polytechnical University,
China

***Correspondence:**
Linglong Kong
lkong@ualberta.ca
Dana Cobzas
dana@cs.ualberta.ca

Specialty section:
This article was submitted to Brain Imaging and Stimulation, a section of the journal Frontiers in Human Neuroscience

Received: 14 December 2020
Accepted: 28 January 2021
Published: 23 February 2021

Citation:
Pietrosanu M, Zhang L, Seres P, Elkady A, Wilman AH, Kong L and Cobzas D (2021) Stable Anatomy Detection in Multimodal Imaging Through Sparse Group Regularization: A Comparative Study of Iron Accumulation in the Aging Brain. Front. Hum. Neurosci. 15:641616. doi: 10.3389/fnhum.2021.641616

Multimodal neuroimaging provides a rich source of data for identifying brain regions associated with disease progression and aging. However, present studies still typically analyze modalities separately or aggregate voxel-wise measurements and analyses to the structural level, thus reducing statistical power. As a central example, previous works have used two quantitative MRI parameters—R2* and quantitative susceptibility (QS)—to study changes in iron associated with aging in healthy and multiple sclerosis subjects, but failed to simultaneously account for both. In this article, we propose a unified framework that combines information from multiple imaging modalities and regularizes estimates for increased interpretability, generalizability, and stability. Our work focuses on joint region detection problems where overlap between effect supports across modalities is encouraged but not strictly enforced. To achieve this, we combine L_1 (lasso), total variation (TV), and L_2 group lasso penalties. While the TV penalty encourages geometric regularization by controlling estimate variability and support boundary geometry, the group lasso penalty accounts for similarities in the support between imaging modalities. We address the computational difficulty in this regularization scheme with an alternating direction method of multipliers (ADMM) optimizer. In a neuroimaging application, we compare our method against independent sparse and joint sparse models using a dataset of R2* and QS maps derived from MRI scans of 113 healthy controls: our method produces clinically-interpretable regions where specific iron changes are associated with healthy aging. Together with results across multiple simulation studies, we conclude that our approach identifies regions that are more strongly associated with the variable of interest (e.g., age), more accurate, and more stable with respect to training data variability. This work makes progress toward a stable and interpretable multimodal imaging analysis framework for studying disease-related changes in brain structure and can be extended for classification and disease prediction tasks.

Keywords: ADMM, geometric regularization, group lasso, joint region, lasso, multiple sclerosis, sparse detection, total variation

1. INTRODUCTION

Following progressive developments in healthcare, the subpopulation of individuals over 60 years old has become the fastest growing worldwide (lr1, 2015). Thanks also in part to rapid advancements in neuroimaging and data storage technology, it is not surprising that much work in recent years has been devoted to studying structural changes in the brain during natural aging and disease progression (e.g., Alzheimer's and Parkinson's diseases Wyss-Coray, 2016 and multiple sclerosis Elkady et al., 2017) as well as differences between healthy and non-normative subjects, particularly in the elderly population.

The naturally high dimensionality of neuroimaging data and their inherent spatial correlation structures present significant challenges to the above goals. Implications of these challenges are apparent in the drawbacks (Davatzikos, 2004) of voxel-based analyses (Ashburner and Friston, 2000) and motivate many of the dimension reduction and regularization techniques commonly applied to neuroimaging data. These methods include pattern identification and discrimination (Fan et al., 2007), which rely on sample sizes not feasible in small neuroimaging studies, and sparse regularization for feature extraction or selection (Batmanghelich et al., 2011; Sabuncu and Van Leemput, 2012; He et al., 2016; Yu et al., 2019; Su et al., 2020). Despite successful applications of the latter to medical data (Krishnapuram et al., 2005; Zou and Hastie, 2005; Ryali et al., 2010), these approaches are unstable with respect to selected or extracted features. In the presence of spatial correlation structures, such as in neuroimaging data where each voxel carries similar information to its neighbors, sparsity comes at the severe detriment of interpretability. To address this, approaches to shape regularization have been developed, notably, total variation (TV) penalties which penalize spatial gradients to encourage a model to apply similar weights to neighboring voxels.

Nonetheless, incorporating multimodal imaging data into analytic techniques remains a difficult problem in general. Previous neuroimaging studies have demonstrated that the simultaneous analysis of multiple imaging modalities can improve statistical power (Elkady et al., 2017), although methods for efficiently doing so are limited. As a result, most studies either analyze different imaging modes independently (Betts et al., 2016) or aggregate voxel-wise observations to the structural level (Cherubini et al., 2009). This approach is inefficient from the perspective of both statistical power and estimate interpretability.

As a focal example and application for this article, we consider specific iron changes in deep gray matter (DGM), which have been histologically associated with healthy aging in the brain (Hallgren and Sourander, 1958). Gradient-echo magnetic resonance imaging (MRI) is used extensively *in vivo* due to its sensitivity to such changes (Peters, 2002). Transverse relaxation rate (R2*) and quantitative susceptibility (QS), both voxel-wise measures derived from gradient-echo MRI, are typically used for this purpose (Haacke et al., 2010; Acosta-Cabronero et al., 2016). Several studies have demonstrated a positive association between iron levels and age in healthy controls using quantitative MRI methods, although they consider only a single MRI measure or anatomical structure (Cherubini et al., 2009; Haacke et al., 2010; Acosta-Cabronero et al., 2016). The combined use of R2* and QS has only recently been introduced, for the purpose of improving statistical power in delineating iron and non-iron changes in studies of multiple sclerosis (Elkady et al., 2017). This earlier study, however, only combines modalities in an initial feature selection stage rather than in a single model.

Related works have similarly investigated, with the previously-discussed methodological limitations, the complex associations between QS and R2* measures, iron, and myelin in brain structures. Through a biochemical and histological analysis of postmortem brains using Pearson correlation (e.g., between myelin and R2*) and linear mixed effect regression (e.g., of R2* on iron and myelin intensities) on region- or structurally-aggregated measures, Hametner et al. (2018) showed that R2* is only weakly sensitive to myelin in white matter regions that do not contain iron, but is strongly sensitive to iron in the basal ganglia and white matter regions that do contain iron. The authors further demonstrated that QS also has mixed sensitivities to iron and myelin in white matter. Taege et al. (2019) applied region of interest-based (i.e., structurally-aggregated) regression analyses using R2* and QS to investigate deep gray matter microstructure in the context of multiple sclerosis. Mangeat et al. (2015) used two-dimensional independent components analysis of magnetization transfer, cortical thickness, B_0 orientation, and R2* to extract information about the fraction of myelin in white matter. Bergsland et al. (2018) used QS and diffusion metrics to perform separate univariate statistical analyses of thalamic white matter tracts and used non-parametric correlation analysis to combine these measures and quantify their association with clinical disease metrics.

While all the previous works provide useful insight into the structure and composition of the brain, the use of region-based analyses relies of the typically incorrect assumption of intra-region homogeneity. Furthermore, these works generally do not jointly incorporate multiple imaging modes as model covariates. These are general limitations in the application of traditional statistical methods to high-dimensional neuroimaging data. In this work, we aim to address these limitations in the context of region-detection problems.

In this article, we propose a unified, multimodal framework for joint region detection associated with a numerical variable of interest such as age. We formulate this problem in terms of sparse regression with L_1 (lasso), TV, and L_2 group lasso penalties, with the last of these combining information across multiple modalities. These penalties have been widely used in the development of robust methods for medical data (He et al., 2016; Yu et al., 2019). Together, the penalties regularize spatial effect estimates for better interpretability, both within and between modalities. This work is concerned primarily with joint region detection, such as in our focal R2*-QS-age problem, where overlap between effect supports across modalities is encouraged but not strictly enforced. To address the computational difficulty in implementing these penalties together, we propose an optimization procedure using the alternating direction method of multipliers (ADMM) algorithm.

Our work addresses the need for multimodal neuroimaging techniques for joint region detection that can provide

interpretable estimates accounting for similarities in spatial effect supports. In our focal example, it is critical to account for both R2* and QS since, voxel-wise, both are positively associated with iron accumulation (Langkammer et al., 2012): the increased statistical power in multimodal MRI analysis has previously detected subtle pathological changes in neurological diseases such as multiple sclerosis (Elkady et al., 2017) and will similarly improve the detection of aging-related neurodegenerative effects. Generally, our approach emphasizes the interpretability and stability of support estimates in terms of spatial smoothness and variability (with respect to perturbations in training data), respectively. Our estimators are much less affected by spatial correlation structures that would otherwise result in severe undersegmentation in other sparse analyses. Furthermore, our work easily accommodates multiple anatomical regions simultaneously: this contrasts with traditional voxel-based analyses, which are generally known to have unsuitable performance when considering multiple regions due to their disregard for spatial correlation (Ashburner and Friston, 2000). In the limited literature addressing multimodal data (Michel et al., 2011; Gramfort et al., 2013), our formulation using sparse regularization is novel.

2. MATERIALS AND METHODS

2.1. Sparse Regression and Image Regularization

We first present more detail on the components of our proposed framework and define the two other models against which the proposed method will be compared. For notational simplicity, we ignore intercept terms in the following subsections and only consider two modalities, although our setup generalizes immediately.

Let X_1 and X_2 be $n \times p$ matrices corresponding to the two imaging modalities (e.g., R2* and QS) after columnwise standardization. These matrices have i-th row $\boldsymbol{x}_{1i}^\top$ and $\boldsymbol{x}_{2i}^\top$, respectively, corresponding to vectorized, observed image data for the i-th subject. In general, p can be smaller than the number of voxels in the image due to the application of a mask (that is constant across subjects). Let $\boldsymbol{\beta}_1$ and $\boldsymbol{\beta}_2$ denote corresponding voxel effects that are to be estimated, and $\boldsymbol{y}$ an observed length-n vector of a continuous variable corresponding to the n subjects. Loosely, we are interested in associations of X_1 and X_2 with $\boldsymbol{y}$, where $p \gg n$.

2.1.1. Sparse Regression

The traditional (least squares) linear regression problem in this setting takes the form $(\hat{\boldsymbol{\beta}}_1, \hat{\boldsymbol{\beta}}_2) = \arg\min_{\boldsymbol{\beta}_1,\boldsymbol{\beta}_2} \|\boldsymbol{y} - X_1\boldsymbol{\beta}_1 - X_2\boldsymbol{\beta}_2\|_2^2$. This estimator is unstable and has extremely high variability, attributable to overfitting in this high-dimensional setting. Furthermore, this estimator typically yields estimates with only non-zero entries, making it useless for region identification. To address both these problems, we introduce a sparsity assumption on $\boldsymbol{\beta} = (\boldsymbol{\beta}_1^\top, \boldsymbol{\beta}_2^\top)^\top$ by adding an L_1 (lasso) penalty to the previous problem, as an approximation of the L_0 penalty used in (NP-hard) best subset selection (Tibshirani, 1996; Huo and Ni, 2007). The lasso penalty is widely-established in both statistical theory and application as a method for variable selection (Tibshirani, 1996; Tibshirani et al., 2005; Simon et al., 2013): loosely-speaking, when applied in 3D imaging contexts, this penalty identifies voxels of interest by shrinking entries of $\hat{\boldsymbol{\beta}}$ corresponding to "non-significant" voxels to zero.

The sparse regression problem becomes

$$\arg\min_{\boldsymbol{\beta}_1,\boldsymbol{\beta}_2} \|\boldsymbol{y} - X_1\boldsymbol{\beta}_1 - X_2\boldsymbol{\beta}_2\|_2^2 + \lambda_1\|\boldsymbol{\beta}_1\|_1 + \lambda_1\|\boldsymbol{\beta}_2\|_1, \quad (1)$$

where the hyperparameter λ_1 controls the balance between model fidelity and model sparsity. We use the same hyperparameter λ_1 for both $\boldsymbol{\beta}_1$ and $\boldsymbol{\beta}_2$ since X_1 and X_2 are standardized.

While the sparse regression problem in (1) is typically encountered in models for predicting y, that is not our primary interest here. We are instead concerned with associations of X_1 and X_2 with $\boldsymbol{y}$: in a neuroimaging context, we wish to identify regions with MRI measures X that vary together with age $\boldsymbol{y}$. In particular, the unpenalized, least squares model maximizes the square sample correlation between y_i and $\boldsymbol{x}_{1i}^\top\boldsymbol{\beta}_1 + \boldsymbol{x}_{2i}^\top\boldsymbol{\beta}_2$, but requires further regularization to become practically usable.

2.1.2. TV Regularization

While the previous sparsity assumption solves initial problems in estimating $\boldsymbol{\beta}$, it does not suitably address estimate interpretability. In neuroimaging contexts, since measures from nearby voxels tend to be correlated, $\hat{\boldsymbol{\beta}}$ will select isolated voxels rather than contiguous, compact regions that are more amenable to interpretation (Kandel et al., 2013; Dubois et al., 2014; Eickenberg et al., 2015).

To encourage interpretability, we add an image-based penalty to (1). Both TV (Michel et al., 2011; Baldassarre et al., 2012; Gramfort et al., 2013; Dohmatob et al., 2014; Dubois et al., 2014; Eickenberg et al., 2015) and GraphNet (Ng et al., 2010; Grosenick et al., 2013; Kandel et al., 2013; Watanabe et al., 2014) penalties have been explored in sparse regression and classification contexts: we use the former as it has demonstrated superior performance with respect to variable selection (Michel et al., 2011; Gramfort et al., 2013; Eickenberg et al., 2015). The anisotropic TV penalty (Tibshirani et al., 2005; Watanabe et al., 2014) is an L_1 penalty on the gradient of an image, which we denote by

$$\|\nabla\boldsymbol{\beta}\|_1 = \|\nabla_1\boldsymbol{\beta}\|_1 + \|\nabla_2\boldsymbol{\beta}\|_1 + \|\nabla_3\boldsymbol{\beta}\|_1,$$

where ∇_i (for $i = 1, 2, 3$) denotes a gradient taken along the i-th orthogonal coordinate direction. The resulting penalized problem is

$$\arg\min_{\boldsymbol{\beta}_1,\boldsymbol{\beta}_2} \|\boldsymbol{y} - X_1\boldsymbol{\beta}_1 - X_2\boldsymbol{\beta}_2\|_2^2 + \lambda_1\|\boldsymbol{\beta}_1\|_1 + \lambda_1\|\boldsymbol{\beta}_2\|_1 + \lambda_2\|\nabla\boldsymbol{\beta}_1\|_1 + \lambda_2\|\nabla\boldsymbol{\beta}_2\|_1, \quad (2)$$

where λ_2 is another hyperparameter.

2.1.3. Sparse Group Lasso Regularization

The TV penalty in (2) addresses the interpretability of $\boldsymbol{\beta}_1$ and $\boldsymbol{\beta}_2$ estimates separately rather than jointly. The latter is a

natural consideration in neuroimaging when interested in the joint support, e.g., regions that are associated with age for both R2* and QS modalities, or if prior knowledge suggests that the effect supports should overlap. We introduce an additional sparse group lasso regularization term to this end.

Group lasso methods apply a penalty to pre-specified groups of variables and are widely used. To encourage overlap in the two estimate supports, we consider p groups of size 2, each composed of voxel-wise measures at the same location. The sparse group lasso penalty (Simon et al., 2013) in this case is given by

$$\lambda_3 \sum_{j=1}^{p} \sqrt{\beta_{1j}^2 + \beta_{2j}^2}.$$

In contrast, the standard group lasso (Tibshirani, 1996) applies an L_1 penalty to the estimates in each group rather than the L_2 penalty above, forcing all estimates in a group to be both either zero or non-zero. This is an undesireably hard constraint in our setting.

The resulting penalized problem and our proposed estimator is given by

$$\begin{aligned} &\arg\min_{\boldsymbol{\beta}_1,\boldsymbol{\beta}_2} \|\boldsymbol{y} - X_1\boldsymbol{\beta}_1 - X_2\boldsymbol{\beta}_2\|_2^2 + \lambda_1\|\boldsymbol{\beta}_1\|_1 + \lambda_1\|\boldsymbol{\beta}_2\|_1 \\ &+\lambda_2\|\nabla\boldsymbol{\beta}_1\|_1 + \lambda_2\|\nabla\boldsymbol{\beta}_2\|_1 + \lambda_3 \sum_{j=1}^{p} \sqrt{\beta_{1j}^2 + \beta_{2j}^2}. \end{aligned} \tag{3}$$

2.2. Optimization

The optimization problem in (3) is difficult to solve due to the non-differentiability of the L_1 norm appearing in the lasso and TV penalties, to which standard gradient-based methods do not apply. Various numerical methods and have been explored for settings with these two penalties, including for logistic regression (Dohmatob et al., 2014).

In this work, we apply the ADMM algorithm (Boyd et al., 2011), an efficient convex optimization scheme amenable to parallel computing. Its computational benefits rely on splitting a given problem into two convex sub-problems. In the present case, denoting $\boldsymbol{\beta} = (\boldsymbol{\beta}_1^\top, \boldsymbol{\beta}_2^\top)^\top$, (3) can be written as

$$\begin{aligned} &\arg\min_{\boldsymbol{\beta},\boldsymbol{\alpha}} L(\boldsymbol{\beta}) + \|\Lambda^\top\boldsymbol{\alpha}\|_1 \\ &\text{subject to } \boldsymbol{\beta} = A\boldsymbol{\alpha}, \end{aligned} \tag{4}$$

where $L(\boldsymbol{\beta}) = \|\boldsymbol{y} - X_1\boldsymbol{\beta}_1 - X_2\boldsymbol{\beta}_2\|_2^2 + \lambda_3 \sum_{i=1}^{p} \sqrt{\beta_{1j}^2 + \beta_{2j}^2}$ is a smooth function of $\boldsymbol{\beta}$, $A = [I_p \mid D^\top]^\top$, $\Lambda = [\lambda_1 I_p \mid \lambda_2 I_{3p}]^\top$, and D is the 3-dimensional differential operator (Rohr, 1997).

The ADMM algorithm solves (4) using the iterative updates

$$\begin{aligned} \boldsymbol{\beta}^{(t+1)} &= \arg\min_{\boldsymbol{\beta}} L_\rho(\boldsymbol{\beta}, \boldsymbol{\alpha}^{(t)}, \boldsymbol{\eta}^{(t)}) \\ \boldsymbol{\alpha}^{(t+1)} &= \arg\min_{\boldsymbol{\alpha}} L_\rho(\boldsymbol{\beta}^{(t+1)}, \boldsymbol{\alpha}, \boldsymbol{\eta}^{(t)}) \\ \boldsymbol{\eta}^{(t+1)} &= \boldsymbol{\eta}^{(t)} + \rho(\boldsymbol{\alpha}^{(t+1)} - A\boldsymbol{\beta}^{(t+1)}), \end{aligned}$$

where $\boldsymbol{\eta}$ is an auxiliary variable and $L_\rho(\boldsymbol{\beta}, \boldsymbol{\alpha}, \boldsymbol{\eta}) = L(\boldsymbol{\beta}) + \|\Lambda^\top\boldsymbol{\alpha}\|_1 + \boldsymbol{\eta}^\top(\boldsymbol{\beta} - A\boldsymbol{\alpha}) + \frac{\rho}{2}\|\boldsymbol{\beta} - A\boldsymbol{\alpha}\|_2^2$ is the augmented Lagrangian with parameter ρ.

The $\boldsymbol{\beta}$-update step minimizes a smooth function (noting that $\boldsymbol{\alpha}$ and $\boldsymbol{\eta}$ are held fixed) and can be performed using standard first-order methods. The $\boldsymbol{\alpha}$-update step, on the other hand, features a non-smooth objective function containing both L_2 and L_1 penalties on $\boldsymbol{\alpha}$. This update admits a closed-form solution using the soft thresholding operator $S_\lambda(x) = \text{sgn}(x)(|x| - \lambda)$, namely,

$$\alpha_i^{(t+1)} = S_{\Lambda_{ii}}\left((A\boldsymbol{\beta}^{(t+1)} - \boldsymbol{\eta}^{(t)})_i\right).$$

For termination criterion, we follow the suggestion of Boyd et al. (2011) based on the problem's primal residuals $\boldsymbol{r}_{\text{primal}}^{(t)} = \boldsymbol{\alpha}^{(t)} - A\boldsymbol{\beta}^{(t)}$ and dual residuals $\boldsymbol{r}_{\text{dual}}^{(t)} = \rho A^\top(\boldsymbol{\alpha}^{(t)} - \boldsymbol{\alpha}^{(t-1)})$, namely,

$$\|\boldsymbol{r}_{\text{primal}}^{(t)}\|_2 \le \epsilon_{\text{primal}} \qquad \text{and} \qquad \|\boldsymbol{r}_{\text{dual}}^{(t)}\|_2 \le \epsilon_{\text{dual}},$$

for positive primal and dual tolerances ϵ_{primal} and ϵ_{primal}, respectively.

2.3. Models and Hyperparameter Tuning

In all subsequent analyses, we compare performance between three models. The first is an independent sparse (IS) model, composed of one model for each imaging modality, each fit with lasso and TV regularization. For this model, "predictions" for $\boldsymbol{y}$ are taken as averages across the independent models. Second, we consider a joint sparse (JS) model, given in (2), including all imaging modalities together with lasso and TV penalties. Third, we consider our proposed sparse group lasso (SGL) method in (3) including all imaging modalities and lasso, TV, and sparse group lasso regularization.

Generally, three hyperparameters λ_1, λ_2, and λ_3 require tuning. We reparameterize these in terms of λ, $r_{1,2}$, and r_3 as

$$(\lambda_1,\ \lambda_2,\ \lambda_3) = \lambda(r_{1,2}(1 - r_3),\ (1 - r_{1,2})(1 - r_3),\ r_3)$$

and use the Bayesian information criterion (BIC) (Fan and Tang, 2013), calculated on the full training dataset, as a performance criterion to choose optimal hyperparameter values. In all analyses, results using the generalized information criterion (GIC) (Fan and Tang, 2013) are similar.

In the following simulation studies, $(\lambda, r_{1,2}, r_3)$ are tuned on a grid over $[e^{-9}, 0] \times [0.1, 0.9] \times [0, 0.9]$. As further restrictions, the IS model enforces $r_3 = 0$ and the SGL model restricts $r_{1,2} = 0.05$ and $r_3 = 0.6$. Tuning in the subsequent neuroimaging analysis restricts the maximum value of λ to e^{-1}, but is otherwise identical.

2.4. Data, Analyses, and Evaluation

2.4.1. Synthetic Data and Simulation Study

Because ground truth for the support regions is not available in real-world imaging, we use synthetic data to more comprehensively investigate the performance of our proposed method. Our setup generalizes that in Zhang et al. (2018) by including a second imaging modality and inter-modality

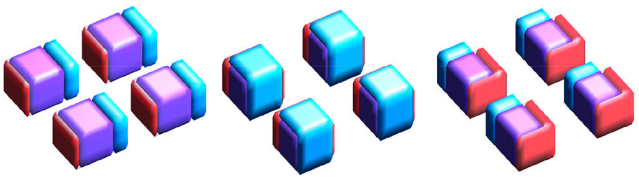

FIGURE 1 | True supports for three of the 10 simulations considered. Purple represents the joint support, while red and cyan are support regions unique to exactly one imaging mode.

correlation. In all simulation studies, we use training datasets of size $n = 100$, which is comparable to the $n = 113$ used in our real-world MRI application.

Imaging data for the first mode is generated with size $32 \times 32 \times 8$. The true support is represented by four disjoint $8 \times 8 \times 4$ regions (which we call "blocks"). Imaging data for the second mode is generated similarly: however, to simulate (partial) overlap in the support between the two modes, we allow block size for the second mode to vary uniform randomly over $\{6, 7, 8, 9, 10\}^2 \times \{4, 5\}$. Example supports are provided in **Figure 1**.

Background noise is independently generated from a $\mathcal{N}(0, I)$ distribution. Voxel measures within a block are correlated only with voxels from the same block and from the corresponding block in the other mode. This inter-voxel correlation is controlled by a spatial coherence parameter ρ that decreases with L_0 distance, and is further multiplied by an inter-mode correlation parameter η for measures in different modes.

The true effect $\boldsymbol{\beta}$ is set to 0.1, 0.2, 0.3, or 0.4 in each block, for varying signal strength, and 0 elsewhere. The simulated response is generated as $\boldsymbol{y} = 0.01 + X_1\boldsymbol{\beta}_1 + X_2\boldsymbol{\beta}_2 + \boldsymbol{\varepsilon}$, where $\boldsymbol{\varepsilon} \sim \mathcal{N}(\mathbf{0}, I_n)$, following the notation in section 2.

We consider two small-sample ($n = 100, p = 32 \times 32 \times 8 \times 2 = 16384$) simulation settings: a "low correlation" ($\rho = 0.5, \eta = 0.2$) and a "high correlation" setting ($\rho = 0.8, \eta = 0.5$). In each case, we run two analyses. The first examines overall performance averaged over 10 simulations, each using independently-generated true supports. The second examines estimate stability over five independent datasets generated using the same true support (i.e., for 10 possible inter-simulation comparisons). From here on, we refer to these two analyses as simulation study #1 and simulation study #2, respectively.

Intuitively, simulation study #1 assesses average performance across a variety of ground truths. On the other hand, simulation study #2 assesses estimate stability across different training datasets for a single, fixed ground truth.

2.4.2. Neuroimaging Data, Pre-processing, and Analyses

The neuroimaging data used in this work is from an in-house study of multiple sclerosis and controls (Walsh et al., 2014; Elkady et al., 2017), similar to that used in Zhang et al. (2018) but composed of only $n = 113$ control scans (mean age 40.25 with SD 10.91, minimum 21.8, and maximum 65.1), of which 40 were obtained from male subjects. Our primary interest is in identifying regions of the brain in which variability in iron levels is associated with age. We focus on four subcortical deep gray matter (DGM) structures: the caudate, putamen, thalamus, and globus pallidus, shown in **Figure 2** (Zhang et al., 2017, 2018). We use R2* and QS modalities, as both are known to be highly sensitive to changes in non-heme iron (Wang and Liu, 2015).

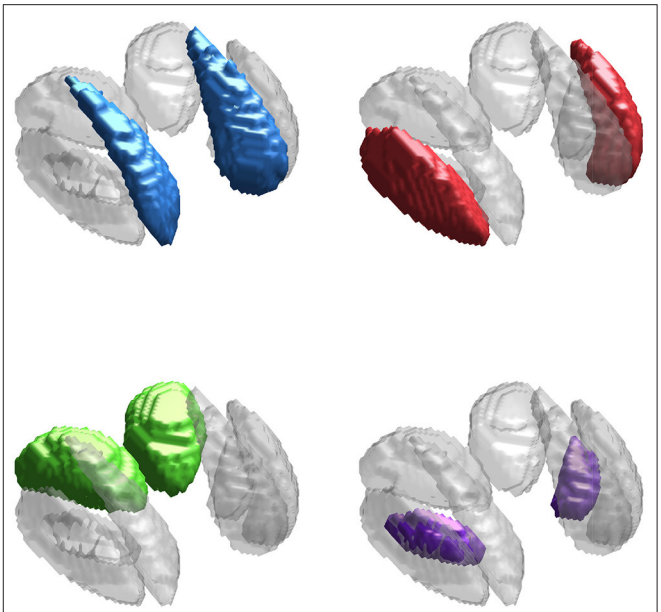

FIGURE 2 | Deep gray matter (DGM) structures considered in this study. The DGM mask applied to the data is shown in gray in all sub-panels. The caudate (blue), putamen (red), thalamus (green), and globus pallidus (purple) are highlighted in each sub-panel.

Imaging was conducted using a 4.7 T system (Varian Inova, Palo Alto, CA), with two imaging sequences obtained per session. R2* and QS maps were calculated using three-dimensional multi-echo gradient echo acquisitions (acquisition time = 9.4 min, repetition time 44 ms, number of echoes = 10, time to first echo = 2.93 ms, echo spacing = 4.1 ms, monopolar readout, flip angle = 10°, number of contiguous slices = 80, field of view = $160 \times 256 \times 160$ mm^3, voxel size $1 \times 1 \times 2$ mm^3). R2* maps were computed using a mono-exponential temporal fit of image magnitude, while QS maps were calculated using an image phase inversion (Bilgic et al., 2012) following phase unwrapping using FSL PRELUDE and background field removal using regularization-enabled sophisticated harmonic removal of phases (RESHARP) (Sun and Wilman, 2013). An anatomical MRI sequence was acquired by 3D T1w volumetric imaging using magnetization-prepared rapid gradient-echo (MPRAGE) (acquisition time = 4.8 min, flip angle = 108°, TE/TR = 4.5/8.5 ms, inversion time to start of readout = 300 ms, sequential phase encoding, number of contiguous slices = 84, voxel size = $0.9 \times 0.9 \times 2$ mm^3).

Prior to analysis, the MRI data was pre-processed and aligned with an in-house unbiased template using ANTs (ANTS, 2011), built from T1w, R2*, and QS data from 10 healthy controls. Pre-processing involved intra-subject alignment of the R2* and QS

TABLE 1 | Performance results for simulation study #1, averaged over 10 independent simulations.

Method	Setting	MAE		Test R^2	Dice	
		Train	Test		Full	Joint
IS	LC	0.187 (0.140)	29.286 (7.895)	0.732 (0.144)	0.427 (0.236)	0.552 (0.152)
	HC	0.147 (0.102)	27.840 (7.334)	0.762 (0.139)	0.532 (0.151)	0.596 (0.128)
JS	LC	**0.127 (0.056)**	29.060 (6.078)	0.734 (0.124)	0.380 (0.148)	0.537 (0.112)
	HC	**0.127 (0.056)**	29.066 (6.072)	0.734 (0.123)	0.380 (0.149)	0.537 (0.113)
SGL	LC	0.128 (0.055)	**8.310 (4.682)**	**0.998 (0.001)**	**0.641 (0.107)**	**0.824 (0.032)**
	HC	0.129 (0.055)	**8.309 (4.682)**	**0.998 (0.001)**	**0.641 (0.107)**	**0.823 (0.031)**

"LC" and "HC" denote the low correlation ($\rho = 0.5, \eta = 0.5$) and high correlation ($\rho = 0.8, \eta = 0.5$) settings, respectively. "IS," "JS," and "SGL" refer to the independent sparse, joint sparse, and proposed sparse group lasso models, respectively. All results are presented in the form "mean (SD)." Entries with the best mean results for the LC and HC settings in each column are in bold.

maps with the T1w map. Non-linear registration in the template space was accomplished by applying SyN (ANTS, 2011) to the multimodal MRI data. Observation row vectors $\boldsymbol{x}_i^\top$ were obtained by taking voxels within a DGM mask manually traced on the atlas, shown in **Figure 5**. Data matrix columns were standardized before analysis.

2.5. Evaluation Methodology

For simulation study #1, we report prediction mean absolute error (MAE) on the training set ($n = 100$) and both MAE and R^2 on the independent testing set ($n = 500$). Since the true support is known for synthetic data, we also report Dice scores between the estimated and true supports (called "full Dice") as well as between the estimated and true joint supports (called "joint Dice"). Here, "joint" refers to the region of overlap in the supports of the two imaging modes.

For simulation study #2, we additionally report Dice scores between estimated supports obtained from different training datasets. This performance measure quantifies the stability of the estimated support with respect to training set variability.

In the neuroimaging analysis, we consider a 23-fold cross-validation approach due to the small sample size. We report training and testing set MAE, testing set R^2, and pairwise Dice scores between the supports estimated using each training dataset.

3. RESULTS

3.1. Simulation Studies

Results for simulation study #1 are provided in **Table 1**. **Figure 3** gives example visualizations of the estimated and true supports for one simulation. These results are similar between the high and low correlation settings. Full and joint Dice scores are significantly higher for the proposed SGL model, with 1.4–4.9 times lower variability across simulations, suggesting more accurate and stable support estimation when using the proposed SGL method. **Figure 3** supports these conclusions and illustrates how the SGL estimator more clearly and accurately identifies the joint support: in contrast, IS and JS estimates suggest higher false-positive voxel selection rates. These points are visually evident though the differences in the size of the joint region (shown in purple) detected by the SGL and the IS/JS estimates, the noise present in the IS (and JS, to a lesser extent) estimate unique to one imaging modality (indicated in red and cyan), and the notable deterioration of IS/JS estimate quality when the true effect size is small. While not the primary goal, the proposed SGL model retains excellent association with the response, shown in testing set MAE and R^2: as hypothesized, this suggests that the proposed SGL model generalizes better to new data and that the

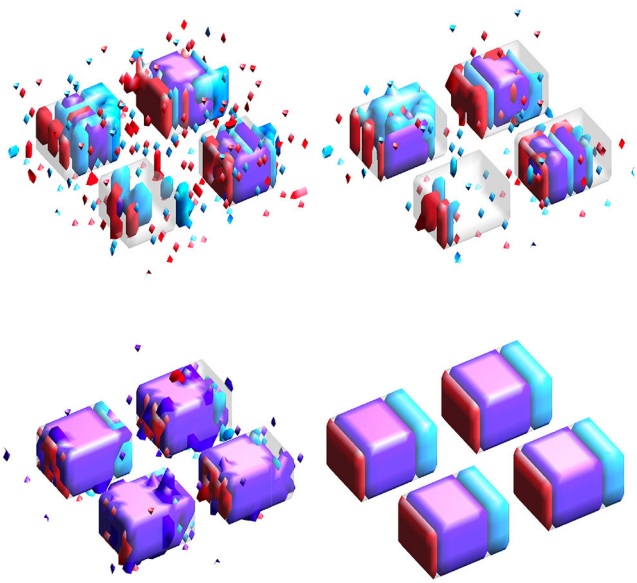

FIGURE 3 | Estimated supports for one simulation in the HC setting. Purple represents the joint support, while red and cyan are support regions unique to exactly one imaging mode. In each sub-panel, the bottom, left, right, and top block corresponds to a true effect size of 0.1, 0.2, 0.3, and 0.4, respectively. **(Top-left)** Independent sparse (IS) model estimates. **(Top-right)** Joint sparse (JS) model estimates. **(Bottom-left)** Proposed sparse group lasso (SGL) model estimates. **(Bottom-right)** True support, also indicated in other sub-panels in gray, for reference.

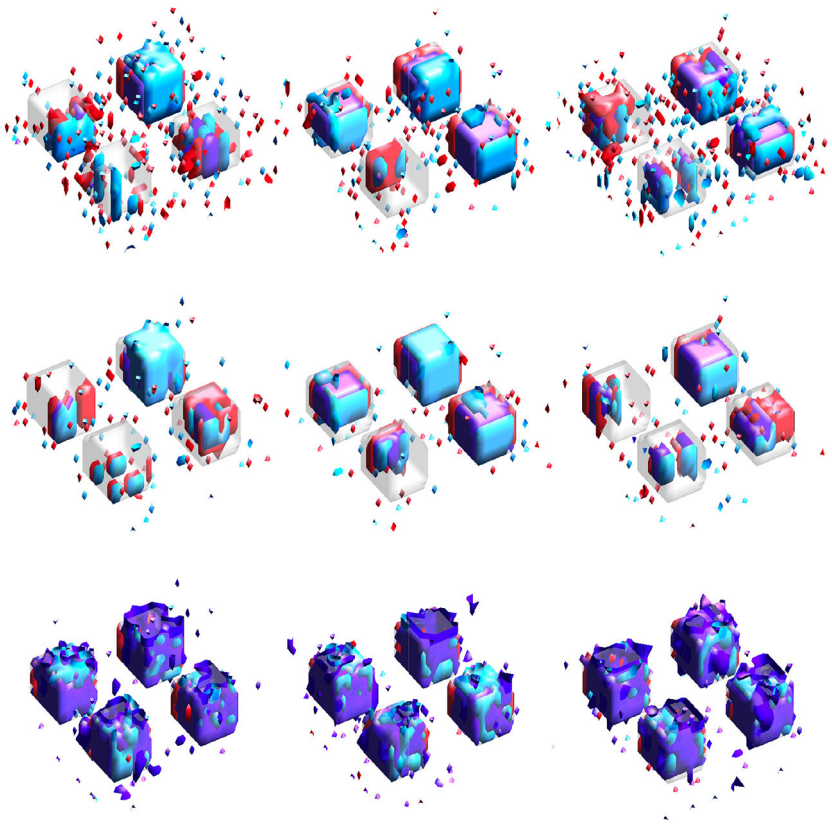

FIGURE 4 | Estimated supports for different simulations with the same ground truth, shown in the middle panel of **Figure 1**. Purple represents the estimated joint support, while red and cyan are estimated support regions unique to exactly one imaging mode. The true support is indicated in gray, for reference. In each sub-panel, the bottom, left, right, and top block corresponds to a true effect size of 0.1, 0.2, 0.3, and 0.4, respectively. Estimates in the same column were obtained using the same dataset. **(Top)** Independent sparse (IS) model estimates. **(Middle)** Joint sparse (JS) model estimates. **(Bottom)** Proposed sparse group lasso (SGL) model estimates.

TABLE 2 | Performance results for simulation study #2.

Method	Setting	MAE		Test R^2	Dice (truth)		Dice (pairwise)	
		Train	Test		Full	Joint	Full	Joint
IS	LC	0.207 (0.129)	25.940 (6.789)	0.811 (0.056)	0.641 (0.069)	0.659 (0.097)	0.579 (0.072)	0.688 (0.080)
	HC	0.207 (0.129)	25.940 (6.789)	0.811 (0.056)	0.641 (0.069)	0.659 (0.097)	0.579 (0.072)	0.688 (.080)
JS	LC	**0.112 (0.026)**	26.426 (6.902)	0.791 (0.067)	0.609 (0.110)	0.568 (0.190)	0.556 (0.076)	0.541 (0.153)
	HC	**0.112 (0.026)**	26.426 (6.902)	0.791 (0.067)	0.609 (0.110)	0.568 (0.190)	0.556 (0.076)	0.541 (0.153)
SGL	LC	0.144 (0.040)	**2.234 (0.402)**	**0.999 (0.001)**	**0.832 (0.012)**	**0.700 (0.024)**	**0.835 (0.007)**	**0.760 (0.011)**
	HC	0.141 (0.042)	**2.241 (0.404)**	**0.999 (0.001)**	**0.831 (0.011)**	**0.700 (0.021)**	**0.835 (0.006)**	**0.760 (0.009)**

"LC" and "HC" denote the low correlation ($\rho = 0.5, \eta = 0.5$) and high correlation ($\rho = 0.8, \eta = 0.5$) settings, respectively. "IS," "JS," and "SGL" refer to the independent sparse, joint sparse, and proposed sparse group lasso models, respectively. All results are presented in the form "mean (SD)." Entries with the best mean results for the LC and HC settings in each column are in bold.

estimated relationship (in $\hat{\boldsymbol{\beta}}$) between voxel-wise measures and the response is less-affected by over-fitting to the training dataset, relative to the IS and JS models.

Results for simulation study #2 are provided in **Table 2**. **Figure 4** gives example visualizations of the estimated supports (obtained from different training datasets) and the true support for one simulation. These results agree with the conclusions of simulation study #1: the proposed SGL method more accurately and stably selects the true support (either full or joint) while retaining high association with the response. Despite a more

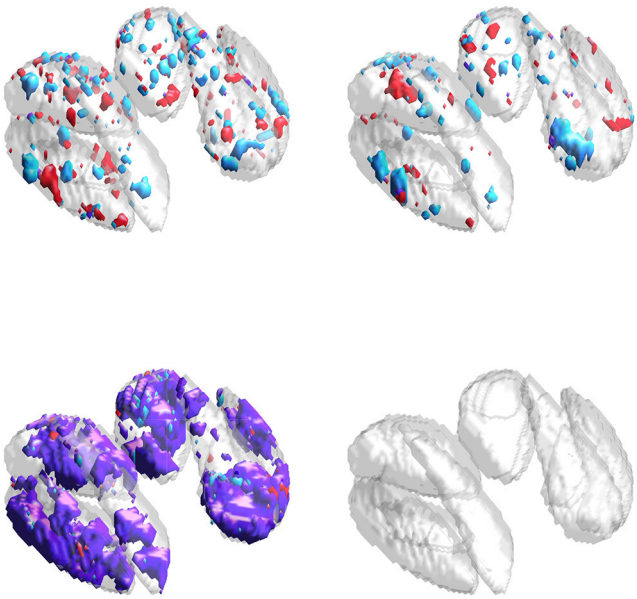

FIGURE 5 | Estimates obtained from one training fold in the neuroimaging data analysis. Purple represents the estimated joint support, while red and cyan are estimated support regions unique to exactly one imaging modality. **(Top-left)** IS model estimates. **(Top-right)** JS model estimates. **(Bottom-left)** SGL model estimates. **(Bottom-right)** DGM mask, also included in other sub-panels for reference.

complex true support, **Figure 4** demonstrates the stability of SGL estimates across independent training sets. This contrasts with IS and JS estimates, which again show higher false-positive voxel selection rates (visually, with red, cyan, or purple outside of the gray true support) and struggle to identify the joint support (visually, with estimates in purple), particularly when the true signal is weak.

3.2. Neuroimaging Data Analysis

Results for the neuroimaging analysis are given in **Table 3**. Examples of the estimated supports are provided for one training fold in **Figure 5** and for multiple folds in **Figure 6**. While no ground truth is available, these results support the simulation studies' conclusions. **Figure 5** illustrates the expected behavior of typical sparse methods in real-world settings: both the IS and JS estimates show many small, non-contiguous regions of selected voxels (although the JS estimates are somewhat smoother). More importantly, the IS and JS estimates suggest little to no joint support (in purple), which is clearly not consistent with findings from previous neuroimaging studies. In contrast, the SGL estimates show a substantial joint support attributable to the proposed sparse group penalty. Furthermore, this region is reasonably smooth, amenable to clinical interpretation, and stable across the (nearly identical) training folds (shown in **Figure 6**), unlike the IS and JS estimates. This conclusion regarding the stability of SGL estimates is supported in **Table 3** by the higher Dice scores (both full and joint) between estimates obtained from different training folds. Numerically, all estimated models retain a comparable and moderate association between predicted and true age (shown by validation set MAE and R^2 in **Table 3**).

4. DISCUSSION

4.1. Summary and Key Findings

Our simulation studies and analysis of a real-world neuroimaging dataset consistently supported our proposed SGL approach over both IS and JS models. In the simulation studies, SGL estimates of the full support gave notably higher (estimate-truth) Dice scores with lower variation across simulations. This result was strengthened when considering joint support detection and can be attributed to our inclusion of a sparse group lasso penalty. **Figures 3**, **4** illustrate the high false-positive rate and instability of IS and JS estimates and the difficulty they have in obtaining the joint support, especially for weaker signals. SGL estimates do not suffer in these ways and still recover the joint support even if the signal is weaker. A second set of simulation studies over independent datasets with the same ground truth similarly confirmed that our proposed method provides more stable estimates.

The neuroimaging analysis highlighted a major disadvantage of typical sparse methods (e.g., IS and JS), namely, their tendency to select a small number of voxels in non-contiguous regions, shown clearly in **Figure 5**. Furthermore, neither IS nor JS estimates suggested the presence of a joint support region, inconsistent with previous neuroimaging studies (Peters, 2002; Langkammer et al., 2012). These estimates again showed high instability, even with minimal variation in the training dataset during 23-fold cross validation (with total sample size $n = 113$). In contrast, our SGL method estimates a substantial joint support that was reasonably smooth, compact, and stable across training folds.

In both the simulation and neuroimaging analyses, all methods demonstrate a difference between the training and testing (or validation) set MAE, as expected. We attribute variation in this difference between the IS/JS and SGL models to the effect of overfitting when using the former methods, which is emphasized in the simulation studies (with about 82–90% of truly non-predictive voxels, much greater than the 32–50% estimated by the SGL model in the neuroimaging analysis). We suspect this variation is lessened in the neuroimaging analysis due to the naturally more complex data for which our simulation is a simple imitation.

4.2. Related Work and Impact

Existing approaches to multimodal neuroimaging data analysis commonly use techniques requiring a large sample size (Fan et al., 2007), analyze modes separately (Cherubini et al., 2009), aggregate voxel-wise measures to the structural level (Betts et al., 2016), or combine modalities in only an initial feature selection stage (Elkady et al., 2017). These approaches are either impractical or come at the cost of statistical power.

In this article, we proposed a unified, multimodal framework for joint region detection associated with a numerical variable of interest. Our work addresses the above limitations in existing

TABLE 3 | Performance results for the neuroimaging data analysis for 23-fold cross-validation.

Method	MAE		Validation R^2	Dice (pairwise)	
	Train	Validation		Full	Joint
IS	**0.193 (0.051)**	**4.548 (1.563)**	**0.845 (0.171)**	0.529 (0.062)	0.395 (0.114)
JS	0.607 (0.188)	5.515 (1.640)	0.784 (0.183)	0.519 (0.070)	0.308 (0.131)
SGL	0.648 (0.117)	5.059 (1.967)	0.824 (0.150)	**0.678 (0.050)**	**0.666 (0.049)**

"IS," "JS," and "SGL" refer to the independent sparse, joint sparse, and proposed sparse group lasso models, respectively. All results are presented in the form "mean (SD)". Entries with the best mean results in each column are in bold.

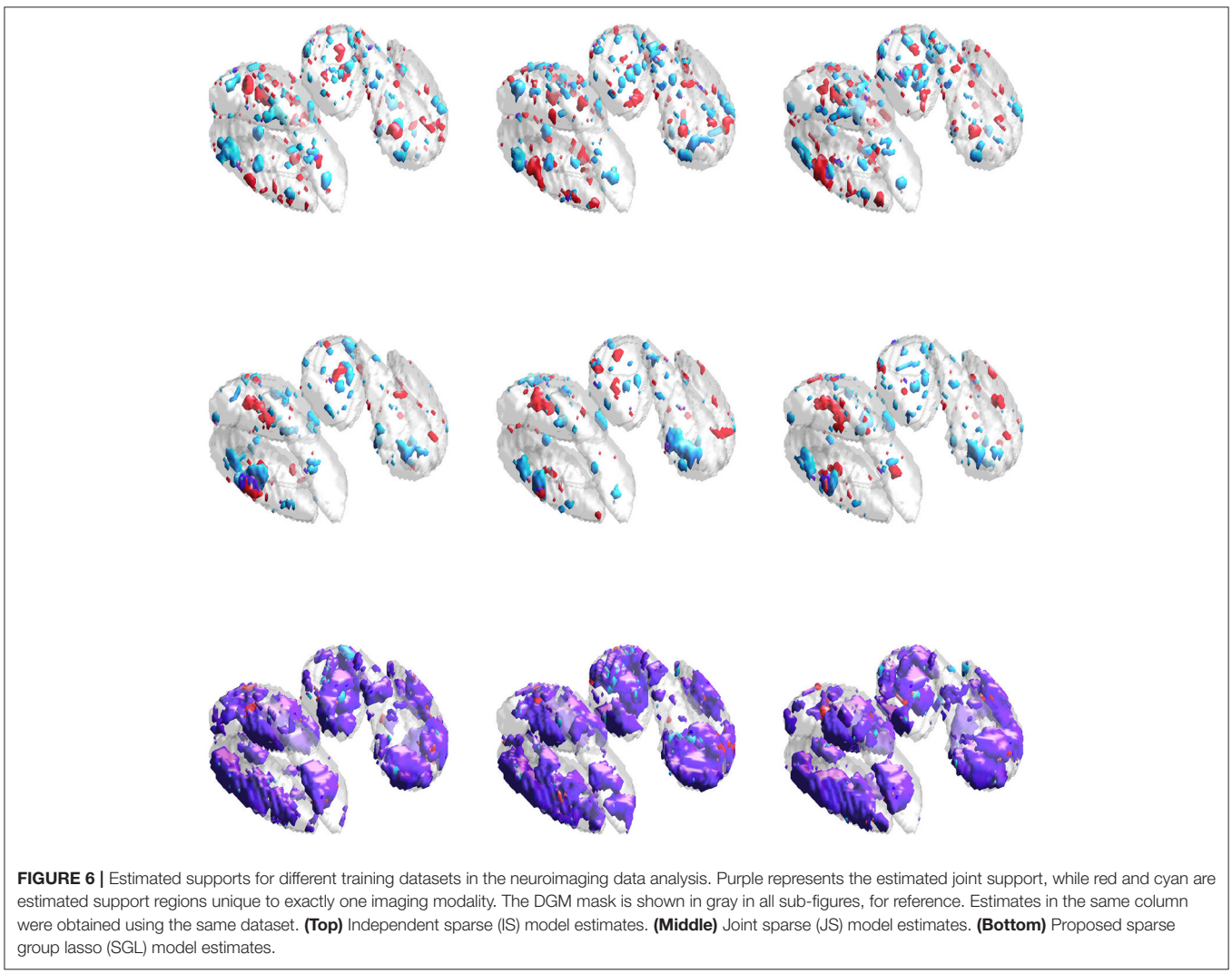

FIGURE 6 | Estimated supports for different training datasets in the neuroimaging data analysis. Purple represents the estimated joint support, while red and cyan are estimated support regions unique to exactly one imaging modality. The DGM mask is shown in gray in all sub-figures, for reference. Estimates in the same column were obtained using the same dataset. **(Top)** Independent sparse (IS) model estimates. **(Middle)** Joint sparse (JS) model estimates. **(Bottom)** Proposed sparse group lasso (SGL) model estimates.

neuroimaging analytic approaches as well as disadvantages of methods that employ sparse regularization. We are primarily interested in settings where overlap in the effect supports between modes is encouraged (rather than enforced) due to prior knowledge or a need for estimate interpretability. Our proposed method combines lasso, TV, and sparse group lasso penalties to this end.

Our primary motivating example concerns the association of R2* and QS MRI maps with age: in particular, previous works have shown that both modalities need to be considered simultaneously to delineate the complex association between iron and myelin levels (Hametner et al., 2018). An understanding of iron accumulation in healthy aging can give insights into the association between brain iron levels and neurological disease such as multiple sclerosis (Elkady et al., 2019). In this article, we considered the problem of identifying deep gray matter regions where variation in R2* and QS measures is jointly associated with aging in healthy controls. Although the main focus of this study

was the detection of specific iron changes in deep gray matter, our work may be extended to delineate iron and myelin changes in myelin-rich white matter tissue.

The neuroimaging literature demonstrates a need for methods that can simultaneously accommodate multiple modalities and yield interpretable results in joint region detection problems, such as in our central R2*-QS-age example. Methods employing sparse regularization suffer due to spatial correlation in imaging data and tend to select a non-compact set of disjoint voxels. Image-based (e.g., TV) penalties help address this, but do not consider relationships between modalities. In practice, this may be problematic when it is expected that relevant brain regions are similar across modalities.

Our introduction of a sparse group lasso penalty is novel in this neuroimaging context and addresses the above gap in the current literature. We have shown that our SGL model is capable of obtaining estimates that are compact, interpretable, and stable, both within and between imaging modalities. Our work here is a first step in more general approaches to the multimodal analysis of age- or disease-related alterations in brain structure and function.

4.3. Limitations and Future Developments

In this article, we only considered a continuous response due to its wide applicability and our primary motivation to study age-related variation in DGM iron levels. However, our approach is readily applied to other tasks by modification of the objective function in (3). For example, Zhang et al. (2018) considers a discriminative anatomy detection problem based on logistic regression using a single MRI modality. This could be developed to include multiple modalities and a sparse group penalty for joint discriminative anatomy detection. To focus on our approach to multiple imaging modalities in this work, we also did not consider subject-level scalar predictors $\boldsymbol{z}_i$ (e.g., demographic or clinical variables). By changing the $\boldsymbol{y} - X_1\boldsymbol{\beta}_1 - X_2\boldsymbol{\beta}_2$ portion of the objective function in (3) to $\boldsymbol{y} - Z\boldsymbol{\gamma} - X_1\boldsymbol{\beta}_1 - X_2\boldsymbol{\beta}_2$, where Z has row vectors $\boldsymbol{z}_i^\top$, scalar covariates can be included with only straightforward changes to the ADMM algorithm. In both cases, our work here is a general framework that supports other standard tools employed in regression analysis.

DATA AVAILABILITY STATEMENT

The datasets presented in this study can be found in online repositories. The names of the repository/repositories and accession number(s) can be found at: https://github.com/pietrosa/qsr2-sim.

ETHICS STATEMENT

The studies involving human participants were reviewed and approved by Health Research Ethics Board, University of Alberta. The patients/participants provided their written informed consent to participate in this study.

AUTHOR CONTRIBUTIONS

MP performed the analyses presented in this article, designed the simulation study, and was responsible for the text, tables, and figures in this work. LZ authored the optimization code used for model-fitting, provided some initial analytic neuroimaging results (not presented), and authored a previous version of this manuscript. PS was heavily involved in subject recruitment, acquired all neuroimaging data used in this study, and provided continued support with neuroimaging data handling and all pre-processing tasks. AE contributed to writing the introduction of the manuscript. AHW designed the image acquisition protocol, funded data collection, and led initial project discussions. LK provided methodological development, modified the general ADMM algorithm for this problem, and provided senior project supervision. DC provided methodological support and senior supervision, motivated this work, and contributed to previous versions of the manuscript. All authors contributed to manuscript editing.

FUNDING

LK was supported by the Natural Sciences and Engineering Research Council of Canada (NSERC) and a Canada Research Chair in Statistical Learning. AHW was supported in imaging data collection by the Canadian Institutes of Health Research (CIHR) (grant number MOP 102582).

ACKNOWLEDGMENTS

The authors thank the two reviewers for their feedback and comments which have improved the presentation of the results in this manuscript.

REFERENCES

(2015). *World Health Organization: World Report on Ageing and Health*.

Acosta-Cabronero, J., Betts, M. J., Cardenas-Blanco, A., Yang, S., and Nestor, P. J. (2016). In vivo MRI mapping of brain iron deposition across the adult lifespan. *J. Neurosci.* 36, 364–374. doi: 10.1523/JNEUROSCI.1907-15.2016

ANTS (2011). Available online at: http://www.picsl.upenn.edu/ants/

Ashburner, J., and Friston, K. J. (2000). Voxel-based morphometry – the methods. *NeuroImage* 11, 805–821. doi: 10.1006/nimg.2000.0582

Baldassarre, L., Mourao-Miranda, J., and Pontil, M. (2012). "Structured sparsity models for brain decoding from fMRI data," in *International Workshop on Pattern Recognition in Neuroimaging* (London, UK), 5–9. doi: 10.1109/PRNI.2012.31

Batmanghelich, N. K., Taskar, B., and Davatzikos, C. (2011). Generative-discriminative basis learning for medical imaging. *IEEE Trans. Med. Imaging* 31, 51–69. doi: 10.1109/TMI.2011.2162961

Bergsland, N., Schweser, F., Dwyer, M. G., Weinstock-Guttman, B., Benedict, R. H. B., and Zivadinov, R. (2018). Thalamic white matter in multiple sclerosis: a combined diffusion-tensor imaging and quantitative susceptibility mapping study. *Hum. Brain Mapp.* 39, 4007–4017. doi: 10.1002/hbm.24227

Betts, M. J., Acosta-Cabronero, J., Cardenas-Blanco, A., Nestor, P. J., and Düzel, E. (2016). High-resolution characterisation of the aging brain using simultaneous quantitative susceptibility mapping (QSM) and R2* measurements at 7T. *NeuroImage* 138, 43–68. doi: 10.1016/j.neuroimage.2016.05.024

Bilgic, B., Pfefferbaum, A., Rohlfing, T., Sullivan, E. V., and Adalsteinsson, E. (2012). MRI estimates of brain iron concentration in normal aging using quantitative susceptibility mapping. *NeuroImage* 59, 2625–2635. doi: 10.1016/j.neuroimage.2011.08.077

Boyd, S., Parikh, N., Chu, E., Peleato, B., and Eckstein, J. (2011). Distributed optimization and statistical learning via the alternating direction method of multipliers. *Found. Trends Mach. Learn.* 3, 1–122. doi: 10.1561/2200000016

Cherubini, A., Peran, P., Caltagirone, C., Sabatini, U., and Spalletta, G. (2009). Aging of subcortical nuclei: microstructural, mineralization and atrophy modifications measured in vivo using MRI. *NeuroImage* 48, 29–36. doi: 10.1016/j.neuroimage.2009.06.035

Davatzikos, C. (2004). Why voxel-based morphometric analysis should be used with great caution when characterizing group differences. *NeuroImage* 23, 17–20. doi: 10.1016/j.neuroimage.2004.05.010

Dohmatob, E., Gramfort, A., Thirion, B., and Varoquaux, G. (2014). "Benchmarking solvers for TV-l_1 least-squares and logistic regression in brain imaging," in *International Workshop on Pattern Recognition in Neuroimaging* (Tübingen), 1–4. doi: 10.1109/PRNI.2014.6858516

Dubois, M., Hadj-Selem, F., Lofstedt, T., Perrot, M., Fischer, C., Frouin, V., et al. (2014). "Predictive support recovery with TV-elastic net penalty and logistic regression: an application to structural MRI," in *International Workshop on Pattern Recognition in Neuroimaging* (Tübingen), 1–4. doi: 10.1109/PRNI.2014.6858517

Eickenberg, M., Dohmatob, E., Thirion, B., and Varoquaux, G. (2015). "Grouping total variation and sparsity: statistical learning with segmenting penalties," in *MICCAI* (Munich), 685–693. doi: 10.1007/978-3-319-24553-9_84

Elkady, A., Cobzas, D., Sun, H., Blevins, G., and Wilman, A. H. (2017). Progressive iron accumulation across multiple sclerosis phenotypes revealed by sparse classification of deep gray matter. *J. Magn. Reson. Imaging* 46, 1464–1473. doi: 10.1002/jmri.25682

Elkady, A. M., Cobzas, D., Sun, H., Seres, P., Blevins, G., and Wilman, A. H. (2019). Five year iron changes in relapsing-remitting multiple sclerosis deep gray matter compared to healthy controls. *Multiple Scleros. Relat. Disord.* 33, 107–115. doi: 10.1016/j.msard.2019.05.028

Fan, Y., Shen, D., Gur, R. C., Gur, R. E., and Davatzikos, C. (2007). COMPARE: Classification of morphological patterns using adaptive regional elements. *IEEE Trans. Med. Imaging* 26, 93–105. doi: 10.1109/TMI.2006.886812

Fan, Y., and Tang, C. Y. (2013). Tuning parameter selection in high dimensional penalized likelihood. *J. R. Stat. Soc. Ser. B* 75, 531–552. doi: 10.1111/rssb.12001

Gramfort, A., Thirion, B., and Varoquaux, G. (2013). "Identifying predictive regions from fMRI with TV-l_1 prior," in *International Workshop on Pattern Recognition in Neuroimaging* (Washington, DC), 17–20. doi: 10.1109/PRNI.2013.14

Grosenick, L., Klingenberg, B., Katovich, K., Brian, K., and Jonathan, E. T. (2013). Interpretable whole-brain prediction analysis with GraphNet. *NeuroImage* 72, 304–321. doi: 10.1016/j.neuroimage.2012.12.062

Haacke, E. M., Miao, Y., Liu, M., Habib, C. A., Katkuri, Y., Liu, T., et al. (2010). Correlation of putative iron content as represented by changes in R2* and phase with age in deep gray matter of healthy adults. *J. Magn. Reson. Imaging* 32, 561–576. doi: 10.1002/jmri.22293

Hallgren, B., and Sourander, P. (1958). The effect of age on the non-haemin iron in the human brain. *J. Neurochem.* 3, 41–51. doi: 10.1111/j.1471-4159.1958.tb12607.x

Hametner, S., Endmayr, V., Deistung, A., Palmrich, P., Prihoda, M., Haimburger, E., et al. (2018). The influence of brain iron and myelin on magnetic susceptibility and effective transverse relaxation: a biochemical and histological validation study. *NeuroImage* 179, 117–133. doi: 10.1016/j.neuroimage.2018.06.007

He, Q., Kong, L., Wang, Y., Wang, S., Chan, T. A., and Holland, E. (2016). Regularized quantile regression under heterogeneous sparsity with application to quantitative genetic traits. *Comput. Stat. Data Anal.* 95, 222–239. doi: 10.1016/j.csda.2015.10.007

Huo, X., and Ni, X. (2007). When do stepwise algorithms meet subset selection criteria? *Ann. Stat.* 35, 870–887. doi: 10.1214/009053606000001334

Kandel, B., Avants, B., Gee, J., and Wolk, D. (2013). "Predicting cognitive data from medical images using sparse linear regression," in *Information Processing in Medical Imaging* (Asilomar, CA), 86–97. doi: 10.1007/978-3-642-38868-2_8

Krishnapuram, B., Carin, L., Figueiredo, M. A., and Hartemink, A. J. (2005). Sparse multinomial logistic regression: fast algorithms and generalization bounds. *IEEE Trans. Pattern Anal. Mach. Intell.* 27, 957–968. doi: 10.1109/TPAMI.2005.127

Langkammer, C., Krebs, N., Goessler, W., Scheurer, E., Yen, K., Fazekas, F., et al. (2012). Susceptibility induced gray-white matter MRI contrast in the human brain. *NeuroImage* 59, 1413–1419. doi: 10.1016/j.neuroimage.2011.08.045

Mangeat, G., Govindarajan, S., Mainero, C., and Cohen-Adad, J. (2015). Multivariate combination of magnetization transfer, t2* and b0 orientation to study the myelo-architecture of the *in vivo* human cortex. *NeuroImage* 119, 89–102. doi: 10.1016/j.neuroimage.2015.06.033

Michel, V., Gramfort, A., and Varoquaux, G. (2011). Total variation regularization for fMRI-based prediction of behaviour. *IEEE Trans. Med. Imaging* 30, 1328–1340. doi: 10.1109/TMI.2011.2113378

Ng, B., Vahdat, A., Hamarneh, G., and Abugharbieh, R. (2010). "Generalized sparse classifiers for decoding cognitive states in fMRI," in *Machine Learning in Medical Imaging 2010* (Beijing), 108–115. doi: 10.1007/978-3-642-15948-0_14

Peters, A. (2002). The effects of normal aging on myelin and nerve fibers: a review. *J. Neurocytol.* 31, 581–593. doi: 10.1023/A:1025731309829

Rohr, K. (1997). On 3D differential operators for detecting point landmarks. *Image Vis. Comput.* 15, 219–233. doi: 10.1016/S0262-8856(96)01127-4

Ryali, S., Supekar, K., Abrams, D. A., and Menon, V. (2010). Sparse logistic regression for whole-brain classification of fMRI data. *NeuroImage* 51, 752–764. doi: 10.1016/j.neuroimage.2010.02.040

Sabuncu, M. R., and Van Leemput, K. (2012). The relevance voxel machine (RVoxM): a self-tuning Bayesian model for informative image-based prediction. *IEEE Trans. Med. Imaging* 31, 2290–2306. doi: 10.1109/TMI.2012.2216543

Simon, N., Friedman, G., Hastie, T., and Tibshirani, R. (2013). A sparse-group lasso. *J. Comput. Graph. Stat.* 22, 231–245. doi: 10.1080/10618600.2012.681250

Su, T., Wang, Y., Liu, Y., Branton, W. G., Asahchop, E., Power, C., et al. (2020). Sparse multicategory generalized distance weighted discrimination in ultra-high dimensions. *Entropy* 22:1257. doi: 10.3390/e22111257

Sun, H., and Wilman, A. H. (2013). Background field removal using spherical mean value filtering and Tikhonov regularization. *Magn. Reson. Med.* 71, 1151–1157. doi: 10.1002/mrm.24765

Taege, Y., Hagemeier, J., Bergsland, N., Dwyer, M. G., Weinstock-Guttman, B., Zivadinov, R., et al. (2019). Assessment of mesoscopic properties of deep gray matter iron through a model-based simultaneous analysis of magnetic susceptibility and r2* – a pilot study in patients with multiple sclerosis and normal controls. *NeuroImage* 186, 308–320. doi: 10.1016/j.neuroimage.2018.11.011

Tibshirani, R. (1996). Regression shrinkage and selection via the lasso. *J. R. Stat. Soc. Ser. B* 58, 267–288. doi: 10.1111/j.2517-6161.1996.tb02080.x

Tibshirani, R., Saunders, M., Rosset, S., Zhu, J., and Knight, K. (2005). Sparsity and smoothness via the fused lasso. *J. R. Stat. Soc. Ser. B* 67, 91–108. doi: 10.1111/j.1467-9868.2005.00490.x

Walsh, A. J., Blevins, G., Lebel, R. M., Seres, P., Emery, D. J., and Wilman, A. H. (2014). Longitudinal MR imaging of iron in multiple sclerosis: an imaging marker of disease. *Radiology* 270, 186–196. doi: 10.1148/radiol.13130474

Wang, Y., and Liu, T. (2015). Quantitative susceptibility mapping (QSM): decoding MRI data for a tissue magnetic biomarker. *Magn. Reson. Med.* 73, 82–101. doi: 10.1002/mrm.25358

Watanabe, T., Kessler, D., Scott, C., Angstadt, M., and Sripada, C. (2014). Disease prediction based on functional connectomes using a scalable and spatially-informed support vector machine. *NeuroImage* 96, 183–202. doi: 10.1016/j.neuroimage.2014.03.067

Wyss-Coray, T. (2016). Ageing, neurodegeneration and brain rejuvenation. *Nature* 539, 180–186. doi: 10.1038/nature20411

Yu, D., Zhang, L., Mizera, I., Jiang, B., and Kong, L. (2019). Sparse wavelet estimation in quantile regression with multiple functional predictors. *Comput. Stat. Data Anal.* 136, 12–29. doi: 10.1016/j.csda.2018.12.002

Zhang, L., Cobzas, D., Wilman, A. H., and Kong, L. (2017). "An unbiased penalty for sparse classification with application to neuroimaging data," in *Medical Image Computing and Computer Assisted Intervention – MICCAI 2017*, eds M. Descoteaux, L. Maier-Hein, A. Franz, P. Jannin, D. L. Collins, and S. Duchesne (Cham: Springer International Publishing), 55–63. doi: 10.1007/978-3-319-66179-7_7

Zhang, L., Cobzas, D., Wilman, A. H., and Kong, L. (2018). Significant anatomy detection through sparse classification: a comparative study. *IEEE Trans. Med. Imaging* 37, 128–137. doi: 10.1109/TMI.2017.2735239

Zou, H. and Hastie, T. (2005). Regularization and variable selection via the elastic net. *J. R. Stat. Soc. Ser. B* 67, 301–320. doi: 10.1111/j.1467-9868.2005.00503.x

Conflict of Interest: The authors declare that the research was conducted in the absence of any commercial or financial relationships that could be construed as a potential conflict of interest.

frontiers in Human Neuroscience

ORIGINAL RESEARCH
published: 24 February 2021
doi: 10.3389/fnhum.2021.637407

Cognitive Impairment in Adolescent Major Depressive Disorder With Nonsuicidal Self-Injury: Evidence Based on Multi-indicator ERPs

*Yujiao Wen, Xuemin Zhang, Yifan Xu, Dan Qiao, Shanshan Guo, Ning Sun, Chunxia Yang, Min Han and Zhifen Liu**

Department of Psychiatry, The First Hospital of Shanxi Medical University, Taiyuan, China

OPEN ACCESS

Edited by:
Wei Liao,
University of Electronic Science and Technology of China, China

Reviewed by:
Suhua Chang,
Peking University Sixth Hospital, China
Zhiliang Long,
Southwest University, China

****Correspondence:***
Zhifen Liu
liuzhifen5518@163.com

Specialty section:
This article was submitted to Brain Imaging and Stimulation, a section of the journal Frontiers in Human Neuroscience

Received: *03 December 2020*
Accepted: *02 February 2021*
Published: *24 February 2021*

Citation:
Wen Y, Zhang X, Xu Y, Qiao D, Guo S, Sun N, Yang C, Han M and Liu Z (2021) Cognitive Impairment in Adolescent Major Depressive Disorder With Nonsuicidal Self-Injury: Evidence Based on Multi-indicator ERPs. Front. Hum. Neurosci. 15:637407. doi: 10.3389/fnhum.2021.637407

The lifetime prevalence of major depressive disorder (MDD) in adolescents is reported to be as high as 20%; thus, MDD constitutes a significant social and public health burden. MDD is often associated with nonsuicidal self-injury (NSSI) behavior, but the contributing factors including cognitive function have not been investigated in detail. To this end, the present study evaluated cognitive impairment and psychosocial factors in associated with MDD with NSSI behavior. Eighteen and 21 drug-naïve patients with first-episode MDD with or without NSSI (NSSI+/– group) and 24 healthy control subjects (HC) were enrolled in the study. The Hamilton Anxiety Scale (HAMA), Hamilton Depression Scale (HAMD), Adolescent Self-injury Questionnaire, Beck Scale for Suicide Ideation–Chinese Version (BSI-CV), Shame Scale for Middle School Students, Sensation Seeking Scale (SSS) and Childhood Trauma Questionnaire (CTQ) were used to assess depression-related behaviors, and event-related potentials (ERPs) were recorded as a measure of cognitive function. The latency of the N1, N2, P3a, P3b, and P50 components of ERPs at the Cz electrode point; P50 amplitude and P50 inhibition (S1/S2) showed significant differences between the 3 groups. CTQ scores also differed across three groups, and the NSSI– and NSSI+ groups showed significant differences in scores on the Shame Scale for Middle School Students. Thus, cognitive function was impaired in adolescents with MDD with NSSI behavior, which was mainly manifested as memory decline, attention and executive function deficits, and low anti-interference ability. We also found that childhood abuse, lack of social support, and a sense of shame contributed to NSSI behavior. These findings provide insight into the risk factors for MDD with NSSI behavior, which can help mental health workers more effectively diagnose and treat these patients.

Keywords: cognitive impairment, adolescent, major depressive disorder, nonsuicidal self-injury behavior, event-related potential

INTRODUCTION

Major depressive disorder (MDD) is a common chronic mental disease characterized by persistent sadness, apathy, and anhedonia. MDD is associated with high rates of morbidity, recurrence, and suicide and has a low cure rate, and is often accompanied by cognitive impairment (Bayes and Parker, 2018). The prevalence of MDD is 4.4% worldwide and 4.2% in China (World Health Organization, 2017). Among adolescents in China, the rate of MDD is 15–20% and the lifetime prevalence may be as high as 20%, with a male-to-female ratio of 1:2 (Zheng et al., 2018).

Nonsuicidal self-injury (NSSI) behavior involves direct, intentional injury to one's body without suicidal intent, and is socially and culturally unacceptable (Ross and Heath, 2002). Common forms of NSSI include skin or wrist cutting, hair pulling, head hitting, biting, beating, scalding, acupuncture, pinching, etc. (Leong et al., 2014). NSSI behavior is listed as an independent clinical disorder in the Diagnostic and Statistical Manual of Mental Disorders, 5th Edition (DSM-V) (Andover, 2014; Zetterqvist, 2015). The incidence of NSSI behavior among adolescents is 10–20% (Zetterqvist et al., 2013; Célia et al., 2017). The co-occurrence of NSSI behavior with MDD in adolescents is mainly related to difficulties in interpersonal relationships, low self-esteem, childhood abuse, and lack of social support (Jiang et al., 2011; VanDerhei et al., 2014; Barreto Carvalho et al., 2017; Wang et al., 2017). One study found that shame and guilt were significant positive and negative predictors, respectively, of NSSI behavior (Xie et al., 2007).

Cognitive distortions and negative cognition contribute to adolescent suicide (Xie et al., 2017). Event-related potentials (ERPs) reflect brain activity and are a reliable indicator of cognitive function, and are thus used to diagnose diseases (Zhang et al., 2019). P1 latency was shown to be significantly delayed in patients with depression, suggesting a poor ability to attend to and discriminate between stimuli (Zhang et al., 2007; Liu W. et al., 2017; Liu Y. H. et al., 2017). Most studies have used ERPs to explore cognitive function in patients with depression but few have focused on adolescent NSSI behavior, although one study demonstrated that ΔFN [To objectively assess initial response to reward, they utilized the feedback negativity (FN) event-related potential, a well-established psychophysiological marker of reward responsiveness. ΔFN (i.e., FN to losses minus FN to gains)] is a psychophysiologic indicator of NSSI risk (Tsypes et al., 2018).

We speculated that cognitive deficits underlie NSSI behavior, and that adolescents with MDD with NSSI behavior show specific alterations in cognitive function. To test this hypothesis, we measured ERPs in adolescent patients with MDD and compared these findings to behavioral test scores from a battery of neuropsychological tests, with the aim of clarifying the features of and factors that contribute to MDD with NSSI behavior.

MATERIALS AND METHODS

Participants

The Research Ethics Committee of Shanxi Medical University First Hospital approved the study protocol. The study included 63 subjects aged 10–22 years: 39 drug-naïve patients with first-episode MDD and 24 HC individuals. The drug-naive, first-episode MDD participants were recruited from the Department of Psychiatry, First Hospital of Shanxi Medical University, Taiyuan, China. The HC subjects were recruited from Taiyuan, China, using advertisement in the community. All participants were evaluated by two trained psychiatrists independently to determine the presence or absence of Axis I psychiatric diagnoses using the Structured Clinical Interview for Diagnostic and Statistical Manual of Mental Disorders, Five Edition (DSM-V) Axis I Disorders (SCID).

Inclusion and Exclusion Criteria for Patients With MDD

The inclusion criteria for MDD patients were as follows: (1) age between 10 and 22 years with no restrictions on gender; (2) met the DSM-V diagnostic criteria for MDD; (3) 24-item Hamilton Depression Scale (HAMD-24) score $\geq$20; (4) first-episode MDD with no previous use of antidepressant or other psychotropic medications; and (5) volunteered to participate in the study and signed the informed consent form. The exclusion criteria were as follows: (1) previous manic or hypomanic episodes; (2) any co-occurring mental disorder; (3) alcohol dependence or abuse; (4) hereditary and organic diseases; (5) intellectual disability; (6) personal or family history of epileptic seizures; (7) history of electroconvulsive therapy; (8) visual or hearing impairment; and (9) other severe physical disabilities or disorders.

Inclusion and Exclusion Criteria for HC Subjects

Inclusion criteria for HC subjects were as follows: (1) age 10–22 years; (2) no mental disorder found in the initial screening; (3) matched to the MDD patients in terms of sex and education level; and (4) participated voluntarily and signed the informed consent form. The exclusion criteria were as follows: (1) organic disease; (2) alcohol abuse within 30 days or alcohol or drug dependence within 6 months prior to the screening; (3) participation in other clinical trials in the previous 3 months; and (4) other conditions that disqualified the subject from the study, as determined by the investigators.

Measures

Eligible participants were asked to provide sociodemographic information including name, gender, age, education years, occupation, ethnicity, residence, religious affiliations, etc. For correlations between clinically related variables and neural measures, we used the HAMD-24, Hamilton Anxiety Scale (HAMA) to assess the severity of depressive and anxiety symptom. Beck Scale for Suicide Ideation–Chinese Version (BSI-CV) was used to evaluate suicide ideation and attempts.

Behavior and severity of NSSI was assessed using the Youth Self-injury Questionnaire, a 18-items self-report scale that assesses NSSI behavior and severity; According to the assessment of the number of NSSI in the "past year," it was divided into four grades: 0, 1, 2–4, 5 and above, and the score was 0–3. The assessment of the degree of physical injury was divided into five grades: no, mild, moderate, severe and extremely severe, and the score was 0–4. Eligible patients were categorized in the NSSI group (NSSI+) if they have self-injurious behavior. Patients were

included in No self-inflicted injury group (NSSI–) if they don't have self-injurious behavior. The final subgroups included 18 patients categorized as NSSI+ and 21 as NSSI–.

Sensation Seeking Scale (SSS) and Shame Scale for Middle School Students were used to assess social support and shame; Childhood abuse was assessed using the Childhood Trauma Questionnaire (CTQ). The questionnaire consists of five subscales, namely emotional abuse, physical abuse, sexual abuse, emotional neglect, and physical neglect. Each subscale contains five items, and each item is rated on a five scale.

Cognitive function was evaluated by measuring ERPs (P300, N400, N170, and P50 were used to assess, respectively, executive function and memory, language function, face recognition ability and ability to selectively process stimuli).

ERP Parameters

ERP data were collected using the 64-electrode NEMUS 2 system (EB Neuro, Florence, Italy). Recording electrodes were placed at the Fz, Cz, and Pz positions; the electrode at the Cz position was the standard and those at the Fz and Pz positions were references for waveform identification. Reference electrodes were placed on the mastoid processes (M1 and M2), and the ground electrode was placed in the middle of the parietal lobe.

P50 Detection

We measured the auditory ERP P50 component in response to 500-Hz, 60-dB short-range pure tones presented 32–64 times in pairs with superposition. The interval between the first and second stimuli (S1 and S2, respectively) was 0.5 s, with a paired stimulus interval of 10 s. The task had a total duration of 6 min. Electrode resistance was <5 kΩ; a bandpass filter of 0.1–300 Hz was applied; and the data were segmented into the time window from −200 to 800 ms.

P300 Detection

The task employed the classic oddball experimental paradigm. The stimulus sequence was composed of a target stimulus (T) and nontarget stimulus (NT) at a probability ratio of 0.2/0.8; T was randomly interspersed among NT, and the task consisted of 60 T and 240 NT. Subjects were required to press a key as soon as T appeared. The stimulus frequency was 0.5–1 time/s; stimulus interval was 1–3 s; and total task duration was 14 min. Electrode resistance was <5 kΩ; bandpass filtering was applied at 0.5–200 Hz; and the time window for data segmentation was −200 to 1,200 ms.

N400 Detection

The subjects were required to sit in a chair with their muscles relaxed and remain awake with eyes fixed on the screen. Three words were sequentially displayed on the screen, and subjects judged whether they could form a logical sentence (e.g., "Xiaoming," "in the playground," and "playing football"). Each word was presented for 100 ms and the time interval between presented words was 1,000 ms, giving the subjects 1,100 ms to respond. The total duration of the task was 3 min. Electrode resistance was <5 kΩ; the filter range was 0.53–60 Hz; and the time window for data segmentation was −200 to 1,000 ms.

N170 Detection

The procedure was similar to that used for N400 detection, except that subjects were presented with images instead of words and had to judge whether these were emotional or nonemotional. Each image was displayed for 300 ms; the time interval between images was 1,500 ms; and total task duration was 8 min. Electrode resistance was <5 kΩ, with bandpass filtering between 0.1 and 100 Hz and data segmented into the time window of −200 to 800 ms.

Statistical Analysis

Data were analyzed using SPSS v22.0 (SPSS Inc., Chicago, IL, USA). The threshold of statistical significance was set as $\alpha = 0.05$ for all analyses.

For general demographic data, categorical variables were evaluated with the χ^2 test and continuous variables were evaluated with the *t*-test or by analysis of variance (ANOVA), which was used for HAMD-24, HAMA, CTQ, SSS, Youth Self-injury Questionnaire, BSI-CV, and Shame Scale for Middle School Students scores. ANOVA was also used to analyze ERP indicators, *post-hoc* analysis was then used to compare the ERP indicators between groups; the major components of ERPs were identified and their index values determined according to the internationally recognized maximum waveforms of the time analysis window.

Pearson's correlation analysis was performed to determine the relationship between the scores of Adolescen Self-injury Questionnaire and the scores of CTQ, SSS and shame scale in NSSI+ group (MDD with NSSI behavior). The results were considered significant if $P < 0.05$, corrected by Bonferroni test.

RESULTS

Demographics, Clinical, and Psychosocial Characteristics of all Participants

The NSSI–, NSSI+ and HC groups showed significant differences in education years ($P < 0.001$); Covariance analysis showed that the influence of education years on the NSSI severity was not affected by grouping ($P > 0.05$) (**Table 1**; **Supplementary Table 1**).

The three groups showed significant differences in HAMD-24, HAMA, Adolescent Self-injury Questionnaire, BSI-CV, emotional and physical abuse, emotional and physical neglect subscales of the CTQ scale scores ($P < 0.05$). Covariance analysis showed that the main effect between grouping and HAMA, HAMD, CTQ, SSS, and BSI-CV was not significant ($P > 0.05$).

There were no significant differences between the three groups in terms of age, gender, only-child status, residence and the SSS total score ($P > 0.05$). There were statistically significant differences in Shame Scale scores between the NSSI- and NSSI+ groups ($P < 0.001$).

TABLE 1 | Demographic, clinical, and psychosocial characteristics of all participants ($N = 63$).

Variable	NSSI+	NSSI–	HC	$\chi^2/F/t$	*P*
Gender				4.179	0.128
Male	7	10	10		
Female	11	11	14		
Age, years	17.11 ± 2.54	18.91 ± 2.77	20.29 ± 0.46	7.965	0.092
Only child				0.04	0.000
Yes	10	11	13		
No	8	10	11		
Education, years	10.17 ± 2.99	11.76 ± 2.88	15.04 ± 0.86	23.649	0.000
Residence				0.948	0.635
City	12	11	13		
Rural	6	10	11		
HAMD-24	27.61 ± 1.01	25.29 ± 0.94	2.708 ± 1.04	417.893	0.000
HAMA	19.94 ± 4.41	17.57 ± 3.07	1.458 ± 0.72	280.824	0.000
Adolescent self-injury questionnaire	31.78 ± 1.55	0.00 ± 0.00	0.00 ± 0.00	531.304	0.000
BSI-CV–suicide ideation[†]	12.11 ± 0.54	0.00 ± 0.00	0.00 ± 0.00	630.180	0.000
BSI-CV–suicide risk[‡]	26.57 ± 4.16	0.00 ± 0.00	0.00 ± 0.00	232.526	0.000
Emotional abuse[a]	10.67 ± 0.75	9.38 ± 1.18	5.63 ± 0.47	10.098	0.000
Physical abuse[b]	8 ± 0.79	7.9 ± 0.82	5.29 ± 0.29	6.048	0.004
Sexual abuse[c]	6.17 ± 0.65	5.67 ± 0.22	5 ± 0	2.894	0.063
Emotional neglect[d]	16.1 ± 1.21	15.08 ± 1.38	12.54 ± 0.62	3.323	0.043
Physical neglect[e]	10.72 ± 0.92	10 ± 0.64	6.33 ± 0.19	16.079	0.000
CTQ total score	49.22 ± 2.5	49.05 ± 2.64	13.13 ± 1.54	16.568	0.000
SSS total score	21.61 ± 0.35	24.67 ± 0.77	32.54 ± 1.57	0.418	0.660

All subjects were students of Han ethnicity, not married, with no religious affiliation.
Data represent number, mean ± standard deviation.
BSI-CV, Beck Scale for Suicide Ideation–Chinese Version; HAMA, Hamilton Anxiety Scale; HAMD, Hamilton Depression Scale; CTQ, Childhood Trauma Questionnaire; SSS, Sensation Seeking Scale; HC, healthy control; NSSI, nonsuicidal self-injury; NSSI+, MDD with nonsuicidal self-injury; NSSI-, MDD with no self-inflicted injury.
[†]*Score on the suicide ideation subscale of the BSI-CV.*
[‡]*Score on the suicide risk subscale of the BSI-CV.*
[a–e]*Scores on the emotional abuse (a), physical abuse (b), sexual abuse (c), emotional neglect (d), and physical neglect (e) subscales of the CTQ.*

Group Differences in Cognitive Function

The results of the ERP analysis showed that compared to HC subjects, the latency of the N1, N2, P3a, P3b, and P50 components was significantly prolonged in the NSSI– and NSSI+ groups; additionally, the amplitude of P50 was decreased, and inhibition of P50 (S1/S2) was increased ($P < 0.05$) (**Table 2**). *Post-hoc* analysis showed that, there were no statistically significant differences between NSSI+ group and NSSI– group for the ERP components ($P > 0.05$); Compared to the HC group, P300 latency was longer in the NSSI– group and the NSSI+ group ($P < 0.05$). On the other hand, N400 latency were shorter, respectively, in the HC group than in the NSSI- group ($P < 0.05$). There were no other statistically significant differences between groups for the other ERP components (**Table 3**).

Correlation Between Psychosocial Factors and NSSI Severity

Pearson correlation was used to analyze the correlation between the NSSI severity and childhood abuse, social support and shame in NSSI+ group, and the results showed that NSSI severity was positively correlated with childhood abuse ($r = 0.667$, $P < 0.01$) and sense of shame ($r = 0.776$, $P < 0.01$), and negatively correlated with social support ($r = -0.464$, $P < 0.01$).

DISCUSSION

The present study explored cognitive impairment and psychosocial factors in first-episode untreated MDD patients with NSSI behavior. To the best of our knowledge, this study investigated for the first time the differences in cognitive function and psychosocial factors between patients diagnosed with major depression (with and without NSSI) and healthy controls. We found that the latencies on N1, N2, P3a, P3b, and P50 were significantly prolonged and the amplitudes on P50 were significantly decreased in NSSI+ group. The cognitive function of adolescents with self-injury behavior in MDD is impaired, which is mainly manifested as memory loss, dysfunction of attention and execution, and low ability of anti-interference. In addition, we also found that childhood abuse, lack of social support and sense of shame are all causes of self-injury.

Cognitive Function to MDD With NSSI Behavior in Adolescents

As the main means and index to detect cognitive function, ERP has important clinical significance in the study of cognitive impairment in patients with depression. Patients with MDD have cognitive impairment to a certain extent, which is mainly related to the dysfunction of frontal lobe (executive function)

TABLE 2 | ANOVA analysis of ERP results among the NSSI+, NSSI–, and HC groups.

ERP component		NSSI+	NSSI–	HC	*F*	*P*
Latency, ms	N1	131 ± 4.41	126 ± 4.78	115 ± 3.33	4.369	0.017
	P2	216 ± 3.28	215 ± 3.15	207 ± 2.58	2.894	0.063
	N2	250 ± 4.56	246 ± 4.29	230 ± 3.56	6.915	0.002
	P3a	343 ± 5.31	330 ± 3.99	313 ± 2.41	13.814	0.000
	P3b	373 ± 4.52	364 ± 5.03	343 ± 3.19	21.159	0.000
	L1	57.2 ± 2.9	55.3 ± 2.3	50.9 ± 1.74	4.718	0.043
	L2	56.7 ± 3.7	54.5 ± 3.2	49.7 ± 1.32	5.726	0.037
	N400	430 ± 4.67	429 ± 4.47	417 ± 3.74	2.564	0.085
	N170	192 ± 5.6	185 ± 5.03	177 ± 2.8	1.526	0.226
Amplitude, μV	N1	−2.5 ± 0.79	−1.9 ± 3.02	−1.5 ± 0.59	1.165	0.319
	P2	3.49 ± 0.87	3.51 ± 1.4	5.51 ± 1.71	0.969	0.385
	N2	2.01 ± 1.25	2.03 ± 0.7	2.54 ± 1.63	0.326	0.723
	P3a	9.8 ± 1.62	10.7 ± 2.5	12.7 ± 2.02	1.366	0.263
	P3b	10.8 ± 1.8	11.2 ± 0.7	13.4 ± 2.1	0.791	0.458
	S1	0.31 ± 0.21	0.52 ± 0.37	−0.49 ± 0.4	4.73	0.730
	S2	0.32 ± 0.26	0.45 ± 0.21	−0.37 ± 0.2	2.965	0.046
	N400	6.26 ± 0.99	5.47 ± 1.67	4.81 ± 2.29	0.509	0.603
	N170	2.86 ± 1.34	2.35 ± 1.01	1.34 ± 0.63	1.800	0.174
S1/S2		0.54 ± 0.13	0.55 ± 0.3	0.48 ± 0.21	5.826	0.008

Data represent mean ± standard deviation.
ERP, event-related potential; HC, healthy control; NSSI, nonsuicidal self-injur; NSSI+, MDD with nonsuicidal self-injury; NSSI-, MDD with no self-inflicted injury.

and temporal lobe (memory) (Hansenne et al., 1996). Based on our findings, compared with NSSI- group and HC group, the latency of N1, N2, P3a, and P3b in NSSI+ group was significantly prolonged and the amplitude decreased. It is speculated that neuronal excitability and cognitive processing speed decreased in NSSI+ group, and there was some impairment of executive function and memory ability.

In this study, we found that the latency and amplitude of P50 in NSSI+ group were worse than those in NSSI– group, and the inhibition of P50 in P50 group was worse than that in NSSI– group. The P50 component of ERP reflects the selective processing of significant external stimuli in the brain. P50 inhibition-measured by S2/S1 ratio-is an indicator of screening or gating intensity (Wang et al., 2011). The weaker the gating function of MDD patients is, the lower the selective processing ability to important external stimuli is. Combined with previous studies (Wang et al., 2012), we found that there are some defects in the screening ability of unrelated stimuli in adolescent depression patients with NSSI behavior.

The N400 is used to test language processing ability; the N400 latency reflects the speed of semantic processing in the brain, while the amplitude reflects the speed at which words are processed in context. A smaller N400 amplitude indicates a higher speed (Kutas and Federmeier, 2011; Zhang et al., 2012). In this group of MDD patients with self-injury behavior, the latency of N400 was longer and the amplitude was higher, which is consistent with previous studies (Liang and Zhou, 2014). Compared with NSSI– group, NSSI+ group has more obvious language barrier, which is mainly manifested in slower language processing speed.

N170, ERP faces specific components, is a negative detection of the occipito-temporal region after 130–190 milliseconds of a face, and reflects the structure of the coding phase faced by the brain processing and early detection of face information (i.e., distinguishing face from non-face) (Itier and Taylor, 2004). The results showed that compared with NSSI- group, the latency of N170 in NSSI+ group was longer, the amplitude was lower, and the speed of face image recognition was slower, so we speculated that the face recognition ability of adolescent depression patients with NSSI behavior decreased.

Psychosocial Factors Contributing to MDD With NSSI Behavior in Adolescents

Childhood Abuse Contributing to MDD With NSSI Behavior in Adolescents

Childhood abuse refers to various forms of physical or mental abuse, sexual abuse, neglect, commercial or other forms of exploitation that cause actual or potential harm to the health, survival, development and dignity of the child, subject to appropriate responsibilities and abilities (Yao et al., 2010). Severe or moderate abuse; emotional abuse; unwanted sexual contact; repeated contact sexual assault/non-contact sexual assault is one of the main risk factors for self-injury behavior (Yu et al., 2013). Our study found that the scores of emotional neglect, physical neglect, emotional abuse and physical abuse in the NSSI+ group were higher than those in the NSSI– group. Patients in the NSSI+ group often reported various kinds of abuse and neglect in childhood. Some literature also showed that emotional and physical abuse and neglect experienced in childhood were risk factors for self-injury behavior (Brodsky

TABLE 3 | *Post-hoc* analysis of ERP latency among the NSSI+, NSSI– and HC groups.

ERP component		NSSI+ vs. NSSI–	NSSI+ vs. HC	NSSI- vs. HC
Latency, ms	N1	−4.913(1.000)	−16.681(0.02)	−11.768(0.04)
	P2	−1.103(1.000)	−9.056(0.112)	−7.952(0.167)
	N2	−3.563(1.000)	−19.778(0.004)	−16.214(0.016)
	P3a	0.635(1.000)	−23.597(0.000)	−24.232(0.000)
	P3b	1.063(1.000)	−31.681(0.000)	−32.744(0.000)
	L1	1.161(0.705)	−1.297(0.039)	−2.458(0.048)
	L2	1.213(0.649)	−1.843(0.041)	−2.159(0.036)
	N400	0.317(1.000)	−11.278(0.205)	−11.595(0.153)
	N170	−74.476(0.431)	−77.708(0.350)	−3.232(1.000)
Amplitude, μV	N1	0.838(1.000)	−1.786(0.405)	0.948(1.000)
	P2	−2.225(0.632)	−2.021(0.723)	0.204(1.000)
	N2	−1.285(1.000)	−0.508(1.000)	0.778(1.000)
	P3a	−2.841(0.543)	−3.137(0.386)	−0.296(1.000)
	P3b	−2.577(1.000)	−2.389(1.000)	0.188(1.000)
	S1	−0.054(1.000)	−0.805(0.937)	−0.751(0.976)
	S2	0.251(1.000)	−0.591(0.746)	−0.649(0.859)
	N400	−2.281(0.965)	−1.492(1.000)	0.789(1.000)
	N170	0.052(1.000)	−2.447(0.372)	−2.499(0.304)
S1/S2		−1.384(1.000)	2.984(1.000)	3.142(1.000)

Data represent mean difference (P).
ERP, event-related potential; HC, healthy control; NSSI, nonsuicidal self-injury; NSSI+, MDD with nonsuicidal self-injury; NSSI–, MDD with no self-inflicted injury.

and Stanley, 2008; Fergusson et al., 2011). Therefore, based on our findings, we speculate that the more abuse and neglect experienced in childhood, the greater the probability of self-injury when they grow up.

Childhood abuse, as a negative experience, will affect the normal function of children's brain neurotransmitters and hormones, including the development of brain regions related to coping problems and emotional control. It will have a series of adverse effects on children's physical and mental health and the development of cognitive function, thus increasing the risk of adolescents' risky behaviors (Gilbert et al., 2015). Factors that affect NSSI behavior include all aspects, although we can't directly determine the childhood abuse and the inevitable cause-and-effect relationship between NSSI behavior (Su et al., 2015), but it exists as a kind of risk factors, should remind us to strengthen the neglect and abuse of children, to give children a certain support and unconditional love, prevent the happening of the risk behavior.

Social Support Contributing to MDD With NSSI Behavior in Adolescents

It is also worth noting that the study showed that the social support score of MDD patients (with or without NSSI) was lower than that of HC subjects, and the social support score of the NSSI+ group was also lower than that of the NSSI– group. Patients in the NSSI+ group often report less family support, their ideas are not understood by others, and there are few companions, so when they encounter stress or setbacks, they cannot or even will not seek help. At this time, self-injury has become an effective way for them to ease their emotions and relieve stress. NSSI behavior is not uncommon in adolescent students, and is particularly common in middle school students between the ages of 13 and 17. Adequate social support can significantly reduce the risk of mental health problems such as NSSI and suicide (Duggan et al., 2015). Conversely, a lack of social support and childhood abuse is linked to NSSI behavior in later life (Liu W. et al., 2017; Liu Y. H. et al., 2017).

Adolescent students are more sensitive, they have extremely unstable emotions, unpredictable and difficult behavior: storms and stress, they are still in an important period of physical and mental development, in this period, we cannot continue to use "storm and stress" to misinterpret adolescent problems. The research on the social development of teenagers mostly focuses on the changes of family and peer roles. In the interaction with their peers, teenagers gradually determine the social factors of their own identity in the process of development, and then determine what kind of person they become (Gao, 2013). During this period, parents' company, friends' communication and teachers' care all become powerful and effective sources of social support for them.

Shame Contributing to MDD With NSSI Behavior in Adolescents

In addition, we also observed the relationship between NSSI behavior and shame. In this study, self-injury was used as a way of self-punishment to study the relationship between NSSI behavior and shame. The results showed that the shame score of NSSI+ group was higher than that of NSSI– group and HC group. Guilt, shame and strong disgust increased before NSSI and decreased after NSSI. According to the results of the study, we found that shame is an important factor affecting self-harm behavior, with the increase of shame, the degree of self-harm will become more and more serious. This result has also been confirmed by many studies (Linehan, 1993; Tanaka et al., 2015).

It has been suggested that NSSI is the expression of anger toward oneself, and self-directed anger and self-deprecation are features of individuals who engage in NSSI (Tanaka et al., 2015; Wang et al., 2019). There are usually negative emotions before self-injury, leading to depression and self-hatred. Individuals take different behaviors to alleviate these emotions and achieve self-coordination and self-balance, including self-injury. In a study on the influencing factors of NSSI behavior among adolescents, it was found that 70% of teenagers reported "I don't like myself" and 63% chose to say "I'm mad at myself" (Laye et al., 2005). Therefore, self-punishment is one of the most common causes of self-injury behavior (Linehan, 1993). In real life, teenagers will have negative emotional experience when they encounter negative life events, and they lack effective ways to deal with emotions, so they choose self-injury to alleviate their negative emotions.

Limitations

This study had certain limitations. Firstly, the sample size was small, and although we found evidence of cognitive impairment

in adolescents with MDD with NSSI behavior, this needs to be validated in a larger cohort. Compared with healthy adolescents, MDD with NSSI behavior in adolescents have obvious cognitive impairment, but compared with adolescent depressive patients without NSSI behavior, there is no significant difference in cognitive function between the two groups. This may be due to the small sample size (18 patients categorized as NSSI+ and 21 as NSSI–), resulting in no significant difference between the two groups. Future studies should include more samples to verify. Secondly, this was a cross-sectional study and there was no long-term follow-up; in the future it would be useful to investigate whether interventions such as psychological counseling, drug treatment, or physical therapy can alter cognitive function in patients with MDD with comorbid NSSI behavior.

CONCLUSION

Compared to adolescent patients with MDD with no self-inflicted injury, those with NSSI behaviors had significantly impaired cognitive function, which was mainly manifested as memory loss, inattention, reduced executive function, and poor resource utilization. Additionally, compared to HC subjects, adolescent patients with MDD with NSSI behavior had poor information screening and anti-interference abilities as well as deficits in language processing and face recognition and processing. The main psychosocial factors associated with NSSI in adolescents with MDD were childhood abuse, lack of social support, and a sense of shame. The results of this study highlight the risk factors for MDD comorbid with NSSI behavior, which can help mental health workers more effectively diagnose and treat these patients.

DATA AVAILABILITY STATEMENT

The raw data supporting the conclusions of this article will be made available by the authors, without undue reservation.

ETHICS STATEMENT

The studies involving human participants were reviewed and approved by Ethics Committee of First Hospital of Shanxi Medical University. Written informed consent to participate in this study was provided by the participants' legal guardian/next of kin. Written informed consent was obtained from the individual(s), and minor(s)' legal guardian/next of kin, for the publication of any potentially identifiable images or data included in this article.

AUTHOR CONTRIBUTIONS

YW, YX, and DQ contributed to study design and were involved in data acquisition, analysis, and interpretation. XZ contributed to data acquisition. SG, NS, CY, MH, and ZL contributed to study design and data interpretation. All authors participated in the drafting or critical review of the article, gave final approval of the version to be published, and agree to be accountable for all aspects of the work.

FUNDING

This work was supported by grants from the National Science Foundation of China (no. 81601193); Key Research and Development Project (International Cooperation) of Shanxi Province (no. 201903D421059); Shanxi Province Science Foundation for Youths (no. 2015021204); Research Project Supported by Shanxi Scholarship Council of China (no. 2015-100); and The First Hospital of Shanxi Medical University Foundation for Youths Innovation (no. YC1409).

SUPPLEMENTARY MATERIAL

The Supplementary Material for this article can be found online at: https://www.frontiersin.org/articles/10.3389/fnhum.2021.637407/full#supplementary-material

REFERENCES

Andover, M. S. (2014). Non-suicidal self-injury disorder in a community sample of adults. *Psychiatry Res.* 219, 305–310. doi: 10.1016/j.psychres.2014.06.001

Barreto Carvalho, C., da Motta, C., Sousa, M., and Cabral, J. (2017). Biting myself so I don't bite the dust: Prevalence and predictors of deliberate self-harm and suicide ideation in Azorean youths. *Braz. J. Psychiatry* 9, 252–262. doi: 10.1590/1516-4446-2016-1923

Bayes, A. J., and Parker, G. B. (2018). Comparison of guidelines for the treatment of unipolar depression: a focus on pharmacotherapy and neurostimulation. *Acta Psychiatr. Scand.* 137, 459–471. doi: 10.1111/acps.12878

Brodsky, B. S., and Stanley, B. (2008). Adverse childhood experiences and suicidal behavior. *Psychiatr. Clin. North Am.* 31, 223–235. doi: 10.1016/j.psc.2008.02.002

Célia, B. C., Da, M. C., Marina, S., Joana, C. (2017). Biting myself so I don't bite the dust: prevalence and predictors of deliberate self-harm and suicide ideation in Azorean youths[J]. *Braz. J. Psychiatry.* 39, 252–262.

Duggan, J., Heath, N., and Hu, T. (2015). Non-suicidal self-injury maintenance and cessation among adolescents: A one-year longitudinal investigation of the role of objectified body consciousness, depression and emotion dysregulation. *Child Adolesc. Psychiatry Ment. Health.* 9:21. doi: 10.1186/s13034-015-0052-9

Fergusson, D. M., Boden, J. M., Horwood, L. J., Miller, A. L., and Kennedy, M. A. (2011). MAOA, abuse exposure and antisocial behaviour: 30-Year longitudinal study. *Br. J. Psychiatry* 198, 457–463. doi: 10.1192/bjp.bp.110.086991

Gao, J. Y. (2013). *Influence Factors of Psychosocial Stress on Blood Glucose Fluctuation in Patients With Type 2 Diabetes Mellitus* (Master's thesis). Soochow University, Jiangsu.

Gilbert, L. K., Breiding, M. J., Merrick, M. T., Tompson, W. W., Ford, D. C., Dhingra, S. S., et al. (2015). Childhood adversity and adult chronic disease. *Am. J. Prev. Med.* 48, 345–349. doi: 10.1016/j.amepre.2014.09.006

Hansenne, M., Pitchot, W., Gonzalez Moreno, A., Zaldua, I. U., and Ansseau, M. (1996). Suicidal behavior in depressive disorder: an event-related potential study. *Biol. Psychiatry.* 40, 116–122. doi: 10.1016/0006-3223(95)00372-X

Itier, R. J., and Taylor, M. J. (2004). N170 or N1? Spatiotemporal differences between object and face processing using ERPs. *Cereb. Cortex.* 14, 132–142. doi: 10.1093/cercor/bhg111

Jiang, G. R., Yu, L. X., and Zheng, Y. (2011). Research on self-injury behavior: current situation, problems and suggestions. *Progr. Psychol. Sci.* 19, 861–873. doi: 10.3724/SP.J.1042.2011.00861

Kutas, M., and Federmeier, K. D. (2011). Thirty years and counting: Finding meaning in the N400 component of the event-related brain potential

(ERP). *Annu. Rev. Psychol.* 62, 621–647. doi: 10.1146/annurev.psych.093008.131123

Laye, G. A., and Schonert-Reichl, K., A. (2005). Nonsuicidal self-harm among community adolescents: understanding the "whats" and "whys" of self-harm. *J. Youth Adolesc.* 34, 447–457. doi: 10.1007/s10964-005-7262-z

Leong, C. H., Wu, A. M., and Poon, M. M. (2014). Measurement of perceived functions of non-suicidal self-injury for Chinese adolescents. *Arch. Suicide Res.* 18, 193–212. doi: 10.1080/13811118.2013.824828

Liang, Y. H., and Zhou, S. (2014). Application of Chinese idiom N400 in the detection of event-related potentials in patients with neurasthenia and depression. *J. Appl. Clin. Med.* 18, 33–35. doi: 10.7619/jcmp.201401010

Linehan, M. M. (1993). *Cognitive-Behavioral Treatment of Borderline Personality Disorder*. New York, NY: The Guilford Press.

Liu, W., Wan, Y. H., Tao, F. B., Hao, J. H. (2017). Mediating role of social support in the association between childhood abuse and adolescent non-suicidal self-injury. *Chin. J. Ment. Health*. 3, 230–234.

Liu, Y. H., Gao, Y. G., and Qing, J. (2017). Analysis of brain evoked potentials in patients with primary depressive disorder. *Guangxi Med. Sci.* 2017, 106–108. doi: 10.11675/j.issn.0253-4304.2017.04.30

Ross, S., and Heath, N. (2002). A study of the frequency of self-mutilation in a community sample of adolescents. *J. Youth Adolesc.* 31, 67–77. doi: 10.1023/A:1014089117419

Su, J., Chen, J., Wan, Y. H., Zhong, C., Hu, X., Tao, F. B., et al. (2015). The relationship between childhood abuse and middle school Students' NSSI. *Chin. J. School Health* 9, 1326–1329.

Tanaka, H., Yagi, A., Komiya, A., Mifune, N., and Ohtsubo, Y. (2015). Shame-prone people are more likely to punish themselves: a test of the reputation-maintenance explanation for self-punishment. *Evol. Behav. Sci.* 9, 1–7. doi: 10.1037/ebs0000016

Tsypes, A., Owens, M., Hajcak, G., and Gibb, B. E. (2018). Neural reward responsiveness in children who engage in nonsuicidal self-injury: an ERP study. *J. Child Psychol. Psychiatry* 59, 1289–1297. doi: 10.1111/jcpp.12919

VanDerhei, S., Rojahn, J., Stuewig, J., and McKnight, P. E. (2014). The effect of shame-proneness, guilt-proneness, and internalizing tendencies on non-suicidal self-injury. *Suicide Life Threat. Behav.* 44, 317–330. doi: 10.1111/sltb.12069

Wang, D., Zhu, K. M., and Tan, S. P. (2011). Characteristics of auditory sensory gated evoked potential P50 in chronic schizophrenia. *Chin. J. Mental Health.* 25, 556–560. doi: 10.3969/j.issn.1000-6729.2011.07.018

Wang, Q. Q., Wei, M., and Liu, X. (2017). Mechanism and influencing factors of adolescent NSSI behavior: From the perspective of emotion management. *Psychol. Dev. Educ.* 33, 759–768. doi: 10.3969/j.issn.1005-3220.2018.04.001

Wang, Y., Li, Z. Z., Huang, J., Chen, X. S., Lou, F. Y., Chen, C., et al. (2012). Auditory P50 and cognitive function in refractory depression and first-episode depression. *Chin. J. Med.* 009, 16–19. doi: 10.1186/1749-8546-7-16

Wang, Y. L., Chen, H. L., Qin, Y. L., and Lin, X. Y. (2019). Self-punishment function of adolescent self-injury: Does it originate from guilt or shame? *Psychol. Dev. Educ.* 35, 3–100. doi: 10.16187/j.cnki.issn1001-4918.2019.02.11

World Health Organization (2017). *Depression and Other Common Mental Disorders. Global Health Estimates.* Geneva: World Health Organization. Available at: https://www.who.int/mental_health/management/depression/prevalence_global_health_estimates/en/ (accessed November 25, 2020).

Xie, L. J., Tang, Q. S., and Huo, A. R. (2007). Effect of Yi nao jie yu prescription on brain evoked potential in patients with primary depressive disorder. *J. Tradit. Chin. Med.* 48, 322–324. doi: 10.3321/j.issn:1001-1668.2007.04.013

Xie, W., Kuang, R. H., Mao, S. J., Tang, H. M., Fu, Y. U., Li, J. N., et al. (2017). Research progress on the relationship between depression and non-suicidal self-injury. *J. Nanchang Univ. Med. Ed.* 57, 100–103. doi: 10.13764/j.cnki.ncdm.2017.02.025

Yao, Y. H., Chen, D. Y., Zhou, F., and Liu, Q. Y. (2010). The relationship between youth violence and childhood abuse by teachers in community. *Chin. J. School Health.* 35, 76–77.

Yu, T. T., Ge, X., Hu, T. J., Liu, Y., Zhang, W. W., Wang, G. F., et al. (2013). Correlation between childhood abuse experience and injury and violence of junior high school students. *Chin. School Doctor* 27, 161–165.

Zetterqvist, M. (2015). The DSM-5 diagnosis of nonsuicidal self-injury disorder: a review of the empirical literature. *Child Adolesc. Psychiatry Ment. Health* 9:31. doi: 10.1186/s13034-015-0062-7

Zetterqvist, M., Lundh, L. G., Dahlström, O., and Svedin, C. G. (2013). Prevalence and function of non-suicidal self-injury (NSSI) in a community sample of adolescents, using suggested DSM-5 criteria for a potential NSSI disorder. *J. Abnorm. Child. Psychol.* 41, 759–773. doi: 10.1007/s10802-013-9712-5

Zhang, C., Chen, X. S., Ren, Q. S., Yi, Z. H., Chen, C., et al. (2012). A comparative study on brain cognition N400 between generalized anxiety disorder and obsessive-compulsive disorder. *Chin. J. Med.* 92, 2468–2472. doi: 10.3760/cma.j.issn.1006-7884.2014.06.009

Zhang, M., Chen, Y. R., Guo, H. D., Ma, Y., and Tang, J. (2019). Mediating role of emotion management between aggression and NSSI in rural middle school students. *Chin. School Health* 7, 980–984. doi: 10.16835/j.cnki.1000-9817.2019.07.006

Zhang, X. K., Zhang, M. Y., and Wu, W. Y. (2007). Clinical follow-up study of five brain evoked potential indexes in patients with depression. *Chin. J. Psychiatry.* 40, 234–237. doi: 10.3760/j.issn:1006-7884.2007.04.011

Zheng, L. F., Yang, L., and Tan, S. (2018). A survey of depressive disorders in adolescents. *Prev. Med.* 4, 338–340. doi: 10.19485/j.cnki.issn2096-5087.2018.04.004

Conflict of Interest: The authors declare that the research was conducted in the absence of any commercial or financial relationships that could be construed as a potential conflict of interest.

frontiers in Human Neuroscience

ORIGINAL RESEARCH
published: 25 February 2021
doi: 10.3389/fnhum.2021.610947

Structural and Functional Changes Are Related to Cognitive Status in Wilson's Disease

Sheng Hu[1,2†], Chunsheng Xu[1,3†], Ting Dong[3], Hongli Wu[2], Yi Wang[2], Anqin Wang[3], Hongxing Kan[2] and Chuanfu Li[3*]*

[1] Center for Biomedical Engineering, University of Science and Technology of China, Hefei, China, [2] School of Medical Information Engineering, Anhui University of Chinese Medicine, Hefei, China, [3] Medical Imaging Center, First Affiliated Hospital of Anhui University of Chinese Medicine, Hefei, China

Patients with Wilson's disease (WD) suffer from prospective memory (PM) impairment, and some of patients develop cognitive impairment. However, very little is known about how brain structure and function changes effect PM in WD. Here, we employed multimodal neuroimaging data acquired from 22 WD patients and 26 healthy controls (HC) who underwent three-dimensional T1-weighted, diffusion tensor imaging (DTI), and resting state functional magnetic resonance imaging (RS-fMRI). We investigated gray matter (GM) volumes with voxel-based morphometry, DTI metrics using the fiber tractography method, and RS-fMRI using the seed-based functional connectivity method. Compared with HC, WD patients showed GM volume reductions in the basal ganglia (BG) and occipital fusiform gyrus, as well as volume increase in the visual association cortex. Moreover, whiter matter (WM) tracks of WD were widely impaired in association and limbic fibers. WM tracks in association fibers are significant related to PM in WD patients. Relative to HC, WD patients showed that the visual association cortex functionally connects to the thalamus and hippocampus, which is associated with global cognitive function in patients with WD. Together, these findings suggested that PM impairment in WD may be modulated by aberrant WM in association fibers, and that GM volume changes in the association cortex has no direct effect on cognitive status, but indirectly affect global cognitive function by its aberrant functional connectivity (FC) in patients with WD. Our findings may provide a new window to further study how WD develops into cognitive impairment, and deepen our understanding of the cognitive status and neuropathology of WD.

Keywords: Wilson's disease, functional connectivity, diffusion tensor imaging, functional magnetic resonance imaging, visual association cortex, association fibers, limbic fibers

OPEN ACCESS

Edited by:
Wei Liao,
University of Electronic Science and Technology of China, China

Reviewed by:
Zhiqun Wang,
Department of Radiology, Aerospace Center Hospital, China
Zhao Qing,
Nanjing Drum Tower Hospital, China

***Correspondence:**
Ting Dong
dongting2002@sina.com
Chuanfu Li
13956078816@126.com

† These authors have contributed equally to this work

Specialty section:
This article was submitted to Brain Imaging and Stimulation, a section of the journal Frontiers in Human Neuroscience

Received: *28 September 2020*
Accepted: *20 January 2021*
Published: *25 February 2021*

Citation:
Hu S, Xu C, Dong T, Wu H, Wang Y, Wang A, Kan H and Li C (2021) Structural and Functional Changes Are Related to Cognitive Status in Wilson's Disease. Front. Hum. Neurosci. 15:610947. doi: 10.3389/fnhum.2021.610947

INTRODUCTION

Wilson's disease (WD) is an inherited disorder of copper metabolism characterized pathologically by the deposition of copper in many organs, particularly the brain and liver, resulting in numerous clinical symptoms (Bandmann et al., 2015; Czlonkowska et al., 2018). Cognitive impairment is relatively frequent in WD patients, mainly with the frontal lobe syndrome and subcortical dementia (Lang, 1989; Lang et al., 1990). Cognitive impairment greatly affects the quality of life of

WD patients. After suffering from cognitive impairment, WD patients will firstly experience prospective memory (PM) impairment. PM, which is a memory component most closely related to the planning or goal-making of daily activities, is defined as the future plans or intention of memory (Arnold et al., 2015). PM include event-based PM (EBPM) and time-based PM (TBPM), which are required to perform purposeful behaviors in the presence of specific target events and goals (McDaniel and Einstein, 2011). Recent studies have reported that PM impairment is associated with gray matter (GM) loss in the basal ganglia (BG) and structural changes in frontal and occipital whiter matter (WM) (Dong et al., 2016, 2019). However, how structural and functional changes affect PM of WD is still unknown.

Advances in neuroimaging have greatly improved the understanding of pathophysiology in WD, especially brain alterations in association with neurological symptoms. Structural brain MRI studies have revealed that widespread alternations in extrapyramidal system nuclei (putaminal and thalamic softening cavitation, caudate nucleus shrinkage, spongy change in the midbrain, and atrophy in thalamus) served as the key features to distinguish the neurological symptoms of WD (Koziæ et al., 2003; Stezin et al., 2016; Zou et al., 2019). Another study reported that GM atrophy in the frontal, parietal, and temporal lobes had a positive correlation with duration of disease (Stezin et al., 2016). One study investigating WM microstructure reported a decreased fractional anisotropy (FA) of frontal and occipital WM, bilateral internal capsules, midbrain, and pons in WD patients with neurological symptoms (Jadav et al., 2013). A recent resting state functional magnetic resonance imaging (RS-fMRI) study using machine learning to classify brain networks discovered that aberrant brain networks in WD patients are associated with severity of clinical symptoms (Jing et al., 2019). However, PM as crucial clinical features in WD patients was not taken into account by the majority of neuroimaging studies.

Association fibers (including superior longitudinal fasciculus, inferior longitudinal fasciculus, inferior fronto-occipital fasciculus, and uncinate fasciculus) and limbic system fibers (including cingulum) are reported to relate to brain function, regarding cognitive control, working memory, and perception of visual space (Delano-Wood et al., 2012; Metzler-Baddeley et al., 2012; Martino and De Lucas, 2014; Motomura et al., 2014; Metoki et al., 2017; Herbet et al., 2018). Therefore, association and limbic system fiber might contribute to PM impairment in patients with WD. Taking this assumption into account, the association and limbic system fibers are structures of interest in the current study.

Here, we hypothesize that WM changes in association and limbic system fibers and GM changes are associated with PM impairment in WD, and furtherly aberrant changes in GM volume would cause brain function deficits that are associated with cognitive status in patients with WD. In order to solve these problems, the present study collected structural magnetic resonance imaging (sMRI) and diffusion tensor imaging (DTI) to investigate structural changes (including the cortical and subcortical GM, and association and limbic fibers of WM) in WD patients compared with healthy controls (HC). In order to identify whether aberrant GM volume changes have an influence on brain function, we further collect RS-fMRI to evaluate functional connectivity (FC) changes in patients with WD. Finally, whether structural and functional changes are associated with PM impairment of WD was investigated by correlation analysis.

MATERIALS AND METHODS

Subjects

Twenty-two native Chinese-speaking WD patients (12 men, 10 women; age: 22.36 ± 8.09 years; age range: 10–36 years) and 26 HC (14 men, 12 women; age: 22.18 ± 7.67 years; age range: 12–35 years) were recruited at the First Affiliated Hospital of Anhui University of Chinese Medicine (AUCM). After comprehensive clinical interviews evaluated by an neurologist expert and a trained neuropsychologist, WD patients based on the diagnosis of clinical symptoms of Kayser–Fleischer (KF) rings, neuroimaging findings, and abnormal copper metabolism were included, they were excluded if they had any other neurological or psychiatric disorder. HC had no history of head injury, neurological, psychiatric disorder, or concomitant medical disorder. All WD patients enrolled in the study have been in stable drug therapy for 2 weeks. Research approval was obtained from the Human Research Committee of the First Affiliated Hospital of AUCM and written informed consent was signed by all subjects before the enrollment. **Table 1** summarizes the clinical and demographic characteristics of all subjects enrolled in the present study.

Neuropsychological Assessment

The neuropsychological assessment of WD patients was performed by an experienced neuropsychologist. WD patients were evaluated by cognitive function measured with the Mini-Mental State Examination (MMSE), and PM. Full details are presented in the supplementary information. The neuropsychological scale is provided in **Table 1**.

TABLE 1 | Clinical features of patients and healthy controls.

	WD (*N* = 22)	HC (*N* = 26)
Gender (male/female)	12/10	14/12
Age (years)	10–36 (22.36 ± 8.09)	12–35 (22.18 ± 7.67)
Education (years)	7–12 (8.73 ± 1.24)	6–14 (9.73 ± 2.55)
Handedness	22 right-handed	26 right-handed
Duration (years)	1–10 (5.25 ± 3.03)	-
MMSE	25–28 (26.59 ± 0.85)	-
EBPM	3–6 (4.73 ± 0.88)	-
TBPM	2–4 (2.68 ± 0.99)	-
KF ring	22 WD with a KF ring	-
SCU (ug/dL)	15–58 (34.34 ± 14.43)	-
SCP (mg/dL)	2–10 (4.74 ± 2.29)	-

WD, Wilson's disease; HC, healthy controls; MMSE, Mini-Mental State Examination; EBPM, event-based prospective memory; TBPM, time-based prospective memory; N, number; KF, Kayser–Fleischer; SCU, serum copper; SCP, serum ceruloplasmin.

MRI Acquisition

Magnetic resonance imaging data were acquired using a 3.0-Tesla MR system (Discovery MR750, General Electric, Milwaukee, WI, United States) with an eight-channel high-resolution radio-frequency head coil. Sagittal 3D T1-weighted images were acquired using a T1-3D BRAVO sequence (repetition time (TR)/echo time (TE), 8.16 ms/3.18 ms; flip angle, 12°; matrix, 256 mm × 256 mm; field of view (FOV), 256 mm × 256 mm; slice thickness, 1 mm) with 170 axial slices with no gap. RS-fMRI images were acquired using a gradient-echo single-shot echo planar imaging sequence (TR/TE, 2,000 ms/30 ms; FOV, 220 mm × 220 mm; matrix 64 mm × 64 mm; flip angle, 90°; slice thickness, 3 mm) with 185 volumes. Diffusion tensor images were acquired by an echo-planar imaging (EPI) sequence (TR/TE, 6,000 ms/81.7; matrix, 128 mm × 128 mm; FOV, 256 mm × 256 mm; slice thickness, 3 mm) with a *b* value of 2,000 s/mm^2 and 64 gradient diffusion directions evenly distributed on a sphere. During scanning, all subjects were instructed to remain motionless and to keep their eyes closed.

MRI Analysis

Structural MRI data were analyzed with FSL version 5.0.2[1], and RS-fMRI data were analyzed with AFNI version 19.2.21[2]. The flowchart of data processing is presented in **Supplementary Figure 1**.

GM Volume Measurement

Gray matter volume measurement was performed using FSL-VBM (Ashburner and Friston, 2000). 3D T1-weighted images were first taken for all the subjects. FSL Automated Segmentation Tool (FAST) was employed to highlight the GM from the 3D T1-weghted image. The segmented GM parietal volume images were then normalized to the MNI152 standard space using the linear image registration (Jenkinson and Smith, 2001) (FLIRT) and non-linear registration (Smith et al., 2004) (FNIRT) tool box. The normalized images were further averaged and flipped along the x-axis to create a study-specific GM template. All native GM images were subsequently non-linearly registered to the study-specific template and modulated for the contraction due to the non-linear component of the transformation by dividing them by the Jacobian of the warp field. The modulated GM images were finally smoothed with an isotropic Gaussian kernel with a sigma of 3 mm. The study-specific GM template was divided into 110 regions of interest (ROIs) based on the Harvard-Oxford cortical and subcortical probabilistic atlases, which included the cerebral cortex and BG but excluded the cerebellum. GM volume for each ROI was measured for further statistical analysis.

Group differences of GM volumes were measured using two-sample *t* test analysis with age as the covariate, and a false discovery rate corrected (FDR) for multiple comparisons. The correlations between GM volumes of significantly different ROI and neuropsychological symptoms were evaluated by linear-regression analysis, FDR was used for multiple comparisons.

[1]http://fsl.fmrib.ox.ac.uk/fsl

[2]https://afni.nimh.nih.gov

Functional Connectivity Analysis

In order to evaluate how GM volume changes have effects on brain function, the aberrant brain regions (BG, visual association cortex) were selected as seeds to perform seed-based FC analysis. The visual association cortex (VAC) was divided into two seeds, including VAC1 (GM volume increased in left angular gyrus, lateral occipital cortex, and precuneus) and VAC2 (GM volume reduced in right occipital fusiform gyrus). Therefore, three seeds (BG, VAC1, and VAC2, **Figure 1**) were selected for FC analysis. For each participant, the Pearson correlation coefficient between the mean time series of seeds and the time series of every voxel across the whole brain was calculated, and the coefficients were further converted to a z-value using a Fisher r-to-z transformation to improve the normality (Biswal et al., 1995). Therefore, each participant acquired a BG-based FC map, VAC1-based FC map, and VAC2-based FC map.

A group-level analysis was applied to identify the FC differences between WD and HC. Group-wise whole brain analysis (AFNI package, version 19.2.21, see text footnote 2) of the belief-photo contrasted with a voxel-wise *p* threshold of 0.001 and cluster-wise threshold of 0.01. The relation between FC of WD patients in significantly different brain regions and neuropsychological symptoms were calculated by linear-regression analysis and the results were corrected by FDR for multiple comparisons.

In order to evaluate relationships between FC and GM volumes, correlation analysis was performed in regions with GM volumes that had significant differences between WD and HC, and the results were corrected by FDR for multiple comparisons.

WM Tracks

Data preprocessing for the diffusion tensor images was carried using a standard pipeline. The diffusion tensor data were skull-stripped using the BET tool (Smith, 2002), and corrected for distortions caused by eddy currents and movements using the eddy tool (Graham et al., 2016). The diffusion tensor was assessed using the DTIFIT toolbox to acquire FA, axial (AD), mean (MD), and radial diffusivities (RD) maps. Using a "seed" method, the reconstructions of association fibers [superior longitudinal fasciculus (SLF), inferior longitudinal fasciculus (ILF), inferior fronto-occipital fasciculus (IFO), and uncinate fasciculus (UNC)] and limbic fibers [cingulate gyrus part of cingulum (CGC) and the parahippocampal part of cingulum (CGH)] were acquired by performing fiber tracking in a native diffusion tensor space with a probabilistic tractography algorithm (Behrens et al., 2007) (PROBTRACKX) as implemented in FDT, which was based on the Bayesian estimation of diffusion parameters (BEDPOSTX) obtained using sampling techniques (Hernández et al., 2015). For each track, the average FA, AD, MD, and RD were extracted in native space.

Group differences of WM were calculated using two-sample *t* test analysis with age as the covariate, and the false discovery rate corrected (FDR) for multiple comparisons. The correlations between metrics (FA, MD, AD, and RD) of significantly different WM and neuropsychological symptoms were evaluated by linear-regression analysis, FDR was used for multiple comparisons.

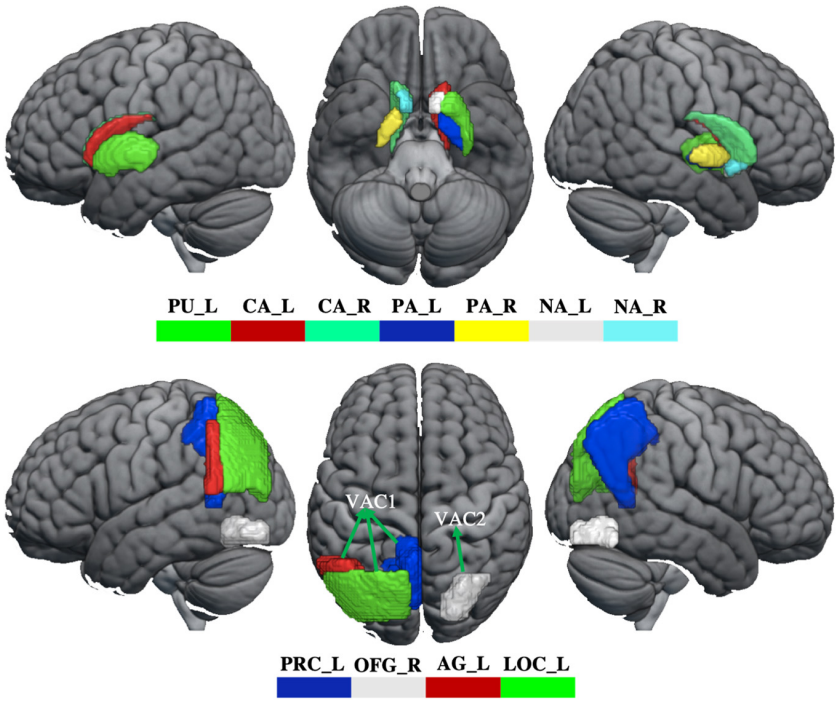

FIGURE 1 | The abnormity of GM volume in WD. The top panel shows that GM volume reduces in the basal ganglia. The bottom panel shows the GM volume changes in the visual association cortex. The GM volume increased in VAC1 and decreased in VAC2. PU_L, left putamen; CA_L, left caudate; CA_R, right caudate; PA_L, left pallidum; PA_R, right pallidum; NA_L, left accumbens; NA_R, right accumbens; PRC_L, left precuneus; OFG_R, right occipital fusiform gyrus; AG_L, left angular gyrus; LOC_L, lateral occipital cortex; VAC1, visual association cortex 1; VAC2, visual association cortex 2.

RESULTS

WM Tracks

Whiter matter tracks of WD patients were widely impaired in association and limbic system fibers (**Figure 2** and **Supplementary Table 2**). Specifically, compared with healthy controls, WD patients showed increased MD and RD in all association and limbic tracks, increased AD in the left CGH, bilateral IFO, SLF, and UNC, and decreased FA in all limbic system fibers, bilateral SLF and UNC. WM tracks had significant correlations with neuropsychological symptoms. Specifically, WD patients showed that AD of the left ILF (r = 0.451, p = 0.035), UNC (r = −0.449, p = 0.036) and right UNC (r = −0.437, p = 0.042) had significant correlations with EBPM (**Figure 3A**), and that FA of the right UNC (r = −0.516, p = 0.014) had significant correlations with TBPM (**Figure 3B**). There were no group differences of head motion between HC and WD (t = −0.5579, p = 0.5796) (**Supplementary Figure 2A**). It suggested that head motion has no influence on results.

GM Volumes

Compared with healthy controls, WD patients showed GM volume loss in the BG, including bilateral caudate, pallidum and accumbens, left putamen, and also in the visual association cortex, located in the right occipital fusiform gyrus (OFG). However, compared with healthy controls, WD patents revealed increased GM volumes in the visual association cortex, including left angular gyrus (AG), lateral occipital gyrus (LOC), and precuneus (**Figure 1** and **Supplementary Table 1**). There were no significant correlations between GM volume and neuropsychological symptoms in patients with WD.

Functional Connectivity

Compared with healthy controls, WD patients demonstrated that FC of BG (**Figure 4A** and **Supplementary Table 3**) was decreased in the bilateral cerebellum, left thalamus, middle cingulate cortex (MCC), and superior medial frontal gyrus (SMEG), and that FC of VAC1 (**Figure 4B** and **Supplementary Table 4**) was decreased in the left thalamus and hippocampus (THA-HIP). No significant FC of VAC2 differences were found between groups. FC between the visual association cortex and THA-HIP was negatively correlated (r = −0.512, p = 0.009) with MMSE (**Figure 4C**). There were no group differences of head motion between HC and WD (t = −1.447, p = 0.1546) (**Supplementary Figure 2B**). It suggested that head motion had no influence on results.

Correlations Between FC and GM Volumes

Based on the BG-based FC map of WD, significant correlation between FC value and gray volume (GV) value was found in BG (R = 0.75, P < 0.001), and no significant correlations were found in VAC1 (R = 0.07, P = 0.77) and VAC2 (R = −0.089,

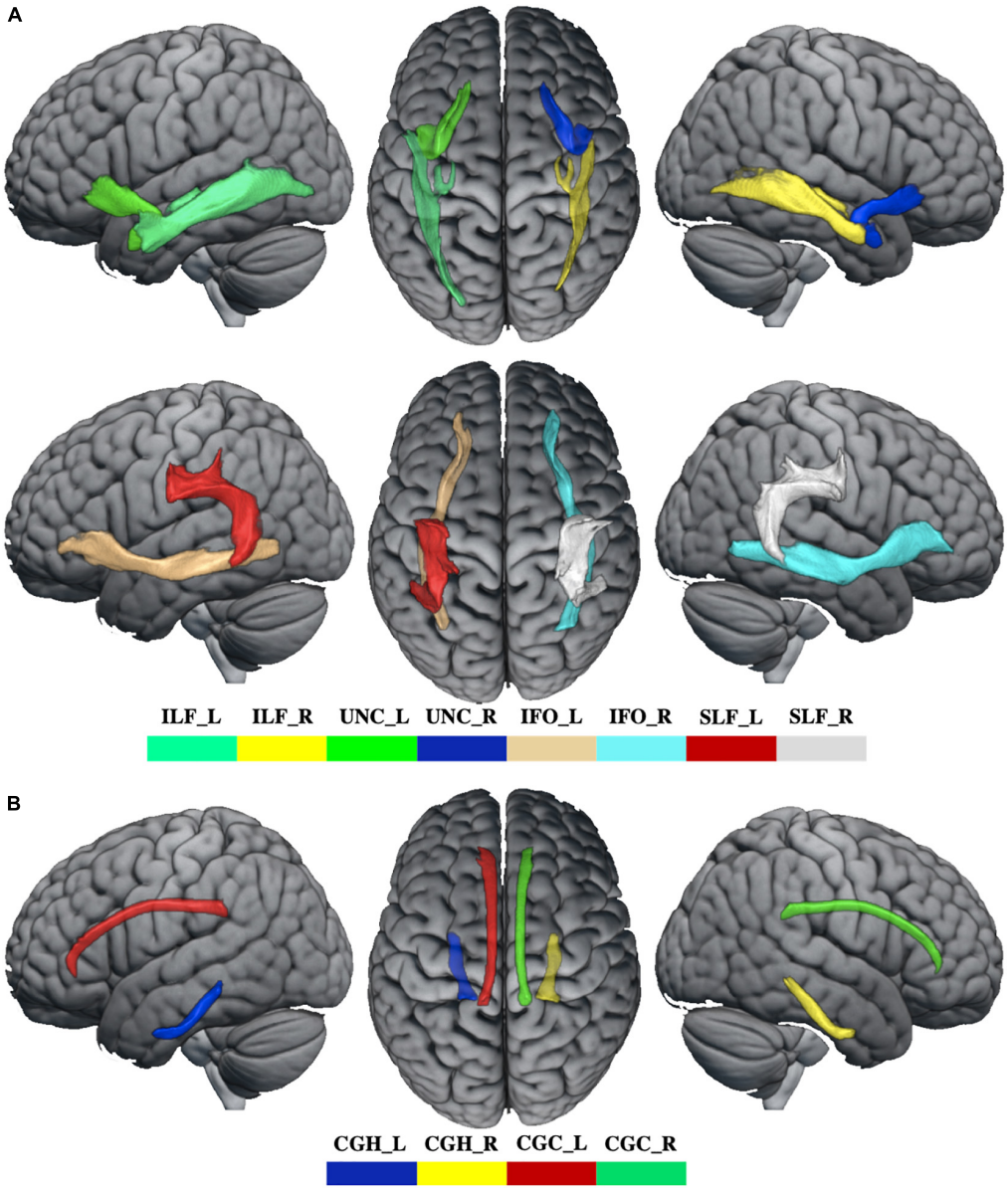

FIGURE 2 | The abnormal WM tracks in WD. **(A)** WM tracks of association fibers. **(B)** WM tracks of limbic system fibers. ILF_L, left inferior longitudinal fasciculus; ILF_R, right inferior longitudinal fasciculus; UNC_L, left uncinate fasciculus; UNC_R, right uncinate fasciculus; IFO_L, left inferior fronto-occipital fasciculus; IFO_R, right inferior fronto-occipital fasciculus; SLF_L, left superior longitudinal fasciculus; SLF_R, right superior longitudinal fasciculus; CGH_L, parahippocampal part of cingulum; CGH_R, right parahippocampal part of cingulum; CGC_L, cingulate gyrus part of cingulum; CGC_R, right cingulate gyrus part of cingulum.

P = 0.69) (**Supplementary Figure 3A**). Based on the VAC1-based FC map, no significant correlations between FC value and GV value were found in VAC1 (R = −0.146, P = 0.52), VAC2 (R = −0.063, P = 0.78), and BG (R = 0.08, P = 0.74) (**Supplementary Figure 3B**).

DISCUSSION

What are the fundamental brain alternations that lead to cognitive impairment in WD patients? Although prior studies have reported that WD can cause frontal lobe syndrome, or subcortical dementia, direct evidence of the correlation between brain alternations and neuropsychology is still lacking. In this study, we used a multimodal approach to analysis brain structural and functional changes to show that WM changes in association fibers are associated with PM, and that GM atrophy in the visual association cortex leads to aberrant FC that effects global cognitive function in WD. These multiparametric MRI finds may have implications in understanding the neural mechanisms underlying cognitive status in WD.

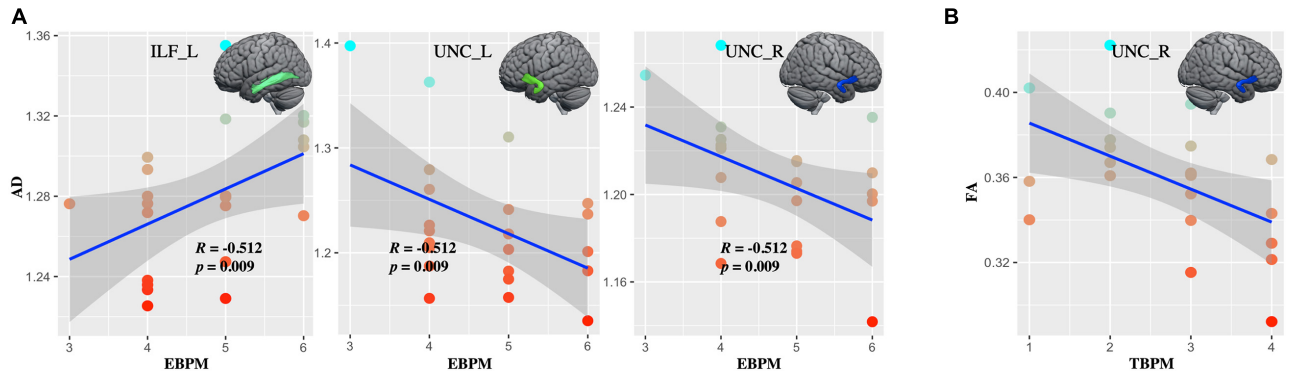

FIGURE 3 | The correlations between diffusion metrics and clinical symptoms. **(A)** Axial diffusivity (AD) in the left ILF and bilateral UNC correlated with the score at EBPM. **(B)** Fractional anisotropy (FA) in right UNC correlated with the score at TBPM. ILF_L, left inferior longitudinal fasciculus; UNC_L, left uncinate fasciculus; UNC_R, right uncinate fasciculus.

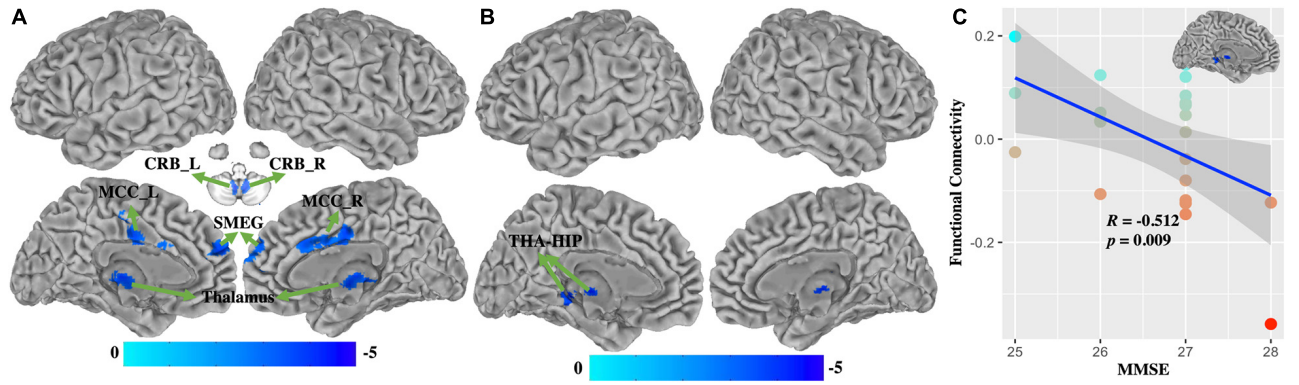

FIGURE 4 | The functional connectivity changes between WD and HC. **(A)** Functional connectivity decreased in the basal ganglia. **(B)** Functional connectivity decreased in VAC1. **(C)** Functional connectivity between VAC1 and THA-HIP was correlated with the score of MMSE in WD patients. THA-HIP, thalamus and hippocampus; CRB_L, left cerebellum; CRB_R, right cerebellum; MCC_L, left middle cingulate cortex; SMEG, superior medial frontal gyrus; MMSE, Mini-Mental State Examination.

In this study, half of the patients had mild neurological symptoms and the other half had no symptoms. Clinical symptoms of the WD patients were not very serious compared to other studies (Stezin et al., 2016). In line with previous neuroimaging studies in WD, we observed similar GM atrophy in the BG (including bilateral caudate, pallidum and accumbens, and left putamen nuclei). GM atrophy is reported to be due to edema, neuronal necrosis, gliosis, demyelination, or cystic degeneration of neurons due to copper overload or hepatic dysfunction (Kim et al., 2006; Bruha et al., 2011; Beinhardt et al., 2014). No significant correlations were found between GM atrophy of BG and PM, which is inconsistent with a previous study (Dong et al., 2016). However, many previous studies have revealed the widespread alternations in BG which mainly lead to extrapyramidal symptoms such as tremors, ataxia, and dystonic syndrome (Ala et al., 2007; Algin et al., 2010). The possible interpretation is that PM impairment is easily masked by other symptoms (Lorincz, 2010) that did not manifest in structural damage in BG in the present study. Interesting, based on the BG-based FC map, we also found that GM volume had significant correlation with FC in BG. This indicated that GM volume atrophy in BG had a significant effect on its function, and further affected the clinical symptoms in WD. Compared to healthy controls, no widespread cortical atrophy was found except in the right OFG; however, GM volumes increased in the visual association cortex (including left AG, LOC, and precuneus) in WD patients. Astrocytes are first impaired by copper accumulation which can cause astrogliosis, followed by cellular swelling, and then the upregulation of the synthesis of metallothionein to increase storage capacity for copper (Scheiber and Dringen, 2011). Due to the lower severity of neuropathology in WD patients, copper toxicity does not have an extensive impact on the cerebral cortex. Therefore, cortical atrophy does not widely occur in WD patients. Several forms of astrocytes exist in the central nervous system including fibrous (in WM), protoplasmic (in GM), and radial (Figley and Stroman, 2011; Khakh and Sofroniew, 2015) astrocytes. Copper accumulation can result in an increase in astrocyte numbers so that increased GM volumes in the visual association cortex may be associated with increased protoplasmic

astrocytes. Another possible interpretation is that medication induces cortical changes to generate a compensatory response to structural impairments in patients with WD. Several prior studies have pointed out that neuroanatomical alternations in patients, such as schizophrenia and Parkinson's disease are associated with drug therapy (Navari and Dazzan, 2009; Fusar-Poli et al., 2013). However, there are no significant correlations between the value of GM volumes in the visual association cortex and the score of PM and MMSE. The visual association cortex is not thought to play a general role in memory function (Rosen et al., 2017). Previous studies have demonstrated that the visual association cortex along with the hippocampus play a role in association memory formation (Rosen et al., 2017). This may indicate that structural damages in the visual association cortex do not have a direct effect on PM and MMSE.

The FC analysis showed that compared with healthy controls, patients' FC of BG was decreased in large-scale networks, including the bilateral cerebellum, right thalamus and MCC, and left SMEG. FC of BG did not correlate with cognitive performance. Previous studies have confirmed that MRI abnormalities in BG are responsible for extrapyramidal or neurological symptoms in WD (Bandmann et al., 2015). The behaviors that have the most striking relationships with FC of BG were limb movements, motivation and, decision making, although measures of cognitive function also showed relationships (Albin et al., 1989; Kreitzer and Malenka, 2008). Taken together, these results suggest that FC changes in BG are important in producing extrapyramidal or neurological disorders in WD patients, instead of PM and global cognitive function impairment. We also demonstrated that FC of VAC1 was decreased in the left THA-HIP. FC between VAC1 and THA-HIP is significantly related to global cognitive function in patients with WD. Connectivity from the thalamus to the visual cortex was investigated to confirm its involvement in visual cognition. Specifically, evidence suggested that the pulvinar, the largest thalamic nucleus, receives input from structures such as the retina and superior colliculus which critically shape the functional organization of the visual cortex, which contributes to visual cognition (Bridge et al., 2016). VAC1 is dorsal stream of the visual system which is proposed to be involved in the perception and interperception of spatial relationships, guidance of actions, and learning tasks that coordinate the body in the space (Galletti and Fattori, 2018). For another, the thalamus is functionally connected to the hippocampus with respect to spatial memory and spatial sensory datum (Stein et al., 2000; Aggleton et al., 2010). A recent study has reported that coactivation of the association visual cortex and hippocampus mediate association memory performances (Rosen et al., 2018). Therefore, these results may suggest that the diminished ability of perception spatial information from the visual cortex impaired FC between VAC1 and THA-HIP, and further affected global cognitive function in WD patients.

Structural changes of WM were widely observed in association and limbic fibers with preservation of the cortex, which can be explained by observation of gliosis and spongiosis in pathology studies (Meenakshi-Sundaram et al., 2002). These results may reflect a reduction of WM microstructural organization in brain locations as the results were compatible with axonal loss and/or demyelination (Jadav et al., 2013). WM changes in bilateral UNC were clinically relevant to the PM scales in WD patients. The UNC, linking anterior portions of the temporal lobe with the inferior frontal lobe, has a role in some types of learning and memory (Alm et al., 2015). In line with a multiple sclerosis study, it suggested that PM deficits are related to alternation of UNC (Pardini et al., 2014). The mean AD of ILF was positively correlated with EBPM. This is an intriguing finding, suggesting that a lower AD may be more prone to develop into PM deficits. Several studies have shown that altered ILF is associated with episodic memory in patients with cognitive decline (Hodgetts et al., 2017; Gao et al., 2019). ILF are thought to connect the temporal gyrus to the fusiform gyrus, occipital gyri, lingual gyrus, and ceneus (Latini et al., 2017). This may imply that increased or reduced GM volume in the visual association cortex is influenced by WM changes in ILF. In this study, we selected regions with GM differences as seed to perform seed-based FC analysis, and found that aberrant FC between the visual association cortex and THA-HIP was associated with global cognitive function. These may indicate that WM and GM have an effect on each other, and further affect brain function in patients with WD. The UNC and ILF may be structural signatures characterizing the PM deficits in WD patients.

In summary, using a multimodal MRI approach, the present study provides a comprehensive picture of structural and functional brain alternations in WD patients relative to healthy controls. On one hand, WM changes in association fibers are related to PM impairment in WD patients. On the other hand, WD patients manifested GM volume decreases in BG and increases in the visual association cortex that is abnormally connected to THA-HIP with respect to impaired global cognitive function in patients with WD. These findings suggested that PM impairment in WD may modulate aberrant WM in association fibers, and that GM volume changes in the association cortex have no direct effect on cognitive status, but indirectly affect global cognitive function by its aberrant FC in patients with WD. Our findings may provide a new window to further study how WD develops into cognitive impairment, and deepen our understanding of the cognitive status and neuropathology of WD.

Limitations

There are several limitations in the present study. The longer scanning time of fMRI makes the results of FC more stable. Patients with WD did not have enough patience to complete the long-term experiment when compared to healthy controls. Therefore, we limited fMRI scanning time to 6 min, which is less than the common scanning time of fMRI. In the future study, we will increase the scanning time appropriately for fMRI data so that the results of FC will be more stable. In the current study, we investigated how WM alternations impact on PM, and how GM volume atrophy causes aberrant FC which has

an impact on cognitive status in patients with WD. However, we do not know how brain function is mediated by WM and GM and further affect the cognitive status in patients with WD. In the future, mediation analysis will be performed in our next study to investigate this problem and provide more useful and interesting results.

DATA AVAILABILITY STATEMENT

The original contributions presented in the study are included in the article/**Supplementary Material**, further inquiries can be directed to the corresponding author/s.

ETHICS STATEMENT

The studies involving human participants were reviewed and approved by Human Research Committee of The First Affiliated Hospital of Anhui University of Chinese Medicine. Written informed consent to participate in this study was provided by the participants' legal guardian/next of kin.

AUTHOR CONTRIBUTIONS

CL and TD designed the current study. SH and CX drafted the manuscript. SH, CX, and AW performed the experiments. SH and HW analyzed the data. SH, YW, and HK revised the manuscript. All authors read and approved the final manuscript.

FUNDING

This study was supported by Borrow to supplement project of Hefei independent innovation policy (Y201710120004), Provincial Foundation for Excellent Young Talents of Colleges and Universities of Anhui Province (gxyqZD2019036), Natural Science Research Project of Anhui University of Chinese Medicine (2019zryb08), and Natural Science Foundation of Anhui Province (1808085MH263).

SUPPLEMENTARY MATERIAL

The Supplementary Material for this article can be found online at: https://www.frontiersin.org/articles/10.3389/fnhum.2021.610947/full#supplementary-material

REFERENCES

Aggleton, J. P., O'Mara, S. M., Vann, S. D., Wright, N. F., Tsanov, M., and Erichsen, J. T. (2010). Hippocampal-anterior thalamic pathways for memory: uncovering a network of direct and indirect actions. *Eur. J. Neurosci.* 31, 2292–2307. doi: 10.1111/j.1460-9568.2010.07251.x

Ala, A., Walker, A. P., Ashkan, K., Dooley, J. S., and Schilsky, M. L. (2007). Wilson's disease. *Lancet* 369, 397–408. doi: 10.1016/s0140-6736(07)60196-2

Albin, R. L., Young, A. B., and Penney, J. B. (1989). The functional anatomy of basal ganglia disorders. *Trends Neurosci.* 12, 366–375. doi: 10.1016/0166-2236(89)90074-x

Algin, O., Taskapilioglu, O., Hakyemez, B., Ocakoglu, G., Yurtogullari, S., Erer, S., et al. (2010). Structural and neurochemical evaluation of the brain and pons in patients with Wilson's disease. *Jap. J. Radiol.* 28, 663–671. doi: 10.1007/s11604-010-0491-4

Alm, K. H., Rolheiser, T., Mohamed, F. B., and Olson, I. R. (2015). Fronto-temporal white matter connectivity predicts reversal learning errors. *Front. Hum. Neurosci.* 9:343. doi: 10.3389/fnhum.2015.00343

Arnold, N. R., Bayen, U. J., and Böhm, M. F. (2015). Is prospective memory related to depression and anxiety? A hierarchical MPT modelling approach. *Memory* 23, 1215–1228. doi: 10.1080/09658211.2014.969276

Ashburner, J., and Friston, K. J. (2000). Voxel-based morphometry–the methods. *Neuroimage* 11(6 Pt 1), 805–821. doi: 10.1006/nimg.2000.0582

Bandmann, O., Weiss, K. H., and Kaler, S. G. (2015). Wilson's disease and other neurological copper disorders. *Lancet Neurol.* 14, 103–113. doi: 10.1016/S1474-4422(14)70190-5

Behrens, T. E. J., Berg, H. J., Jbabdi, S., Rushworth, M. F. S., and Woolrich, M. W. (2007). Probabilistic diffusion tractography with multiple fibre orientations: what can we gain? *Neuroimage* 34, 144–155.

Beinhardt, S., Leiss, W., Stättermayer, A. F., Graziadei, I., Zoller, H., Stauber, R., et al. (2014). Long-term outcomes of patients with Wilson disease in a large Austrian cohort. *Clin. Gastroenterol. Hepatol.* 12, 683–689. doi: 10.1016/j.cgh.2013.09.025

Biswal, B., Yetkin, F. Z., Haughton, V. M., and Hyde, J. S. (1995). Functional connectivity in the motor cortex of resting human brain using echo-planar MRI. *Magn. Reson. Med.* 34, 537–541. doi: 10.1002/mrm.1910340409

Bridge, H., Leopold, D. A., and Bourne, J. A. (2016). Adaptive pulvinar circuitry supports visual cognition. *Trends Cogn. Sci.* 20, 146–157. doi: 10.1016/j.tics.2015.10.003

Bruha, R., Marecek, Z., Pospisilova, L., Nevsimalova, S., Vitek, L., Martasek, P., et al. (2011). Long-term follow-up of Wilson disease: natural history, treatment, mutations analysis and phenotypic correlation. *Liver Int.* 31, 83–91. doi: 10.1111/j.1478-3231.2010.02354.x

Czlonkowska, A., Litwin, T., Dusek, P., Ferenci, P., Lutsenko, S., Medici, V., et al. (2018). Wilson disease. *Nat. Rev. Dis. Primers* 4:21. doi: 10.1038/s41572-018-0018-3

Delano-Wood, L., Stricker, N. H., Sorg, S. F., Nation, D. A., Jak, A. J., Woods, S. P., et al. (2012). Posterior cingulum white matter disruption and its associations with verbal memory and stroke risk in mild cognitive impairment. *J. Alzheimers Dis.* 29, 589–603. doi: 10.3233/JAD-2012-102103

Dong, T., Qiu, J., Cheng, H. D., Dong, W. W., Huang, P., Xu, C. S., et al. (2016). Impairment of time-based prospective memory in patients with Wilson's disease. *Eur. Rev. Med. Pharmacol. Sci.* 20, 1845–1851.

Dong, T., Yang, W. M., Wu, M. C., Zhang, J., Huang, P., Xu, C. S., et al. (2019). Microstructure changes in whiter matter relate to cognitive impairment in Wilson's disease. *Biosci. Rep.* 39:BSR20181651. doi: 10.1042/bsr20181651

Figley, C. R., and Stroman, P. W. (2011). The role(s) of astrocytes and astrocyte activity in neurometabolism, neurovascular coupling, and the production of functional neuroimaging signals. *Eur. J. Neurosci.* 33, 577–588. doi: 10.1111/j.1460-9568.2010.07584.x

Fusar-Poli, P., Smieskova, R., Kempton, M. J., Ho, B. C., Andreasen, N. C., and Borgwardt, S. (2013). Progressive brain changes in schizophrenia related to antipsychotic treatment? A meta-analysis of longitudinal MRI studies. *Neurosci. Biobehav. Rev.* 37, 1680–1691. doi: 10.1016/j.neubiorev.2013.06.001

Galletti, C., and Fattori, P. (2018). The dorsal visual stream revisited: stable circuits or dynamic pathways? *Cortex* 98, 203–217. doi: 10.1016/j.cortex.2017.01.009

Gao, S., Chen, Y., Sang, F., Yang, Y., Xia, J., Li, X., et al. (2019). White matter microstructural change contributes to worse cognitive function in patients with type 2 diabetes. *Diabetes* 68, 2085–2094. doi: 10.2337/db19-0233

Graham, M. S., Drobnjak, I., and Zhang, H. (2016). Realistic simulation of artefacts in diffusion MRI for validating post-processing correction techniques. *Neuroimage* 125, 1079–1094. doi: 10.1016/j.neuroimage.2015.11.006

Herbet, G., Zemmoura, I., and Duffau, H. (2018). Functional anatomy of the inferior longitudinal fasciculus: from historical reports to current hypotheses. *Front. Neuroanat.* 12:77. doi: 10.3389/fnana.2018.00077

Hernández, M., Guerrero, G. D., Cecilia, J. M., García, J. M., Inuggi, A., Jbabdi, S., et al. (2015). Correction: accelerating fibre orientation estimation from diffusion weighted magnetic resonance imaging using GPUs. *PLoS One* 10:e0130915. doi: 10.1371/journal.pone.0130915

Hodgetts, C. J., Postans, M., Warne, N., Varnava, A., Lawrence, A. D., and Graham, K. S. (2017). Distinct contributions of the fornix and inferior longitudinal fasciculus to episodic and semantic autobiographical memory. *Cortex* 94, 1–14. doi: 10.1016/j.cortex.2017.05.010

Jadav, R., Saini, J., Sinha, S., Bagepally, B., Rao, S., and Taly, A. B. (2013). Diffusion tensor imaging (DTI) and its clinical correlates in drug naïve Wilson's disease. *Metab. Brain Dis.* 28, 455–462. doi: 10.1007/s11011-013-9407-1

Jenkinson, M., and Smith, S. (2001). A global optimisation method for robust affine registration of brain images. *Med. Image Anal.* 5, 143–156. doi: 10.1016/s1361-8415(01)00036-6

Jing, R., Han, Y., Cheng, H., Han, Y., Wang, K., Weintraub, D., et al. (2019). Altered large-scale functional brain networks in neurological Wilson's disease. *Brain Imaging Behav.* 14, 1445–1455. doi: 10.1007/s11682-019-00066-y

Khakh, B. S., and Sofroniew, M. V. (2015). Diversity of astrocyte functions and phenotypes in neural circuits. *Nat. Neurosci.* 18, 942–952. doi: 10.1038/nn.4043

Kim, T. J., Kim, I. O., Kim, W. S., Cheon, J. E., Moon, S. G., Kwon, J. W., et al. (2006). MR imaging of the brain in Wilson disease of childhood: findings before and after treatment with clinical correlation. *AJNR Am. J. Neuroradiol.* 27, 1373–1378.

Kozić, D., Svetel, M., Petrović, B., Dragasević, N., Semnic, R., and Kostić, V. S. (2003). MR imaging of the brain in patients with hepatic form of Wilson's disease. *Eur. J. Neurol.* 10, 587–592. doi: 10.1046/j.1468-1331.2003.00661.x

Kreitzer, A. C., and Malenka, R. C. (2008). Striatal plasticity and basal ganglia circuit function. *Neuron* 60, 543–554. doi: 10.1016/j.neuron.2008.11.005

Lang, C. (1989). Is Wilson's disease a dementing condition? *J. Clin. Exp. Neuropsychol.* 11, 569–570. doi: 10.1080/01688638908400914

Lang, C., Müller, D., Claus, D., and Druschky, K. F. (1990). Neuropsychological findings in treated Wilson's disease. *Acta Neurol. Scand.* 81, 75–81. doi: 10.1111/j.1600-0404.1990.tb00934.x

Latini, F., Martensson, J., Larsson, E. M., Fredrikson, M., Ahs, F., Hjortberg, M., et al. (2017). Segmentation of the inferior longitudinal fasciculus in the human brain: a white matter dissection and diffusion tensor tractography study. *Brain Res.* 1675, 102–115. doi: 10.1016/j.brainres.2017.09.005

Lorincz, M. T. (2010). Neurologic Wilson's disease. *Ann. N. Y. Acad. Sci.* 1184, 173–187. doi: 10.1111/j.1749-6632.2009.05109.x

Martino, J., and De Lucas, E. M. (2014). Subcortical anatomy of the lateral association fascicles of the brain: a review. *Clin. Anat.* 27, 563–569. doi: 10.1002/ca.22321

McDaniel, M. A., and Einstein, G. O. (2011). The neuropsychology of prospective memory in normal aging: a componential approach. *Neuropsychologia* 49, 2147–2155. doi: 10.1016/j.neuropsychologia.2010.12.029

Meenakshi-Sundaram, S., Taly, A. B., Kamath, V., Arunodaya, G. R., Rao, S., and Swamy, H. S. (2002). Autonomic dysfunction in Wilson's disease –a clinical and electrophysiological study. *Clin. Auton. Res.* 12, 185–189. doi: 10.1007/s10286-002-0038-6

Metoki, A., Alm, K. H., Wang, Y., Ngo, C. T., and Olson, I. R. (2017). Never forget a name: white matter connectivity predicts person memory. *Brain Struct. Funct.* 222, 4187–4201. doi: 10.1007/s00429-017-1458-3

Metzler-Baddeley, C., Jones, D. K., Steventon, J., Westacott, L., Aggleton, J. P., and O'Sullivan, M. J. (2012). Cingulum microstructure predicts cognitive control in older age and mild cognitive impairment. *J. Neurosci.* 32, 17612–17619. doi: 10.1523/JNEUROSCI.3299-12.2012

Motomura, K., Fujii, M., Maesawa, S., Kuramitsu, S., Natsume, A., and Wakabayashi, T. (2014). Association of dorsal inferior frontooccipital fasciculus fibers in the deep parietal lobe with both reading and writing processes: a brain mapping study. *J. Neurosurg.* 121, 142–148. doi: 10.3171/2014.2.JNS131234

Navari, S., and Dazzan, P. (2009). Do antipsychotic drugs affect brain structure? A systematic and critical review of MRI findings. *Psychol. Med.* 39, 1763–1777. doi: 10.1017/s0033291709005315

Pardini, M., Bergamino, M., Bommarito, G., Bonzano, L., Luigi Mancardi, G., and Roccatagliata, L. (2014). Structural correlates of subjective and objective memory performance in multiple sclerosis. *Hippocampus* 24, 436–445. doi: 10.1002/hipo.22237

Rosen, M. L., Sheridan, M. A., Sambrook, K. A., Peverill, M. R., Meltzoff, A. N., and Mclaughlin, K. A. (2017). The role of visual association cortex in associative memory formation across development. *J. Cogn. Neurosci.* 30, 365–380.

Rosen, M. L., Sheridan, M. A., Sambrook, K. A., Peverill, M. R., Meltzoff, A. N., and McLaughlin, K. A. (2018). The role of visual association cortex in associative memory formation across development. *J. Cogn. Neurosci.* 30, 365–380. doi: 10.1162/jocn_a_01202

Scheiber, I. F., and Dringen, R. (2011). Copper-treatment increases the cellular GSH content and accelerates GSH export from cultured rat astrocytes. *Neurosci. Lett.* 498, 42–46. doi: 10.1016/j.neulet.2011.04.058

Smith, S. M. (2002). Fast robust automated brain extraction. *Hum. Brain Mapp.* 17, 143–155. doi: 10.1002/hbm.10062

Smith, S. M., Jenkinson, M., Woolrich, M. W., Beckmann, C. F., Behrens, T. E., Johansen-Berg, H., et al. (2004). Advances in functional and structural MR image analysis and implementation as FSL. *Neuroimage* 23(Suppl. 1), S208–S219. doi: 10.1016/j.neuroimage.2004.07.051

Stein, T., Moritz, C., Quigley, M., Cordes, D., Haughton, V., and Meyerand, E. (2000). Functional connectivity in the thalamus and hippocampus studied with functional MR imaging. *AJNR Am. J. Neuroradiol.* 21, 1397–1401.

Stezin, A., George, L., Jhunjhunwala, K., Lenka, A., Saini, J., Netravathi, M., et al. (2016). Exploring cortical atrophy and its clinical and biochemical correlates in Wilson's disease using voxel based morphometry. *Parkinsonism Relat. Disord.* 30, 52–57. doi: 10.1016/j.parkreldis.2016.06.017

Zou, L., Song, Y., Zhou, X., Chu, J., and Tang, X. (2019). Regional morphometric abnormalities and clinical relevance in Wilson's disease. *Mov. Disord.* 34, 545–554. doi: 10.1002/mds.27641

Conflict of Interest: The authors declare that the research was conducted in the absence of any commercial or financial relationships that could be construed as a potential conflict of interest.

frontiers in Human Neuroscience

ORIGINAL RESEARCH
published: 20 April 2021
doi: 10.3389/fnhum.2021.641961

BCCT: A GUI Toolkit for Brain Structural Covariance Connectivity Analysis on MATLAB

Qiang Xu[1,2†], Qirui Zhang[2†], Gaoping Liu[2†], Xi-jian Dai[2,3†], Xinyu Xie[2], Jingru Hao[2], Qianqian Yu[2], Ruoting Liu[2], Zixuan Zhang[2], Yulu Ye[2], Rongfeng Qi[2], Long Jiang Zhang[2], Zhiqiang Zhang[2,4] and Guangming Lu[1,2,4*]*

[1] College of Automation Engineering, Nanjing University of Aeronautics and Astronautics, Nanjing, China, [2] Department of Radiology, School of Medicine, Jinling Hospital, Nanjing University, Nanjing, China, [3] Sleep Assessment Unit, Department of Psychiatry, Faculty of Medicine, Chinese University of Hong Kong, Hong Kong, China, [4] State Key Laboratory of Analytical Chemistry of Life Science, Nanjing University, Nanjing, China

OPEN ACCESS

Edited by:
Jurong Ding,
Sichuan University of Science and Engineering, China

Reviewed by:
Yifeng Wang,
Sichuan Normal University, China
Jinping Xu,
Shenzhen Institutes of Advanced Technology, Chinese Academy of Sciences (CAS), China

***Correspondence:**
Guangming Lu
cjr.luguangming@vip.163.com
Zhiqiang Zhang
zhangzq2001@126.com

† These authors have contributed equally to this work

Specialty section:
This article was submitted to Brain Imaging and Stimulation, a section of the journal Frontiers in Human Neuroscience

Received: 15 December 2020
Accepted: 25 February 2021
Published: 20 April 2021

Citation:
Xu Q, Zhang Q, Liu G, Dai X-j, Xie X, Hao J, Yu Q, Liu R, Zhang Z, Ye Y, Qi R, Zhang LJ, Zhang Z and Lu G (2021) BCCT: A GUI Toolkit for Brain Structural Covariance Connectivity Analysis on MATLAB. Front. Hum. Neurosci. 15:641961. doi: 10.3389/fnhum.2021.641961

Brain structural covariance network (SCN) can delineate the brain synchronized alterations in a long-range time period. It has been used in the research of cognition or neuropsychiatric disorders. Recently, causal analysis of structural covariance network (CaSCN), winner-take-all and cortex–subcortex covariance network (WTA-CSSCN), and modulation analysis of structural covariance network (MOD-SCN) have expended the technology breadth of SCN. However, the lack of user-friendly software limited the further application of SCN for the research. In this work, we developed the graphical user interface (GUI) toolkit of brain structural covariance connectivity based on MATLAB platform. The software contained the analysis of SCN, CaSCN, MOD-SCN, and WTA-CSSCN. Also, the group comparison and result-showing modules were included in the software. Furthermore, a simple showing of demo dataset was presented in the work. We hope that the toolkit could help the researchers, especially clinical researchers, to do the brain covariance connectivity analysis in further work more easily.

Keywords: structural covariance connectivity, causal network analysis of structural covariance, modulation, winner-take-all, GUI

INTRODUCTION

The brain is a connectome that collects network architectures by fragmental and coalescent organizations (Bullmore and Sporns, 2009). The human brain could be described by anatomical pathways and functional interactions among distinct brain regions (Bullmore and Sporns, 2009; Sporns, 2011). The human brain connectome can be separated into functional connectivity based on signal process (Biswal et al., 1995; Liao et al., 2010; Sporns, 2018), structural connectivity based on fiber tracts (Liao et al., 2011; Zhang et al., 2011a; Watson et al., 2019), and covariance connectivity based on structural covariance analysis (He et al., 2007; Zhang et al., 2011b;

Liao et al., 2013). The covariance connectivity, mainly referred to as the structural covariance network (SCN) constructed by morphological images, could be used to measure the synchronized topological patterns of brain regions in a long-range time period (He et al., 2007; Liao et al., 2013; Zhang et al., 2017; Xu et al., 2020). Using a cross-sectional morphological image dataset, the structural covariance connectivity could measure the undergoing pathological processes between brain regions during development, plasticity, or diseases (He et al., 2007; Seeley et al., 2009; Sanabria-Diaz et al., 2010; Liao et al., 2013; Jiang et al., 2018; Li et al., 2019).

Recently, new techniques have expended the breadth of SCN. Based on the Granger causality algorithm, the causal analysis of structural covariance network (CaSCN) could be used to detect the progression patterns of SCN (Zhang et al., 2017; Jiang et al., 2018; Li et al., 2019; Guo et al., 2020). The strategy of CaSCN was to assign the temporal order to the structural covariance analysis (Zhang et al., 2017). The temporal order could be based on the variables with sequential order, such as the duration of diseases or disorders, age of participants, etc., (Zhang et al., 2017). With the temporal order, the Granger causality analysis (GCA) could be used to calculate the influences among the brain regions (Zhang et al., 2017). The winner-take-all and cortex–subcortex covariance network (WTA-CSSCN) was the combination of winner-take-all strategy and structural covariance analysis between cortex and subcortex regions (Xu et al., 2020). It could be used to build the parcelations of subcortex regions according to the cortex parcelations. And it could provide novel insight of the subcortex by using structural covariance analysis (Xu et al., 2020). Additionally, modulation analysis of structural covariance network (MOD-SCN) was developed for the detection of the influence of clinical variables onto the structural covariance connectivity (Bernhardt et al., 2014; Sharda et al., 2016; Valk et al., 2017; Xu et al., 2020). These developments of SCN widely extended the applications of the technique.

However, until now, there was no dedicated software for the analysis of brain structural covariance connectivity. Meanwhile, it was difficult to do the statistical analysis of SCN, especially for the clinical researchers. Hence, we developed this user-friendly graphical user interface (GUI) software, Brain Covariance Connectivity Toolkit (BCCT), which was based on MATLAB platform, to operate the related process of structural covariance connectivity. We hope it could help researchers who would like to do the structural covariance analysis in their studies.

INTERFACE AND MAIN FUNCTIONS OF THE BRAIN COVARIANCE CONNECTIVITY TOOLKIT

Brain Covariance Connectivity Toolkit was developed by the Department of Radiology, Jinling Hospital, Medical School of Nanjing University. It was scripted on the MATLAB platform. It is suggested that the MATLAB version is later than R2014a. It could be downloaded from the website of github[1]. The supported operation systems include the Linux and Windows systems, while the MAC system has not been tested. It is suggested that the memory (RAM) should be larger than 8 GB for running the toolkit for seed-to-brain SCN analysis. It would be better that the RAM is larger than 16 GB for the large voxel and vertex numbers of gray matter volume (GMV) in MNI space and thickness in fsaverage space. It would cost large RAM and time for the permutation test. The toolkit needs spm[2], freesurfer matlab tools[3], and SurfStat toolkit[4] for the I/O operation of the related image dataset.

Four kinds of SCN methods were included in the toolkit: SCN, CaSCN, MOD-SCN, and WTA-CSSCN. Apart from the WTA-CSSCN, the other SCN methods could deal with the morphological image datasets either on volume space or on surface space. The WTA-CSSCN could only process the volume-based morphological dataset currently.

Meanwhile, two kinds of statistical analysis methods were included in the toolkit, the interaction analysis (Lerch et al., 2006; Valk et al., 2017; Xu et al., 2020), and the permutation test (Liao et al., 2013; Teipel et al., 2016; Xu et al., 2020). Currently, the software only supported the comparison between two groups. Additionally, the simple result-showing mode was included in the utilities of the toolkit (**Figure 1**). Also, the utilities included the mask generation function and help documents.

For SCN, CaSCN, and MOD-SCN, the input datasets should be the processed morphological indices, such as GMV from voxel-based morphometry (VBM) analysis[5]/Computational Anatomy Toolbox toolkit (CAT12)[6], brain area, thickness from FreeSurfer software (see text footnote 3), etc. The "ROI signals" were conducted with the mean values of region of interest (ROI) of the morphological indices in participants, and the "voxel/vertex signal" was produced by the value of the related vortex/vertex of the indices in participants.

There were four kinds of ROI definitions in the toolkit: the MNI coordinate mode, the ROI image mode, the mat mode, and the ASCII text mode.

After extracting the "ROI signals" and/or whole brain "voxel/vertex signal," the related analysis methods of different SCN modes were used for further analysis: correlation analysis for SCN, GCA for CaSCN, and generalized linear model (GLM) analysis for MOD-SCN.

Then, the statistical analysis was applied to the group comparison analysis. For SCN and MOD-SCN, the interaction analysis could be used for the comparison. And for SCN and CaSCN, the permutation test could be used for the comparison (**Figure 2A**).

For WTA-CSSCN, the "ROI signals" were extracted from the parcelation of the cortex. Then, the correlation analysis was used to gain the correlation coefficients between "ROI signals" of the cortex and the "voxel signals" of the subcortex

[1]https://github.com/JLhos-fmri/BrainCovarianceConnectToolkitV2.1
[2]https://www.fil.ion.ucl.ac.uk/spm/
[3]https://www.freesurfer.net/
[4]http://www.math.mcgill.ca/keith/surfstat/#ICBMagain
[5]http://dbm.neuro.uni-jena.de/wordpress/vbm/
[6]http://www.neuro.uni-jena.de/cat/

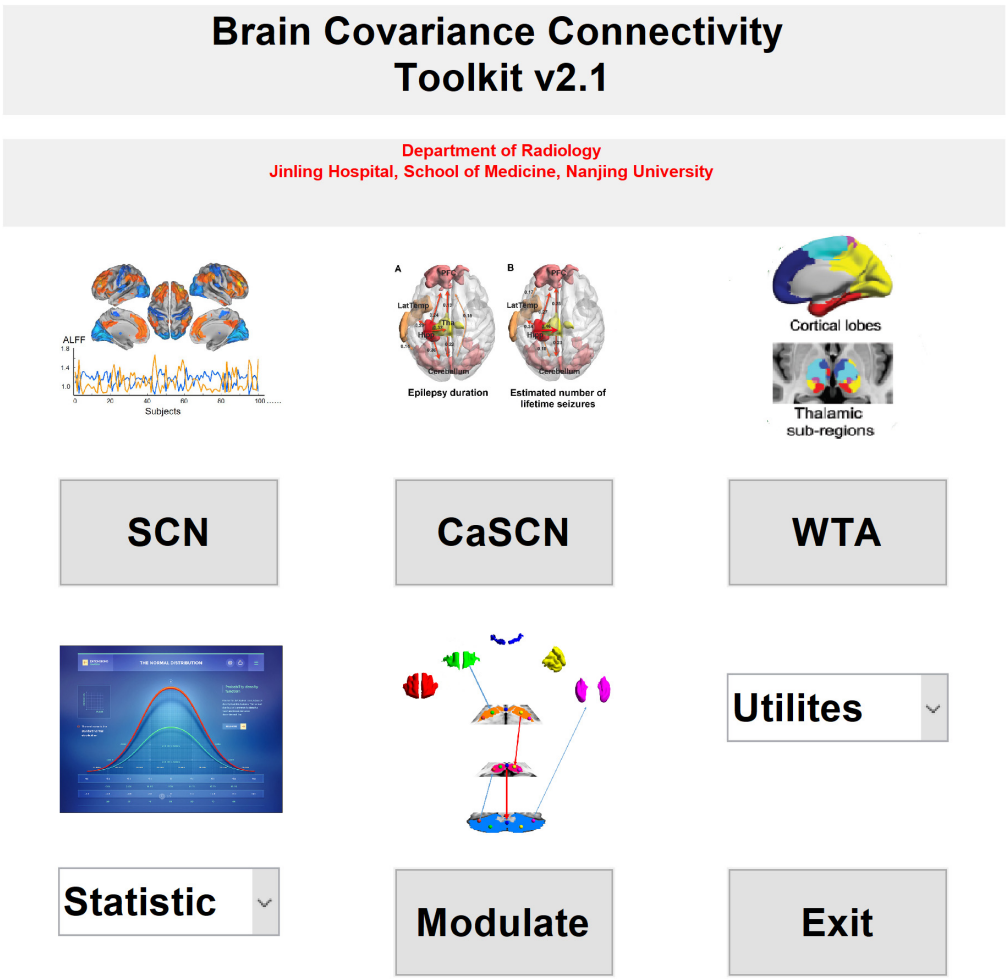

FIGURE 1 | The main interface of the brain covariance connectivity toolkit (BCCT) toolkit. CaSCN, causal analysis of structural covariance network; SCN, structural covariance network; WTA, winner-take-all.

structure. Each voxel of the subcortex structure was labeled according to the cortical parcelation with the highest correlation coefficient, respectively. Then, the permutation test was used for the group comparison of the connectivity numbers of the subcortex structure in WTA-CSSCN (**Figure 2B**).

STRUCTURAL COVARIANCE NETWORK

Structural covariance network was the basic function of the brain structural covariance analysis. The SCN in the toolkit was constructed by correlation analysis. Two kinds of SCN were implemented in the toolkit: the voxel-/vertex-wise seed-to-brain structural covariance connectivity of volume-/surface-based morphological images and ROI-wise structural covariance connectivity of volume-based morphological images. Additionally, the regression of variables of no interest could be selected in the analysis. According to the advisement of VBM/CAT, the total intracranial volume (TIV) should be regressed out during the morphological analysis. There were two kinds of correlation methods in the toolkit, the Pearson correlation and partial correlation analysis. It was noted that it should make sure that the number of participants was larger than the number of the ROIs.

CAUSAL ANALYSIS OF STRUCTURAL COVARIANCE NETWORK

Causal analysis of structural covariance network was firstly developed in 2017 (Zhang et al., 2017). In the study, the duration of disease was selected as the sequential order of participants. The GCA was applied to the seed-to-brain analysis and ROI-wise analysis. There were two kinds of GCA algorithms in the toolkit, one was the residual-based GCA (John, 1982; Goebel et al., 2003; Wu et al., 2013) and the other was the coefficient-based GCA (Chen et al., 2009; Zang et al., 2012).

The formulas of the residual-based GCA are as follows:

$$Y_n = \beta Y_{n-k} + \varepsilon$$

$$Y_n = \alpha X_{n-k} + \bar{\beta} Y_{n-k} + \delta$$

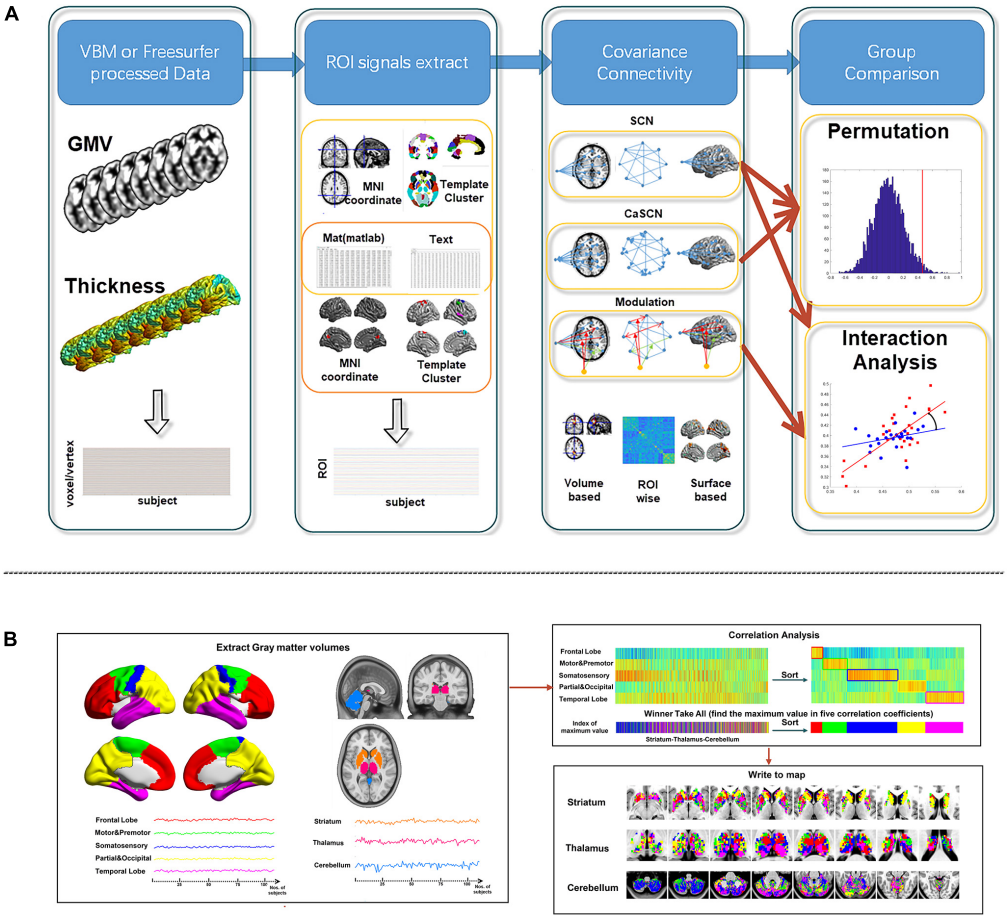

FIGURE 2 | Workflow of BCCT toolkit. **(A)** Workflow of SCN, CaSCN, and modulation analysis of structural covariance network (MOD-SCN). **(B)** Workflow of winner-take-all and cortex–subcortex covariance network (WTA-CSSCN). Here, the gray matter volume (GMV) from VBM/CAT12 could be used for the voxel-wise seed-to-brain analysis of volume-based morphological images and region of interest (ROI)-wise analysis of volume-based morphological images. The thickness from FreeSurfer could be used for the vertex-wise seed-to-brain analysis of surface-based morphological images.

Here, Y_n represents the current value of Y signal, X_{n-k} and Y_{n-k} represent the former values of X and Y signals with k-order, and ε and δ represent the residual of the linear fit modes. When $\varepsilon > \delta$, the X shows Granger causal effect on Y. The residual-based GCA is defined like this:

$$F_{x \to y} = \frac{\ln(\varepsilon)}{\ln(\delta)}$$

The formula of coefficient-based GCA is as follows:

$$Y_n = \alpha X_{n-k} + \beta Y_{n-k} + \varepsilon$$

Here, Y_n represents the current value of Y signal, X_{n-k} and Y_{n-k} represent the former values of X signal and Y signals with k-order, and ε represents the residual of the linear fit modes. The coefficient of α represents the causal effect of X to Y.

According to the distributions of the residual-based GCA and coefficient-based GCA, the significance of GC values could be calculated.

The permutation test analysis could be used for the significance of GC values. The null distribution of GC values was conducted by random realigning the orders of participants. Then, the normal distribution function was used to calculate the significance of the GC values.

Similar to the SCN, the CaSCN mode supported the analysis of the voxel-/vertex-wise seed-to-brain analysis of volume-/surface-based morphological images and ROI-wise analysis of volume-based morphological images.

Please note that since the large number of the voxel/vertex of morphological images, the permutation analysis of CaSCN in voxel-/vertex-wise seed-to-brain analysis of volume-/surface-based morphological images would cost a related long time and need large memory.

MODULATION ANALYSIS OF STRUCTURAL COVARIANCE NETWORK

Modulation analysis of structural covariance network was based on the GLM. It could evaluate the modulation effect of clinical variables on the structural covariance connectivity. The SurfStat

toolkit (see text footnote 4) was applied for the analysis (Lerch et al., 2006; Bernhardt et al., 2009; Worsley et al., 2009).

The formula of the modulation analysis is as follows:

$$Y = \beta_1 \times X + \beta_2 \times \text{Var Of Clinic} + \beta_3 \times X \times \text{Val Of Clinic} + \beta_4 \times \text{Cov Of No Int}$$

Here, $\times$ indicates an interaction between terms, and Cov Of No Int is the covariate of no interest. Y is the "Signal" of target ROI, and X was the "Signal" of seed ROI. Var Of Clinic is the clinical variance for the modulation analysis. The significance of β_3 could represent the power of modulation effect on the structural covariance connectivity between X and Y.

Similar to the SCN, the MOD-SCN mode supported the analysis of the voxel-/vertex-wise seed-to-brain analysis of volume-/surface-based morphological images and ROI-wise analysis of volume-based morphological images.

WINNER-TAKE-ALL AND CORTEX–SUBCOTEX COVARIANCE NETWORK

Winner-take-all and cortex–subcotex covariance network was introduced in 2020 (Xu et al., 2020). It described the parcelations of the subcortex structure according to the parcelations of the cortex. In the study, the WTA-CSSCN analysis was used to find the differences of cortico-striato-thalamo-cerebellar covariance connectivity between different types of epilepsy patients with generalized tonic–clonic seizures. In the toolkit, the WTA-CSSCN mode included the setup, calculation, group comparison, and result showing.

STATISTICAL ANALYSIS OF STRUCTURAL COVARIANCE CONNECTIVITY

Two kinds of statistical analysis methods were included in the toolkit, the permutation test (Liao et al., 2013; Teipel et al., 2016) and the interaction analysis (Lerch et al., 2006; Xu et al., 2020). These two kinds of methods were only suitable for the comparison of two groups in the toolkit.

In the permutation test, the null distribution was conducted by random disarrangement and regroupment of the two groups of participants. The differences between the regrouped datasets could be used to make up the null distribution, and the significance of the true difference between two groups could be calculated by the normal distribution functions. Let I_A and I_B represent the indices of Group A and Group B, $\Delta_{A-B} = I_A - I_B$ represent the difference between Group A and Group B. Then, Group A and Group B were randomly disarranged and regrouped to be Group A' and Group B'. I'_A and I'_B represent the indices of Group A' and Group B', and $\Delta'_{A-B} = I'_A - I'_B$ represent the difference between Group A' and Group B'. Repeat the random disarrangement and regroupment of Group A and Group B many times, such as 5,000 times. Then, Δ'_{A-B} could build a null distribution. After that, the significance of Δ_{A-B} could be calculated by using the normal distribution function according to the null distribution. The permutation test could be used in the group comparison of SCN, CaSCN, and WTA-CSSCN.

In the interaction analysis, the GLM model was applied in the analysis. It was based on the differences of coefficient of the SCN and MOD-SCN (Bernhardt et al., 2009; Sharda et al., 2016; Xu et al., 2020).

The formula of the SCN group comparison using the interaction analysis is as follows:

$$Y = \beta_1 \times \text{Group}_1 + \beta_2 \times \text{Group}_2 + \beta_3 \times X + \beta_4 \times \text{Group}_1 \times X + \beta_5 \times \text{Group}_2 \times X + \beta_6 \times \text{Var Of Clinic}$$

Here, $\times$ indicates an interaction between terms, and Cov Of No Int is the covariate of no interest. X is the "signal" of the seed region, Y is the "signals" of target region, Group_1 and Group_2 represent the labels of two groups. The difference of β_3 and β_4 presents the difference of covariance connectivity between seed region and target region.

The formula of MOD-SCN group comparison using the interaction analysis is as follows:

$$Y = \beta_1 \times \text{Group} + \beta_2 \times X + \beta_3 \times \text{Var Of Clinic} + \beta_4 \times \text{Group} \times \text{Val Of Clinic} + \beta_5 \times X \times \text{Val Of Clinic} + \beta_6 \times \text{Group} \times X + \beta_7 \times \text{Group} \times X \times \text{Val Of Clinic} + \beta_8 \times \text{Cov Of No Int}$$

Here, $\times$ indicates an interaction between terms, and Cov Of No Int is the covariate of no interest. Y is the "Signal" of target ROI, and X is the "Signal" of seed ROI. Group is the labels of two groups of participants. Val Of Clinic is the clinical

TABLE 1 | The parameters of the demo dataset for BCCT.

Seed	Seed	Template
MNI coordinate 0–53 30, radius 10 mm	MNI coordinate 0–53 30	Automated anatomical labeling
SCN: GMV	SCN: thickness	SCN: GMV
seed-to-brain	seed-to-brain	ROI-wise
Interaction Analysis for Group Comparison	Interaction Analysis for Group Comparison	Permutation Test for Group Comparison
CaSCN: GMV	CaSCN: thickness	CaSCN: GMV
Seed-to-brain, sorted by age	Seed-to-brain, sorted by age	ROI-wise, sorted by age
Residual-based	Coefficient-based	Coefficient-based
Permutation test for group comparison	Permutation test for group comparison	Permutation test for group comparison
Modulation: GMV	Modulation: thickness	Modulation: GMV
Seed-to-brain	Seed-to-brain	ROI-wise
Clinical variable: age	Clinical variable: age	Clinical variable: age
Interaction Analysis for Group Comparison	Interaction Analysis for Group Comparison	Interaction Analysis for Group Comparison

BCCT, brain covariance connectivity toolkit; CaSCN, causal analysis of structural covariance network; GMV, gray matter volume; ROI, region of interest; SCN, structural covariance network.

variance for the modulation analysis. The significance of β_7 could represent the power of modulation effect on the structural covariance connectivity between X and Y between two groups of participants.

The interaction analysis in the toolkit was based on the SurfStat Toolkit (see text footnote 4) (Lerch et al., 2006; Bernhardt et al., 2009; Worsley et al., 2009).

RESULTS-SHOWING MODE

Six modes of result showing were included in the toolkit: Map (SCN&Modulate), Matrix (SCN&Modulate), Map (GCA), Matrix (GCA), Winner-Take-All, and View for Surf. The Map (SCN&Modulate) and Map (GCA) were suitable for the result showing of SCN, MOD-SCN, and CaSCN of voxel-wise analysis of volume-based morphological images. The Matrix (SCN&Modulate) and Matrix (GCA) were suitable for the result showing of SCN, MOD-SCN, and CaSCN of ROI-wise analysis of the morphological images. The Winner-Take-All was designed for the result showing of WTA-CSSCN. And the View for Surf was suitable for the result showing of the SCN, MOD-SCN, and CaSCN of vertex-wise analysis of surface-based morphological images. For each mode, the parameter results and group comparison results could be shown. In parameter result showing, the related p information should be selected for the threshold selection. The permutation p result could be shown in each mode independently. The Winner-Take-All mode provided the radar map and cross-sectional slice maps of parcelation and the group comparison result of the permutation test. More detailed description of the result showing would be listed in the help document.

DEMO DATASET

For demo, 52 healthy participants (28 female, age range 20–40 years, 25.82 ± 6.59 years; 24 male, age range 21–46 years, 27.5 ± 7.09 years) were included in the study. All healthy participants were collected in Jinling Hospital, Medical School of Nanjing University. This study was approved by the Medical Ethics Committee in Jinling Hospital, Medical School of Nanjing University. Written informed consent was obtained from all the participants. There was no significant difference in age between the two groups ($T = -0.884$, $p = 0.381$).

All participants were scanned in 3T MRI scanner (Siemens Trio, Germany). High-resolution T1-weighted anatomical

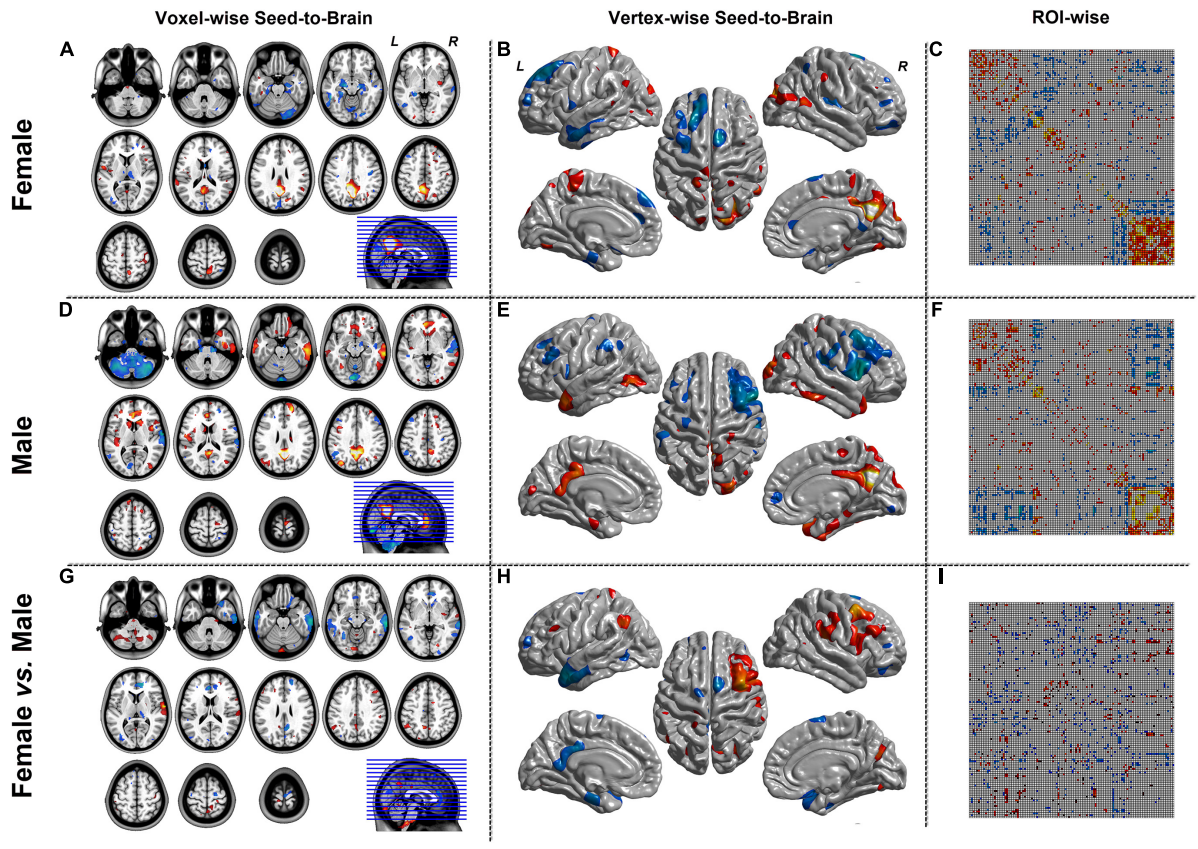

FIGURE 3 | The results of SCN mode. Panels **(A,D,G)** were the results of seed-to-brain connectivity of the GMV. Panels **(B,E,H)** were the results of seed-to-brain connectivity of thickness. Panels **(C,F,I)** were the results of ROI-wise connectivity of the GMV with the automated anatomical labeling (AAL) template. All results were set at the threshold of $p < 0.05$ uncorrected.

images were acquired in the sagittal orientation using a magnetization-prepared rapid gradient-echo sequence with the following parameters: repetition time (TR) = 2,300 ms, echo time (TE) = 2.98 ms, flip angle = 9°, field of view (FOV) = 25.6 × 25.6 cm^2, acquisition matrix = 256 × 256, slice thickness = 1 mm, 176 slices without interslice gap.

Before being used for the toolkit, the two indices were processed in advance. The GMVs were conducted by CAT12 (see text footnote 6) implemented in SPM12 (see text footnote 2). And the cortical thickness indices were conducted by FreeSurfer 5.3 (see text footnote 3). The TIV was used as the variable of no interest during the following brain structural covariance connectivity analysis.

For a whole view of the software, the showing results of different combinations were listed in **Table 1**. The sex factor was used as the group label in the group comparison.

For WTA-CSSCN analysis, we employed a cortical parcelation by dividing bilateral hemispheres into five non-overlapping lobes: (1) frontal lobe, (2) motor/premotor lobe, (3) somatosensory lobe, (4) parietal/occipital lobe, and (5) temporal lobe (Zhang et al., 2008; Ji et al., 2015). The cerebellum from automated anatomical labeling (AAL) (Tzourio-Mazoyer et al., 2002) was set to be the subcortex structure for analysis. In the toolkit, there were templates of thalamus, striatum, and cerebellum available for the WTA-CSSCN analysis. Here, we took the cerebellum for the demo. Additionally, the subcortex did not fully fit the usage range of this mode, since this mode could be used to analyze the winner-take-all and SCN between parcelations of brain part A and regions of brain part B, such as cortex parcelations to the thalamus, parcelations of the thalamus to the cerebellum, etc. The permutation test was used for the comparison of numbers of connected voxels. The sex factor was used as the group label in the group comparison.

RESULTS OF DEMO DATASET

Here, we only presented the results of the software. We would not discuss the meaning of the results. The results were presented according to the setting in **Table 1**.

Figure 3 represented the results of the SCN mode. The left column was the seed-to-brain connectivity maps of volume-based morphological images in the female group, the male group separately, and the group comparison result. The middle

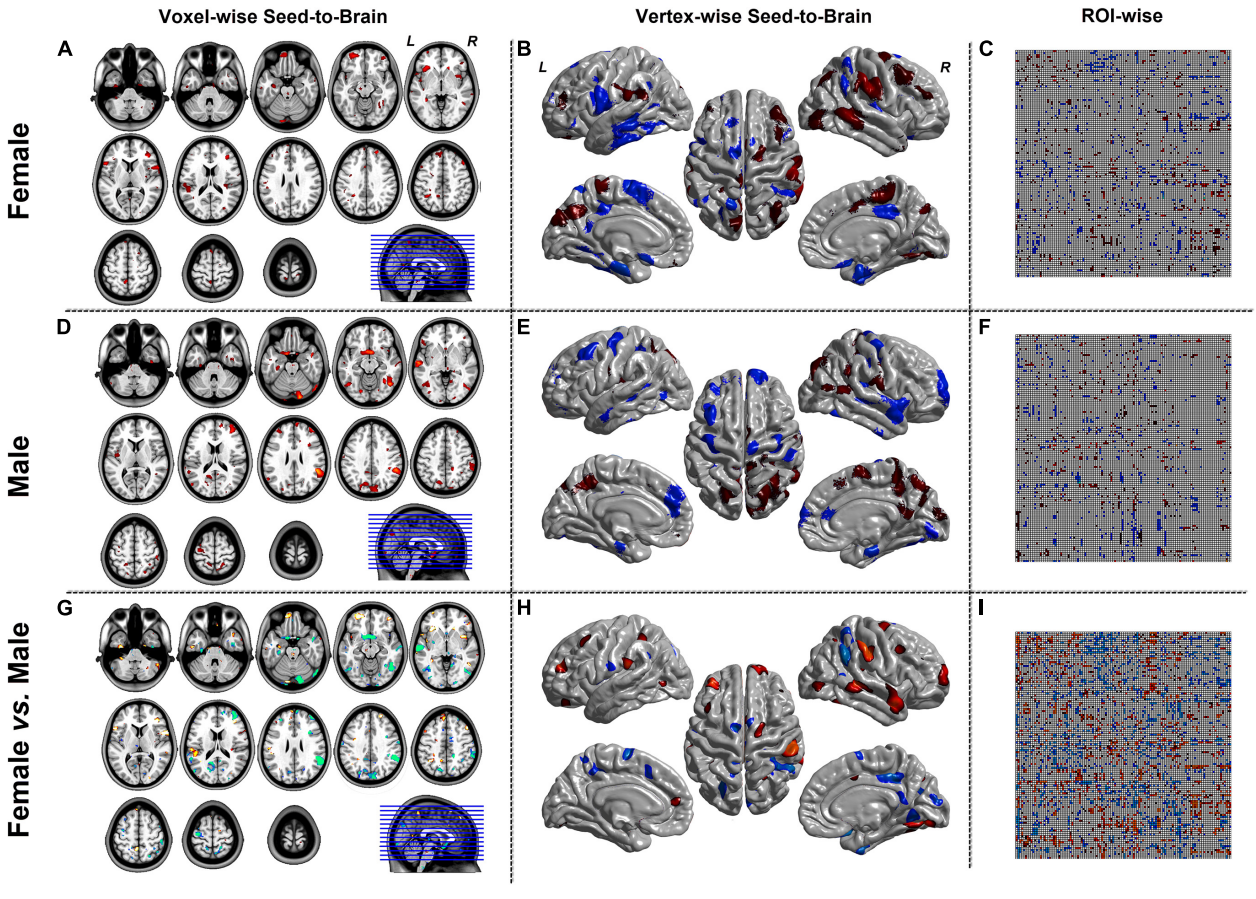

FIGURE 4 | The results of CaSCN mode with X (seed)-to-Y (Brain/Target ROI). Panels **(A,D,G)** were the results of seed-to-brain connectivity of the GMV. Panels **(B,E,H)** were the results of seed-to-brain connectivity of thickness. Panels **(C,F,I)** were the results of ROI-wise connectivity of the GMV with the AAL template. All results were set at the threshold of $p < 0.05$ uncorrected.

column was the seed-to-brain connectivity maps of surface-based morphological images in the female group, the male group separately, and the group comparison result. The right column was the ROI-wise connectivity matrices of volume-based morphological images in the female group, the male group separately, and the group comparison result. All results were set to be $p < 0.05$ uncorrected. The hot color represented the positive values, and the winter color represented the negative values.

Figures 4, **5** were the results of the CaSCN mode. **Figure 4** represented the out effect of GCA of the seed region, and **Figure 5** represented the in effect of GCA of the seed region. Similar to the SCN result-showing mode (**Figure 3**), the left column was the results of seed-to-brain connectivity maps of volume-based morphological images, the middle column was the results of seed-to-brain connectivity maps of surface-based morphological images, and the right column was the results of ROI-wise connectivity matrices of volume-based morphological images. All results were presented as the female group (top), the male group (middle), and the comparison result (bottom). All results were set to be $p < 0.05$ uncorrected. The hot color represented the positive values, and the winter color represented the negative values.

Figure 6 represented the results of the MOD-SCN mode. Similar to the SCN result-showing mode (**Figure 3**), the left column was the results of seed-to-brain connectivity maps of volume-based morphological images, the middle column was the results of seed-to-brain connectivity maps of surface-based morphological images, and the right column was the results of ROI-wise connectivity matrices of volume-based morphological images. All results were presented as the female group (top), the male group (middle), and the comparison result (bottom). All results were set to be $p < 0.05$ uncorrected. The hot color represented the positive values, and the winter color represented the negative values. The seed-to-brain results represented the modulation effect of the connectivity with seed region to whole brain. The upper triangular of the ROI-wise connectivity matrix represented the seed-to-target effects, while the lower triangular represented the target-to-seed effects. It was an asymmetric matrix.

Figure 7 represented the results of the WTA-SCN mode with the female group (upper left), the male group (left bottom) separately, and the group comparison result (right). The colors in the cerebellum represented the corresponding brain regions of the cortex. The group comparison represented the significance of

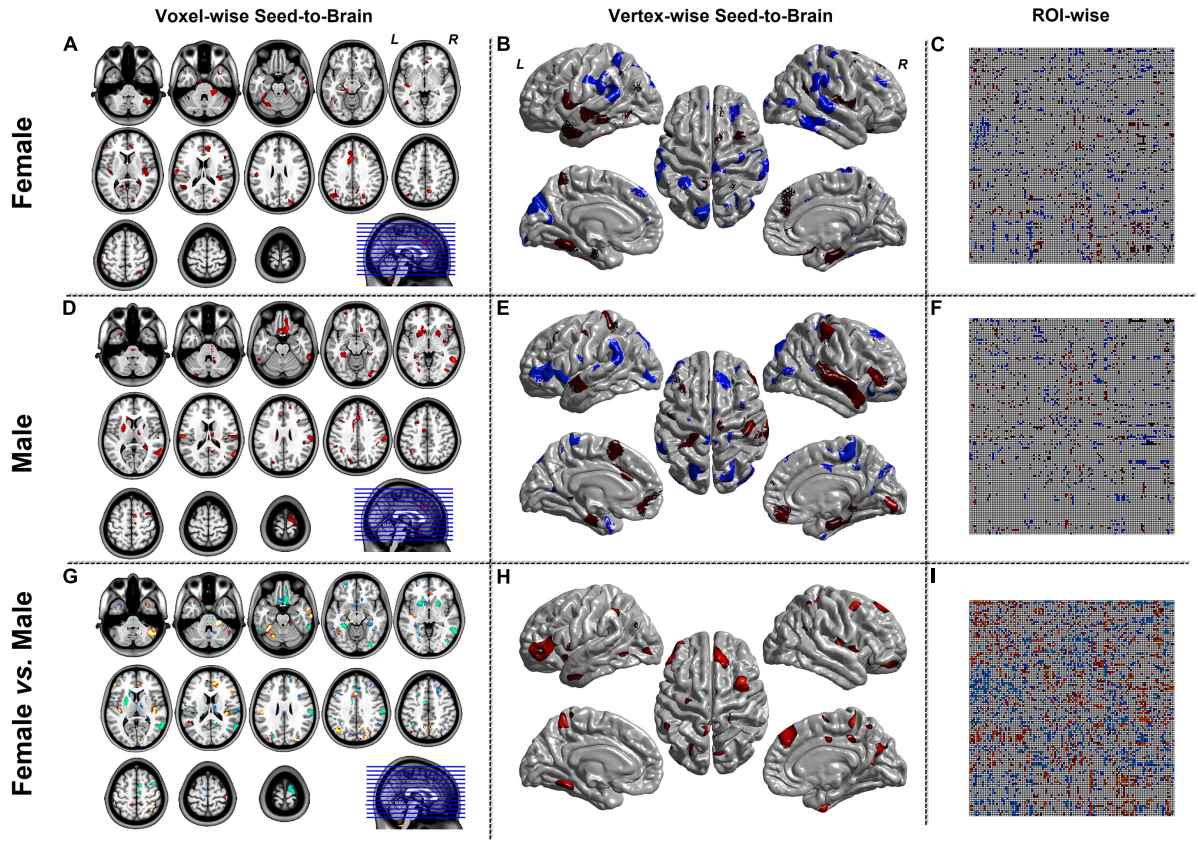

FIGURE 5 | The results of CaSCN mode with Y (Brain/Target ROI)-to-X (seed). Panels **(A**,**D**,**G)** were the results of seed-to-brain connectivity of the GMV. Panels **(B**,**E**,**H)** were the results of seed-to-brain connectivity of thickness. Panels **(C**,**F**,**I)** were the results of ROI-wise connectivity of the GMV with the AAL template. All results were set at the threshold of $p < 0.05$ uncorrected.

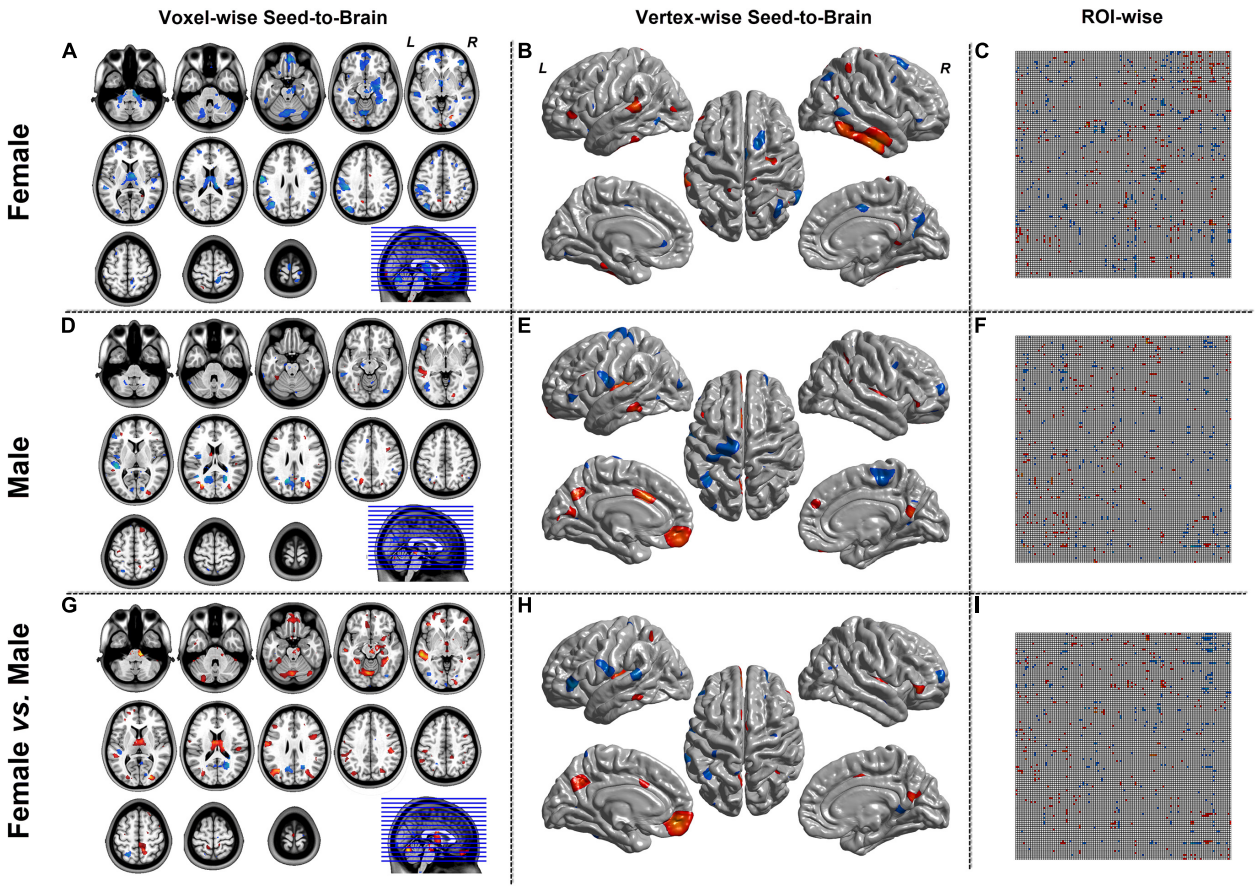

FIGURE 6 | The results of modulation mode with X (seed)-to-Y (Brain/Target ROI). Panels **(A**,**D**,**G)** were the results of seed-to-brain connectivity of the GMV. Panels **(B**,**E**,**H)** were the results of seed-to-brain connectivity of thickness. Panels **(C**,**F**,**I)** were the results of ROI-wise connectivity of the GMV with the AAL template. All results were set at the threshold of $p < 0.05$ uncorrected. The ROI-wise connectivity contained the seed-to-Target and Target-to-seed effects.

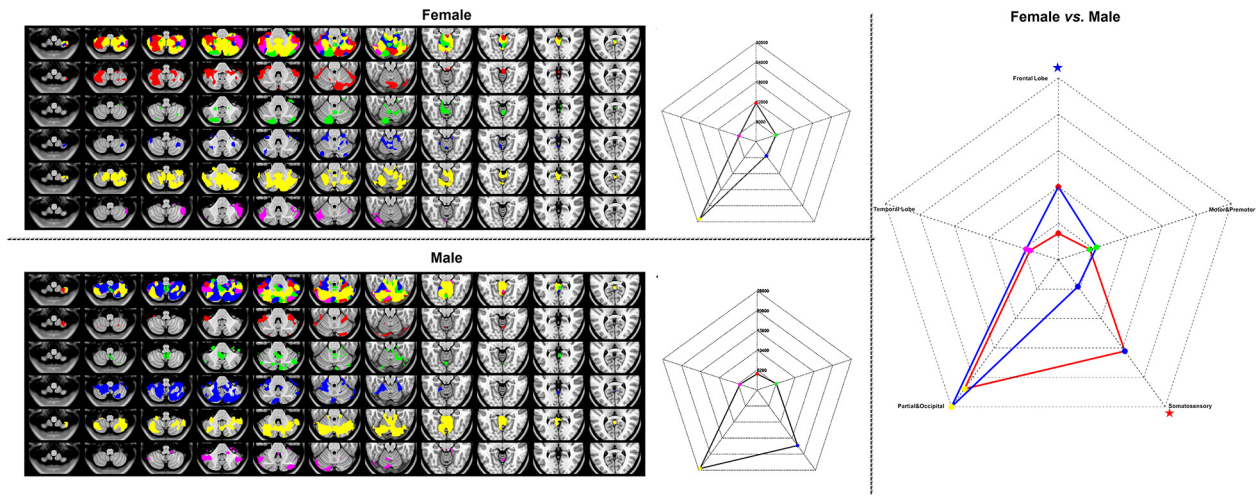

FIGURE 7 | The results of WTA-CSSCN mode. Red, frontal lobe; green, motor and premotor; blue, somatosensory; yellow, parietal and occipital; and violet, temporal lobe. The red star represented the female group > male group, and the blue star represented the male group < female group.

the numbers of cortex ROI-to-cerebellum connectivity between female and male groups.

DISCUSSION

In the current work, we developed a user-friendly GUI BCCT in MATLAB platform. We also present the results of BCCT toolkit with the demo dataset. A completed workflow of structural covariance connectivity analysis was presented to the researchers who would like to use the toolkit.

As far as we know, this toolkit is the first software dedicated to structural covariance analysis. Additionally, for the first time, the toolkit integrated the group comparison, which formerly restricted the application of structural covariance analysis for clinical researchers. Furthermore, the advanced methods, CaSCN, MOD-SCN, and WTA-CSSCN, have extended the application areas of SCN. Structural covariance analysis holds great promise in many areas of neuroscience (Bermudez et al., 2009; Lv et al., 2010; Zielinski et al., 2010) and neuropsychiatric disorders (Ge et al., 2020; Zhang et al., 2020).

The result showings of SCN, CaSCN, and MOD-SCN of demo dataset could help researchers to be familiar with the toolkit. Furthermore, the volume-based and surface-based analysis could help meet more requirements of the researcher. The WTA-CSSCN could be used for the parcelation of subcortex structures (Xu et al., 2020). The MOD-SCN connected the covariance connectivity and the clinical variables (Bernhardt et al., 2009; Xu et al., 2020). The statistical analysis of structural covariance connectivity could give the researcher more useful information.

The results of the toolkit could be used for the later analysis of other toolkits, such as the graph theoretic analysis. Additionally, the functional covariance connectivity, such as hemodynamic (Tzourio-Mazoyer et al., 2002), metabolic (Di and Biswal, 2012), and amplitude of low-frequency fluctuation (Zhang et al., 2011b; Taylor et al., 2012; Liao et al., 2013) descriptor, could be done in the toolkit. The text-based and mat-based mode of ROI-wise connectivity could be used for other kinds of neuroimage mode, such as electroencephalogram (EEG) signals of sensors.

METHODOLOGICAL CONSIDERATION

For the limitation of time and abilities of the developer, there were several methodological considerations in the toolkit. Firstly, the surface-based analysis was only limited to the data structures of FreeSurfer software. The support of other types of surface-based images would be added in future versions. Secondly, the group comparison was restricted into two groups, and only two kinds of statistical analysis tools were included in the toolkit. The statistical analysis beyond two groups and other statistical tools need to be discussed later. Additionally, some other kinds of covariance connectivity analysis and statistical tools require new ideas from the user of the toolkit. The result-showing mode of the toolkit needed further update in the later version.

DATA AVAILABILITY STATEMENT

The raw data supporting the conclusions of this article will be made available by the authors, without undue reservation.

ETHICS STATEMENT

The studies involving human participants were reviewed and approved by Jinling Hospital, School of Medicine, Nanjing University. The patients/participants provided their written informed consent to participate in this study.

AUTHOR CONTRIBUTIONS

QX and QZ: draft writing. GLi, X-jD, XX, JH, QY, RL, ZiZ, and YY: data collection. GLi and X-jD: data process. ZhZ and GLu: topic propose. RQ and LZ: draft modification. QX, QZ, and XD: software developer. All authors contributed to the article and approved the submitted version.

FUNDING

This work was supported by grants of National Natural Science Foundation of China (Grant Nos. 81871345, 81790653, 81790650, and 81701680), National Key Research and Development Program of Ministry of Science and Technology of People's Republic of China (Grant Nos. 2018YFA0701703 and 2017YFC0108805), grants of the key talent project in Jiangsu province (Grant No. ZDRCA2016093), Natural scientific foundation-social development (Grant No. BE2016751), Post-doctoral grants of China (Grant No. 2016M603064) and Jiangsu Province (1501169B).

REFERENCES

Bermudez, P., Lerch, J. P., Evans, A. C., and Zatorre, R. J. (2009). Neuro-anatomical correlates of musicianship as revealed cortical thickness and voxel-based morphometry. *Cereb. Cortex* 19, 1583–1596. doi: 10.1093/cercor/bhn196

Bernhardt, B. C., Klimecki, O. M., Leiberg, S., and Singer, T. (2014). Structural covariance networks of the dorsal anterior insula predict females' individual differences in empathic responding. *Cereb. Cortex* 24, 2189–2198. doi: 10.1093/cercor/bht072

Bernhardt, B. C., Rozen, D. A., Worsley, K. J., Evans, A. C., Bernasconi, N., and Bernasconi, A. (2009). Thalamo-cortical network pathology in idiopathic generalized epilepsy: insights from MRI-based morphometric correlation analysis. *Neuroimage* 46, 373–381. doi: 10.1016/j.neuroimage.2009.01.055

Biswal, B., Yetkin, F. Z., Haughton, V. M., and Hyde, J. S. (1995). Functional connectivity in the motor cortex of resting human brain using echo-planar MRI. *Magn. Reson. Med.* 34, 537–541. doi: 10.1002/mrm.1910340409

Bullmore, E., and Sporns, O. (2009). Complex brain networks: graph theoretical analysis of structural and functional systems. *Nat. Rev. Neurosci.* 10, 186–198. doi: 10.1038/nrn2575

Chen, G., Hamilton, J. P., Thomason, M. E., Gotlib, I. H., Saad, Z. S., and Cox, R. W. (2009). Granger causality via vector auto-regression tuned for fMRI data analysis. *Proc. Int. Soc. Magn. Reson. Med.* 17:1718.

Di, X., and Biswal, B. B. (2012). Metabolic brain covariant networks as revealed by FDG-PET with reference to resting-state fMRI networks. *Brain Connect.* 2, 275–283. doi: 10.1089/brain.2012.0086

Ge, R., Hassel, S., Arnott, S. R., Davis, A. D., Harris, J. K., Zamyadi, M., et al. (2020). Structural covariance pattern abnormalities of insula in major depressive disorder: a CAN-BIND study report. *Prog. Neuropsychopharmacol. Biol. Psychiatry.* 2020:110194. doi: 10.1016/j.pnpbp.2020.110194

Goebel, R., Roebroeck, A., Kim, D. S., and Formisano, E. (2003). Investigating directed cortical interactions in time-resolved fMRI data using vector autoregressive modeling and Granger causality mapping. *Magn. Reson. Imaging* 21, 1251–1261. doi: 10.1016/j.mri.2003.08.026

Guo, J., Chen, H., Biswal, B. B., Guo, X., Zhang, H., Dai, L., et al. (2020). Gray matter atrophy patterns within the cerebellum-neostriatum-cortical network in SCA3. *Neurology* 95, e3036–e3044. doi: 10.1212/wnl.0000000000010986

He, Y., Chen, Z. J., and Evans, A. C. (2007). Small-world anatomical networks in the human brain revealed by cortical thickness from MRI. *Cereb. Cortex* 17, 2407–2419. doi: 10.1093/cercor/bhl149

Ji, G. J., Zhang, Z., Xu, Q., Wang, Z., Wang, J., Jiao, Q., et al. (2015). Identifying Corticothalamic Network Epicenters in Patients with Idiopathic Generalized Epilepsy. *AJNR Am. J. Neuroradiol.* 36, 1494–1500. doi: 10.3174/ajnr.A4308

Jiang, Y., Luo, C., Li, X., Duan, M., He, H., Chen, X., et al. (2018). Progressive Reduction in Gray Matter in Patients with Schizophrenia Assessed with MR Imaging by Using Causal Network Analysis. *Radiology* 287:729. doi: 10.1148/radiol.2018184005

John, G. (1982). Measurement of Linear Dependence and Feedback between Multiple Time Series. *J. Am. Stat. Assoc.* 77, 304–313.

Lerch, J. P., Worsley, K., Shaw, W. P., Greenstein, D. K., Lenroot, R. K., Giedd, J., et al. (2006). Mapping anatomical correlations across cerebral cortex (MACACC) using cortical thickness from MRI. *Neuroimage* 31, 993–1003. doi: 10.1016/j.neuroimage.2006.01.042

Li, Y., Wang, C., Teng, C., Jiao, K., Song, X., Tan, Y., et al. (2019). Hippocampus-driving progressive structural alterations in medication-naïve major depressive disorder. *J. Affect. Disord.* 256, 148–155. doi: 10.1016/j.jad.2019.05.053

Liao, W., Zhang, Z., Mantini, D., Xu, Q., Wang, Z., Chen, G., et al. (2013). Relationship between large-scale functional and structural covariance networks in idiopathic generalized epilepsy. *Brain Connect.* 3, 240–254. doi: 10.1089/brain.2012.0132

Liao, W., Zhang, Z., Pan, Z., Mantini, D., Ding, J., Duan, X., et al. (2010). Altered functional connectivity and small-world in mesial temporal lobe epilepsy. *PLoS One* 5:e8525. doi: 10.1371/journal.pone.0008525

Liao, W., Zhang, Z., Pan, Z., Mantini, D., Ding, J., Duan, X., et al. (2011). Default mode network abnormalities in mesial temporal lobe epilepsy: a study combining fMRI and DTI. *Hum. Brain Mapp.* 32, 883–895. doi: 10.1002/hbm.21076

Lv, B., Li, J., He, H., Li, M., Zhao, M., Ai, L., et al. (2010). Gender consistency and difference in healthy adults revealed bycortical thickness. *NeuroImage* 53, 373–382. doi: 10.1016/j.neuroimage.2010.05.020

Sanabria-Diaz, G., Melie-García, L., Iturria-Medina, Y., Alemán-Gómez, Y., Hernández-González, G., Valdés-Urrutia, L., et al. (2010). Surface area and cortical thickness descriptors reveal different attributes of the structural human brain networks. *Neuroimage* 50, 1497–1510. doi: 10.1016/j.neuroimage.2010.01.028

Seeley, W. W., Crawford, R. K., Zhou, J., Miller, B. L., and Greicius, M. D. (2009). Neurodegenerative diseases target large-scale human brain networks. *Neuron* 62, 42–52. doi: 10.1016/j.neuron.2009.03.024

Sharda, M., Khundrakpam, B. S., Evans, A. C., and Singh, N. C. (2016). Disruption of structural covariance networks for language in autism is modulated by verbal ability. *Brain Struct. Funct.* 221, 1017–1032. doi: 10.1007/s00429-014-0953-z

Sporns, O. (2011). The human connectome: a complex network. *Ann. N. Y. Acad. Sci.* 1224, 109–125. doi: 10.1111/j.1749-6632.2010.05888.x

Sporns, O. (2018). Graph theory methods: applications in brain networks. *Dialogues Clin. Neurosci.* 20, 111–121. doi: 10.31887/DCNS.2018.20.2/osporns

Taylor, P. A., Gohel, S., Di, X., Walter, M., and Biswal, B. B. (2012). Functional covariance networks: obtaining resting-state networks from intersubject variability. *Brain Connect.* 2, 203–217. doi: 10.1089/brain.2012.0095

Teipel, S., Raiser, T., Riedl, L., Riederer, I., Schroeter, M. L., Bisenius, S., et al. (2016). Atrophy and structural covariance of the cholinergic basal forebrain in primary progressive aphasia. *Cortex* 83, 124–135. doi: 10.1016/j.cortex.2016.07.004

Tzourio-Mazoyer, N., Landeau, B., Papathanassiou, D., Crivello, F., Etard, O., Delcroix, N., et al. (2002). Automated anatomical labeling of activations in SPM using a macroscopic anatomical parcellation of the MNI MRI single-subject brain. *Neuroimage* 15, 273–289. doi: 10.1006/nimg.2001.0978

Valk, S. L., Bernhardt, B. C., Böckler, A., Trautwein, F. M., Kanske, P., and Singer, T. (2017). Socio-Cognitive Phenotypes Differentially Modulate Large-Scale Structural Covariance Networks. *Cereb. Cortex* 27, 1358–1368. doi: 10.1093/cercor/bhv319

Watson, C. G., DeMaster, D., and Ewing-Cobbs, L. (2019). Graph theory analysis of DTI tractography in children with traumatic injury. *Neuroimage Clin.* 21:101673. doi: 10.1016/j.nicl.2019.101673

Worsley, K. J., Taylor, J. E., Carbonell, F., Chung, M. K., and Evans, A. C. J. N. (2009). SurfStat: a Matlab toolbox for the statistical analysis of univariate and multivariate surface and volumetric data using linear mixed effects models and random field theory. *NeuroImage* 47:S102.

Wu, G. R., Stramaglia, S., Chen, H., Liao, W., and Marinazzo, D. (2013). Mapping the voxel-wise effective connectome in resting state FMRI. *PLoS One* 8:e73670. doi: 10.1371/journal.pone.0073670

Xu, Q., Zhang, Q., Yang, F., Weng, Y., Xie, X., Hao, J., et al. (2020). Cortico-striato-thalamo-cerebellar networks of structural covariance underlying different epilepsy syndromes associated with generalized tonic-clonic seizures. *Hum. Brain Mapp.* 42, 1102–1115. doi: 10.1002/hbm.25279

Zang, Z. X., Yan, C. G., Dong, Z. Y., Huang, J., and Zang, Y. F. (2012). Granger causality analysis implementation on MATLAB: a graphic user interface toolkit for fMRI data processing. *J. Neurosci. Methods* 203, 418–426. doi: 10.1016/j.jneumeth.2011.10.006

Zhang, D., Snyder, A. Z., Fox, M. D., Sansbury, M. W., Shimony, J. S., and Raichle, M. E. (2008). Intrinsic functional relations between human cerebral cortex and thalamus. *J. Neurophysiol.* 100, 1740–1748. doi: 10.1152/jn.90463.2008

Zhang, X., Liu, W., Guo, F., Li, C., Wang, X., Wang, H., et al. (2020). Disrupted structural covariance network in first episode schizophrenia patients: evidence from a large sample MRI-based morphometric study. *Schizophr. Res.* 224, 24–32. doi: 10.1016/j.schres.2020.11.004

Zhang, Z., Liao, W., Chen, H., Mantini, D., Ding, J. R., Xu, Q., et al. (2011a). Altered functional-structural coupling of large-scale brain networks in idiopathic generalized epilepsy. *Brain* 134, 2912–2928. doi: 10.1093/brain/awr223

Zhang, Z., Liao, W., Xu, Q., Wei, W., Zhou, H. J., Sun, K., et al. (2017). Hippocampus-associated causal network of structural covariance measuring structural damage progression in temporal lobe epilepsy. *Hum. Brain Mapp.* 38, 753–766. doi: 10.1002/hbm.23415

Zhang, Z., Liao, W., Zuo, X. N., Wang, Z., Yuan, C., Jiao, Q., et al. (2011b). Resting-state brain organization revealed by functional covariance networks. *PLoS One* 6:e28817. doi: 10.1371/journal.pone.0028817

Zielinski, B. A., Gennatas, E. D., Zhou, J., and Seeley, W. W. (2010). Network-level structural covariance in the developing brain. *PNAS* 107, 18191–18196. doi: 10.1073/pnas.1003109107

Conflict of Interest: The authors declare that the research was conducted in the absence of any commercial or financial relationships that could be construed as a potential conflict of interest.

frontiers in Human Neuroscience

ORIGINAL RESEARCH
published: 07 June 2021
doi: 10.3389/fnhum.2021.654381

Characterization of Brain Iron Deposition Pattern and Its Association With Genetic Risk Factor in Alzheimer's Disease Using Susceptibility-Weighted Imaging

Peiting You[1,2†], Xiang Li[2†], Zhijiang Wang[3,4,5†], Huali Wang[3,4,5], Bin Dong[1]* and Quanzheng Li[2]**

[1] Beijing International Center for Mathematical Research, Peking University, Beijing, China, [2] Massachusetts General Hospital and Harvard Medical School, Boston, MA, United States, [3] Peking University Institute of Mental Health (Sixth Hospital), Beijing, China, [4] National Clinical Research Center for Mental Disorders and Key Laboratory of Mental Health, Ministry of Health, Peking University, Beijing, China, [5] Beijing Municipal Key Laboratory for Translational Research on Diagnosis and Treatment of Dementia, Beijing, China

The presence of iron is an important factor for normal brain functions, whereas excessive deposition of iron may impair normal cognitive function in the brain and lead to Alzheimer's disease (AD). MRI has been widely applied to characterize brain structural and functional changes caused by AD. However, the effectiveness of using susceptibility-weighted imaging (SWI) for the analysis of brain iron deposition is still unclear, especially within the context of early AD diagnosis. Thus, in this study, we aim to explore the relationship between brain iron deposition measured by SWI with the progression of AD using various feature selection and classification methods. The proposed model was evaluated on a 69-subject SWI imaging dataset consisting of 24 AD patients, 21 mild cognitive impairment patients, and 24 normal controls. The identified AD progression-related regions were then compared with the regions reported from previous genetic association studies, and we observed considerable overlap between these two. Further, we have identified a new potential AD-related gene (MEF2C) closely related to the interaction between iron deposition and AD progression in the brain.

Keywords: Alzheimer's disease, brain iron deposition, SWI, feature selection, genetic risk factor

OPEN ACCESS

Edited by:
Dajiang Zhu,
University of Texas at Arlington, United States

Reviewed by:
Jingwen Yan,
Indiana University, United States
Yong Liu,
Beijing University of Posts and Telecommunications (BUPT), China

***Correspondence:**
Huali Wang
huali_wang@bjmu.edu.cn
Bin Dong
dongbin@math.pku.edu.cn
Quanzheng Li
Li.Quanzheng@mgh.harvard.edu

[†]These authors share first authorship

Specialty section:
This article was submitted to Brain Imaging and Stimulation, a section of the journal Frontiers in Human Neuroscience

Received: *16 January 2021*
Accepted: *27 April 2021*
Published: *07 June 2021*

Citation:
You P, Li X, Wang Z, Wang H, Dong B and Li Q (2021) Characterization of Brain Iron Deposition Pattern and Its Association With Genetic Risk Factor in Alzheimer's Disease Using Susceptibility-Weighted Imaging. Front. Hum. Neurosci. 15:654381. doi: 10.3389/fnhum.2021.654381

INTRODUCTION

Alzheimer's disease (AD) is among the leading causes of death in the United States and has been on the rising trend in the past decade with the aging populations (Alzheimer's Association, 2011). More than 47 million people worldwide are estimated to have AD and related dementias. This number is expected to reach 152 million by 2050, with one new case of dementia diagnosed every 3 s (Patterson, 2018). As no effective treatment has been found to delay the onset and progression of AD (Selkoe, 2012), early diagnosis of AD and understanding of the progression

from mild cognitive impairment (MCI) to AD is essential for preventative and therapeutic strategies (Gauthier et al., 2006).

Progression of AD can lead to structural and functional changes in the brain, which various imaging techniques can capture. Differential brain structural diagnostic markers derived from T1-weighted magnetic resonance imaging (MRI) have been reported for AD (Cuingnet et al., 2011), MCI (Driscoll et al., 2009), and MCI–AD conversion (Davatzikos et al., 2011) based on brain atrophy measurement (Jack et al., 2004) and its spatial pattern (Davatzikos et al., 2008). Diffusion MRI can measure white matter connectivity and microstructural integrity. It may also be supportive for the diagnosis of AD, based on both change in white matter tracts (Douaud et al., 2011) and global/local fractional anisotropy (FA) (Medina et al., 2006; Zhang et al., 2007). Functional magnetic resonance imaging (fMRI) has also been explored to characterize cognitive and behavior changes caused by AD progression (Li et al., 2019). Previous studies observed that disruption of resting-state functional networks could differentiate MCI/AD with normal controls (Rombouts et al., 2005); so does the decreased activation in cognition-related brain regions measured by memory encoding task (Machulda et al., 2003). Other functional imaging techniques, such as electroencephalography (EEG) and magnetoencephalography (MEG), have been demonstrated to detect the brain signal spectrum shift (Fernández et al., 2006) and coherence (Jeong, 2004). Previous studies also reported the utility of these techniques in modeling brain network alterations in MCI patients after cognitive training (Xu et al., 2020). Besides, PET imaging has been established as a standard approach to investigate pathological features and imaging biomarkers for AD, including neuritic plaques of amyloid-β peptide fibrils (Nordberg, 2004), hyper-phosphorylated tau neurofibrillary tangles (Ossenkoppele et al., 2016), as well as their respective propagation patterns (Sepulcre et al., 2018; Guo et al., 2019). Recently, the fusion of multiple imaging modalities for the early diagnosis of MCI and AD has been well studied and demonstrated improved performance over single-modality biomarkers (Zhang et al., 2011).

Among all potential imaging biomarkers for AD, one crucial marker is the excessive iron deposition in the brain. In vitro and in vivo studies have observed that excessive iron deposition in the brain might promote neurotoxicity, which causes neuronal injury and has been recognized as a putative factor in AD pathogenesis (Stankiewicz et al., 2007). Previous literature on the iron content measured with MR susceptibility-weighted imaging (SWI) (Halefoglu and Yousem, 2018) has reported significant iron deposition in brain regions related to brain cognitive and memory functions in AD, including substantia nigra, globus pallidum, hippocampus, putamen, and caudate nucleus. It has also been found that iron can induce the production and accumulation of amyloid-β plaques and bind to tau protein to induce tau protein phosphorylation aggregation (Liu et al., 2018). A meta-analysis on 1,813 AD patients and 2,401 normal controls concluded that specific brain regions had statistically significantly higher iron concentrations that can be related to AD (Tao et al., 2014). Besides, genetic factors have been found to play an essential role in the development of neurodegenerative disease in the context of iron deposition. It has been reported that the circulation of iron in the brain involves a complex interaction between metabolic and genetic processes (Rouault, 2013). It has been widely reported that genetic mutations can cause excessive iron deposition at the systemic level, posing as risk factors for several diseases such as acute myocardial infarction (Roest et al., 1999; Tuomainen et al., 1999). Similar gene mutations have also been reported to be related to neurodegenerative diseases (Hagemeier et al., 2012), for example, through the oxidative stress process that ultimately leads to the formation of neurofibrillary tangles senile plaques in AD (Crichton et al., 2011).

However, the predictive value of iron deposition to AD progression, especially with the current advancement of machine learning methods, is still unclear and largely understudied. With the aging of the brain, the excessive iron deposition could be related to many factors besides AD, such as increased permeability of the blood–brain barrier, dilation of blood vessels, redistribution of iron, and iron homeostasis changes (Ward et al., 2014). In the initial stage of AD patients, increasing iron is always along with β-amyloid peptide gathering, which provides the theoretical basis of MRI-based diagnosis (Ward et al., 2014). In addition, while region-specific iron deposition in the normal aging population has been investigated and observed in substantia nigra, putamen, globus pallidum, and caudate nuclei, iron-related pathogenic mechanisms are needed to explain the cause of such selectivity (Zecca et al., 2004). The regional heterogeneity and age-related brain iron have been confirmed by MRI (Zecca et al., 2004; Ramos et al., 2014).

Susceptibility-weighted imaging plays a vital role in the estimation of iron deposition (Sheelakumari et al., 2016). Thus, it could be used to detect abnormal iron deposition related to the progress of AD. Most diagnostic works using SWI imaging technology are currently based on manual or semi-manual measurement of the region of interest (ROI) in MRI images, which relies on previous knowledge and is usually confined to the hippocampus and entorhinal cortex (Zhang et al., 2015). In the past decade, with the advancement of machine learning methodologies, various computer-assisted models have been developed for the early diagnosis of AD, including SVM-based classifier (Davatzikos et al., 2011), Random Forest (Lebedev et al., 2014), and most recently, deep learning methods (Ortiz et al., 2016). However, there is little work on using machine learning methods to analyze iron deposition in the brain and facilitate automatic AD/MCI detection by SWI.

Thus, in this work, we used feature selection techniques and classification algorithms to analyze SWI image data acquired from a group of 69 subjects. After image pre-processing, iron deposition characteristics were extracted from SWI images based on different brain atlases. We then investigated the prediction power of different feature selection methods/atlas/classifier combinations. The best set of brain regions selected by the feature selection procedure were analyzed and compared to neuroscientific findings. We also obtained human gene expression data from the public Allen Human Brain Atlas Microarray dataset to investigate the relationship between iron deposition, genetic risk factor, and AD progression. This integrated analysis framework could lead us to answer the

questions of (1) whether iron deposition as characterized by SWI images can be used to differentiate the three groups of subjects (healthy control, MCI, and AD), (2) which brain regions are involved in the differentiation, and (3) whether those brain regions have common genetic factors.

The organization of the rest of this paper is as follows: in the Materials and Methods section, we will introduce the SWI imaging dataset, its pre-processing pipeline, as well as the feature selection and classification methods used in this work. The Result section will showcase and discuss the classification performance and discriminative brain regions identified by the feature selection method. The identified brain regions are then combined with gene expression data to analyze their underlying relationship and discover new AD-related genes.

MATERIALS AND METHODS

Study Population and Image Acquisition

All participants were recruited to establish a registry at the Dementia Care and Research Center, Peking University Institute of Mental Health. The clinical diagnosis of AD was made according to the International Classification of Disease, 10th Revision (ICD-10) (World Health Organization, 2004) and the criteria for probable AD of the National Institute of Neurological and Communicative Disorders and the Stroke/Alzheimer's Disease and Related Disorders Association (NINCDS-ADRDA) (McKhann et al., 1984). The clinical diagnosis of MCI was made according to Petersen's MCI criteria with the MMSE score of no less than 24. All the healthy controls had no history of neurological or psychiatric disorders, and subjective cognitive complaints or objectively abnormal cognitive assessment. Other inclusion criteria were as follows: age $\geq$55 years, right-handed, and primary school education ($\geq$6 years). Exclusion criteria were as follows: current or previous neuropsychiatric diseases, such as Parkinson's disease, epilepsy, alcohol or substance abuse/dependence, and head injury with loss of consciousness that could affect cognition or psychiatric behavior. This study was approved by the ethics committee of Peking University Institute of Mental Health (Sixth Hospital), Beijing, China. All participants were fully informed regarding the study protocol and provided written informed consent.

Participants were scanned on a 3-Tesla MR system (Siemens Magnetom Trio, A Tim System, Germany) using a standard 8-channel head coil at Peking University Third Hospital. T1-weighted magnetization-prepared rapidly acquired gradient-echo (MPRAGE) sequence was used to acquire high-resolution 3D MR anatomical images using the following parameters: repetition time (TR)/echo time (TE) = 2,530 ms/3.44 ms; time inversion (TI) = 1,100 ms; slice number = 192; slice thickness = 1.0 mm; gap = 0 mm; matrix = 256 × 256; field of view (FOV) = 256 mm × 256 mm; flip angle = 7°. SWI images were acquired using the following parameters: repetition time (TR)/echo time (TE) = 27 ms/20 ms; flip angle = 15°; slice thickness = 1.5 mm; voxel resolution = 0.8984 mm × 0.8984 mm × 1.5 mm. The Institutional Review Board of Peking University Sixth Hospital approved this study.

Similar to our previous genetic data studies on Allen Mouse Brain Atlas (AMBA) dataset (Li et al., 2017a,b), in this work, we used the Human Brain Atlas Microarray[1] data (Shen et al., 2012) to search the anatomical brain regions associated with a specific gene. The microarray data provided by Human Brain Atlas Microarray includes the expression value (normalized Z-score) on each brain region from each subject (donor), where we would average these Z-scores across different subjects. In case there were multiple probes used to detect the same gene, Z-scores across different probes would also be averaged. After calculating the averaged Z-scores of the target gene, we applied a threshold of 0.3 to determine whether that gene is considered highly expressed in each brain region. Finally, we would obtain a list of "highly expressed" brain regions associated with it for each target gene, which could be further matched to the regions in SWI data.

Image Preprocessing

Susceptibility-weighted imaging data were normalized into the MNI space based on transformation parameters derived from aligning T1 images to the MNI standard template using diffeomorphic anatomical registration through the exponentiated lie algebra (DARTEL) method (Ashburner, 2007) using Statistical Parametric Mapping (SPM12:[2]), then resampled to 1.5-mm isotropic voxels followed by spatially smoothing with a 6-mm full width at half maximum Gaussian kernel. We then applied three types of brain atlas: AAL (anatomical automatic labeling, 116 regions with 90 cerebral cortex and 26 cerebellar cortex regions), Harvard–Oxford (48 regions), and MMP (matrix metalloproteinase, 180 regions) to extract iron deposition information in the corresponding brain regions from SWI images. Specifically, each brain region (defined by one type of atlas) in the registered SWI images were characterized by the collection of voxels:

$$v_{i,j}, i \ = 1, \ldots, T, j \in S$$

where T is the number of subjects in the dataset (69 in this study), S consists of the R number of regions in the atlas, $S \ = 1, \ldots, S_1, S_1 + 1, \ldots, S_2, \ldots, S_R$. S_k denotes the number of voxels in the k-th region. In this way, we can obtain the phase value (i.e., iron content) of the i-th subject in the k-th region by

$$b_{ik}^{mean} \ = \frac{1}{S_k - S_{k-1}} \sum_{j \ =S_{k-1}+1}^{S_k} v_{i,j}$$

The final iron content vector for the i-th subject in the k-th region is then

$$X_{ik} \ = \frac{-b \ \times \pi}{4096},$$

where value in X varies from $-\pi$ to π, and b varies from −4,096 to 4,095.

[1] https://human.brain-map.org/microarray/search

[2] http://www.fil.ion.ucl.ac.uk/spm

Feature Selection and Classification

To identify the most discriminative brain regions toward classification of AD, MCI, and NC, we explored the commonly used supervised feature selection methods of Lasso and Adaptive Lasso for the analysis.

(1) Lasso: for dataset $D = (x_1, y_1), (x_2, y_2), \ldots, (x_m, y_m)$, where $x \in R^d$, $y \in R$, in this work x denotes the iron content vector and y denotes the patient label (AD/MCI/NC), we consider the simple linear regression model with the squared error as a loss function:

$$\min_w \sum_{i=1}^{m} (y_i - w^T x_i)^2$$

When there are much more features than samples, the above equation is prone to be overfitting. To solve the problem, the regularization term is introduced. With $l-1$ norm regularization, the Lasso (Least Absolute Shrinkage and Selection Operator) algorithm is

$$\min_w \sum_{i=1}^{m} (y_i - w^T x_i)^2 + \lambda ||w||_1,$$

with the regularization parameter $\lambda > 0$.

(2) Adaptive Lasso: by adding weights to the penalty term in the original Lasso, the Adaptive Lasso can counteract the possible biased estimate in LASSO, with the following loss function:

$$\min_w \sum_{i=1}^{m} (y_i - w^T x_i)^2 + \lambda \sum_j \frac{|\beta_j|}{w_j},$$

where $w_j = \beta_j (OLS)$.

Both Lasso and Adaptive Lasso can identify a subset of all regions (termed "regional feature") in a given atlas by the non-zero weights found in regression. Iron content information from the selected regional features were then used to train various classifiers, including AdaBoost, LinearSVC, Randomtree, and XGBoost, to perform a three-class (healthy control/MCI/AD) classification. We set the basic classifier of AdaBoost algorithm to cycle 100 times with a learning rate of 0.1. The depth of Randomtree is four. For the XGBoost algorithm, we used the tree model with maximum depth of five and softmax as activation function.

RESULTS

Results of this study are organized into two parts: in the first part we will describe the performance of the models we used for classifying AD and MCI patients from healthy controls. More importantly, we will analyze the region-specific feature extracted for making the classification. In the second part, we will connect the identified regions with gene expression data, both for the purpose of investigating the validity of the identified regions and to discover potentially new AD-related gene(s). A sample set of SWI images and the three different brain atlases used in this study are visualized in **Figure 1**.

Classification Performance and the Regional Features Extracted

By using Lasso and adaptive Lasso to extract discriminative features (i.e., brain regions) on SWI images defined on three different types of brain atlas, we now obtained the AD-predictive regions for each feature selection method (Lasso/adaptive Lasso) and each atlas (AAL, Harvard–Oxford, MMP) combination. To investigate the discriminative power of the obtained AD-predictive regions, we designed a 10-fold cross-validation scheme where the dataset would be randomly divided into training/validation set (62 subjects) and testing set (7 subjects), where regional features based on feature selection

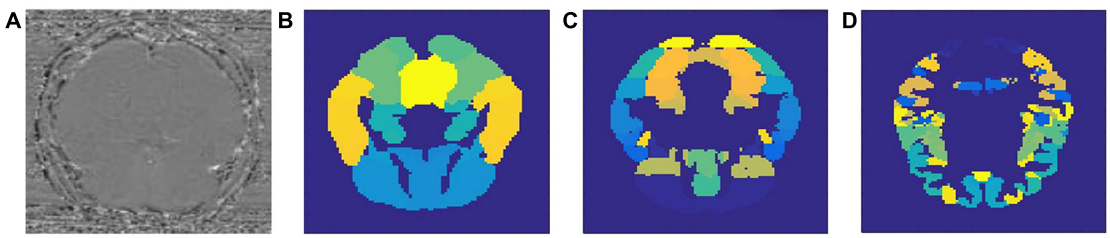

FIGURE 1 | Sample SWI image **(A)** and three types of brain atlases used: **(B)** AAL atlas, **(C)** Harvard–Oxford atlas, **(D)** MMP atlas.

TABLE 1 | Classification accuracy of different classifiers (listed in each row) on different atlases (listed in each column), based on the regional feature selected by Lasso or Adaptive Lasso Highest classification accuracies achieved for Lasso and Adaptive Lasso are marked by bold.

	Lasso			Adaptive Lasso		
Classifier	**AAL**	**Harvard**	**MMP**	**AAL**	**Harvard**	**MMP**
Adaboost	0.3145	0.3116	0.4304	0.3665	0.4415	0.4126
LinearSVC	**0.7388**	0.3578	0.3939	**0.7157**	0.5382	0.5497
Randomtree	0.4141	0.3564	0.3448	0.4747	0.4098	0.4415
XGBoost	0.4242	0.4227	0.404	0.4862	0.4747	0.518

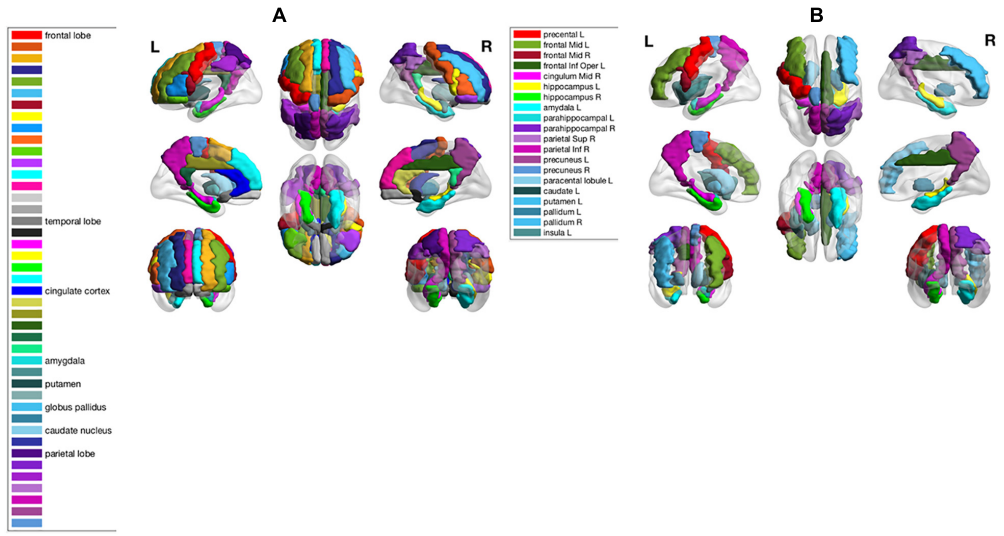

FIGURE 2 | (A) Names of 8 brain regions reported in Tao et al. (2014) and their visualizations as colored brain surface areas, according to the color bar to the left. **(B)** Names of the selected brain regions by Lasso algorithm in this study. The brain regions were visualized using the BrainNet Viewer (Xia et al., 2013).

method/atlas combination will be extracted correspondingly. Different classification methods would be then trained and tested on the extracted features in this cross-validation experiment. The experiment was repeated for 100 times, the average classification performance with regarding to different feature selection method (Lasso/Adaptive Lasso), atlas (AAD/Harvard/MMP), and classifiers (AdaBoost/LinearSVC/Randomtree /XGBoost) are summarized in **Table 1**.

As shown in the performance matrices, the best classification accuracy (0.7388) was obtained by the LinearSVC classifier on AAL atlas, using Lasso for the feature selection. Thus, in later analysis, we will investigate the feature regions and the corresponding neuroscience implications based on Lasso feature selection on AAL atlas. In total, 20 AAL regions that were selected as discriminative features by Lasso are listed and visualized as colored brain surfaces in **Figure 2B**. In addition, a meta-analysis study in Tao et al. (2014) have found that eight brain regions are closely related to AD, including frontal lobe (FL), parietal lobe (PL), temporal lobe, amygdala (Amg), putamen, cingulate cortex, globus pallidus (GP), and caudate nucleus, which are listed and visualized in **Figure 2A**.

Analysis of Gene Expression Distribution on Selected Regional Features

The AD-predictive regions identified by our models were then compared with the brain regions associated with three commonly known AD risk factor genes (APOE, MAPT, and CLU). As reported in our previous study, apolipoprotein E (APOE) genotype has been found to account for the majority of AD risk and pathology (Marioni et al., 2017; Sepulcre et al., 2018). Microtubule-associated protein tau (MAPT) gene is related to the encoding of tau protein and can cause potential vulnerability to tau accumulation as found in our work (Sepulcre et al., 2018), leading to frontotemporal dementia-spectrum (FTD-s) disorders (Coppola et al., 2012). The clusterin gene (CLU) has been reported to be associated with degraded regional cerebral blood flow (Thambisetty et al., 2013) and white matter integrity

TABLE 2 | List of regions identified by our method as predicative to AD (first column), as well as regions associated with APOE, MAPT, and CLU gene.

Regions identified by our method	Regions asscociated with APOE	Regions asscociated with MAPT	Regions asscociated with CLU
amygdala!	amygdala	cingulate gyrus	amygdala
caudate nucleus.L	dorsal thalamus	frontal lobe	cingulate gyrus
hippocampus!	globus pallidus	insula	dorsal thalamus
hippocampus.R	hypothalamus	occipital lobe	frontal lobe
inferior frontal gyrus, opercular part.L	striatum	parahippocampal gyms	globus pallidus
inferior parietal, supramarginal and angular gyri.R	subthalamus	parietal lobe	insula
insula!	ventral thalamus	temporal lobe	occipital lobe
lenticular nucleus, putamen.L			parietal lobe
median cingulate and paracingulate gyri.R			striatum
middle frontal gyrus.L			temporal lobe
middle frontal gyrus.R			
pallidum!			
pallidum.R			
paracental Lobule!			
parahippocampal!			
parahippocampal.R			
precentral gyms!			
precuneus!			
precuneus.R			
superior parietal gyrus.R			

TABLE 3 | Calculated gene presence frequency (in column "Frequency") from the 21 preselected genes as listed in each row.

Gene	Frequency	FL	Ins	CgG	HP	PHG	OL	PL	TL	Amy	BF	GP	Str	Cla	ET	HT	ST	DT	VT
MART	**12.52**	1.5	1.5	1.3	0.29	0.14	1.2	1.4	1.5	−0.48	0.18	−0.67	−1.3	0.11	−2.2	−0.36	−0.45	−0.09	−0.85
APOE	−2.86	−0.87	−0.63	−0.57	−1.2	−0.03	−0.48	−0.79	−0.58	1	1.4	2.4	1.2	−0.48	0.34	0.71	0.38	1	0.8
PICALM	−11.88	−1	−1.3	−0.94	−0.39	−0.76	−0.75	−0.9	−1	0.04	0.74	0.97	−0.33	0.4	−0.75	−0.61	0	−0.06	2
BIN1	−5.42	−0.55	−0.6	−0.39	0.53	−0.67	−0.42	−0.51	−0.47	−0.06	0.65	0.88	−0.55	0.2	−2.1	−1.3	0.45	0.32	1.4
CLU	**14.91**	0.61	0.76	0.73	0.76	0.48	0.51	0.55	0.73	0.55	0.86	0.25	2.4	0.13	−1.2	−0.13	−0.29	0.02	−0.57
CR1	−5.62	−0.24	−0.25	−0.12	−1.1	0.19	−0.68	−0.04	0.39	−0.25	−1.1	−0.62	−0.38	−0.43	−0.87	−0.96	0.4	−0.55	1.4
ABCA7	−15.14	−0.7	−1	−0.55	1	−1.6	−0.24	−0.8	−0.94	0.93	1.6	−1.5	−1.8	0.84	−0.49	−0.48	1.4	0.11	0.73
SORL1	−1.75	0.31	−0.38	−0.07	0.31	−0.6	0.93	0.56	−0.08	−1.6	−1.1	0.79	−2.4	−0.12	0.73	−0.95	0.8	−0.31	0.85
PLEKHC1	−5.22	−0.97	−0.84	−0.47	−0.85	0.04	−0.94	−0.83	−0.79	1.6	1.1	1.8	0.26	0.79	−0.19	0.15	0.48	0.34	1.2
CD2AP	−10.16	−1	−1.5	−1.3	−0.59	−0.67	−0.01	−0.59	−0.83	0.08	−1.3	0.62	0.4	−1.1	1.1	0.17	−0.12	0.52	−0.1
CD33	−11.74	−0.86	−0.85	−1.2	−0.76	−0.31	−1.4	−0.95	−0.65	0.54	−0.41	0.86	−0.79	0.57	0.36	−0.49	1.2	−0.32	1.3
APP	0.12	−0.29	−0.43	−0.12	0.42	0.16	0.09	−0.05	−0.2	0.7	0.01	0.47	−0.36	2	−1.1	−1.1	−0.29	0.11	1.3
PSEN1	−10.81	−0.56	−0.82	−0.56	−1.1	−0.98	−0.75	−0.68	−0.66	−1	0.66	1.1	−0.34	−0.59	−0.61	−1.1	0.41	−0	1.3
PSEN2	−14.85	−0.86	−0.79	−0.77	−0.43	−0.75	−1.3	−0.98	−0.85	−0.23	0.8	−0.5	−0.68	1.8	−0.93	0.59	1.5	0.83	0.77
CASS	−3.31	−0.36	−0.28	−1.1	−0.88	−0.37	−0.64	−0.75	0.41	0.14	1.2	1.8	0.97	−0.77	−1.7	0.89	−0.51	0.83	0.77
EPHA1	−3.68	−0.21	−0.31	−0.29	−0.48	0.05	−0.53	0.29	0.03	−0.05	−0.6	−0.9	−0.49	0.4	−0.72	−0.86	0.07	−0.32	0.78
PTK2B	7.19	0.58	0.35	0.36	2.2	−0.21	0.4	0.54	0.34	1.6	0.54	−1.6	−0.51	0.73	−1.8	−1.5	−0.75	0.89	0.73
INPP5D	−10.02	−0.89	−0.82	−1.1	−1.2	−1.1	0.43	−0.68	−0.77	−0.43	0.21	1.5	0.43	−0.49	1.7	0.04	1.1	−0.12	0.47
MEF2C	**14.59**	1.3	1.4	1.3	−0.21	1.1	1.4	1.4	1.4	0.64	−0.35	−0.73	−0.66	1.5	−0.81	−0.8	−0.73	−0.74	−0.4
CUGBP1	11.38	0.34	0.18	0.48	1.7	0.76	0.93	0.61	0.42	1.6	0.84	−0.64	0.55	1.8	−0.52	−0.48	−1.1	0.82	−0.46
MAAD	4.38	−0.37	−0.41	0.27	1.6			0.04	−0.15	2.3	0.48	−0.98	0.3	2.1	−0.96	−0.59	−0.01	−0.72	1.3

Normalized Z-scores of each gene are provided in the corresponding top-level structure (column). A higher value indicates gene located in that structure has higher expression. Three genes with the highest presence frequencies (MAPT, CLU, and MEF2C) are highlighted in bold.

(Braskie et al., 2011). Regions that are highly expressed by APOE, MAPT, and CLU were identified from Allen Human Brain Atlas Microarray data based on the thresholding of their normalized Z-Scores as previously introduced. The names of these regions, along with the AD-predictive regions identified in this work, are summarized in **Table 2**.

In addition to these three genes, we preselected a total of 21 genes based on the literature reports on aging, dementia, and MCI/AD progression, and obtained their correspondingly highly expressed regions in the Allen Human Brain Atlas. Based on the premise that the 20 AD-predictive regions as identified in this work from SWI data are associated with AD both at imaging and genetic level, we investigated how frequent each of the 21 genes are expressed in these regions, and used the derived gene presence frequency as a measurement for the association between each gene and AD development. However, the brain region definition used in the Allen Human Brain Atlas (shown as "top-level structure name" in the downloaded expression data) is different from the AAL atlas used in this work, where the top-level structures are usually larger and can cover multiple regions in the AAL atlas. Thus, we firstly identified a total of 18 top-level structures from the microarray data with higher expressions for either of these 21 genes (i.e., the union of highly expressed regions), including structures of FL, cingulate gyrus (CgG), hippocampus formation (HiF), parahippocampal gyrus (PHG), PL, Amg, GP, and striatum (Str). As shown in **Table 3**, each gene (row) has its corresponding normalized Z-score at each top-level structure (column). After that, we mapped these top-level structures with the regions in AAL atlas by comparing their spatial distributions in the MNI space. Based on this many-to-many mapping, we can find which AAL region(s) are included in each top-level structure. Between the 18 top-level structures and the 20 AD-predictive regions, we obtained the following 18×1 weight vector [4, 1, 1, 2, 2, 0, 2, 0, 5, 0, 1, 0, 2, 2, 0, 0, 0, 0, 0, 0]. Each value in the vector indicates how many of the 20 AD-predictive region(s) are presented in that top-level structure, for example, the first value of four indicates that the top-level structure of FL includes four AD-predictive regions. Finally, we can calculate the presence frequency for each gene by multiplying the normalized Z-score in each top-level structure with the corresponding weight value and adding them together, as listed in the "Frequency" column in **Table 3**. Higher value of presence frequency indicates that the target gene in overall is more frequently expressed in regions that are predictive to AD, thus could be potentially more associated with AD.

DISCUSSION AND CONCLUSION

In this study of analyzing the association between the development AD and iron deposition as characterized by SWI images, we used Lasso family algorithms for supervised dimensionality reduction to identify important regions that are discriminative to AD to overcome the challenge of small sample size and large feature number. We then applied different classification methods to investigate the diagnostic capability of SWI towards MCI and AD. Ten-fold cross-validation experiment results show that >70% accuracy can be achieved for this three-class classification task. Further investigation into the identified AD-related regions revealed that they are consistent with previous literature reports. The regions identified in this work cover all the eight regions previously reported.

We then co-analyzed the SWI-derived imaging features with the genetic data provided by Allen's brain atlas. We found that the regions identified by the feature selection method are identical with the regions rich in gene expression associated with protein precipitation and the blood–brain barrier, as measured by the microarray data (Shen et al., 2012). Specifically, our study has found that:

(1) AD-predicative regions identified in this work cover most of the APOE-associated regions except for the dorsal thalamus and striatum. Iron is involved in the formation of astrocytes that might affect the permeability of the blood–brain barrier. It has been reported that AD patients have a breakdown of the blood–brain barrier before dementia, neurodegenerative diseases, and brain atrophy. APOE gene has been found to be the strongest AD risk gene involved in the damage of the blood–brain barrier (Montagne et al., 2015). On the other hand, the UCLA team (Raven et al., 2013) used FDRI to detect cerebral iron and studied the difference of iron content in the hippocampus and thalamus regions. As detected in our study, the iron levels increase at the hippocampus, not the thalamus, might be linked to an injury to the hippocampus.
(2) Our identified regions also include CLU/MAPT-associated regions except for the striatum, as well as the occipital lobe, which is commonly known as non-specific to AD. In the initial lesion regions of AD patients, increased iron concentration was associated with the accumulation of Aβ (amyloid β) and *tau* protein. Our previous study in Sepulcre et al. (2018) shows that CLU and MAPT genes are responsible for the high expression of Aβ and *tau* protein, respectively. Studies have shown that iron deposition was detected in microglia and astrocytes in the amygdala, and ferritin concentrations increase with age (Zecca et al., 2004). A study of 143 healthy individuals shows that iron deposition in the caudate nucleus increases with age, peaking at age 60 (Wang et al., 2012). Other literature reported similar iron increases with age in the putamen, globus pallidus, and caudate nucleus (Ward et al., 2014). Further studies on iron deposition in AD, MCI, and NC also revealed significant differences in the caudate nucleus and putamen (Wang et al., 2013).
(3) From the gene expression frequency analysis, our study observed that the top three genes presented in the identified AD-predictive regions are CLU, MEF2C, and MAPT. Besides the two previously reported AD-related genes (CLU/MAPT), the MEF2C gene plays a key role in the development of multiple types of tissues. It is currently known to be related to epilepsy, autism, and mental retardation (Rashid et al., 2014). However, its role in the adult brain is largely understudied. Recent evidence suggests that the MEF2C gene regulates memory forming structures (Cole et al., 2012), which implies its potential role in the memory degradation of AD patients.

There are several limitations of the current study, both on the method design and the data used. Specifically, the current feature selection and classification scheme are relatively simple due to the limited sample size. With a larger dataset, we can try more advanced data analytics methods such as deep learning to better map imaging features and disease development. We also recognized that the regional features identified in the current study are limited because the AAL atlas is relatively coarse for the detailed spatial analysis. In later studies, we will try more fine-grained parcellation of the brain or performing voxel-level analysis.

Our conclusions on the effectiveness of using SWI for AD diagnosis need to be validated by external datasets. Nevertheless, in this study, we have only collected susceptibility-weighted images as one single dataset. We have implemented the complete feature selection and classification pipeline into an integrated framework. We will publish the code onto a public repository so that external researchers can use the same regional features to test their prediction power and compare the classification performance. The possible role of the MEF2C gene also needs to be validated, both by testing the consistency of its expression in the MCI/AD population on another dataset other than the Allen brain atlas and by exploring the biological pathway of the MEF2C's expression using bioinformatics tools.

DATA AVAILABILITY STATEMENT

The raw data supporting the conclusions of this article will be made available by the authors, without undue reservation.

ETHICS STATEMENT

The studies involving human participants were reviewed and approved by Institutional Review Board of Peking University Sixth Hospital. The patients/participants provided their written informed consent to participate in this study.

AUTHOR CONTRIBUTIONS

PY was responsible for the model implementation, experiment, and manuscript writing. XL was responsible for the experiment design, image processing, and manuscript writing. ZW was responsible for the data curation and image processing of this work. HW, BD, and QL were responsible for the funding acquisition, project administration, and supervision of this work. All authors contributed to the article and approved the submitted version.

FUNDING

BD is supported in part by National Natural Science Foundation of China (NSFC) grant no. 12090022, Beijing Natural Science Foundation (No. 180001), and Beijing Academy of Artificial Intelligence (BAAI).

REFERENCES

Alzheimer's Association. (2011). 2011 Alzheimer's disease facts and figures. *Alzheimers Dement.* 7, 208–244. doi: 10.1016/j.jalz.2011.02.004

Ashburner, J. (2007). A fast diffeomorphic image registration algorithm. *NeuroImage* 38, 95–113. doi: 10.1016/j.neuroimage.2007.07.007

Braskie, M. N., Jahanshad, N., Stein, J. L., Barysheva, M., McMahon, K. L., de Zubicaray, G. I., et al. (2011). Common Alzheimer's disease risk variant within the CLU gene affects white matter microstructure in young adults. *J. Neurosc.* 31:6764. doi: 10.1523/jneurosci.5794-10.2011

Cole, C. J., Mercaldo, V., Restivo, L., Yiu, A. P., Sekeres, M. J., Han, J. H., et al. (2012). MEF2 negatively regulates learning-induced structural plasticity and memory formation. *Nat. Neurosci.* 15, 1255–1264. doi: 10.1038/nn.3189

Coppola, G., Chinnathambi, S., Lee, J. J., Dombroski, B. A., Baker, M. C., Soto-Ortolaza, A. I., et al. (2012). Evidence for a role of the rare p.A152T variant in MAPT in increasing the risk for FTD-spectrum and Alzheimer's diseases. *Hum. Mol. Genet.* 21, 3500–3512.

Crichton, R. R., Dexter, D. T., and Ward, R. J. (2011). Brain iron metabolism and its perturbation in neurological diseases. *J. Neural Transm.* 118, 301–314. doi: 10.1007/s00702-010-0470-z

Cuingnet, R., Gerardin, E., Tessieras, J., Auzias, G., Lehéricy, S., Habert, M.-O., et al. (2011). Automatic classification of patients with Alzheimer,s disease from structural MRI: a comparison of ten methods using the ADNI database. *NeuroImage* 56, 766–781. doi: 10.1016/j.neuroimage.2010.06.013

Davatzikos, C., Bhatt, P., Shaw, L. M., Batmanghelich, K. N., and Trojanowski, J. Q. (2011). Prediction of MCI to AD conversion, via MRI, CSF biomarkers, and pattern classification. *Neurobiol. Aging* 32, 2322.e19–27. doi: 10.1016/j.neurobiolaging.2010.05.023

Davatzikos, C., Fan, Y., Wu, X., Shen, D., and Resnick, S. M. (2008). Detection of prodromal Alzheimer's disease via pattern classification of magnetic resonance imaging. *Neurobiol. Aging* 29, 514–523. doi: 10.1016/j.neurobiolaging.2006.11.010

Douaud, G., Jbabdi, S., Behrens, T. E. J., Menke, R. A., Gass, A., Monsch, A. U., et al. (2011). DTI measures in crossing-fibre areas: increased diffusion anisotropy reveals early white matter alteration in MCI and mild Alzheimer's disease. *NeuroImage* 55, 880–890. doi: 10.1016/j.neuroimage.2010.12.008

Driscoll, I., Davatzikos, C., An, Y., Wu, X., Shen, D., Kraut, M., et al. (2009). Longitudinal pattern of regional brain volume change differentiates normal aging from MCI. *Neurology* 72, 1906–1913. doi: 10.1212/wnl.0b013e3181a82634

Fernández, A., Hornero, R., Mayo, A., Poza, J., Gil-Gregorio, P., and Ortiz, T. (2006). MEG spectral profile in Alzheimer's disease and mild cognitive impairment. *Clin. Neurophysiol.* 117, 306–314. doi: 10.1016/j.clinph.2005.10.017

Gauthier, S., Reisberg, B., Zaudig, M., Petersen, R. C., Ritchie, K., Broich, K., et al. (2006). Mild cognitive impairment. *Lancet* 367, 1262–1270.

Guo, J., Qiu, W., Li, X., Zhao, X., Guo, N., and Li, Q. (2019). "Predicting Alzheimer's disease by hierarchical graph convolution from positron emission tomography imaging," in *Proceedings of the 2019 IEEE International Conference on Big Data (Big Data)* (Los Angeles, CA), 5359–5363.

Hagemeier, J., Geurts, J. J. G., and Zivadinov, R. (2012). Brain iron accumulation in aging and neurodegenerative disorders. *Expert Rev. Neurother.* 12, 1467–1480. doi: 10.1586/ern.12.128

Halefoglu, A. M., and Yousem, D. M. (2018). Susceptibility weighted imaging: clinical applications and future directions. *World J. Radiol.* 10, 30–45. doi: 10.4329/wjr.v10.i4.30

Jack, C. R., Shiung, M. M., Gunter, J. L., O'Brien, P. C., Weigand, S. D., Knopman, D. S., et al. (2004). Comparison of different MRI brain atrophy rate measures with clinical disease progression in AD. *Neurology* 62, 591–600. doi: 10.1212/01.wnl.0000110315.26026.ef

Jeong, J. (2004). EEG dynamics in patients with Alzheimer's disease. *Clin. Neurophysiol.* 115, 1490–1505.

Lebedev, A. V., Westman, E., Van Westen, G. J. P., Kramberger, M. G., Lundervold, A., Aarsland, D., et al. (2014). Random Forest ensembles for detection and prediction of Alzheimer's disease with a good between-cohort robustness. *NeuroImage* 6, 115–125. doi: 10.1016/j.nicl.2014.08.023

Li, X., Guo, N., and Li, Q. (2019). Functional neuroimaging in the new era of big data. *Genomics Proteom. Bioinform.* 17, 393–401. doi: 10.1016/j.gpb.2018.11.005

Li, Y., Chen, H., Jiang, X., Li, X., Lv, J., Li, M., et al. (2017a). Transcriptome architecture of adult mouse brain revealed by sparse coding of genome-wide in situ hybridization images. *Neuroinformatics* 15, 285–295. doi: 10.1007/s12021-017-9333-1

Li, Y., Chen, H., Jiang, X., Li, X., Lv, J., Peng, H., et al. (2017b). Discover mouse gene coexpression landscapes using dictionary learning and sparse coding. *Brain Struct. Funct.* 222, 4253–4270. doi: 10.1007/s00429-017-1460-9

Liu, J.-L., Fan, Y.-G., Yang, Z.-S., Wang, Z.-Y., and Guo, C. (2018). Iron and Alzheimer's disease: from pathogenesis to therapeutic implications. *Front. Neurosci.* 12:632. doi: 10.3389/fnins.2018.00632

Machulda, M. M., Ward, H. A., Borowski, B., Gunter, J. L., Cha, R. H., O'Brien, P. C., et al. (2003). Comparison of memory fMRI response among normal, MCI, and Alzheimer's patients. *Neurology* 61, 500–506. doi: 10.1212/01.wnl.0000079052.01016.78

Marioni, R. E., Campbell, A., Hagenaars, S. P., Nagy, R., Amador, C., Hayward, C., et al. (2017). Genetic stratification to identify risk groups for Alzheimer's disease. *J. Alzheimers Dis.* 57, 275–283. doi: 10.3233/jad-161070

McKhann, G., Drachman, D., Folstein, M., Katzman, R., Price, D., and Stadlan, E. M. (1984). Clinical diagnosis of Alzheimer's disease: report of the NINCDS-ADRDA Work Group under the auspices of department of health and human services task force on Alzheimer's disease. *Neurology* 34, 939–944. doi: 10.1212/wnl.34.7.939

Medina, D., deToledo-Morrell, L., Urresta, F., Gabrieli, J. D. E., Moseley, M., Fleischman, D., et al. (2006). White matter changes in mild cognitive impairment and AD: a diffusion tensor imaging study. *Neurobiol. Aging* 27, 663–672. doi: 10.1016/j.neurobiolaging.2005.03.026

Montagne, A., Barnes, S. R., Sweeney, M. D., Halliday, M. R., Sagare, A. P., Zhao, Z., et al. (2015). Blood-brain barrier breakdown in the aging human hippocampus. *Neuron* 85, 296–302. doi: 10.1016/j.neuron.2014.12.032

Nordberg, A. (2004). PET imaging of amyloid in Alzheimer's disease. *Lancet Neurol.* 3, 519–527.

Ortiz, A., Munilla, J., Górriz, J. M., and Ramírez, J. (2016). Ensembles of deep learning architectures for the early diagnosis of the Alzheimer's disease. *Int. J. Neural Syst.* 26, 1650025. doi: 10.1142/s0129065716500258

Ossenkoppele, R., Schonhaut, D. R., Schöll, M., Lockhart, S. N., Ayakta, N., Baker, S. L., et al. (2016). Tau PET patterns mirror clinical and neuroanatomical variability in Alzheimer's disease. *Brain* 139, 1551–1567. doi: 10.1093/brain/aww027

Patterson, C. (2018). *World Alzheimer Report 2018: The State of the art of Dementia Research: New Frontiers*. London: Alzheimer's Disease International (ADI), 32–36.

Ramos, P., Santos, A., Pinto, N. R., Mendes, R., Magalhães, T., and Almeida, A. (2014). Iron levels in the human brain: a post-mortem study of anatomical region differences and age-related changes. *J. Trace Elem. Med. Biol.* 28, 13–17. doi: 10.1016/j.jtemb.2013.08.001

Rashid, A. J., Cole, C. J., and Josselyn, S. A. (2014). Emerging roles for MEF2 transcription factors in memory. *Genes Brain Behav.* 13, 118–125. doi: 10.1111/gbb.12058

Raven, E. P., Lu, P. H., Tishler, T. A., Heydari, P., and Bartzokis, G. (2013). Increased iron levels and decreased tissue integrity in hippocampus of Alzheimer's disease detected in vivo with magnetic resonance imaging. *J. Alzheimers Dis.* 37, 127–136. doi: 10.3233/jad-130209

Roest, M., van der Schouw, Y. T., de Valk, B., Marx, J. J., Tempelman, M. J., de Groot, P. G., et al. (1999). Heterozygosity for a hereditary hemochromatosis gene is associated with cardiovascular death in women. *Circulation* 100, 1268–1273.

Rombouts, S. A. R. B., Barkhof, F., Goekoop, R., Stam, C. J., and Scheltens, P. (2005). Altered resting state networks in mild cognitive impairment and mild Alzheimer's disease: an fMRI study. *Hum. Brain Mapp.* 26, 231–239. doi: 10.1002/hbm.20160

Rouault, T. A. (2013). Iron metabolism in the CNS: implications for neurodegenerative diseases. *Nat. Rev. Neurosci.* 14, 551–564. doi: 10.1038/nrn3453

Selkoe, D. J. (2012). Preventing Alzheimer's disease. *Science* 337, 1488–1492.

Sepulcre, J., Grothe, M. J., d'Oleire Uquillas, F., Ortiz-Terán, L., Diez, I., Yang, H.-S., et al. (2018). Neurogenetic contributions to amyloid beta and tau spreading in the human cortex. *Nat. Med.* 24, 1910–1918. doi: 10.1038/s41591-018-0206-4

Sheelakumari, R., Madhusoodanan, M., Radhakrishnan, A., Ranjith, G., and Thomas, B. (2016). A potential biomarker in amyotrophic lateral sclerosis: can assessment of brain iron deposition with swi and corticospinal tract degeneration with DTI help? *AJNR. American journal of neuroradiology.* 37, 252–258. doi: 10.3174/ajnr.a4524

Shen, E. H., Overly, C. C., and Jones, A. R. (2012). The allen human brain atlas: comprehensive gene expression mapping of the human brain. *Trends Neurosci.* 35, 711–714.

Stankiewicz, J., Panter, S. S., Neema, M., Arora, A., Batt, C. E., and Bakshi, R. (2007). Iron in chronic brain disorders: imaging and neurotherapeutic implications. *Neurotherapeutics* 4, 371–386. doi: 10.1016/j.nurt.2007.05.006

Tao, Y., Wang, Y., Rogers, J. T., and Wang, F. (2014). Perturbed iron distribution in Alzheimer's disease serum, cerebrospinal fluid, and selected brain regions: a systematic review and meta-analysis. *J. Alzheimers Dis.* 42, 679–690. doi: 10.3233/jad-140396

Thambisetty, M., Beason-Held, L. L., An, Y., Kraut, M., Nalls, M., Hernandez, D. G., et al. (2013). Alzheimer risk variant clu and brain function during aging. *Biol. Psychiatry* 73, 399–405. doi: 10.1016/j.biopsych.2012.05.026

Tuomainen, T. P., Kontula, K., Nyyssönen, K., Lakka Timo, A., Heliö, T., and Salonen Jukka, T. (1999). Increased risk of acute myocardial infarction in carriers of the hemochromatosis gene Cys282Tyr mutation. *Circulation* 100, 1274–1279. doi: 10.1161/01.cir.100.12.1274

Wang, D., Szyf, M., Benkelfat, C., Provençal, N., Turecki, G., Caramaschi, D., et al. (2012). Peripheral SLC6A4 DNA methylation is associated with in vivo measures of human brain serotonin synthesis and childhood physical aggression. *PLoS One* 7:e39501. doi: 10.1371/journal.pone.0039501

Wang, D., Zhu, D., Wei, X. E., Li, Y. H., and Li, W. B. (2013). Using susceptibility-weighted images to quantify iron deposition differences in amnestic mild cognitive impairment and Alzheimer's disease. *Neurol. India* 61, 26–34. doi: 10.4103/0028-3886.107924

Ward, R. J., Zucca, F. A., Duyn, J. H., Crichton, R. R., and Zecca, L. (2014). The role of iron in brain ageing and neurodegenerative disorders. *Lancet Neurol.* 13, 1045–1060. doi: 10.1016/s1474-4422(14)70117-6

World Health Organization. (2004). *International Statistical Classification of Diseases and Related Health Problems: Tabular List*. Geneva: World Health Organization.

Xia, M., Wang, J., and He, Y. (2013). BrainNet viewer: a network visualization tool for human brain connectomics. *PLoS One* 8:e68910. doi: 10.1371/journal.pone.0068910

Xu, M., Wang, Z., Zhang, H., Pantazis, D., Wang, H., and Li, Q. (2020). A new Graph Gaussian embedding method for analyzing the effects of cognitive training. *PLoS Comput. Biology.* 16:e1008186. doi: 10.1371/journal.pcbi.1008186

Zecca, L., Stroppolo, A., Gatti, A., Tampellini, D., Toscani, M., Gallorini, M., et al. (2004). The role of iron and copper molecules in the neuronal vulnerability of locus coeruleus and substantia nigra during aging. *Proc. Natl. Acad. Sci. U.S.A.* 101, 9843–9848. doi: 10.1073/pnas.0403495101

Zhang, D., Wang, Y., Zhou, L., Yuan, H., and Shen, D. (2011). Multimodal classification of Alzheimer's disease and mild cognitive impairment. *NeuroImage* 55, 856–867.

Zhang, Y., Dong, Z., Phillips, P., Wang, S., Ji, G., Yang, J., et al. (2015). Detection of subjects and brain regions related to Alzheimer's disease using 3D MRI scans based on eigenbrain and machine learning. *Front. Comput. Neurosci.* 9:66. doi: 10.3389/fncom.2015.00066

Zhang, Y., Schuff, N., Jahng, G.-H., Bayne, W., Mori, S., Schad, L., et al. (2007). Diffusion tensor imaging of cingulum fibers in mild cognitive impairment and Alzheimer disease. *Neurology* 68, 13–19. doi: 10.1212/01.wnl.0000250326.77323.01

Conflict of Interest: The authors declare that the research was conducted in the absence of any commercial or financial relationships that could be construed as a potential conflict of interest.

frontiers in Human Neuroscience

ORIGINAL RESEARCH
published: 15 June 2021
doi: 10.3389/fnhum.2021.643410

Narrowband Resting-State fNIRS Functional Connectivity in Autism Spectrum Disorder

Weiting Sun[1], *Xiaoyin Wu*[1], *Tingzhen Zhang*[1], *Fang Lin*[1], *Huiwen Sun*[1] *and Jun Li*[1,2]*

[1] South China Academy of Advanced Optoelectronics, South China Normal University, Guangzhou, China, [2] Key Lab for Behavioral Economic Science & Technology, South China Normal University, Guangzhou, China

Hemispheric asymmetry in the power spectrum of low-frequency spontaneous hemodynamic fluctuations has been previously observed in autism spectrum disorder (ASD). This observation may imply a specific narrow-frequency band in which individuals with ASD could show more significant alteration in resting-state functional connectivity (RSFC). To test this assumption, we evaluated narrowband RSFC at several frequencies for functional near-infrared spectroscopy signals recorded from the bilateral temporal lobes on 25 children with ASD and 22 typically developing (TD) children. In several narrow-frequency bands, we observed altered interhemispheric RSFC in ASD. However, in the band of 0.01–0.02 Hz, more mirrored channel pairs (or cortical sites) showed significantly weaker RSFC in the ASD group. Receiver operating characteristic analysis further demonstrated that RSFC in the narrowband of 0.01–0.02 Hz might have better differentiation ability between the ASD and TD groups. This may indicate that the narrowband RSFC could serve as a characteristic for the prediction of ASD.

Keywords: functional near-infrared spectroscopy, autism spectrum disorder, resting-state functional connectivity, narrow frequency bands, discrimination

OPEN ACCESS

Edited by:
Wei Liao,
University of Electronic Science and Technology of China, China

Reviewed by:
Heng Chen,
Guizhou University, China
Han Zhang,
University of North Carolina at Chapel Hill, United States

***Correspondence:**
Jun Li
jun.li@coer-scnu.org

Specialty section:
This article was submitted to Brain Imaging and Stimulation, a section of the journal Frontiers in Human Neuroscience

Received: *18 December 2020*
Accepted: *12 May 2021*
Published: *15 June 2021*

Citation:
Sun W, Wu X, Zhang T, Lin F, Sun H and Li J (2021) Narrowband Resting-State fNIRS Functional Connectivity in Autism Spectrum Disorder. Front. Hum. Neurosci. 15:643410. doi: 10.3389/fnhum.2021.643410

INTRODUCTION

Over decades, the prevalence of autism spectrum disorder (ASD) has an astonishing rise in children (Goldson, 2016). It has been acknowledged that genetic, developmental, and environmental factors could be related to the effects toward developing autism (Arbabshirani et al., 2017). Individuals in the spectrum often present with symptoms such as impairments in social interaction and communication, restricted interests, and repetitive patterns of behaviors (Veenstra-VanderWeele et al., 2004). These symptoms generally appear in the first 2–3 years of life, and thereafter ASD can be reliably diagnosed based on the observation of these children's behaviors (Lord et al., 2006), e.g., *via* the Autism Diagnostic Observation Schedule (Luyster et al., 2009). Although ASD can be a lifelong disorder, early intervention for ASD is still extremely important, as proper care and function training can improve individuals' condition and help them learn new skills and find their places in the world as happy and productive human beings. For this reason, the earlier ASD is diagnosed, the sooner the intervention can be started.

Despite rapid progress on the study of ASD, the fact is that the diagnosis still relies solely on the behavioral observation, as to date there is no reliable biological indicator directly related to the disorder. Children with suspected ASD cannot receive a final diagnosis until they are much older, e.g., 2–3 years old, as only by then the consistent behaviors can be observed. This delay often prevents children with ASD from getting necessary and timely help.

In order to improve this situation, a great number of imaging studies for revealing intrinsic characteristics in the brains of ASD have been performed. Among these studies, cortical temporal correlation of the spontaneous brain activity in distinct but functionally related regions, termed as resting-state functional connectivity (RSFC), has become a research focus (Biswal et al., 1995; White et al., 2009; Lu et al., 2010; Van Den Heuvel and Pol, 2010; Zhang et al., 2010; Chuang and Sun, 2014; Li and Qiu, 2014; Smitha et al., 2017), because RSFC reveals concurrent spontaneous activity of spatially segregated regions (Friston, 2007). Studying RSFC may generate fresh insight into understanding of ASD, as well as other neurological and psychiatric disorders. Functional magnetic resonance imaging (fMRI) (Monk et al., 2009; Assaf et al., 2010) studies have demonstrated the existence of abnormalities in the functional connection in the brains of ASD. However, it is usually difficult to measure brain activity for young children because of their inability to remain still for several minutes, e.g., 5–10 min, a typical time duration required for studying resting state by using brain imaging modalities such as MRI/fMRI, positron emission tomography (PET), and magnetoencephalography (MEG). These brain imaging modalities usually require the subject to keep motionless during measurement. However, for functional near-infrared spectroscopy (fNIRS) it might not be a severe problem. It is because as compared to the aforementioned imaging techniques, fNIRS is more tolerant to motion artifact (MA) caused by head movement; thus, it is more suitable on studying children's brains. Besides this, the unrealistic environment required for fMRI, PET, and MEG measurement may cause claustrophobia, which may induce extra unexpected effect on the resting-state data. In addition, several fNIRS studies on ASD have already shown that children with ASD present atypical cortical activity (Kita et al., 2011), even in resting state (Zhu et al., 2014; Li et al., 2016; Xu et al., 2019, 2020a,b,c).

Resting-state fNIRS studies on ASD can be roughly divided into two categories: one is uncovering various characteristics associated with ASD in a single or several fNIRS channels (e.g., Xu et al., 2019, 2020a,b,c), and the other is investigating the difference between ASD and TD in the interhemispheric RSFC (e.g., Zhu et al., 2014; Li et al., 2016). The two categories of studies reveal resting-state features associated with ASD from different aspects, e.g., one is from a single or a few cortical sites and the other from brain network.

Previous studies have demonstrated that as compared to typically developing (TD) children, children with ASD show weaker RSFC between the bilateral temporal lobes (Zhu et al., 2014; Li et al., 2016) and asymmetry between the left and right hemispheres in the power spectrum of the low-frequency hemodynamic fluctuations. Moreover, the deviation in the power spectrum occurred mostly in the frequency band of 0.01–0.06 Hz (Cheng et al., 2019). In an fNIRS study, Sasai et al. found frequency-specific RSFC, implying that the correlation of spontaneous brain activity between different regions depended also on the frequency band (Sasai et al., 2011). In several fMRI studies, altered oscillation in Slow-5 band (0.010–0.027 Hz) was found in healthy aging adults and ischemic stroke patients, which was believed to be associated with the disruptions on the brain network (La et al., 2016a,b,c). Cheng et al. (2017) have found that dynamic functional connectivity (i.e., the temporal variation in RSFC) in Slow-5 band reflects the capacity of sustaining attention in performing a cognitive task during pain. As children with ASD have weaker interhemispheric brain network and usually show deficit in sustaining attention, it might be reasonable to infer their brain spontaneous fluctuations, and functional connectivity may also show pronounced alteration in Slow-5 band. Therefore, we assume that the most alteration in the functional connectivity between ASD and TD may occur in a specific narrow-frequency band, rather than in a broad low-frequency band, e.g., 0.009–0.08 Hz (hereafter referred to as broadband). To test this hypothesis and locate precisely a specific narrow-frequency band in which RSFC has a higher discriminative ability between ASD and TD, the fNIRS data collected in a prior study (Li et al., 2016) were reanalyzed. The frequency range from 0.01 to 0.06 Hz was focused on. The reason why we focused on this frequency range was because of our previous work (Cheng et al., 2019), in which we analyzed power spectrum of resting-state fNIRS signals recorded from bilateral temporal lobes on children with ASD and normal TD controls. We found within the broadband range that the significant alteration occurred mostly in 0.01–0.06 Hz in ASD, and also in this range, children with ASD exhibited an asymmetry between right and left brain hemispheres in the power spectrum. This asymmetry implies children with ASD may show an atypical homotopic RSFC within the range of 0.01–0.06 Hz. To find a specific bandwidth in which RSFC shows the most pronounced alteration in ASD, several narrow bandwidths including 0.01, 0.02, and 0.03 Hz were used for bandpass filter. After bandpass filtering, an independent component analysis (ICA) algorithm was applied to remove MA and suppress global component in the fNIRS signals. Narrowband RSFC was then obtained at each frequency band by calculating Pearson correlation coefficient between each mirrored channel pair. To demonstrate the significant difference between the ASD and TD groups in the narrowband RSFC, statistical hypothesis test and power analysis were performed. To further show the discrimination ability of the narrowband RSFC between the two groups, receiver operating characteristic (ROC) curve and area under curve (AUC) value were presented.

MATERIALS AND METHODS

Participants

Twenty-five children with ASD (18 boys and 7 girls, 9.3 ± 1.4 years old) and 22 age-matched TD children (18 boys and 4 girls, 9.5 ± 1.6 years old) participated in the study. The children with ASD were recruited from a local autism rehabilitation school. They were all diagnosed by experienced pediatricians and child psychiatrists in hospitals on the basis of *Diagnostic and Statistical Manual of Mental Disorders, Fourth Edition, Text Revision* (American Psychiatry Association, 2000). The TD children were recruited from a local elementary school. Intelligence quotient (IQ) for both groups were measured with Raven's Standard Progressive Matrices Test (Raven and Court, 1998). IQ was 91 ± 15 for the ASD group and 106 ± 12 for the TD group. IQ difference between the two groups was significant (two-sample

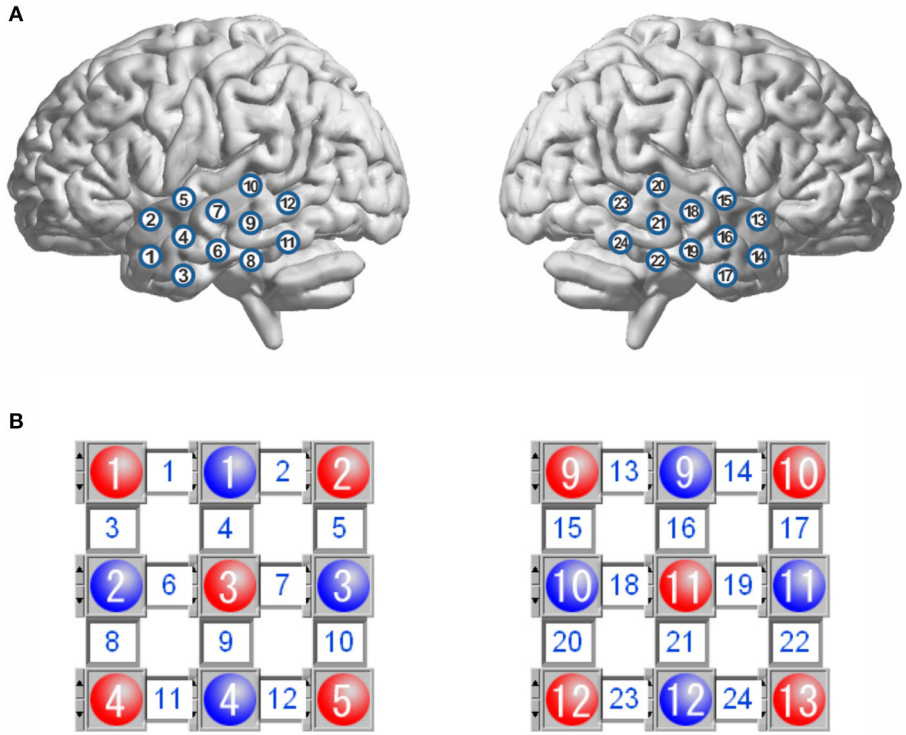

FIGURE 1 | Schematic representation of channel locations over the bilateral temporal lobes **(A)**, and layout for the sources and detectors **(B)**. The red circles represent the sources, and the blue circles represent the detectors, and the square between a source and a detector is a channel. There are 12 channels in each hemisphere.

t-test: $p < 0.05$). Ethical approval was obtained from South China Normal University's Ethical Review Board, and informed consents were obtained from all participants' parents prior to the experiments.

Data Acquisition

During resting-state fNIRS data acquisition, all participants were awake with their eyes closed and sat comfortably in a dark room. They were asked to try to keep as motionless as possible. The fNIRS used in this study was a commercial continuous-wave fNIRS system (FOIRE 3000, Shimadzu Corporation, Japan). To ensure a good optode-scalp contact, all optodes were secured on the scalp by a headgear. Twenty-four optical channels (a channel consisted of a source-detector pair) were used with 12 channels on each side of the head (**Figure 1**). The source-detector distance was fixed to be 3.0 cm. For each subject, spontaneous fluctuations of cortical oxygenated hemoglobin (HbO_2), deoxygenated Hb, and total Hb ($HbT = HbO_2 + Hb$) were recorded from the bilateral temporal lobes for about 8 min with 70-ms temporal resolution (i.e., 14.3-Hz sampling frequency). The output parameters of this fNIRS were concentration changes in HbO_2, Hb, and HbT, which were converted from changes in optical density of three wave lengths (780, 805, and 830 nm) based on the modified Beer–Lambert law. The international 10/20 system was referenced for identifying channel locations on the bilateral temporal lobes.

Data Analysis

The raw data we collected included HbO_2, Hb, and HbT, where HbT is the sum of HbO_2 and Hb. As overlapping information can hardly make a better contribution for the discrimination between ASD and TD, only HbO_2 and Hb were analyzed. Each time series of the hemodynamic signal S (HbO_2 and Hb) was first transformed into its *Z*-score *via* $Z = (S - \text{mean}(S))/\text{std}(S)$, and then a detrending process with a second-order polynomial fit was applied to *Z*-score to remove slow drift. To select different frequency components for computing frequency-dependent RSFC, a zero-phase second-order Butterworth bandpass filter was applied with a variety of pass-bands (**Table 1**). As the upper limit of these pass-bands was <0.08 Hz, most systemic interferences were filtered out, such as those originated from cardiac cycles (∼1 Hz), respirations (∼0.2 Hz), and Mayer waves (∼0.1 Hz). After the filtering, an ICA algorithm was employed to suppress global component and remove MA. In this ICA algorithm, we assumed that the global component would make similar contribution to all channels, which could be identified from the mixing matrix, whereas an MA could be an independent component whose peak value was 10 times larger than the standard deviation of this component. For more details on the ICA algorithm, readers can refer to Li et al. (2016).

After detrending, bandpass filtering, and ICA processing, narrowband hemodynamic signals were obtained for all

TABLE 1 | The number of channel pairs with significant difference in RSFC between ASD and TD in each frequency band for HbO_2 and Hb, respectively.

Frequency band (FB)		HbO_2	Hb
FB1	0.01–0.02 Hz	6	2
FB2	0.02–0.03 Hz	0	0
FB3	0.03–0.04 Hz	0	0
FB4	0.04–0.05 Hz	1	1
FB5	0.05–0.06 Hz	0	0
FB6	0.01–0.03 Hz	3	1
FB7	0.02–0.04 Hz	1	0
FB8	0.03–0.05 Hz	0	0
FB9	0.04–0.06 Hz	1	1
FB10	0.01–0.04 Hz	2	1
FB11	0.02–0.05 Hz	1	0
FB12	0.03–0.06 Hz	0	0
Broadband	0.009–0.08 Hz	2	0
Slow-5	0.010–0.027 Hz	3	1

optical channels. These signals were then used to compute interhemispheric RSFC for each subject. The RSFC was indicated *via* the Pearson correlation coefficient of the hemodynamic fluctuations for each mirrored channel pair locating symmetrically on the left and right hemispheres. As there were 12 optical channels on each hemisphere, 12 correlation coefficients were obtained for each subject. To test whether the difference in RSFC was significant between the two groups (ASD vs. TD) in each narrow-frequency band, two-sample *t*-test was first performed. Because of non-Gaussianity of the correlation coefficients, before performing *t*-test, each correlation coefficient was transformed into Fisher *Z* value by Fisher *Z* transform. For multiple comparisons, the false discovery rate (FDR) correction (i.e., FDR-corrected *q* value) was utilized. To control type II error, the statistical powers were also calculated for the differences with the current sample size. We defined significant difference in this study as both FDR-corrected $q < 0.05$ and power > 0.8. To further show the discrimination ability of RSFC in narrowbands, ROC curves and AUC values were presented.

RESULTS

RSFC was indicated as a Pearson correlation coefficient for each mirrored channel pair (**Figure 1**, 12 channel pairs in total) in hemodynamic signals (HbO_2 and Hb). For all frequency bands, including 12 narrowbands (FB1–FB12), the broadband, and Slow-5 band, we counted the number of the mirrored channel pairs for which the correlation coefficients (in HbO_2 and Hb) showed significant difference (defined as FDR-corrected $q < 0.05$ and statistical power >0.8) between the ASD and TD groups. The number in each band is listed in **Table 1**.

In FB1 frequency band (0.01–0.02 Hz), there were eight correlation coefficients (six in HbO_2 and two in Hb) showing significant difference between the ASD and TD groups, more than those in the other frequency bands including the broadband (0.009–0.08 Hz) and Slow-5 band (0.010–0.027 Hz). In the broadband, only two correlation coefficients in HbO_2 were observed to show significant difference between the two groups; whereas in Slow-5 band, three correlation coefficients in HbO_2 and one in Hb showed significant difference, same as the number in FB6 (0.01–0.03 Hz), which almost fully overlay with the frequency range of Slow-5.

Figure 2 displays the grand average of correlation coefficients for the 12 (FB1–FB12) frequency bands. Two-sample *t*-test with FDR correction showed that the RSFC for both HbO_2 and Hb in the frequency band of 0.01–0.02 Hz (FB1) had the smallest FDR-corrected *q* values: $q(HbO_2) = 0.0024$, $q(Hb) = 0.0116$, indicating that in the band of 0.01–0.02 Hz, the homotopic RSFC for both HbO_2 and Hb showed more pronounced difference between the ASD and TD groups. In addition, the power analysis showed with the current sample size (ASD = 25, TD = 22) that the difference (more strictly speaking the effect size) resulted in the power of 0.99 for HbO_2 and 0.87 for Hb, both larger than 0.80, implying the current sample size was suitable for obtaining the conclusion that the difference between the two groups was statistically significant. As in the FB1 band, both the grand average of RSFC (**Figure 2**) and the group average of RSFC for mirrored channels (or cortical sites) (**Table 1**) showed more pronounced differences between the two groups, indicating that in the frequency band of 0.01–0.02 Hz, asynchronization in the spontaneous fluctuations between the two hemispheres was more obvious in ASD; thereafter, we focused on FB1 band for the further analysis.

Figure 3 shows RSFC in HbO_2 and Hb for the 12 mirrored channel pairs in FB1 band. As **Figure 3** illustrates, children with ASD showed clearly weaker interhemispheric RSFC than TD children in both HbO_2 and Hb, particularly between Ch5 and 15, Ch7 and 18, Ch8 and 22, Ch9 and 21, Ch10 and 20, and Ch11 and 24 in HbO_2, and between Ch9 and 21, and Ch11 and 24 in Hb. For these channel pairs, the differences in the correlation coefficients were statistically significant, indicating the disruption in the synchronization of the spontaneous fluctuations in these mirrored cortical regions occurred more pronouncedly in the band of 0.01–0.02 Hz in autism brains.

To demonstrate the discrimination ability of FB1-RSFC between ASD and TD, we took the mean of all 12 RSFCs of each hemodynamic variable as a discriminative feature to draw ROC curves, as shown in **Figure 4**, for FB1 and the other bands in which the grand average of RSFC also showed a significant difference between the ASD and TD groups, for example, FB2, FB6, FB7, FB9, and FB10 (**Figure 2**). The ROC curve was generated by varying a criterion value for RSFC. An individual whose HbO_2-RSFC and Hb-RSFC both were smaller than the criterion was classified as ASD, while classified as TD. The AUC value was calculated for each of these frequency bands: AUC (FB1) = 0.806, AUC (FB2) = 0.783, AUC (FB6) = 0.797, AUC (FB9) = 0.734, and AUC (FB10) = 0.783. AUC of FB1 was the largest among these bands, indicating FB1-RSFC is superior to RSFC in other frequency bands on the discrimination ability.

As not all mirrored channel pairs in FB1-RSFC showed significant difference between the ASD and TD groups, to

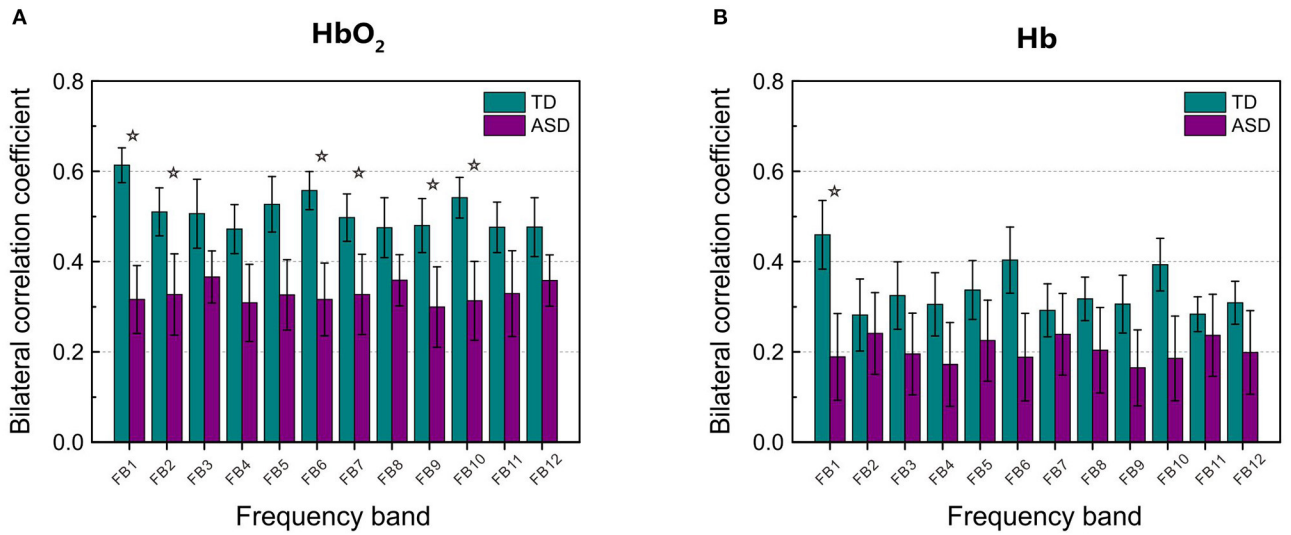

FIGURE 2 | The grand average of the correlation coefficients for HbO_2 **(A)** and Hb **(B)** between the left and right hemisphere in each frequency band (from FB1 to FB12, in total 12 bands) for TD and ASD groups. The asterisks indicate that the differences in the correlation coefficient between ASD and TD are statistically significant (FDR-corrected $q < 0.05$), and the statistical powers are larger than 0.8. FDR-corrected q values on HbO_2 are 0.0024, 0.0048, 0.0032, 0.0106, 0.0144, and 0.0048 for FB1, FB2, FB6, FB7, FB9, and FB10, respectively. FDR-corrected q value on Hb is 0.0116 for FB1. The error bar for each correlation coefficient is the standard error of mean.

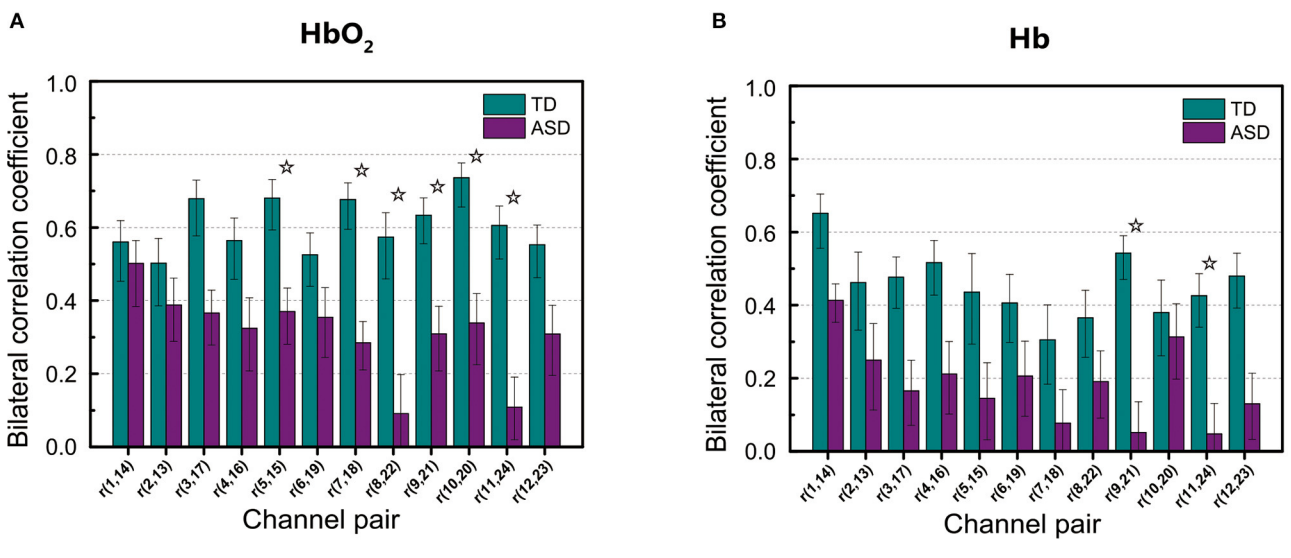

FIGURE 3 | The group average of correlation coefficients of HbO_2 **(A)** and Hb **(B)** in FB1 band for each mirrored channel pair located symmetrically on the left and right temporal lobes. The digit pair in the parenthesis indicates the corresponding channel pair, e.g., $r(1,14)$ is the temporal correlation coefficient between channel 1 and channel 14. The asterisks indicate the differences in the correlation coefficient between ASD and TD are statistically significant (FDR-corrected $q < 0.05$) for the channel pair, and the statistical powers are larger than 0.8. The error bar for each correlation coefficient is the standard error of mean.

enhance the discrimination ability, we could calculate an average only over those channel pairs showing significant difference and took this average as a discriminative feature. To show the discriminative ability of this averaged FB1-RSFC, ROC curve was generated, as shown in **Figure 5**. For comparisons, ROC curves were also generated by using the averaged Slow-5 and broadband RSFC as discriminative feature. For these two bands, the average of RSFC was also calculated only over those channel pairs showing significant difference between the ASD and TD groups. The AUC value for the narrowband (FB1) was 0.867, larger than that using the averaged RSFC over all channel pairs (i.e., 0.806). This was because including the RSFC showing no significant difference between ASD and TD as discriminative feature could not make positive contribution to the discrimination, but could

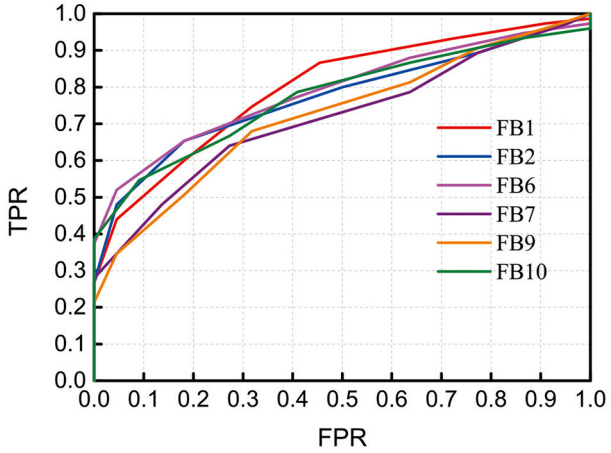

FIGURE 4 | Receiver operating characteristic (ROC) curves obtained by using RSFC as discriminative features at several frequency bands in which RSFC is significantly different between the ASD and TD groups. The RSFC in each band is the mean of RSFC averaged over all channel pairs. AUC (FB1) = 0.806, AUC (FB2) = 0.783, AUC (FB6) = 0.797, AUC (FB9) = 0.734, and AUC (FB10) = 0.783. FPR, false-positive rate; TPR, true-positive rate.

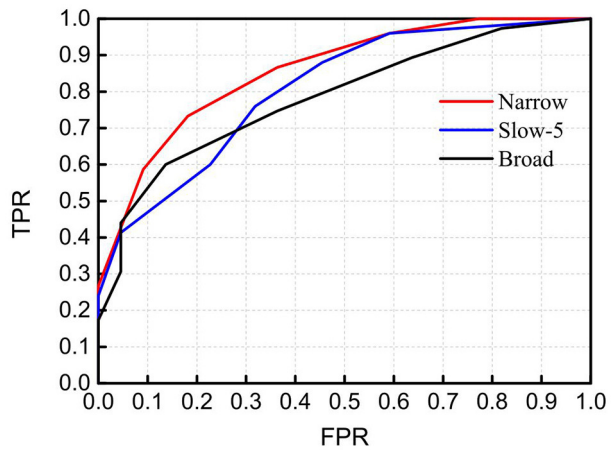

FIGURE 5 | Receiver operating characteristic (ROC) curves obtained by using RSFC as discriminative features in the narrowband of 0.01–0.02 Hz (Narrow), Slow-5 band (Slow-5), and broadband of 0.009–0.08 Hz (Broad). The RSFC for each band is the mean of RSFC averaged over channel pairs showing significantly different connectivity between the ASD and TD groups. AUC (Narrow) = 0.867, AUC (Slow-5) = 0.817, and AUC (Broad) = 0.793. FPR, false-positive rate; TPR, true-positive rate.

lead to some degradation. The AUC value was 0.817 for Slow-5 and 0.793 for the broadband, both smaller than the AUC value for the narrow FB1 band.

DISCUSSION

As FB6 (0.01–0.03 Hz) and FB10 (0.01–0.04 Hz) fully cover FB1 (0.01–0.02 Hz) in frequency range, it is not surprising that their AUC values are similar, e.g., 0.806, 0.797, and 0.783 for FB1, FB6, and FB10, respectively (**Figure 4**). However, from FB1 to FB6 and FB10, AUC shows a decreasing trend, which may imply that including those components in the frequency range beyond FB1 (such as 0.02–0.03 Hz and 0.02–0.04 Hz) cannot make better contribution to the differentiation than using FB1 only. The possible reason would be those bands provide either no useful information for the discrimination or redundant (e.g., overlapping) information with respect to FB1. To clarify this, we investigated the relationship between RSFCs in FB1, FB2 (0.02–0.03 Hz), FB7 (0.02–0.04 Hz), FB6, and FB10 by calculating the correlation coefficients between each other. The correlation coefficient was 0.733 between FB1- and FB2-RSFC, 0.722 between FB1- and FB7-RSFC, 0.973 between FB1- and FB6-RSFC, and 0.965 between FB1- and FB10-RSFC. As the correlation between FB1- and FB2-RSFC (also between FB1- and FB7-RSFC) was high (e.g., >0.7), RSFC in FB2 (0.02–0.03 Hz) and FB7 (0.02–0.04 Hz) could not provide additional discriminative information than FB1-RSFC. This could also be verified by the very high correlation between BF1- and FB6-RSFC (i.e., 0.973) and between BF1- and FB10-RSFC (i.e., 0.965). This correlation analysis could demonstrate that the most useful discriminative information was contained in FB1 band.

In an autism study with fMRI, Dinstein et al. (2011) observed the reduced interhemispheric fMRI-RSFC in autism, in particular RSFC between the bilateral superior temporal gyrus. To make a classification between all the participants with ASD (the number was 29) and all non-autistic controls (the number was 43), they selected a criterion value of 0.38 for the RSFC. With this criterion, all participants were classified as two categories: those with lower RSFC than the criterion were classified as ASD, otherwise classified as TD. This method yielded a classification with a sensitivity of 72.4%, specificity of 83.7%, and accuracy of 79.2%. As both the present and Dinstein and colleagues' studies used the homotopic RSFC in temporal lobes as a classification feature, to make a quantitative comparison on the classification ability between the fNIRS and fMRI data, we could use the same approach by selecting a criterion value on fNIRS-RSFC for best differentiating between the two groups. The result showed that by using the mean of RSFC showing significant difference between ASD and TD in FB1 band as discriminative feature and selecting a criterion value of 0.53, the classification could be achieved with a sensitivity of 80.0%, specificity of 81.8%, and accuracy of 80.9%, slightly better in sensitivity and accuracy than the classification obtained with fMRI. However, because of the difference in sample size (in Dinstein and colleagues' work, ASD = 29, non-ASD = 43, whereas in our study, ASD = 25, non-ASD = 22) and individuals, we could not conclude that fNIRS was superior to fMRI in RSFC-based classification between individuals with ASD and TD controls. Nevertheless, the discrimination ability of fNIRS is comparable to fMRI, demonstrating the promise of this optical imaging technique in the application of ASD study.

As seen in **Table 1**, in the narrow-frequency band of 0.01–0.02 Hz (FB1), the number of channel pairs showing significant differences in RSFC between ASD and TD is 8 (i.e., 6 in HbO_2 and 2 in Hb), the largest number in all these frequency bands. In 0.01–0.03 Hz (FB6), the number is 4 (3 in HbO_2, 1 in Hb), the second largest number. This frequency band mostly overlaps

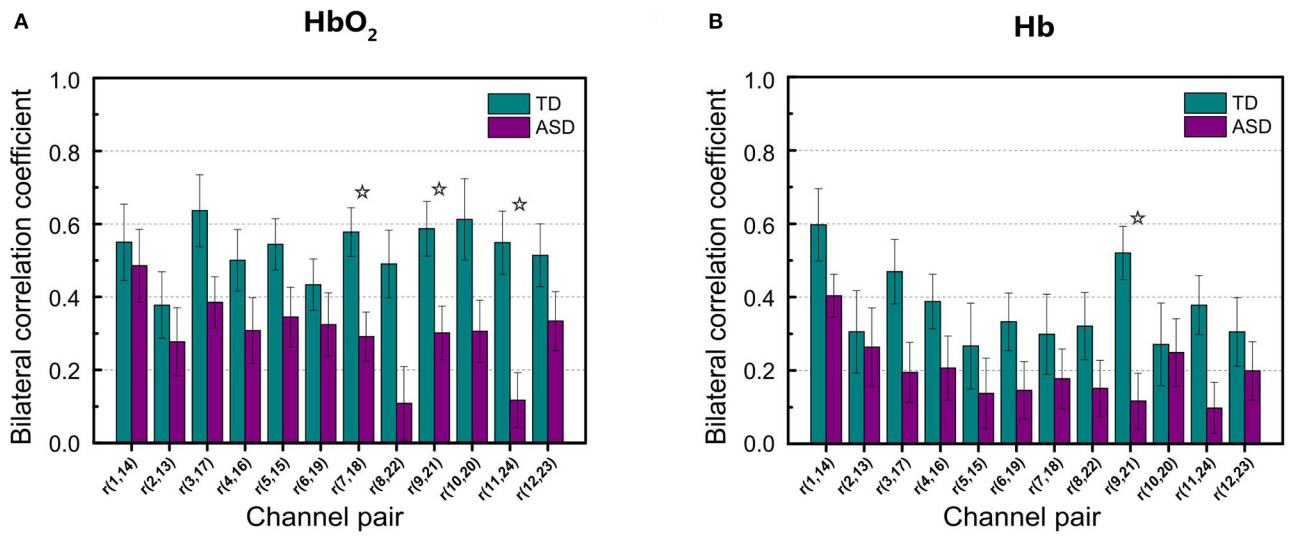

FIGURE 6 | Group average of the correlation coefficients in HbO_2 **(A)** and Hb **(B)** for each mirrored channel pair locating symmetrically on the left and right temporal lobes in Slow-5 band. The digit pair in the parenthesis indicates the corresponding channel pair, e.g., $r(1,14)$ is the temporal correlation coefficient between channel 1 and channel 14. The asterisks indicate the differences in the correlation coefficient between ASD and TD are statistically significant (FDR-corrected $q < 0.05$) for the channel pair, and the statistical powers are larger than 0.8. The error bar for each correlation coefficient is the standard error of mean.

with Slow-5 band (0.010–0.027 Hz). As already discussed in the introduction, the reduced brain network connectivity could be manifested by the alteration in Slow-5 oscillation (La et al., 2016a,b,c); we further investigated if children with ASD could show altered Slow-5 RSFC. **Figure 6** shows Slow-5 RSFC for each mirrored channel pair in TD and ASD groups. Not surprisingly, in Slow-5 band, there were three channel pairs, i.e., $r(7,18)$, $r(9,21)$, and $r(11,24)$ in HbO_2 and one channel pair, i.e., $r(9,21)$, in Hb showing significant difference between the ASD and TD groups in the correlation coefficient, the same as seen in FB6 (0.01–0.03 Hz) (**Table 1**), and all pairs were included in those channel pairs observed in FB1 (**Figure 3**). As in the present study the minimal resolution of the frequency scanning was 0.1 Hz, the characteristics in Slow-5 might be reflected in FB1 (0.01–0.02 Hz) and FB6 (0.01–0.03 Hz), which could also be seen in **Figures 3**, **5**, **6** and **Table 1**. From the ROC curve and AUC value, we could roughly evaluate the discrimination ability of RSFC between ASD and TD at the three frequency bands: 0.01–0.02 Hz (Narrow FB1), 0.010–0.027 Hz (Slow-5), and 0.009–0.08 Hz (broadband): narrow FB1 > Slow-5 > broadband (**Figure 5**).

In the present study, we observed in several frequency bands including FB1, FB2, FB6, FB7, FB9, and FB10 that the grand average of RSFC in HbO_2 showed significant difference between the ASD and TD groups (**Figure 2**). However, the discrimination ability was different, as AUC value showed FB1-RSFC was superior to RSFC in the other frequency bands (**Figure 4**). In addition, correlation analysis demonstrated that RSFC in the other frequency bands was highly correlated to FB1-RSFC. Therefore, FB1-RSFC might contain more rich discriminative information than RSFC in the other bands. Besides that, only in the FB1 band that the grand average of RSFC in Hb showed significant difference between the ASD and TD groups. On the other hand, from the number of channel pairs (corresponding to the mirrored cortical sites) showing significant difference in RSFC, we found more mirrored cortical sites exhibited significantly weaker RSFC in ASD in the narrowband of FB1. Therefore, our fNIRS data and analysis suggested that FB1 (0.01–0.02 Hz) might be an important frequency band for studying atypical RSFC in ASD.

fNIRS, as a rapidly developing brain imaging technique, allows mapping human brain non-invasively. Its unique and beneficial characteristics, in particular relatively low sensitivity to head movement and natural environment for measurement, have made fNIRS gain more popularity in recent years, particularly in studying brains of young children. The discrimination ability between ASD and TD with fNIRS 0.01–0.02-Hz frequency band RSFC is comparable to fMRI-RSFC, making this optical imaging modality a potential tool for the prediction of ASD in children. Suffice to say, it might be of great significance to promote fNIRS with more clinical applications on ASD.

As the sample size (i.e., 25 children with ASD and 22 TD children) was limited in the present study, to effectively restrain type II error, we also performed statistical power analysis for the differences already passing through *t*-test and FDR correction. We defined significant difference by using two criteria: FDR-corrected $q < 0.05$ and statistical power >0.8. By this definition, both type I error (controlled by *t*-test and FDR correction) and type II error (controlled by the statistical power analysis) would be strictly restrained; thus, the results observed were more statistically reliable, implying the revealed discriminative features should likely be still valid when the sample (children with ASD and TD children) size is enlarged. Another limitation of this study is that we cannot completely exclude the possibility that the difference in RSFC is due to the difference in IQ between

the two groups, although several fMRI studies (Song et al., 2008; Van Den Heuvel et al., 2009; Pamplona et al., 2015) on whole head have revealed that IQ is correlated to the functional connectivity between the frontal and other brain regions such as parietal, occipital, and limbic lobes, but have not reported any evidence that IQ is related to RSFC between the bilateral temporal lobes.

CONCLUSION

We applied narrowband pass filters with different bandwidths to resting-state fNIRS data and found that children with ASD showed significantly weaker RSFC than TD children in a variety of frequency bands. However, the difference between ASD and TD in RSFC was more pronounced in 0.01–0.02 Hz than the other frequency bands including the widely used broadband (0.009–0.08 Hz) and Slow-5 band. ROC curve and AUC value also demonstrated 0.01–0.02-Hz RSFC could be a good characteristic feature for the discrimination between children with ASD and TD children.

DATA AVAILABILITY STATEMENT

The raw data supporting the conclusions of this article will be made available by the authors, without undue reservation.

ETHICS STATEMENT

The studies involving human participants were reviewed and approved by South China Normal University's Ethical Review Board. Written informed consent to participate in this study was provided by the participants' legal guardian/next of kin.

AUTHOR CONTRIBUTIONS

JL and WS conceptualized the manuscript. WS, XW, and TZ analyzed the data. WS wrote the original draft. HS and FL drew pictures. JL reviewed and edited its intellectual content. All authors contributed to the article and approved the submitted version.

FUNDING

This study was supported by the National Natural Science Foundation of China (NSFC) (Grant No. 81771876), Guangdong Provincial Key Laboratory of Optical Information Materials and Technology (Grant No. 2017B030301007), Guangdong Science and Technology Program (Grant No. 2017A010101023), Special Funds for the Cultivation of Guangdong College Students' Scientific and Technological Innovation (Climbing Program Special Funds) (No. pdjh2020b0155), and Science and Technology Program of Guangzhou (No. 2019050001).

REFERENCES

American Psychiatry Association (2000). *Diagnostic and Statistical Manual of Mental Disorders: DSM-IV-TR*. Washington, DC: American Psychiatric Publishing. p. 157.

Arbabshirani, M. R., Plis, S., Sui, J., and Calhoun, V. D. (2017). Single subject prediction of brain disorders in neuroimaging: promises and pitfalls. *Neuroimage* 145, 137–165. doi: 10.1016/j.neuroimage.2016.02.079

Assaf, M., Jagannathan, K., Calhoun, V. D., Miller, L., Stevens, M. C., Sahl, R., et al. (2010). Abnormal functional connectivity of default mode sub-networks in autism spectrum disorder patients. *Neuroimage* 53, 247–256. doi: 10.1016/j.neuroimage.2010.05.067

Biswal, B., Zerrin Yetkin, F., Haughton, V. M., and Hyde, J. S. (1995). Functional connectivity in the motor cortex of resting human brain using echo-planar MRI. *Magn. Reson. Med.* 34, 537–541. doi: 10.1002/mrm.1910340409

Cheng, H., Yu, J., Xu, L., and Li, J. (2019). Power spectrum of spontaneous cerebral homodynamic oscillation shows a distinct pattern in autism spectrum disorder. *Biomed. Opt. Express* 10, 1383–1392. doi: 10.1364/BOE.10.001383

Cheng, J. C., Bosma, R. L., Hemington, K. S., Kucyi, A., Lindquist, M. A., and Davis, K. D. (2017). Slow-5 dynamic functional connectivity reflects the capacity to sustain cognitive performance during pain. *Neuroimage* 157, 61–68. doi: 10.1016/j.neuroimage.2017.06.005

Chuang, C.-C., and Sun, C.-W. (2014). Gender-related effects of prefrontal cortex connectivity: a resting-state functional optical tomography study. *Biomed. Opt. Express* 5, 2503–2516. doi: 10.1364/BOE.5.002503

Dinstein, I., Pierce, K., Eyler, L., Solso, S., and Courchesne, E. (2011). Disrupted neural synchronization in toddlers with autism. *Neuron* 70, 1218–1225. doi: 10.1016/j.neuron.2011.04.018

Friston, K. J. (2007). *Statistical Parametric Mapping: The Analysis of Functional Brain Images*. London: Elsevier Academic.

Goldson, E. (2016). Advances in autism-2016. *Adv. Pediatr.* 63, 333–355. doi: 10.1016/j.yapd.2016.04.014

Kita, Y., Gunji, A., Inoue, Y., Goto, T., Sakihara, K., Kaga, M., et al. (2011). Self-face recognition in children with autism spectrum disorders: a near-infrared spectroscopy study. *Brain Dev.* 33, 494–503. doi: 10.1016/j.braindev.2010.11.007

La, C., Mossahebi, P., Nair, V. A., Young, B. M., Stamm, J., Birn, R., et al. (2016a). Differing patterns of altered slow-5 oscillations in healthy aging and ischemic stroke. *Front. Hum. Neurosci.* 10:156. doi: 10.3389/fnhum.2016.00156

La, C., Nair, V. A., Mossahebi, P., Stamm, J., Birn, R., Meyerand, M. E., et al. (2016b). Recovery of slow-5 oscillations in a longitudinal study of ischemic stroke patients. *Neuroimage Clin.* 11, 398–407. doi: 10.1016/j.nicl.2016.03.008

La, C., Nair, V. A., Mossahebi, P., Young, B. M., Chacon, M., Jensen, M., et al. (2016c). Implication of the slow-5 oscillations in the disruption of the default-mode network in healthy aging and stroke. *Brain Connect.* 6, 482–495. doi: 10.1089/brain.2015.0375

Li, J., and Qiu, L. (2014). Temporal correlation of spontaneous hemodynamic activity in language areas measured with functional near-infrared spectroscopy. *Biomed. Opt. Express* 5, 587–595. doi: 10.1364/BOE.5.000587

Li, J., Qiu, L., Xu, L., Pedapati, E. V., Erickson, C. A., and Sunar, U. (2016). Characterization of autism spectrum disorder with spontaneous hemodynamic activity. *Biomed. Opt. Express* 7, 3871–3881. doi: 10.1364/BOE.7.003871

Lord, C., Risi, S., Dilavore, P. S., Shulman, C., Thurm, A., and Pickles, A. (2006). Autism from 2 to 9 years of age. *Arch. Gen. Psychiatry* 63, 694–701. doi: 10.1001/archpsyc.63.6.694

Lu, C.-M., Zhang, Y.-J., Biswal, B. B., Zang, Y.-F., Peng, D.-L., and Zhu, C.-Z. (2010). Use of fNIRS to assess resting state functional connectivity. *J. Neurosci. Methods* 186, 242–249. doi: 10.1016/j.jneumeth.2009.11.010

Luyster, R., Gotham, K., Guthrie, W., Coffing, M., Petrak, R., Pierce, K., et al. (2009). The autism diagnostic observation schedule—toddler module: a new module of a standardized diagnostic measure for autism spectrum disorders. *J. Autism Dev. Disord.* 39, 1305–1320. doi: 10.1007/s10803-009-0746-z

Monk, C. S., Peltier, S. J., Wiggins, J. L., Weng, S.-J., Carrasco, M., Risi, S., et al. (2009). Abnormalities of intrinsic functional connectivity in autism spectrum disorders. *Neuroimage* 47, 764–772. doi: 10.1016/j.neuroimage.2009.04.069

Pamplona, G. S., Santos Neto, G. S., Rosset, S. R., Rogers, B. P., and Salmon, C. E. (2015). Analyzing the association between functional connectivity of the brain and intellectual performance. *Front. Hum. Neurosci.* 9:61. doi: 10.3389/fnhum.2015.00061

Raven, J., and Court, J. (1998). *Raven Manual: Section 3. Standard Progressive Matrices.* Oxford: Oxford Psychologists Press.

Sasai, S., Homae, F., Watanabe, H., and Taga, G. (2011). Frequency-specific functional connectivity in the brain during resting state revealed by NIRS. *Neuroimage* 56, 252–257. doi: 10.1016/j.neuroimage.2010.12.075

Smitha, K., Akhil Raja, K., Arun, K., Rajesh, P., Thomas, B., Kapilamoorthy, T., et al. (2017). Resting state fMRI: a review on methods in resting state connectivity analysis and resting state networks. *Neuroradiol. J.* 30, 305–317. doi: 10.1177/1971400917697342

Song, M., Zhou, Y., Li, J., Liu, Y., Tian, L., Yu, C., et al. (2008). Brain spontaneous functional connectivity and intelligence. *Neuroimage* 41, 1168–1176. doi: 10.1016/j.neuroimage.2008.02.036

Van Den Heuvel, M. P., and Pol, H. E. H. (2010). Exploring the brain network: a review on resting-state fMRI functional connectivity. *Eur. Neuropsychopharmacol.* 20, 519–534. doi: 10.1016/j.euroneuro.2010.03.008

Van Den Heuvel, M. P., Stam, C. J., Kahn, R. S., and Pol, H. E. H. (2009). Efficiency of functional brain networks and intellectual performance. *J. Neurosci.* 29, 7619–7624. doi: 10.1523/JNEUROSCI.1443-09.2009

Veenstra-VanderWeele, J., Christian, S. L., and Cook, J., Edwin, H. (2004). Autism as a paradigmatic complex genetic disorder. *Annu. Rev. Genomics Hum. Genet.* 5, 379–405. doi: 10.1146/annurev.genom.5.061903.180050

White, B. R., Snyder, A. Z., Cohen, A. L., Petersen, S. E., Raichle, M. E., Schlaggar, B. L., et al. (2009). Resting-state functional connectivity in the human brain revealed with diffuse optical tomography. *Neuroimage* 47, 148–156. doi: 10.1016/j.neuroimage.2009.03.058

Xu, L., Geng, X., He, X., Li, J., and Yu, J. (2019). Prediction in autism by deep learning short-time spontaneous hemodynamic fluctuations. *Front. Hum. Neurosci.* 13:1120. doi: 10.3389/fnins.2019.01120

Xu, L., Guo, Y., Li, J., Yu, J., and Xu, H. (2020a). Classification of autism spectrum disorder based on fluctuation entropy of spontaneous hemodynamic fluctuations. *Biomed. Signal Process. Control* 60:101958. doi: 10.1016/j.bspc.2020.101958

Xu, L., Hua, Q., Yu, J., and Li, J. (2020b). Classification of autism spectrum disorder based on sample entropy of spontaneous functional near infra-red spectroscopy signal. *Clin. Neurophysiol.* 131, 1365–1374. doi: 10.1016/j.clinph.2019.12.400

Xu, L., Liu, Y., Yu, J., Li, X., Yu, X., Cheng, H., et al. (2020c). Characterizing autism spectrum disorder by deep learning spontaneous brain activity from functional near-infrared spectroscopy. *J. Neurosci. Methods* 331:108538. doi: 10.1016/j.jneumeth.2019.108538

Zhang, Y.-J., Lu, C.-M., Biswal, B. B., Zang, Y.-F., Peng, D., and Zhu, C.-Z. (2010). Detecting resting-state functional connectivity in the language system using functional near-infrared spectroscopy. *J. Biomed. Opt.* 15:047003. doi: 10.1117/1.3462973

Zhu, H., Fan, Y., Guo, H., Huang, D., and He, S. (2014). Reduced interhemispheric functional connectivity of children with autism spectrum disorder: evidence from functional near infrared spectroscopy studies. *Biomed. Opt. Express* 5, 1262–1274. doi: 10.1364/BOE.5.001262

Conflict of Interest: The authors declare that the research was conducted in the absence of any commercial or financial relationships that could be construed as a potential conflict of interest.

frontiers in Human Neuroscience

ORIGINAL RESEARCH
published: 10 September 2021
doi: 10.3389/fnhum.2021.720596

Impact of Antiepileptic Drugs on Cognition and Neuromagnetic Activity in Childhood Epilepsy With Centrotemporal Spikes: A Magnetoencephalography Study

*Kai Niu[1], Yihan Li[1], Tingting Zhang[1,2], Jintao Sun[1], Yulei Sun[1], Mingzhu Shu[1], Pengfei Wang[1], Ke Zhang[1], Qiqi Chen[3] and Xiaoshan Wang[1]**

[1] Department of Neurology, The Affiliated Brain Hospital of Nanjing Medical University, Nanjing, China, [2] Department of Neurology, Affiliated Hospital of Jiangsu University, Zhenjiang, China, [3] MEG Center, The Affiliated Brain Hospital of Nanjing Medical University, Nanjing, China

OPEN ACCESS

Edited by:
Dajiang Zhu, University of Texas at Arlington, United States

Reviewed by:
Jacopo Lanzone, Sant'Isidoro Hospital Ferb Onlus Trescore Balneario, Italy
Lorenzo Ricci, Policlinico Universitario Campus Bio-Medico, Italy

***Correspondence:**
Xiaoshan Wang
lidou2005@126.com

Specialty section:
This article was submitted to Brain Imaging and Stimulation, a section of the journal Frontiers in Human Neuroscience

Received: *04 June 2021*
Accepted: *13 August 2021*
Published: *10 September 2021*

Citation:
Niu K, Li Y, Zhang T, Sun J, Sun Y, Shu M, Wang P, Zhang K, Chen Q and Wang X (2021) Impact of Antiepileptic Drugs on Cognition and Neuromagnetic Activity in Childhood Epilepsy With Centrotemporal Spikes: A Magnetoencephalography Study. Front. Hum. Neurosci. 15:720596. doi: 10.3389/fnhum.2021.720596

Objective: Childhood epilepsy with centrotemporal spikes (CECTS), the most common childhood epilepsy, still lacks longitudinal imaging studies involving antiepileptic drugs (AEDs). In order to examine the effect of AEDs on cognition and brain activity. We investigated the neuromagnetic activities and cognitive profile in children with CECTS before and after 1 year of treatment.

Methods: Fifteen children with CECTS aged 6–12 years underwent high-sampling magnetoencephalography (MEG) recordings before treatment and at 1 year after treatment, and 12 completed the cognitive assessment (The Wechsler Intelligence Scale for Children). Next, magnetic source location and functional connectivity (FC) were investigated in order to characterize interictal neuromagnetic activity in the seven frequency sub-bands, including: delta (1–4 Hz), theta (4–8 Hz), alpha (8–12 Hz), beta (12–30 Hz), gamma (30–80 Hz), ripple (80–250 Hz), and fast ripple (250–500 Hz).

Results: After 1 year of treatment, children with CECTS had increased scores on full-scale intelligence quotient, verbal comprehension index (VCI) and perceptual reasoning index (PRI). Alterations of neural activity occurred in specific frequency bands. Source location, in the 30–80 Hz frequency band, was significantly increased in the posterior cingulate cortex (PCC) after treatment. Moreover, FC analysis demonstrated that after treatment, the connectivity between the PCC and the medial frontal cortex (MFC) was enhanced in the 8–12 Hz frequency band. Additionally, the whole-brain network distribution was more dispersed in the 80–250 Hz frequency band.

Conclusion: Intrinsic neural activity has frequency-dependent characteristic. AEDs have impact on regional activity and FC of the default mode network (DMN). Normalization of aberrant DMN in children with CECTS after treatment is likely the reason for improvement of cognitive function.

Keywords: magnetoencephalography, cognition, source location, functional connectivity, antiepileptic drug, childhood epilepsy with centrotemporal spikes

INTRODUCTION

Childhood epilepsy with centrotemporal spikes (CECTS) is the most common idiopathic focal epilepsy syndrome, and accounts for 13–23% of childhood epilepsy (Heijbel et al., 1975; Panayiotopoulos et al., 2008). In the past, CECTS was called "benign epilepsy with centrotemporal spikes," however, recent studies have revealed that children with CECTS tend to exhibit extensive cognitive difficulties, which makes the definition of "benign" no longer applicable (Wickens et al., 2017). Therefore, rational treatments of antiepileptic drugs (AEDs) are recommended to control seizures, as well as alleviate cognitive impairment (Hughes, 2010; Mellish et al., 2015). However, the exact long-term effect of AEDs on the intrinsic brain activity and cognitive function among children with CECTS remains unclear.

To date, numerous studies have demonstrated that the resting-state brain activity of children with CECTS has been altered (McGinnity et al., 2017; Bourel-Ponchel et al., 2019; Zhang et al., 2020). On this basis, several studies based on functional magnetic resonance (fMRI) have further investigated brain alterations in CECTS during AEDs treatment, the results of which have shown that AEDs have an effect on functional connectivity (FC) (Jiang et al., 2019, 2020), and regional activity (Zhang et al., 2017, 2018). Unfortunately, these studies are all cross-sectional studies, rather than longitudinal follow-up studies, and lead to limited convincing results. Besides, although the effect of AEDs on cognitive function has been widely reported among previous studies (Tacke et al., 2016; Han and Kim, 2018; Operto et al., 2019), the lack of synchronized cognitive assessment weakens the clinical significance of neuroimaging results.

In addition, increasing evidence suggests that high-frequency oscillations may be a specific biomarker for measuring disease activity, as well as assessing treatment response (van Klink et al., 2016; Frauscher et al., 2017; Lanzone et al., 2020, 2021a). However, fMRI studies only retain low-frequency amplitudes, and may lose high-frequency information of neural activity (Wang et al., 2014). Also, studies that are based on fMRI and electroencephalogram show that brain activity exhibit frequency-dependent properties (Gohel and Biswal, 2015; Jiang et al., 2019; Jun et al., 2019; Lanzone et al., 2021b). Magnetoencephalography (MEG) is a non-invasive technique with high spatiotemporal resolution that records brain activity by detecting magnetic fields generated by neural currents (Guggisberg et al., 2008; Burgess, 2011). These magnetic fields are not attenuated by the scalp and skull, allowing MEG to detect the higher frequency electromagnetic oscillations of the brain (Guggisberg et al., 2008; Burgess, 2011; Harmsen et al., 2018). Furthermore, compared to other neuroimaging techniques, MEG has several advantages for use among young children, including fewer constraints and the absence of radiation and unpleasant sounds (Kikuchi et al., 2016). Overall, MEG is known to be suitable for multifrequency analysis of brain activity among children with CECTS.

In this study, we utilized MEG to directly compare the neuromagnetic signatures and FC network before and after drug treatment from low- to high-frequency bands in order to explore the changes in brain activity of children with CECTS that receive AEDs. We also simultaneously performed cognitive assessment to link cognitive profile changes that are caused by AEDs with neuroimaging results. Our finding likely contributed to gain better insight into the neural mechanisms of AEDs on CECTS therapy.

Abbreviations: CECTS, childhood epilepsy with centrotemporal spikes; AEDS, antiepileptic drugs; FC, functional connectivity; DMN, default mode network; fMRI, functional magnetic resonance; MEG, magnetoencephalography; ASI, accumulated source imaging; WISC-IV, Wechsler Intelligence Scale for Children, fourth edition; FSIQ, full-scale intelligence quotient; VCI, verbal comprehension index; PRI, perceptual reasoning index; WMI, working memory index; MFC, medial frontal cortex; PCC, posterior cingulate cortex; PR, peri-Rolandic area; MTL, medial temporal lobe; DBA, deep brain area.

EXPERIMENTAL PROCEDURES

Participants

Children that are diagnosed with CECTS were recruited from the Department of Neurology at Nanjing Children's Hospital and Nanjing Brain Hospital between November 2018 and November 2019. All children started taking AEDs within 1 week after completing the initial MEG recording, and performed the second recording after a period of treatment. The time interval was 8.8–18.3 months (average 11.9 months).

The inclusion criteria for subjects were as follows: (1) a clinical diagnosis of CECTS, according to the ILAE 2017 classification of epilepsy syndrome (Scheffer et al., 2017); (2) normal brain MRI, no history of other neurological diseases or major diseases; (3) 6–12 years old, undergoing normal development and receiving formal education; (4) drug naive at enrollment; and (5) requirement of drug intervention as judged by an experienced neurologist.

The exclusion criteria are as follows: (1) a history of taking AEDs, (2) metal implants within the body, (3) atypical evolution, (4) interruption of treatment or combined use of multiple drugs during follow-up, and (5) lost to follow-up.

MEG Recording

A whole-head, CTF-275 channel MEG system (VSM Medical Technology Company, Canada) was utilized to collect the MEG data in a magnetically shielded room. The MEG date was collected at a sampling rate of 6000 Hz, with noise cancelation of the third-order gradients. Prior to MEG recording, three small electromagnetic coils were pasted on the nasion and bilateral pre-auricular points of each subject, which helped monitor the subject's head position relative to the MEG sensors. The accuracy of the head position was 1 mm. During the recording, subjects were instructed to relax, stay still, gently close their eyes and slightly open their mouths. Each MEG recording lasted for 2 min. Data with head movement >5 mm was discarded so as not to affect accuracy of the source localization. For each subject, at least ten valid data files for a total of 20 min were collected.

MRI Scan

The MRI date was obtained on a 3.0T MRI scanner (Siemens, Germany). The T1-weighted images were acquired using the following parameters: sagittal orientation, slices = 176,

thickness = 1 mm, TR = 1,900 ms, TE = 2.48 ms, matrix = 512 × 512, and field of view = 250 mm × 250 mm. Prior to scanning, three fiduciary marks were also pasted on positions of the coils in the MEG recording, in order to accurately co-register the MRI and MEG data.

Data Preprocessing

We performed data processing via the following steps: First, we deleted the data with discernible noise and artifacts (waveform > 6pT deflection) by visually inspecting the MEG waveform (Xiang et al., 2015b). Then, we filtered the remaining MEG data with a band pass filter of 1–70 Hz so that the characteristic spikes can be clearly displayed in the waveform. Next, we selected a segment of interictal waveform with no spikes for up to 60 s. Finally, we analyzed the selected waveform segments in the following seven frequency bands, including: delta (1–4 Hz), theta (4–8 Hz), alpha (8–12 Hz), beta (12–30 Hz), gamma (30–80 Hz), ripple (80–250 Hz), and fast ripple (250–500 Hz). Notch filters for 50 Hz and its harmonics were utilized to eliminate the interference from ambient alternating current power.

Source Localization

Based on the previous studies (Xiang et al., 2014, 2015b), we utilized accumulated source imaging (ASI), which is a specific approach to analyze neuromagnetic activity among multiple frequency ranges, as well as to analyze MEG signals at the source level. In brief, ASI is the volumetric summation of source activity over a period of time (Xiang et al., 2015b), which can be depicted by the following equation:

$$Asi\,(r, s) = \sum_{t=1}^{t=n} Q\,(r, t) \tag{1}$$

Where Asi is accumulated source strength at location r, s is the time slice, t is the time point of MEG data, n is the total time points of MEG data and Q is the source activity at source r and at time point t. We defined $s \geq 1$ and $s \leq n/2$.

We used two-step beamforming to localize the magnetic sources (Xiang et al., 2015b). Specific steps were as follows. First, we computed the lead fields for each source (or voxel position) to generate matrices with MEG data. The next crucial step was selecting sensors for partial sensor coverage for each voxel, which was done to minimize the effect of coherent sources in source localization (Xiang et al., 2015a). Then, we computed the covariance for all sensors. Furthermore, we computed two sets of magnetic source images using a 3D vector beamformer grid, and estimated the coherent source and source orientation with a covariance matrix vector beamformer (Xiang et al., 2015a). Finally, we generated source activity (or virtual sensor waveform) using a scalar beamformer (Xiang et al., 2015a). The detailed mathematical algorithms and validations were described in the previously published articles (Xiang et al., 2014, 2015b).

Functional Connectivity Analysis

We analyzed FC at the source level, and specific procedures and algorithms of this method were elaborated in the previous reports (Xiang et al., 2014, 2015b). In summary, the virtual sensor waveforms of each source were calculated using the ASI algorithm mentioned above. Next, the source neural network was estimated via analysis of the signal correlation of each pair of virtual sensors in the 60 s time window. Finally, the relationship between the virtual sensor signals from the two source pairs was statistically analyzed by calculating the correlation factor (or the correlation coefficient). The correlation factor is calculated via the following formula:

$$R\,(Xa, Xb) = \frac{C\,(Xa, Xb)}{SXa, Xb} \tag{2}$$

Where R (X_a, X_b) represent the correlation between the pair of magnetic sources "a" and "b," while X_a and X_b represent signals from two of the magnetic sources calculated in pairs. C (X_a, X_b), respectively, represent the average signals of the two magnetic sources, while SX_a and SX_b are the standard deviations of signals of the two magnetic sources.

In order to avoid possible bias, source-level analysis was utilized to calculate all possible connections for each source pair. All possible FC distributions of each pair of voxel-based virtual sensors were co-registered to MRI of each participant (Xiang et al., 2014, 2015b). In order to analyze source connections, the neural network was visualized in axial, coronal, and sagittal views. Excitatory and inhibitory connections were depicted in red and blue, respectively. In order to ensure the quality of the data, a threshold was utilized as a checkpoint. *T* values were computed for all source pairs to determine the thresholding of connections.

$$Tp = R\sqrt{\frac{K-2}{1-R^2}} \tag{3}$$

Where T_p is the *t*-value of a correlation, R is the correlation of a source pair, and K is the number of data points for the connection. In this study, we used a threshold of a T_p value with a corresponding *p*-value < 0.05 to obtain the FC networks.

Neurocognitive Assessment

The Wechsler Intelligence Scale for Children, fourth edition (WISC-IV) is a standardized test designed to measure intelligence of children and adolescents from 6 to 16 years old. The scale consists of 10 subscales core subtests and five additional subtests through which it is possible to calculate one full-scale intelligence quotient (FSIQ) and four indices. The details are as follows: The verbal comprehension index (VCI) represents language and verbal skills, the perceptual reasoning index (PRI) reflects nonverbal and fluid reasoning, the working memory index (WMI) reflects working memory and auditory attention, and the processing speed index (PSI) reflects selective attention and speed of visual information processing. We previously reported that, prior to treatment, children with CECTS showed significantly poorer performance compared to health controls in all aspects (Li et al., 2020a). The WISC-IV was utilized in the present study to determine whether treatment with AEDs would cause a change in cognitive function.

TABLE 1 | Demographic and clinical characteristics of the patients.

Patients	Onset age, y	Sex	Seizure type	Seizure frequency	Duration, m		Initial AED	Maintenance Dose, mg	Seizure controlled
					Enrollment	Follow-up			
1	6.95	F	FS with PA	Four episodes	8.9	22.6	LEV	1000	Y
2	4.64	M	Focal to bilateral TCS	Three episodes	9.7	22.9	VPA	750	N
3	7.93	F	Focal to bilateral TCS	Weekly	4.6	15.8	LEV	1750	N
4	4.43	M	FS with IA	Four episodes	10.9	20.3	LEV	750	Y
5	9.65	F	Focal to bilateral TCS	One episode	5.6	14.7	LEV	750	N
6	9.46	M	Focal to bilateral TCS	Two episodes	6.1	24.4	LEV	1000	N
7	8.89	M	Focal to bilateral TCS	Three episodes	0.5	9.3	OXC	450	Y
8	8.25	F	FS with PA	Two episodes	5.7	16.5	OXC	600	N
9	7.23	F	FS with IA	Two episodes	9.5	25.1	LEV	1250	N
10	9.60	F	FS with IA	Three episodes	7.7	16.6	OXC	750	N
11	7.18	M	Focal to bilateral TCS	Two episodes	1.3	11.9	VPA	500	Y
12	8.93	M	FS with PA	Four episodes	14.5	28.7	LEV	1500	Y
13	5.15	F	FS with IA	Four episodes	4.5	15.5	OXC	450	Y
14	7.30	F	FS with PA	Two episodes	0.8	13.4	LEV	1000	Y
15	6.21	M	Focal to bilateral TCS	Three episodes	5.7	17.3	OXC	600	N

F, female; M, male; FS, focal seizures; PA, preserved awareness; IA, impaired awareness; TCS, tonic-clonic seizures; AED, antiepileptic drug; LEV, levetiracetam; VPA, valproic acid; OXC, oxcarbazepine; Y, yes; N, no.

Statistical Analyses

The McNemar's test was conducted on predominant neuromagnetic source locations and FC network patterns. For WISC-IV scores, statistical analyses were carried out using a paired sample *T*-test after demonstrating normal distribution with a Shapiro–Wilk test. Bonferroni correction was utilized for multiple comparisons [i.e., for seven frequency bands, $p < 0.007$ (0.05/7 = 0.00714)]. Probability values < 0.05 (two-tailed) were considered to be statistically significant. All statistical analyses were conducted using SPSS version 23.0 for Windows (SPSS Inc., Chicago, IL, United States).

RESULTS

Clinical Characteristics

A total of 22 children were recruited for this study. Among them, children who were lost to follow-up ($n = 5$) and children with atypical evolution ($n = 2$) were excluded from the study. Data from the remaining 15 patients (eight female and seven male) were analyzed. Their average age of onset was 7.65 ± 1.44 years. Their average course of disease was 6.40 ± 3.92 months at the time of enrollment, and 18.33 ± 5.45 months at the time of follow-up. The average follow-up interval is 11.93 ± 2.80 months. Seven children no longer experienced seizures after treatment, while the other eight continued to have seizures. Detailed data is described in **Table 1**.

The WISC-IV Score

In total, 12 children completed the two tests at the time of enrollment and follow-up. Comparing the mean scores before and after treatment, we discovered found that treatment led to better scores in FSIQ, VCI, PRI, WMI, and PSI. The improvement in FSIQ, VCI and PRI was found to be statistically significant. **Table 2** and **Figure 1** summarizes the mean scores of the two times.

Source Localization

Accumulative magnetic source imaging demonstrated that each patient has 1–3 sources stronger than the rest of the brain activity during the resting state. Regarding the location of the main magnetic source (**Figure 2**), we discovered similar patterns were present before and after treatment. Specifically, in the 1–4, 4–8, and 8–12 Hz frequency bands, the main magnetic source was found to be located in the medial frontal cortex (MFC), posterior cingulate cortex (PCC), and peri-Rolandic area (PR). In the 12–30 Hz frequency band, the main magnetic source was located in the MFC and PCC. We did not find any significant difference in the magnetic source location before and after treatment in these frequency bands. In the 30–80 Hz frequency band, the main magnetic source was located in the MFC, PCC, and medial temporal lobe (MTL). The brain activity before and after treatment was significantly different at this frequency band, while activation of the PCC after treatment was higher compared to before treatment ($P = 0.004$). In the 80–250 and 250–500 Hz

TABLE 2 | WISC-IV scores before and after treatment.

WISC-IV	Pre-treatment	Post-treatment	Difference	*P*-value
FSIQ	96.08 ± 11.91	105.08 ± 10.00	9.00 ± 11.40	0.019*
VCI	93.42 ± 17.19	101.33 ± 16.54	7.92 ± 9.46	0.014*
PRI	97.33 ± 15.31	110.33 ± 8.65	13.00 ± 17.71	0.027*
WMI	98.00 ± 11.32	102.00 ± 11.10	4.00 ± 14.21	0.350
PSI	100.42 ± 12.68	101.75 ± 6.80	1.33 ± 13.51	0.739

*FSIQ, Full-scale Intelligence Quotient; VCI, verbal comprehension index; PRI, perceptual reasoning index; WMI, working memory index; PSI, processing speed index. *The p-value was statistically significant.*

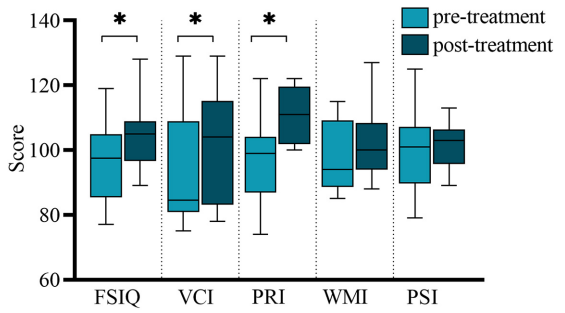

FIGURE 1 | Comparison of WISC-IV scores before and after treatment. FSIQ, Full-scale Intelligence Quotient; VCI, verbal comprehension index; PRI, perceptual reasoning index; WMI, working memory index; PSI, processing speed index. *The *p*-value was statistically significant.

Frequency bands, the main magnetic sources were located in the MFC, MTL, and deep brain area (DBA). Changes in these frequency band were found not to be statistically significant. Detailed statistical results were shown in **Table 3**.

Functional Network

Both positive and negative connections of seven frequency bands before and after treatment was analyzed and compared. We found that there were differences in the frequency bands of 1–4, 8–12, and 80–250 Hz. Among them, in the 1–4 Hz frequency band, the functional connection involving the PR tended to decrease post-treatment, compared to before treatment. The *P*-value ($P = 0.031$), however, was not statistically significant after Bonferroni correction. In the 8–12 Hz frequency band, the functional connection between the anterior and posterior brain regions (mainly the connection between the MFC and the PCC) was significantly enhanced after treatment ($p = 0.001$, $p < 0.05$ after Bonferroni correction). In the 80–250 Hz frequency band, the functional network was limited to the MFC before treatment, while it involved more brain regions after treatment ($p = 0.004$, $p < 0.05$ after Bonferroni correction). No statistically significant difference emerged in other frequency bands. **Figure 3** demonstrates the typical functional network under untreated and treated conditions.

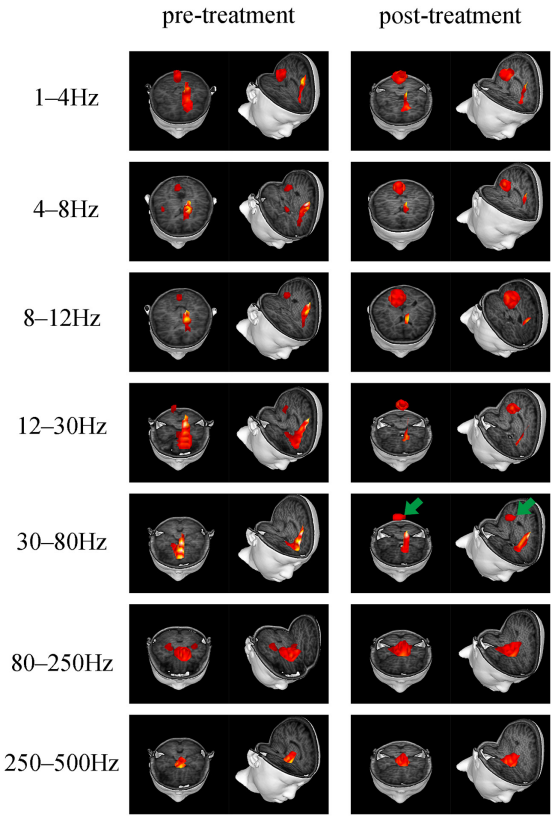

FIGURE 2 | Typical predominant magnetic source locations in the 1–500 Hz frequency range before and after treatment. Activation of the PCC in the 30–80 Hz frequency band increased after treatment, which is indicated by green arrows.

DISCUSSION

Herein, we investigated intrinsic neural activity at the source level from both local and global aspects in CECTS patients prior to and after AEDs treatment, providing novel insights into mechanisms of drug treatment. The results demonstrate that neuromagnetic activity exhibited great differences between the various frequency bands, but relative stability before and after treatment on the same frequency band. Notably, in specific frequency bands, children administered AEDs for 1 year seemed to present with increased neuromagnetic activity in the PCC, increased FC involving the default mode network (DMN), as well as altered distribution of the whole brain network. Moreover, we showed that the cognitive profile of children with CECTS is affected by AEDs, as children have better performance on verbal comprehension and perceptual reasoning post-treatment. Thus, changes in regional neuromagnetic activity and whole-brain functional networks based on analysis of multiple frequency bands have potential significance as an imaging biomarker for clinical drug treatment and cognitive development.

We illustrated how cognitive functions in children with CECTS evolve over 1 year of antiepileptic treatment. After treatment, the children performed significantly better on verbal comprehension and perceptual reasoning, and had stable scores on working memory and processing speed. Thus, our results indicate that AEDs do not cause deterioration of cognitive function among children with BECT, which shows good consistency with previous studies (Tacke et al., 2016; Operto et al., 2019). In addition, according to a report (Garcia-Ramos et al., 2015), without drug intervention, children with CECTS show only mild cognitive improvement over time, and still retain deficits. Therefore, we cautiously infer that the improved cognitive response after 1 year of medication in this study is likely attributable to treatment, and not to the natural course of the disease. This positive cognitive trajectory induced by AEDs has also been observed in other different childhood epilepsies. In mixed samples, the neutral-to-beneficial effects of lamotrigine

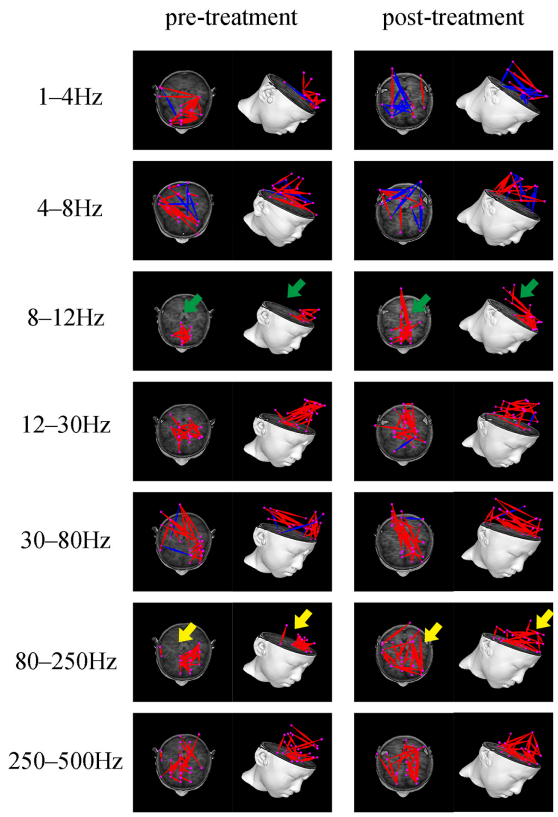

FIGURE 3 | Typical FC networks patterns in the 1–500 Hz frequency range before and after treatment. The FC network patterns before and after treatment are significantly different in the 8–12 and 80–250 Hz frequency bands. The green arrow indicates increased anterior-posterior connection (mainly the connection between the MFC and PCC) after treatment. The yellow arrow indicates a more dispersed whole-brain network distribution pattern after treatment.

TABLE 3 | Predominant source locations before and after treatment.

Frequency band (Hz)	Source location	Pre-treatment	Post-treatment	*p*-value
1–4 Hz	PR	6	4	0.625
	PCC	6	8	0.625
	MFC	13	14	1.000
	MTL	1	0	1.000
	DBA	0	0	–
4–8 Hz	PR	6	4	0.625
	PCC	7	8	1.000
	MFC	14	15	1.000
	MTL	0	0	–
	DBA	0	0	–
8–12 Hz	PR	1	2	1.000
	PCC	7	11	0.219
	MFC	13	9	0.219
	MTL	0	0	–
	DBA	0	0	–
12–30 Hz	PR	0	1	1.000
	PCC	5	10	0.065
	MFC	14	14	1.000
	MTL	1	0	1.000
	DBA	2	1	1.000
30–80 Hz	PR	1	0	1.000
	PCC	2	11	0.004**
	MFC	13	14	1.000
	MTL	4	4	1.000
	DBA	2	1	1.000
80–250 Hz	PR	0	0	–
	PCC	0	0	–
	MFC	10	7	0.508
	MTL	10	11	1.000
	DBA	6	9	0.289
250–500 Hz	PR	0	0	–
	PCC	0	0	–
	MFC	10	9	1.000
	MTL	11	11	1.000
	DBA	7	10	0.250

*PR, peri-Rolandic area; PCC, posterior cingulate cortex; MFC, medial frontal cortex; MTL, medial temporal lobe; DBA, deep brain area. **The p-value was statistically significant after Bonferroni correction.*

on cognition and vigilance of children with epilepsy during long term treatment has been validated (Brodbeck et al., 2006). Furthermore, a study on childhood absence epilepsy also suggests that AEDs likely improve children's neurocognitive functions in attention, fine-motor fluency, and visual memory by reducing seizures (Sirén et al., 2007). Although there are differences with regards to research results based on diverse AEDs (Moavero et al., 2017; Han and Kim, 2018), collectively, these findings question the long-standing view that chronic cognitive deficits in children with epilepsy are largely caused by drugs.

Our neuromagnetic findings reveal the frequency-dependent characteristic of intrinsic neural activity in CECTS, which indicates that the source locations vary with frequency bands, exhibiting obvious differences and regularities, both before and after treatment. In brief, the higher the frequency band, the more concentrated the source locations in the deep brain regions. This further supports the theory that neuromagnetic signals of different frequency bands represent distinct inherent physiological activities (Tenney et al., 2014; Tang et al., 2016; Zhang et al., 2020).

In agreement with fMRI evidence based on amplitude of low frequency fluctuation (Jiang et al., 2020) and functional covariance connectivity (Jiang et al., 2019), our results suggest that AEDs have effects on brain regional activity and functional networks. The analysis of the magnetic source location exhibited that, after treatment, activation of PCC increased in multiple frequency bands, and the differences were evident in the 30–80 Hz frequency band. Interestingly, our exploration of the global brain network also demonstrated changes involving DMN, with increased FC between the MFC and PCC after treatment in the 8–12 Hz frequency band. It is well known that MFC and PCC are core regions in the DMN (Buckner et al., 2008; Buckner and DiNicola, 2019),

which suggests that DMN may be a potential key target for drug therapy.

The brain is a large-scale network which dynamically regulates information interaction between various systems. The DMN is considered to be a fundamental network for maintaining baseline state of the nervous system, which is inhibited during the working state or in response to significant external stimuli, and resumes and remains active during the resting state (Lin et al., 2016). The proper operation of DMN is very important to the maintenance of normal neurophysiological functions, and many neuropsychiatric diseases are thought to be related to abnormal activation pattern of DMN (Greicius et al., 2004; Ibarretxe-Bilbao et al., 2011; Washington et al., 2014). There is now accumulating evidence that abnormal DMN exists among children with BECT (Oser et al., 2014; Ofer et al., 2018) and plays a pivotal role in the occurrence and development of cognitive and behavioral disorders (Gusnard et al., 2001; Oser et al., 2014). Functionally, DMN can be separated into anterior DNM, which is centered around the MFC, and posterior DMN, which is centered on the PCC (Buckner et al., 2008; Raichle, 2015). The execution of different physiological functions depends on the interaction between the sub-networks (Buckner et al., 2008; Buckner and DiNicola, 2019). Herein, children with BECT demonstrated reduced FC between anterior DMN and posterior DMN prior to treatment. It is intriguing that reduced connectivity between PCC and bilateral MFC is consistently demonstrated in CAE, another childhood epilepsy (Luo et al., 2011). Moreover, reduced connectivity between the anterior and posterior areas of the DMN is related to the duration of epilepsy (McGill et al., 2012). The enhanced activation of PCC and increased FC within DMN after treatment are, therefore, likely to reflect repair or compensation of damaged DMN. This is completely consistent with the view of a previous cross-sectional study (Zeng et al., 2015). That is, due to intervention of AEDs, abnormal brain function in the DMN of children with CECTS has been reversed. Additionally, given that PCC and DMN are closely related to cognitive processes such as remembering and making social inferences (Buckner and DiNicola, 2019), we speculated that normalization of DMN after treatment is a basis for cognitive improvement.

Furthermore, our results indicated that in the 80–250 Hz frequency band, compared to the functional network pattern confined to the MFC before treatment, brain networks of the BECT children after 1 year of treatment tend to be more decentralized and involve more brain regions. This may reflect compensation for the integration of high-frequency information. In the future, this specific mechanism needs to be further explored. In addition, although the results of the 1–4 Hz frequency band in this study were not statistically different after multiple corrections, it is worth noting that previous EEG study of temporal lobe epilepsy also showed similar results, that is, slow wave activity reduces after initial AED therapy (Ricci et al., 2021). In focal epilepsy, the enhancement of slow wave activity is considered to be related to the activity of epileptic focus (Pellegrino et al., 2017). Therefore, the reduction in slow frequency can be explained by the effect of AEDs on epileptic activity and cortical excitability, which is a manifestation of the normalization of brain activity (Ricci et al., 2021). We noticed that the alteration of source location and FC occurred in different frequency bands, respectively. This phenomenon can be attributed to the weak statistical power that is caused by a small sample. Another reasonable explanation can be that different types of neural activities and information processing require different frequencies (Cha et al., 1991; Lopes et al., 2003; Palva and Palva, 2018).

Several limitations to our research exist. First, the number of participants who completed the follow-up was less than expected, and the small sample size weakened the statistical power and the generalizability of the conclusions, to some extent. Meanwhile, this study design was not able to compare brain activity between untreated CECTS children and matched healthy controls, so while several previous studies have reported comparative results for this purpose among untreated children and healthy controls (Jiang et al., 2019, 2020; Li et al., 2020b), we still cannot assert that all the cognitive improvements can be attributed to AEDs. Additionally, this study, limited by sample size, did not group the types of AEDs and the prognosis of the children, which can cause mixed effects. Whether different types of AEDs have different effects on neural activity, or whether there are differences in the brain network patterns among children with different outcomes needs to be clarified in future studies.

CONCLUSION

This longitudinal study investigated the effects of long-term use of AEDs on brain activity and cognitive function among children with CECTS. We demonstrated that compensation or normalization of DMN caused by AEDs likely contributes to the improvement of cognition. The dispersed distribution of the whole brain network may be a compensation of AEDs for integration of brain function. The above-mentioned alterations occur in specific frequency bands, which supports the frequency-dependent characteristic of neural activity, and proves the feasibility and effectiveness of MEG technology based on multi-frequency analysis in epilepsy research. Overall, our findings provide novel insights into the effects of AEDs on abnormal brain activity and cognitive deficits among CECTS children.

DATA AVAILABILITY STATEMENT

The original contributions presented in the study are included in the article/supplementary material, further inquiries can be directed to the corresponding author.

ETHICS STATEMENT

The studies involving human participants were reviewed and approved by the Medical Ethics Committee of Nanjing Brain Hospital. Written informed consent to participate in this study was provided by the participants' legal guardian/next of kin. Written informed consent was obtained from the individual(s), and minor(s)' legal guardian/next of kin, for the publication of any potentially identifiable images or data included in this article.

AUTHOR CONTRIBUTIONS

KN, YL, and TZ designed the study. KN, YL, TZ, PW, and QC acquired the raw data. JS, YS, MS, and KZ analyzed the data. KN wrote the manuscript. XW revised the manuscript. All authors read and approved the final submitted manuscript.

FUNDING

This work was supported by the National Natural Science Foundation of China (Grant No. 81471324), General Program of Natural Science Foundation of Jiangsu Province (Grant No. BK20191127), Health Department of Jiangsu Province (Grant No. H2018062), and Medical Health International Cooperation Project of Nanjing Municipal Science and Technology Bureau (Grant No. 201911044).

ACKNOWLEDGMENTS

We would like to thank all the children and families who took an active part in our study. We would also like to thank Xiang Jing for technical assistance, Zheng Hu for recruitment of participants, and the medical staff from Child Mental Health Research Center of Nanjing Brain Hospital for cognitive assessment.

REFERENCES

Bourel-Ponchel, E., Mahmoudzadeh, M., Adebimpe, A., and Wallois, F. (2019). Functional and structural network disorganizations in typical epilepsy with centro-temporal spikes and impact on cognitive neurodevelopment. *Front. Neurol.* 10:809.

Brodbeck, V., Jansen, V., Fietzek, U., Muehe, C., Weber, G., and Heinen, F. (2006). Long-term profile of lamotrigine in 119 children with epilepsy. *Eur. J. Paediatr. Neurol.* 10, 135–141. doi: 10.1016/j.ejpn.2006.05.003

Buckner, R. L., and DiNicola, L. M. (2019). The brain's default network: updated anatomy, physiology and evolving insights. *Nat. Rev. Neurosci.* 20, 593–608. doi: 10.1038/s41583-019-0212-7

Buckner, R. L., Andrews-Hanna, J. R., and Schacter, D. L. (2008). The brain's default network: anatomy, function, and relevance to disease. *Ann. N. Y. Acad. Sci.* 1124, 1–38. doi: 10.1196/annals.1440.011

Burgess, R. C. (2011). Evaluation of brain connectivity: the role of magnetoencephalography. *Epilepsia* 52 Suppl 4, 28–31. doi: 10.1111/j.1528-1167.2011.03148.x

Cha, K., Zatorre, R. J., and Schönwiesner, M. (1991). Frequency selectivity of voxel-by-voxel functional connectivity in human auditory cortex. *Cereb. Cortex (New York, N.Y.)* 26, 211–224. doi: 10.1093/cercor/bhu193

Frauscher, B., Bartolomei, F., Kobayashi, K., Cimbalnik, J., van 't Klooster, M. A., Rampp, S., et al. (2017). High-frequency oscillations: the state of clinical research. *Epilepsia* 58, 1316–1329.

Garcia-Ramos, C., Jackson, D. C., Lin, J. J., Dabbs, K., Jones, J. E., Hsu, D. A., et al. (2015). Cognition and brain development in children with benign epilepsy with centrotemporal spikes. *Epilepsia* 56, 1615–1622.

Gohel, S. R., and Biswal, B. B. (2015). Functional integration between brain regions at rest occurs in multiple-frequency bands. *Brain Connect.* 5, 23–34. doi: 10.1089/brain.2013.0210

Greicius, M. D., Srivastava, G., Reiss, A. L., and Menon, V. (2004). Default-mode network activity distinguishes Alzheimer's disease from healthy aging: evidence from functional MRI. *Proc. Natl. Acad. Sci. U.S.A.* 101, 4637–4642. doi: 10.1073/pnas.0308627101

Guggisberg, A. G., Honma, S. M., Findlay, A. M., Dalal, S. S., Kirsch, H. E., Berger, M. S., et al. (2008). Mapping functional connectivity in patients with brain lesions. *Ann. Neurol.* 63, 193–203.

Gusnard, D. A., Akbudak, E., Shulman, G. L., and Raichle, M. E. (2001). Medial prefrontal cortex and self-referential mental activity: relation to a default mode of brain function. *Proc. Natl. Acad. Sci. U.S.A.* 98, 4259–4264. doi: 10.1073/pnas.071043098

Han, M. J., and Kim, S. J. (2018). Effects of antiepileptic drugs on language abilities in benign epilepsy of childhood with centrotemporal spikes. *J. Clin. Neurol. (Seoul, Korea)* 14, 523–529. doi: 10.3988/jcn.2018.14.4.523

Harmsen, I. E., Rowland, N. C., Wennberg, R. A., and Lozano, A. M. (2018). Characterizing the effects of deep brain stimulation with magnetoencephalography: a review. *Brain Stimul.* 11, 481–491. doi: 10.1016/j.brs.2017.12.016

Heijbel, J., Blom, S., and Bergfors, P. G. (1975). Benign epilepsy of children with centrotemporal EEG foci. A study of incidence rate in outpatient care. *Epilepsia* 16, 657–664. doi: 10.1111/j.1528-1157.1975.tb04748.x

Hughes, J. R. (2010). Benign epilepsy of childhood with centrotemporal spikes (BECTS): to treat or not to treat, that is the question. *Epilepsy Behav.* 19, 197–203. doi: 10.1016/j.yebeh.2010.07.018

Ibarretxe-Bilbao, N., Zarei, M., Junque, C., Marti, M. J., Segura, B., Vendrell, P., et al. (2011). Dysfunctions of cerebral networks precede recognition memory deficits in early Parkinson's disease. *NeuroImage* 57, 589–597. doi: 10.1016/j.neuroimage.2011.04.049

Jiang, S., Luo, C., Huang, Y., Li, Z., Chen, Y., Li, X., et al. (2020). Altered static and dynamic spontaneous neural activity in drug-naïve and drug-receiving benign childhood epilepsy with centrotemporal spikes. *Front. Hum. Neurosci.* 14:361.

Jiang, Y., Song, L., Li, X., Zhang, Y., Chen, Y., Jiang, S., et al. (2019). Dysfunctional white-matter networks in medicated and unmedicated benign epilepsy with centrotemporal spikes. *Hum. Brain Mapp.* 40, 3113–3124.

Jun, Y. H., Eom, T. H., Kim, Y. H., Chung, S. Y., Lee, I. G., and Kim, J. M. (2019). Changes in background electroencephalographic activity in benign childhood epilepsy with centrotemporal spikes after oxcarbazepine treatment: a standardized low-resolution brain electromagnetic tomography (sLORETA) study. *BMC Neurol.* 19:3.

Kikuchi, M., Yoshimura, Y., Mutou, K., and Minabe, Y. (2016). Magnetoencephalography in the study of children with autism spectrum disorder. *Psychiatry Clin. Neurosci.* 70, 74–88. doi: 10.29070/31/58287

Lanzone, J., Boscarino, M., Ricci, L., Insola, A., Tombini, M., Di Lazzaro, V., et al. (2020). The effects of antiepileptic drugs on high-frequency oscillations in somatosensory evoked potentials. *Clin. Neurophysiol.* 131, 1917–1924. doi: 10.1016/j.clinph.2020.05.022

Lanzone, J., Boscarino, M., Ricci, L., Insola, A., Tombini, M., Di Lazzaro, V., et al. (2021a). Effects of the noncompetitive AMPA receptor antagonist perampanel on thalamo-cortical excitability: a study of high-frequency oscillations in somatosensory evoked potentials. *Clin. Neurophysiol.* 132, 1049–1056. doi: 10.1016/j.clinph.2020.12.030

Lanzone, J., Ricci, L., Tombini, M., Boscarino, M., Mecarelli, O., Pulitano, P., et al. (2021b). The effect of Perampanel on EEG spectral power and connectivity in patients with focal epilepsy. *Clin. Neurophysiol.* 132, 2176–2183. doi: 10.1016/j.clinph.2021.05.026

Li, Y., Sun, Y., Niu, K., Wang, P., Xiang, J., Chen, Q., et al. (2020a). The relationship between neuromagnetic activity and cognitive function in benign childhood epilepsy with centrotemporal spikes. *Epilepsy Behav.* 112, 107363. doi: 10.1016/j.yebeh.2020.107363

Li, Y., Sun, Y., Zhang, T., Shi, Q., Sun, J., Xiang, J., et al. (2020b). The relationship between epilepsy and cognitive function in benign childhood epilepsy with centrotemporal spikes. *Brain Behav.* 10:e01854.

Lin, P., Yang, Y., Jovicich, J., De Pisapia, N., Wang, X., Zuo, C. S., et al. (2016). Static and dynamic posterior cingulate cortex nodal topology of default mode network predicts attention task performance. *Brain Imaging Behav.* 10, 212–225. doi: 10.1007/s11682-015-9384-6

Lopes, F., da Silva, W., Blanes, S.N. Kalitzin, Parra, J., Suffczynski, P., and Velis, D. N. (2003). Epilepsies as dynamical diseases of brain systems: basic models of the transition between normal and epileptic activity. *Epilepsia* 44 Suppl 12, 72–83. doi: 10.1111/j.0013-9580.2003.12005.x

Luo, C., Li, Q., Lai, Y., Xia, Y., Qin, Y., Liao, W., et al. (2011). Altered functional connectivity in default mode network in absence epilepsy: a resting-state fMRI study. *Hum. Brain Mapp.* 32, 438–449. doi: 10.1002/hbm.21034

McGill, M. L., Devinsky, O., Kelly, C., Milham, M., Castellanos, F. X., Quinn, B. T., et al. (2012). Default mode network abnormalities in idiopathic generalized epilepsy. *Epilepsy Behav.* 23, 353–359. doi: 10.1016/j.yebeh.2012.01.013

McGinnity, C. J., Smith, A. B., Yaakub, S. N., Weidenbach Gerbase, S., Gammerman, A., Tyson, A. L., et al. (2017). Decreased functional connectivity within a language subnetwork in benign epilepsy with centrotemporal spikes. *Epilepsia Open* 2, 214–225. doi: 10.1002/epi4.12051

Mellish, L. C., Dunkley, C., Ferrie, C. D., and Pal, D. K. (2015). Antiepileptic drug treatment of rolandic epilepsy and Panayiotopoulos syndrome: clinical practice survey and clinical trial feasibility. *Arch. Dis. Child.* 100, 62–67.

Moavero, R., Santarone, M. E., Galasso, C., and Curatolo, P. (2017). Cognitive and behavioral effects of new antiepileptic drugs in pediatric epilepsy. *Brain Dev.* 39, 464–469.

Ofer, I., Jacobs, J., Jaiser, N., Akin, B., Hennig, J., Schulze-Bonhage, A., et al. (2018). Cognitive and behavioral comorbidities in Rolandic epilepsy and their relation with default mode network's functional connectivity and organization. *Epilepsy Behav.* 78, 179–186.

Operto, F. F., Pastorino, G. M. G., Mazza, R., Roccella, M., Carotenuto, M., Margari, L., et al. (2019). Cognitive profile in BECTS treated with levetiracetam: A 2-year follow-up. *Epilepsy Behav.* 97, 187–191.

Oser, N., Hubacher, M., Specht, K., Datta, A. N., Weber, P., and Penner, I. K. (2014). Default mode network alterations during language task performance in children with benign epilepsy with centrotemporal spikes (BECTS). *Epilepsy Behav.* 33, 12–17. doi: 10.1016/j.yebeh.2014.01.008

Palva, J. M., and Palva, S. (2018). Functional integration across oscillation frequencies by cross-frequency phase synchronization. *Eur. J. Neurosci.* 48, 2399–2406.

Panayiotopoulos, C. P., Michael, M., Sanders, S., Valeta, T., and Koutroumanidis, M. (2008). Benign childhood focal epilepsies: assessment of established and newly recognized syndromes. *Brain A J. Neurol.* 131, 2264–2286.

Pellegrino, G., Tombini, M., Curcio, G., Campana, C., Di Pino, G., Assenza, G., et al. (2017). Slow activity in focal epilepsy during sleep and wakefulness. *Clin. EEG Neurosci.* 48, 200–208. doi: 10.1177/1550059416652055

Raichle, M. E. (2015). The brain's default mode network. *Ann. Rev. Neurosci.* 38, 433–447. doi: 10.1146/annurev-neuro-071013-014030

Ricci, L., Assenza, G., Pulitano, P., Simonelli, V., Vollero, L., Lanzone, J., et al. (2021). Measuring the effects of first antiepileptic medication in temporal lobe epilepsy: predictive value of quantitative-EEG analysis. *Clin. Neurophysiol.* 132, 25–35. doi: 10.1016/j.clinph.2020.10.020

Scheffer, I. E., Berkovic, S., Capovilla, G., Connolly, M. B., French, J., Guilhoto, L., et al. (2017). ILAE classification of the epilepsies: position paper of the ILAE Commission for classification and terminology. *Epilepsia* 58, 512–521. doi: 10.1111/epi.13709

Sirén, A., Kylliäinen, A., Tenhunen, M., Hirvonen, K., Riita, T., and Koivikko, M. (2007). Beneficial effects of antiepileptic medication on absence seizures and cognitive functioning in children. *Epilepsy Behav.* 11, 85–91. doi: 10.1016/j.yebeh.2007.04.009

Tacke, M., Gerstl, L., Heinen, F., Heukaeufer, I., Bonfert, M., Bast, T., et al. (2016). Effect of anticonvulsive treatment on neuropsychological performance in children with BECTS. *Eur. J. Paediatric Neurol.* 20, 874–879.

Tang, L., Xiang, J., Huang, S., Miao, A., Ge, H., Liu, H., et al. (2016). Neuromagnetic high-frequency oscillations correlate with seizure severity in absence epilepsy. *Clin. Neurophysiol.* 127, 1120–1129.

Tenney, J. R., Fujiwara, H., Horn, P. S., Vannest, J., Xiang, J., Glauser, T. A., et al. (2014). Low- and high-frequency oscillations reveal distinct absence seizure networks. *Ann. Neurol.* 76, 558–567. doi: 10.1002/ana.24231

van Klink, N. E., van 't Klooster, M. A., Leijten, F. S., Jacobs, J., Braun, K. P., and Zijlmans, M. (2016). Ripples on rolandic spikes: a marker of epilepsy severity. *Epilepsia* 57, 1179–1189. doi: 10.1111/epi.13423

Wang, Z., Zhang, Z., Liao, W., Xu, Q., Zhang, J., Lu, W., et al. (2014). Frequency-dependent amplitude alterations of resting-state spontaneous fluctuations in idiopathic generalized epilepsy. *Epilepsy Res.* 108, 853–860. doi: 10.1016/j.eplepsyres.2014.03.003

Washington, S. D., Gordon, E. M., Brar, J., Warburton, S., Sawyer, A. T., Wolfe, A., et al. (2014). Dysmaturation of the default mode network in autism. *Hum. Brain Mapp.* 35, 1284–1296. doi: 10.1002/hbm.22252

Wickens, S., Bowden, S. C., and D'Souza, W. (2017). Cognitive functioning in children with self-limited epilepsy with centrotemporal spikes: a systematic review and meta-analysis. *Epilepsia* 58, 1673–1685. doi: 10.1111/epi.13865

Xiang, J., Korman, A., Samarasinghe, K. M., Wang, X., Zhang, F., Qiao, H., et al. (2015a). Volumetric imaging of brain activity with spatial-frequency decoding of neuromagnetic signals. *J. Neurosci. Methods* 239, 114–128.

Xiang, J., Luo, Q., Kotecha, R., Korman, A., Zhang, F., Luo, H., et al. (2014). Accumulated source imaging of brain activity with both low and high-frequency neuromagnetic signals. *Front. Neuroinform.* 8:57. doi: 10.3389/fninf.2014.00057

Xiang, J., Tenney, J. R., Korman, A. M., Leiken, K., Rose, D. F., Harris, E., et al. (2015b). Quantification of interictal neuromagnetic activity in absence epilepsy with accumulated source imaging. *Brain Topogr.* 28, 904–914.

Zeng, H., Ramos, C. G., Nair, V. A., Hu, Y., Liao, J., La, C., et al. (2015). Regional homogeneity (ReHo) changes in new onset versus chronic benign epilepsy of childhood with centrotemporal spikes (BECTS): a resting state fMRI study. *Epilepsy Res.* 116, 79–85. doi: 10.1016/j.eplepsyres.2015.06.017

Zhang, Q., Yang, F., Hu, Z., Xu, Q., Bernhardt, B. C., Quan, W., et al. (2018). Antiepileptic drug of levetiracetam decreases centrotemporal spike-associated activation in rolandic epilepsy. *Front. Neurosci.* 12:796. doi: 10.3389/fnins.2018.00796

Zhang, Q., Yang, F., Hu, Z., Zhang, Z., Xu, Q., Dante, M., et al. (2017). Resting-state fMRI revealed different brain activities responding to valproic acid and levetiracetam in benign epilepsy with central-temporal spikes. *Eur. Radiol.* 27, 2137–2145. doi: 10.1007/s00330-016-4531-z

Zhang, T., Shi, Q., Li, Y., Gao, Y., Sun, J., Miao, A., et al. (2020). Frequency-dependent interictal neuromagnetic activities in children with benign epilepsy with centrotemporal spikes: a magnetoencephalography (MEG) study. *Front. Hum. Neurosci.* 14:264. doi: 10.3389/fnhum.2020.00264

Conflict of Interest: The authors declare that the research was conducted in the absence of any commercial or financial relationships that could be construed as a potential conflict of interest.

Publisher's Note: All claims expressed in this article are solely those of the authors and do not necessarily represent those of their affiliated organizations, or those of the publisher, the editors and the reviewers. Any product that may be evaluated in this article, or claim that may be made by its manufacturer, is not guaranteed or endorsed by the publisher.

frontiers in Human Neuroscience

ORIGINAL RESEARCH
published: 16 December 2021
doi: 10.3389/fnhum.2021.778807

Changes in the Shape and Volume of Subcortical Structures in Patients With End-Stage Renal Disease

Wen Gu[1], Ronghua He[2], Hang Su[2], Zhuanqin Ren[2], Lei Zhang[1,3], Huijie Yuan[1], Ming Zhang[1] and Shaohui Ma[1]**

[1] Department of Medical Imaging, The First Affiliated Hospital of Xi'an Jiaotong University, Xi'an, China, [2] Department of Radiology, Baoji Center Hospital, Baoji, China, [3] Department of Radiology, Baoji High-Tech Hospital, Baoji, China

OPEN ACCESS

Edited by:
Jurong Ding,
Sichuan University of Science and Engineering, China

Reviewed by:
Shigeki Hirano,
Chiba University, Japan
Bochao Cheng,
Sichuan University, China
Qiang Xu,
Nanjing University, China

***Correspondence:**
Ming Zhang
zhangming01@xjtu.edu.cn
Shaohui Ma
shh_ma@xjtu.edu.cn

Specialty section:
This article was submitted to Brain Imaging and Stimulation, a section of the journal Frontiers in Human Neuroscience

Received: 17 September 2021
Accepted: 15 November 2021
Published: 16 December 2021

Citation:
Gu W, He R, Su H, Ren Z, Zhang L, Yuan H, Zhang M and Ma S (2021) Changes in the Shape and Volume of Subcortical Structures in Patients With End-Stage Renal Disease. Front. Hum. Neurosci. 15:778807. doi: 10.3389/fnhum.2021.778807

Introduction: End-stage renal disease (ESRD) typically causes changes in brain structure, and patients with ESRD often experience cognitive and sleep disorders. We aimed to assess the changes in the subcortical structure of patients with ESRD and how they are associated with cognitive and sleep disorders.

Methods: We involved 36 adult patients for maintenance hemodialysis and 35 age- and gender-matched control individuals. All participants underwent neuropsychological examination and 3T magnetic resonance imaging (MRI) to acquire T1 anatomical images. The laboratory blood tests were performed in all patients with ESRD close to the time of the MR examination. We used volumetric and vertex-wise shape analysis approaches to investigate the volumes of 14 subcortical structural (e.g., bilateral accumbens, amygdala, hippocampus, caudate, globus pallidus, putamen, and thalamus) abnormalities in the two groups. Analyses of partial correlations and shape correlations were performed in order to identify the associations between subcortical structure, cognition, and sleep quality in patients with ESRD.

Results: The volumetric analysis showed that compared with the healthy control group, patients with ESRD had less bilateral thalamus (left: $p < 0.001$; right: $p < 0.001$), bilateral accumbens (left: $p < 0.001$; right: $p = 0.001$), and right amygdala ($p = 0.002$) volumes. In the vertex-wise shape analysis, patients with ESRD had abnormal regional surface atrophy in the bilateral thalamus, right accumbens, left putamen, and bilateral caudate. Moreover, the Montreal Cognitive Assessment (MoCA) score was associated with volume reduction in the bilateral thalamus (left: Spearman $\rho = 0.427$, $p = 0.009$; right: $\rho = 0.319$, $p = 0.018$), and the Pittsburgh Sleep Quality Index (PSQI) score was associated with volume reduction in the bilateral accumbens (left: $\rho = -0.546$, $p = 0.001$; right: $\rho = -0.544$, $p = 0.001$). In vertex-wise shape correlation analysis, there was a positive significant correlation between regional shape deformations on the bilateral thalamus and MoCA score in patients with ESRD.

Conclusion: Our study suggested that patients with ESRD have subcortical structural atrophy, which is related to impaired cognitive performance and sleep disturbances. These findings may help to further understand the underlying neural mechanisms of brain changes in patients with ESRD.

Keywords: end-stage renal disease, magnetic resonance imaging, subcortical, shape analysis, volumetric analysis

INTRODUCTION

End-stage renal disease (ESRD), also known as uremia, is defined by a glomerular filtration rate of <15 ml/min/1.73 m^2 (with the persistence of <10% renal function) or the development of chronic kidney disease (CKD) to stage 5 (Meyer and Hostetter, 2007; Jha et al., 2013). Patients with uremia require dialysis to maintain kidney function (Himmelfarb and Ikizler, 2010). Although hemodialysis and peritoneal dialysis can significantly prolong the survival of patients with ESRD, dialysis does not resolve complications experienced by patients with ESRD (Mettang and Kremer, 2015), which seriously affects the quality of life of patients (Zhang et al., 2012).

Patients with ESRD often have varying degrees of brain damage. According to the kidney–brain axis and cross-talk theory, both structural and functional changes are observed in the brain of patients with ESRD (Bugnicourt et al., 2013; Lu et al., 2015). The underlying pathophysiology of comorbid neurological diseases in patients with ESRD is related to the shared anatomical and vascular regulation systems and the bidirectional pathways of humoral and non-humoral systems that influence the kidneys and the brain. Therefore, different degrees of subcortical structural volume abnormalities are often observed in patients with ESRD. Although studies investigating these alterations have been conducted, results are inconsistent (Zhang et al., 2013; Chang et al., 2017; Jin et al., 2020). Recently, subcortical structural atrophy was reported in patients with ESRD who had been treated using hemodialysis (Prohovnik et al., 2007; Chiu et al., 2019). However, the effect of subcortical structural abnormalities on cognition and sleep in patients with ESRD remains unknown. Cognitive control deficits and sleep disturbance are common symptoms experienced by patients with ESRD (Scherer et al., 2017; Drew et al., 2019). Data have shown that the incidences of insomnia in patients undergoing maintenance hemodialysis and peritoneal dialysis are 79 and 73%, respectively, whereas the incidence of insomnia in the general population is only 12% (Hui et al., 2000, 2002). Moreover, approximately 60% of patients with ESRD have cognitive dysfunction (Kalirao et al., 2011). Various subcortical structural abnormalities have been reported in patients with cognitive impairment (Chang et al., 2017; Chiu et al., 2019) and insomnia (Alperin et al., 2019; Li et al., 2019). In fact, the kidney–brain axis and cross-talk theory suggested that subcortical structural volume abnormalities contribute to impaired sleep and cognition in patients with ESRD (Lu et al., 2015; Miranda et al., 2017).

Numerous methods can be used to study the volume and morphology of subcortical structures, which include, but are not limited to, vertex-wise analysis and voxel-based morphometry (VBM). Among these methods, vertex-wise shape analysis is a fully automated segmentation method that can provide the location and pattern of shape changes in subcortical structures. Furthermore, this method has advantages in detecting morphological changes of subcortical structures and is not dependent on tissue classification methods or arbitrary smoothing. Therefore, it can precisely locate the regional atrophy of the subcortical structure and detect the structural changes (Patenaude et al., 2011). At present, shape analysis is a precise approach for exploring atrophy-related lesions. It is used widely in the investigations of neurological diseases, such as Parkinson's disease (PD) (Nemmi et al., 2015), temporal lobe epilepsy (TLE) (Weng et al., 2020), chronic insomnia disorder (Gong et al., 2019), and Alzheimer's disease (AD) (de Jong et al., 2008). To date, only few studies have applied these methods to investigate subcortical structures in patients with ESRD.

In this study, we used vertex-wise shape analysis to compare the shape changes of subcortical structures between patients with ESRD and matched healthy controls (HCs). In addition, we also measured the volumes of the 14 subfields of the subcortical structure to compare the two groups. Analyses of partial correlations and shape correlations were then performed in order to detect associations between subcortical structural volume and neuropsychology in patients with ESRD.

MATERIALS AND METHODS

Participants

The study was approved by the Ethics Committee of the First Affiliated Hospital of Xi'an Jiaotong University. After receiving a full explanation of the study, all participants provided an informed consent before participation.

In this study, we involved 36 patients with ESRD (26 males, 10 females; age range 25–65 years; mean age 43.64 years), and 35 healthy age- and gender-matched right-handed HCs (20 males, 15 females; age range 20–64 years; mean age 43.60 years), who underwent neuropsychological and magnetic resonance imaging (MRI) examinations, and laboratory blood tests were performed before single hemodialysis within 24 h. The underlying cause of all ESRD in patients was glomerulonephritis. The diagnosis of ESRD was based on serum creatinine levels (Stevens and Levin, 2013).

Inclusion criteria for the ESRD group were as follows: (a) age >18 years; (b) confirmed clinical diagnosis of ESRD (estimated glomerular filtration rate <15 ml/min/1.73 m^2); and (c) on maintenance hemodialysis for more than 3 months.

Exclusion criteria for the ESRD group were as follows: (a) kidney transplantation; (b) history of drug or alcohol abuse; (c) severe neurological disease, psychiatric disorder (other than cognitive impairment), or organic brain disease (e.g., brain tumor and stroke); (d) severe complications, such as advanced liver, infections, and heart failure; (e) diabetic nephropathy or primary hypertensive nephropathy; (f) history of neurodegenerative disease (e.g., PD or AD); and (g) MRI examination contraindications (e.g., cardiac pacemaker implants or claustrophobia).

Neuropsychological Assessments

The Pittsburgh Sleep Quality Index (PSQI) was used to evaluate sleep quality in the ESRD group (Buysse et al., 1989; Backhaus et al., 2002). The Montreal Cognitive Assessment (MoCA) was employed to evaluate cognitive function (Nasreddine et al., 2005). All neuropsychological assessments were carried out 1 h before MRI scanning was performed.

Laboratory Blood Tests

Laboratory blood tests of patients with ESRD have included serum creatinine, serum blood urea nitrogen, cystatin-C, hemoglobin, and hematocrit. All laboratory variables were obtained close to the time of MR imaging. All blood samples were collected in the same laboratory using the same method. Blood samples were not collected from the HC group.

Image Acquisition

All MRI structural images were acquired using a 3.0-Tesla MRI scanner (GE Discovery MR750w Healthcare, Milwaukee, WI, United States) equipped with an eight-channel phased-array coil. High-resolution T1-weighted scans of the whole brain were acquired for each participant using a 3D BRAVO (brain volume) pulse sequence with the following parameters: repetition time 8.2 ms, echo time 3.1 ms, 12° flip angle, 256 × 256 matrix resolution (voxel size: 1 mm × 1 mm × 1 mm), and 140 contiguous slices. Scans were used to conduct shape analysis of the subcortical structures. The conventional T2-weighted imaging and fluid-attenuated inversion recovery sequences were obtained in our study design to exclude severe neurological disease, psychiatric disorder, or organic brain diseases.

Image Preprocessing

Segmentation of all subcortical structure and volume calculations were performed using FreeSurfer Version 6.0 (Fischl, 2012). Preprocessing of the imaging data mainly included the following steps: motion correction and intensity normalization (Reuter et al., 2010); labeling the volumes of each segmentation (Fischl et al., 2002); and removal of non-brain tissue using skull-stripping (Ségonne et al., 2004). We then applied the Bayesian algorithm to measure subcortical structural volume and Talairach registration (Fischl et al., 2004). Finally, manual quality checks were performed on the data by trained researchers.

Furthermore, we also used estimated total intracranial volume (eTIV) of all the subjects as a covariate in the subsequent analysis, which was calculated using SIENAX (Smith et al., 2004), a part of the FMRIB Software Library (FSL version 6.0.3[1]; Oxford University, Oxford, United Kingdom) (Jenkinson et al., 2012).

FMRIB's Integrated Registration and Segmentation Tool (FIRST) (Patenaude et al., 2011) is a model-based segmentation and registration module contained in FSL (Jenkinson et al., 2012). The shape and appearance of the subcortical structures used in this method were established from 336 manually labeled brain images provided by the Center for Morphometric Analysis, Massachusetts General Hospital, Boston. FIRST uses a deformable mesh model to create a surface mesh that consists of a set of triangles for each subcortical structure, and the vertices of adjacent triangles are called vertices. Therefore, this approach, which is based on a Bayesian framework model, was used to process the data. Briefly, images were registered to Montreal Neurological Institute 152 space; all subcortical structures were constructed subcortical structures were automatically segmented; and the quality of segmentation was manually checked for every participant. Then, the outcome file output from FIRST was used for the vertex analysis.

Statistical Analysis

Statistical analysis was performed using IBM SPSS Statistics (version 26.0 IBM Corp., Armonk, NY, United States). A two-sample *t*-test was used to compare various demographic data between the ESRD and HC groups, and a Mann–Whitney *U* test was used for non-normally distributed data. The Chi-squared test was used to analyze gender differences between the two groups. In addition, we used the Kolmogorov–Smirnov test to evaluate normality and Levene's test to determine the equality of variances.

An analysis of covariance (ANCOVA) was used to estimate group differences in subcortical structural volume, with age, gender, and eTIV as covariates. Partial eta squared was a proportion of variance accounted for by effect, and we also calculated their values (Chen et al., 2017). Pearson correlations were performed to examine the relationships between the results of neuropsychological test and laboratory blood test and subcortical structure volume in the ESRD group, and the Spearman correlations were used for non-normally distributed data. Partial Pearson correlations were performed to examine the relationships between the results of neuropsychological test and laboratory blood test and subcortical structure volume in the ESRD group after controlling for the effects of age, gender, and eTIV, and partial Spearman correlation coefficients (ρ) were used for non-normally distributed data. Bonferroni correction was performed for the results of ANCOVA [$p < 0.004$ (0.05/14) was considered statistically significant] and correlation analysis [$p < 0.025$ (0.05/2) was considered statistically significant].

A permutation-based non-parametric analysis of subcortical shape data and general linear models comprise age and gender as covariates (Winkler et al., 2014). Results were corrected for multiple comparisons using threshold-free cluster enhancement and FWE methods ($p < 0.05$) (Smith and Nichols, 2009).

[1]https://fsl.fmrib.ox.ac.uk/

TABLE 1 | Demographic and clinical characteristics of participants.

Variables	ESRD (n = 36)	HC (n = 35)	p-Value	Comparison
Age (years)	43.64 (11.37)	43.60 (12.35)	0.989[a]	NS
Gender (male/female)	26/10	20/16	0.184[b]	NS
Education (years)	10.78 (2.55)	11.63 (1.89)	0.115[a]	NS
Dialysis duration (months)	27.89 (26.11)			
Laboratory blood tests				
Blood urea nitrogen				
(mmol/L)	22.81 (8.80)			
Creatinine (μmol/L)	800.33 (250.99)			
Cystatin-C (mg/L)	5.00 (1.58)			
Hemoglobin (g/L)	94.53 (19.44)			
Hematocrit	27.95 (9.00)[d]			
Psychometric				
MoCA (scores)	25.00 (6.00)[d]	28.00 (1.00)[d]	<0.001[c]	HC > ESRD
PSQI (scores)	7.50 (4.00)[d]	4.00 (2.00)[d]	<0.001[c]	HC < ESRD

PSQI, Pittsburgh Sleep Quality Index; MoCA, Montreal Cognitive Assessment; NS, not significant; ESRD, end-stage renal disease; HC, healthy controls; SD, standard deviation; IQR, interquartile range.
Data are shown as means (SDs).
[a] *Independent-samples t-test was used for data analysis.*
[b] χ^2 *test was used for data analysis.*
[c] *Mann–Whitney U test was used for data analysis.*
[d] *Medians (IQRs).*

RESULTS

Demographic, Clinical, and Neuropsychological Data

The MoCA and PSQI scores were non-normally distributed data. Demographic information and clinical characteristics of participants are summarized in **Table 1**. There were no significant differences in age (p = 0.989), gender (p = 0.184), or education (p = 0.115) between patients with ESRD and HCs. Patients with ESRD had significantly lower MoCA scores ($p < 0.001$) and had higher PSQI scores ($p < 0.001$) compared with HCs.

Subcortical Volume Analyses

After Bonferroni correction, subcortical volumes are significantly different between the ESRD and HC groups in the bilateral thalamus (left: $F = 31.479$, $p < 0.001$; right: $F = 22.820$, $p < 0.001$), bilateral accumbens (left: $F = 15.321$, $p < 0.001$; right: $F = 13.148$, $p = 0.001$), and right amygdala ($F = 9.924$, $p = 0.002$), as shown in **Table 2**. Compared with the HC group, the ESRD group had greater volume atrophy in the bilateral thalamus, bilateral accumbens, and right amygdala (**Figure 1**).

Subcortical Shape Analyses

Comparisons of the vertex-wise shape of subcortical structures between patients with ESRD and HCs are shown in **Figure 2**. Significantly different subcortical structures are shown in a three-dimensional model: the blue models represent the subcortical structures and the orange layers represent regions with significant differences. Automated subcortical structure vertex-wise analysis revealed significant subcortical volumetric reductions in patients with ESRD in the bilateral thalamus, right accumbens, left putamen, and bilateral caudate. However, in contrast to the results of the subcortical volume analysis, there were no significant differences between groups in the left accumbens and the right amygdala.

Correlation Analyses

In the ESRD group, there was a significant correlation between the bilateral thalamus volume and MoCA score (left: Spearman $\rho = 0.427$, $p = 0.009$; right: $\rho = 0.391$, $p = 0.018$; **Figure 3**) by correlation analyses after adjustment for age, gender, and eTIV. Similarly, there was also a significant negative correlation between the bilateral accumbens volume and PSQI score after adjustment for age, gender, and eTIV (left: $\rho = -0.546$,

TABLE 2 | Results of subcortical volumes group comparisons.

	ESRDMean volumes (SD) (mm^3)	HCMean volumes (SD) (mm^3)	F	Partial eta squared	p-Value
Left thalamus	**7135.78 (595.41)**	**7719.50 (732.23)**	**31.479**	**0.323**	**<0.001**
Left caudate	3652.33 (420.38)	3596.26 (336.63)	0.074	0.001	0.787
Left putamen	4960.81 (428.24)	5117.30 (420.89)	6.002	0.083	0.017
Left globus pallidus	1825.13 (188.20)	1857.63 (130.90)	4.019	0.049	0.057
Left hippocampus	3936.08 (337.32)	4106.19 (353.27)	8.554	0.115	0.005
Left amygdala	1676.83 (219.50)	1731.37 (222.25)	2.575	0.038	0.113
Left accumbens	**478.63 (98.61)**	**549.65 (79.19)**	**15.321**	**0.188**	**<0.001**
Right thalamus	**6940.78 (534.16)**	**7180.01 (618.19)**	**22.820**	**0.257**	**<0.001**
Right caudate	3788.63 (533.11)	3678.91 (349.31)	0.388	0.006	0.536
Right putamen	4993.29 (472.63)	5113.54 (476.52)	3.059	0.044	0.085
Right globus pallidus	1816.54 (230.91)	1858.42 (154.08)	2.870	0.042	0.095
Right hippocampus	4186.49 (300.52)	4327.37 (383.52)	4.151	0.046	0.059
Right amygdala	**1797.43 (195.44)**	**1926.83 (283.57)**	**9.924**	**0.131**	**0.002**
Right accumbens	**477.57 (70.72)**	**530.40 (72.61)**	**13.148**	**0.166**	**0.001**

eTIV, estimated total intracranial volume.
Bold figures represent significant volumetric reductions after adjustment for age, gender, and eTIV. Threshold for significance $\alpha = 0.004$ (0.05/14) after Bonferroni correction.

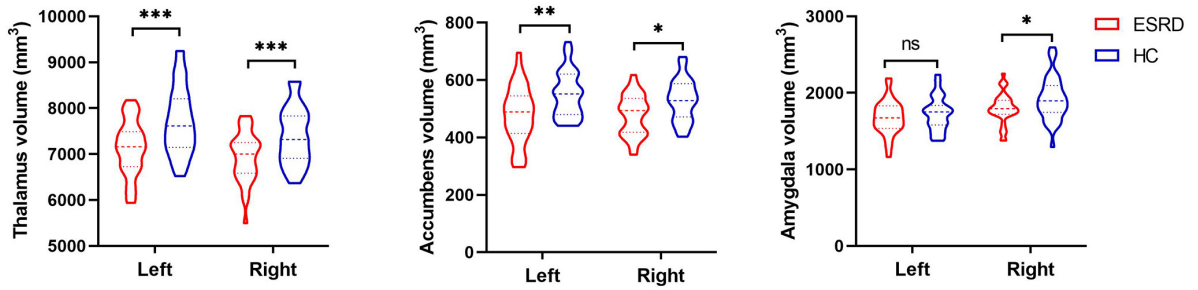

FIGURE 1 | The violin plot depicts significantly different subcortical structural volumes between patients with end-stage renal disease (ESRD) and healthy controls (HCs), which included the bilateral thalamus, bilateral accumbens, and right amygdala, after adjustment for age, gender, and estimated total intracranial volume. Red color represents patients with ESRD, and blue color represents HCs. Inner violin plot shows the quartile and the median. *Significance after Bonferroni correction. *$p < 0.05/14$, **$p < 0.01/14$, ***$p < 0.001/14$; ns, not significant.

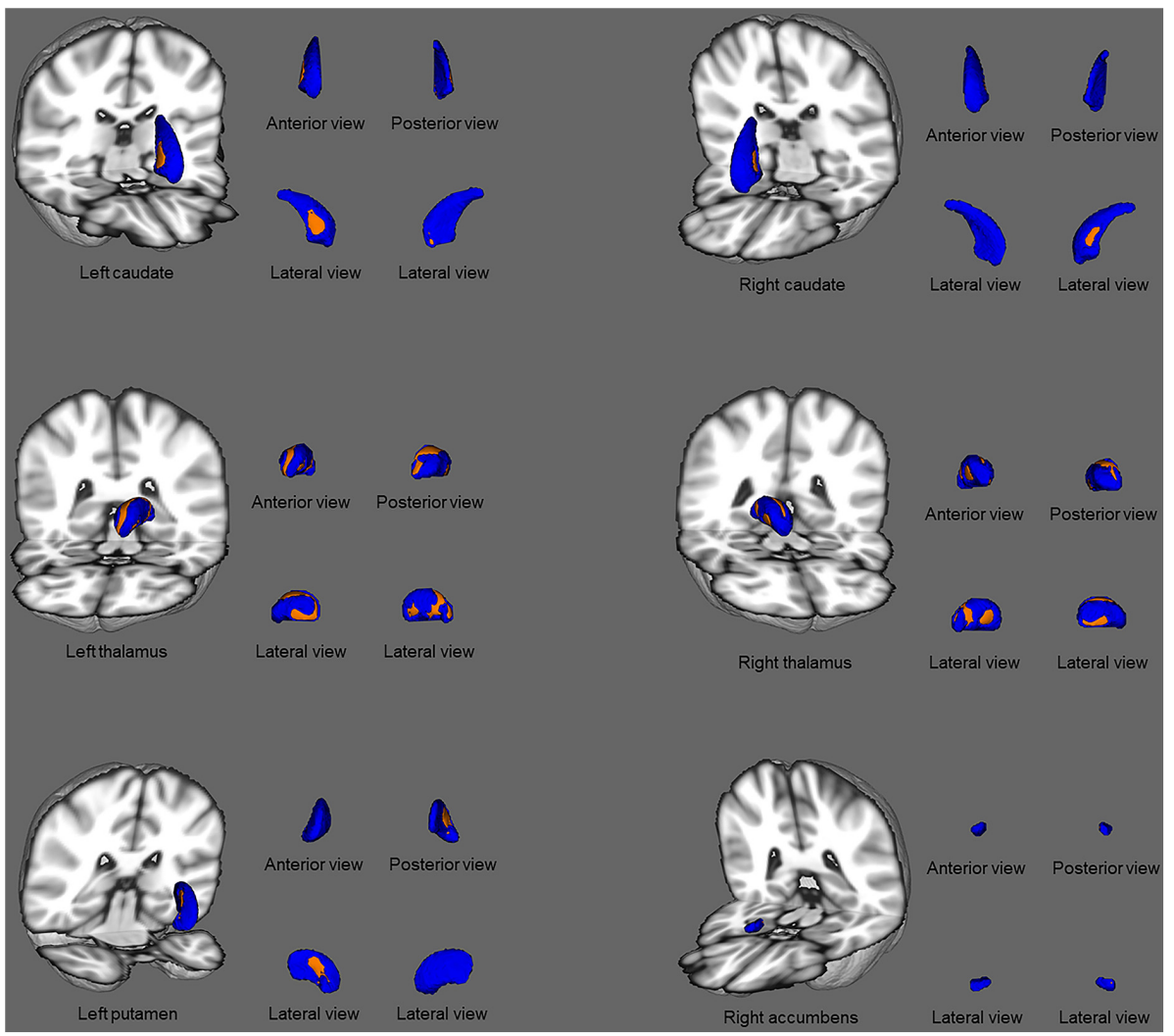

FIGURE 2 | Subcortical structural shape differences between the ESRD group and healthy controls using vertex-wise surface analyses. Subcortical surface alterations were observed in the bilateral thalamus, right accumbens, left putamen, and bilateral caudate, after adjustment for age and gender. The blue models indicate the three-dimensional subcortical structure mesh, and the orange layers represent the significant reductions. Results were corrected for multiple comparisons using threshold-free cluster enhancement and family-wise error methods ($p < 0.05$).

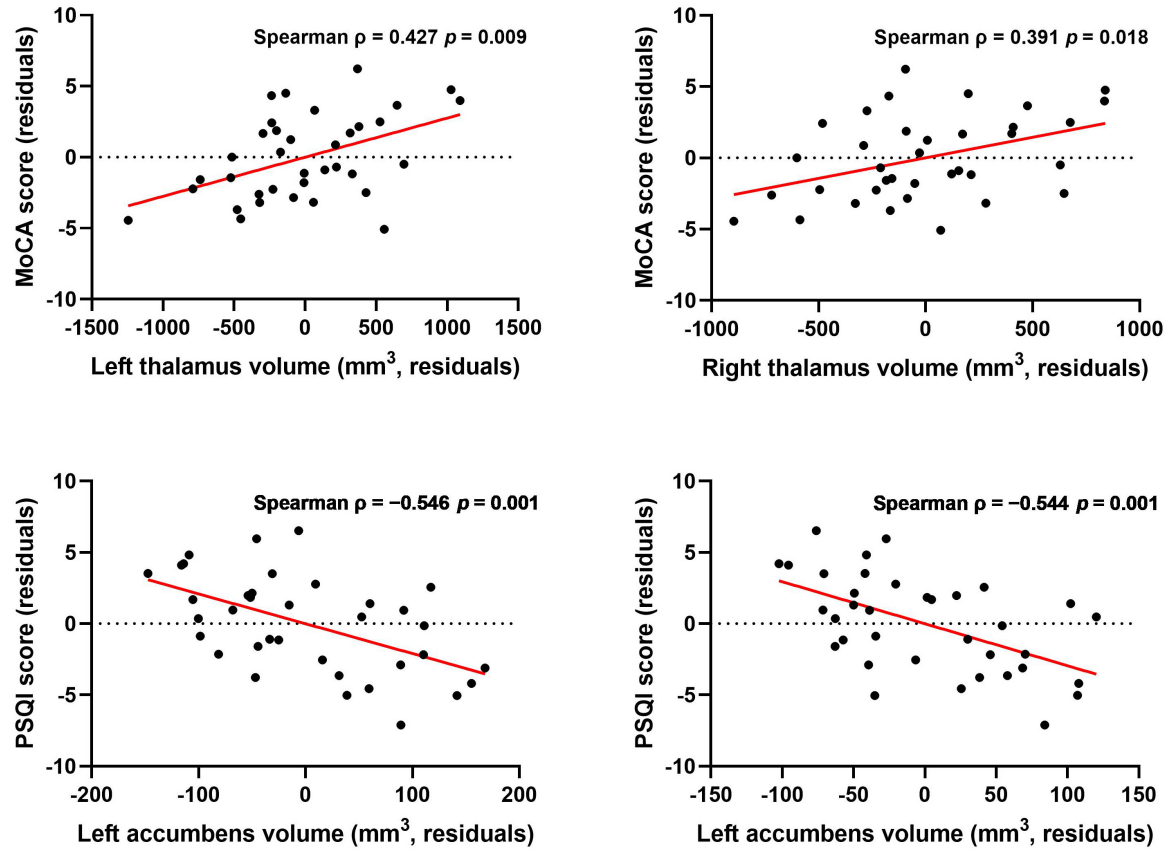

FIGURE 3 | Association between subcortical structure volume and MoCA and PSQI scores after controlling for age, gender, and eTIV. Thalamus volume was correlated with MoCA score, and accumbens volume was correlated with PSQI score after controlling for age, gender, and eTIV [$p < 0.025$ (0.05/2) was considered statistically significant after Bonferroni correction].

p = 0.001; right: ρ = −0.544, p = 0.001; **Figure 3**). In addition, there was a significant correlation between the left thalamus volume and serum creatinine after adjustment for age, gender, and eTIV (r = −0.518, p = 0.002). Moreover, there were no significant correlations between right amygdala volume and neuropsychological scores (i.e., PSQI or MoCA scores) after adjustment for age, gender, and eTIV. There was no correlation between the dialysis duration and the bilateral thalamus or bilateral accumbens volume after adjustment for age, gender, and eTIV.

In shape analysis correlations, there was a significant positive correlation between regional shape deformation on the ventral and dorsal sides of the bilateral thalamus and MoCA score in patients with ESRD after adjustment for age and gender (**Figure 4**). However, there were no correlations of PSQI score with regional shape deformation on the bilateral accumbens in patients with ESRD after adjustment for age and gender.

DISCUSSION

In this study, we investigated the relationship between changes in subcortical structural volume and cognitive and sleep symptoms in patients with ESRD using automated volumetric and vertex-wise shape analyses. We found atrophy of various subcortical structures in patients with ESRD, particularly the thalamus and accumbens. Moreover, in patients, cognition was associated with thalamic volume, and sleep quality had a trend relationship with accumbens volume. In addition, our results highlighted the impact that the changes in subcortical structures have on cognition and sleep of patients. Furthermore, shape analysis and volumetric analysis play a role in cross-validation, which can be used to study the changes of subcortical structures in patients with ESRD.

Abnormalities of subcortical structures have been reported previously in patients with ESRD, irrespective of dialysis status. Our study showed that patients with ESRD undergoing dialysis have atrophy of the bilateral thalamus, bilateral accumbens, and right amygdala. A recent study found the reduced volume of all subcortical structures in patients undergoing dialysis, including the thalamus, accumbens, and amygdala (Chiu et al., 2019). The study used the same processing software (FreeSurfer) to analyze the volume of the subcortical structure. Similarly, a previous study reported that patients with ESRD had reduced volume in the bilateral amygdala (Li A. et al., 2018). In addition, previous studies reported hippocampal volume atrophy

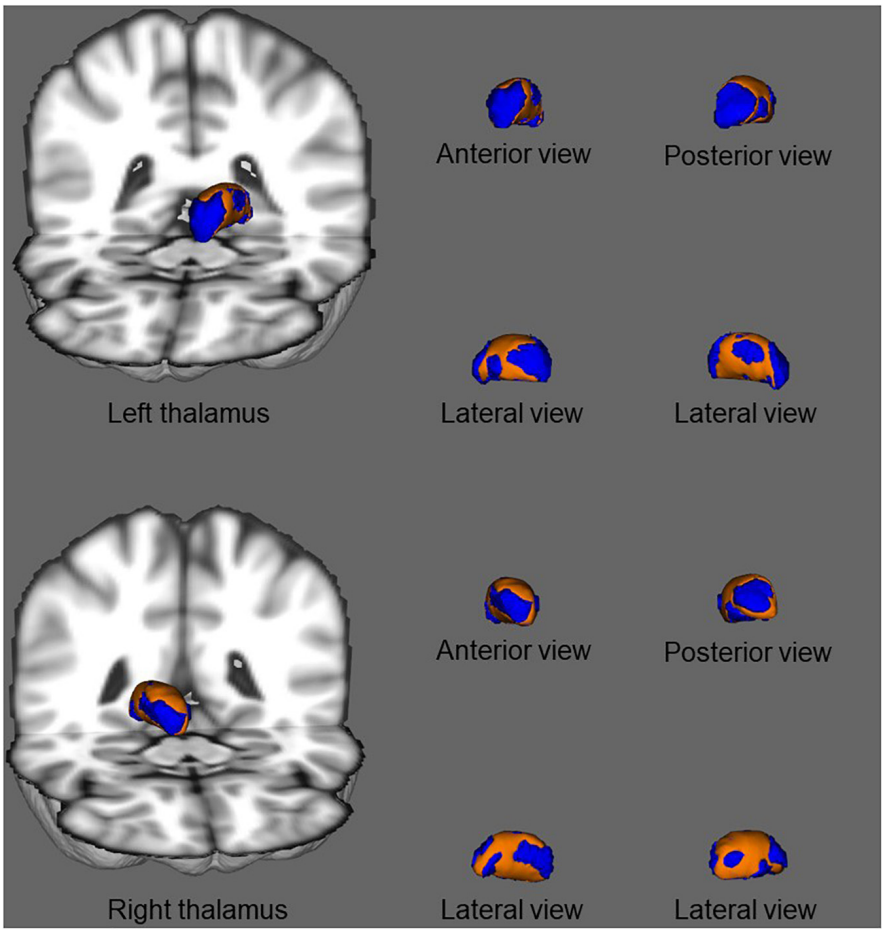

FIGURE 4 | In shape analysis correlations, association between regional shape deformation on the ventral and dorsal side of the bilateral thalamus and MoCA score in patients with ESRD after adjustment for age and gender. The regions in orange color indicate the area associated with the MoCA score. Results were corrected for multiple comparisons using threshold-free cluster enhancement and family-wise error methods ($p < 0.05$).

in patients with ESRD (Chang et al., 2017). We also detected atrophy of the left hippocampus, albeit without Bonferroni correction. However, in contrast, it is different from our research results, and a recent study found significantly higher bilateral thalamus volumes in hemodialysis patients compared with HCs, although their results on the caudate and amygdala volumes were similar to our observations (Jin et al., 2020). Previous researchers found that compared with HCs, patients with minimal nephro-encephalopathy ESRD had lower brain volumes of the right amygdala and hippocampus, and those with non-nephro-encephalopathy ESRD had higher brain volumes of the right caudate and right thalamus (Zhang et al., 2013). However, the previous neuroimaging study included 19 hemodialysis patients and 14 HCs bilateral caudate volumes lower in patients (Prohovnik et al., 2007). These different findings are likely related to differences in study patients and methods used. For example, some researchers used VBM to analyze subcortical volumes instead of the volumetric analysis methods used in our study (Prohovnik et al., 2007; Zhang et al., 2013; Jin et al., 2020). Moreover, our study subjects differed from those of previous studies; the previous study selected patients with ESRD with non-nephro-encephalopathy, whereas the patients in our study had general cognitive and sleep disorders (Zhang et al., 2013). Furthermore, the use of stringent statistical correction may also contribute to inconsistent findings.

Vertex-wise analysis was used for the first time to study subcortical structural abnormalities in patients with ESRD undergoing maintenance hemodialysis, and we demonstrated its feasibility as an analysis method to detect atrophy. Using vertex-wise analysis, we found subcortical atrophy not only in the bilateral thalamus and accumbens and right amygdala but also in the bilateral caudate and left putamen. However, using volume analysis, we found that the volume of the bilateral thalamus, bilateral nucleus accumbens, and right amygdala decreased in patients with ESRD compared with the HC group. Similarly, inconsistent results between the two analysis methods were reported in a study exploring subcortical structures in patients with chronic insomnia (Gong et al., 2019) and alcohol dependence (Shim et al., 2019). Although the results of the vertex-wise shape analysis and volumetric analysis are different,

they complement each other and play a role in cross-validation. In other words, these two methods are used to observe the changes of subcortical structures in patients with ESRD from different perspectives.

By combining vertex-wise and automated volumetric analysis results, we can study both volumetric and morphological abnormalities of the thalamus and accumbens in patients with ESRD. The vertex-wise analysis results showed that the atrophy shape of the thalamus roughly reflected the ventral anterior, mediodorsal, ventral posterior, and ventral lateral nuclei. Different areas of thalamic infarction can cause different cognitive impairments, such as a decline in memory and learning ability, lowered levels of consciousness, and decreased orientation, depending on the blood supply arteries (Chen et al., 2019). The anatomical and physiological bases of the kidney–brain axis and kidney–brain cross-talk hypothesis are related to the similarity in the structure and function of the blood supply arteries between the kidneys and the brain (Bugnicourt et al., 2013; Lu et al., 2015). Furthermore, a recent review reported that uremic neurotoxins that interact with the brain vasculature, neural progenitor cells, monoaminergic neurons, and the glymphatic system cause brain dysfunction in patients with CKD due to vascular insults and neurodegeneration (Viggiano et al., 2020). This was confirmed by a recent kidney transplant study, which demonstrated that the normalization of cerebral blood flow and neurochemicals in the bodies of patients with CKD after transplantation was related to improvements in cognition (Lepping et al., 2020). In fact, we observed that the MoCA score of patients with ESRD was positively correlated with bilateral thalamus volume, supporting the kidney–brain axis hypothesis. In addition, patients with ESRD have anemia that manifests as a decrease in hemoglobin and hematocrit (Kuwabara et al., 2002). Although we did not find a correlation between hemoglobin and hematocrit and thalamus and accumbens volumes in patients with ESRD, we observed a negative correlation between serum creatinine and volume of the left thalamus. This may carry some significance in terms of the relationship between the kidneys and the brain. Some scholars have also observed a similar relationship between serum creatinine and brain volume. They found that serum creatinine was negatively correlated with the volumes of right frontal lobe, left uncus, and left temporal pole (Zhang et al., 2013). It is suggested that the accumulation of major uremic toxins is one of the main risk factors for the change of volume of subcortical structures and the results are also consistent with the neurodegenerative disease in the kidney–brain axis hypothesis (Bugnicourt et al., 2013). Serum creatinine reflects the degree of renal impairment in patients with ESRD (Levey et al., 1999). The above results indicate that the severity of renal damage may be related to the changes in the volume of brain structures.

Similar findings were also revealed in the accumbens, and the volumetric analysis showed bilateral atrophy. Furthermore, slight atrophy was found in the right medial accumbens using vertex-wise analysis. The accumbens is a major component of the ventral striatum and is an area of continuity between the head of the caudate nucleus and the putamen; this region is primarily supplied by the recurrent artery of Heubner (Feekes and Cassell, 2006). The accumbens plays an important role in sleep and wakefulness and comprises two parts, namely, the shell and the core. Most neurons in the accumbens are gamma-aminobutyric acidergic neurons, which project fibers to the ventral pallidum, parabrachial nucleus, lateral hypothalamus, and ventral tegmental area, and the activation of these nuclei causes cortical awakening (Lazarus et al., 2012). Some researchers found that damage to both the core and shell of the accumbens causes a significant increase in wakefulness and a significant reduction in the sleep homeostatic response (Qiu et al., 2012). Similar to the thalamus volume results, we found that the severity of sleep disorders in patients with ESRD was related to the volume of the bilateral accumbens. In summary, based on the vascular insult and neurodegeneration hypothesis, direct neuronal toxicity, endothelial dysfunction, and vascular injury may cause subcortical atrophy, which would cause subsequent relative symptoms in patients with ESRD.

In addition, the relationship of morphometric alterations between thalamus or accumbens and the other network regions in patients with ESRD may also have value for exploration. Some studies have been reported the relationship between them in patients with TLE by the network of structural covariance (Zhang et al., 2017; Xu et al., 2020). This method can reveal the effect of changes in different subcortical gray matter (GM) nuclei on cortical GM in patients with ESRD.

Dialysis as a treatment measure does affect the state of a patient and will influence brain volumes, since this therapy will eliminate water from the subjects. Previous studies on single dialysis session in patients with ESRD focused on changes in the brain activity of a patient, and functional MRI (fMRI) was used in these studies (Li P. et al., 2018; Peng et al., 2021). Previous studies on the brain structure of patients with ESRD also did not involve the impact of a single dialysis (Li A. et al., 2018; Chiu et al., 2019; Jin et al., 2020). The possible reason for the different study methods mentioned earlier is that it is generally considered that changes in brain structure are a long-term process, and brain activity can change in a short time. Moreover, we found that there was no correlation between the dialysis duration and the bilateral thalamus volume or bilateral accumbens volume after adjustment for age, gender, and eTIV. This result is inconsistent with a previous study, which shows that the GM volume was strongly related to the duration of hemodialysis treatment on patients with ESRD (Prohovnik et al., 2007). The above results may be caused by the difference between the method (VBM vs. volumetric analysis) and the selected subject (global GM vs. thalamus). Therefore, the effect of a single dialysis session on changes in the brain structure of patients with ESRD may require further study in future.

The strengths of this study are as follows. First, vertex-wise analysis was used to study subcortical structures in patients with ESRD. Although this method has been applied to the study of subcortical structures in patients with various neurological diseases (de Jong et al., 2008; Nemmi et al., 2015; Gong et al., 2019), it has rarely been used in patients with ESRD. Second, the subcortical structures of ESRD patients were explored more objectively and clearly using vertex-wise shape analysis and the volumetric analysis than previous reports (Chang et al., 2017; Chiu et al., 2019; Jin et al., 2020). Third, we investigated correlations between subcortical structural changes and related symptoms, such as cognitive and sleep disorders.

However, the limitations of this study should also be mentioned. First, there were no non-dialysis-dependent ESRD patients and ESRD patients after a single dialysis as controls; therefore, it was not possible to determine the effect of dialysis on the subcortical structures of patients with ESRD. Thus, the patient group should be included in future studies. Second, the number of patients with ESRD was small, and a multicenter collaborative study is warranted. Third, we did not follow up patients; long-term longitudinal studies will help to understand the subcortical structural changes in patients with ESRD over time.

CONCLUSION

We confirmed that patients with ESRD have atrophy of subcortical structures, especially the thalamus and accumbens. In addition, atrophy of the thalamus was associated with cognitive dysfunction, and accumbens atrophy was related to sleep disorders in patients with ESRD. These findings contribute to a deeper understanding of the mechanisms underlying the neurological symptoms of patients with ESRD.

DATA AVAILABILITY STATEMENT

The original contributions presented in the study are included in the article/supplementary material, further inquiries can be directed to the corresponding authors.

ETHICS STATEMENT

The studies involving human participants were reviewed and approved by the Medical Ethics Review Board of the First Affiliated Hospital of the Medical College in Xi'an Jiaotong University. The patients/participants provided their written informed consent to participate in this study.

AUTHOR CONTRIBUTIONS

WG, SM, and MZ contributed to the research idea and study design. WG, HS, and RH performed the data acquisition and analysis. WG and RH performed manual quality checks on the data. WG and HY wrote this manuscript. LZ and ZR interpreted the data and managed the selection. All authors read and approved the final manuscript.

FUNDING

This work was supported by the National Natural Science Foundation of China (Grant No. 82071879) and the Health Research Program of Shaanxi Province (Grant No. 2018C001).

ACKNOWLEDGMENTS

We would like to thank all participants and staff involved in this research.

REFERENCES

Alperin, N., Wiltshire, J., Lee, S. H., Ramos, A. R., Hernandez-Cardenache, R., Rundek, T., et al. (2019). Effect of sleep quality on amnestic mild cognitive impairment vulnerable brain regions in cognitively normal elderly individuals. *Sleep* 42:zsy254. doi: 10.1093/sleep/zsy254

Backhaus, J., Junghanns, K., Broocks, A., Riemann, D., and Hohagen, F. (2002). Test-retest reliability and validity of the pittsburgh sleep quality index in primary insomnia. *J. Psychosom. Res.* 53, 737–740. doi: 10.1016/s0022-3999(02)00330-6

Bugnicourt, J. M., Godefroy, O., Chillon, J. M., Choukroun, G., and Massy, Z. A. (2013). Cognitive disorders and dementia in CKD: the neglected kidney-brain axis. *J. Am. Soc. Nephrol.* 24, 353–363. doi: 10.1681/ASN.2012050536

Buysse, D. J., Reynolds, C. F. III, Monk, T. H., Berman, S. R., and Kupfer, D. J. (1989). The Pittsburgh Sleep Quality Index: a new instrument for psychiatric practice and research. *Psychiatry Res.* 28, 193–213. doi: 10.1016/0165-1781(89)90047-4

Chang, C. Y., Lin, C. C., Tsai, C. F., Yang, W. C., Wang, S. J., Lin, F. H., et al. (2017). Cognitive impairment and hippocampal atrophy in chronic kidney disease. *Acta Neurol. Scand.* 136, 477–485. doi: 10.1111/ane.12753

Chen, G., Taylor, P. A., and Cox, R. W. (2017). Is the statistic value all we should care about in neuroimaging? *Neuroimage* 147, 952–959. doi: 10.1016/j.neuroimage.2016.09.066

Chen, L., Luo, T., Wang, K., Zhang, Y., Shi, D., Lv, F., et al. (2019). Effects of thalamic infarction on the structural and functional connectivity of the ipsilesional primary somatosensory cortex. *Eur. Radiol.* 29, 4904–4913. doi: 10.1007/s00330-019-06068-0

Chiu, Y. L., Tsai, H. H., Lai, Y. J., Tseng, H. Y., Wu, Y. W., Peng, Y. S., et al. (2019). Cognitive impairment in patients with end-stage renal disease: accelerated brain aging? *J. Formos. Med. Assoc.* 118, 867–875. doi: 10.1016/j.jfma.2019.01.011

de Jong, L. W., van der Hiele, K., Veer, I. M., Houwing, J. J., Westendorp, R. G., Bollen, E. L., et al. (2008). Strongly reduced volumes of putamen and thalamus in Alzheimer's disease: an MRI study. *Brain* 131(Pt 12), 3277–3285. doi: 10.1093/brain/awn278

Drew, D. A., Weiner, D. E., and Sarnak, M. J. (2019). Cognitive impairment in CKD: pathophysiology. Management, and prevention. *Am. J Kidney Dis.* 74, 782–790. doi: 10.1053/j.ajkd.2019.05.017

Feekes, J. A., and Cassell, M. D. (2006). The vascular supply of the functional compartments of the human striatum. *Brain* 129(Pt 8), 2189–2201. doi: 10.1093/brain/awl158

Fischl, B. (2012). FreeSurfer. *Neuroimage* 62, 774–781. doi: 10.1016/j.neuroimage.2012.01.021

Fischl, B., Salat, D. H., Busa, E., Albert, M., Dieterich, M., Haselgrove, C., et al. (2002). Whole brain segmentation: automated labeling of neuroanatomical structures in the human brain. *Neuron* 33, 341–355. doi: 10.1016/s0896-6273(02)00569-x

Fischl, B., Salat, D. H., van der Kouwe, A. J., Makris, N., Ségonne, F., Quinn, B. T., et al. (2004). Sequence-independent segmentation of magnetic resonance images. *Neuroimage* 23(Suppl. 1), S69–S84. doi: 10.1016/j.neuroimage.2004.07.016

Gong, L., Liao, T., Liu, D., Luo, Q., Xu, R., Huang, Q., et al. (2019). Amygdala changes in chronic insomnia and their association with sleep and anxiety symptoms: insight from shape analysis. *Neural. Plast* 2019:8549237. doi: 10.1155/2019/8549237

Himmelfarb, J., and Ikizler, T. A. (2010). Hemodialysis. *N. Engl. J. Med.* 363, 1833–1845. doi: 10.1056/NEJMra0902710

Hui, D. S., Wong, T. Y., Ko, F. W., Li, T. S., Choy, D. K., Wong, K. K., et al. (2000). Prevalence of sleep disturbances in chinese patients with end-stage renal failure on continuous ambulatory peritoneal dialysis. *Am. J. Kidney Dis.* 36, 783–788. doi: 10.1053/ajkd.2000.17664

Hui, D. S., Wong, T. Y., Li, T. S., Ko, F. W., Choy, D. K., Szeto, C. C., et al. (2002). Prevalence of sleep disturbances in Chinese patients with end stage renal failure on maintenance hemodialysis. *Med. Sci. Monit.* 8, Cr331–Cr336.

Jenkinson, M., Beckmann, C. F., Behrens, T. E., Woolrich, M. W., and Smith, S. M. (2012). FSL. *Neuroimage* 62, 782–790. doi: 10.1016/j.neuroimage.2011.09.015

Jha, V., Garcia-Garcia, G., Iseki, K., Li, Z., Naicker, S., Plattner, B., et al. (2013). Chronic kidney disease: global dimension and perspectives. *Lancet* 382, 260–272. doi: 10.1016/s0140-6736(13)60687-x

Jin, M., Wang, L., Wang, H., Han, X., Diao, Z., Guo, W., et al. (2020). Structural and functional alterations in hemodialysis patients: a voxel-based morphometry and functional connectivity study. *Front. Hum. Neurosci.* 14:80. doi: 10.3389/fnhum.2020.00080

Kalirao, P., Pederson, S., Foley, R. N., Kolste, A., Tupper, D., Zaun, D., et al. (2011). Cognitive impairment in peritoneal dialysis patients. *Am. J. Kidney Dis.* 57, 612–620. doi: 10.1053/j.ajkd.2010.11.026

Kuwabara, Y., Sasaki, M., Hirakata, H., Koga, H., Nakagawa, M., Chen, T., et al. (2002). Cerebral blood flow and vasodilatory capacity in anemia secondary to chronic renal failure. *Kidney Int.* 61, 564–569. doi: 10.1046/j.1523-1755.2002.00142.x

Lazarus, M., Huang, Z. L., Lu, J., Urade, Y., and Chen, J. F. (2012). How do the basal ganglia regulate sleep-wake behavior? *Trends Neurosci.* 35, 723–732. doi: 10.1016/j.tins.2012.07.001

Lepping, R. J., Montgomery, R. N., Sharma, P., Mahnken, J. D., Vidoni, E. D., Choi, I. Y., et al. (2020). Normalization of cerebral blood flow, neurochemicals, and white matter integrity after kidney transplantation. *J. Am. Soc. Nephrol.* 32, 177–187. doi: 10.1681/ASN.2020050584

Levey, A. S., Bosch, J. P., Lewis, J. B., Greene, T., Rogers, N., and Roth, D. (1999). A more accurate method to estimate glomerular filtration rate from serum creatinine: a new prediction equation. Modification of diet in renal disease study group. *Ann. Intern. Med.* 130, 461–470. doi: 10.7326/0003-4819-130-6-199903160-00002

Li, A., Mu, J., Huang, M., Zhang, Z., Liu, J., and Zhang, M. (2018). Altered amygdala-related structural covariance and resting-state functional connectivity in end-stage renal disease patients. *Metab. Brain Dis.* 33, 1471–1481. doi: 10.1007/s11011-018-0254-y

Li, M., Wang, R., Zhao, M., Zhai, J., Liu, B., Yu, D., et al. (2019). Abnormalities of thalamus volume and resting state functional connectivity in primary insomnia patients. *Brain Imaging Behav.* 13, 1193–1201. doi: 10.1007/s11682-018-9932-y

Li, P., Ding, D., Ma, X. Y., Zhang, H. W., Liu, J. X., and Zhang, M. (2018). Altered intrinsic brain activity and memory performance improvement in patients with end-stage renal disease during a single dialysis session. *Brain Imaging Behav.* 12, 1640–1649. doi: 10.1007/s11682-018-9828-x

Lu, R., Kiernan, M. C., Murray, A., Rosner, M. H., and Ronco, C. (2015). Kidney-brain crosstalk in the acute and chronic setting. *Nat. Rev. Nephrol.* 11, 707–719. doi: 10.1038/nrneph.2015.131

Mettang, T., and Kremer, A. E. (2015). Uremic pruritus. *Kidney Int.* 87, 685–691. doi: 10.1038/ki.2013.454

Meyer, T. W., and Hostetter, T. H. (2007). Uremia. *N. Engl. J. Med.* 357, 1316–1325. doi: 10.1056/NEJMra071313

Miranda, A. S., Cordeiro, T. M., Dos Santos Lacerda Soares, T. M., Ferreira, R. N., and Simoes, E. S. A. C. (2017). Kidney-brain axis inflammatory cross-talk: from bench to bedside. *Clin. Sci.* 131, 1093–1105. doi: 10.1042/CS20160927

Nasreddine, Z. S., Phillips, N. A., Bédirian, V., Charbonneau, S., Whitehead, V., Collin, I., et al. (2005). The montreal cognitive assessment, MoCA: a brief screening tool for mild cognitive impairment. *J. Am. Geriatr. Soc.* 53, 695–699. doi: 10.1111/j.1532-5415.2005.53221.x

Nemmi, F., Sabatini, U., Rascol, O., and Péran, P. (2015). Parkinson's disease and local atrophy in subcortical nuclei: insight from shape analysis. *Neurobiol. Aging* 36, 424–433. doi: 10.1016/j.neurobiolaging.2014.07.010

Patenaude, B., Smith, S. M., Kennedy, D. N., and Jenkinson, M. (2011). A bayesian model of shape and appearance for subcortical brain segmentation. *Neuroimage* 56, 907–922. doi: 10.1016/j.neuroimage.2011.02.046

Peng, C., Yang, H., Ran, Q., Zhang, L., Liu, C., Fang, Y., et al. (2021). Immediate abnormal intrinsic brain activity patterns in patients with end-stage renal disease during a single dialysis session : resting-state functional MRI study. *Clin. Neuroradiol.* 31, 373–381. doi: 10.1007/s00062-020-00915-0

Prohovnik, I., Post, J., Uribarri, J., Lee, H., Sandu, O., and Langhoff, E. (2007). Cerebrovascular effects of hemodialysis in chronic kidney disease. *J. Cereb. Blood Flow Metab.* 27, 1861–1869. doi: 10.1038/sj.jcbfm.9600478

Qiu, M. H., Liu, W., Qu, W. M., Urade, Y., Lu, J., and Huang, Z. L. (2012). The role of nucleus accumbens core/shell in sleep-wake regulation and their involvement in modafinil-induced arousal. *PLoS One* 7:e45471. doi: 10.1371/journal.pone.0045471

Reuter, M., Rosas, H. D., and Fischl, B. (2010). Highly accurate inverse consistent registration: a robust approach. *Neuroimage* 53, 1181–1196. doi: 10.1016/j.neuroimage.2010.07.020

Scherer, J. S., Combs, S. A., and Brennan, F. (2017). Sleep disorders, restless legs syndrome, and uremic pruritus: diagnosis and treatment of common symptoms in dialysis patients. *Am. J. Kidney Dis.* 69, 117–128. doi: 10.1053/j.ajkd.2016.07.031

Ségonne, F., Dale, A. M., Busa, E., Glessner, M., Salat, D., Hahn, H. K., et al. (2004). A hybrid approach to the skull stripping problem in MRI. *Neuroimage* 22, 1060–1075. doi: 10.1016/j.neuroimage.2004.03.032

Shim, J. H., Kim, Y. T., Kim, S., and Baek, H. M. (2019). Volumetric reductions of subcortical structures and their localizations in alcohol-dependent patients. *Front. Neurol.* 10:247. doi: 10.3389/fneur.2019.00247

Smith, S. M., Jenkinson, M., Woolrich, M. W., Beckmann, C. F., Behrens, T. E., Johansen-Berg, H., et al. (2004). Advances in functional and structural MR image analysis and implementation as FSL. *Neuroimage* 23(Suppl. 1), S208–S219. doi: 10.1016/j.neuroimage.2004.07.051

Smith, S. M., and Nichols, T. E. (2009). Threshold-free cluster enhancement: addressing problems of smoothing, threshold dependence and localisation in cluster inference. *Neuroimage* 44, 83–98. doi: 10.1016/j.neuroimage.2008.03.061

Stevens, P. E., and Levin, A. (2013). Evaluation and management of chronic kidney disease: synopsis of the kidney disease: improving global outcomes 2012 clinical practice guideline. *Ann. Intern. Med.* 158, 825–830. doi: 10.7326/0003-4819-158-11-201306040-00007

Viggiano, D., Wagner, C. A., Martino, G., Nedergaard, M., Zoccali, C., Unwin, R., et al. (2020). Mechanisms of cognitive dysfunction in CKD. *Nat. Rev. Nephrol.* 16, 452–469. doi: 10.1038/s41581-020-0266-9

Weng, Y., Lariviere, S., Caciagli, L., Vos de Wael, R., Rodriguez-Cruces, R., Royer, J., et al. (2020). Macroscale and microcircuit dissociation of focal and generalized human epilepsies. *Commun. Biol.* 3:244. doi: 10.1038/s42003-020-0958-5

Winkler, A. M., Ridgway, G. R., Webster, M. A., Smith, S. M., and Nichols, T. E. (2014). Permutation inference for the general linear model. *Neuroimage* 92, 381–397. doi: 10.1016/j.neuroimage.2014.01.060

Xu, Q., Zhang, Q., Yang, F., Weng, Y., Xie, X., Hao, J., et al. (2020). Cortico-striato-thalamo-cerebellar networks of structural covariance underlying different epilepsy syndromes associated with generalized tonic–clonic seizures. *Hum. Brain Mapp.* 42, 1102–1115. doi: 10.1002/hbm.25279

Zhang, L., Wang, F., Wang, L., Wang, W., Liu, B., Liu, J., et al. (2012). Prevalence of chronic kidney disease in China: a cross-sectional survey. *Lancet* 379, 815–822. doi: 10.1016/s0140-6736(12)60033-6

Zhang, L. J., Wen, J., Ni, L., Zhong, J., Liang, X., Zheng, G., et al. (2013). Predominant gray matter volume loss in patients with end-stage renal disease: a voxel-based morphometry study. *Metab. Brain Dis.* 28, 647–654. doi: 10.1007/s11011-013-9438-7

Zhang, Z., Liao, W., Xu, Q., Wei, W., Zhou, H. J., Sun, K., et al. (2017). Hippocampus-associated causal network of structural covariance measuring structural damage progression in temporal lobe epilepsy. *Hum. Brain Mapp.* 38, 753–766. doi: 10.1002/hbm.23415

Conflict of Interest: The authors declare that the research was conducted in the absence of any commercial or financial relationships that could be construed as a potential conflict of interest.

Publisher's Note: All claims expressed in this article are solely those of the authors and do not necessarily represent those of their affiliated organizations, or those of the publisher, the editors and the reviewers. Any product that may be evaluated in this article, or claim that may be made by its manufacturer, is not guaranteed or endorsed by the publisher.

frontiers in Human Neuroscience

STUDY PROTOCOL
published: 31 January 2022
doi: 10.3389/fnhum.2022.788037

Prediction of Communication Impairment in Children With Bilateral Cerebral Palsy Using Multivariate Lesion- and Connectome-Based Approaches: Protocol for a Multicenter Prospective Cohort Study

Jie Hu[1], Jingjing Zhang[1], Yanli Yang[1], Ting Liang[2], Tingting Huang[3], Cheng He[4], Fuqin Wang[1], Heng Liu[1] and Tijiang Zhang[1]**

[1] Department of Radiology, Medical Imaging Center of Guizhou Province, The Affiliated Hospital of Zunyi Medical University, Zunyi, China, [2] Department of Diagnostic Radiology, The First Affiliated Hospital of Xi'an Jiaotong University, Xi'an, China, [3] Department of Radiology, The First Affiliated Hospital of Henan University of TCM, Zhengzhou, China, [4] Department of Radiology, Chongqing University Central Hospital, Chongqing, China

OPEN ACCESS

Edited by:
Wei Liao, University of Electronic Science and Technology of China, China

Reviewed by:
Fanpei G. Yang, National Tsing Hua University, Taiwan
Jessica Girault, University of North Carolina at Chapel Hill, United States

***Correspondence:**
Heng Liu
zmcliuh@163.com
Tijiang Zhang
tijzhang@163.com

Specialty section:
This article was submitted to Brain Imaging and Stimulation, a section of the journal Frontiers in Human Neuroscience

Received: *01 October 2021*
Accepted: *10 January 2022*
Published: *31 January 2022*

Citation:
Hu J, Zhang J, Yang Y, Liang T, Huang T, He C, Wang F, Liu H and Zhang T (2022) Prediction of Communication Impairment in Children With Bilateral Cerebral Palsy Using Multivariate Lesion- and Connectome-Based Approaches: Protocol for a Multicenter Prospective Cohort Study. Front. Hum. Neurosci. 16:788037. doi: 10.3389/fnhum.2022.788037

Background: Bilateral cerebral palsy (BCP) is the most common type of CP in children and is often accompanied by different degrees of communication impairment. Several studies have attempted to identify children at high risk for communication impairment. However, most prediction factors are qualitative and subjective and may be influenced by rater bias. Individualized objective diagnostic and/or prediction methods are still lacking, and an effective method is urgently needed to guide clinical diagnosis and treatment. The aim of this study is to develop and validate an objective, individual-based model for the prediction of communication impairment in children with BCP by the time they enter school.

Methods: A multicenter prospective cohort study will be conducted in four Chinese hospitals. A total of 178 children with BCP will undergo advanced brain magnetic resonance imaging (MRI) at baseline (corrected age, before the age of 2 years). At school entry, communication performance will be assessed by a communication function classification system (CFCS). Three-quarters of children with BCP will be allocated as a training cohort, whereas the remaining children will be allocated as a test cohort. Multivariate lesion- and connectome-based approaches, which have shown good predictive ability of language performance in stroke patients, will be applied to extract features from MR images for each child with BCP. Multiple machine learning models using extracted features to predict communication impairment for each child with BCP will be constructed using data from the training cohort and externally validated using data from the test cohort. Prediction accuracy across models in the test cohort will be statistically compared.

Discussion: The findings of the study may lead to the development of several translational tools that can individually predict communication impairment in children newly diagnosed with BCP to ensure that these children receive early, targeted therapeutic intervention before they begin school.

Trial registration: The study has been registered with the Chinese Clinical Trial Registry (ChiCTR2100049497).

Keywords: cerebral palsy, children, magnetic resonance imaging, prediction, communication

INTRODUCTION

Cerebral palsy (CP) is the most common physical disability in childhood and occurs in 2–3 per 1,000 live births (Patel et al., 2020). Recently, the majority of individuals with CP achieve a life expectancy close to that of the general population. Clinical and research interests now focus on improving the ability of children with CP to perform activities of daily living and socially interact. Communication plays an integral role in people's daily activities and social participation, yet only a few studies have examined the prevalence and features of communication impairment in children with CP (Mei et al., 2016; Kristoffersson et al., 2020). Communication (receptive and/or expressive language) impairments are common comorbidities in patients with CP, with a prevalence ranging from 46 to 78% (Coleman et al., 2015, 2016; Mei et al., 2016; Kristoffersson et al., 2020). Communication problems result in poor prospects of engagement and social participation in children with CP across a range of activities, including self-development, social functioning, and learning (Pennington et al., 2019; Vaillant et al., 2020). Particularly by the time these children enter school, communication skills greatly impact school readiness, which affects later social and academic success as well as economic and health outcomes (High, 2008).

Language development from birth to 2 years, when brain plasticity is at its greatest, presents multiple opportunities for intervention (Chorna et al., 2017). During this period, language perception (receptive) and production (expressive) are accompanied by the development of cortical areas responsible for improvements in working memory and pattern recognition in the first year and the multiplication of associations between different cortical processing areas in the second year (McMahon et al., 2012). Social interactions and interventions leveraging cortical development and cortical associations between language and motor systems at this critical time represent a promising role in improving long-term language outcomes and social functions (Goldstein et al., 2003; McMahon et al., 2012; Lipscombe et al., 2016; Chorna et al., 2017). Therefore, the key to interventions in these individuals lies in the importance of the early identification of children with CP at high risk for communication impairments (Coleman et al., 2015).

Several studies (Coleman et al., 2015; Hustad et al., 2018; Pennington et al., 2020; Tan et al., 2020) have attempted to explore demographic variables, early clinical characteristics, and environmental factors in predicting communication ability in children with CP at school entry. Studies have demonstrated that communication, cognition, and motor performance at an early age are critical for predicting future functional communication in children with CP (Coleman et al., 2015; Hustad et al., 2018; Pennington et al., 2020; Tan et al., 2020). However, most standardized tests require behavioral repertoires that exceed the capabilities of young children with CP, which makes these measures too difficult to use to assess these children reliably (Geytenbeek et al., 2010; Nordberg, 2018). Other non-standardized tests, such as parent-completed measures and grade-level classification systems, are unlikely to easily and adequately capture the scope of information necessary to track impairment-related changes (Geytenbeek et al., 2010; Potter, 2016). All these limitations make these methods less accurate in identifying or predicting children with CP at high risk for communication impairment.

In recent decades, progress in magnetic resonance imaging (MRI) techniques has increased the number of opportunities to search for more precise and objective biomarkers in various pediatric neurological diseases; additionally, MRI has been recommended and widely used for diagnosis, prognosis, treatment monitoring and research in CP (Graham et al., 2016; Novak et al., 2017). Three studies (Geytenbeek et al., 2015; Coleman et al., 2016; Choi et al., 2017) used qualitative categorical descriptions from MRI to investigate the characteristics of brain abnormalities associated with communication performance in children with CP. All these studies found that communication is related to the type of brain lesion on MRI (qualitative measurement); specifically, more severe periventricular white matter lesions (PWMLs) are associated with worse communication performance for the patient. Moreover, some researchers (Coleman et al., 2016; Laporta-Hoyos et al., 2018) used a semiquantitative MRI scale that provides scores by evaluating the extent of brain injury—assigning higher scores for increased lesion involvement—to assess the severity of brain damage in children with CP. The results demonstrated that children with CP with more severe lesions in the presumed language pathway regions (the left frontal, left temporal, left thalamus, left posterior internal capsule, left caudate and lenticular nuclei) had poorer overall communication skills and lower Communication and Symbolic Behavior Scales Developmental Profile (CSBS-DP) total scores (Coleman et al., 2016). All these results indicate that MRI has potential value in predicting communication impairment in children with CP. However, the above studies had a cross-sectional design, and variables reported as risk factors were qualitative or semiquantitative. Thus, an early quantitative and individualized prediction model for communication

outcomes based on patient characteristics and MRI parameters is still lacking.

Multivariate lesion- and connectome-based approaches (Gleichgerrcht et al., 2017) are emerging techniques that provide an objective and quantifiable way to statistically evaluate the relationship between whole-brain structure connections and behavioral function. Notably, a prediction model constructed from this approach had high efficacy in the prediction of language deficits in post-stroke patients (Yourganov et al., 2016) and motor outcomes in neonates with arterial ischemic stroke (Al Harrach et al., 2021). Therefore, this study aims to develop individual prediction models based on multivariate lesion- and connectome-based approaches at an early age to predict communication ability in children with CP by the time they enter school. Among all types of CP, bilateral cerebral palsy (BCP) is the most common subtype, comprising 64.7% of all cases (Colver et al., 2014). Furthermore, different neuroimaging findings have revealed different patterns of insult to the brain in CP; recent research has noted that white matter lesions are the most common findings in imaging, accounting for 49.1% of all cases, and the severity of PWMLs has been verified to be linked with communication performance in children with CP (Geytenbeek et al., 2015; Coleman et al., 2016; Choi et al., 2017). Thus, we will also limit study participants to those with BCP and PWMLs (the most common subtype and neuroimaging finding in children with CP) to reduce the heterogeneity within the study population to improve the accuracy of prediction models. The results of this study may lead to the development of several translational tools that can be used to make individualized predictions of communication impairments in children newly diagnosed with BCP and PWMLs to ensure that these children receive early, targeted therapeutic intervention before they begin school.

AIMS

Primary Aim

The aim of this study is to develop and validate an individual-based model that can be used to predict the communication impairment of children with BCP and PWMLs at school entry based on advanced brain MRI at an early age (before 2 years).

Secondary Aims

(1) To establish a practical method for multivariate lesion- and connectome-based approaches of children with BCP and PWMLs.
(2) To identify injuries to cortical regions and connectomes associated with communication impairment in children with BCP with PWMLs.

MATERIALS AND METHODS

Study Design

This study will be implemented as a multicenter prospective cohort study at four centers. This study has been registered with the Chinese Clinical Trial Registry (ChiCTR2100049497) and will be reported in accordance with the Standard Protocol Items: Recommendations for clinical Trials (SPIRIT) (Chan et al., 2013).

Study Setting

The study will take place at the Affiliated Hospital of Zunyi Medical University (No. 149, Dalian Road, Huichuan District, Zunyi City, Guizhou Province, China), the First Affiliated Hospital of Xi'an Jiaotong University (No. 277 Yanta West Road, Xi'an, Shaanxi, China), the First Affiliated Hospital of Henan University of Chinese Medicine (No. 19 Renmin Road, Zhengzhou, Henan, China), and Chongqing University Central Hospital (No. 1 Jiankang Road, Yuzhong District, Chongqing, China). The study will begin in December 2021 and is expected to be completed in June 2025.

Ethics and Dissemination

All participating centers approved this study protocol. Full ethics committee approval was obtained from the Institutional Review Board of The Affiliated Hospital of Zunyi Medical University (KLL-2021-108). A signed, informed consent form will be obtained from the legal parents/guardians of each participant. Participating subjects will receive a summary of the results, including clinical phenotype descriptions, imaging reports, and results of the behavioral assessments they have completed. The results of the present study will be submitted to peer-reviewed journals and/or reported at relevant conferences. Subjects will be able to withdraw from the study at any time without explanation. They will not suffer any penalty from the staff, nor will any repercussions be evident in their care due to this decision.

Participants

Some investigators have noted that predictors of communication difficulties may differ for the subgroup of children with CP in early life (Pennington et al., 2020). Therefore, we will limit our study participants to those with BCP (associated with more serious complications and a more common prevalence of communication problems) (Geytenbeek et al., 2015) to find reliable prognostic markers for this population. Brain MRI-based classification systems have been widely recommended and used for classifying different types of brain lesions in children with CP, and different neuroimaging methods may reveal the different pathogenic patterns responsible for CP (Ditchfield, 2017; Himmelmann et al., 2017). Among all the types of lesions, PWMLs are the most common neuroimaging finding in this population (Himmelmann and Uvebrant, 2011; Coleman et al., 2016; Himmelmann et al., 2017), and the severity of PWMLs has been shown to be associated with the severity of communication impairment (Geytenbeek et al., 2015; Coleman et al., 2016; Choi et al., 2017). Thus, we will also constrain neuroimaging to children with BCP and PWMLs to reduce the heterogeneity within our study population.

Inclusion Criteria

Children meeting the following criteria will be considered for enrollment in this study: (I) confirmed diagnosis of BCP by

pediatric neurologists (Novak et al., 2017), (II) age 6 months to 2 years at the time of recruitment, (III) PWMLs as described on the MRI imaging report, and (IV) willingness by participants and parents to participate in the study.

Exclusion Criteria

Children will be excluded if they have any one of the following criteria: (I) blindness, severe visual impairment or hearing impairment (given the requirements of some language assessment modules); (II) other diseases (i.e., hereditary disease, cancer, severe infectious disease, severe heart disease, or progressive central nervous system diseases); (III) MRI artifacts affecting any further image processing analysis; (IV) insufficient cooperation to participate in the communication assessment; and (VI) a primary language other than Chinese among the family members.

Withdrawal Criteria

Subjects will be withdrawn from this study at the discretion of the researchers if there are safety concerns or if the children are unable to complete follow-up examinations.

Sample Size

There are no directly available data to assess the relationship between connectome-based features and clinical assessments of children with BCP to predict their communication ability at school entry. The sample size was calculated according to a previous study (Coleman et al., 2016). In that study of children with CP with a total sample size of n = 131, the number of children with communication abnormalities was 62 (47.0%). Multiple linear regression showed that lesion type and five semiquantitative indices that reflected the severity of brain lesions were related to the communication assessment score. However, the efficient size f2 cannot be directly calculated because the R2 and residual variance in the multiple regression model were not reported in the study (Coleman et al., 2016). Geytenbeek et al. (2015) used multiple linear regression based on MRI measures to evaluate language comprehension in non-speaking children with severe CP and PWMLs; that study revealed that the R2 of the model was 0.36. Choi et al. (2017) also found significant negative relationships between the severity of PWMLs and expressive language and between the severity of PWMLs and receiving language performance. Although the above results indicate that the MRI measures could be used to adequately predict communication performance in children with CP, we still assumed a lower efficient size for the MRI measures (f2 as 0.10) to ensure a sufficient sample size for an accurate prediction of communication performance in children with CP. Based on previous studies (Geytenbeek et al., 2015; Coleman et al., 2016; Choi et al., 2017), the number of predictors was set as 6. If $\alpha = 0.05$, $1\text{-}\beta = 0.80$, then the study requires enrollment of 143 participants according to the power calculation by G*Power, version 3.1.9 (Faul et al., 2009). According to previous follow-up experience and given a maximum anticipated dropout rate of 20%, a total sample size of 178 children with BCP and PWMLs will be needed.

Study Procedures

The study procedures are shown in **Figure 1**. Following the inclusion and exclusion criteria, eligible participants (children with BCP and PWMLs) will be entered from corrected ages of 6 to 24 months. Participants will be assessed for diagnostic criteria, differential diagnosis and comorbidities by a pediatrician or child neurologist. The participants will undergo at least 1 advance brain MRI examination according to a standardized protocol. A variety of clinical data and data pertaining to socioeconomic status will be collected. Neurobehavioral development will be assessed by experienced physiotherapists blinded to the MRI findings and related medical information (such as other examination results relevant to the content of the current assessment) at each center.

At the age of 48–60 months, the participants will be invited back to the hospital for a follow-up assessment. Experienced speech and language therapists (SLTs) blinded to the medical history will assess each child's communication ability using multiple classification systems and scales. The primary outcome measure for this study is the communication function classification system (CFCS) rating. Secondary outcome measures include ratings from the Functional Communication Classification System (FCCS), Viking Speech Scale (VSS), Peabody Picture Vocabulary Test-Revised (PPTV-R), verb comprehension subtest of the Wechsler Preschool and Primary Scale of Intelligence (WPPSI-IV), and CSBS-DP Infant-Toddler Checklist. The questionnaire data (CSBS-DP) will be collected by trained researchers during a telephone survey for participants who are reluctant to return to the hospital for follow-up. Other measures, such as Gross Motor Function Classification (GMFCS), Manual Ability Classification System (MACS), WPPSI-IV, and advanced brain imaging, will also be used to evaluate the development of participants during the follow-up assessment.

Blinding

The neuroradiologists involved in lesion delineation and MRI analysis will be blinded to other clinical information and assessment findings. The child neurologists and physiotherapists conducting the neurobehavioral assessment at baseline will be blinded to the MRI findings. Follow-up assessments will be implemented once the children are old enough for preschool by SLTs blinded to the children's clinical history, baseline assessment and MRI findings.

Clinical Data Collection

Demographic Data

Basic demographic and clinical information will be collected from families and health records. The following general information will be collected: age at MRI examination, sex, body weight, height, medical history, comorbidities, epilepsy, family makeup, seizure history, and medication. In addition to the above information, prenatal factors have also been shown to be related to brain injury and affect language development outcomes. Thus, birth history variables, including delivery mode, gestational age, birth weight, head circumference, body length, and Apgar score, will also be documented.

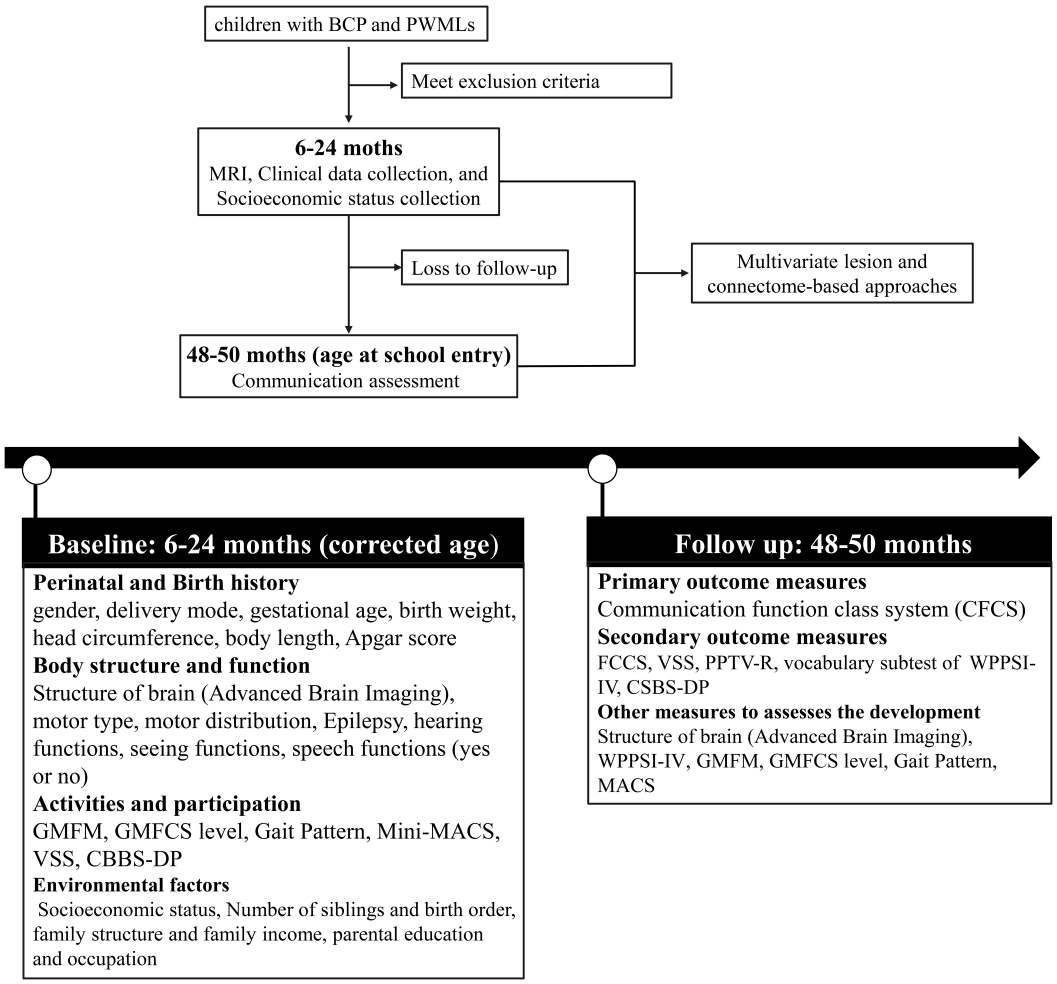

FIGURE 1 | Flow chart of the study protocol. BCP, Bilateral Cerebral Palsy; PWML, Periventricular White Matter Lesion; MRI, Magnetic Resonance Imaging; GMFM, Gross Motor Function Measure; GMFCS, Gross Motor Function Classification System; MACS, Manual Ability Classification System; VSS, Viking Speech Scale; CBBS-DP, Communication and Symbolic Behavior Scales Developmental Profile; FCCS, Function Communication Classification System; PPTV-R, Peabody Picture Vocabulary Test-Revised; WPPSI-IV, Wechsler Preschool and Primary Scale of Intelligence.

Furthermore, a systematic review (Vaillant et al., 2020) indicated that the factors in some domains of the International Classification of Functioning, Disability and Health – Children and Youth framework are relevant for language comprehension in children with CP. According to this concept, children's motor type, motor distribution, hand function (MACS), gross motor function (GMFCS), hearing function, visual function, speech function, socioeconomic status, parental educational level, parental occupation, and birth order will be recorded.

Primary Outcome Measures

The aim of the present study is to predict communication performance in children with CP at school entry. This will be assessed using the CFCS, which contains 5 levels (I-V), with level I being the best functional and level V being the least functional level. Children will be classified into one of the 5 levels based on their performance in sending and receiving information with familiar and unfamiliar communication partners. The CFCS is the most widely used system designed to classify communication function in children with CP in daily life. To increase the accuracy of the assessment, this study will establish a standardized assessment process according to a previous study (Wang and Wei, 2017). In this process, (I) SLTs will question parents regarding different aspects of the child's daily function and simultaneously observe children's movements during the initial contact (understanding and discovering the ways in which the child usually communicates), (II) the child's communication with the family will be observed and recorded, and (III) SLTs will further communicate with the child through play to allow the child to fully demonstrate his or her communication skills.

While the SLTs are conducting the on-site CFCS rating, a caregiver will be asked to read the CFCS-Chinese version and conduct a retrospective assessment of the child's communication performance in daily life. Then, the caregiver will be asked to determine his or her child's CFCS level by taking into account the communication performance status on site. If there are 2

caregivers in the field, the ratings will be made simultaneously without discussion, and the one who spends more time with the child will be marked as the first caregiver and the other one will be marked as the second caregiver. The SLT will explain the CFCS language but will not discuss the CFCS outcome with the parents. The final CFCS levels will be determined by professionals (SLTs) in close collaboration with parents. The CFCS has good reliability with high intraclass correlation coefficients across different language versions (Hidecker et al., 2011; Vander Zwart et al., 2016; Wang and Wei, 2017; Choi et al., 2018; Mutlu et al., 2018) and has been widely used in multiple CP registries (Coleman et al., 2015; Hustad et al., 2016; Mei et al., 2016; Vander Zwart et al., 2016; Wang and Wei, 2017; Mutlu et al., 2018) as a recommended, suitable tool for evaluating everyday communication in children with CP. The CFCS-Chinese version has also shown good reliability with intraclass correlation coefficients of 0.88 between an SLT and a caregiver and of 0.86 between the first and second caregivers for children with CP (Wang and Wei, 2017).

Secondary Outcome Measures

The secondary outcome measures include the levels/scores of the FCCS, VSS, PPTV-R, CSBS-DP, and the vocabulary subtest of WPPSI-IV for implementing a comprehensive communication assessment of children with CP. **Table 1** describes the classification systems of the CFCS, FCCS, and VSS.

(1) FCCS: The FCCS is a 5-level system, with the highest level (level V) indicating the worst performance. The FCCS classifies children's performance in sending communicative messages and considers their observable communication performance using speech, gestures, and/or augmentative and alternative communication. The reliability and validity of the FCCS for classifying the functional communication of children with CP aged 4 to 5 years have been previously tested (Barty et al., 2016).

(2) VSS: The VSS (Pennington et al., 2013) was developed to classify the speech production of children with CP. The VSS is a four-level rating scale used to classify speech intelligibility in children with CP aged 4 years and above when they are speaking to unfamiliar partners and strangers. It has substantial to almost perfect test-retest reliability ($\kappa > 0.68$) and moderate to substantial interrater reliability between pairings of professionals and/or parents ($\kappa = 0.58–0.81$) (Pennington et al., 2013).

(3) PPTV-R: The PPTV-R is often used to assess the receptive vocabulary abilities of people ranging in age from 2.5 to 40 years old, and the reliability and validity of the Chinese version have been previously tested (Sang and Miao, 1990). The test is composed of 175 items, and its test-retest reliability and split-half reliability are 0.94 and 0.99, respectively. One point is recorded each time a picture is correctly matched to the given word. The raw score is obtained by summing all the correct item scores.

(4) CSBS-DP: The CSBS-DP (Wetherby and Prizant, 2002) is a parent questionnaire containing 24 questions and investigates children's expressive and receptive language skills; verb/non-verbal communication skills; and symbolic skills, such as participation in pretend play and appropriate use of objects. The total raw scores are converted to a standardized score, with mean = 100 and standard deviation (SD) = 15 among typically developing children (Wetherby and Prizant, 2002). Scores below 80 imply developmental delay of communication and referral for further language and speech assessment. The test–retest reliability of the CSBS-DP for the composite and total scores ranged from 0.79 to 0.88 (Wetherby and Prizant, 2002), and the reliability and validity of the Chinese version were previously tested (Lin et al., 2015).

(5) WPPSI-IV: The Chinese version of the WPPSI (Zhang, 2009) is divided into two groups of tests: group 1 for children aged 2.5 years to 3 years and 11 months and group 2 for children aged 4 years and 0 months to 6 years and 11 months. The WPPSI-IV comprises 3 subtests (verbal comprehension, working memory and visuospatial ability) for group 1 but 5 subtests (verbal comprehension, working memory, visuospatial ability, fluid intelligence and processing speed) for group 2. The verbal comprehension test includes three subtests: similarity, comprehension, vocabulary, and a supplemental subtest—common sense. Verbal comprehension index scores have a mean = 100 and standard deviation = 15. If children with CP are unable to complete the verb comprehension subtest due to fine motor impairment, language impairment or reduced intellectual ability, a composite score will be calculated.

TABLE 1 | Descriptors for levels of the CFCS, FCCS, and VSS.

Level	CFCS	FCCS	VSS
I	Effective sender/receiver with familiar/unfamiliar partners	Effective communicator in most situations	No speech motor disorder indicated
II	Effective, but slower-paced sender and/or receiver with familiar and/or unfamiliar partners	Effective communicator in most situations but may need help	Speech motor disorder indicated but is usually understandable to unfamiliar listeners
III	Effective sender and receiver with familiar partners; not effective with unfamiliar partners	An effective communicator in some situations	Speech motor disorder indicated and is not typically understandable to unfamiliar listeners out of context
IV	Inconsistent sender and/or receiver with familiar partners; not effective with unfamiliar partners	Assistance required in most situations, especially with unfamiliar partners	No understandable speech
V	Seldom effective sender/receiver with familiar partners; not effective with unfamiliar partners	Communicates unintentionally using movements and behavior	–

CFCS, Communication Function Classification System; FCCS, Functional Communication Classification System; VSS, Viking Speech Scale.

Clinical Data Collection

Acquisition of MR Images

Brain MR images will be acquired using 3.0-T GE scanners with 8-channel head coils at baseline. All participants will be scanned during natural sleep, as their sleep times will be adjusted based on the experimental schedule, and earplugs will be used to reduce the scanning noise from the MRI chamber. In cases where the child cannot fall asleep to comply with the MRI examination, sedation will be administered after obtaining parental or guardian consent. The potential risks of sedation will be fully explained to the parents or guardians. Each subject's vital signs will be monitored closely, and head motion will be limited by the placement of foam padding around the child's head during the MRI examination. Three sequences will be acquired: 3-dimensional fast spoiled gradient-recalled echo (3D-FSPGR) T_1-weighted imaging (T_1WI), T_2-fluid attenuated inversion recovery (T_2-FLAIR) imaging and diffusion tensor imaging (DTI). Image acquisition parameters of 3D-FSPGR, T1WI, T2-FLAIR, and DTI will be held consistent across sites to reduce the variability of imaging data. The detail scan parameters of the MRI sequences are shown in **Table 2**.

Lesion Masks

Periventricular white matter lesions will be characterized as areas of T_2 hyperintensity with or without cystic degeneration. The lesion masks will be manually delineated on T_2-FLAIR images using ITK-snap software (Yushkevich et al., 2006) by two neuroradiologists. Intrarater and interrater reliability in lesion segmentation will be evaluated using the Dice κ consistency test (Guo et al., 2017). If there is an evident discrepancy, a third neuroradiologist will be invited to make the final decision. Then, the T_2-FLAIR image will be coregistered to the T_1 image, and these parameters will be used to reslice the lesion mask into the native T_1 space. The resliced lesion masks will be binarized using a 50% probability threshold. The alignment between the resliced lesion masks and the lesions in native T_2 space will be visually inspected by two experienced neuroradiologists by comparing the overlay of the resliced lesion mask to the patient's native T_1 image to the overlay of the original lesion mask on the patient's native T_2-FLAIR image. Cases of misalignment will be manually corrected directly in the normalized lesion mask using ITK-snap software.

TABLE 2 | Scan parameters of the MRI sequences.

Variable	T_2-FLAIR	3D-FSPGR T_1WI	DTI
Repetition time (ms)	7500	7.8	12500
Echo time (ms)	145	3.0	86.8
Number of diffusion gradient directions	NA	NA	64
b values (s/mm^2)	NA	NA	0,1000
Slice thickness (mm)	3	1.0	2.5
Gap (mm)	1.5	0	0
Field of view (mm^2)	240 × 240	256 × 256	240 × 240
Matrix size	256 × 256	256 × 256	256 × 256

T_2-FLAIR, T_2-fluid attenuated inversion recovery; 3D-FSPGR T_1WI, 3-dimensional fast spoiled gradient-recalled echo T_1 weighted imaging; DTI, diffusion tensor imaging; NA, not available.

Lesion (Voxel)-Based Analysis

Two complimentary approaches (lesion- and connectome-based) will be used to characterize brain damage. Both of them will use a brain atlas developed by Oishi et al. (2011) to divide the brain into 122 regions to reduce the feature dimensions. For lesion-based and connectome-based analysis, the brain atlas containing the parcelation information will be aligned to each individual's native T_1 images. First, the T_1 target image of patients will be created by using a groupwise template creation method (Li et al., 2016). Then the patients T_1 target image will be registered to the infant T_1WI template provided by Oishi et al. (2011) in the standard space. Subsequently, these deformation parameters will be inverted and applied on the brain atlas in the standard space to obtain the brain atlas in the local patient target space and individual's native T_1 space. The unified segmentation function of SPM12 (Ashburner and Friston, 2005) will be used to obtain the probabilistic gray and white matter maps from T_1 images. These probabilistic gray maps (in native T_1 space) will be further divided into regions of interest (ROIs) corresponding to the brain atlas. Then, lesion-based analysis will be computed as the proportion of lesioned voxels per ROI (each cortical and subcortical gray matter region corresponding to the brain atlas).

Connectome-Based Analysis

The structural brain connectome will be computed as the number of white matter streamlines that connect each pair of cortical and subcortical gray matter regions, and probabilistic tractography will be performed in individual's diffusion space to construct the connectome. Thus, the tissue maps (including the ROI-segmented gray matte map) will be registered into an individual's diffusion-weighted imaging (DWI) space. First, since tissue contrast is comparable between B0 and T_2 images, the registered T_2-FLAIR image (coregistered into the native T_1 image) will be linearly normalized into the mean B0 image from the diffusion MRI sequence using the FMRIB Software Library (FSL) Linear Image Registration Tool (Greve and Fischl, 2009) (correlation ratio cost function, affine registration with 12 parameters and nearest neighbor interpolation). The transformation matrices will then be used to register the probabilistic maps of white and gray matter, and segmented cortical ROIs in native T_1 space into DWI space.

Probabilistic tractography will be applied to evaluate the structural connectivity of pairwise cortical regions, which will be separately defined according to the brain atlas. Structural connectivity will be obtained by the probabilistic method of the FMRIB Diffusion Toolbox (FDT) (Behrens et al., 2007) for fiber tracking. FDT BEDPOST will be used to build the default distributions of diffusion parameters at each voxel. Probabilistic tractography will be obtained using FDT's probtrackx (Behrens et al., 2007) (parameters: 5,000 individual streamlines drawn through the probability distributions on principle fiber direction, step length of 0.5 mm, 200 maximum steps, curvature threshold set at 0.2, and distance correction) since probabilistic tractography is theoretically capable of

accommodating intravoxel fiber crossings. The probabilistic white matter map will be used as the waypoint mask (Yourganov et al., 2016; Gleichgerrcht et al., 2017). The cortical ROIs (corresponding to the brain atlas) in diffusion space will be used as seed regions for tractography. For each subject, the connectivity between cortical ROIs i and j will be calculated, defined as the number of streamlines arriving at j when i is seeded, averaged with the number of streamlines arriving at i when j is seeded. The calculation of the streamlines will be corrected based on the distance traveled ("distance correction" built into probtrackx). In addition, the number of streamlines between ROIs i and j will be divided by the sum of the volume of the two regions to eliminate the effects of the unequal sizes of the different cortical regions. These steps will be repeated iteratively to ensure that all cortical ROIs are used as seed regions. Once all iterations are completed, a connectivity matrix A will be constructed, where each entry Aij represents the connection weight between cortical ROIs i and j.

Harmonization

Multisite imaging studies are prone to technical variability across scans, including differences between the manufacturers, heterogeneity in the protocol and variations in the scanning parameters. Such unwanted variation can hinder the detection of important features and/or cause spurious findings. There is a need to remove the bias and non-biological variance caused by unwanted site effects. In this study, we will use ComBat (Fortin et al., 2017, 2018), a method that adjusts the mean value and variance between different groups by combining an empirical Bayes framework and the location/scale model, to harmonize the data. Studies have shown that the ComBat method performs well in preserving biological variability and removing the unwanted variation introduced by site for harmonizing the $3DT_1$ imaging (Fortin et al., 2018) and DTI (Fortin et al., 2017).

Models for Predicting Communication Impairment

Preselection of Predictive Features

Since the number of streamlines between two cortical regions is averaged, the connectivity matrix is symmetrical with respect to the diagonal, and only the lower triangular matrix will be used for further analyses. For both lesion-based and connectome-based analyses, the feature set will include hundreds to thousands of feature vectors, and such high-dimensional data can cause the "curse of dimensionality." To reduce the number of potential features introduced into the predictive model, a preselection procedure will be performed to exclude noisy or uninformative predictors from being fed into the prediction model, which can reduce the chance of model overfitting. First, for lesion-based analyses, only gray matter regions that are lesioned in more than 10% of the patients will be entered into the analysis. Second, for the links in the connectome matrix-based analyses, only those that are present in more than 75% of the patients will be entered into the analysis. After the above steps, each subject will have three feature sets: the lesion feature set, connectome feature set, and combination feature set.

Development and Validation of Prediction Models

According to previously reported literature, for children with CP, the distribution of their CFCS grades is unbalanced and skewed. None or mild communication impairment (CFCS level I, II, III) in children with CP and PWMLs is more common than in those with severe communication impairment (CFCS level IV, V) (Kristoffersson et al., 2020). Such an imbalance distribution will cause misprediction during the process of predictive model generation (Saethang et al., 2016). Thus, we defined individuals who communicate at CFCS level I (defined as "effective sender and receiver communication with unfamiliar and familiar partners") as having an absence of communication impairment. Patients with CFCS level I will be classified into the absence of communication impairment group, and those with CFCS levels II, III, IV, and V will be classified into the communication impairment group. In this way, the CFCS grade will be converted to a binary indicator, and our study will focus on identifying whether children with BCP have any communication impairment and improving the efficacy of the predictive model. All the variables will be centered and standardized before being entered into each model, which will be created with machine learning algorithms. In machine learning, the no-free-lunch theorem states that there is no one model (or, more generically, machine learning tool) that will work best for every problem (Wolpert and Macready, 1997). Therefore, several classification algorithms with varying hyperparameters will be evaluated using support vector machine, random forest, logistic regression, and other methods to investigate which algorithm will outperform competing approaches across all settings. The workflow of data processing and communication prediction is outlined in **Figure 2**. The detailed model building and validation steps are as follows.

Images from four sites (four hospitals) will be randomly partitioned into four equal portions. Approximately three-quarters of these images will be used as a "training cohort," and the remaining one-quarter of these images will be used as a "test cohort." In the "training cohort," the proportion of lesioned voxels in the ROI and the links of the connectome matrix that are not shown difference between absence of communication impairment group and communication impairment group will be excluded, where the significance level is defined as $P < 0.05$ without multiple comparison correction in the two-sample test. The selected features will be used to define models predicting presence or absence of communication impairment in children with BCP. For each prediction model, 10-fold cross-validation (CV) will be used to evaluate the performance. This means that the "training cohort" will be divided into a training (nine folds) and a validation dataset (one fold), leaving 9 of 10 participants in the training dataset and the remaining participants in the testing dataset. For the training cohort, the various hyperparameters within each algorithm will be used to determine the prediction model. Then, the model will be applied to the validation dataset to predict children with the presence or absence of communication impairment (predicted label). The same procedure will be repeated with each of the one-fold participants or the left-out participants in the leave-one-out procedure, serving as the validation dataset for 10

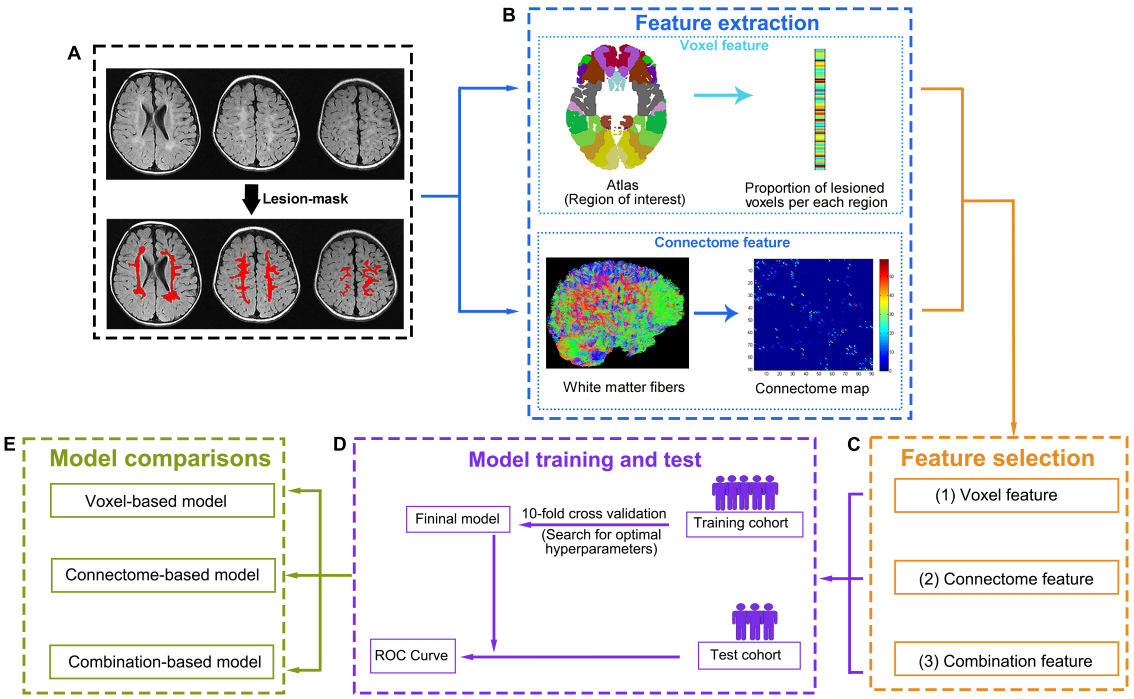

FIGURE 2 | Data processing and analysis workflow. **(A)** First, the lesion will be manually defined on T_2-FLAIR images. **(B)** Two complementary methods, one based on lesions and the other on the connectome, will be used to characterize brain damage. To compute lesion-based damage (top row), the brain atlas and each individual's lesion mask will be aligned with each individual's native T_1 space. The gray matter regions will be divided into regions of interest (ROIs) according to the atlas. Then, lesion-based damage will be computed as the proportion of lesioned voxels per ROI based on the lesion mask. Connectome-based damage (bottom row) will be computed as the number of diffusion tensor imaging (DTI) tracts that connect each pair of ROIs (tractography for reconstructing tracts will be performed guided by the white matter probabilistic map). **(C)** For each individual, three feature sets (lesion features, connectome features, and combination features) will be generated from the corresponding features after feature selection. **(D)** For each feature set, a "training cohort" will be used to build an optimal model based on a 10-fold cross-validation, and the prediction performance of the optimal model will be tested with the "test cohort" using ROC curve. **(E)** Then, three optimal models will be generated based on different feature sets (the lesion feature set for voxel model, the connectome feature set for connectome model, and the combination feature set for combination model). The prediction performance of each model will be compared, and the best-performing model will be selected.

iterations. Thus, each subject will receive a predicted label, and the accuracy of predictive model will be evaluate by comparing predicted labels to true labels of BCP children. The CV step will be repeated 100 times with random cohort designation to select the model with the best prediction accuracy. The whole "training cohort" will be reused in its entirety to retrain the model based on the classification algorithm and hyperparameters of the prior selected model. Then, the retrained model will be used to evaluate the "test cohort," and the communication performance of every subject of the "test cohort" will be predicted by the model. The final accuracy of the prediction model will be defined by comparing predicted labels to true labels of BCP children in the "test cohort," The Receiver Operating Characteristic (ROC) curve and the area under curve (AUC) will be calculated to evaluate the predictive ability of built models. A two-sided Hotelling-Williams test (Steiger, 1980) will be used to determine whether the multimodality prediction model is more accurate than any of the single-modality prediction models. P values < 0.05 will be considered indicative of statistically significant differences across models. Given the possible effects of age on imaging measures, the "test cohort" will be divided into three groups: younger (6–12 months), middle-aged (12–18 months), and elderly (18–24 months years), according to their age at MRI scan. The optimal model will be applied to all subgroups to exam whether the prediction accuracy changes with age at MRI scan.

Confidentiality and Data Management

The original data will be kept confidential throughout the study and preserved by The Affiliated Hospital of Zunyi Medical University, China. The electronic data will be gathered at each site and supervised by the two specially trained investigators. The data will be stored in a secure computer, and only research staff will have access to the data. Unless required by law, none of the above information will be divulged. Anonymized study data will be published for scientific purposes.

Trial Status

This trial is currently recruiting participants.

DISCUSSION

This study protocol reports the procedures for a prospective, multicenter, longitudinal cohort study that will establish an

individual-based model for the prediction of communication impairment in children with BCP and PWMLs at school entry.

This study will have some potential strengths. Previous studies (Geytenbeek et al., 2015; Coleman et al., 2016; Choi et al., 2017; Laporta-Hoyos et al., 2018) have demonstrated that the type and severity of brain injury shown on MRI scans is associated with communication impairment. However, all these studies were retrospective in design and were performed to identify risk factors for communication impairment, and an individualized prediction model for communication is still lacking. Moreover, wide ranges of communication performance in the specified type or degree of injuries suggest the limited value of predicting communication outcomes based on quantitative and semiqualitative parameters (Geytenbeek et al., 2015; Coleman et al., 2016; Laporta-Hoyos et al., 2018). In this study, a large representative sample of children with BCP will be recruited, and the data will be collected prospectively using standardized neuroimaging protocols and outcome measures. An individual-based prediction model for communication ability will be developed based on quantitative MRI parameters. This model can provide information that can contribute to the determination of the appropriate time for intervention and guide decision-making. In addition, only a few articles (Geytenbeek et al., 2015; Coleman et al., 2016; Choi et al., 2017) have reported brain-communication relationships in children with CP, and neuroimaging characteristics identified as risk factors in these studies are quantitative and/or semiqualitative parameters. Hence, the neuroanatomic basis for communication impairment remains unclear (Vaillant et al., 2020). We will use voxel-based analyses to examine which regions are typically associated with communication impairment. Connectome-based analyses, a novel approach for identifying key connections for neurological function, will also be used to provide unique insights into communication deficits. In this light, it can be foreseen that the abovementioned methods would greatly help in the understanding of the neural basis of communication impairment in these children.

With the growing number of multisite neuroimaging studies, there is a great challenge in handling non-biological variance due to site-level factors, such as differences in MRI scanners and/or acquisition protocols. Such unwanted sources of variability and bias may mask true associations of interest and/or generate spurious findings. In this multisite neuroimaging study, we will use ComBat (Fortin et al., 2017, 2018), a well-established methodology for controlling unwanted variation induced by scanner and/or acquisition protocol differences, to remove site effects. Moreover, due to difficulties in obtaining neuroimaging data in children with CP (accompanied by multiple complications), our hospital will develop an individualized examination procedure for these children and extend it to other participating sites to ensure the feasibility of the process. During this period, translation of specialist knowledge and dissemination of research results into clinical practice will begin immediately via site investigators. The university affiliations across this study will provide opportunities to integrate research fronts and introduce this collaborative effort into undergraduate education. Knowledge translation will also target parents and/or guardians of children with CP to improve their quality of life.

This study will have several limitations. Given the multidimensional nature of communication, attempting to reduce communication skills to a single linear scale will be fraught with the problems of overlooking impairment-related data and important, informative developments (Potter, 2016; Nordberg, 2018). Therefore, the CFCS may not be able to capture the full scope of information necessary to evaluate cross-sectional performance and track the longitudinal development of communication ability. However, quantitative communication tests in the Chinese version for children with CP are scarce. The CFCS has been translated into different languages (Hidecker et al., 2011; Vander Zwart et al., 2016; Wang and Wei, 2017; Choi et al., 2018; Mutlu et al., 2018) and has often been used in multiple CP registries (Coleman et al., 2015; Hustad et al., 2016; Mei et al., 2016; Vander Zwart et al., 2016; Wang and Wei, 2017; Mutlu et al., 2018) worldwide. It shows good reliability and validity across different cultures and languages (including the Chinese version) and is quick and user friendly, making it ideally suited for multicenter trials. Thus, we will still consider CFCS as the primary outcome measure, and a search for precise scales in the Chinese version that enable quantitative evaluation of communication ability for these children will be continued. Functional MRI has great potential for characterizing typical development and detecting abnormalities early; however, it will not be included in our present study because of the poor ability of infants to tolerate MRI scanning (furthermore, after conventional and diffusion sequences, the evaluation time would be too long to include MRI examination). Finally, it should be noted that our study population is limited to children with BCP and PWMLs to reduce the heterogeneity in constructing more accurate predictive models. Thus, the prediction models constructed by this protocol will likely not be generalizable to other CP subtypes or BCP with other neuroimaging findings.

ETHICS STATEMENT

The studies involving human participants were reviewed and approved by the Institutional Review Board of The Affiliated Hospital of Zunyi Medical University (KLL-2021-108). All participating centers approved this study protocol. Written informed consent form will be obtained from the legal parents/guardians of all participants.

AUTHOR CONTRIBUTIONS

JH, HL, and TZ designed and conceptualized the study and developed the first version of the manuscript. YY, TL, TH, and CH will provide assistance with the data acquisition protocol and methodology. JZ and FW helped to perform the statistical analyses and revised the manuscript for important intellectual content. HL carried out the design and critically revised the final version of the manuscript. All authors contributed to the article and approved the submitted version.

FUNDING

This work was supported by the National Natural Science Foundation of China (Grant No. 81901732), Science and Technology Supporting Program of Guizhou Province (Grant No. qiankehezhicheng [2020]4Y122), Young Outstanding Scientific and Technological Talent of Guizhou Province (Grant No. Qiankehepingtairencai [2021]5620), Chongqing Medical Scientific Research Project (Joint project of Chongqing Health Commission and Science and Technology Bureau, No 2020MSXM081), and Science and Technology Plan Project of Zunyi City (Grant No. zunshikeheHZzi [2019]109).

REFERENCES

Al Harrach, M., Pretzel, P., Groeschel, S., Rousseau, F., Dhollander, T., Hertz-Pannier, L., et al. (2021). A connectome-based approach to assess motor outcome after neonatal arterial ischemic stroke. *Ann. Clin. Transl. Neurol.* 8, 1024–1037. doi: 10.1002/acn3.51292

Ashburner, J., and Friston, K. J. (2005). Unified segmentation. *Neuroimage* 26, 839–851.

Barty, E., Caynes, K., and Johnston, L. M. (2016). Development and reliability of the functional communication classification system for children with cerebral palsy. *Dev. Med. Child Neurol.* 58, 1036–1041. doi: 10.1111/dmcn.13124

Behrens, T. E. J., Berg, H. J., Jbabdi, S., Rushworth, M. F. S., and Woolrich, M. W. (2007). Probabilistic diffusion tractography with multiple fibre orientations: what can we gain? *Neuroimage* 34, 144–155. doi: 10.1016/j.neuroimage.2006.09.018

Chan, A.-W., Tetzlaff, J. M., Altman, D. G., Laupacis, A., Gøtzsche, P. C., Krleža-Jerić, K., et al. (2013). SPIRIT 2013 statement: defining standard protocol items for clinical trials. *Annals Intern. Med.* 158, 200–207. doi: 10.7326/0003-4819-158-3-201302050-00583

Choi, J. Y., Choi, Y. S., and Park, E. S. (2017). Language development and brain magnetic resonance imaging characteristics in preschool children with cerebral palsy. *J. Speech Lang. Hear. Res.* 60, 1330–1338. doi: 10.1044/2016_JSLHR-L-16-0281

Choi, J. Y., Hwang, E. H., Rha, D., and Park, E. S. (2018). Reliability and validity of the Korean-language version of the communication function classification system in children with cerebral palsy. *Child Care Health Dev.* 44, 140–146. doi: 10.1111/cch.12507

Chorna, O., Hamm, E., Cummings, C., Fetters, A., and Maitre, N. L. (2017). Speech and language interventions for infants aged 0 to 2 years at high risk for cerebral palsy: a systematic review. *Dev. Med. Child Neurol.* 59, 355–360. doi: 10.1111/dmcn.13342

Coleman, A., Fiori, S., Weir, K. A., Ware, R. S., and Boyd, R. N. (2016). Relationship between brain lesion characteristics and communication in preschool children with cerebral palsy. *Res. Dev. Disabil.* 58, 55–64. doi: 10.1016/j.ridd.2016.08.015

Coleman, A., Weir, K., Ware, R. S., and Boyd, R. (2015). Predicting functional communication ability in children with cerebral palsy at school entry. *Dev. Med. Child Neurol.* 57, 279–285. doi: 10.1111/dmcn.12631

Colver, A., Fairhurst, C., and Pharoah, P. O. D. (2014). Cerebral palsy. *Lancet* 383, 1240–1249.

Ditchfield, M. (2017). Creating a neuroimaging classification system for children with cerebral palsy. *Dev. Med. Child Neurol.* 59:9. doi: 10.1111/dmcn.13188

Faul, F., Erdfelder, E., Buchner, A., and Lang, A.-G. (2009). Statistical power analyses using G*Power 3.1: tests for correlation and regression analyses. *Behav. Res. Methods* 41, 1149–1160. doi: 10.3758/BRM.41.4.1149

Fortin, J.-P., Cullen, N., Sheline, Y. I., Taylor, W. D., Aselcioglu, I., Cook, P. A., et al. (2018). Harmonization of cortical thickness measurements across scanners and sites. *Neuroimage* 167, 104–120. doi: 10.1016/j.neuroimage.2017.11.024

Fortin, J.-P., Parker, D., Tunç, B., Watanabe, T., Elliott, M. A., Ruparel, K., et al. (2017). Harmonization of multi-site diffusion tensor imaging data. *Neuroimage* 161, 149–170. doi: 10.1016/j.neuroimage.2017.08.047

Geytenbeek, J., Harlaar, L., Stam, M., Ket, H., Becher, J. G., Oostrom, K., et al. (2010). Utility of language comprehension tests for unintelligible or non-speaking children with cerebral palsy: a systematic review. *Dev. Med. Child Neurol.* 52:1098. doi: 10.1111/j.1469-8749.2010.03807.x

Geytenbeek, J. J., Oostrom, K. J., Harlaar, L., Becher, J. G., Knol, D. L., Barkhof, F., et al. (2015). Language comprehension in nonspeaking children with severe cerebral palsy: neuroanatomical substrate? *Eur. J. Paediatr. Neurol.* 19, 510–520. doi: 10.1016/j.ejpn.2015.06.001

Gleichgerrcht, E., Fridriksson, J., Rorden, C., and Bonilha, L. (2017). Connectome-based lesion-symptom mapping (CLSM): a novel approach to map neurological function. *Neuroimage Clin.* 16, 461–467. doi: 10.1016/j.nicl.2017.08.018

Goldstein, M. H., King, A. P., and West, M. J. (2003). Social interaction shapes babbling: testing parallels between birdsong and speech. *Proc. Natl. Acad. Sci. U S A* 100, 8030–8035. doi: 10.1073/pnas.1332441100

Graham, H. K., Rosenbaum, P., Paneth, N., Dan, B., Lin, J. P., Damiano, D. L., et al. (2016). Cerebral palsy. *Nat. Rev. Dis. Primers* 2:15082. doi: 10.1038/nrdp.2015.82

Greve, D. N., and Fischl, B. (2009). Accurate and robust brain image alignment using boundary-based registration. *Neuroimage* 48, 63–72. doi: 10.1016/j.neuroimage.2009.06.060

Guo, T., Duerden, E. G., Adams, E., Chau, V., Branson, H. M., Chakravarty, M. M., et al. (2017). Quantitative assessment of white matter injury in preterm neonates: association with outcomes. *Neurology* 88, 614–622. doi: 10.1212/WNL.0000000000003606

Hidecker, M. J. C., Paneth, N., Rosenbaum, P. L., Kent, R. D., Lillie, J., Eulenberg, J. B., et al. (2011). Developing and validating the Communication Function Classification System for individuals with cerebral palsy. *Dev. Med. Child Neurol.* 53, 704–710. doi: 10.1111/j.1469-8749.2011.03996.x

High, P. C. (2008). School readiness. *Pediatrics* 121, e1008–e1015. doi: 10.1542/peds.2008-0079

Himmelmann, K., Horber, V., De La Cruz, J., Horridge, K., Mejaski-Bosnjak, V., Hollody, K., et al. (2017). MRI classification system (MRICS) for children with cerebral palsy: development, reliability, and recommendations. *Dev. Med. Child Neurol.* 59, 57–64. doi: 10.1111/dmcn.13166

Himmelmann, K., and Uvebrant, P. (2011). Function and neuroimaging in cerebral palsy: a population-based study. *Dev. Med. Child Neurol.* 53, 516–521. doi: 10.1111/j.1469-8749.2011.03932.x

Hustad, K. C., Oakes, A., McFadd, E., and Allison, K. M. (2016). Alignment of classification paradigms for communication abilities in children with cerebral palsy. *Dev. Med. Child Neurol.* 58, 597–604. doi: 10.1111/dmcn.12944

Hustad, K. C., Sakash, A., Broman, A. T., and Rathouz, P. J. (2018). Longitudinal growth of receptive language in children with cerebral palsy between 18 months and 54 months of age. *Dev. Med. Child Neurol.* 60, 1156–1164. doi: 10.1111/dmcn.13904

Kristoffersson, E., Dahlgren Sandberg, A., and Holck, P. (2020). Communication ability and communication methods in children with cerebral palsy. *Dev. Med. Child Neurol.* 62, 933–938. doi: 10.1111/dmcn.14546

Laporta-Hoyos, O., Fiori, S., Pannek, K., Ballester-Plane, J., Leiva, D., Reid, L. B., et al. (2018). Brain lesion scores obtained using a simple semi-quantitative scale from MR imaging are associated with motor function, communication and cognition in dyskinetic cerebral palsy. *Neuroimage Clin.* 19, 892–900. doi: 10.1016/j.nicl.2018.06.015

Li, X., Gao, J., Wang, M., Wan, M., and Yang, J. (2016). Rapid and reliable tract-based spatial statistics pipeline for diffusion tensor imaging in the neonatal brain: Applications to the white matter development and lesions. *Magn. Reson. Imaging* 34, 1314–1321. doi: 10.1016/j.mri.2016.07.011

Lin, C.-S., Chang, S.-H., Cheng, S.-F., Chao, P.-C., and Chiu, C.-H. (2015). The preliminary analysis of the reliability and validity of the Chinese Edition of the CSBS DP. *Res. Dev. Disabil.* 38, 309–318. doi: 10.1016/j.ridd.2014.12.023

Lipscombe, B., Boyd, R. N., Coleman, A., Fahey, M., Rawicki, B., and Whittingham, K. (2016). Does early communication mediate the relationship between motor ability and social function in children with cerebral palsy? *Res. Dev. Disabil.* 5, 279–286. doi: 10.1016/j.ridd.2016.02.013

McMahon, E., Wintermark, P., and Lahav, A. (2012). Auditory brain development in premature infants: the importance of early experience. *Annals N Y Acad. Sci.* 1252, 17–24. doi: 10.1111/j.1749-6632.2012.06445.x

Mei, C., Reilly, S., Reddihough, D., Mensah, F., Pennington, L., and Morgan, A. (2016). Language outcomes of children with cerebral palsy aged 5 years and 6 years: a population-based study. *Dev. Med. Child Neurol.* 58, 605–611. doi: 10.1111/dmcn.12957

Mutlu, A., Kara, O. K., Livanelioglu, A., Karahan, S., Alkan, H., Yardimci, B. N., et al. (2018). Agreement between parents and clinicians on the communication function levels and relationship of classification systems of children with cerebral palsy. *Disabil. Health J.* 11, 281–286. doi: 10.1016/j.dhjo.2017.11.001

Nordberg, A. (2018). Early receptive language comprehension ability in children with cerebral palsy. *Dev. Med. Child Neurol.* 60:1073. doi: 10.1111/dmcn.13901

Novak, I., Morgan, C., Adde, L., Blackman, J., Boyd, R. N., Brunstrom-Hernandez, J., et al. (2017). Early, accurate diagnosis and early intervention in cerebral palsy: advances in diagnosis and treatment. *JAMA Pediatrics* 171, 897–907. doi: 10.1001/jamapediatrics.2017.1689

Oishi, K., Mori, S., Donohue, P. K., Ernst, T., Anderson, L., Buchthal, S., et al. (2011). Multi-contrast human neonatal brain atlas: application to normal neonate development analysis. *Neuroimage* 56, 8–20. doi: 10.1016/j.neuroimage.2011.01.051

Patel, D. R., Neelakantan, M., Pandher, K., and Merrick, J. (2020). Cerebral palsy in children: a clinical overview. *Transl. Pediatr.* 9, S125–S135. doi: 10.21037/tp.2020.01.01

Pennington, L., Dave, M., Rudd, J., Hidecker, M. J. C., Caynes, K., and Pearce, M. S. (2020). Communication disorders in young children with cerebral palsy. *Dev. Med. Child Neurol.* 62, 1161–1169. doi: 10.1111/dmcn.14635

Pennington, L., Stamp, E., Smith, J., Kelly, H., Parker, N., Stockwell, K., et al. (2019). Internet delivery of intensive speech and language therapy for children with cerebral palsy: a pilot randomised controlled trial. *BMJ Open* 9:e024233. doi: 10.1136/bmjopen-2018-024233

Pennington, L., Virella, D., Mjoen, T., da Graca Andrada, M., Murray, J., Colver, A., et al. (2013). Development of The Viking Speech Scale to classify the speech of children with cerebral palsy. *Res. Dev. Disabil.* 34, 3202–3210. doi: 10.1016/j.ridd.2013.06.035

Potter, N. L. (2016). Not there yet: the classification of communication in cerebral palsy. *Dev. Med. Child Neurol.* 58, 224–225. doi: 10.1111/dmcn.12879

Saethang, T., Payne, D. M., Avihingsanon, Y., and Pisitkun, T. (2016). A machine learning strategy for predicting localization of post-translational modification sites in protein-protein interacting regions. *BMC Bioinfor.* 17:307. doi: 10.1186/s12859-016-1165-8

Sang, B., and Miao, X. (1990). The revision of trial norm of peabody picture vocabulary test revised (PPVT- R). *Psychol. Sci.* 5, 20–25. doi: 10.16719/j.cnki.1671-6981.1990.05.004

Steiger, J. H. (1980). Tests for comparing elements of a correlation matrix. *Psychol. Bull.* 87, 245–251. doi: 10.1037/0033-2909.87.2.245

Tan, S. S., van Gorp, M., Voorman, J. M., Geytenbeek, J. J., Reinders-Messelink, H. A., Ketelaar, M., et al. (2020). Development curves of communication and social interaction in individuals with cerebral palsy. *Dev. Med. Child Neurol.* 62, 132–139. doi: 10.1111/dmcn.14351

Vaillant, E., Geytenbeek, J. J. M., Jansma, E. P., Oostrom, K. J., Vermeulen, R. J., and Buizer, A. I. (2020). Factors associated with spoken language comprehension in children with cerebral palsy: a systematic review. *Dev. Med. Child Neurol.* 62, 1363–1373. doi: 10.1111/dmcn.14651

Vander Zwart, K. E., Geytenbeek, J. J., de Kleijn, M., Oostrom, K. J., Gorter, J. W., Hidecker, M. J. C., et al. (2016). Reliability of the Dutch-language version of the Communication Function Classification System and its association with language comprehension and method of communication. *Dev. Med. Child Neurol.* 58, 180–188. doi: 10.1111/dmcn.12839

Wang, Y. N., and Wei, S. (2017). Reliability and validity of Chinese Communication Function Classification System (Fudan). *Chinese J. Evid. Based Pediatrics* 12, 321–327. doi: 10.3233/VES-190675

Wetherby, A. M., and Prizant, B. M. (2002). "Communication and symbolic behaviour scales developmental profile," in *American Psychological Association*, ed. H. Paul (Baltimore: Brookes Publishing Co).

Wolpert, D. H., and Macready, W. G. (1997). No Free Lunch Theorems for Optimization. *IEEE Trans. Evol. Comp.* 1, 67–82. doi: 10.1109/4235.585893

Yourganov, G., Fridriksson, J., Rorden, C., Gleichgerrcht, E., and Bonilha, L. (2016). Multivariate Connectome-Based Symptom Mapping in Post-Stroke Patients: Networks Supporting Language and Speech. *J. Neurosci.* 36, 6668–6679. doi: 10.1523/JNEUROSCI.4396-15.2016

Yushkevich, P. A., Piven, J., Hazlett, H. C., Smith, R. G., Ho, S., Gee, J. C., et al. (2006). User-guided 3D active contour segmentation of anatomical structures: significantly improved efficiency and reliability. *Neuroimage* 31, 1116–1128. doi: 10.1016/j.neuroimage.2006.01.015

Zhang, H. (2009). The Revision of WISC-IV Chinese Version. *Psychol. Sci.* 32, 1177–1179. doi: 10.16719/j.cnki.1671-6981.2009.05.026

Conflict of Interest: The authors declare that the research was conducted in the absence of any commercial or financial relationships that could be construed as a potential conflict of interest.

Publisher's Note: All claims expressed in this article are solely those of the authors and do not necessarily represent those of their affiliated organizations, or those of the publisher, the editors and the reviewers. Any product that may be evaluated in this article, or claim that may be made by its manufacturer, is not guaranteed or endorsed by the publisher.

Advantages of publishing in Frontiers

OPEN ACCESS
Articles are free to read for greatest visibility and readership

FAST PUBLICATION
Around 90 days from submission to decision

HIGH QUALITY PEER-REVIEW
Rigorous, collaborative, and constructive peer-review

TRANSPARENT PEER-REVIEW
Editors and reviewers acknowledged by name on published articles

Frontiers
Avenue du Tribunal-Fédéral 34
1005 Lausanne | Switzerland

Visit us: www.frontiersin.org
Contact us: frontiersin.org/about/contact

REPRODUCIBILITY OF RESEARCH
Support open data and methods to enhance research reproducibility

DIGITAL PUBLISHING
Articles designed for optimal readership across devices

FOLLOW US
@frontiersin

IMPACT METRICS
Advanced article metrics track visibility across digital media

EXTENSIVE PROMOTION
Marketing and promotion of impactful research

LOOP RESEARCH NETWORK
Our network increases your article's readership